Fluid and gas emissions in a submarine eruption context offshore Mayotte Island : geochemical impact on the water column

Manon Mastin

COLLEGE SCIENCES DOCTORAL DE LA MER BRETAGNE ET DU LITTORAL

Université de Bretagne Occidentale

geo-ocean
CNRS | Ifremer | UBO | UBS

THESE DE DOCTORAT DE

Ifremer

TotalEnergies

L'UNIVERSITE DE BRETAGNE OCCIDENTALE

ECOLE DOCTORALE N° 598
Sciences de la Mer et du Littoral
Spécialité : *Géosciences Marines*

Par

Manon MASTIN

Fluid and gas emissions in a submarine eruption context offshore Mayotte Island: Geochemical impact on the water column

Thèse présentée et soutenue à l'Institut Universitaire Européen de la Mer, le 12 octobre 2023
Unité de recherche : Geo-Ocean UMR6538, Ifremer, CNRS, UBO, UBS, F-29280 Plouzané, France

Rapporteurs avant soutenance :

	Magali ADER	Professeure des universités, IPGP, France
	Joseph RESING	Senior research scientist, NOAA/University of Washington, Etats-Unis

Composition du Jury :

Président :	Géraldine SARTHOU	Directrice de recherche CNRS, IUEM, France
Examinateurs :	Magali ADER	Professeure des universités, IPGP, France
	Joseph RESING	Senior research scientist, NOAA/University of Washington, Etats-Unis
	Valérie CHAVAGNAC	Directrice de recherche CNRS, GET, France
	Andrea RIZZO	Professeur associé, Université de Milan, Italie
Dir. de thèse :	Olivier ROUXEL	Cadre de recherche, Ifremer, France
Co-dir. de thèse :	Emmanuel RINNERT	Chercheur, Ifremer, France
	Cécile CATHALOT	Chercheure, Ifremer, France

Invité(s)

Sébastien DEHEZ	Ingénieur de recherche, TotalEnergies, France
Stéphane JOUENNE	Ingénieur de recherche, TotalEnergies, France
Eric GAUCHER	Chercheur, Lavoisier H_2, France

Acknowledgements | Remerciements

Acknowledgements | Remerciements

Dans un premier temps, je tiens à remercier mes encadrants, Olivier Rouxel, Emmanuel Rinnert et Cécile Cathalot, pour m'avoir offert l'opportunité de réaliser cette thèse et pour m'avoir accordé leur confiance. Vos conseils et votre expertise ont été d'une importance cruciale pour l'aboutissement de ce travail de recherche. Je vous remercie mille fois de m'avoir donné la possibilité de participer à trois campagnes océanographiques, qui ont été une magnifique découverte, tant sur l'aspect scientifique qu'humain.

Ce travail a été possible grâce au financement de TotalEnergies, dans le cadre du projet MAYFLUID. Ainsi, je remercie Eric Gaucher pour avoir permis que cette thèse est lieu, et pour la formation qu'il m'a dispensée sur l'utilisation du logiciel PHREEQC. Je remercie également Sébastien Dehez et Stéphane Jouenne pour m'avoir suivi tout au long du projet. Merci à tous les trois pour l'intérêt porté au sujet, et pour avoir toujours été si enthousiaste au sujet des résultats. Merci également pour les suggestions et conseils apportés au cours de la thèse.

Je souhaite ensuite remercier sincèrement Magali Ader et Joseph Resing pour avoir accepté d'être les rapporteurs de mon manuscrit de thèse, mais également Géraldine Sarthou, Valérie Chavagnac et Andrea Rizzo de prendre place dans mon jury final.

I would like to sincerely thank Magali Ader and Joseph Resing for agreeing to review my thesis manuscript, and Géraldine Sarthou, Valérie Chavagnac and Andrea Rizzo for agreeing to be part of my final jury.

Je tiens également à remercier l'ensemble des membres de mon comité de thèse, Andrea Di Muro, Thomas Giunta et Joël Knoery, d'avoir donné de leur temps pour m'accompagner dans cette thèse. Vos remarques et suggestions m'ont permis de me projeter dans mes recherches et d'améliorer la qualité de mon travail.

Au cours de ma thèse, de nombreuses personnes m'ont accompagnées et aidées dans le prélèvement et l'analyse de mes échantillons. Je tiens en particulier à remercier Jean-Pierre Donval, qui m'a convertie à l'analyse des gaz et m'a transmis son savoir et sa passion. Je remercie aussi Yoan Germain pour m'avoir initiée à la spectrométrie de masse mais aussi pour toutes les analyses d'échantillons et pour sa disponibilité pour préparer ou analyser des échantillons en urgence. I would like to thank Jürgen Sültenfuß for welcoming me in his laboratory, for teaching me the fundamentals of helium analysis and for involving me in the analysis of my samples.

Je tiens à remercier tous les membres de l'unité Géosciences Marines de l'Ifremer qui ont interagi avec le projet, mais aussi toutes les personnes avec qui j'ai eu des échanges, scientifiques ou non.

Les campagnes océanographiques ont pris une part importante dans mes années de thèse, ainsi je souhaite remercier toutes les personnes avec qui j'ai pu réaliser les échantillonnages, les analyses, et tous ceux qui ont participer à l'acquisition de données pour ce projet, je pense à Johanne Aube, Audrey Boissier, Claire Charles, Romain Davy, Olivia Fandino, Nicolas Gayet, Jérémie Gouriou, Vivien Guyader, Carla Scalabrin, Julien Vialat, et bien d'autres… Je ne pourrais citer tout le monde mais je suis reconnaissante de chacune de ces rencontres. Ainsi, je remercie aussi l'ensemble des personnes présentes à bord – équipes scientifiques et équipages du bord – qui ont permis que ces campagnes se déroulent dans la convivialité, merci pour tous les échanges et la bonne humeur.

Je tiens également à remercier tous les stagiaires, doctorants, post-docs, tous ceux qui sont passé par nos bureaux et qui ont croisé ma route. Je pense notamment à Matthieu, Quentin, Alissia, Danaé, Gwenn, Agathe, Clément, Simon, Manon, Constant, Ikenna, Dhishna, Manyano… et tant d'autres. Merci pour la bonne humeur générale, et une pensée au bon vieux temps où on pouvait encore faire des parties de fléchettes. Je remercie particulièrement Maud et Sophie, pour toujours avoir été présentes et pour avoir su me remonter le moral quand cela était nécessaire. Même si cette dernière année nous a un peu éloigné, vous restez pour moi deux très belles rencontres.

Je souhaite remercier tous mes amis, pour tous les moments passés ces trois dernières années, et qui m'ont permis de mettre la thèse de côté. Merci à toi Coco, pour m'avoir incité à faire des pauses de temps à autres, et pour notre routine d'apéros qu'on a un peu laissé tomber ces derniers temps. Merci Aude pour ta bienveillance et ton soutien, je suis ravie de t'avoir rencontré sur notre première campagne en mer.

Je remercie toute la team *A fond la fonte*, pour tous ces moments de sueur, mais surtout pour tous les moments géniaux passés avec vous. Merci à vous de rigoler à toutes mes blagues nulles, et promis, je continuerai à vous en faire même à l'autre bout du globe. Soyez soulager, vous allez enfin pouvoir manger en moins de trente minutes.

Un grand merci à la *Fine Equipe* pour tous nos repas de seigneurs et pour nos escapades. Vous avez su me remonter le moral, me motiver, me faire changer d'air dès qu'il le fallait.

Je remercie tout particulièrement Boubou la Truffe et Pataf. Vous avez été d'un soutien inestimable, toujours là pour moi, avec votre bonne humeur débordante. Nos fous rires et nos bêtises resteront toujours gravés dans ma mémoire, mais ce n'est que le début.

Je tiens sincèrement à remercier Mathieu pour m'avoir encouragée sur la dernière ligne droite de ma thèse. Merci pour toutes tes relectures, pour ton aide, pour ton immense soutien et pour ta patience. Je t'en serai toujours reconnaissante.

J'en profite aussi pour remercier ma famille. Merci d'avoir toujours cru en moi, d'avoir été un tel soutien tout au long de la thèse et de m'avoir permis d'aller jusqu'au bout. Je remercie ma sœur, Marine, pour son immense soutien dans les derniers jours de rédaction.

Merci à tous.

Table of Contents | Sommaire

Table of Contents | Sommaire

List of Figures | Liste des Figures

CHAPTER 1.

CHAPITRE 1.

CHAPTER 2.

CHAPTER 3.

CHAPTER 4.

CHAPTER 5.

CHAPTER 6.

CHAPTER 7.

List of Tables | Liste des Tableaux

CHAPTER 1.

CHAPITRE 1.

CHAPTER 2.

CHAPTER 4.

CHAPTER 6.

CHAPTER 7.

CHAPTER 1. Introduction (English)

Abstract

Submarine volcanism accounts for 85% of the volcanic activity present on Earth and involves substantial and immediate transfers of heat, chemical elements, and microbes from the mantle to the ocean. It plays a role in the regional fertilization of oceans and creates habitats for microbial communities. It is also the primary mechanism for releasing deep-seated carbon to the surface, potentially exerting a significant impact on climate over geological timescales.

Thus, underwater eruptions significantly alter the bathymetry of the seafloor, the chemical composition, and the physical structure of seawater, disrupting the local ecosystem. However, the physical and chemical processes controlling these transfers remain poorly understood.

This chapter provides an overview of current knowledge about submarine volcanism, the mechanisms of fluid generation at the seafloor and in the water column, and the geochemistry of these fluid emissions. Additionally, this chapter outlines the scientific objectives of the thesis that fit into this context.

1.1. General background

This PhD thesis is grounded in the current context of climate change wherein the concentration of carbon dioxide (CO_2) in the atmosphere has dramatically increased since the pre-industrial era (Masson-Delmotte et al., 2021). The continued growth of atmospheric CO_2 concentrations over the industrial era is unequivocally due to emissions from human activities, particularly the burning of fossil fuels (Masson-Delmotte et al., 2021). Yet, natural sources are also involved in CO_2 emissions including organic matter decomposition and respiration by microorganisms but also volcanism. Since 1750, atmospheric concentrations of CO_2 and methane (CH_4) have risen by 47% and 156%, respectively, far exceeding the natural multi-millennial variations between glacial and interglacial periods over at least the past 800,000 years. (Masson-Delmotte et al., 2021). These concentrations are predicted to further increase over the next decades (IPCC, Intergovernmental Panel on Climate Change). CO_2 and CH_4 are greenhouse gases, absorbing thermal radiation emitted by the land and ocean and radiating it back to Earth, ultimately fostering global warming and triggering long-lasting changes in the climate system. Such increase in the global carbon budget (i.e. increase of CO_2 and CH_4), by modifying the climate system, have profound effects on the biodiversity, the functioning of ecosystems and ultimately the services provided by these ecosystems to human societies (e.g. pollination, water access, CO_2 storage, water purification, etc.) (Pörtner et al., 2022). For example, field manipulations of seawater CO_2 have shown that ocean acidification causes carbonate saturation state to fall below levels suitable for coral reef calcification (Albright et al., 2018). Similarly, laboratory studies showed that ocean acidification can reduce the nutritional value of seafood by lowering the caloric content and levels of protein, lipid and carbohydrate (Lemasson et al., 2019). Thus, increased CO_2 concentrations and related acidification have the potential to put at risk many of the valuable ecosystem services that ocean provides to society, such as fisheries, aquaculture, and shoreline protection (Hall-Spencer and Harvey, 2019; Doney et al., 2020).

During the past decade (2010-2019), CO_2 emissions related to human activities (10.9 ± 0.9 PgC/yr) accumulated in three Earth system components: 46% accumulated in the atmosphere (5.1 ± 0.02 PgC yr–1), 23% taken up by oceans (2.5 ± 0.6 PgC/yr) and 31% stored by vegetation in terrestrial ecosystems (3.4 ± 0.9 PgC/yr) (Masson-Delmotte et al., 2021). Therefore, ocean is a particularly important component in the climate system due to their role regarding the absorption and long-term deep storage of CO_2 that can henceforth limit the impact of greenhouse gases on climate change (Houghton, 2014). Although the ocean can act as a carbon sink, with increasing atmospheric concentrations of CO_2, the fraction of emissions taken up by the ocean is expected to decline (Masson-

Delmotte et al., 2021), and further it might act as a carbon source depending on the concentration balance between the atmosphere and the ocean.

The oceanic biological carbon pump regulates the Earth carbon cycle by transporting the organic matter – created by phytoplankton productivity in photic zone – to the dark ocean interior, where it is consumed by heterotrophic animals and microbes that is then remineralized into inorganic forms (Honjo et al., 2014; Le Moigne, 2019). The biological carbon pump is composed of (i) organic carbon particles sinking out the surface ocean, into neutrally buoyant organic carbon (dissolved or particulate) entrained by downward water masses movements and/or mixing, and (ii) active transport of organic carbon allowing by the migration of animals such as zooplankton and fishes (Honjo et al., 2014; Le Moigne, 2019). This downward transport of organic matter constitutes the main mechanism where the carbon from the atmosphere is stored in the deep ocean on sub-millennium time scales (Honjo et al., 2014; Le Moigne, 2019; Siegel et al., 2023).

While ocean absorption of atmospheric CO_2 is increasing, oceans are also fed by another important source of CO_2. Submarine volcanism accounts for about 85% of volcanic activity on Earth (White et al., 2015b), and involves the immediate and massive transfer of heat, chemical elements and micro-organisms from the mantle to the ocean. More generally, volcanism is the main mechanism responsible for deep CO_2 release (and other greenhouse gases such as CH_4) within the ocean (Baker et al., 2012; Rubin et al., 2012).

Subaerial volcanism represents ~53–88 $TgCO_2$/year (Fischer and Aiuppa, 2020), which would correspond to about 40 to 60 million cars covering 10,000 km. The eruptive mechanism of subaerial volcanism, its geochemical manifestations and its impacts on the atmosphere are well described with a large panel of monitoring methods (e.g. satellites, land-based seismic networks, atmospheric sensors, etc.). In the geological record, massive volcanic eruptions have been often linked to large extinction events marking the transition between various geological periods. For example, the Deccan Traps, in India, which is the youngest mafic large igneous provinces, is associated with the mass extinction of the dinosaurs and many other groups, and defines the transition between the Cretaceous and the Paleogene (Courtillot et al., 1988; Bond et al., 2014), albeit the relative timing of volcanogenic outgassing, impact, and extinction remains highly debated (Hull et al., 2020). More recently, studies have shown that volcanic eruptions can have large effects on the climate. For example, the eruption of the Pinatubo volcano (Philippines) in 1991 caused global cooling due to sulfur dioxide (SO_2) emissions (Self et al., 1993). Similarly, the eruption of Tambora (Indonesia) in April 1815 had considerable effects on the global climate, triggering a "year without summer" in 1816 over Europe

and North America (Oppenheimer, 2003; Raible et al., 2016). Contrary to aerial volcanism, submarine volcanism is much more difficult to detect, observe and study. Compared to the number of presumed submarine volcanoes, too few have been observed and studied (Rubin et al., 2012). Thus, submarine volcanism impact on ocean and on the atmosphere is not well apprehended.

At mid-ocean ridges, submarine eruptions of magma are a fundamental process in the formation of oceanic crust (Rubin et al., 2012; White et al., 2015b), making submarine volcanism the main mechanism for releasing deep-sea carbon to the surface. In particular, it is considered that the net carbon flux into the basaltic oceanic crust (stored as reduced and inorganic carbon, e.g. carbonate, resulting from basalt-seawater interaction processes) is rivaling with the outgassing CO_2 flux (Martinez et al., 2021). However, the large diversity of geological contexts (e.g. fast vs slow spreading ridges, back-arc vs. mid-ocean settings), types of eruption, products of eruptions, etc., makes the knowledge of carbon budget still limited.

In addition, volcanic activity generates very significant fluxes of gases (e.g. H_2, CO_2, CH_4), particles and fluids rich in chemical elements (e.g. iron, manganese, sulfur species) from the crust into the water column (Resing et al., 2007; Fischer, 2008; Resing et al., 2009; Baumberger et al., 2014; Buck et al., 2018), thereby influencing the regional fertilization of the oceans (Langmann et al., 2010a; Wilson et al., 2019) ultimately providing support for microbial communities (Tagliabue et al., 2010; Edwards et al., 2011; Achterberg et al., 2013; Spietz et al., 2018; Longman et al., 2022). Submarine eruptions also affect the bathymetry of the seabed, the chemical composition and physical structure of seawater, and the local functioning of ecosystems. However, the physical and chemical processes controlling these transfers remain poorly understood.

CO_2 release through submarine eruption can alter the ocean acidity and have potential consequences on biogeochemical cycles. Ocean acidification, as defined by the Intergovernmental Panel on Climate Change (IPCC) (Masson-Delmotte et al., 2021), is a reduction in the ocean pH over an extended period of time, typically decades or longer, that is caused primarily by the uptake of CO_2 from the atmosphere, but that can also be caused by other chemical additions or subtractions from the ocean (i.e. by an increased volcanic activity). Ocean acidification is currently increasing as a result of an increased uptake up CO_2 from human-caused emissions. This increasing acidification is associated with reductions in the saturation state of calcium carbonate, which is a main constituent of the skeletons or shells of a variety of marine organisms. Once dissolved in the seawater, CO_2 reacts with water to form carbonic acid (H_2CO_3), which in turn dissociates into hydrogenocarbonate ions (HCO_3^-) and then carbonate ions (CO_3^{2-}), leading to an increase in hydrogen ions (H^+) (Emerson and Hedges,

2008). These trends towards ocean acidification are clear at the global scale, with an estimated rate of pH decrease in the surface layer of the ocean comprised between 0.016 and 0.020 per decade in subtropical areas and between 0.002 and 0.026 per decade in subpolar and polar areas since the 1980s. Ocean acidification has also been evidenced deeper in the ocean, exceeding 2000 m depth in the North Atlantic and Southern Ocean (Masson-Delmotte et al., 2021). Submarine volcanism can also alter the carbon cycle by increasing the carbon budget of the ocean. More specifically, if the carbon budget of the ocean becomes larger than the one of the atmosphere, oceans will no longer act as a carbon sink but as a carbon source, with potential dramatic effects on the climate. It is therefore of paramount importance to better understand the impact of submarine volcanism on the already acidifying trend of the ocean caused by increased CO_2 emissions.

To date, less than a dozen of active submarine volcanoes have been monitored. Although they are few in numbers, they show a variety of manifestations within the water column, depending on the geotectonic context. For instance, submarine volcanism can take place in an intraplate context (e.g. Loihi Seamount, Hawaii, lastly erupted in 1996) (Karl et al., 1988; Garcia et al., 2006; Schipper et al., 2010), at mid-ocean ridges (e.g. West Mata, Lau Basin, erupted in 2008, 2009, 2012) (Resing et al., 2011; Baumberger et al., 2014; Embley et al., 2014; Dziak et al., 2015; Chadwick et al., 2019), or in a subduction context (e.g. Northwest Rota-1 volcano, Mariana arc, erupted in 2003-2010) (Resing et al., 2007; Resing et al., 2009; Butterfield et al., 2011). Overall, these different eruptive systems have in common to be characterized by the emission of fluids very rich in volatile elements (He, H_2, CH_4, CO_2, Mn^{2+}, Fe^{2+}), although the relative proportion of these elements strongly vary among systems. Currently, how and to which extent these volatile elements affect the ocean geochemistry is poorly known. Therefore, the main question this thesis focuses on is: how does submarine volcanism contribute in terms of gas release into the ocean and how does it affect the geochemistry of the water column? More specifically, this thesis-overarching objective is to study the geochemical manifestations occurring within the ocean water column during and after an eruptive event, as well as the impact of fluid and gas emissions on the water column geochemistry.

For this purpose, we took advantage of a newly born submarine volcano – the Fany Maoré volcano – whose activity started in 2018-2019, to study the water column geochemistry during the setting of the volcano (i.e. eruption and formation of the edifice) and after the eruptive event (i.e. lava flows installation and possibly hydrothermal circulation initiation). The description of the geological setting of this submarine eruption offshore Mayotte Island is provided in CHAPTER 2. Below we provide a description of current knowledge of submarine volcanism, and its characteristics in terms of tectonic settings, volcanic product emissions and known consequences on the open ocean.

1.2. The submarine volcanism

About 85 % of current global volcanic activity occurs on the seafloor, building oceanic crust along mid-ocean ridges, forming abundant intraplate seamounts, and building island arcs (Rubin et al., 2012; White et al., 2015b; Tepp and Dziak, 2021) (Figure 1.1, Table 1.1). Nonetheless, observational technics in the ocean are limited and there may be many more active sites in the interior of tectonic plates than what is currently known.

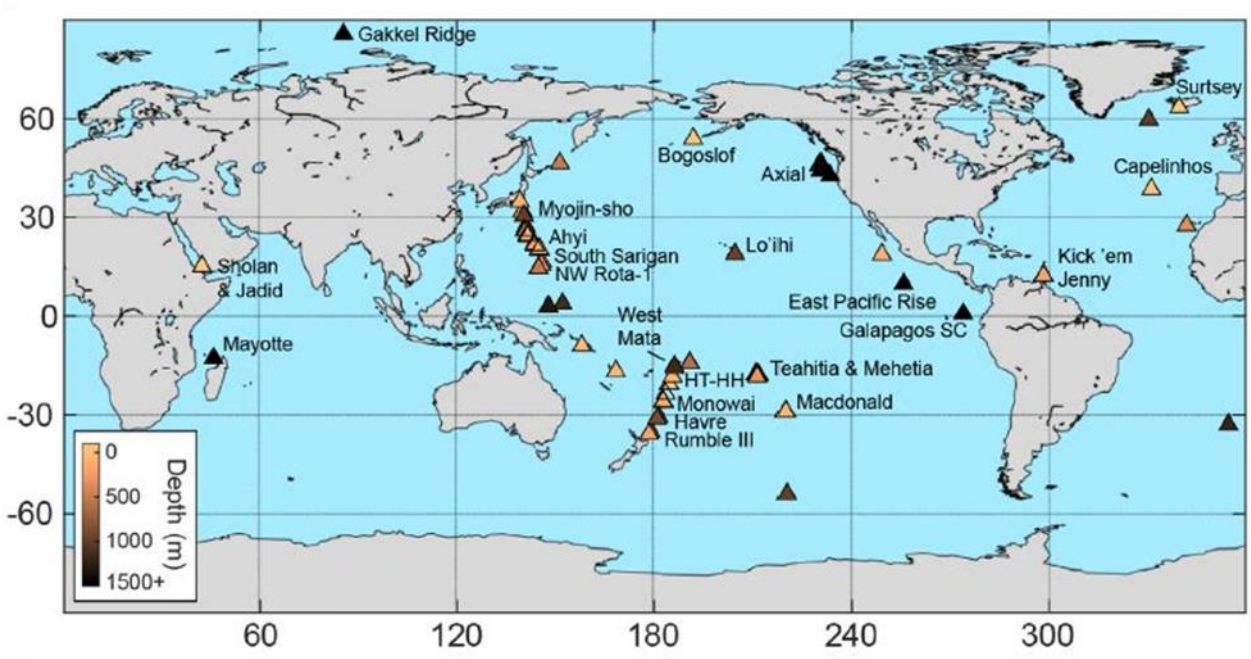

Figure 1.1. World map showing the locations of known submarine eruptions (triangles). The color scale indicate the depth of the seamount's summit or the depth of the spreading center (from Tepp and Dziak (2021)).

While subaerial volcanoes have been extensively monitored, the methods used are barely applicable to submarine volcanoes. The first submarine eruption was discovered by chance in 1986 at the Juan de Fuca Ridge on the Cleft Segment (Baker et al., 1987). Since then, 35 magmatic events have been studied (Baker et al., 2012). Only in a few cases, it has been possible to accurately capture the volcanic activity, either using remotely operated vehicles (Chadwick et al., 2008; Chadwick et al., 2019) or seismometer deployments (Tolstoy et al., 2006; Kelley et al., 2014). Despite the technological achievements of the last 30 to 40 years that have significantly improved our ability to observe, map, access, sample, and study the seafloor, submarine eruptions are still rarely detected, even more rarely observed, and their eruptive products are difficult and expensive to sample. Hence, the range of eruption styles and geochemical manifestations in the deep sea still remains largely unknown (Rubin et al., 2012), particularly regarding their impact on the global ocean geochemistry.

Table 1.1. Abundance and significance of submarine eruptions compared to subaerial eruptions (White et al., 2015b). Submarine eruptions are quantitatively dominated by eruptions at spreading ridge, are more commonly basaltic than subaerial eruptions, and make up a much larger share of total global volcanism. Given total submarine eruptive volumes, even a small proportion of such eruptions is likely to have a large impact in the global transfer of heat and volatiles in the oceans.

	Subaerial Eruption	**Submarine Eruption**
Estimated % global volcanism	15% (0.6 km^3/yr)	85% (3.5 km^3/yr)
Basaltic volcanism	30% (0.19 km^3/yr)	80% (2.8 km^3/yr)
Non-basaltic volcanism	70% (0.43 km^3/yr)	20% (0.697 km^3/yr)
Volcanic heat released as percentage of global total	14% (30% at 1200°C + 70% at 800°C)	86% (80% at 1200°C + 20% at 800°C)
Estimated proportion explosive	80% of 15% (i.e. 12% of all eruptions are explosive subaerial ones)	5% of 85% (i.e. ~4% of all eruptions are explosive submarine ones)

The main difference between submarine and subaerial volcanism is obviously the presence of water as the ambient environmental medium in submarine environments. The interaction between magma and surrounding seawater can produce a variety of interaction styles, processes and deposits (Cas and Giordano, 2014). Submarine eruptions are thus subject to physical constraints that are very different from those of subaerial eruptions. The heat capacity, thermal conductivity, density, viscosity, pressure gradient and bulk modulus of seawater are each generally orders of magnitude larger than the properties of the atmosphere surrounding subaerial vents. These differences greatly affect the eruption processes, including fragmentation, particle cooling, plume dynamics, transport and dispersal (White et al., 2015b; Cas and Simmons, 2018). Only in-conduit processes, those occurring before the magma interacts with the surrounding environment, have the potential to be equivalent between subaerial and submarine eruptions. Generally, the exsolved volatile content of the erupting magma will be lower in the ocean than on land because magmas decompress at hydrostatic pressures orders of magnitude greater than atmospheric pressure. At water depths and pressures greater than those equivalent to the critical points of H_2O and CO_2, exsolved volatiles are supercritical fluids, not gas, and so have limited ability to expand, let alone explosively. Gas overpressures are lower in deep submarine magmas relative to subaerial counterparts, limiting explosive expansion of gas bubbles to shallower waters (Cas and Simmons, 2018). Overall, while submarine volcanism differs in many way from aerial volcanism, differences also exist between submarine volcanoes depending on tectonic settings. We

present hereafter the various tectonic settings behind the formation of submarine volcanoes, the mechanisms of fluid and gas discharges depending on the submarine volcanic activity, and the consequences and hazard of submarine volcanism.

1.2.1. Tectonic settings

Tectonic setting plays a major role in the volcano distribution, behavior and chemistry of the eruptive products (Siebert et al., 2015a). Most submarine volcanoes occur where tectonic plates move towards or away from each other. There are four main types of submarine volcanoes (Figure 1.2):

(i) Volcanoes from spreading centers (i.e. divergent plate boundaries), also called Mid-Ocean Ridge (MOR) volcanoes. They form where two tectonic plates move away from one another with basalt lava rising out from beneath the seafloor (Soule, 2015). These volcanoes arise as a result of episodic melt production beneath ridges near fracture zones (Batiza and Vanko, 1983). The basalt flows at these locations often have a distinctive "pillow" shape, but can also appear smooth depending on the speed and viscosity of the flow (Siebert et al., 2015a). The East Pacific Rise is an example of such volcano (Wu et al., 2022).

(ii) Volcanoes from subduction zones (i.e. convergent plate boundaries), are differentiated into arc and back-arc volcanoes. Those volcanoes form where two tectonic plates collide, with one plate subducting underneath the other and re-melting. As cold water-laden oceanic plates descend into the hot interior at oceanic arcs, they dehydrate. The efflux of water lowers the temperature at which the overlying rocks of the solid mantle melt, leading to magma generation where it would not otherwise occur. In this context, the primary rock composition is felsic, producing a lava with high viscosity and high gas content. This lava is generally associated with very violent eruptions, although much of their explosiveness is mitigated by the depths at which they occur (Siebert et al., 2015a). Volcanoes found at the Mariana Arc, such as Ahyi Seamount (Buck et al., 2018) or NW Rota-1 (Chadwick et al., 2008; Resing et al., 2009), were formed by the melting of the subducting Pacific Plate.

(iii) Volcanoes from hotspots, occur as a consequence of a magma plume rising through the Earth's crust overlying a melting area in the Earth's mantle. These eruptions often lead to chains of volcanic islands and seamounts that are older with increased distance from the surface location of the rising magma plume. Hot spots leave linear "tracks" of seamounts across the ocean basins and build some of the Earth's largest volcanoes (Siebert et al.,

2015a; Staudigel and Koppers, 2015). Example include Loihi Seamount (Garcia et al., 2006; Malahoff et al., 2006).

(iv) Volcanoes in intraplate settings occur within tectonic plates, far away from plate boundaries. This type of submarine volcanoes has been little observed so far. The origins of intraplate volcanism are still a matter of debate among geologists, and different mechanisms have been proposed to explain it. Volcanoes in intraplate settings are typically attributed to the activity of mantle plumes or hot spots, and in some cases to mantle upwelling due to plate extension. Those volcanoes can also be found near large offsets in ridge system and near topographic highs of the faster spreading ridges (Staudigel and Koppers, 2015).

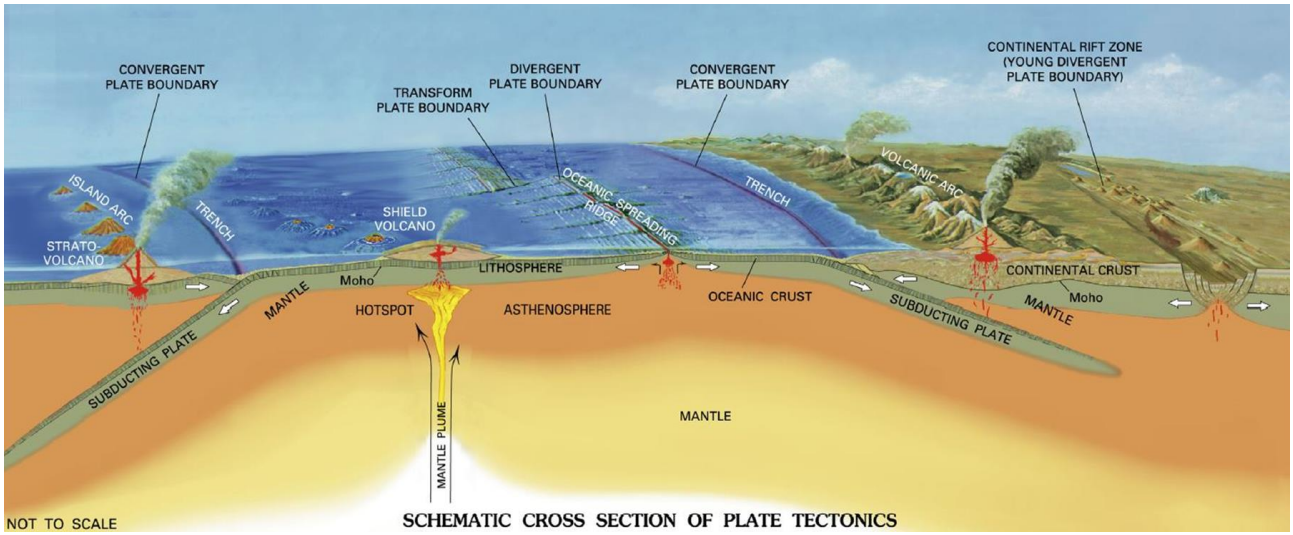

Figure 1.2. Schematic representation of the tectonic setting behind the different types of submarine volcanoes, after Siebert et al. (2015a).

1.2.2. Mechanisms of fluid and gas discharges depending on the volcanic activity

Submarine volcanic eruption are generally associated with water-rock interactions leading in some cases to the formation of hydrothermal vent systems at the seafloor, which present various chemical signatures depending on geologic and tectonic context, sub-seafloor processes and magma composition. These settings control the manifestation of the emissions and thus the geochemical composition of the fluid released into the seawater at the ocean seafloor, and therefore the impact on the water column geochemistry.

1.2.2.1. Volcanic eruption

The supply of magma, whether constant or variable over time, leads to an increase in pressure in the magma chamber, which in turn triggers an increase in seismicity rates (Tolstoy et al., 2006). Changes in hydrothermal fluid chemistry and temperature are related to this seismicity due to the vertical migration of the thermal boundary layer associated with magma recharge (Kelley et al., 2002; Fornari et al., 2012). Once sufficient pressure has been reached in the magma chamber, magma upwelling is initiated and, with sufficient overpressure, can reach the surface. This upwelling is probably linked to the formation of event plumes (Dziak et al., 2007) by advection of magmatic heat to the seafloor and/or release of hydrothermal fluids stored in the crust (Baker et al., 2011; Baker et al., 2012).

The eruption mode is determined by the depth of the eruption, the magma composition, the volatile segregation conditions and the tectonic context, while eruption frequency depends on episodes of magma overpressure and changes in the geometry of the magma chamber. The amount of magma gas in the system and the depth of eruption, determine the level of explosive activity that may accompany the effusiveness of the eruption. Submarine volcanic eruptions are influenced by the pressure of the surrounding water (Rubin et al., 2012; Cas and Giordano, 2014).

1.2.2.1.1. Types of volcanic eruptions

Volcanic eruptions can be divided into effusive styles that produce lava flows versus explosive styles that produce pyroclastic deposits. One fundamental control on this behavior is the silica (SiO_2) content of the magma that erupts. Basaltic magma with <52 wt% (mass percentage) SiO_2 is hot and very fluid (low viscosity) so it is commonly erupted as a spray of droplets (fountains) or as lava flows. In contrast, magmas that are richer in SiO_2, such as andesite (52-64 wt % SiO_2), dacite, and rhyolite (>69 wt% SiO_2), are generally erupted at lower temperatures and have higher viscosities, which commonly result in eruptions being potentially explosive. Most submarine eruptions in deep water are basaltic in composition and so are generally not, or only weakly, explosive but may form hyaloclastite when molten lava is quenched on contact with water. In most cases, basaltic magmas have lost volatiles during ascent and reach the seafloor with only minor volatiles which, at high hydrostatic pressures, remain mostly in solution. Exsolved volatiles form bubbles. As a rule of thumb, vesicles are less voluminous in basaltic lavas generated by deep-water eruptions (White et al., 2015a).

Explosive eruptions can occur when magma reaches the seafloor without losing its original volatiles, or when shallow magma is fluxed by volatiles from a deeper magma (White et al., 2015b). Explosions can also be caused by a rapid transfer of heat from the magma to the water (Zimanowski et al., 2015).

The nature of the eruptive site, particularly whether covered with thick loose sediment or with rigid rocks, provides another control on the eruptive behavior. Magma approaches the surface in dikes that advance by crack propagation. Unconsolidated sediment is insufficiently rigid to crack, and the dike tip stalls. Simultaneously, the heat of the magma heats and expands water in the sediment; the expansion pushes grains apart and allows the mixture to behave as a soft plastic or viscous fluid. These effects allow the magma to spread laterally into the sediment at shallow depths below the seafloor, commonly resulting in intrusions of complex form, and mingled combinations of magma and sediment termed peperite (Cas and Giordano, 2014; White et al., 2015b).

To date, only two small submarine explosive eruptions have been observed at their vents: the eruption of NW Rota-1 Volcano in the Marianas Arc (Chadwick et al., 2008), and the eruption of West Mata Volcano in the Lau Basin (Resing et al., 2011).

1.2.2.1.2. Types of lava flows

The entry of lava into the ocean is often a violent process as molten lava is rapidly quenched and fractured by the relatively cold seawater. In return, the lava heats the seawater creating a large pool of warm water with very distinctive hydrographic features (Sansone and Resing, 1995). Depending on the gas content, magma chemistry, and eruptive style, products range from gentle flows, through near-vent spatter, to scoria, cinder, ash, and pumice, which results in widely varying volcanic landforms (Siebert et al., 2015a), as well as emissions that are very diverse in terms of their chemical composition.

When magma reaches the ocean, the cold water causes rapid cooling and solidification of the lava, forming volcanic glass structures known as "pillow lavas". Lava flows progress over several hours or days for each eruption pulse, which may continue as long as the pressure released is not sufficient, or as the pressure continues to increase in the magma chamber through magma recharge (Rubin et al., 2012). By far the most voluminous submarine volcanic facies are of basaltic composition. Lava of this type is dominant along the global mid-ocean ridges, in back-arc basins, at intraplate seamounts, ocean volcanic islands, and oceanic plateaus (White et al., 2015a). Submarine basaltic lavas differ morphologically from subaerial lavas due primarily to efficient crust formation (i.e., quenching) that results from eruption into cold seawater rather than cool air (White et al., 2015a).

Pillow lava is commonly cited as the most abundant geologic landform on Earth’s surface. Pillows are formed at low, though imprecisely known, flow rates (White et al., 2015a). They are of tubular shape, often with circular or oval cross-sections. They commonly have a distinct top-to bottom

asymmetry, whereby the bottoms of these lava tubes tend to be molded around the preexisting topography into “V-shapes” while the tops are round and often flattened as pillows grow larger (Staudigel and Koppers, 2015). Pillow lavas have been observed while forming on the West Mata Volcano in the NE Lau back-arc basin (Resing et al., 2011).

Lobate lava is the dominant morphology on many fast and intermediate spreading-rate ridges, and reflects higher eruption rates than pillow lavas. Single lobes are many times wider than they are thick. Lobate lava is similar to pillow lava in that individual flow units (lobes) are easily recognized on the flow surfaces, but boundaries between lobes are commonly destroyed within the lava interior (White et al., 2015a).

At the highest eruption/flow rates, sheet lavas are produced. Their interiors are fully interconnected and the surfaces lack any indication of separate units. Instead, the surfaces may be smooth, ropey, lineated in the direction of flow, or jumbled. Jumbled surfaces reflect continued deformation of a folded or lineated surface causing the crust to brecciate. Sheet lavas are typically restricted to near-vent regions and areas where flow is constricted (White et al., 2015a).

1.2.2.1.3. Gas and fluid products of eruption

Eruptions produce lava flows, but can also produce gas plumes, and steam explosions (Rubin et al., 2012).Submarine volcanic liquids include hot water and mineral-rich hydrothermal solutions. These liquids are typically the result of seawater interaction with hot magma and can contain high concentrations of sulfides, metals, and other chemical elements (Resing and Sansone, 2002; Hawco et al., 2020). Submarine volcanic liquids exhibit unique physicochemical properties, such as high temperatures, high pressures, and acidic pH levels.

Volcanic gas emissions can occur continuously or intermittently. Their distribution in seawater depends on ocean currents, submarine topography, and the depth of the volcano. Volcanic gases can have a significant impact on the environment, contributing to seawater acidification, influencing climate, and participating in the formation of aerosol particle clouds in the case of shallow volcanoes.

Gaseous submarine eruption columns and hot water plumes form above both explosive and non-explosive eruptions, and these can entrain pyroclasts and pumice autoclasts upward (Cas and Simmons, 2018) (Figure 1.3). Dispersal and sedimentation of clasts in water is affected by the rate at which buoyant clasts become water-logged and sink, and by waves, and oceanic currents, which can produce very circuitous dispersal patterns in floating pumice rafts (Cas and Simmons, 2018). The behaviour of pyroclasts in a submarine explosive eruption column will be complex and depend on

their density, whether the ambient medium they are entrained in is low density gas-steam, or higher density water, and the concentration of pyroclasts in this fluid medium.

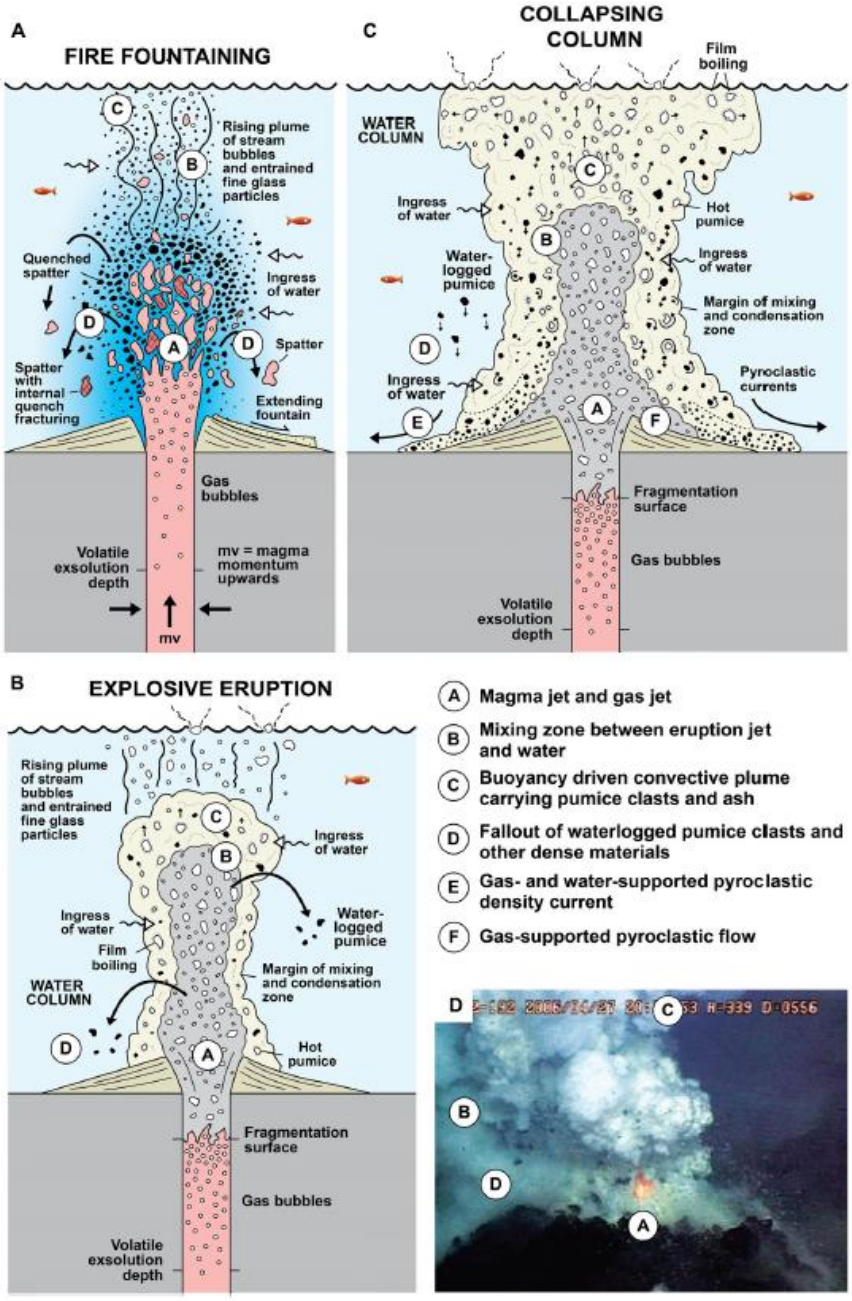

Figure 1.3. Example of submarine eruption characteristics from Cas and Simmons (2018) – and references therein. (A) Deep-water fire fountain column, showing quench fragmentation of spatter clasts in the column and the water mass above the vent. (B) Complex processes contributing to the dynamics of a relatively deep-water, submarine explosive eruption column as a result of initial bubble decompression and expansion, then cooling, condensation and water ingress into a submarine eruption column upward. (C) Schematic diagram of a relatively shallow water (tens to hundreds of meters) explosive eruption column collapsing around the vent. The rising buoyant column is subject to condensation of gasses and mixing in of ambient water. Large pumice clasts become water-logged, contributing to collapse of the column, forming a hot mass-flow of pyroclastic debris, steam and water on the seafloor. (D) Small, suppressed explosion of small ejecta, with a core of incandescent lava or fire fountain, in 2006, Brimbank Crater, NW Rota 1 volcano, Marianas arc, water depth ~550 m.

From deep-water vents, eruptive plumes can be significantly modified above the vent by cooling, condensation of gasses and mixing in cold, dense ambient water, so that their heights are often limited to the depth of the ocean/water body at the location of the eruption. Considering that all submarine eruptions occur at depths <5000 m, submarine eruption columns are generally limited in height to a few kilometers to hundreds of meters (Cas and Simmons, 2018).

1.2.2.2. Hydrothermal fluid circulation

Seawater infiltration through fractured oceanic crust is at the origin of hydrothermal circulation (Figure 1.4). By penetrating the cracks in the oceanic crust, the cold seawater is heated and undergoes a gradual chemical change. During its migration, it moves closer to the heat source (i.e. the magma chamber) and can reach maximum temperatures in excess of 400°C. This modified seawater, referred to as hydrothermal fluid, rises through the crust due to density differences, before being expelled into the rocks of the ocean floor. Hydrothermal fluids are significantly enriched or depleted in chemical components compared to ambient seawater, as a result of sub-seafloor reaction conditions. These hydrothermal vents host a unique biodiversity and play a crucial role in oceanic geochemical cycles (Massoth et al., 1989; Massoth et al., 2003).

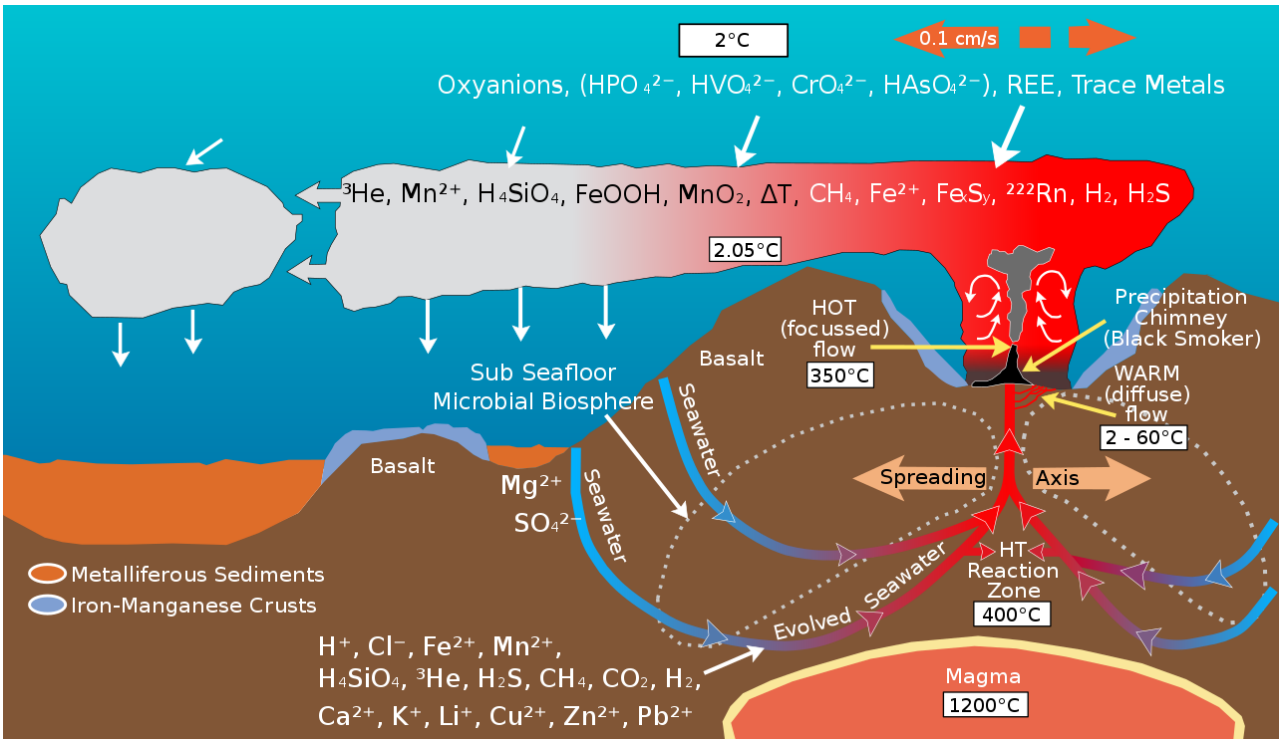

Figure 1.4. Schematic diagram of hydrothermal fluid circulation drive by volcanic heat at the mid-ocean ridge axis as adapted from Massoth et al. (1988). Image courtesy of Submarine Ring of Fire 2002, NOAA/OER.

In a submarine volcanic system, hydrothermal circulation generally occurs at post-eruptive stage due to increased permeability of the crust and the creation of new heat sources such as sub-seafloor magma and freshly erupted lava fields that are still cooling (Baker, 1998; Baker et al., 2004). Long after the eruption has subsided, the diffuse circulation of hydrothermal fluids continues through the shell of new lava flows (Rubin et al., 2012). Also, active deep-sea volcanoes, such as Loihi Seamount, are often associated with low-temperature (< 55°C) hydrothermal systems between periods of volcanic eruptions (Sedwick et al., 1992; Glazer and Rouxel, 2009), with higher temperature venting (> 250°C) associated to eruptive periods (Davis and Clague, 1998).

Composition of high-temperature hydrothermal fluids is controlled primarily by the pressure-temperature conditions, reaction kinetics, rock composition in the high temperature reaction zone and the input of magmatic volatiles. Diffuse fluids result from a sub-seafloor dilution of hotter hydrothermal fluids, and the range of compositions of diffuse fluids can be influenced by the degree of dilution, the time between dilution and venting, and by microbially-mediated and inorganic chemical reactions occurring throughout the upflow-mixing zone (Butterfield et al., 1997). Ultra-diffuse venting may occur away from the volcanic summit, as previously discovered at 5000 m depth off the southern flank of Loihi seamount that is characterized by laterally extensive massive Fe-oxyhydroxide deposition, with no detectable hydrothermal fluid flux to overlying seawater (Edwards et al., 2011).

Butterfield et al. (1997) have proposed a general model of how fluid vents evolve following a volcanic event, accounting for the difference in the location of the heat source within the oceanic crust. Immediately following a volcanic eruption or dyke injection, heat flux increases greatly, triggering phase separation and preferential venting of the more buoyant vapor phase. Continuous venting of brines observed in some systems means the conjugate brine phase must be temporarily retained around the heat source (by virtue of higher density or other physical properties), while higher-enthalpy vapor rich fluids with low chlorinities remove heat, volatiles (H_2S, CO_2, He and H_2 from magmatic degassing and water-rock interaction partition into the vapor phase) and metals. As the system cools, phase separation slows down and stops, and the fluids go through a transition from vapor-dominated to brine-dominated (chloride and metals increase while volatiles decrease). Brine content in the vented fluids may reach a peak and then decline as heat from the system runs out and fluid compositions decay back toward seawater.

The post-eruptive fluid evolution has been attributed to cooling of magma injected into the permeable upper layer of the oceanic crust. In the absence of recent volcanic perturbations, it appears that low-

chlorinity volatile-rich fluids are associated with high heat flux systems driving deeper phase separation (e.g. Endeavour Main Field), while brine-dominated fluids are associated with lower heat flux systems (e.g. Cleft segment) (Butterfield et al., 1997).

Beginning of hydrothermal circulation is characterized by the venting of magmatic volatiles (such as SO_2 and CO_2), resulting in highly acidic fluids and bulk dissolution of the host rocks. When the eruptive phase ends, the front of molten material recedes due both to magma chamber collapse and cooling by fluid circulation. As the reaction path of the hydrothermal fluids lengthens, contact between water and rock increases causing fluid temperatures to rise. As the volcano continues to age, less magmatic gas escape, the edifice cools, and the hydrothermal activity decreases (Resing et al., 2009).

A range of temperatures have observed at the Brothers hydrothermal system, from near-ambient seawater values to ~300°C leading to black-smoker type hydrothermal deposits (De Ronde et al., 2011). The different rock alteration assemblages were influenced by the interaction between seawater, magmatic fluid, the degree of hydrothermal water-rock interaction, and changing reduction-oxidation potential and temperature. These parameters appear to have varied over time and space throughout the evolution of the hydrothermal system (De Ronde et al., 2019). Periodic influx of magmatic hydrothermal fluids also may have initiated cycles of hydrothermal activity. With a decrease in magmatic input and an increase in hydrothermal water-rock interaction, the hydrothermal fluid become more evolved and alteration mineral assemblages change accordingly with temperature, depth, and distance from the main magmatic influx zone (De Ronde et al., 2005).

1.2.2.3. CO_2 cold seeps

CO_2 seeps are described by (González-Delgado and Hernández, 2018) as subtidal areas affected by the emission of gases originated from the discharge at the seafloor of CO_2-rich volcanic-hydrothermal fluids. In the literature, these are also mentioned as shallow hydrothermal CO_2 seeps, steaming fumaroles or submerged seeps (Price and Giovannelli, 2017; González-Delgado and Hernández, 2018; Aiuppa et al., 2021). They are more likely to exist where there is or has been a recent underwater volcanic activity, such as mid-oceanic ridges, island arcs, intra-plate magmatism, or around any active coastal or island volcano (Price and Giovannelli, 2017). These active zones have been found in several areas of the planet. Price and Giovannelli (2017) have reported 70 shallow (< 200 m) volcano-related seep locations over 23 CO_2 vent systems (Figure 1.5). Among those CO_2 seeps, one of the most

studied, Baia di Levante off Vulcano Island (Aeolian Islands, Sicily), presents CO_2 seeps composed of CO_2 at ~90 mol% that are interpreted as vapors deriving from the boiling of hydrothermal brines rising from a shallow geothermal aquifer (Boatta et al., 2013; Aiuppa et al., 2021) (Figure 1.6.A). CO_2 seeps were also reported offshore the island of Panarea, Sicily (Romano et al., 2019; Li et al., 2020); in the southern North Sea, about 30 km offshore the East Frisian Island Juist, Germany (McGinnis et al., 2011), or within the D'Entrecasteaux Island group in Milne Bay Province, Papua New Guinea (Morrow et al., 2015).

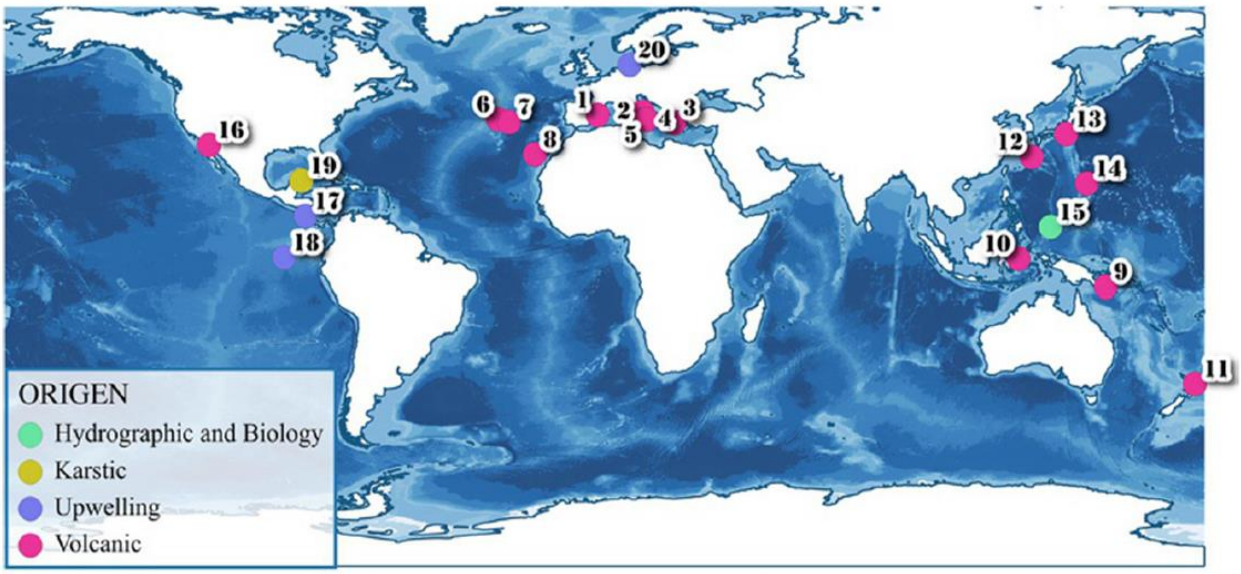

1	Columbretes Islands (Spain)	8	La Palma (Canary Islands)	15	Palau (Oceania)
2	Ischia (Italy)	9	Papua New Guinea	16	Wagner Basin (Northern Gulf of California)
3	Methana (Greece)	10	Indonesia	17	Bahia Culebra (Gulf of Papagayo)
4	Panarea (Italy)	11	White Island (New Zealand)	18	Eastern Tropical Pacific
5	Vulcano (Italy)	12	Iwatorishima (Japan)	19	Puerto Morelos (Mexico)
6	Faial (Azores)	13	Shikine Island (Japan)	20	Kiel Fjord (Baltic Sea)
7	San Miguel (Azores)	14	Maug (Mariana Islands)		

Figure 1.5. World map of the locations of shallow CO_2 seeps, after González-Delgado and Hernández (2018)

Overall, at those sites, emissions are in the gaseous form, with mean CO_2 content of 87.0 ± 20.7 vol% over 207 gas analyses (Aiuppa et al., 2021). Usually, the remaining volume (1–20%) consists in other gases or elements that are associated with volcanic emissions, such as nitrogen (N_2), oxygen (O_2), argon (Ar), dihydrogen (H_2), helium (He), mercury (Hg), methane (CH_4), hydrogen sulfide (H_2S) (González-Delgado and Hernández, 2018). Dissolution of CO_2 in seawater leads to water acidification. Lower pH, and thus differences in other chemical parameters, has been particularly detected in the vent system of the island of Shikine, in Japan, where the ambient pH has decreased by 1.3 units (Agostini et al., 2015). These volcanic seeps being located at shallow depths, results in

the discharge of CO_2 and reducing species (H_2S, CH_4, and H_2) into the surface oceans where they influence surface ocean chemistry and productivity. Rising the partial pressure of CO_2 in seawater reduces the concentration of carbonate ions and the saturation state of calcium carbonate minerals, which are essential for calcification in carbonate accreting invertebrates such as corals. It has been shown that some organisms can benefit from these changing conditions, but many more are hindered (e.g. reductions in coral diversity), leading to complex changes in communities and ecosystem functioning (Fabricius et al., 2011; Morrow et al., 2015). In addition to chemical inputs, the gases dissolved in seawater come from continuous bubbling in areas with volcanic activity. This can both prevent the establishment of some organisms but also generate acoustic turbulence that can alter the perception of the surrounding environment by some animals, thus affecting the development and behavior of larvae and juveniles seeking refuge or food (De Soto et al., 2013).

Other comparable CO_2 seep systems were found in other volcanic systems (Table 1.2), such as the young intraplate submarine volcano of El Hierro, Canary Island, that has been studied for ocean acidification concern, showing significant discharge of CO_2 at ~350 mbsl (Santana-Casiano et al., 2016). Bubble stream were also observed at Kick'em Jenny submarine volcano, in the Caribbean Sea. Two sites, named Champagne vent and Shrimp vent, presenting bubbles mainly composed of CO_2 of magmatic origin were observed at ~265 mbsl, with flux measurements of individual focused vent ranging from 10 to 100 kg of CO_2 per day (Carey et al., 2016; Michel et al., 2018). Numerous CO_2 vents were identified at ~500 mbsl in the crater of Kolumbo submarine volcano, in the Aegean Sea (Greece) inducing pH values as low as 5 pH units, which points to acidic conditions within the crater (Carey et al., 2013). Rizzo et al. (2019) suggest that the gases emitted originate from a homogeneous mantle contaminated with CO_2, probably due to decarbonation of subducting limestone. Also in the Hellenic Volcanic Arc, bubble venting with CO_2 as major component, and high temperature, were found at shallow depths around the Island of Milos (Dando et al., 1995). In addition, Lupton et al. (2008) gave evidence of CO_2-rich gas bubbles discharges at three submarine volcanoes located on the Mariana Arc (NW Rota-1, Nikko, and Daikoku) and two volcanoes on the Tonga-Kermadec Arc (Giggenbach and Volcano-1).

At those CO_2 seeps, CO_2 is discharged as gas bubbles and vents present high temperatures. However, in some rare cases, discharges have been observed deeper (> 1300 m) in the ocean as cold droplets of liquid CO_2 (Table 1.2). The first reported case was at the Okinawa Trough, in the JADE hydrothermal field, where they suggest the presence of CO_2 hydrates in the sediment associated with the liquid CO_2 (Sakai et al., 1990a; Sakai et al., 1990b). Liquid CO_2 venting was then observed in the Yonaguni

Knoll IV hydrothermal system, also at the Okinawa Trough, where it was suggested that this liquid CO_2 must result from a series of sub-seafloor processes including phase separation of hydrothermal fluid due to boiling, formation of solid CO_2-hydrate due to cooling of vapor phase, and melting of the solid CO_2-hydrate to liquid CO_2 due to a temperature increase within the sedimentary layer (Sakai et al., 1990a; Sakai et al., 1990b; Konno et al., 2006). The third site reported is the Champagne vent site on NW Eifuku in the northern Mariana Arc, which is discharging cold droplets of liquid CO_2 at an estimated rate of 23 mol CO_2/s, about 0.1% of the global mid-ocean ridge carbon flux. Here to, CO_2 is supposed to be directly degassing from a magma chamber, then cooled while migrating to the seafloor, ultimately forming CO_2 liquid and hydrate near the surface (Lupton et al., 2006) (Figure 1.6.B).

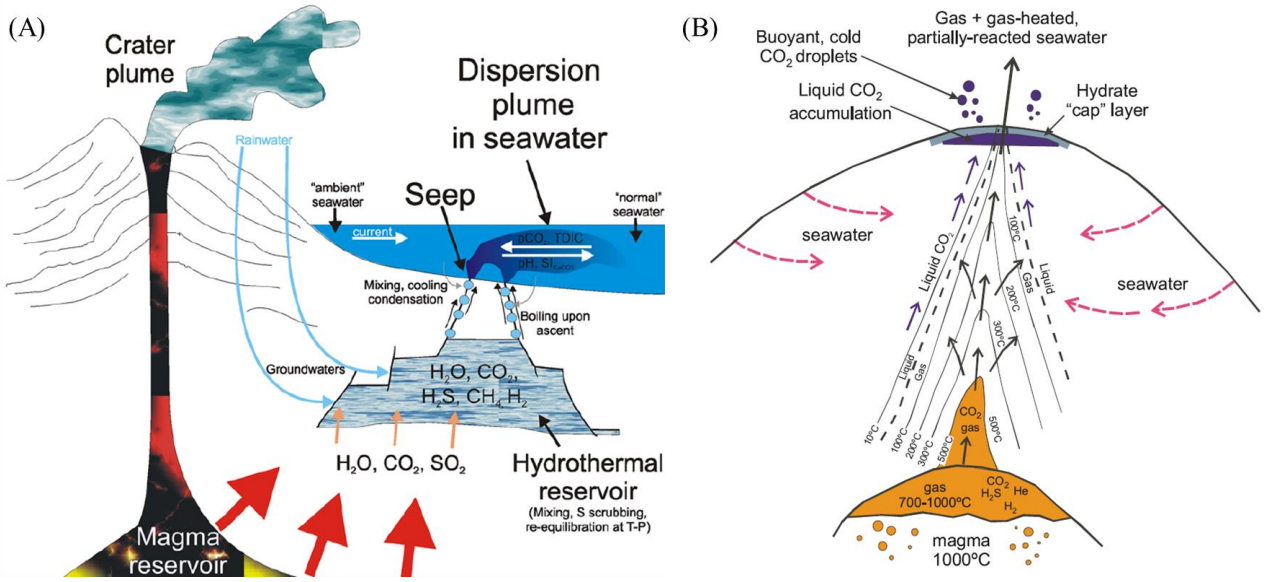

Figure 1.6. Schematic diagrams of the suggested sub-seafloor mechanism underlying (A) the CO_2 degassing at costal and insular volcanoes, after Aiuppa et al. (2021) , and (B) the liquid CO_2 venting at deep volcanic systems after Lupton et al. (2006).

Overall, venting of CO_2-rich gas bubbles and liquid CO_2 droplets is probably more common in submarine volcanic areas than we thought, but observations remains limited by the lack of resources and difficulty to access a number of sites. More generally, the impact of submarine volcanic eruptions on the global carbon budget, ocean acidification and oceanic ecosystems is largely unknown.

Table 1.2. Summary of the physicochemical properties of some CO_2 venting sites.

Vent site name	Location	Depth	Setting	CO_2	Phase	Temperature	References
Champagne and Shrimp vents, Kick'em Jenny submarine volcano	Caribbean Sea, Lesser Antilles	265 m	Back-arc	93-96%	gas	160-180°C	(Carey et al., 2016; Michel et al., 2018)
Kolumbo submarine volcano	Aegean Sea, Greece	500 m	Hellenic Volcanic Arc	>97%	gas	>220°C	(Carey et al., 2013; Rizzo et al., 2019)
Island of Milos	Greece	3-110 m	Hellenic Volcanic Arc	54.9-91.9%	gas	~80-110°C	(Dando et al., 1995)
Champagne vent field, NW Eifuku	Mariana Arc	1600 m	Arc	98%	liquid	<4°C	(Lupton et al., 2006)
JADE hydrothermal field	Mid-Okinawa Trough	1335-1550m	Back-arc	86%	liquid		(Sakai et al., 1990a; Sakai et al., 1990b)
Yonaguni Knoll IV hydrothermal system	Okinawa Trough	1360-1400 m	Back-arc	85%	liquid		(Konno et al., 2006)

1.2.3. The geochemistry of fluid emissions

Submarine eruptions are associated with fluid and gas discharged that present various chemical compositions controlled by numerous characteristics, such as geotectonic context, tectonic processes, depth, spatial and temporal sampling, or lava composition (Karl et al., 1988; Massoth et al., 1989; Malahoff et al., 2006; Kilias et al., 2013). Volcanic fluid and gas discharge are generally characterized by a high concentration of volatiles (including H_2O, CH_4, CO_2, SO_2, H_2S, ^3He, H_2), metal enrichment (Fe, Mn), hydrothermal precipitates (including particulate S) and large decreases in alkalinity and pH values in comparison with the ambient seawater (Massoth et al., 2003; Resing et al., 2009; Resing et al., 2011; Wen et al., 2016). Here, this section presents an overview on the chemicals that are found in submarine volcanic context, which provide insights into their origin and inherent processes of generation, and into their impact on the seawater geochemistry.

1.2.3.1. Noble gases: helium and neon

Helium is a very efficient tracer for studying volatile sources because of its gaseous state, its inertness and its multiple origins (radiogenic, magmatic; Figure 1.7). Helium is a stable and conservative nuclide that is not involve in any chemical or biological process. Helium has two stable isotopes:

helium-3 (^{3}He) and helium-4 (^{4}He). The ^{3}He is essentially primordial, stored in Earth's mantle since the accretion, but can also be produced by the radioactive decay of tritium (^{3}H) (Jenkins and Clarke, 1976; Jenkins et al., 2019). ^{3}He can also be produced via cosmic-ray-induced spallation (cosmogenic) reactions on planetary surfaces, which produce ^{3}H and ^{3}He in equal proportions, with subsequent decay of ^{3}H to ^{3}He, but this is a relatively minor source of noble gases. The ^{4}He is mainly radiogenic, produced by the radioactive decay of uranium (U) and thorium (Th) (Craig and Weiss, 1971).

Therefore, helium in the ocean originates from three different sources (Figure 1.7): (i) gas dissolution in equilibrium with atmospheric helium (He_{eq}), (ii) radioactive decay of tritium forming tritiogenic helium (^{3}He), and (iii) injection of terrigenic ^{3}He and ^{4}He by the submarine volcanic activity and addition of radiogenic ^{4}He from the crust and sedimentary cover (Lupton, 1983; Ayache et al., 2015).

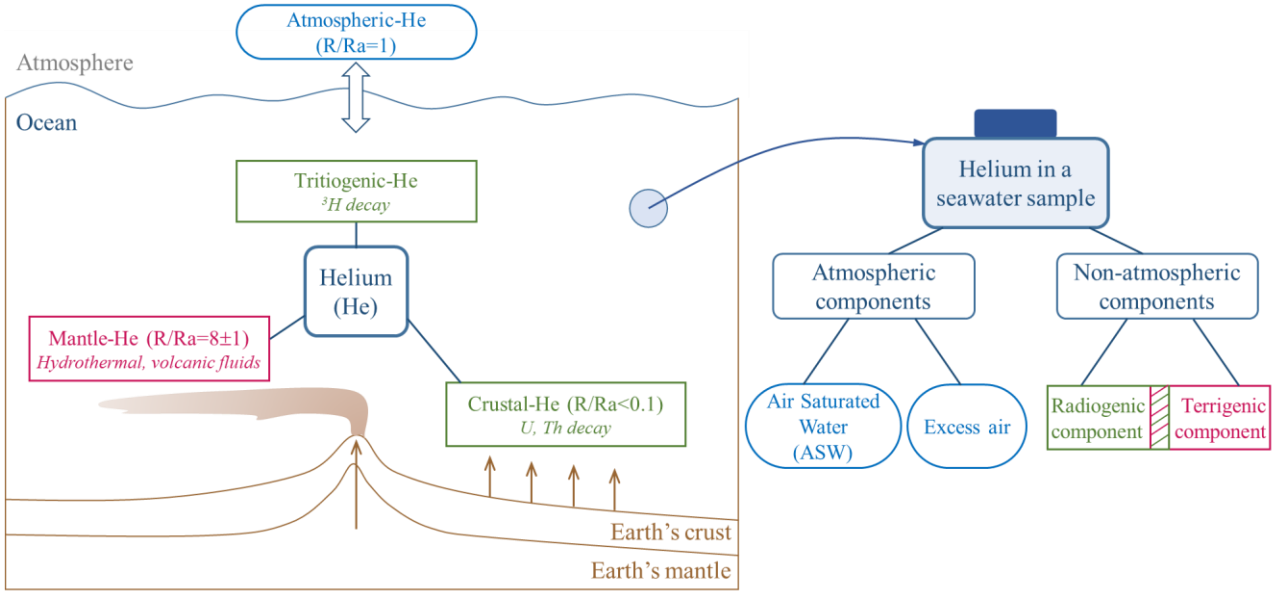

Figure 1.7. Schematic of helium components in the ocean, and terminology and classification of helium components that can be found in a seawater sample, adapted from Ayache et al. (2015) and Brennwald et al. (2013). Radiogenic noble gases are often, but not always of terrigenic origin (e.g. tritiogenic-^{3}He is not terrigenic). At the ocean surface, helium is essentially in solubility equilibrium with atmospheric He.

Apart from terrigenic origin, the main source of noble gases in the ocean is from the atmosphere through the process of air-sea gas exchange (Figure 1.7). The noble gases are usually close to being in equilibrium with the atmosphere, according to Henry laws constants, although rapid warming or cooling, ice formation or ice melting, and bubble injection can lead to departures from equilibrium (Stanley and Jenkins, 2013). Noble gases are partitioned between the atmosphere and the water by exchange across the air-water surface. The air-saturated water (ASW) corresponds to the solubility equilibrium of the noble gas between the atmosphere and the seawater. Excess air is formed by the (partial) dissolution of air bubble in the water (Brennwald et al., 2013). The overall concentration of

helium (i.e. measures) in seawater is thus given by the sum of the ASW concentration (noted He_{eq} hereafter), the excess air component (He_{air}), the terrigenic helium component (He_{xs}) and the tritiogenic ^{3}He (Brennwald et al., 2013).

Neon has three isotopes, ^{20}Ne, ^{21}Ne, and ^{22}Ne. These three isotopes can be produced via cosmogenic reactions but are also nucleogenic in the mantle, though the production rates for ^{20}Ne and ^{22}Ne are negligible in the Earth's mantle compared to their natural abundances. ^{21}Ne is a rare isotope and is thus more affected by cosmogenic and nucleogenic production, in contrast to the more abundant ^{20}Ne and ^{22}Ne. In the solid Earth, production of nucleogenic ^{21}Ne is coupled to that of radiogenic ^{4}He. This is because production of ^{21}Ne is directly proportional to the α-particle production ratio from the uranium and thorium series (Hilton and Porcelli, 2003). Neon isotopes are often used to correct for air contamination (i.e. atmospheric helium components). Indeed, the $^{20}Ne/^{22}Ne$ isotopic ratios can be considered as a stable isotopic ratio in the mantle. Both ^{20}Ne and ^{22}Ne are produced by nucleogenic pathways, but these productions are sufficiently slow to be considered as negligible. The correction is generally made by assuming that all neon is atmospheric and exploiting the contrast in He/Ne ratios between the mantle (>1000, Sano and Fischer (2013)) and the air (0.226, Weiss (1971) and Hilton (1996)) (Marty et al., 1989; Ozima and Podosek, 2002; Moreira and Kurz, 2013).

At the ocean surface, helium is essentially in solubility equilibrium with the atmosphere. However, several important processes alter the helium isotopic ratio ($^{3}He/^{4}He$) depending on depth. Present-day mantle contains both primordial (^{3}He) and radiogenic isotopes (^{4}He), but in different proportions depending on the geological context (Ayache et al., 2015). Helium isotope values are attributed to mixing between mantle-derived and crustal-derived radiogenic components. As a result, the helium isotopic ratio in fluids and gases provides information about the origin of volatiles (i.e. mantle vs. crust). The release of helium from submarine volcanic activity at mid-ocean ridges (MORB) and volcanic centers presents elevated helium isotopic ratios typical of their mantle source, while release of radiogenic ^{4}He from the crust and sedimentary cover lead to the addition of helium with a low helium isotopic ratio (Lupton et al., 1977b; a; Lupton, 1979; Craig and Lupton, 1981; Jean-Baptiste et al., 1991a; Jean-Baptiste et al., 1991b).

The atmospheric helium isotopic ratio (noted Ra) is of 1.384×10^{-6} (Clarke et al., 1976) and can be considered constant due to the long residence time of helium, which is ~10^{6} times longer than the mixing time of the atmosphere (based on the total helium content of the atmosphere and the global helium degassing flux estimated by (Torgersen, 1989)). Relative to this atmospheric ratio, typical helium isotopic ratios vary from < 0.1 Ra in the Earth's crust to an average of 8.0 ± 1.5 Ra in the

upper mantle (i.e. MORB-type), and up to some 40 to 50 Ra in products of plume-related ocean islands, such as in Hawaii and Iceland (Ballentine and Burnard, 2002; Graham, 2002; Hilton et al., 2002; Sano and Fischer, 2013; Wang et al., 2020). Global-mean subcontinental lithospheric mantle (SCLM) helium isotopic ratio has been estimated to be 6.1 ± 0.9 Ra (Gautheron and Moreira, 2002)

Because helium has such a high concentration in hydrothermal vent fluids relative to the surrounding seawater, ^{3}He can be used to trace hydrothermal plumes for thousands of kilometers from the source regions (Lupton, 1998). Oceanic helium isotopic ratio variations are usually expressed as δ^3He, which is the percentage deviation from the atmospheric ratio, defined as $\delta^3 He = 100 \times \left(\frac{R_m}{R_a} - 1\right)$, where R_m corresponds to the measured helium isotopic ratio (Benson and Krause, 1980; Stanley and Jenkins, 2013). In several areas of the Pacific, such as at the East Pacific Rise, Juan de Fuca Ridge or Loihi seamount, the hydrothermal activity is of sufficient strength to produce intense ^{3}He-rich plumes, which are clearly associated to important ^{3}He enrichment in deep water masses in the Pacific, about 20% above background seawater values (Lupton, 1998). Over the Mozambique Channel, δ^3He value in the deep ocean (~2500 mbsl) is about 10-15 %, while the tritiogenic helium appears negligible (Jenkins et al., 2019).

1.2.3.2. Volatile species

1.2.3.2.1. Carbon dioxide (CO_2)

CO_2 is the second most common gas in volcanic exhalations after H_2O, generated through lava outgassing (Craig and Lupton, 1981; Symonds et al., 1994; Lowenstern, 2001), although in gases exsolved from basaltic magmas, CO_2 can exceeds water in concentration (Giggenbach, 1997), presumably due to its greater abundance in some mantle source region. As the magma rises and cools, the low solubility of CO_2 relative to H_2O will cause it to partition preferentially into any exsolving vapor phase and gas bubbles that can segregate from the melt at different depths (Giggenbach, 1997). The composition of the exsolved gas phase will thus change as a function of the pressure-related solubility of each volatile species. CO_2 is extensively lost during the gas phase generation at high pressure and exsolve at all depth before H_2O does (Métrich and Wallace, 2008). Because the exsolved fluids are less dense than the melt they ascent faster to the surface, given place to fluid emissions with a very high concentration in a specific volatile. CO_2 may also be generated through a separate CO_2-rich gas phase directly degassing from the magma chamber, as it was observed at NW Rota-1, where

CO_2-rich gas bubbles exsolve from slowly erupting lava (Chadwick et al., 2008; Lupton et al., 2008). When the CO_2-rich gas phase encounters circulating seawater during its ascent through the volcano edifice, a two-phase mixture of CO_2–rich gas and an aqueous phase undersaturated with CO_2 can coexist as buoyant gas bubbles ascend through and exchange with the aqueous phase (Lupton et al., 2008). The behavior of CO_2 released into seawater is governed primarily by the pressure (i.e. depth) and the temperature of the water into which it is released, and to a lesser extent its salinity.

Since CO_2 emitted by volcanic eruption or hydrothermal fluid mainly originate from magmatic degassing, the isotopic composition of carbon dioxide ($\delta^{13}C$-CO_2) of magmatic origin, ranges between -8‰ and -4‰ (Pineau and Javoy, 1983; Sano and Marty, 1995). Nevertheless, the CO_2 isotopic composition can result from a mixing between the one of marine limestone $\delta^{13}C$-CO_2 = 0 ‰ (Sano and Marty, 1995), and the one of organic-rich sediments $\delta^{13}C$-CO_2 = -30 ‰ (Sano and Marty, 1995), depending on the fractionation process and the substrate through which the fluids and gases go through.

Once reaching the ocean seafloor, CO_2 can exist in different phases, according to pressure-temperature conditions (Figure 1.8). For instance, it can appear as CO_2-hydrates within sediments and on the seafloor (Sakai et al., 1990a; Lupton et al., 2006), as liquid CO_2 droplets (Sakai et al., 1990a; Sakai et al., 1990b; Konno et al., 2006; Lupton et al., 2006), or as gaseous CO_2 that occurs generally above 500 mbsl in the ocean (Lupton et al., 2008).

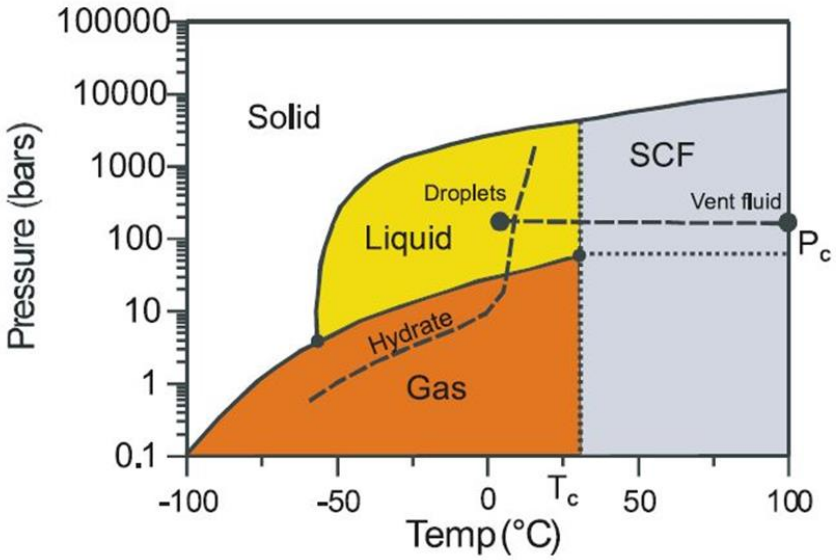

Figure 1.8. Phase diagram of CO_2 (from Lupton et al. (2006)) with regions where solid, liquid, gas, and super-critical fluid (SCF) exist. P_C and T_C denote the critical pressure and temperature. The dashed line denotes the boundary of hydrate stability. This diagram also presents the pressure-temperature conditions found for the liquid droplets and the 103°C vent fluid at Champagne site (Lupton et al., 2006).

1.2.3.2.2. Methane (CH_4)

Methane can be considered as a tracer for volcanic and hydrothermal activities. Since the fluids emitted are gas-rich and have a global composition very different from that of the surrounding seawater, this tracer allows the detection of plumes in the water column beyond tens to thousands of kilometers.

In submarine volcanic systems, CH_4 is generally produced through hydrothermal circulation that is initiated after an eruptive event, such as at Ahyi, NW Rota, West Mata, Nikko, Daikoku or Kasuga-2 (Resing et al., 2009; Resing et al., 2011; Baumberger et al., 2014; Buck et al., 2018), although it is also released during the eruptive event (Craig and Lupton, 1981; Baumberger et al., 2014; Baumberger et al., 2020).

Four processes are generally considered for CH_4 production in volcanic and hydrothermal systems (Schoell, 1988; Welhan, 1988; Fiebig et al., 2004):

(i) the biologic production of microbial CH_4 by bacteria at temperatures below 100°C (Rice and Claypool, 1981; Schoell, 1988; McLaughlin-West et al., 1999);
(ii) the thermogenic CH_4 production by thermal decomposition of organic matter at temperatures above 100°C (Schoell, 1980; 1988);
(iii) the outgassing of juvenile carbon as CH_4 rises through the mantle, similar to that of juvenile He (Craig and Lupton, 1981);
(iv) the inorganic synthesis in reactions to high temperatures (>300-400°C) involving CO_2 and H_2 or other C-H molecules which may be derived from various sources. An example of inorganic synthesis is the formation hydrocarbons and other organic compounds in geologic environments during chemical reactions such as the Fischer-Tropsch-type reaction: $CO_2 + 4H_2 \leftrightharpoons CH_4 + 2H_2O$ (Craig, 1953; Zolotov and Shock, 2000; McCollom, 2013).

Those processes can be classified into two categories: (i) and (ii) are considered as biogenic sources that includes both bacterial and thermocatalytic activities, while (iii) and (iv) are abiogenic sources (although a prior biogenic carbon history is not precluded under (iv)).

Looking at the carbon isotopic composition of methane ($\delta^{13}C$-CH_4), gas dominated by CH_4 with $\delta^{13}C$ values < -55‰ is typically considered to have a microbial origin, while gas with CH_4 that has $\delta^{13}C$ values from -30‰ to -50‰ is typically interpreted as being of thermogenic. Abiotic CH_4 is commonly assumed to be ^{13}C-enriched, with $\delta^{13}C$ values > -20‰ (Schoell, 1980; 1988; Welhan, 1988).

However, post-generation processes of mixing, migration, biodegradation, thermochemical sulfate reduction, and oxidation may occur in which case the interpretation of the isotopic signature is more complex. Milkov and Etiope (2018) have proposed new diagrams covering the vast majority of hydrocarbon-containing gases currently known to exist in nature.

Gases observed in hydrothermal fluids from mid-ocean ridge regions generally display $\delta^{13}C\text{-}CH_4$ values between -8.6 and -20‰, whereas $\delta^{13}C\text{-}CH_4$ values of -23 ± 6 ‰ are reported along the East Pacific Rise (EPR) and -12 ± 4 ‰ along the Mid-Atlantic Ridge (MAR) (Kawagucci et al., 2008; Sano and Fischer, 2013; Wen et al., 2016), and references therein). In addition, warm vents and gas bubbles from back arc submarine volcano with $\delta^{13}C\text{-}CH_4$ ranging from -24.8‰ to -41.4‰ have been reported suggesting a primarily thermogenic origin for CH_4 (Michel et al., 2018).

1.2.3.2.3. Dihydrogen (H_2)

In submarine volcanic systems, the dihydrogen (H_2) is described as an immediate tracer of the eruptive activity and provide strong evidence for on-going or very recent reactions between seawater or magmatic water and molten or extremely hot rocks (Baker et al., 2011; Resing et al., 2011; Baumberger et al., 2014; Baumberger et al., 2020).

H_2 comes either from a magmatic gas source (Symonds et al., 1994) or may be generated by the contact between molten lava and seawater (Sansone and Resing, 1995). More generally, H_2 is produced by all forms of Fe(II) oxidation (Truche et al., 2020), resulting from water reduction by iron-bearing compounds, following the reaction $2(FeO)_{magma} + (H_2O)_{seawater} \rightarrow (Fe_2O_3)_{rock} + H_2$ (Perfit et al., 2003; Baker et al., 2011; Worman et al., 2020).

Possible abiogenic processes for H_2 origins, have recently been listed by Worman et al. (2020) (Figure 1.9), and includes:

(i) Lava-seawater interaction: this is the most common process of H_2 generation during a volcanic eruption, taking place in the extruding high temperature lava during its interaction with seawater (Sansone et al., 1991);

(ii) Serpentinization: H_2 is released through hydration reactions of ultramafic materials such as olivine and pyroxene (McCollom, 2016; McCollom and Donaldson, 2016). This mechanism is generally considered to be the main H_2 production route during hydrothermal circulation at slow and ultra-slow spreading ridges, but likely requires a mature hydrothermal system (Charlou et al., 2010);

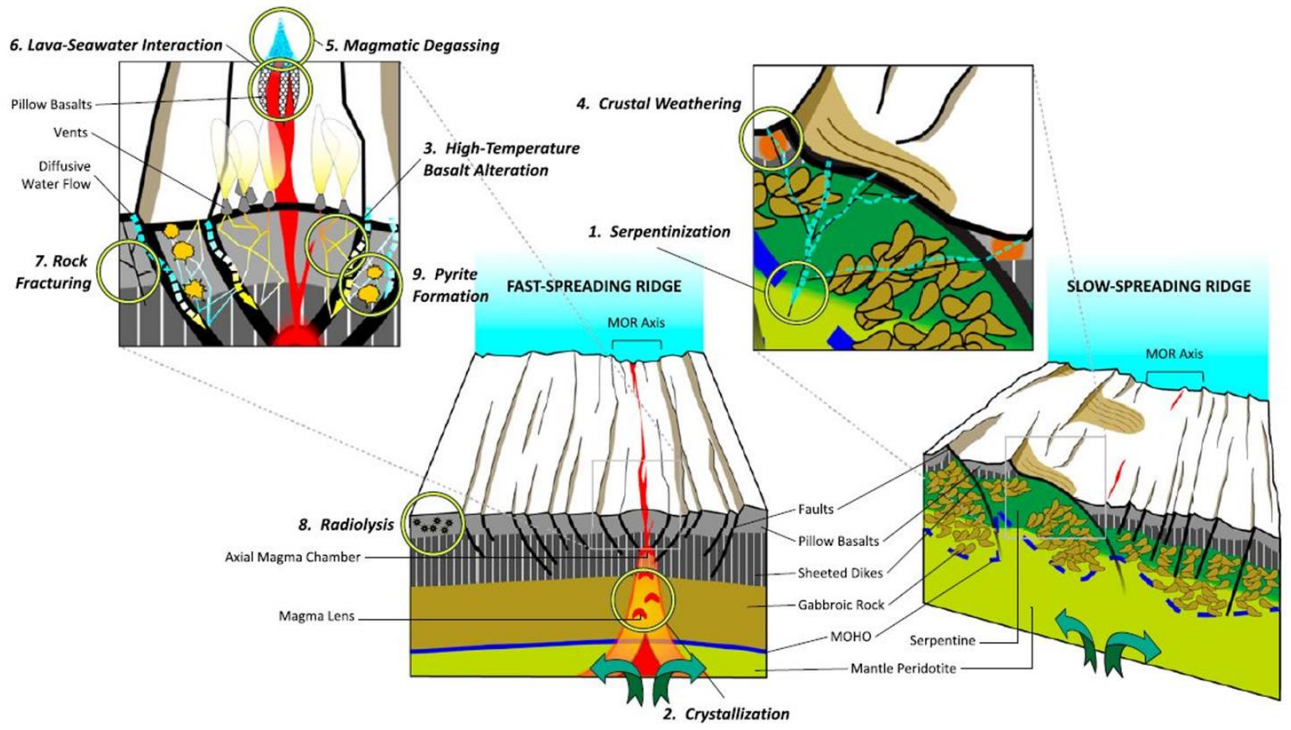

Figure 1.9. Schematic diagram of the nine different abiogenic processes that can produce H_2 within young oceanic crust, after Worman et al. (2020).

(iii) Crystallization of basaltic magma: H_2 production occurs during the late-stage of crystallization, as water is dissolved within magma oxidizes ferrous iron (Christie et al., 1986);

(iv) High-temperature basalt alteration: during the high-temperature (~350 to 400 °C) alteration of oceanic crust by seawater, a small number of ferrous silicates alter to ferric-bearing minerals and produce H_2 (Reed and Palandri, 2008).

(v) Crustal weathering: oceanic crust is altered by seawater as it cools and ages, forming lower-temperature (< 250°C) ferric-bearing minerals and H_2 (Bach and Edwards, 2003);

(vi) Magmatic degassing: at magmatic temperatures (~1200°C), the equilibrium of the reaction $CH_4 + 2H_2O \leftrightharpoons CO_2 + 4H_2$ is displaced strongly to the right, suggesting that H_2 may be a component of magmas (Apps and Kamp, 1993);

(vii) Radiolysis : the radiation released by decaying radioactive elements within oceanic rocks such as uranium (^{238}U and ^{235}U), thorium (^{232}Th), and potassium (^{40}K) can excite and ionize water, producing free radicals that may lead to the radiolysis of water, source of H_2 (Jørgensen and D'Hondt, 2006; Dzaugis et al., 2016);

(viii) Rock fracturing: this process breaks chemical bonds, producing radicals that can react with water to generate H_2 (Kita et al., 1982; Hirose et al., 2011);

(ix) Pyrite formation: H_2 can be produced as a result of metal sulfide mineral precipitation reactions (such as pyrite) from hydrothermal fluids (Gallant and Von Damm, 2006).

Regardless of the mechanism, once H_2 is produced it can be consumed by oxidation through abiotic reactions or microbial processes, usually within the timespan of a few hours to a few days (McLaughlin-West et al., 1999; Worman et al., 2020).

1.2.3.2.4. Hydrogen sulfide (H_2S) and sulfur dioxide (SO_2)

Despite its reduced abundance in magmas compared to water or carbon dioxide, the degassing of sulfur compounds related to volcanic eruptions is a very important phenomenon. Indeed, it exerts a substantial influence on magma evolution (and its eruptive potential) and has major impacts on the atmosphere (for terrestrial volcanoes), climate, and adjacent oceanic ecosystems, at different time and spatial scales. The complex behavior of sulfur in magmas is partly due to its multiple valence states (−II, 0, IV, VI), chemical speciation (e.g., S_2, H_2S, SO_2, OCS and SO_3 in gaseous phase ; S^{2-}, SO_4^{2-} and SO_3^{2-} in lavas and liquid phase) and its variations in stable isotopic composition (^{32}S, ^{33}S, ^{34}S and ^{36}S ; e.g. Metrich and Mandeville (2010), Labidi et al. (2015)). The redox ratio (H_2S/SO_2) notably increases with pressure (and therefore depth) and decreases with magma temperature and oxygen fugacity, and also depends on the tectonic context (Hoshyaripour et al., 2012). In seafloor hydrothermal systems, H_2S typically originates from leaching of basaltic-sulfide and seawater-derived sulfate that is reduced during high temperature water rock interaction (Shanks, 2001; Ono et al., 2007). In back-arc and arc related settings, magmatic volatiles enriched in SO_2 can produce highly acidic and H_2S-rich hydrothermal fluids through the reaction of disproportionation (Herzig et al., 1998): $4SO_2 + 4H_2O = 3H_2SO_4 + H_2S$.

The impact of degassing sulfur species activity on the biosphere, related to volcanism is also significant since a wide variety of microorganisms has their metabolism based on the redox chemistry of sulfides: reducing sulfides, thiosulfate, sulfite, and sulfate to H_2S, or oxidizing sulfur and H_2S to sulfates (Amend and Shock, 2001; Shock et al., 2010). Understanding volcanic sulfur degassing is therefore of paramount interest to understand the impact of magmatic, volcanic, and hydrothermal processes on the Earth system, and oceanic biogeochemical cycles.

1.2.3.2.5. Iron (Fe) and manganese (Mn)

Submarine eruptions and hydrothermal circulation produce strong discharge of trace elements such as iron (Fe) and manganese (Mn), which are biologically essential. In both cases, the source of the

metals is the lava, either solid or molten and the metals are released in their dissolved forms. Fe and Mn are the most commonly chemically enriched ionic species (Fe^{2+} and Mn^{2+}) in vent fluids, and hydrothermal discharge is the major source of these metals in seawater. Thus, Fe and Mn are ideal tracers of hydrothermal emissions when diluted as plumes, where they transform to particulate compounds that are important moderators of geochemical processes in seawater (Massoth et al., 2003).

For a long time, hydrothermal emissions from the seafloor were not considered as a major source of dissolved iron in the ocean, unlike manganese. However, recent studies showed the opposite. In the East Pacific Rise, hydrothermal activity could be responsible for plumes of dissolved iron extending over nearly 4000 km (Resing et al., 2015). In the Tonga Arc region, a shallow hydrothermal source was assumed to be responsible for fertilizing the photic waters of the southwestern Pacific with dissolved iron (Guieu et al., 2018).

As hydrothermal plumes age, Fe and Mn oxidize and are scavenged by particles. Iron is thought to remain in the dissolved form for hours to days, while Mn persists for months (Klinkhammer et al., 1985; Cowen et al., 1990; Field and Sherrell, 2000; German and Von Damm, 2004).

The concentrations of dissolved Fe in the open ocean are very low, with typical values in the 0.02 to 2 nmol/L range (e.g. Wu et al. (2001)), while typical concentrations of dissolved iron in hydrothermal vents are 1–3 mmol/L, with extreme values of about 18.7 mmol/L measured in the Juan de Fuca Ridge (De Baar H. J, 2001). In hydrothermal fluids, dissolved Fe occurs as stable Fe(II) species due to low pH and reduced potential conditions. After hydrothermal emission, Fe(II) is oxidized under the presence of dissolved oxygen and precipitates into various mineral forms, mainly Fe-sulfides and Fe-oxyhydroxides. Fe-oxyhydroxides deposits are widespread in seafloor hydrothermal systems along mid-ocean ridge and back-arc spreading centers, and form the main type of hydrothermal deposits associated with active submarine volcanoes. Fe-oxyhydroxides precipitate directly at the seafloor from diffuse low-temperature (from 10 to 100 °C) hydrothermal fluids mixing with cold seawater. Fe-oyhydroxides have been reported along the East Pacific Rise (EPR), the Mid-Atlantic Ridge (MAR), at arc and back-arc seamounts, and at intraplate submarine volcanoes in the Pacific (Boyd and Scott, 2001; Kennedy et al., 2003; Edwards et al., 2011; Sun et al., 2011; Rouxel et al., 2018). Around 4% of the total emitted iron is stabilized against loss from solution due to complexation by dissolved organic ligands (Bennett et al., 2008; Resing et al., 2015; Fitzsimmons et al., 2017), or by incorporation into inorganic or organic colloids which reside within the dissolved size fraction (Resing et al., 2015). Moreover, reduced species of Fe and S form FeS colloidal complex, which

remains suspended in the water and is modified as the pH changes (Luther et al., 2001). These nanoparticles can remain suspended in the deep sea for years with slower settling rates (Yücel et al., 2011), solubilizing and releasing the Fe(II). The complexation significantly increases metal content from hydrothermal systems, increasing trace-metal flux to the global ocean. Large and widespread deep-water Fe anomalies attributed from seafloor hydrothermal systems have been found in the Pacific, the Indian and the Atlantic basins (Tagliabue et al., 2010).

The relationship between Fe and Mn in hydrothermal plume water is complex and varies depending on a myriad of different reaction conditions. The Fe/Mn ratio (in term of total dissolvable fraction) can provide insights into the origin of fluids being discharged and the magmatic-hydrothermal state. Active hydrothermal centers within the Marianas present ratios ranging from 5 to 30 (Buck et al., 2018), which is within the range of Fe/Mn ratios measured in low-temperature vent fluids at Loihi Seamount (Glazer and Rouxel, 2009). Mid-ocean ridges and deep-seated hydrothermal systems have vent fluids with higher pH values and longer water-rock reaction pathways, and thus present ratios from 0.2 to 4 (German and Seyfried, 2014). Magmatic fluids found in eruptive and early post-eruptive evolution that are rich in SO_2 and CO_2 produce Fe/Mn ratios that have similar values than those in host rock (Massoth et al., 2003; De Ronde et al., 2005). Elevated Fe to Mn ratios in hydrothermal plumes have several possible origins, the emission of metal-rich magmatic volatiles (~54) (Rubin, 1997), congruent dissolution of the host rock either during lava-seawater interactions (~52) (Resing and Sansone, 2002) or by the reaction between hot sulfurous acid-rich fluids and the host lavas (~50) (Butterfield et al., 2011). Interaction between lava and seawater is governed by enrichment of the major seawater elements due to the loss of water vapor, the release of magmatic volatiles to generate both elemental enrichments (Resing and Sansone, 2002) and acidity (Resing and Sansone, 1999), the exchange of ions in seawater with that of the lava to produce acid (Resing and Sansone, 1999), the congruent dissolution of the lava (Resing and Sansone, 2002), and the reaction between water and the reduced Fe in lava to produce H_2 (Sansone and Resing, 1995).

1.2.3.3. The carbonate system

In the study of fluid and gas emissions from submarine volcanoes, the carbonate system reflects the venting of fluids rich in CO_2, acid (H^+) and alkalinity.

The carbonate system controls the acidity of seawater and acts as a governor for the carbon cycle (Emerson and Hedges, 2008). Within the mix of acids and bases in the Earth-surface environment, the carbonate system is the primary buffer for the acidity of water, which determines the reactivity of

most chemical compounds and solids. The carbonate system of the ocean by controlling the pressure of the CO_2 in the atmosphere, plays a key role in regulating the temperature of the planet (Menon et al., 2007; Michard, 2008; Houghton, 2014). The formation rate of the most prevalent authigenic mineral in the environment, $CaCO_3$, is also the major sink for dissolved carbon in the long-term global carbon balance.

The carbonate system is therefore described as the chemical equilibrium between the dissolved forms of CO_2 in water, the pH and both the solid and dissolved forms of carbonates. The dissolved compounds that make up the carbonate system in water (CO_2, HCO_3^- and CO_3^{2-}) are in chemical equilibrium on time scales longer than a few minutes (Emerson and Hedges, 2008).

Dissolving CO_2 in water results in the formation of carbonic acid, whose dissociation leads to a drop in pH:

$$CO_2 + H_2O \leftrightharpoons H_2CO_3 \leftrightharpoons HCO_3^- + H^+ \leftrightharpoons CO_3^{2-} + 2H^+ \quad (1.1)$$

In seawater, this acidification is attenuated based on the total alkalinity (A_T) relative to the concentration of dissolved inorganic carbon (DIC). The A_T is the sum of all weak bases contained in the water that can be titrated by a strong acid to the equivalent point of CO_2. In seawater, the majority of alkalinity is made up of carbonate and bicarbonate ions (Figure 1.10). The H^+ ions are primarily neutralized by the transformation of CO_3^{2-} ions into HCO_3^-. Thus, the concentration of CO_3^{2-} is an indicator of the buffering capacity of seawater. When the concentration of carbonate ions becomes limiting, the pH of seawater decreases. The dissociation of carbonic acid (HCO_3^-) increases the absorption capacity of atmospheric CO_2 compared to the dissolution of CO_2 as described by the Henry's law. This absorption capacity is expressed by the Revelle factor, describing the evolution of DIC concentrations when the partial pressure of CO_2 increases in the seawater (Egleston et al., 2010).

Seawater is therefore a buffered system whereby different forms of DIC, A_T, and pH constitute the carbonate system. This system is governed by a set of acid-base equilibria of carbonic acid, depending on temperature and pressure (Millero, 1979; Emerson and Hedges, 2008).

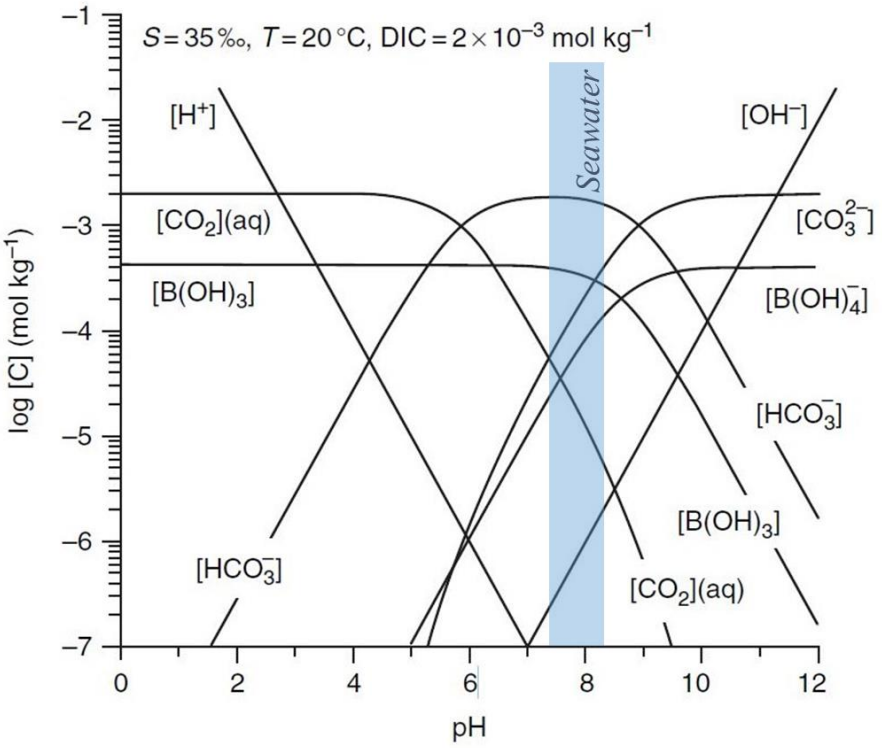

Figure 1.10. Concentrations of the species of the acid-base pairs of carbonate, borate and water in seawater as a function of pH, and for a salinity (S) of 35 psu, a temperature (T) of 20 °C, and a DIC of 2.0×10^{-3} mol/kg (modified from Emerson and Hedges (2008)). The seawater pH is generally comprised between 7.5 and 8.2, and DIC for this range is composed by more than 90 % of bicarbonates ions (HCO_3^-).

1.2.3.3.1. pH

In seawater, pH is a crucial parameter of the carbonate system as it determines the chemical equilibria of acid-base systems, such as the speciation of dissolved inorganic carbon, and thus has a significant influence on marine ecosystems.

The dissociation of the carbonic acid (H_2CO_3) by lowering the pH, alters the normal seawater dissolved carbon speciation, and lowers the seawater saturation state of calcite and aragonite (Aiuppa et al., 2021). The lowering of this saturation state (Ω) directly affects the biocalcifying organisms (i.e. corals, foraminifera, bivalves, etc.) by making it difficult for them to form and maintain their shells. This can lead to the local disappearance of species leading to complex community reorganization with potential consequences for ecosystem functioning (Fabricius et al., 2011). Thus, the balance of carbon exchanges between the ocean, atmosphere, and lithosphere is directly linked to the chemical conditions of marine ecosystems (Mostofa et al., 2016).

1.2.3.3.2. Dissolved inorganic carbon

In seawater, inorganic carbon exists in four distinct forms: the gas in solution or aqueous carbon dioxide ($CO_{2\,(aq)}$), and the three products of hydration reactions, namely carbonic acid (H_2CO_3), bicarbonate (HCO_3^-) and carbonate (CO_3^{2-}). The dissolved inorganic carbon (DIC), also named as total CO_2 (ΣCO_2), is described by the sum of the dissolved CO_2 forms in the water (Emerson and Hedges, 2008):

$$DIC = \Sigma CO_2 = [CO_{2\,(aq)}] + [H_2CO_3] + [HCO_3^-] + [CO_3^{2-}] \quad (1.2)$$

Concentrations of those forms in seawater are linked by equilibrium constants that depend on pH, salinity, and temperature (Dickson et al., 2007; Emerson and Hedges, 2008):

$$CO_{2\,(g)} \leftrightharpoons CO_{2\,(aq)} \quad (1.3)$$

$$CO_{2\,(aq)} + H_2O \leftrightharpoons H_2CO_3 \qquad K'_{CO_2} = \frac{[CO_{2\,(aq)}]}{[H_2CO_3]} \quad (1.4)$$

$$H_2CO_3 \leftrightharpoons HCO_3^- + H^+ \qquad K'_{H_2CO_3} = \frac{[HCO_3^-][H^+]}{[H_2CO_3]} \quad (1.5)$$

$$HCO_3^- \leftrightharpoons CO_3^{2-} + H^+ \qquad K'_2 = \frac{[CO_3^{2-}][H^+]}{[HCO_3^-]} \quad (1.6)$$

It is difficult to distinguish analytically the species $CO_{2\,(aq)}$ and $H_2CO_{3\,(aq)}$. It is common to combine the concentrations of $CO_{2\,(aq)}$ and $H_2CO_{3\,(aq)}$ by their sum and to represent it either with the symbol $[CO_2]$ or $H_2CO^*_3$, resulting in:

$$[CO_2] = [CO_{2\,(aq)}] + [H_2CO_3] \quad (1.7)$$

Equations (1.4) and (1.5) can then be combined to eliminate $[H_2CO_3]$ and give a new composite first dissociation constant of CO_2 in seawater. Assuming that $[CO_{2\,(aq)}] = [CO_2]$, the first dissociation constant of carbonic acid, K'_1, is (Emerson and Hedges, 2008):

$$CO_2 + H_2O \leftrightharpoons HCO_3^- + H^+ \qquad K'_1 = \frac{[HCO_3^-][H^+]}{[CO_2]} \quad (1.8)$$

Three important processes (and corresponding back processes) are able to modify the DIC of seawater: dissolution (outgassing) of gas; respiration or oxidation of living organisms

(photosynthesis); dissolution (precipitation) of $CaCO_3$ (Michard, 2008). Carbonate ions react with calcium ions to give solid calcium carbonate under two possible forms: calcite and aragonite.

1.2.3.3.3. Total alkalinity

The total alkalinity in seawater corresponds to the excess in bases (i.e. proton acceptors) over acids (i.e. proton donors) in the solution (Emerson and Hedges, 2008). The precise definition of total alkalinity from Dickson (1981) is:

$$\begin{aligned} A_T = [HCO_3^-] + 2[CO_3^{2-}] + [B(OH)_4^-] + [H_3SiO_4^-] + [HPO_4^{2-}] + 2[PO_4^{3-}] \\ +[OH^-] - [H^+] - [HSO_4^-] - [HF] - [H_3PO_4] \end{aligned} \quad (1.9)$$

This expression includes all known inorganic proton acceptors and donors in oxic seawater (Dickson, 1981). It includes two uncharged species at the very end, so it is not exactly consistent with the previous charge balance definition; however, in practice, the concentrations of acidic species in seawater (H+, HSO4- , HF, and H_3PO_4) are too low in the seawater pH range of 7.0–8.0 to be significant and are frequently not included in the alkalinity definition.

$$A_T = [HCO_3^-] + 2[CO_3^{2-}] + [B(OH)_4^-] + [OH^-] - [H^+] \quad (1.10)$$

In seawater, ions of carbonate and borate define about 99 % of the total alkalinity, while carbonate species alone define about 96 % of the total alkalinity and is expressed as the carbonate alkalinity (A_C):

$$A_C = [HCO_3^-] + 2[CO_3^{2-}] \quad (1.11)$$

The major source of alkalinity for many waters is calcium carbonate. The solubility of calcium carbonate is described as $CaCO_3 = Ca^{2+} + CO_3^{2-}$. In seawater, the carbon dioxide reacts with calcite ($CaCO_3$) and dolomite ($CaCO_3.MgCO_3$) to forms bicarbonate ions (Boyd, 2015):

$$CaCO_3 + CO_2 + H_2O \leftrightharpoons Ca^{2+} + 2HCO_3^- \quad (1.12)$$

$$CaCO_3 \cdot MgCO_3 + 2CO_2 + 2H_2O \leftrightharpoons Ca^{2+} + Mg^{2+} + 4HCO_3^- \quad (1.13)$$

1.2.4. Consequences and hazards of submarine volcanism

Submarine volcanic eruptions present a lower risk to life than subaerial eruptions, but there are still a number of hazards associated with submarine volcanism. Submarine eruption may lead to submarine debris avalanches, tephra fallout, large earthquakes, flank collapse events, slope instabilities, submarine landslides, and even tsunami generation (Lindsay et al., 2005; Paris et al., 2014). Tsunamis of eruptive origin occur when part of the energy released during an eruption is directly or indirectly transmitted to the sea, generating impulsive waves by the displacement of water (Begét, 2000). Up to eight mechanisms are implied in the generation of volcanic tsunamis: underwater explosions, pyroclastic flows and lahars entering the water, earthquake preceding or occurring during a volcanic eruption, flank failure, collapse of coastal lava bench, caldera collapse and shock wave produced by large explosion. Also, intense eruption-related seismicity may trigger submarine slope collapse (Nomikou et al., 2014; Paris et al., 2014; Mutaqin et al., 2019). Additionally, the proximity of volcanoes to the coasts may present significant risks for the population. Direct hazards include ballistic ejecta, water disturbances and lowered water density due to degassing, which may thus cause a decrease in buoyancy of boats above the volcano (Lindsay et al., 2005).

Volcanic activities include the release of gases, particles and fluids to the ocean, which are acidic and potentially toxic to many species (e.g. CO_2, CH_4, SO_2, H_2S, HS^-, HCl and HF) (Fischer, 2008; Oppenheimer et al., 2011; Buck et al., 2018; Romano et al., 2019; Aiuppa et al., 2021). Those emissions may disrupt the physicochemical features of the surrounding ocean, with potential impact on the functioning of ecosystems present on the seafloor and/or within the water column. Submarine eruptive plumes can transport small particles (e.g. ash) with slow settling velocities over large spatial scales along with the gravity currents (White et al., 2001; Deardorff et al., 2011; Murch, 2018), exporting themselves hundreds of kilometers away from the eruption location (Mittal and Delbridge, 2019). In addition, submarine eruption and lava discharge have been reported to act as a potential fertilizer for the ocean (Langmann et al., 2010b; Guieu et al., 2018; Wilson et al., 2019). Submarine volcanism support diverse microbial communities through hydrothermal venting (Spietz et al., 2018), acting as an exogenous source of nutrient, generating surface phytoplanktonic blooms through the upwelling of nutrient-rich and low O_2 deep waters (Wilson et al., 2019). The mixing zones between the reduced hydrothermal plume and the seawater provide local enrichments of electron donors capable of feeding complex chemosynthetic metabolisms (Jannasch and Wirsen, 1979; Dick et al., 2013). Studies have suggested the presence of autotrophic processes and microorganisms involved in the oxidation of sulfides, hydrogen, methane and ammonia, which dominate these mixing zones

(Baker et al., 2012; Li et al., 2014). Conversely, underwater eruptions may destroy entire biologic populations, with significant impacts on sessile benthic fauna that cannot escape burial in lava, or exposure to heat and gases. Colonization and re-establishment of benthic communities on newly created seafloor, depends on exogeneous larval supply from other populations and on the modifications of the physicochemical conditions in seawater. The shifts in benthic communities observed between the pre-eruptive state and the re-establishment of communities can present drastic changes (Kelley et al., 2002; Staudigel et al., 2006; Resing et al., 2011).

1.2.5. Summary of studied submarine volcanic systems

Up to now, only a dozen of deep submarine eruptions have been documented worldwide (Baker et al., 2011; Rubin et al., 2012). They were observed in different tectonic contexts (spreading center, hotspot, arc context), but very few of the detected volcanoes occurs in the deep ocean (>2000 mbsl). These main studied submarine volcanic systems are presented in Table 1.3.

Table 1.3. The main studied submarine volcanic systems. Data are issued from Baker et al. (2012), Price and Giovannelli (2017), Rubin et al. (2012), Siebert et al. (2015b), Tepp and Dziak (2021), and references cited in the table. NA stands for missing information.

Volcano	Location	Tectonic setting	Latitude	Longitude	Base depth (m)	Summit depth (m)	Geologic context	Observed eruptive events
East Pacific Rise	Central Pacific	spreading center	9.83	-104.3	2500	NA	basalt	1991-1992, 2005-2006
Axial Seamount	Juan de Fuca Ridge	spreading center	45.95	-130	2200-2400	1540	basalt	1998, 2011, 2015
CoAxial Segment	Juan de Fuca Ridge	spreading center	46.52	-129.58	2400	NA	basalt	1993
Loihi Seamount	Hawaii	hotspot	18.92	-155.27	~1200	969	alkalic basalt	1996
Vailulu'u Seamount	American Samoa	hotspot/spreading center	-14.22	-169.06	1000	593	NA	2005, 1995, 1973
Macdonald	South Pacific, Austral Islands	hotspot	-28.98	-140.25	150	40	NA	1987-89
Tagoro	El Hierro, Canary Islands	hotspot	27.62	-17.99	350	88	basanite	2011-2012
Brothers Volcano	Kermadec Arc, New Zealand	arc	-34.86	179.06	1650	1500	NA	NA
Havre Seamount	Kermadec Arc, New Zealand	arc	-31.11	-179.04	1750-2000	650	rhyolite, dacite	2012
Kick 'em Jenny	Caribbean Sea, Lesser Antilles	back-arc	12.30	-61.64	265	NA	basaltic, andesite	12 times between 1939 and 2001
NW Rota-1	Mariana Arc	arc	14.6	144.78	2800	517	basaltic, andesite	2003-2010
Ahyi	Mariana Arc	arc	20.4375	145.0292	90	25	basaltic	2014
West Mata	NE Lau Basin, Tonga Islands	rear-arc	-15.1	-173.75	3000	1165	boninite	2008-2009
Northeast Lau Spreading Center	NE Lau Basin, Tonga Islands	back-arc	-15.4	-174.27	1800	NA	basaltic, andesite	2008
Fani Maoré Seamount	Comoros Archipelago, Indian Ocean	Intraplate, lithospheric deformation	-12.7	45.65	3500	2680	basaltic	2018-2019

Volcano	Activity observed	Water column geochemistry	References
East Pacific Rise	Lava flow, hydrothermal activivity	High-temperature fluids (>410°C); High levels of CH_4; Presence of H_2S	(Tolstoy et al., 2006; Cowen et al., 2007; Dziak et al., 2009; Fornari et al., 2012; Wu et al., 2022)
Axial Seamount	Lava flow, hydrothermal plume	Low hydrothermal heat flux; Elevated ^3He/heat; Elevated CH_4, Mn and H_2	(Baker et al., 1990; McLaughlin-West et al., 1999; Baker et al., 2004; Wilcock et al., 2018)
CoAxial Segment	Megaplume, lava flow, microbial activity	Elevated dissolved Mn and CH_4; Fe-rich and H_2S-rich fluids	(Baker et al., 1995; Butterfield et al., 1997; Dziak et al., 2007)
Loihi Seamount	Lava flow, Hydrothermal fluid	High (~200°C) and low (<95°C) temperature hydrothermal fluids; Rich in CH_4, ^3He, CO_2, Fe, Mn	(Wheat et al., 2000; Garcia et al., 2006; Malahoff et al., 2006; Glazer and Rouxel, 2009; Schipper et al., 2010)
Vailulu'u Seamount	Hydrothermal activity, microbial communities	Low (~28°C) and high (~81°C) temperature hydrothermal fluids; Enrichment in particulates, ^3He and reduce Fe and Mn	(Staudigel et al., 2004; Staudigel et al., 2006; Connell et al., 2009)
Macdonald	Explosive eruption, hydrothermal activity, magmatic gases, volcanic ash	Large amount of CH_4, CO_2, SO_2; Enriched in H_2S, Fe, Mn and Si; Extremly low pH	(Cheminée et al., 1991)
Tagoro	Hydrothermal activity, active CO_2 degassing	Low temperature hydrothermal fluids (<40°C); Enriched in CO_2, CH_4, H_2S, Si, Fe^{2+}	(Santana-Casiano et al., 2013; Santana-Casiano et al., 2016; Santana-González et al., 2017; Santana-Casiano et al., 2018; González et al., 2020)
Brothers Volcano	Hydrothermal activity, episodic injection of magmatic fluid	Low (<200°C) and high (up to 320°C) temperature hydrothermal fluids; High levels of CO_2, H_2S, ^3He, particulate Cu, total dissolvable Fe	(De Ronde et al., 2003; Massoth et al., 2003; De Ronde et al., 2005; Stucker et al., 2022)
Havre Seamount	Eruption		(Murch, 2018; Mittal and Delbridge, 2019)
Kick 'em Jenny	Hydrothermal activity, cold seeps with chemosynthetic-based ecosystems, bacterial mats	Fluids up to 180°C; 93-96% CO_2; Diffuse venting of low temperature	(Lindsay et al., 2005; Carey et al., 2014; Carey et al., 2016; Michel et al., 2018)
NW Rota-1	Eruption, hydrothermal activivity, magma degassing	Gas-rich fluid; CO_2 bubble discharged, Fluid rich in Fe, Mn, CO_2, and ^3He; Acid flows rich in SO_2, Al, Si	(Embley et al., 2006; Resing et al., 2007; Chadwick et al., 2008; Resing et al., 2009; Chadwick et al., 2014)
Ahyi	Hydrothermal activity	Enriched concentrations of H_2, ^3He, CH_4, particulate S, Mn, and Fe	(Buck et al., 2018)
West Mata	Eruption, lava flow, strong effusive and explosive activity	Elevated volatile concentrations: H_2, CH_4, CO_2, He, Mn^{2+}, Fe^{2+}	(Clague et al., 2011; Resing et al., 2011; Baumberger et al., 2014; Embley et al., 2014; Dziak et al., 2015; Chadwick et al., 2019; Walker et al., 2019; Murch et al., 2022)
Northeast Lau Spreading Center	Possibly short-live explosive and effusive	Event plume rich in H_2, poor in ^3He; Diffuse plume rich in CH_4 and ^3He	(Baker et al., 2011; Embley and Rubin, 2018; Baumberger et al., 2020)
Fani Maoré Seamount	Eruption (possibly explosive and effusive), lava flow, liquid CO2 venting	Elevated concentrations of ^3He, CH_4, CO_2, H_2; Event plume with extremely high H_2; Fe and Mn enrichment near seafloor	(Feuillet et al., 2021); this thesis

1.3. Scientific aims

The overarching objective of this thesis is to better understand how a volcanic edifice is built through time in a deep environment, how different processes of construction influence the interaction between the eruptive products and the seawater, and what is the extent of the impact of such eruption.

For this purpose, we took advantage of a newly born volcano: Fani Maoré located ~50 km offshore Mayotte Island. Fani Maoré's eruption is the largest and deepest eruption reported to date with possible explosive eruptive event. The volcano's edifice is probably the youngest ever observed. In addition, the volcanic system is associated to liquid CO_2 venting in a geologic structure called the Horseshoe, which is only the fourth case observed.

Therefore, investigating the Fani Maoré volcano is a unique opportunity to investigate the overarching objective of this thesis. Below, we detail the main scientific questions associated to the main problematic of the thesis, which involve investigating the origin of the emissions observed in the water column, the styles of manifestation of the volcanic products and their geochemical composition, and the overall impact of a deep-sea volcano on the geochemistry of the water column (Figure 1.11).

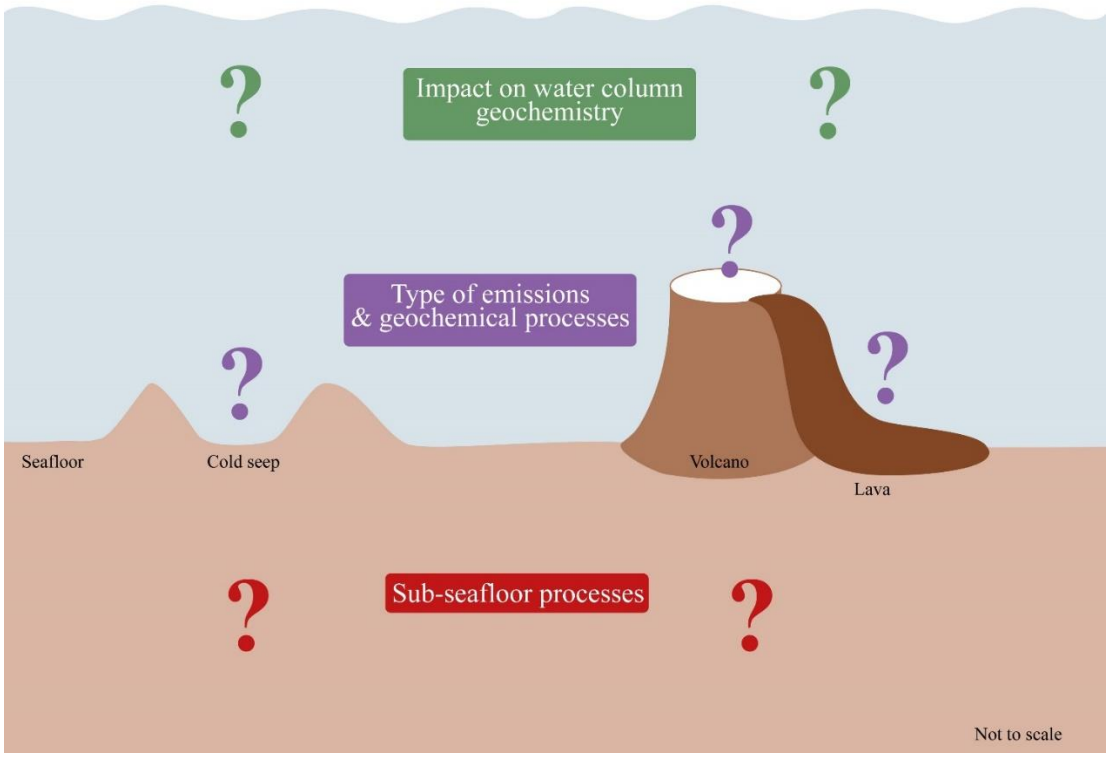

Figure 1.11. Schematic diagram of the three main objectives underlying this PhD work. This diagram is reused for the conclusion of this manuscript, in Chapter 7, and filled from the findings of this thesis.

1.3.1. Origin of the emissions observed within the water column

The first objective of this thesis is to define, within the water column, the origin of the fluid and gas discharged during an eruption. To do so, we will use helium isotopes measured from discrete water column samples taken over the area of the Fani Maoré volcanic system. Thanks to the different cruises carried out on this area, we were able to sample different periods of constructions (ongoing eruption and post-eruption at several times) and different activity manifestations (such as eruptive plume, lava flows, possible hydrothermal circulation, liquid CO_2 venting).

Helium is a noble gas released through the magmatic fluids and gases, and its non-reactive property makes it an ideal tracer of these emissions within the water column. In addition, the isotopic helium composition (also named as signature) provides valuable information on the fluid and gas origin by giving evidence of mantle-derived or crust-derived materials. Up until now, the use of helium isotopes for signature determination was performed on fluid samples and rarely in water column samples due to elevated dilution factors implying low concentrations in noble gas. Helium isotopes quantification is therefore a challenge, and requires careful sampling choices.

Helium determination is very useful when it is associated to the emissions observed in the water column (with the corresponding fluid or gas vent), and further the sub-seafloor mechanism, making the possibility to study the continuum from the endmember, and even a sub-seafloor reservoir, to the open ocean.

In this objective, we aimed to examine if there is (or not) a spatial and temporal homogeneity of the fluid signature observed in the water column. For this, we used data from sampling carried out during and after the eruptive event, as well as samples performed on various activity manifestations (e.g. liquid CO_2 degassing). A change in the water column helium signature would provides information on the change in the sub-seafloor magma or fluid path. Given the water column signature, we investigated whether the sub-seafloor mechanism responsible for the emissions can be defined.

What is the origin of the emissions within the water column?

Are there spatial and temporal variations that indicate changes in subsurface processes?

Can sub-seafloor processes be defined from water column helium signature?

1.3.2. Manifestations and geochemical processes in the water column

The second objective of this thesis consist in determining the various types of manifestation of the volcanic discharges and the geochemical processes involved. The type of manifestation includes two components: the style of manifestation and the composition of the emissions. The style of manifestation may be defined as an eruptive plume, fluid and gas released through lava-seawater interaction, hydrothermal plumes, gas bubbles, droplets. The composition of the emissions consists on the physicochemical composition, concentration in gas, metals and non-metals. The geochemical processes involved in the fluid and gas emissions may include magma degassing, lava-seawater interaction, fluid circulation, or degassing of a sub-seafloor reservoir. It has been observed that the type of the manifestation plays an important role on how the water column is affected.

To fulfill this objective, we used a large panel of data acquired during the cruises performed over the area of the Fani Maoré volcanic system. Those includes gas concentrations (H_2, CH_4, CO_2), trace metals concentrations (Fe, Mn) and physicochemical characteristics (pH, dissolved inorganic carbon, alkalinity). Gases in a volcanic system are generated through different processes, and their concentrations in the water column can give clues on the processes involved. However, the relationship between gas concentrations and processes is still unclear. For instance, iron and manganese are very good tools that could reflect lava-seawater interactions but that can also indicate the re-entrainment of seafloor deposits. The physicochemical parameters give indications on the nature of the fluid. For instance, if physicochemical parameters are acid-rich, they would indicate fluid-rock interactions. In this part, we particularly studied the link between the manifestation types and the inherent geochemical processes observed within the water column, considering different variables including the eruptive activity level, the lava freshness, the localization (i.e. the geologic setting), and the origin of the emissions.

How do volcanic emissions manifest within the water column and what are the geochemical processes involved?

What are the different type of manifestations (style and composition)?

What are the geochemical processes associated?

What is the link between the geochemical characteristics of the emissions, the geochemical processes, the eruptive activity, the geological context, and the origin of the emissions?

1.3.3. Impact on the water column geochemistry

The third objective of this thesis consist in evaluating the impact of a submarine eruption, and therefore of the fluid and volcanic gases released, on the geochemistry of the water column. To tackle this question, we focused on the carbonate system (concentration of CO_2, dissolved inorganic carbon, alkalinity) to estimate the budget of carbon released through the global ocean, evaluate the buffering power of the water column, and estimate the impact in term of acidification.

On one hand, we evaluated the impact on the water column of the Fani Maoré submarine eruption, both during and after the event. On the other hand, we estimated the impact of the exceptional released of liquid CO_2 happening at the Horseshoe structure, ~40 km from the volcano.

Over both areas, we studied the impact through time and space, and defined whether the carbon budget in the water column is increasing, diluted through export and water masses renewing, or is buffered by seawater chemical compounds. We also evaluated the relationship between the impact level and the geo-physicochemical characteristics of the emissions, considering the phase of the emissions (gas, liquid, dissolved), the chemical composition, and the flux.

What is the impact of the volcanic emissions on the water column geochemistry?

What is the impact over time and space?

How does the carbon budget evolves in the local area?

How the water column will be affected depending on the geo-physicochemical characteristics of the emission?

1.4. Structure of the manuscript

This manuscript is constituted by seven chapters. They aim to better understand the emissions released in a submarine volcanic context and their impact on the water column geochemistry.

CHAPTER 2. Geologic Setting & Context of the Study

This chapter presents the regional geological settings of the Mayotte area. It describes the main features known before the seismo-volcanic crisis, as well as the geological and seismic context

during the ongoing crisis. This chapter also includes the societal aspects and the scientific mobilization that ensues.

CHAPTER 3. Methodology

This chapter describes the different instruments used for the observation, the sampling and the analysis of the water column, as well as the analytical methods.

CHAPTER 4. Strong geochemical anomalies following active submarine eruption offshore Mayotte

In this study, we present a compilation of geochemical data taken at the Fani Maoré submarine volcano, during the main eruptive event in May 2019 and from two cruises performed in July 2019 and October 2020, leading to monitor the continuous lava flow installation. These data provide valuable information on geochemical mechanisms during the setup of a volcanic edifice and on the impact of an eruptive activity on the water column at a local scale.

CHAPTER 5. Submarine venting of liquid carbon dioxide in a volcanic context

In this study, we present a compilation of geochemical data taken above the Horseshoe degassing sites and we aim to determine the origin of the liquid CO_2 emissions observed and the relationship with the known emissions in the area. In addition, we seek to understand the geochemical processes that occur in seawater during the ascent of the liquid CO_2 droplets and, consequently, their dissolution. Furthermore, we intend to assess the impact of this dissolution on the water column, particularly concerning water column acidification across spatial scales. By closely examining the interactions between liquid CO_2 droplets and the surrounding water, we aspire to gain a deeper understanding of the environmental implications of these phenomena.

CHAPTER 6. Injection of CO_2 into the water column from the Horseshoe degassing: a numerical modeling

In this chapter, we are exploring a first approach to give an estimate of the amount of carbon dioxide injected all along the water column by the Horseshoe degassing. To this end, we use the PHREEQC geochemical software and the CO2Sys Excel Macro, and we compare *in situ* data with model results. We first perform this approach at several depths within the water column above two sites, one with venting and one without venting presence at seafloor. Then, we test the model for various sites at one depth to give a spatial analysis over the Horseshoe area. Finally, we extrapolate the estimation of the injected CO_2 for calculation of CO_2 budgets within the water column.

CHAPTER 7. Conclusions and Perspectives:

This chapter concludes with the work conducted during the course of this PhD thesis, and outlines a few perspectives of research for future work.

1.5. Bibliographical References

Achterberg, E.P., Moore, C.M., Henson, S.A., Steigenberger, S., Stohl, A., Eckhardt, S., et al. (2013). Natural iron fertilization by the Eyjafjallajökull volcanic eruption. *Geophysical Research Letters* 40(5)**,** 921-926. doi: 10.1002/grl.50221.

Agostini, S., Wada, S., Kon, K., Omori, A., Kohtsuka, H., Fujimura, H., et al. (2015). Geochemistry of two shallow CO2 seeps in Shikine Island (Japan) and their potential for ocean acidification research. *Regional Studies in Marine Science* 2**,** 45-53. doi: 10.1016/j.rsma.2015.07.004.

Aiuppa, A., Hall-Spencer, J.M., Milazzo, M., Turco, G., Caliro, S., and Di Napoli, R. (2021). Volcanic CO2 seep geochemistry and use in understanding ocean acidification. *Biogeochemistry* 152(1)**,** 93-115. doi: 10.1007/s10533-020-00737-9.

Albright, R., Takeshita, Y., Koweek, D.A., Ninokawa, A., Wolfe, K., Rivlin, T., et al. (2018). Carbon dioxide addition to coral reef waters suppresses net community calcification. *Nature* 555(7697)**,** 516-519. doi: 10.1038/nature25968.

Amend, J.P., and Shock, E.L. (2001). Energetics of overall metabolic reactions of thermophilic and hyperthermophilic Archaea and Bacteria. *FEMS Microbiology Reviews* 25(2)**,** 175-243. doi: 10.1111/j.1574-6976.2001.tb00576.x.

Apps, J.A., and Kamp, P.C.v.d. (1993). Energy gases of abiogenic origin in the Earth's crust. *United States Geological Survey, Professional Paper; (United States)* 1570**,** Medium: X; Size: Pages: 81-132.

Ayache, M., Dutay, J.C., Jean-Baptiste, P., and Fourré, E. (2015). Simulation of the mantle and crustal helium isotope signature in the Mediterranean Sea using a high-resolution regional circulation model. *Ocean Science* 11(6)**,** 965-978. doi: 10.5194/os-11-965-2015.

Bach, W., and Edwards, K.J. (2003). Iron and sulfide oxidation within the basaltic ocean crust: implications for chemolithoautotrophic microbial biomass production. *Geochimica et Cosmochimica Acta* 67(20)**,** 3871-3887. doi: 10.1016/S0016-7037(03)00304-1.

Baker, E.T. (1998). Patterns of event and chronic hydrothermal venting following a magmatic intrusion: new perspectives from the 1996 Gorda Ridge eruption. *Deep Sea Research Part II: Topical Studies in Oceanography* 45(12)**,** 2599-2618. doi: 10.1016/S0967-0645(98)00085-X.

Baker, E.T., Chadwick, W.l.l.i.W.J., Cowen, J.P., Dziak, R.P., Rubin, K.H., and Fornari, D.J. (2012). Hydrothermal Discharge During Submarine Eruptions The Importance of Detection, Response, and New Technology. *Oceanography* 25(1)**,** 128-141. doi: 10.5670/oceanog.2012.11.

Baker, E.T., German, C.R., and Elderfield, H. (1995). "Hydrothermal Plumes Over Spreading-Center Axes: Global Distributions and Geological Inferences," in *Seafloor Hydrothermal Systems: Physical, Chemical, Biological, and Geological Interactions*.), 47-71.

Baker, E.T., Lowell, R.P., Resing, J.A., Feely, R.A., Embley, R.W., Massoth, G.J., et al. (2004). Decay of hydrothermal output following the 1998 seafloor eruption at Axial Volcano: Observations and models. *Journal of Geophysical Research: Solid Earth* 109(B1). doi: 10.1029/2003jb002618.

Baker, E.T., Lupton, J.E., Resing, J.A., Baumberger, T., Lilley, M.D., Walker, S.L., et al. (2011).

Unique event plumes from a 2008 eruption on the Northeast Lau Spreading Center. *Geochemistry, Geophysics, Geosystems* 12(9). doi: 10.1029/2011gc003725.

Baker, E.T., Massoth, G.J., and Feely, R.A. (1987). Cataclysmic hydrothermal venting on the Juan de Fuca Ridge. *Nature* 329(6135)**,** 149-151. doi: 10.1038/329149a0.

Baker, E.T., McDuff, R.E., and Massoth, G.J. (1990). Hydrothermal venting from the summit of a ridge axis Seamount: Axial Volcano, Juan de Fuca Ridge. *Journal of Geophysical Research* 95(B8)**,** 12843. doi: 10.1029/jb095ib08p12843.

Ballentine, C.J., and Burnard, P.G. (2002). Production, Release and Transport of Noble Gases in the Continental Crust. *Reviews in Mineralogy and Geochemistry* 47(1)**,** 481-538. doi: 10.2138/rmg.2002.47.12.

Batiza, R., and Vanko, D. (1983). Volcanic development of small oceanic central volcanoes on the flanks of the East Pacific Rise inferred from narrow-beam echo-sounder surveys. *Marine Geology* 54(1)**,** 53-90. doi: 10.1016/0025-3227(83)90008-7.

Baumberger, T., Lilley, M.D., Lupton, J.E., Baker, E.T., Resing, J.A., Buck, N.J., et al. (2020). Dissolved Gas and Metal Composition of Hydrothermal Plumes From a 2008 Submarine Eruption on the Northeast Lau Spreading Center. *Frontiers in Marine Science* 7. doi: 10.3389/fmars.2020.00171.

Baumberger, T., Lilley, M.D., Resing, J.A., Lupton, J.E., Baker, E.T., Butterfield, D.A., et al. (2014). Understanding a submarine eruption through time series hydrothermal plume sampling of dissolved and particulate constituents: West Mata, 2008-2012. *Geochemistry, Geophysics, Geosystems* 15(12)**,** 4631-4650. doi: 10.1002/2014gc005460.

Begét, J. (2000). "Volcanic tsunamis," in *Encyclopedia of volcanoes,* ed. H.B. Sigurdsson H, Mc Nutt SR, Rymer H, Stix J. (New York: Academic Press), 1005-1013.

Bennett, S.A., Achterberg, E.P., Connelly, D.P., Statham, P.J., Fones, G.R., and German, C.R. (2008). The distribution and stabilisation of dissolved Fe in deep-sea hydrothermal plumes. *Earth and Planetary Science Letters* 270(3-4)**,** 157-167. doi: 10.1016/j.epsl.2008.01.048.

Benson, B.B., and Krause, D. (1980). Isotopic fractionation of helium during solution: A probe for the liquid state. *Journal of Solution Chemistry* 9(12)**,** 895-909. doi: 10.1007/bf00646402.

Boatta, F., D'Alessandro, W., Gagliano, A.L., Liotta, M., Milazzo, M., Rodolfo-Metalpa, R., et al. (2013). Geochemical survey of Levante Bay, Vulcano Island (Italy), a natural laboratory for the study of ocean acidification. *Marine Pollution Bulletin* 73(2)**,** 485-494. doi: 10.1016/j.marpolbul.2013.01.029.

Bond, D.P.G., Wignall, P.B., Keller, G., and Kerr, A.C. (2014). "Large igneous provinces and mass extinctions: An update," in *Volcanism, Impacts, and Mass Extinctions: Causes and Effects*. Geological Society of America).

Boyd, C.E. (2015). "pH, Carbon Dioxide, and Alkalinity." Springer International Publishing), 153-178.

Boyd, T., and Scott, S. (2001). Microbial and hydrothermal aspects of ferric oxyhydroxides and ferrosic hydroxides: the example of Franklin Seamount, Western Woodlark Basin, Papua New Guinea. *Geochemical Transactions* 2(1). doi: 10.1186/1467-4866-2-45.

Brennwald, M.S., Vogel, N., Scheidegger, Y., Tomonaga, Y., Livingstone, D.M., and Kipfer, R. (2013). "Noble Gases as Environmental Tracers in Sediment Porewaters and Stalagmite Fluid Inclusions," in *The Noble Gases as Geochemical Tracers,* ed. P. Burnard. (Berlin, Heidelberg: Springer Berlin Heidelberg), 123-153.

Buck, N.J., Resing, J.A., Baker, E.T., and Lupton, J.E. (2018). Chemical Fluxes From a Recently Erupted Shallow Submarine Volcano on the Mariana Arc. *Geochemistry, Geophysics, Geosystems* 19(5)**,** 1660-1673. doi: 10.1029/2018gc007470.

Butterfield, D.A., Jonasson, I.R., Massoth, G.J., Feely, R.A., Roe, K.K., Embley, R.E., et al. (1997). Seafloor eruptions and evolution of hydrothermal fluid chemistry. *Philosophical Transactions of the Royal Society of London. Series A: Mathematical, Physical and Engineering Sciences* 355(1723)**,** 369-386. doi: doi:10.1098/rsta.1997.0013.

Butterfield, D.A., Nakamura, K.i., Takano, B., Lilley, M.D., Lupton, J.E., Resing, J.A., et al. (2011). High SO2 flux, sulfur accumulation, and gas fractionation at an erupting submarine volcano. *Geology* 39(9)**,** 803-806. doi: 10.1130/g31901.1.

Carey, S., Ballard, R., Bell, K.L.C., Bell, R.J., Connally, P., Dondin, F., et al. (2014). Cold seeps associated with a submarine debris avalanche deposit at Kick'em Jenny volcano, Grenada (Lesser Antilles). *Deep Sea Research Part I: Oceanographic Research Papers* 93**,** 156-160. doi: 10.1016/j.dsr.2014.08.002.

Carey, S., Nomikou, P., Bell, K.C., Lilley, M., Lupton, J., Roman, C., et al. (2013). CO2 degassing from hydrothermal vents at Kolumbo submarine volcano, Greece, and the accumulation of acidic crater water. *Geology* 41(9)**,** 1035-1038. doi: 10.1130/g34286.1.

Carey, S., Olsen, R., Bell, K.L.C., Ballard, R., Dondin, F., Roman, C., et al. (2016). Hydrothermal venting and mineralization in the crater of Kick'em Jenny submarine volcano, Grenada (Lesser Antilles). *Geochemistry, Geophysics, Geosystems* 17(3)**,** 1000-1019. doi: 10.1002/2015gc006060.

Cas, R.A.F., and Giordano, G. (2014). Submarine Volcanism: a Review of the Constraints, Processes and Products, and Relevance to the Cabo de Gata Volcanic Succession. *Italian Journal of Geosciences* 133(3)**,** 362-377. doi: 10.3301/Ijg.2014.46.

Cas, R.A.F., and Simmons, J.M. (2018). Why Deep-Water Eruptions Are So Different From Subaerial Eruptions. *Frontiers in Earth Science* 6. doi: 10.3389/feart.2018.00198.

Chadwick, W.W., Cashman, K.V., Embley, R.W., Matsumoto, H., Dziak, R.P., De Ronde, C.E.J., et al. (2008). Direct video and hydrophone observations of submarine explosive eruptions at NW Rota-1 volcano, Mariana arc. *Journal of Geophysical Research: Solid Earth* 113(B8). doi: 10.1029/2007jb005215.

Chadwick, W.W., Merle, S.G., Buck, N.J., Lavelle, J.W., Resing, J.A., and Ferrini, V. (2014). Imaging of CO2bubble plumes above an erupting submarine volcano, NW Rota-1, Mariana Arc. *Geochemistry, Geophysics, Geosystems* 15(11)**,** 4325-4342. doi: 10.1002/2014gc005543.

Chadwick, W.W., Rubin, K.H., Merle, S.G., Bobbitt, A.M., Kwasnitschka, T., and Embley, R.W. (2019). Recent Eruptions Between 2012 and 2018 Discovered at West Mata Submarine Volcano (NE Lau Basin, SW Pacific) and Characterized by New Ship, AUV, and ROV Data. *Frontiers in Marine Science* 6. doi: 10.3389/fmars.2019.00495.

Charlou, J.L., Donval, J.P., Konn, C., OndréAs, H., Fouquet, Y., Jean-Baptiste, P., et al. (2010). "High production and fluxes of H2 and CH4 and evidence of abiotic hydrocarbon synthesis by serpentinization in ultramafic-hosted hydrothermal systems on the Mid-Atlantic Ridge," in *Diversity Of Hydrothermal Systems On Slow Spreading Ocean Ridges*.), 265-296.

Cheminée, J.L., Stoffers, P., McMurtry, G., Richnow, H., Puteanus, D., and Sedwick, P. (1991). Gas-rich submarine exhalations during the 1989 eruption of Macdonald Seamount. *Earth and Planetary Science Letters* 107(2)**,** 318-327. doi: 10.1016/0012-821x(91)90079-w.

Christie, D.M., Carmichael, I.S.E., and Langmuir, C.H. (1986). Oxidation states of mid-ocean ridge basalt glasses. *Earth and Planetary Science Letters* 79(3)**,** 397-411. doi: 10.1016/0012-821X(86)90195-0.

Clague, D.A., Paduan, J.B., Caress, D.W., Thomas, H., Chadwick, W.W., and Merle, S.G. (2011). Volcanic morphology of West Mata Volcano, NE Lau Basin, based on high-resolution bathymetry and depth changes. *Geochemistry, Geophysics, Geosystems* 12(11)**,** n/a-n/a. doi: 10.1029/2011gc003791.

Clarke, W.B., Jenkins, W.J., and Top, Z. (1976). Determination of tritium by mass spectrometric measurement of 3He. *The International Journal of Applied Radiation and Isotopes* 27(9)**,** 515-522. doi: 10.1016/0020-708x(76)90082-x.

Connell, L., Barrett, A., Templeton, A., and Staudigel, H. (2009). Fungal Diversity Associated with an Active Deep Sea Volcano: Vailulu'u Seamount, Samoa. *Geomicrobiology Journal* 26(8)**,** 597-605. doi: 10.1080/01490450903316174.

Courtillot, V., Féraud, G., Maluski, H., Vandamme, D., Moreau, M.G., and Besse, J. (1988). Deccan flood basalts and the Cretaceous/Tertiary boundary. *Nature* 333(6176)**,** 843-846. doi: 10.1038/333843a0.

Cowen, J.P., Fornari, D.J., Shank, T.M., Love, B., Glazer, B., Treusch, A., et al. (2007). Volcanic Eruptions at East Pacific Rise Near 9°50′N. *Eos, Transactions American Geophysical Union* 88(7)**,** 81. doi: 10.1029/2007eo070001.

Cowen, J.P., Massoth, G.J., and Feely, R.A. (1990). Scavenging rates of dissolved manganese in a hydrothermal vent plume. *Deep Sea Research Part A. Oceanographic Research Papers* 37(10)**,** 1619-1637. doi: 10.1016/0198-0149(90)90065-4.

Craig, H. (1953). The geochemistry of the stable carbon isotopes. *Geochimica et Cosmochimica Acta* 3(2)**,** 53-92. doi: 10.1016/0016-7037(53)90001-5.

Craig, H., and Lupton, J.E. (1981). Helium-3 and mantle volatiles in the ocean and the oceanic crust. *The oceanic lithosphere* 7**,** 391.

Craig, H., and Weiss, R.F. (1971). Dissolved gas saturation anomalies and excess helium in the ocean. *Earth and Planetary Science Letters* 10(3)**,** 289-296. doi: 10.1016/0012-821X(71)90033-1.

Dando, P.R., Hughes, J.A., Leahy, Y., Niven, S.J., Taylor, L.J., and Smith, C. (1995). Gas venting rates from submarine hydrothermal areas around the island of Milos, Hellenic Volcanic Arc. *Continental Shelf Research* 15(8)**,** 913-929. doi: 10.1016/0278-4343(95)80002-u.

Davis, A.S., and Clague, D.A. (1998). Changes in the hydrothermal system at Loihi Seamount after the formation of Pele's pit in 1996. *Geology* 26(5)**,** 399-402. doi: 10.1130/0091-7613(1998)026<0399:Cithsa>2.3.Co;2.

De Baar H. J, W. (2001). Distributions, sources and sinks of iron in seawater. *The Biogeochemistry of iron in seawater*.

De Ronde, C.E., Faure, K., Bray, C.J., Chappell, D.A., and Wright, I.C. (2003). Hydrothermal fluids associated with seafloor mineralization at two southern Kermadec arc volcanoes, offshore New Zealand. *Mineralium Deposita* 38(2)**,** 217-233. doi: 10.1007/s00126-002-0305-4.

De Ronde, C.E.J., Hannington, M.D., Stoffers, P., Wright, I.C., Ditchburn, R.G., Reyes, A.G., et al. (2005). Evolution of a Submarine Magmatic-Hydrothermal System: Brothers Volcano, Southern Kermadec Arc, New Zealand. *Economic Geology* 100(6)**,** 1097-1133. doi: 10.2113/gsecongeo.100.6.1097.

De Ronde, C.E.J., Humphris, S.E., Höfig, T.W., and Reyes, A.G. (2019). Critical role of caldera collapse in the formation of seafloor mineralization: The case of Brothers volcano. *Geology* 47(8)**,** 762-766. doi: 10.1130/g46047.1.

De Ronde, C.E.J., Massoth, G.J., Butterfield, D.A., Christenson, B.W., Ishibashi, J., Ditchburn, R.G., et al. (2011). Submarine hydrothermal activity and gold-rich mineralization at Brothers Volcano, Kermadec Arc, New Zealand. *Mineralium Deposita* 46(5-6)**,** 541-584. doi: 10.1007/s00126-011-0345-8.

De Soto, N.A., Delorme, N., Atkins, J., Howard, S., Williams, J., and Johnson, M. (2013). Anthropogenic noise causes body malformations and delays development in marine larvae. *Scientific Reports* 3(1). doi: 10.1038/srep02831.

Deardorff, N.D., Cashman, K.V., and Chadwick, W.W. (2011). Observations of eruptive plume dynamics and pyroclastic deposits from submarine explosive eruptions at NW Rota-1, Mariana arc. *Journal of Volcanology and Geothermal Research* 202(1)**,** 47-59. doi: 10.1016/j.jvolgeores.2011.01.003.

Dick, G.J., Anantharaman, K., Baker, B.J., Li, M., Reed, D.C., and Sheik, C.S. (2013). The microbiology of deep-sea hydrothermal vent plumes: ecological and biogeographic linkages to seafloor and water column habitats. *Front Microbiol* 4**,** 124. doi: 10.3389/fmicb.2013.00124.

Dickson, A.G. (1981). An exact definition of total alkalinity and a procedure for the estimation of alkalinity and total inorganic carbon from titration data. *Deep Sea Research Part A. Oceanographic Research Papers* 28(6)**,** 609-623. doi: 10.1016/0198-0149(81)90121-7.

Dickson, A.G., Sabine, C.L., and Christian, J.R. (2007). "Guide to best practices for ocean CO2 measurements", in: *PICES Special Publication 3, IOCCP Report 8*. (North Pacific Marine Science Organization, Sidney, British Columbia).

Doney, S.C., Busch, D.S., Cooley, S.R., and Kroeker, K.J. (2020). The Impacts of Ocean Acidification on Marine Ecosystems and Reliant Human Communities. *Annual Review of Environment and Resources* 45(1)**,** 83-112. doi: 10.1146/annurev-environ-012320-083019.

Dzaugis, M.E., Spivack, A.J., Dunlea, A.G., Murray, R.W., and D'Hondt, S. (2016). Radiolytic Hydrogen Production in the Subseafloor Basaltic Aquifer. *Frontiers in Microbiology* 7. doi: 10.3389/fmicb.2016.00076.

Dziak, R.P., Bohnenstiehl, D.R., Baker, E.T., Matsumoto, H., Caplan-Auerbach, J., Embley, R.W., et al. (2015). Long-term explosive degassing and debris flow activity at West Mata submarine volcano. *Geophysical Research Letters* 42(5)**,** 1480-1487. doi: 10.1002/2014gl062603.

Dziak, R.P., Bohnenstiehl, D.R., Cowen, J.P., Baker, E.T., Rubin, K.H., Haxel, J.H., et al. (2007). Rapid dike emplacement leads to eruptions and hydrothermal plume release during seafloor spreading events. *Geology* 35(7)**,** 579-582. doi: 10.1130/g23476a.1.

Dziak, R.P., Bohnenstiehl, D.R., Matsumoto, H., Fowler, M.J., Haxel, J.H., Tolstoy, M., et al. (2009). January 2006 seafloor-spreading event at 9°50′N, East Pacific Rise: Ridge dike intrusion and transform fault interactions from regional hydroacoustic data. *Geochemistry, Geophysics, Geosystems* 10(6)**,** n/a-n/a. doi: 10.1029/2009gc002388.

Edwards, K.J., Glazer, B.T., Rouxel, O.J., Bach, W., Emerson, D., Davis, R.E., et al. (2011). Ultra-diffuse hydrothermal venting supports Fe-oxidizing bacteria and massive umber deposition at 5000 m off Hawaii. *The ISME Journal* 5(11)**,** 1748-1758. doi: 10.1038/ismej.2011.48.

Egleston, E.S., Sabine, C.L., and Morel, F.M.M. (2010). Revelle revisited: Buffer factors that quantify the response of ocean chemistry to changes in DIC and alkalinity. *Global Biogeochemical Cycles* 24(1)**,** n/a-n/a. doi: 10.1029/2008gb003407.

Embley, R.W., Chadwick, W.W., Baker, E.T., Butterfield, D.A., Resing, J.A., de Ronde, C.E.J., et al. (2006). Long-term eruptive activity at a submarine arc volcano. *Nature* 441(7092)**,** 494-497. doi: 10.1038/nature04762.

Embley, R.W., Merle, S.G., Baker, E.T., Rubin, K.H., Lupton, J.E., Resing, J.A., et al. (2014). Eruptive modes and hiatus of volcanism at West Mata seamount, NE Lau basin: 1996-2012. *Geochemistry, Geophysics, Geosystems* 15(10)**,** 4093-4115. doi: 10.1002/2014gc005387.

Embley, R.W., and Rubin, K.H. (2018). Extensive young silicic volcanism produces large deep submarine lava flows in the NE Lau Basin. *Bulletin of Volcanology* 80(4). doi: 10.1007/s00445-018-1211-7.

Emerson, S., and Hedges, J. (2008). *Chemical Oceanography and the Marine Carbon Cycle*.

Fabricius, K.E., Langdon, C., Uthicke, S., Humphrey, C., Noonan, S., De'Ath, G., et al. (2011). Losers and winners in coral reefs acclimatized to elevated carbon dioxide concentrations. *Nature Climate Change* 1(3)**,** 165-169. doi: 10.1038/nclimate1122.

Feuillet, N., Jorry, S., Crawford, W.C., Deplus, C., Thinon, I., Jacques, E., et al. (2021). Birth of a large volcanic edifice offshore Mayotte via lithosphere-scale dyke intrusion. *Nature Geoscience* 14**,** 787-795. doi: 10.1038/s41561-021-00809-x.

Fiebig, J., Chiodini, G., Caliro, S., Rizzo, A., Spangenberg, J., and Hunziker, J.C. (2004). Chemical and isotopic equilibrium between CO2 and CH4 in fumarolic gas discharges: Generation of CH4 in arc magmatic-hydrothermal systems 1 1Associate editor: M. Kusakabe. *Geochimica et Cosmochimica Acta* 68(10)**,** 2321-2334. doi: 10.1016/j.gca.2003.10.035.

Field, M.P., and Sherrell, R.M. (2000). Dissolved and particulate Fe in a hydrothermal plume at 9°45′N, East Pacific Rise. *Geochimica et Cosmochimica Acta* 64(4)**,** 619-628. doi: 10.1016/s0016-7037(99)00333-6.

Fischer, T.P. (2008). Fluxes of volatiles (H2O, CO2, N2, Cl, F) from arc volcanoes. *GEOCHEMICAL JOURNAL* 42(1)**,** 21-38. doi: 10.2343/geochemj.42.21.

Fischer, T.P., and Aiuppa, A. (2020). AGU Centennial Grand Challenge: Volcanoes and Deep Carbon Global CO2 Emissions From Subaerial Volcanism—Recent Progress and Future Challenges. *Geochemistry,*

Geophysics, Geosystems 21(3). doi: 10.1029/2019gc008690.

Fitzsimmons, J.N., John, S.G., Marsay, C.M., Hoffman, C.L., Sarah, Toner, B.M., et al. (2017). Iron persistence in a distal hydrothermal plume supported by dissolved–particulate exchange. *Nature Geoscience* 10(3)**,** 195-201. doi: 10.1038/ngeo2900.

Fornari, D.J., Von Damm, K.L., Bryce, J.G., Cowen, J.P., Ferrini, V., Fundis, A., et al. (2012). The East Pacific Rise Between 9°N and 10°N: Twenty-five years of integrated, multidisciplinary oceanic spreading center studies. *Oceanography* 25(1)**,** 18-43.

Gallant, R.M., and Von Damm, K.L. (2006). Geochemical controls on hydrothermal fluids from the Kairei and Edmond Vent Fields, 23°-25°S, Central Indian Ridge. *Geochemistry, Geophysics, Geosystems* 7(6)**,** n/a-n/a. doi: 10.1029/2005gc001067.

Garcia, M.O., Caplan-Auerbach, J., De Carlo, E.H., Kurz, M.D., and Becker, N. (2006). Geology, geochemistry and earthquake history of Lòihi Seamount, Hawaìi's youngest volcano. *Geochemistry* 66(2)**,** 81-108. doi: 10.1016/j.chemer.2005.09.002.

Gautheron, C., and Moreira, M. (2002). Helium signature of the subcontinental lithospheric mantle. *Earth and Planetary Science Letters* 199(1)**,** 39-47. doi: 10.1016/S0012-821X(02)00563-0.

German, C.R., and Seyfried, W.E. (2014). "8.7 - Hydrothermal Processes," in *Treatise on Geochemistry (Second Edition)*, eds. H.D. Holland & K.K. Turekian. (Oxford: Elsevier), 191-233.

German, C.R., and Von Damm, K.L. (2004). "Hydrothermal processes," in *Treatise on geochemistry, Vol. 6. The oceans and marine geochemistry*, eds. H.D. Holland, K.K. Turekian & H. Elderfield. Elsevier-Pergamon), 181-222.

Giggenbach, W. (1997). The origin and evolution of fluids in magmatic-hydrothermal systems. *Geochemistry of hydrothermal ore deposits*.

Glazer, B.T., and Rouxel, O.J. (2009). Redox Speciation and Distribution within Diverse Iron-dominated Microbial Habitats at Loihi Seamount. *Geomicrobiology Journal* 26(8)**,** 606-622. doi: 10.1080/01490450903263392.

González-Delgado, S., and Hernández, J.C. (2018). "Chapter Two - The Importance of Natural Acidified Systems in the Study of Ocean Acidification: What Have We Learned?," in *Advances in Marine Biology*, ed. C. Sheppard. Academic Press), 57-99.

González, F.J., Rincón-Tomás, B., Somoza, L., Santofimia, E., Medialdea, T., Madureira, P., et al. (2020). Low-temperature, shallow-water hydrothermal vent mineralization following the recent submarine eruption of Tagoro volcano (El Hierro, Canary Islands). *Marine Geology* 430**,** 106333. doi: 10.1016/j.margeo.2020.106333.

Graham, D.W. (2002). Noble Gas Isotope Geochemistry of Mid-Ocean Ridge and Ocean Island Basalts: Characterization of Mantle Source Reservoirs. *Reviews in Mineralogy and Geochemistry* 47(1)**,** 247-317. doi: 10.2138/rmg.2002.47.8.

Guieu, C., Bonnet, S., Petrenko, A., Menkes, C., Chavagnac, V., Desboeufs, K., et al. (2018). Iron from a submarine source impacts the productive layer of the Western Tropical South Pacific (WTSP). *Scientific Reports* 8(1). doi: 10.1038/s41598-018-27407-z.

Hall-Spencer, J.M., and Harvey, B.P. (2019). Ocean acidification impacts on coastal ecosystem services due to habitat degradation. *Emerging Topics in Life Sciences* 3(2)**,** 197-206. doi: 10.1042/etls20180117.

Hawco, N.J., Yang, S.-C., Foreman, R.K., Funkey, C.P., Dugenne, M., White, A.E., et al. (2020). Metal isotope signatures from lava-seawater interaction during the 2018 eruption of Kīlauea. *Geochimica et Cosmochimica Acta* 282**,** 340-356. doi: 10.1016/j.gca.2020.05.005.

Herzig, P.M., Hannington, M.D., and Arribas Jr, A. (1998). Sulfur isotopic composition of hydrothermal precipitates from the Lau back-arc: implications for magmatic contributions to seafloor hydrothermal systems. *Mineralium Deposita* 33(3)**,** 226-237. doi: 10.1007/s001260050143.

Hilton, D.R. (1996). The helium and carbon isotope systematics of a continental geothermal system: results from monitoring studies at Long Valley caldera (California, U.S.A.). *Chemical Geology* 127(4)**,** 269-295. doi: 10.1016/0009-2541(95)00134-4.

Hilton, D.R., Fischer, T.P., and Marty, B. (2002). Noble Gases and Volatile Recycling at Subduction Zones. *Reviews in Mineralogy and Geochemistry* 47(1)**,** 319-370. doi: 10.2138/rmg.2002.47.9.

Hilton, D.R., and Porcelli, D. (2003). "2.06 - Noble Gases as Mantle Tracers," in *Treatise on Geochemistry*, eds. H.D. Holland & K.K. Turekian. (Oxford: Pergamon), 277-318.

Hirose, T., Kawagucci, S., and Suzuki, K. (2011). Mechanoradical H2 generation during simulated faulting: Implications for an earthquake-driven subsurface biosphere. *Geophysical Research Letters* 38(17)**,** n/a-n/a. doi: 10.1029/2011gl048850.

Honjo, S., Eglinton, T.I., Taylor, C.D., Ulmer, K.M., Sievert, S.M., Bracher, A., et al. (2014). Understanding the role of the biological pump in the global carbon cycle: An Imperative for Ocean Science. *Oceanography* 27(3)**,** 10-16.

Hoshyaripour, G., Hort, M., and Langmann, B. (2012). How does the hot core of a volcanic plume control the sulfur speciation in volcanic emission? *Geochemistry, Geophysics, Geosystems* 13(7)**,** n/a-n/a. doi: 10.1029/2011gc004020.

Houghton, R.A. (2014). "10.10 - The Contemporary Carbon Cycle," in *Treatise on Geochemistry (Second Edition)*, eds. H.D. Holland & K.K. Turekian. (Oxford: Elsevier), 399-435.

Hull, P.M., Bornemann, A., Penman, D.E., Henehan, M.J., Norris, R.D., Wilson, P.A., et al. (2020). On impact and volcanism across the Cretaceous-Paleogene boundary. *Science* 367(6475)**,** 266-272. doi: doi:10.1126/science.aay5055.

Jannasch, H.W., and Wirsen, C.O. (1979). Chemosynthetic Primary Production at East Pacific Sea Floor Spreading Centers. *BioScience* 29(10)**,** 592-598. doi: 10.2307/1307765.

Jean-Baptiste, P., Charlou, J.L., Stievenard, M., Donval, J.P., Bougault, H., and Mevel, C. (1991a). Helium and methane measurements in hydrothermal fluids from the mid-Atlantic ridge: The Snake Pit site at 23°N. *Earth and Planetary Science Letters* 106(1)**,** 17-28. doi: 10.1016/0012-821X(91)90060-U.

Jean-Baptiste, P., Mantisi, F., Mémery, L., and Jamous, D. (1991b). 3He and chlorofluorocarbons (CFC) in the Southern Ocean: tracers of water masses. *Marine Chemistry* 35(1)**,** 137-150. doi: 10.1016/S0304-4203(09)90013-5.

Jenkins, W.J., and Clarke, W.B. (1976). The distribution of 3He in the western Atlantic ocean. *Deep Sea Research and Oceanographic Abstracts* 23(6)**,** 481-494. doi: 10.1016/0011-7471(76)90860-3.

Jenkins, W.J., Doney, S.C., Fendrock, M., Fine, R., Gamo, T., Jean-Baptiste, P., et al. (2019). A comprehensive global oceanic dataset of helium isotope and tritium measurements. *Earth System Science Data* 11(2)**,** 441-454. doi: 10.5194/essd-11-441-2019.

Jørgensen, B.B., and D'Hondt, S. (2006). A Starving Majority Deep Beneath the Seafloor. *Science* 314(5801)**,** 932-934. doi: 10.1126/science.1133796.

Karl, D.M., McMurtry, G.M., Malahoff, A., and Garcia, M.O. (1988). Loihi Seamount, Hawaii: a mid-plate volcano with a distinctive hydrothermal system. *Nature* 335(6190)**,** 532-535. doi: 10.1038/335532a0.

Kawagucci, S., Okamura, K., Kiyota, K., Tsunogai, U., Sano, Y., Tamaki, K., et al. (2008). Methane, manganese, and helium-3 in newly discovered hydrothermal plumes over the Central Indian Ridge, 18°-20°S. *Geochemistry, Geophysics, Geosystems* 9(10). doi: 10.1029/2008gc002082.

Kelley, D.S., Baross, J.A., and Delaney, J.R. (2002). Volcanoes, Fluids, and Life at Mid-Ocean Ridge Spreading Centers. *Annual Review of Earth and Planetary Sciences* 30(1)**,** 385-491. doi: 10.1146/annurev.earth.30.091201.141331.

Kelley, D.S., Delaney, J.R., and Juniper, S.K. (2014). Establishing a new era of submarine volcanic observatories: Cabling Axial Seamount and the Endeavour Segment of the Juan de Fuca Ridge. *Marine Geology* 352**,** 426-450. doi: 10.1016/j.margeo.2014.03.010.

Kennedy, C.B., Scott, S.D., and Ferris, F.G. (2003). Characterization of Bacteriogenic Iron Oxide Deposits from Axial Volcano, Juan de Fuca Ridge, Northeast Pacific Ocean. *Geomicrobiology Journal* 20(3)**,** 199-214. doi: 10.1080/01490450303873.

Kilias, S.P., Nomikou, P., Papanikolaou, D., Polymenakou, P.N., Godelitsas, A.,

Argyraki, A., et al. (2013). New insights into hydrothermal vent processes in the unique shallow-submarine arc-volcano, Kolumbo (Santorini), Greece. *Scientific Reports* 3(1). doi: 10.1038/srep02421.

Kita, I., Matsuo, S., and Wakita, H. (1982). H2 generation by reaction between H2O and crushed rock: An experimental study on H2 degassing from the active fault zone. *Journal of Geophysical Research: Solid Earth* 87(B13)**,** 10789-10795. doi: 10.1029/jb087ib13p10789.

Klinkhammer, G., Rona, P., Greaves, M., and Elderfield, H. (1985). Hydrothermal manganese plumes in the Mid-Atlantic Ridge rift valley. *Nature* 314(6013)**,** 727-731. doi: 10.1038/314727a0.

Konno, U., Tsunogai, U., Nakagawa, F., Nakaseama, M., Ishibashi, J.-I., Nunoura, T., et al. (2006). Liquid CO2 venting on the seafloor: Yonaguni Knoll IV hydrothermal system, Okinawa Trough. *Geophysical Research Letters* 33(16). doi: 10.1029/2006gl026115.

Labidi, J., Cartigny, P., and Jackson, M.G. (2015). Multiple sulfur isotope composition of oxidized Samoan melts and the implications of a sulfur isotope 'mantle array' in chemical geodynamics. *Earth and Planetary Science Letters* 417**,** 28-39. doi: 10.1016/j.epsl.2015.02.004.

Langmann, B., Zaksek, K., and Hort, M. (2010a). Atmospheric distribution and removal of volcanic ash after the eruption of Kasatochi volcano: A regional model study. *Journal of Geophysical Research-Atmospheres* 115. doi: 10.1029/2009jd013298.

Langmann, B., Zakšek, K., Hort, M., and Duggen, S. (2010b). Volcanic ash as fertiliser for the surface ocean. *Atmos. Chem. Phys.* 10(8)**,** 3891-3899. doi: 10.5194/acp-10-3891-2010.

Le Moigne, F.A.C. (2019). Pathways of Organic Carbon Downward Transport by the Oceanic Biological Carbon Pump. *Frontiers in Marine Science* 6. doi: 10.3389/fmars.2019.00634.

Lemasson, A.J., Hall-Spencer, J.M., Kuri, V., and Knights, A.M. (2019). Changes in the biochemical and nutrient composition of seafood due to ocean acidification and warming. *Marine Environmental Research* 143**,** 82-92. doi: 10.1016/j.marenvres.2018.11.006.

Li, J., Roche, B., Bull, J.M., White, P.R., Davis, J.W., Deponte, M., et al. (2020). Passive acoustic monitoring of a natural CO2 seep site – Implications for carbon capture and storage. *International Journal of Greenhouse Gas Control* 93**,** 102899. doi: 10.1016/j.ijggc.2019.102899.

Li, M., Toner, B.M., Baker, B.J., Breier, J.A., Sheik, C.S., and Dick, G.J. (2014). Microbial iron uptake as a mechanism for dispersing iron from deep-sea hydrothermal vents. *Nat Commun* 5. doi: 10.1038/ncomms4192.

Lindsay, J.M., Shepherd, J.B., and Wilson, D. (2005). Volcanic and Scientific Activity at Kick 'em Jenny Submarine Volcano 2001-2002: Implications for Volcanic Hazard in the Southern Grenadines, Lesser Antilles. *Natural Hazards* 34(1)**,** 1-24. doi: 10.1007/s11069-004-1566-2.

Longman, J., Palmer, M.R., Gernon, T.M., Manners, H.R., and Jones, M.T. (2022). Subaerial volcanism is a potentially major contributor to oceanic iron and manganese cycles. *Communications Earth & Environment* 3(1). doi: 10.1038/s43247-022-00389-7.

Lowenstern, J. (2001). Carbon dioxide in magmas and implications for hydrothermal systems. *Mineralium Deposita* 36(6)**,** 490-502. doi: 10.1007/s001260100185.

Lupton, J. (1998). Hydrothermal helium plumes in the Pacific Ocean. *Journal of Geophysical Research: Oceans* 103(C8)**,** 15853-15868. doi: 10.1029/98jc00146.

Lupton, J., Butterfield, D., Lilley, M., Evans, L., Nakamura, K.-I., Chadwick, W., et al. (2006). Submarine venting of liquid carbon dioxide on a Mariana Arc volcano. *Geochemistry, Geophysics, Geosystems* 7(8). doi: 10.1029/2005gc001152.

Lupton, J., Lilley, M., Butterfield, D., Evans, L., Embley, R., Massoth, G., et al. (2008). Venting of a separate CO2-rich gas phase from submarine arc volcanoes: Examples from the Mariana and Tonga-Kermadec arcs. *Journal of Geophysical Research: Solid Earth* 113(B8). doi: 10.1029/2007jb005467.

Lupton, J.E. (1979). Helium-3 in the Guaymas Basin: Evidence for injection of mantle volatiles in the Gulf of California. *Journal of*

Geophysical Research: Solid Earth 84(B13)**,** 7446-7452. doi: 10.1029/jb084ib13p07446.

Lupton, J.E. (1983). TERRESTRIAL INERT GASES: Isotope Tracer Studies and Clues to Primordial Components in the Mantle. *Annual Review of Earth and Planetary Sciences* 11(1)**,** 371-414. doi: 10.1146/annurev.ea.11.050183.002103.

Lupton, J.E., Weiss, R.F., and Craig, H. (1977a). Mantle helium in hydrothermal plumes in the Galapagos Rift. *Nature* 267(5612)**,** 603-604. doi: 10.1038/267603a0.

Lupton, J.E., Weiss, R.F., and Craig, H. (1977b). Mantle helium in the Red Sea brines. *Nature* 266(5599)**,** 244-246. doi: 10.1038/266244a0.

Malahoff, A., Kolotyrkina, I.Y., Midson, B.P., and Massoth, G.J. (2006). A decade of exploring a submarine intraplate volcano: Hydrothermal manganese and iron at Lō'ihi volcano, Hawai'i. *Geochemistry, Geophysics, Geosystems* 7(6)**,** n/a-n/a. doi: 10.1029/2005gc001222.

Martinez, I., Shilobreeva, S., Alt, J., Polyakov, V., and Agrinier, P. (2021). The origin and fate of C during alteration of the oceanic crust. *Comptes Rendus. Géoscience* 353(1)**,** 319-336. doi: 10.5802/crgeos.61.

Marty, B., Jambon, A., and Sano, Y. (1989). Helium isotopes and CO2 in volcanic gases of Japan. *Chemical Geology* 76(1-2)**,** 25-40. doi: 10.1016/0009-2541(89)90125-3.

Masson-Delmotte, V.P., Zhai, P., Pirani, S.L., Connors, C., Péan, S., Berger, N., et al. (2021). IPCC, 2021, Climate Change 2021: The Physical Science Basis. Contribution of Working Group I to the Sixth Assessment Report of the Intergovernmental Panel on Climate Change.

Massoth, G.J., Butterfield, D.A., Lupton, J.E., McDuff, R.E., Lilley, M.D., and Jonasson, I.R. (1989). Submarine venting of phase-separated hydrothermal fluids at Axial Volcano, Juan de Fuca Ridge. *Nature* 340(6236)**,** 702-705. doi: 10.1038/340702a0.

Massoth, G.J., Milburn, H.B., Hammond, S.R., Butterfield, D.A., McDuff, R.E., and Lupton, J.E. (1988). "The geochemistry of submarine venting fluids at Axial Volcano, Juan de Fuca Ridge: New sampling methods and a VENTS program rationale," in *Global venting, midwater, and benthic ecological processes*. NOAA Rockville, MD), 29-59.

Massoth, G.J., Ronde, C.E.J.D., Lupton, J.E., Feely, R.A., Baker, E.T., Lebon, G.T., et al. (2003). Chemically rich and diverse submarine hydrothermal plumes of the southern Kermadec volcanic arc (New Zealand). *Geological Society, London, Special Publications* 219(1)**,** 119-139. doi: doi:10.1144/GSL.SP.2003.219.01.06.

McCollom, T.M. (2013). Laboratory Simulations of Abiotic Hydrocarbon Formation in Earth's Deep Subsurface. *Reviews in Mineralogy and Geochemistry* 75(1)**,** 467-494. doi: 10.2138/rmg.2013.75.15.

McCollom, T.M. (2016). Abiotic methane formation during experimental serpentinization of olivine. *Proceedings of the National Academy of Sciences* 113(49)**,** 13965-13970. doi: 10.1073/pnas.1611843113.

McCollom, T.M., and Donaldson, C. (2016). Generation of Hydrogen and Methane during Experimental Low-Temperature Reaction of Ultramafic Rocks with Water. *Astrobiology* 16(6)**,** 389-406. doi: 10.1089/ast.2015.1382.

McGinnis, D.F., Schmidt, M., Delsontro, T., Themann, S., Rovelli, L., Reitz, A., et al. (2011). Discovery of a natural CO2seep in the German North Sea: Implications for shallow dissolved gas and seep detection. *Journal of Geophysical Research* 116(C3). doi: 10.1029/2010jc006557.

McLaughlin-West, E.A., Olson, E.J., Lilley, M.D., Resing, J.A., Lupton, J.E., Baker, E.T., et al. (1999). Variations in hydrothermal methane and hydrogen concentrations following the 1998 eruption at Axial Volcano. *Geophysical Research Letters* 26(23)**,** 3453-3456. doi: 10.1029/1999gl002336.

Menon, S., Denman, K.L., Brasseur, G., Chidthaisong, A., Ciais, P., Cox, P.M., et al. (2007). *Couplings between changes in the climate system and biogeochemistry*. United States.

Metrich, N., and Mandeville, C.W. (2010). Sulfur in Magmas. *Elements* 6(2)**,** 81-86. doi: 10.2113/gselements.6.2.81.

Métrich, N., and Wallace, P.J. (2008). Volatile Abundances in Basaltic Magmas and Their Degassing Paths Tracked by Melt Inclusions. *Reviews in Mineralogy and Geochemistry*

69(1), 363-402. doi: 10.2138/rmg.2008.69.10.

Michard, G. (2008). Can we explain atmospheric carbon dioxide oscillations during the past 400,000 years? *Comptes Rendus Geoscience* 340(8), 483-494. doi: 10.1016/j.crte.2008.06.004.

Michel, A.P.M., Wankel, S.D., Kapit, J., Sandwith, Z., and Girguis, P.R. (2018). In situ carbon isotopic exploration of an active submarine volcano. *Deep Sea Research Part II: Topical Studies in Oceanography* 150, 57-66. doi: 10.1016/j.dsr2.2017.10.004.

Milkov, A.V., and Etiope, G. (2018). Revised genetic diagrams for natural gases based on a global dataset of >20,000 samples. *Organic Geochemistry* 125, 109-120. doi: 10.1016/j.orggeochem.2018.09.002.

Millero, F.J. (1979). The thermodynamics of the carbonate system in seawater. *Geochimica et Cosmochimica Acta* 43(10), 1651-1661. doi: 10.1016/0016-7037(79)90184-4.

Mittal, T., and Delbridge, B. (2019). Detection of the 2012 Havre submarine eruption plume using Argo floats and its implications for ocean dynamics. *Earth and Planetary Science Letters* 511, 105-116. doi: 10.1016/j.epsl.2019.01.035.

Moreira, M.A., and Kurz, M.D. (2013). "Noble Gases as Tracers of Mantle Processes and Magmatic Degassing," in *The Noble Gases as Geochemical Tracers*, ed. P. Burnard. (Berlin, Heidelberg: Springer Berlin Heidelberg), 371-391.

Morrow, K.M., Bourne, D.G., Humphrey, C., Botté, E.S., Laffy, P., Zaneveld, J., et al. (2015). Natural volcanic CO2 seeps reveal future trajectories for host–microbial associations in corals and sponges. *The ISME Journal* 9(4), 894-908. doi: 10.1038/ismej.2014.188.

Mostofa, K.M.G., Liu, C.-Q., Zhai, W., Minella, M., Vione, D., Gao, K., et al. (2016). Reviews and Syntheses: Ocean acidification and its potential impacts on marine ecosystems. *Biogeosciences* 13(6), 1767-1786. doi: 10.5194/bg-13-1767-2016.

Murch, A. (2018). *Ash Generation in the 2012 Eruption of Havre Volcano, Kermadec Arc: The Largest Deep Subaqueous Eruption of the Last Century*. Doctor of Philosophy, University of Otago.

Murch, A.P., Portner, R.A., Rubin, K.H., and Clague, D.A. (2022). Deep-subaqueous implosive volcanism at West Mata seamount, Tonga. *Earth and Planetary Science Letters* 578, 117328. doi: 10.1016/j.epsl.2021.117328.

Mutaqin, B.W., Lavigne, F., Hadmoko, D.S., and Ngalawani, M.N. (2019). Volcanic Eruption-Induced Tsunami in Indonesia: A Review. *IOP Conference Series: Earth and Environmental Science* 256(1), 012023. doi: 10.1088/1755-1315/256/1/012023.

Nomikou, P., Carey, S., Bell, K.L.C., Papanikolaou, D., Bejelou, K., Cantner, K., et al. (2014). Tsunami hazard risk of a future volcanic eruption of Kolumbo submarine volcano, NE of Santorini Caldera, Greece. *Natural Hazards* 72(3), 1375-1390. doi: 10.1007/s11069-012-0405-0.

Ono, S., Shanks, W.C., Rouxel, O.J., and Rumble, D. (2007). S-33 constraints on the seawater sulfate contribution in modern seafloor hydrothermal vent sulfides. *Geochimica et Cosmochimica Acta* 71(5), 1170-1182. doi: 10.1016/j.gca.2006.11.017.

Oppenheimer, C. (2003). Climatic, environmental and human consequences of the largest known historic eruption: Tambora volcano (Indonesia) 1815. *Progress in Physical Geography: Earth and Environment* 27(2), 230-259. doi: 10.1191/0309133303pp379ra.

Oppenheimer, C., Scaillet, B., and Martin, R. (2011). *Sulfur Degassing From Volcanoes: Source Conditions, Surveillance, Plume Chemistry and Earth System Impacts*.

Ozima, M., and Podosek, F.A. (2002). *Noble gas geochemistry*. Cambridge University Press.

Paris, R., Switzer, A.D., Belousova, M., Belousov, A., Ontowirjo, B., Whelley, P.L., et al. (2014). Volcanic tsunami: a review of source mechanisms, past events and hazards in Southeast Asia (Indonesia, Philippines, Papua New Guinea). *Natural Hazards* 70(1), 447-470. doi: 10.1007/s11069-013-0822-8.

Perfit, M.R., Cann, J.R., Fornari, D.J., Engels, J., Smith, D.K., Ian Ridley, W., et al. (2003). Interaction of sea water and lava during submarine eruptions at mid-ocean ridges. *Nature* 426(6962), 62-65. doi: 10.1038/nature02032.

Pineau, F., and Javoy, M. (1983). Carbon isotopes and concentrations in mid-oceanic ridge

basalts. *Earth and Planetary Science Letters* 62(2), 239-257. doi: 10.1016/0012-821X(83)90087-0.

Pörtner, H.-O., Roberts, D.C., Tignor, M., Poloczanska, E.S., Mintenbeck, K., Alegría, A., et al. (2022). "IPCC, 2022, Climate Change 2022: Impacts, Adaptation and Vulnerability Working Group II Contribution to the Sixth Assessment Report of the Intergovernmental Panel on Climate Change", (ed.) C.U. Press. (Cambridge University Press, Cambridge, UK and New York, NY, USA).

Price, R.E., and Giovannelli, D. (2017). "A Review of the Geochemistry and Microbiology of Marine Shallow-Water Hydrothermal Vents," in *Reference Module in Earth Systems and Environmental Sciences*. Elsevier).

Raible, C.C., Brönnimann, S., Auchmann, R., Brohan, P., Frölicher, T.L., Graf, H.F., et al. (2016). Tambora 1815 as a test case for high impact volcanic eruptions: Earth system effects. *WIREs Climate Change* 7(4), 569-589. doi: 10.1002/wcc.407.

Reed, M.H., and Palandri, J. (2008). Hydrogen Produced by Reduction of H2O in Rock Reaction: Peridotite vs Basalt. *AIP Conference Proceedings* 987(1), 100-104. doi: 10.1063/1.2896951.

Resing, J.A., Baker, E.T., Lupton, J.E., Walker, S.L., Butterfield, D.A., Massoth, G.J., et al. (2009). Chemistry of hydrothermal plumes above submarine volcanoes of the Mariana Arc. *Geochemistry, Geophysics, Geosystems* 10(2). doi: 10.1029/2008gc002141.

Resing, J.A., Lebon, G., Baker, E.T., Lupton, J.E., Embley, R.W., Massoth, G.J., et al. (2007). Venting of Acid-Sulfate Fluids in a High-Sulfidation Setting at NW Rota-1 Submarine Volcano on the Mariana Arc. *Economic Geology* 102(6), 1047-1061. doi: 10.2113/gsecongeo.102.6.1047.

Resing, J.A., Rubin, K.H., Embley, R.W., Lupton, J.E., Baker, E.T., Dziak, R.P., et al. (2011). Active submarine eruption of boninite in the northeastern Lau Basin. *Nature Geoscience* 4(11), 799-806. doi: 10.1038/ngeo1275.

Resing, J.A., and Sansone, F.J. (1999). The chemistry of lava–seawater interactions: the generation of acidity. *Geochimica et Cosmochimica Acta* 63(15), 2183-2198. doi: 10.1016/S0016-7037(99)00193-3.

Resing, J.A., and Sansone, F.J. (2002). The chemistry of lava-seawater interactions II: the elemental signature. *Geochimica et Cosmochimica Acta* 66(11), 1925-1941. doi: 10.1016/S0016-7037(01)00897-3.

Resing, J.A., Sedwick, P.N., German, C.R., Jenkins, W.J., Moffett, J.W., Sohst, B.M., et al. (2015). Basin-scale transport of hydrothermal dissolved metals across the South Pacific Ocean. *Nature* 523(7559), 200-203. doi: 10.1038/nature14577.

Rice, D.D., and Claypool, G.E. (1981). Generation, Accumulation, and Resource Potential of Biogenic Gas1. *AAPG Bulletin* 65(1), 5-25. doi: 10.1306/2F919765-16CE-11D7-8645000102C1865D.

Rizzo, A.L., Caracausi, A., Chavagnac, V., Nomikou, P., Polymenakou, P.N., Mandalakis, M., et al. (2019). Geochemistry of CO2-Rich Gases Venting From Submarine Volcanism: The Case of Kolumbo (Hellenic Volcanic Arc, Greece). *Frontiers in Earth Science* 7. doi: 10.3389/feart.2019.00060.

Romano, D., Gattuso, A., Longo, M., Caruso, C., Lazzaro, G., Corbo, A., et al. (2019). Hazard Scenarios Related to Submarine Volcanic-Hydrothermal Activity and Advanced Monitoring Strategies: A Study Case from the Panarea Volcanic Group (Aeolian Islands, Italy). *Geofluids* 2019, 1-15. doi: 10.1155/2019/8728720.

Rouxel, O., Toner, B., Germain, Y., and Glazer, B. (2018). Geochemical and iron isotopic insights into hydrothermal iron oxyhydroxide deposit formation at Loihi Seamount. *Geochimica et Cosmochimica Acta* 220, 449-482. doi: 10.1016/j.gca.2017.09.050.

Rubin, K. (1997). Degassing of metals and metalloids from erupting seamount and mid-ocean ridge volcanoes: Observations and predictions. *Geochimica et Cosmochimica Acta* 61(17), 3525-3542. doi: 10.1016/s0016-7037(97)00179-8.

Rubin, K.H., Soule, S.A., Chadwick, W.W., Fornari, D.J., Clague, D.A., Embley, R.W., et al. (2012). Volcanic Eruptions in the Deep Sea. *Oceanography* 25(1), 142-157. doi: 10.5670/oceanog.2012.12.

Sakai, H., Gamo, T., Kim, E.-S., Tsutsumi, M., Tanaka, T., Ishibashi, J., et al. (1990a). Venting of Carbon Dioxide-Rich Fluid and Hydrate Formation in Mid-Okinawa Trough Backarc Basin. *Science* 248(4959)**,** 1093-1096. doi: doi:10.1126/science.248.4959.1093.

Sakai, H., Gamo, T., Kim, E.S., Shitashima, K., Yanagisawa, F., Tsutsumi, M., et al. (1990b). Unique chemistry of the hydrothermal solution in the mid-Okinawa Trough Backarc Basin. *Geophysical Research Letters* 17(12)**,** 2133-2136. doi: 10.1029/gl017i012p02133.

Sano, Y., and Fischer, T.P. (2013). "The Analysis and Interpretation of Noble Gases in Modern Hydrothermal Systems," in *The Noble Gases as Geochemical Tracers*, ed. P. Burnard. (Berlin, Heidelberg: Springer Berlin Heidelberg), 249-317.

Sano, Y., and Marty, B. (1995). Origin of carbon in fumarolic gas from island arcs. *Chemical Geology* 119(1)**,** 265-274. doi: 10.1016/0009-2541(94)00097-R.

Sansone, F.J., and Resing, J.A. (1995). Hydrography and geochemistry of sea surface hydrothermal plumes resulting from Hawaiian coastal volcanism. *Journal of Geophysical Research* 100(C7)**,** 13555. doi: 10.1029/95jc01120.

Sansone, F.J., Resing, J.A., Tribble, G.W., Sedwick, P.N., Kelly, K.M., and Hon, K. (1991). Lava-seawater interactions at shallow-water submarine lava flows. *Geophysical Research Letters* 18(9)**,** 1731-1734. doi: 10.1029/91gl01279.

Santana-Casiano, J.M., Fraile-Nuez, E., González-Dávila, M., Baker, E.T., Resing, J.A., and Walker, S.L. (2016). Significant discharge of CO2 from hydrothermalism associated with the submarine volcano of El Hierro Island. *Scientific Reports* 6(1)**,** 25686. doi: 10.1038/srep25686.

Santana-Casiano, J.M., González-Dávila, M., and Fraile-Nuez, E. (2018). "The Emissions of the Tagoro Submarine Volcano (Canary Islands, Atlantic Ocean): Effects on the Physical and Chemical Properties of the Seawater." InTech).

Santana-Casiano, J.M., González-Dávila, M., Fraile-Nuez, E., De Armas, D., González, A.G., Domínguez-Yanes, J.F., et al. (2013). The natural ocean acidification and fertilization event caused by the submarine eruption of El Hierro. *Scientific Reports* 3(1). doi: 10.1038/srep01140.

Santana-González, C., Santana-Casiano, J.M., González-Dávila, M., and Fraile-Nuez, E. (2017). Emissions of Fe(II) and its kinetic of oxidation at Tagoro submarine volcano, El Hierro. *Marine Chemistry* 195**,** 129-137. doi: 10.1016/j.marchem.2017.02.001.

Schipper, C.I., White, J.D.L., Houghton, B.F., Shimizu, N., and Stewart, R.B. (2010). Explosive submarine eruptions driven by volatile-coupled degassing at Lō`ihi Seamount, Hawai`i. *Earth and Planetary Science Letters* 295(3-4)**,** 497-510. doi: 10.1016/j.epsl.2010.04.031.

Schoell, M. (1980). The hydrogen and carbon isotopic composition of methane from natural gases of various origins. *Geochimica et Cosmochimica Acta* 44(5)**,** 649-661. doi: 10.1016/0016-7037(80)90155-6.

Schoell, M. (1988). Multiple origins of methane in the Earth. *Chemical Geology* 71(1)**,** 1-10. doi: 10.1016/0009-2541(88)90101-5.

Sedwick, P.N., McMurtry, G.M., and Macdougall, J.D. (1992). Chemistry of hydrothermal solutions from Pele's Vents, Loihi Seamount, Hawaii. *Geochimica et Cosmochimica Acta* 56(10)**,** 3643-3667. doi: 10.1016/0016-7037(92)90159-G.

Self, S., Zhao, J.-X., Holasek, R.E., Torres, R.C., and King, A.J. (1993). The atmospheric impact of the 1991 Mount Pinatubo eruption.

Shanks, W.C., III (2001). Stable Isotopes in Seafloor Hydrothermal Systems: Vent fluids, hydrothermal deposits, hydrothermal alteration, and microbial processes. *Reviews in Mineralogy and Geochemistry* 43(1)**,** 469-525. doi: 10.2138/gsrmg.43.1.469.

Shock, E.L., Holland, M., Meyer-Dombard, D.A., Amend, J.P., Osburn, G.R., and Fischer, T.P. (2010). Quantifying inorganic sources of geochemical energy in hydrothermal ecosystems, Yellowstone National Park, USA. *Geochimica et Cosmochimica Acta* 74(14)**,** 4005-4043. doi: 10.1016/j.gca.2009.08.036.

Siebert, L., Cottrell, E., Venzke, E., and Andrews, B. (2015a). "Chapter 12 - Earth's Volcanoes and Their Eruptions: An Overview," in *The*

Encyclopedia of Volcanoes (Second Edition), ed. H. Sigurdsson. (Amsterdam: Academic Press), 239-255.

Siebert, L., Cottrell, E., Venzke, E., and Edwards, B. (2015b). "Appendix 2 - Catalog of Earth's Documented Holocene Eruptions," in *The Encyclopedia of Volcanoes (Second Edition)*, ed. H. Sigurdsson. (Amsterdam: Academic Press), 1367-1400.

Siegel, D.A., Devries, T., Cetinić, I., and Bisson, K.M. (2023). Quantifying the Ocean's Biological Pump and Its Carbon Cycle Impacts on Global Scales. *Annual Review of Marine Science* 15(1)**,** 329-356. doi: 10.1146/annurev-marine-040722-115226.

Soule, S.A. (2015). "Chapter 21 - Mid-Ocean Ridge Volcanism," in *The Encyclopedia of Volcanoes (Second Edition)*, ed. H. Sigurdsson. (Amsterdam: Academic Press), 395-403.

Spietz, R.L., Butterfield, D.A., Buck, N.J., Larson, B.I., Chadwick, W.W., Walker, S.L., et al. (2018). Deep-Sea Volcanic Eruptions Create Unique Chemical and Biological Linkages Between the Subsurface Lithosphere and the Oceanic Hydrosphere. *Oceanography* 31(1)**,** 128-135.

Stanley, R.H.R., and Jenkins, W.J. (2013). "Noble Gases in Seawater as Tracers for Physical and Biogeochemical Ocean Processes," in *The Noble Gases as Geochemical Tracers*, ed. P. Burnard. (Berlin, Heidelberg: Springer Berlin Heidelberg), 55-79.

Staudigel, H., Hart, S.R., Koppers, A.A.P., Constable, C., Workman, R., Kurz, M., et al. (2004). Hydrothermal venting at Vailulu'u Seamount: The smoking end of the Samoan chain. *Geochemistry, Geophysics, Geosystems* 5(2)**,** n/a-n/a. doi: 10.1029/2003gc000626.

Staudigel, H., Hart, S.R., Pile, A., Bailey, B.E., Baker, E.T., Brooke, S., et al. (2006). Vailulu'u Seamount, Samoa: Life and death on an active submarine volcano. *Proceedings of the National Academy of Sciences* 103(17)**,** 6448-6453. doi: 10.1073/pnas.0600830103.

Staudigel, H., and Koppers, A.A.P. (2015). "Chapter 22 - Seamounts and Island Building," in *The Encyclopedia of Volcanoes (Second Edition)*, ed. H. Sigurdsson. (Amsterdam: Academic Press), 405-421.

Stucker, V.K., de Ronde, C.E.J., Laurence, K.J., and Phillips, A.M. (2022). Rare Time Series of Hydrothermal Fluids for a Submarine Volcano: 14 Years of Vent Fluid Compositions for Brothers Volcano, Kermadec Arc New Zealand. *Economic Geology*. doi: 10.5382/econgeo.4922.

Sun, Z., Zhou, H., Yang, Q., Sun, Z., Bao, S., and Yao, H. (2011). Hydrothermal Fe–Si–Mn oxide deposits from the Central and South Valu Fa Ridge, Lau Basin. *Applied Geochemistry* 26(7)**,** 1192-1204. doi: 10.1016/j.apgeochem.2011.04.008.

Symonds, R.B., Rose, W.I., Bluth, G.J.S., and Gerlach, T.M. (1994). Volcanic-gas studies; methods, results, and applications. *Reviews in Mineralogy and Geochemistry* 30(1)**,** 1-66.

Tagliabue, A., Bopp, L., Dutay, J.-C., Bowie, A.R., Chever, F., Jean-Baptiste, P., et al. (2010). Hydrothermal contribution to the oceanic dissolved iron inventory. *Nature Geoscience* 3(4)**,** 252-256. doi: 10.1038/ngeo818.

Tepp, G., and Dziak, R.P. (2021). The Seismo-Acoustics of Submarine Volcanic Eruptions. *Journal of Geophysical Research: Solid Earth* 126(4). doi: 10.1029/2020jb020912.

Tolstoy, M., Cowen, J.P., Baker, E.T., Fornari, D.J., Rubin, K.H., Shank, T.M., et al. (2006). A Sea-Floor Spreading Event Captured by Seismometers. *Science* 314(5807)**,** 1920-1922. doi: doi:10.1126/science.1133950.

Torgersen, T. (1989). Terrestrial helium degassing fluxes and the atmospheric helium budget: Implications with respect to the degassing processes of continental crust. *Chemical Geology: Isotope Geoscience section* 79(1)**,** 1-14. doi: 10.1016/0168-9622(89)90002-X.

Truche, L., McCollom, T.M., and Martinez, I. (2020). Hydrogen and Abiotic Hydrocarbons: Molecules that Change the World. *Elements* 16(1)**,** 13-18. doi: 10.2138/gselements.16.1.13.

Walker, S.L., Baker, E.T., Lupton, J.E., and Resing, J.A. (2019). Patterns of Fine Ash Dispersal Related to Volcanic Activity at West Mata Volcano, NE Lau Basin. *Frontiers in Marine Science* 6. doi: 10.3389/fmars.2019.00593.

Wang, Y., Liu, Y., Zhao, C., Li, Q., Zhou, Y., and Ran, H. (2020). Helium and carbon isotopic signatures of thermal spring gases in southeast Yunnan, China. *Journal of*

Volcanology and Geothermal Research 402**,** 106995. doi: 10.1016/j.jvolgeores.2020.106995.

Weiss, R.F. (1971). Solubility of helium and neon in water and seawater. *Journal of Chemical & Engineering Data* 16(2)**,** 235-241. doi: 10.1021/je60049a019.

Welhan, J.A. (1988). Origins of methane in hydrothermal systems. *Chemical Geology* 71(1-3)**,** 183-198. doi: 10.1016/0009-2541(88)90114-3.

Wen, H.-Y., Sano, Y., Takahata, N., Tomonaga, Y., Ishida, A., Tanaka, K., et al. (2016). Helium and methane sources and fluxes of shallow submarine hydrothermal plumes near the Tokara Islands, Southern Japan. *Scientific Reports* 6(1)**,** 34126. doi: 10.1038/srep34126.

Wheat, C.G., Jannasch, H.W., Plant, J.N., Moyer, C.L., Sansone, F.J., and McMurtry, G.M. (2000). Continuous sampling of hydrothermal fluids from Loihi Seamount after the 1996 event. *Journal of Geophysical Research: Solid Earth* 105(B8)**,** 19353-19367. doi: 10.1029/2000jb900088.

White, J.D., Manville, V., Wilson, C.J., Houghton, B.F., Riggs, N.R., and Ort, M. (2001). "Settling and Deposition of AD 181 Taupo Pumice in Lacustrine and Associated Environments," in *Volcaniclastic Sedimentation in Lacustrine Settings*.), 141-150.

White, J.D.L., McPhie, J., and Soule, S.A. (2015a). "Chapter 19 - Submarine Lavas and Hyaloclastite," in *The Encyclopedia of Volcanoes (Second Edition)*, ed. H. Sigurdsson. (Amsterdam: Academic Press), 363-375.

White, J.D.L., Schipper, C.I., and Kano, K. (2015b). "Chapter 31 - Submarine Explosive Eruptions," in *The Encyclopedia of Volcanoes (Second Edition)*, ed. H. Sigurdsson. (Amsterdam: Academic Press), 553-569.

Wilcock, W.S.D., Dziak, R.P., Tolstoy, M., Chadwick Jr., W.W., Nooner, S.L., Bohnenstiehl, D.R., et al. (2018). The Recent Volcanic History of Axial Seamount: Geophysical Insights into Past Eruption Dynamics with an Eye Toward Enhanced Observations of Future Eruptions. *Oceanography* 31.

Wilson, S.T., Hawco, N.J., Armbrust, E.V., Barone, B., Björkman, K.M., Boysen, A.K., et al. (2019). Kīlauea lava fuels phytoplankton bloom in the North Pacific Ocean. *Science* 365(6457)**,** 1040-1044. doi: 10.1126/science.aax4767.

Worman, S.L., Pratson, L.F., Karson, J.A., and Schlesinger, W.H. (2020). Abiotic hydrogen (H2) sources and sinks near the Mid-Ocean Ridge (MOR) with implications for the subseafloor biosphere. *Proceedings of the National Academy of Sciences of the United States of America* 117(24)**,** 13283-13293. doi: 10.1073/pnas.2002619117.

Wu, J., Boyle, E., Sunda, W., and Wen, L.-S. (2001). Soluble and Colloidal Iron in the Oligotrophic North Atlantic and North Pacific. *Science* 293(5531)**,** 847-849. doi: 10.1126/science.1059251.

Wu, J.N., Parnell-Turner, R., Fornari, D.J., Kurras, G., Berrios-Rivera, N., Barreyre, T., et al. (2022). Extent and Volume of Lava Flows Erupted at 9°50′N, East Pacific Rise in 2005–2006 From Autonomous Underwater Vehicle Surveys. *Geochemistry, Geophysics, Geosystems* 23(3). doi: 10.1029/2021gc010213.

Yücel, M., Gartman, A., Chan, C.S., and Luther, G.W. (2011). Hydrothermal vents as a kinetically stable source of iron-sulphide-bearing nanoparticles to the ocean. *Nature Geoscience* 4(6)**,** 367-371. doi: 10.1038/ngeo1148.

Zimanowski, B., Büttner, R., Dellino, P., White, J.D.L., and Wohletz, K.H. (2015). "Chapter 26 - Magma–Water Interaction and Phreatomagmatic Fragmentation," in *The Encyclopedia of Volcanoes (Second Edition)*, ed. H. Sigurdsson. (Amsterdam: Academic Press), 473-484.

Zolotov, M.Y., and Shock, E.L. (2000). A thermodynamic assessment of the potential synthesis of condensed hydrocarbons during cooling and dilution of volcanic gases. *Journal of Geophysical Research: Solid Earth* 105(B1)**,** 539-559. doi: 10.1029/1999jb900369

CHAPITRE 1. Introduction (Français)

Résumé

Le volcanisme sous-marin représente 85% de l'activité volcanique présente sur Terre, et met en jeu des transferts considérables et immédiats de chaleur, d'éléments chimiques et de microbes du manteau vers l'océan. Il intervient alors sur la fertilisation régionale des océans et génère des supports pour les communautés microbiennes. C'est aussi le principal mécanisme permettant le relargage vers la surface du carbone stocké en profondeur et pouvant ainsi avoir un impact significatif sur le climat à l'échelle des temps géologiques.

Ainsi, les éruptions sous-marines modifient significativement la bathymétrie du fond marin, la composition chimique et la structure physique de l'eau de mer et perturbent l'écosystème local. Cependant, les processus physiques et chimiques contrôlant ces transferts restent peu compris.

Ce chapitre présente un état des lieux des connaissances actuelles sur le volcanisme sous-marin, sur les mécanismes de générations de fluides au niveau du fond marin et dans la colonne d'eau, et sur la géochimie de ces émissions de fluide. Aussi, ce chapitre expose les objectifs scientifiques de la thèse qui s'intègre à ce contexte.

1.1. Contexte général

Cette thèse de doctorat s'inscrit dans le contexte actuel du changement climatique, où la concentration de dioxyde de carbone (CO_2) dans l'atmosphère a considérablement augmenté depuis l'ère préindustrielle (Masson-Delmotte et al., 2021). Cette croissance continue est indiscutablement due aux émissions d'origine humaine, en particulier à la combustion de ressources fossiles (Masson-Delmotte et al., 2021). Cependant, des sources naturelles sont également impliquées dans les émissions de CO_2, notamment la décomposition de la matière organique et la respiration des microorganismes, mais aussi le volcanisme. Depuis 1750, les concentrations atmosphériques de CO_2 et de méthane (CH_4) ont augmenté respectivement de 47 % et 156 %, dépassant largement les variations naturelles multimillénaires entre les périodes glaciaires et interglaciaires sur au moins les 800 000 dernières années. (Masson-Delmotte et al., 2021). Et il a été prédit que ces concentrations augmenteront encore au cours des prochaines décennies (IPCC, Groupe d'experts intergouvernemental sur l'évolution du climat). Le CO_2 et le CH_4 sont des gaz à effet de serre, absorbant le rayonnement thermique émis par la terre et l'océan pour le réémettre vers la Terre, favorisant ainsi le réchauffement global et déclenchant des changements durables dans le système climatique. Une telle augmentation du bilan carbone mondial (c'est-à-dire l'augmentation du CO_2 et du CH_4), en modifiant le système climatique, a des effets profonds sur la biodiversité, le fonctionnement des écosystèmes et finalement sur les services fournis par ces écosystèmes aux sociétés humaines (par exemple, la pollinisation, l'accès à l'eau, le stockage de CO_2, la purification de l'eau, etc.) (Pörtner et al., 2022). Par exemple, des expérimentations de terrain sur la concentration en CO_2 de l'eau de mer ont montré que l'acidification des océans entraîne une saturation en carbonate qui tombe en dessous des niveaux appropriés pour la calcification des récifs coralliens (Albright et al., 2018). De même, des études en laboratoire ont montré que l'acidification des océans peut réduire la valeur nutritionnelle des fruits de mer en réduisant la teneur en calories, en protéines, en lipides et en glucides (Lemasson et al., 2019). Ainsi, l'augmentation des concentrations de CO_2 et l'acidification associée ont le potentiel de mettre en danger bon nombre des précieux services écosystémiques que l'océan offre à la société, tels que la pêche, l'aquaculture et la protection des littoraux (Hall-Spencer and Harvey, 2019 ; Doney et al., 2020).

Au cours de la dernière décennie (2010-2019), les émissions de CO_2 liées aux activités humaines (10,9 ± 0,9 PgC/an) se sont accumulées dans trois composantes du système terrestre : 46 % se sont accumulés dans l'atmosphère (5,1 ± 0,02 PgC/an), 23 % ont été absorbés par les océans (2,5 ± 0,6 PgC/an) et 31 % ont été stockés par la végétation dans les écosystèmes terrestres (3,4 ± 0,9 PgC/an)

(Masson-Delmotte et al., 2021). Par conséquent, l'océan est une composante particulièrement importante du système climatique en raison de son rôle dans l'absorption et le stockage à long terme du CO_2, ce qui peut limiter l'impact des gaz à effet de serre sur le changement climatique (Houghton, 2014). Bien que l'océan puisse agir en tant que puits de carbone, avec l'augmentation des concentrations atmosphériques de CO_2, la fraction d'émissions absorbée par l'océan devrait diminuer (Masson-Delmotte et al., 2021), et il pourrait même agir en tant que source de carbone en fonction de l'équilibre de concentration entre l'atmosphère et l'océan.

La pompe biologique océanique régule le cycle du carbone terrestre en transportant la matière organique - créée par la productivité du phytoplancton dans la zone photique - vers l'intérieur obscur de l'océan, où elle est consommée par des animaux et des microbes hétérotrophes, puis reminéralisée sous forme inorganique (Honjo et al., 2014 ; Le Moigne, 2019). La pompe biologique océanique est composée de (i) de carbone organique neutre (dissous ou particulaire) qui s'enfoncent dans l'océan de surface entraîné par des mouvements d'eau descendant et/ou de mélange, et (ii) du transport actif du carbone organique par la migration du zooplancton et des poissons (Honjo et al., 2014 ; Le Moigne, 2019). Ce transport descendant de la matière organique constitue le principal mécanisme par lequel le carbone de l'atmosphère est stocké dans l'océan profond à l'échelle des sous-millénaires (Honjo et al., 2014 ; Le Moigne, 2019; Siegel et al., 2023).

Alors que l'absorption du CO_2 atmosphérique par les océans augmente, les océans sont également alimentés par une autre source importante de CO_2. Le volcanisme sous-marin représente environ 85 % de l'activité volcanique sur Terre (White et al., 2015b), et implique le transfert immédiat et considérable de chaleur, d'éléments chimiques et de micro-organismes du manteau vers l'océan. Plus généralement, le volcanisme est le principal mécanisme responsable de la libération profonde de CO_2 (et d'autres gaz à effet de serre tels que le CH_4) dans l'océan (Baker et al., 2012 ; Rubin et al., 2012).

Le volcanisme subaérien représente environ 53 à 88 $TgCO_2$/an (Fischer and Aiuppa, 2020), ce qui correspondrait à environ 40 à 60 millions de voitures parcourant chacune 10 000 km. Le mécanisme éruptif du volcanisme subaérien, ses manifestations géochimiques et ses impacts sur l'atmosphère sont bien décrits avec un large éventail de méthodes de surveillance (par exemple, satellites, réseaux sismiques terrestres, capteurs atmosphériques, etc.). Dans les archives géologiques, de vastes éruptions volcaniques ont souvent été liées à de grands événements d'extinction marquant la transition entre différentes périodes géologiques. Par exemple, les Trapps du Deccan, en Inde, qui constituent les provinces magmatiques mafiques les plus jeunes, sont associés à l'extinction de masse des dinosaures et de nombreux autres groupes, et définissent la transition entre le Crétacé et le Paléogène

(Courtillot et al., 1988; Bond et al., 2014), bien que le timing relatif du dégazage volcanique, de l'impact et de l'extinction reste largement débattu (Hull et al., 2020). Plus récemment, des études ont montré que les éruptions volcaniques peuvent avoir de grands effets sur le climat. Par exemple, l'éruption du volcan Pinatubo (Philippines) en 1991 a provoqué un refroidissement mondial en raison des émissions de dioxyde de soufre (SO_2) (Self et al., 1993). De même, l'éruption du Tambora (Indonésie) en avril 1815 a eu des effets considérables sur le climat mondial, déclenchant une "année sans été" en 1816 en Europe et en Amérique du Nord (Oppenheimer, 2003; Raible et al., 2016). Contrairement au volcanisme aérien, le volcanisme sous-marin est beaucoup plus difficile à détecter, à observer et à étudier. Comparé au nombre de volcans sous-marins présumés, trop peu ont été observés et étudiés (Rubin et al., 2012). Ainsi, l'impact du volcanisme sous-marin sur l'océan et sur l'atmosphère n'est pas bien appréhendé.

Au niveau des dorsales médio-océaniques, les éruptions sous-marines de magma sont un processus fondamental dans la formation de la croûte océanique (Rubin et al., 2012 ; White et al., 2015b), faisant du volcanisme sous-marin le principal mécanisme de libération du carbone des profondeurs marines à la surface. En particulier, on considère que le flux net de carbone dans la croûte océanique basaltique (stocké sous forme de carbone réduit et inorganique, par exemple les carbonates résultant des processus d'interaction entre le basalte et l'eau de mer) rivalise avec le flux de CO_2 issu des dégazages (Martinez et al., 2021). Cependant, la grande diversité des contextes géologiques (par exemple, dorsales à extension rapide vs lente, dorsales arrière-arc vs dorsales médio-océaniques), des types d'éruption, des produits des éruptions, etc., limite encore les connaissances sur le bilan carbone.

De plus, l'activité volcanique génère des flux très importants de gaz (ex. H_2, CO_2, CH_4), de particules et de fluides riches en éléments chimiques (ex. fer, manganèse, espèces sulfurées) depuis la croûte vers la colonne d'eau (Resing et al., 2007; Fischer, 2008 ; Resing et al., 2009 ; Baumberger et al., 2014 ; Buck et al., 2018), influençant ainsi la fertilisation régionale des océans (Langmann et al., 2010a ; Wilson et al., 2019), et servant de support aux populations microbiennes (Tagliabue et al., 2010 ; Edwards et al., 2011; Achterberg et al., 2013 ; Spietz et al., 2018 ; Longman et al., 2022). Les éruptions sous-marines affectent également la bathymétrie du fond marin, la composition chimique et la structure physique de l'eau de mer, ainsi que le fonctionnement local des écosystèmes. Cependant, les processus physiques et chimiques contrôlant ces transferts restent encore mal compris.

Le relargage de CO_2 lors d'éruptions sous-marines peut altérer l'acidité de l'océan et avoir des conséquences potentielles sur les cycles biogéochimiques. L'acidification des océans, telle que définie par le groupe d'experts intergouvernemental sur l'évolution du climat (Intergovernmental Panel on

Climate Change, IPCC) (Masson-Delmotte et al., 2021), correspond à une diminution du pH de l'océan sur une période prolongée, généralement de plusieurs décennies ou plus, causée principalement par l'absorption de CO_2 de l'atmosphère, mais qui peut également être provoquée par d'autres ajouts ou soustractions chimiques dans l'océan (tel que par une activité volcanique accrue). L'acidification des océans augmente actuellement en raison de l'absorption importante de CO_2 provenant des émissions d'origine humaine. Cette acidification croissante est associée à des réductions de l'état de saturation du carbonate de calcium, qui est un constituant principal des squelettes ou coquilles de divers organismes marins. Une fois dissous dans l'eau de mer, le CO_2 réagit avec l'eau pour former de l'acide carbonique (H_2CO_3), qui se dissocie à son tour en ions hydrogenocarbonate (HCO_3^-) et ensuite en ions carbonate (CO_3^{2-}), entraînant ainsi une augmentation des ions hydrogène (H^+) (Emerson and Hedges, 2008). Les tendances vers l'acidification des océans sont claires à l'échelle mondiale, avec un taux estimé de diminution du pH dans la couche de surface de l'océan compris entre 0,016 et 0,020 par décennie dans les zones subtropicales et entre 0,002 et 0,026 par décennie dans les zones subpolaires et polaires depuis les années 1980. L'acidification des océans a également été constatée en profondeur, dépassant les 2000 m de profondeur dans l'Atlantique Nord et l'océan Austral (Masson-Delmotte et al., 2021). Le volcanisme sous-marin peut également altérer le cycle du carbone en augmentant le bilan carbone de l'océan. Plus précisément, si le bilan carbone de l'océan devient plus élevé que celui de l'atmosphère, les océans ne fonctionneront plus comme un puits de carbone mais comme une source de carbone, avec des effets potentiellement dramatiques sur le climat. Il est donc de la plus haute importance de mieux comprendre l'impact du volcanisme sous-marin sur la tendance déjà acidifiante de l'océan due à l'augmentation des émissions de CO_2.

À ce jour, moins d'une douzaine de volcans sous-marins actifs ont fait l'objet d'un suivi. Bien qu'ils soient peu nombreux, ils présentent une variété de manifestations dans la colonne d'eau, en fonction du contexte géotectonique. En effet, le volcanisme sous-marin peut avoir lieu dans un contexte intraplaque (ex. Loihi Seamount à Hawaii, en éruption pour la dernière fois en 1996) (Karl et al., 1988; Garcia et al., 2006 ; Schipper et al., 2010), au niveau des dorsales médio-océaniques (ex. West Mata dans le bassin de Lau, en éruption en 2008, 2009, 2012) (Resing et al., 2011; Baumberger et al., 2014 ; Embley et al., 2014 ; Dziak et al., 2015 ; Chadwick et al., 2019), ou dans un contexte de subduction (ex. le volcan Northwest Rota-1 sur l'arc des Mariannes, en éruption en 2003-2010) (Resing et al., 2007; Resing et al., 2009 ; Butterfield et al., 2011). Globalement, ces différents systèmes éruptifs ont en commun d'être caractérisés par l'émission de fluides très riches en éléments volatils (He, H_2, CH_4, CO_2, Mn^{2+}, Fe^{2+}), bien que la proportion relative de ces éléments varie

fortement d'un système à l'autre. Actuellement, la manière dont ces éléments volatils affectent la géochimie de l'océan est mal connue. Par conséquent, la question principale sur laquelle se concentre cette thèse est la suivante : comment le volcanisme sous-marin contribue-t-il en termes de libération de gaz dans l'océan et comment affecte-t-il la géochimie de la colonne d'eau ? Plus spécifiquement, l'objectif général de cette thèse est d'étudier les manifestations géochimiques survenant dans la colonne d'eau de l'océan pendant et après un événement éruptif, ainsi que l'impact des émissions de fluides et de gaz sur la géochimie de la colonne d'eau.

À cette fin, nous avons profité d'un volcan sous-marin récemment formé - le volcan Fany Maoré - dont l'activité a commencé en 2018-2019, pour étudier la géochimie de la colonne d'eau pendant la mise en place du volcan (éruption et formation de l'édifice) et après l'événement éruptif (installation des coulées de lave et éventuellement initiation de la circulation hydrothermale). La description du contexte géologique de cette éruption sous-marine au large de Mayotte est fournie dans le CHAPTER 2. Ci-dessous, nous fournissons une description des connaissances actuelles sur le volcanisme sous-marin, et ses caractéristiques en termes de contextes tectoniques, d'émissions de produits volcaniques et de conséquences connues sur l'océan ouvert.

1.2. Le volcanisme sous-marin

Environ 85 % de l'activité volcanique mondiale actuelle se produit en profondeur, construisant la croûte océanique le long des dorsales médio-océaniques, formant de nombreux monts sous-marins intraplaques et érigeant des arcs insulaires (Rubin et al., 2012 ; White et al., 2015b; Tepp and Dziak, 2021) (Figure 1. 1, Tableau 1. 1. Abondance et importance des éruptions sous-marines par rapport aux éruptions subaériennes (White et al., 2015b). Les éruptions sous-marines sont quantitativement dominées par les éruptions au niveau des dorsales de propagation, sont plus souvent basaltiques que les éruptions subaériennes et représentent une part beaucoup plus importante du volcanisme mondial total. Étant donné les volumes éruptifs sous-marins totaux, même une petite proportion de telles éruptions est susceptible d'avoir un impact important sur le transfert mondial de chaleur et de volatils dans les océans.). Néanmoins, les techniques d'observation en milieu océanique sont limitées et il pourrait y avoir beaucoup plus de sites actifs à l'intérieur des plaques tectoniques que ce qui est actuellement connu.

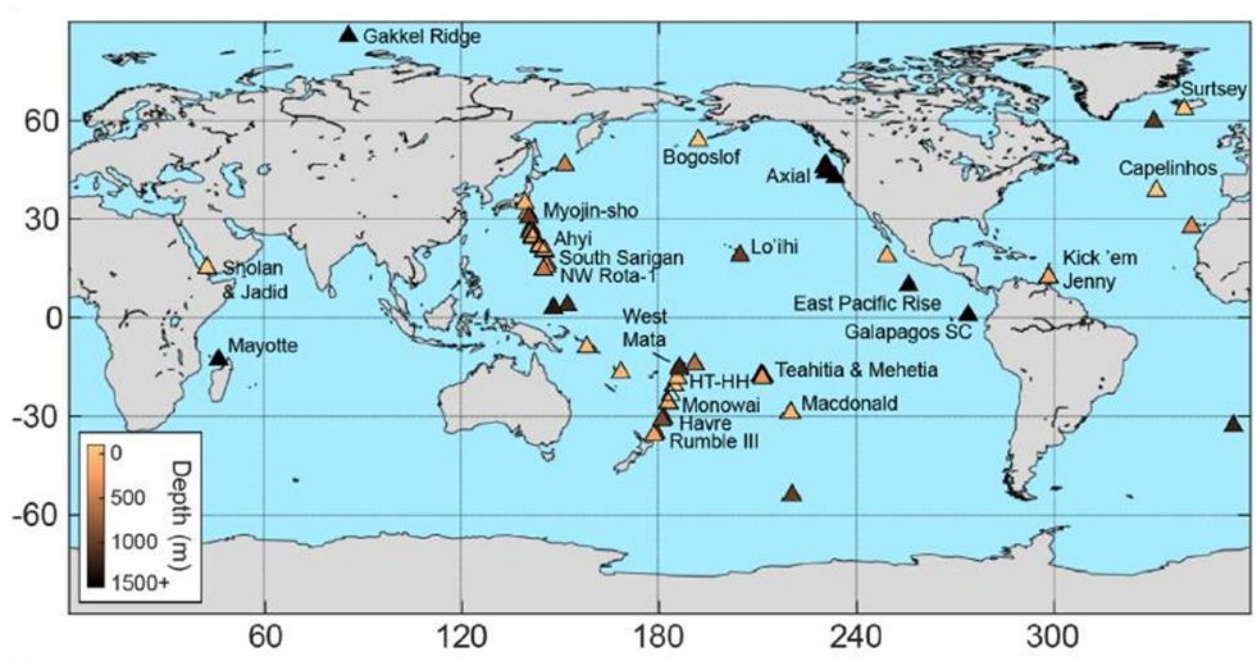

Figure 1. 1. Carte mondiale montrant les emplacements des éruptions sous-marines connues (triangles). L'échelle de couleur indique la profondeur du sommet du mont sous-marin ou la profondeur du centre de propagation, d'après (Tepp and Dziak, 2021).

Alors que les volcans subaériens ont été largement surveillés, les méthodes utilisées peu applicables aux volcans sous-marins. La première éruption sous-marine a été découverte par hasard en 1986 sur la dorsale Juan de Fuca, sur le segment Cleft (Baker et al., 1987). Depuis, 35 événements magmatiques ont été étudiés (Baker et al., 2012). Dans seulement quelques cas, il a été possible de capturer avec précision l'activité volcanique, soit en utilisant des véhicules sous-marins télécommandés (Chadwick et al., 2008 ; Chadwick et al., 2019), soit en déployant des sismomètres (Tolstoy et al., 2006 ; Kelley et al., 2014). Malgré les avancées technologiques des 30 à 40 dernières années qui ont considérablement amélioré notre capacité à observer, cartographier, accéder, prélever et étudier le fond marin, les éruptions sous-marines sont encore rarement détectées, encore plus rarement observées, et leurs produits éruptifs sont difficiles et coûteux à prélever. Par conséquent, la gamme de styles éruptifs et de manifestations géochimiques dans l'océan profond reste largement inconnue (Rubin et al., 2012), en particulier en ce qui concerne leur impact sur la géochimie globale de l'océan.

Tableau 1. 1. Abondance et importance des éruptions sous-marines par rapport aux éruptions subaériennes (White et al., 2015b). Les éruptions sous-marines sont quantitativement dominées par les éruptions au niveau des dorsales de propagation, sont plus souvent basaltiques que les éruptions subaériennes et représentent une part beaucoup plus importante du volcanisme mondial total. Étant donné les volumes éruptifs sous-marins totaux, même une petite proportion de telles éruptions est susceptible d'avoir un impact important sur le transfert mondial de chaleur et de volatils dans les océans.

	Eruption subaérienne	**Eruption sous-marine**
% estimé du volcanisme global	15% (0.6 km^3/yr)	85% (3.5 km^3/yr)
Volcanism basaltique	30% (0.19 km^3/yr)	80% (2.8 km^3/yr)
Volcanisme non-basaltique v	70% (0.43 km^3/yr)	20% (0.697 km^3/yr)
% chaleur volcanique dégagée par rapport à la quantité totale	14% (30% à 1200°C + 70% à 800°C)	86% (80% à 1200°C + 20% à 800°C)
Proportion explosive estimée	80% de 15% (c-à-d. 12% de toutes les éruptions sont subaériennes explosives)	5% de 85% (c-à-d. ~4% de toutes les éruptions sont sous-marines explosives)

La principale différence entre le volcanisme sous-marin et le volcanisme subaérien réside évidemment dans la présence de l'eau en tant que milieu environnemental ambiant dans les environnements sous-marins. L'interaction entre le magma et l'eau de mer environnante peut produire une variété de styles d'interaction, de processus et de dépôts (Cas and Giordano, 2014). Les éruptions sous-marines sont ainsi soumises à des contraintes physiques très différentes de celles des éruptions subaériennes. La capacité thermique, la conductivité thermique, la densité, la viscosité, le gradient de pression et le module volumique de l'eau de mer sont généralement chacun plusieurs ordres de grandeur plus élevés que les propriétés de l'atmosphère entourant les éruptions subaériennes. Ces différences affectent considérablement les processus éruptifs, y compris la fragmentation, le refroidissement des particules, la dynamique du panache, le transport et la dispersion (White et al., 2015b; Cas and Simmons, 2018). Seuls les processus intra-conduits, c'est-à-dire ceux se produisant avant que le magma n'interagisse avec l'environnement environnant, ont le potentiel d'être équivalents entre les éruptions subaériennes et sous-marines. En général, la teneur en volatils exsolués du magma en éruption sera plus faible dans l'océan que sur terre car les magmas se décompressent à des pressions hydrostatiques de plusieurs ordres de grandeur supérieures à la pression atmosphérique. À des profondeurs et à des pressions supérieures à celles équivalentes aux points critiques de H_2O et CO_2, les volatils exsolués sont des fluides supercritiques, et non des gaz, et ont donc une capacité limitée

à se dilater, encore moins de manière explosive. Les surpressions de gaz sont plus faibles dans les magmas sous-marins profonds par rapport à leurs équivalents subaériens, limitant l'expansion explosive des bulles de gaz aux eaux plus peu profondes (Cas and Simmons, 2018). Dans l'ensemble, bien que le volcanisme sous-marin diffère de nombreuses manières du volcanisme aérien, des différences existent également entre les volcans sous-marins en fonction des contextes tectoniques. Nous présentons ci-après les différents contextes tectoniques à l'origine de la formation des volcans sous-marins, les mécanismes d'émissions de fluides et de gaz en fonction de l'activité volcanique sous-marine, ainsi que les conséquences et les risques du volcanisme sous-marin.

1.2.1. Contextes tectoniques

Le contexte tectonique joue un rôle majeur dans la répartition, le comportement et la chimie des produits éruptifs des volcans (Siebert et al., 2015a). La plupart des volcans sous-marins se trouvent là où les plaques tectoniques se déplacent l'une vers l'autre ou s'éloignent l'une de l'autre. Il existe quatre principaux types de volcans sous-marins (Figure 1. 2) :

(i) Les volcans des centres d'expansion (c.-à-d. limites divergentes des plaques), également appelés volcans de dorsales médio-océaniques. Ils se forment lorsque deux plaques tectoniques s'éloignent l'une de l'autre et que la lave basaltique monte depuis le dessous du plancher océanique (Soule, 2015). Ces volcans se forment en raison de la production épisodique de magma sous les dorsales, près des zones de fracture (Batiza and Vanko, 1983). Les coulées de basalte à ces endroits ont souvent une forme caractéristique en "coussin", mais peuvent aussi paraître lisses en fonction de la vitesse et de la viscosité de l'écoulement (Siebert et al., 2015a). La dorsale East Pacific en est un exemple (Wu et al., 2022).

(ii) Les volcans des zones de subduction (c.-à-d. limites convergentes des plaques) se divisent en volcans d'arc et d'arrière arc. Ces volcans se forment là où deux plaques tectoniques entrent en collision, avec une plaque s'enfonçant sous l'autre et entrant en fusion. Lorsque des plaques océaniques chargées d'eau froide descendent dans l'intérieur chaud des arcs océaniques, elles se déshydratent. L'efflux d'eau abaisse la température à laquelle les roches surmontant le manteau solide fondent, conduisant à la génération de magma là où cela ne se produirait pas autrement. Dans ce contexte, la composition minéralogique principale est felsique, produisant une lave à haute viscosité et à forte teneur en gaz. Cette lave est généralement associée à des éruptions très violentes, bien que leur explosivité soit en grande partie atténuée par les profondeurs auxquelles elles se produisent (Siebert et al.,

2015a). Les volcans trouvés dans l'arc des Mariannes, tels que le mont Ahyi (Buck et al., 2018) ou le NW Rota-1 (Chadwick et al., 2008 ; Resing et al., 2009), ont été formés par la fusion de la plaque du Pacifique plongeante.

(iii) Les volcans des points chauds se produisent en conséquence d'un panache de magma montant à travers la croûte terrestre recouvrant une zone de fusion dans le manteau terrestre. Ces éruptions conduisent souvent à des chaînes d'îles volcaniques et de monts sous-marins qui sont plus anciens à mesure que l'on s'éloigne de l'emplacement de surface du panache de magma montant. Les points chauds laissent des "traces" linéaires de monts sous-marins à travers les bassins océaniques et construisent certains des plus grands volcans observés sur Terre (Siebert et al., 2015a; Staudigel and Koppers, 2015). Un exemple est le mont Loihi (Garcia et al., 2006 ; Malahoff et al., 2006).

(iv) Les volcans dans les contextes d'intraplaque se produisent à l'intérieur des plaques tectoniques, loin des limites des plaques. Ce type de volcans sous-marins a été peu observé jusqu'à présent. Les origines du volcanisme intraplaque sont encore un sujet de débat parmi les géologues, et différents mécanismes ont été proposés pour l'expliquer. Les volcans dans les contextes intraplaques sont généralement attribués à l'activité de panaches mantelliques ou de points chauds, et dans certains cas à la remontée du manteau due à l'extension de la plaque. Ces volcans peuvent également être situés près de grands décrochements dans les systèmes de dorsales et près des sommets topographiques des dorsales à propagation plus rapide (Staudigel and Koppers, 2015).

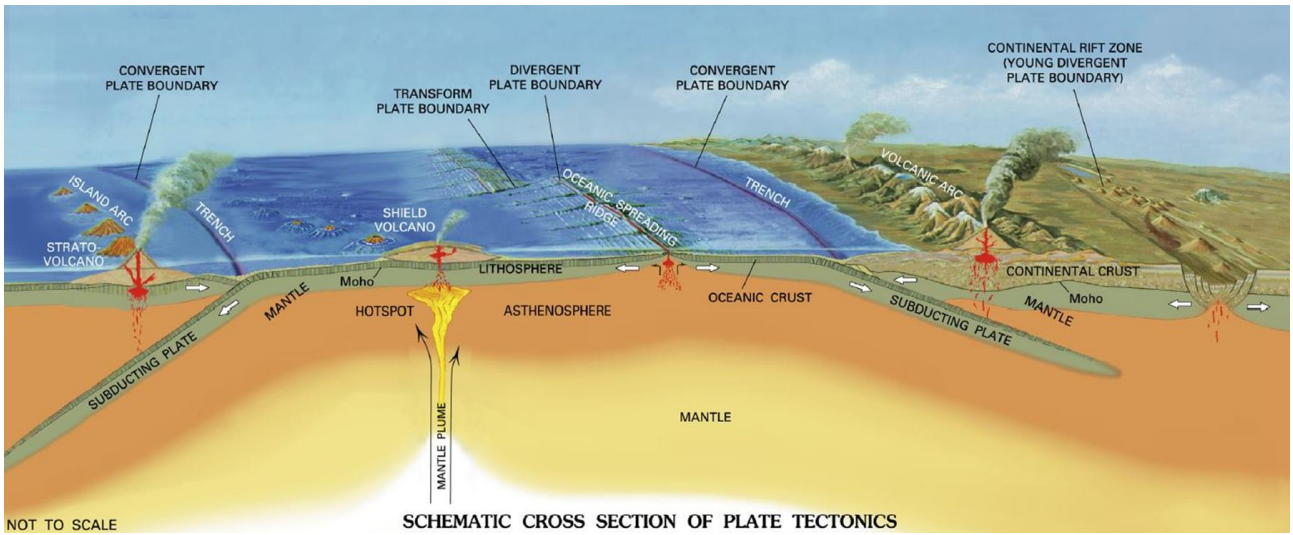

Figure 1. 2. Représentation schématique des contextes tectoniques à l'origine des différents types de volcans sous-marins, after Siebert et al. (2015a).

1.2.2. Mécanismes des émissions de fluides et de gaz dépendants de l'activité volcanique sous-marine

Les éruptions volcaniques sous-marines sont généralement associées à des interactions entre l'eau et la roche, conduisant dans certains cas à la formation de systèmes de sources hydrothermales au fond de la mer. Ces systèmes présentent diverses signatures chimiques en fonction du contexte géologique et tectonique, des processus du sous-sol et de la composition du magma. Ces paramètres contrôlent ainsi la manifestation des émissions et donc la composition géochimique du fluide libéré dans l'eau de mer au fond de l'océan, et par conséquent l'impact sur la géochimie de la colonne d'eau.

1.2.2.1. Eruption volcanique

L'approvisionnement en magma, qu'il soit constant ou variable dans le temps, entraîne une augmentation de la pression dans la chambre magmatique, ce qui à son tour déclenche une augmentation des taux de sismicité (Tolstoy et al., 2006). Les changements dans la chimie et la température des fluides hydrothermaux sont liés à cette sismicité en raison de la migration verticale de la couche limite thermique associée à la recharge en magma (Kelley et al., 2002; Fornari et al., 2012). Une fois qu'une pression suffisante a été atteinte dans la chambre magmatique, la remontée du magma est initiée et, avec une surpression suffisante, peut atteindre la surface. Cette remontée est probablement liée à la formation de panaches (Dziak et al., 2007) par advection de chaleur magmatique vers le fond marin et/ou libération de fluides hydrothermaux stockés dans la croûte (Baker et al., 2011; Baker et al., 2012).

Le mode d'éruption est déterminé par la profondeur de l'éruption, la composition du magma, les conditions de ségrégation des volatiles et le contexte tectonique, tandis que la fréquence des éruptions dépend des épisodes de surpression du magma et des changements dans la géométrie de la chambre magmatique. La quantité de gaz de magma dans le système et la profondeur de l'éruption déterminent le niveau d'activité explosive qui peut accompagner l'effusivité de l'éruption. Les éruptions volcaniques sous-marines sont influencées par la pression de l'eau environnante (Rubin et al., 2012 ; Cas and Giordano, 2014).

1.2.2.1.1. Types d'éruptions sous-marines

Les éruptions volcaniques peuvent être divisées en deux styles de comportement le style effusif qui produit des coulées de lave, et le style explosif qui produit des dépôts pyroclastiques. Un contrôle fondamental de ce comportement est la teneur en silice (SiO_2) du magma qui entre en éruption. Le

magma basaltique avec une teneur en SiO_2 <52 % (pourcentage en masse) est chaud et très fluide (faible viscosité), il est donc généralement érupté sous forme de gouttelettes (fontaines) ou de coulées de lave. En revanche, les magmas riches en SiO_2, tels que l'andésite (52-64 % de SiO_2), la dacite et la rhyolite (>69 % de SiO_2), sont généralement éruptés à des températures plus basses et ont des viscosités plus élevées, ce qui peut entraîner des éruptions potentiellement explosives. La plupart des éruptions sous-marines en eau profonde ont une composition basaltique et ne sont donc généralement pas, ou seulement faiblement, explosives, mais peuvent former des hyaloclastites lorsque la lave en fusion est refroidie au contact de l'eau. Dans la plupart des cas, les magmas basaltiques ont perdu des volatiles pendant leur ascension et atteignent le fond marin avec seulement de faibles quantités de volatiles qui, à des pressions hydrostatiques élevées, restent principalement en solution. Les volatiles exsolvés forment des bulles. En règle générale, les vésicules sont moins volumineuses dans les laves basaltiques générées par des éruptions en eau profonde (White et al., 2015a).

Des éruptions explosives peuvent se produire lorsque le magma atteint le fond marin sans perdre ses volatiles d'origine, ou lorsque le magma peu profond est enrichi en volatiles provenant d'un magma plus profond (White et al., 2015b). Les explosions peuvent également être causées par un transfert rapide de chaleur du magma vers l'eau (Zimanowski et al., 2015). La nature du site éruptif, en particulier lorsque le fond marin est recouvert de sédiments épais ou de roches rigides, constitue un autre facteur de contrôle sur le comportement éruptif. Le magma s'approche de la surface dans des filons qui progressent par propagation de fissures. Les sédiments non consolidés ne sont pas suffisamment rigides pour se fissurer, et l'extrémité du filon stagne. En même temps, la chaleur du magma chauffe et dilate l'eau dans le sédiment ; l'expansion sépare les grains et permet au mélange de se comporter comme un plastique mou ou un fluide visqueux. Ces effets permettent au magma de se propager latéralement dans le sédiment à faible profondeur sous le fond marin, ce qui entraîne généralement des intrusions de forme complexe et des combinaisons mélangées de magma et de sédiment appelées pépérites (Cas and Giordano, 2014; White et al., 2015b).

À ce jour, seules deux petites éruptions explosives sous-marines ont été observées : l'éruption du volcan NW Rota-1 dans l'arc des Mariannes (Chadwick et al., 2008) et l'éruption du volcan West Mata dans le bassin de Lau (Resing et al., 2011).

1.2.2.1.2. Types de coulées de lave

L'entrée de la lave dans l'océan est souvent un processus violent car la lave en fusion est rapidement refroidie et fracturée par l'eau de mer relativement froide. En retour, la lave chauffe l'eau de mer,

créant un grand volume d'eau chaude avec des caractéristiques hydrographiques très distinctes (Sansone and Resing, 1995). Selon la teneur en gaz, la composition du magma et le style éruptif, les produits vont des coulées douces, aux éclaboussures près de l'évent, aux scories, cendres et ponces, ce qui entraîne des formes volcaniques très variées (Siebert et al., 2015a), mais aussi des émissions très variées dans leur composition en éléments chimiques.

Lorsque le magma atteint l'océan, l'eau froide provoque un refroidissement et une solidification rapides de la lave, formant des structures de verre volcanique connues sous le nom de "pillow lavas" (coulées en coussin). Les coulées de lave progressent sur plusieurs heures ou jours pour chaque impulsion d'éruption, qui peut se poursuivre tant que la pression libérée n'est pas suffisante, ou que la pression continue d'augmenter dans la chambre magmatique par le biais de la recharge en magma (Rubin et al., 2012).

De loin, les faciès volcaniques sous-marins les plus volumineux sont de composition basaltique. Les laves de ce type dominent le long des dorsales océaniques mondiales, dans les bassins arrière-arc, sur les monts sous-marins intraplaciques, les îles volcaniques océaniques et les plateaux océaniques (White et al., 2015a). Les laves basaltiques sous-marines diffèrent morphologiquement des laves subaériennes principalement en raison de la formation efficace de la croûte qui résulte de l'éruption dans l'eau froide de la mer plutôt que dans l'air frais (c.-à-d. par l'extinction) (White et al., 2015a).

Le "pillow lava" est souvent cité comme la forme géologique la plus abondante à la surface de la Terre. Les "pillows" se forment à des débits faibles, bien que mal connus, et ont une forme tubulaire, souvent avec des sections circulaires ou ovales. Ils ont généralement une asymétrie distincte de haut en bas, les parties inférieures de ces tubes de lave ayant tendance à être moulées autour de la topographie préexistante en formant des "V" tandis que les parties supérieures sont rondes et souvent aplaties à mesure que les "pillows" grandissent (Staudigel and Koppers, 2015). Les "pillow lavas" ont été observés en formation sur le volcan West Mata dans le bassin arrière-arc du NE Lau (Resing et al., 2011).

La "lobate lava" est la morphologie dominante sur de nombreuses dorsales à taux d'extansion rapide et intermédiaire, et reflète des taux d'éruption plus élevés que les "pillow lavas". Un seul lobe est souvent beaucoup plus large qu'il n'est épais. La "lobate lava" est similaire au "pillow lava" de par les unités de flux individuelles (lobes) qui sont facilement reconnaissables, mais les limites entre les lobes sont couramment détruites à l'intérieur de la lave (White et al., 2015a).

Aux taux d'éruption/écoulement les plus élevés, des "sheet lavas" sont produites. Leurs intérieurs sont entièrement interconnectés et les surfaces ne montrent aucune indication d'unités séparées. Au lieu de cela, les surfaces peuvent être lisses, nervurées, linéarisées dans la direction de l'écoulement, ou mélangées. Les surfaces mélangées reflètent la déformation continue d'une surface pliée ou linéarisées, ce qui provoque la fragmentation de la croûte. Les "sheet lavas" sont généralement limitées aux régions près de la sortie de magma et aux zones où l'écoulement est restreint (White et al., 2015a).

1.2.2.1.3. Production de gaz et de fluides par l'éruption

Les éruptions produisent des coulées de lave, mais peuvent aussi produire des panaches de gaz et des explosions de vapeur (Rubin et al., 2012). Les liquides volcaniques sous-marins incluent de l'eau chauffée et des solutions hydrothermales riches en minéraux. Ces liquides sont généralement le résultat de l'interaction de l'eau de mer avec le magma chaud et peuvent contenir des concentrations élevées de sulfures, de métaux et d'autres éléments chimiques (Resing and Sansone, 2002; Hawco et al., 2020). Les fluides volcaniques sous-marins présentent des propriétés physico-chimiques uniques, telles que des températures élevées, des pressions élevées et des niveaux de pH acides.

Les émissions de gaz volcaniques peuvent être continues ou intermittentes. Leur répartition dans l'eau de mer dépend des courants océaniques, de la topographie sous-marine et de la profondeur du volcan. Les gaz volcaniques peuvent avoir un impact significatif sur l'environnement, contribuant à l'acidification de l'eau de mer, influençant le climat et participant à la formation de nuages de particules d'aérosol dans le cas des volcans peu profonds.

Des colonnes éruptives sous-marines gazeuses et des panaches d'eau chaude se forment au-dessus des éruptions explosives et non explosives, et ceux-ci peuvent entraîner des pyroclastes et des autoclastes de ponces vers le haut (Cas and Simmons, 2018) (Figure 1. 3). La dispersion et la sédimentation des fragments dans l'eau sont affectées par la vitesse à laquelle les fragments flottants deviennent imbibés d'eau et coulent, ainsi que par les vagues et les courants océaniques, qui peuvent produire des schémas de dispersion très complexes dans les pumices (Cas and Simmons, 2018). Le comportement des pyroclastes dans une colonne éruptive sous-marine sera complexe et dépendra de leur densité, que le milieu ambiant dans lequel ils sont entraînés soit un gaz-vapeur de faible densité ou une eau de densité plus élevée, et de la concentration de pyroclastes dans ce milieu fluide.

En profondeur dans l’océan, les panaches éruptifs peuvent être considérablement modifiés par le refroidissement, la condensation des gaz et le mélange avec l'eau ambiante froide et dense, de sorte

que leur hauteur est souvent limitée à la profondeur de l'océan à l'emplacement de l'éruption. Étant donné que toutes les éruptions sous-marines se produisent à des profondeurs <5000 m, les colonnes d'éruption sous-marines sont généralement limitées en hauteur à quelques kilomètres à quelques centaines de mètres (Cas and Simmons, 2018).

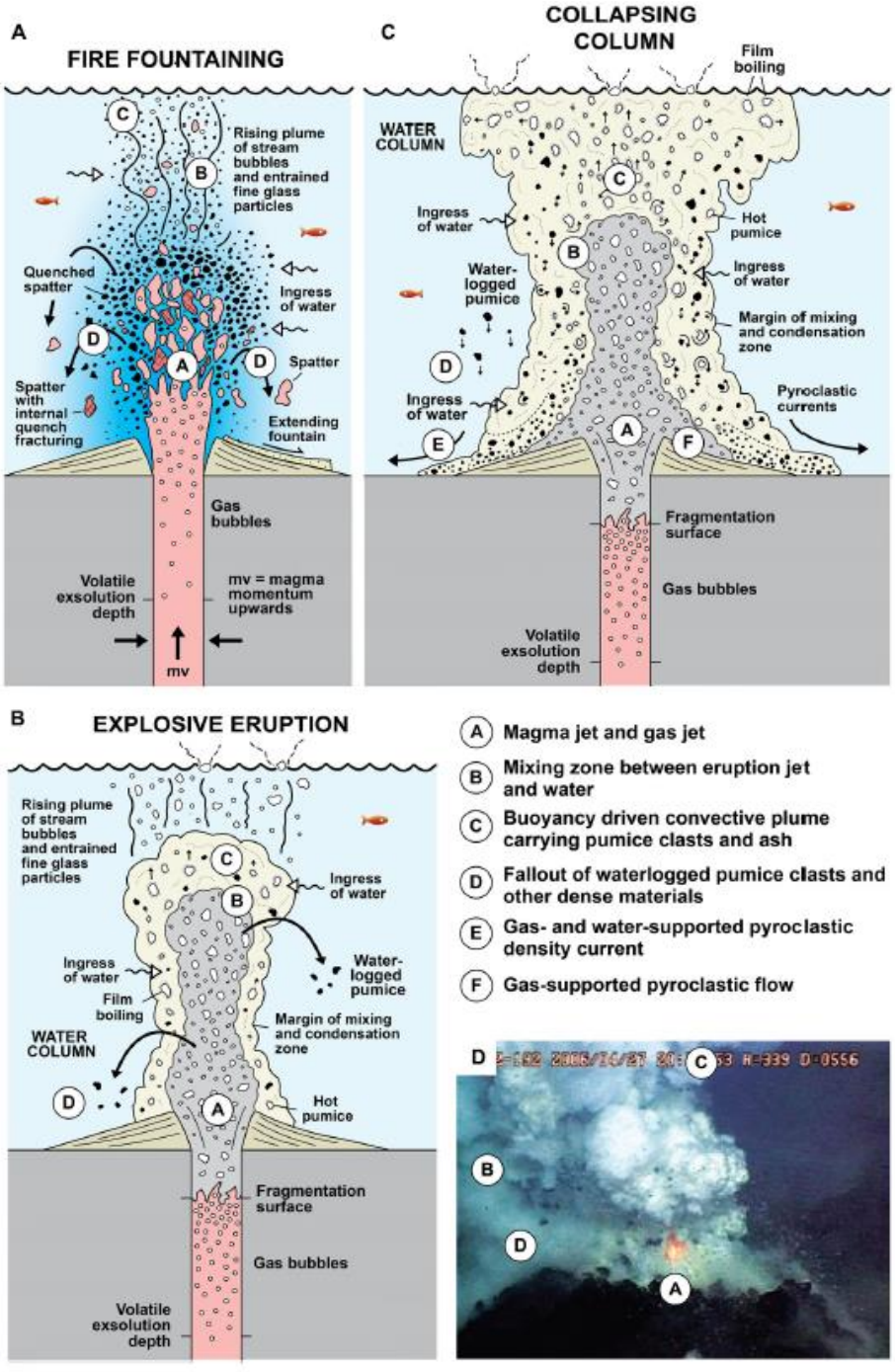

Figure 1. 3. Exemple des caractéristiques d'une éruption sous-marine (d'après Cas and Simmons (2018) – et les références qui y figurent). (A) Colonne en "fire fountain" en profondeur, montrant la fragmentation des clastes dispersés dans la colonne et la masse d'eau au-dessus de l'évent. (B) Processus complexes contribuant à la dynamique d'une colonne éruptive sous-marine relativement en profondeur, résultant de la décompression et de l'expansion initiales des bulles, puis du refroidissement, de la condensation et de l'entrée d'eau dans une

colonne éruptive sous-marine vers le haut. (C) Colonne éruptive explosive relativement peu profonde (d'une dizaine à centaine de mètres) s'effondrant autour de l'évent. La colonne montante et flottante est soumise à la condensation des gaz et à l'incorporation d'eau ambiante. Les éclats de ponce deviennent imbibés d'eau, contribuant à l'effondrement de la colonne et formant un flux de masse chaude de débris pyroclastiques, de vapeur et d'eau sur le plancher océanique. (D) Petite explosion atténuée par des éjectas de petite taille, avec au centre de la lave incandescente ou "fire fountain", en 2006, cratère Brimbank, volcan NW Rota 1, arc des Mariannes, profondeur ~550 mètres.

1.2.2.2. Circulation de fluides hydrothermaux

L'infiltration de l'eau de mer à travers la croûte océanique fracturée est à l'origine de la circulation hydrothermale (Figure 1. 4). En pénétrant dans les fissures de la croûte océanique, l'eau de mer froide est chauffée et subit un changement chimique progressif. Pendant sa migration, elle se rapproche de la source de chaleur (c.-à-d. la chambre magmatique) et peut atteindre des températures maximales dépassant 400°C. Cette eau de mer modifiée, appelée fluide hydrothermal, remonte à travers la croûte en raison des différences de densité, avant d'être expulsée au sein des roches du fond marin. En raison des conditions de réaction sous le plancher océanique, les fluides hydrothermaux sont significativement enrichis ou appauvris en composants chimiques par rapport à l'eau de mer ambiante. Ces sources hydrothermales abritent une biodiversité unique et jouent un rôle crucial dans les cycles géochimiques océaniques (Massoth et al., 1989; Massoth et al., 2003).

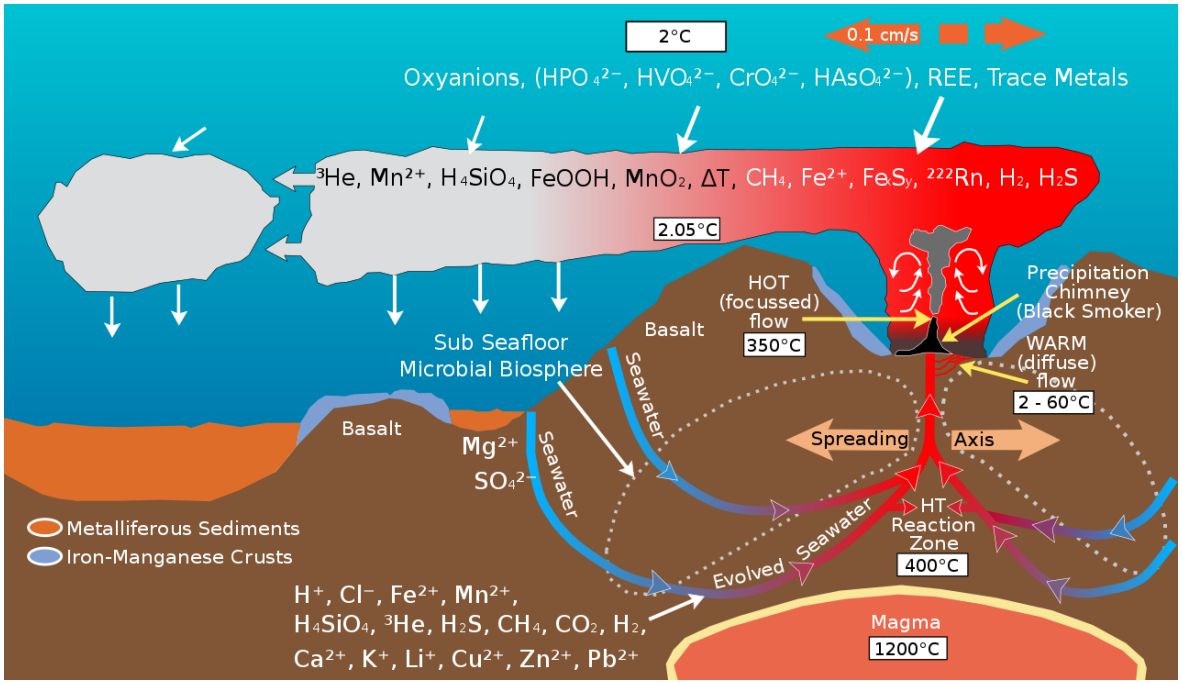

Figure 1. 4. Représentation schématique de la circulation des fluides hydrothermaux induite par la chaleur volcanique au niveau de l'axe de la dorsale médio-océanique, adapté de Massoth et al. (1988). Image de Submarine Ring of Fire 2002, NOAA/OER.

Dans un système volcanique sous-marin, la circulation hydrothermale se produit généralement au stade post-éruptif en raison de l'augmentation de la perméabilité de la croûte et de la création de nouvelles sources de chaleur telles que le magma sous-plancher et les champs de lave fraîchement éruptés qui sont encore en train de refroidir (Baker, 1998; Baker et al., 2004). Longtemps après que l'éruption se soit calmée, la circulation diffuse des fluides hydrothermaux se poursuit à travers l'enveloppe des nouvelles coulées de lave (Rubin et al., 2012). De plus, les volcans sous-marins actifs profonds, tels que Loihi,Seamount sont souvent associés à des systèmes hydrothermaux à basse température (< 55°C) entre les périodes d'éruptions volcaniques (Sedwick et al., 1992; Glazer and Rouxel, 2009), avec un dégazage à haute température (> 250°C) associé aux périodes éruptives (Davis and Clague, 1998).

La composition des fluides hydrothermaux à haute température est principalement contrôlée par les conditions de pression et de température, la cinétique des réactions, la composition des roches dans la zone de réaction à haute température et l'apport de volatils magmatiques. Les fluides diffus résultent d'une dilution en sous-plancher de fluides hydrothermaux plus chauds, et la gamme de compositions des fluides diffus peut être influencée par le degré de dilution, le temps entre la dilution et le dégazage, ainsi que par les réactions chimiques inorganiques et induites par les micro-organismes qui se produisent dans toute la zone de mélange en remontée (Butterfield et al., 1997). Le dégazage ultra-diffus peut se produire loin du sommet volcanique, comme précédemment découvert à une profondeur de 5000 m au large du flanc sud du mont sous-marin Loihi, qui se caractérise par un dépôt massif latéralement étendu d'oxyhydroxyde de fer, sans flux détectable de fluide hydrothermal vers l'eau de mer sus-jacente (Edwards et al., 2011).

Butterfield et al. (1997) ont proposé un modèle général de l'évolution des émissions de fluides à la suite d'un événement volcanique, en tenant compte de la différence de localisation de la source de chaleur dans la croûte océanique. Immédiatement après une éruption volcanique ou l'injection d'un dyke, le flux de chaleur augmente considérablement, déclenchant la séparation des phases et l'évacuation préférentielle de la phase vapeur, de densité faible. Le dégazage continu de saumures observé dans certains systèmes signifie que la phase de saumure conjuguée doit être temporairement retenue autour de la source de chaleur (en raison de sa densité plus élevée ou d'autres propriétés physiques), tandis que des fluides riches en vapeur à haute enthalpie avec de faibles teneurs en chlorure éliminent la chaleur, les volatils (H_2S, CO_2, He et H_2 issus du dégazage magmatique et de l'interaction eau-roche se partitionnent dans la phase vapeur) et les métaux. À mesure que le système refroidit, la séparation des phases ralentit puis s'arrête, et les fluides passent d'une dominance de vapeur à une domination de saumure (c.-à-d. la teneur en chlorure et en métaux augmente tandis que

les volatils diminuent). La teneur en saumure dans les fluides évacués peut atteindre un pic, puis diminuer à mesure que la chaleur du système s'épuise et que les compositions des fluides se dégradent en se rapprochant de l'eau de mer.

L'évolution des fluides post-éruptifs a été attribuée au refroidissement du magma injecté dans la couche supérieure perméable de la croûte océanique. En l'absence de perturbations volcaniques récentes, il semble que les fluides riches en volatils à faible teneur en chlorure soient associés à des systèmes à haut flux thermique entraînant une séparation des phases plus profonde (par exemple, le champ principal Endeavour), tandis que les fluides dominés par la saumure sont associés à des systèmes à faible flux thermique (par exemple, le segment Cleft) (Butterfield et al., 1997).

Le début de la circulation hydrothermale se caractérise par le dégazage de volatils magmatiques (comme le SO_2 et le CO_2), ce qui entraîne des fluides fortement acides et la dissolution globale des roches hôtes. Lorsque la phase éruptive prend fin, le front de matériau fondu recule en raison de l'effondrement de la chambre magmatique et du refroidissement par la circulation des fluides. À mesure que le chemin réactionnel des fluides hydrothermaux s'allonge, le contact entre l'eau et la roche augmente, ce qui fait monter la température des fluides. À mesure que le volcan vieillit, moins de gaz magmatiques s'échappent, l'édifice se refroidit et l'activité hydrothermale diminue (Resing et al., 2009).

Une gamme de températures a été observée dans le système hydrothermal de Brothers, allant des valeurs proches de la température ambiante de l'eau de mer à environ 300°C, ce qui conduit à la formation de dépôts hydrothermaux de type "cheminée noire". Les différents assemblages d'altération des roches ont été influencés par l'interaction entre l'eau de mer et le fluide magmatique, le degré d'interaction eau-roche hydrothermale et la variation du potentiel d’oxydation-réduction et de la température. Ces paramètres semblent avoir varié au fil du temps et de l'espace tout au long de l'évolution du système hydrothermal (De Ronde et al., 2019). Des apports périodiques de fluides hydrothermaux magmatiques peuvent également avoir initié des cycles d'activité hydrothermale. Avec une diminution de l'apport magmatique et une augmentation de l'interaction fluide hydrothermal-roche, les fluides hydrothermaux deviennent plus évolués et les assemblages de minéraux d'altération changent en conséquence en fonction de la température, de la profondeur et de la distance par rapport à la zone principale d'afflux magmatique (De Ronde et al., 2005).

1.2.2.3. Dégazage de CO_2

Les dégazages de CO_2 sont décrits par González-Delgado and Hernández (2018) comme des zones subtidales affectées par l'émission de gaz provenant de fluides volcaniques-hydrothermaux riches en CO_2 au niveau du fond marin. Dans la littérature, elles sont également mentionnées comme des émissions de CO_2 hydrothermal ou des fumerolles (Price and Giovannelli, 2017; González-Delgado and Hernández, 2018; Aiuppa et al., 2021). Elles sont plus susceptibles d'exister là où il y a eu ou il y a une activité volcanique sous-marine récente, telle qu'au niveau des dorsales médio-océaniques, des arcs insulaires, du magmatisme intra-plaque ou autour de tout volcan côtier ou insulaire (Price and Giovannelli, 2017). Ces zones actives ont été observées dans plusieurs régions de la planète. Price and Giovannelli (2017) ont recensé 70 sites de sorties de CO_2 liées à des volcans, à moins de 200 mètres de profondeur répartis sur 23 systèmes de dégazage de CO_2 (Figure 1. 5). Parmi ces sorties de CO_2, l'une des plus étudiées, Baia di Levante au large de l'île de Vulcano (îles Éoliennes, Sicile), présente des émissions de CO_2 composées à environ 90 mol% de CO_2, qui sont interprétées comme des vapeurs provenant de l'ébullition de saumures hydrothermales montant depuis une nappe géothermique peu profonde (Boatta et al., 2013; Aiuppa et al., 2021) (Figure 1. 6.A). Des émissions de CO_2 à faibles profondeurs ont également été observées au large de l'île de Panarea, en Sicile (Romano et al., 2019; Li et al., 2020); dans le sud de la mer du Nord, à environ 30 km au large d'East Frisian Island Juist, en Allemagne (McGinnis et al., 2011), ou dans les îles D'Entrecasteaux dans la province de Milne Bay, en Papouasie-Nouvelle-Guinée (Morrow et al., 2015).

De manière générale, sur ces sites, les émissions se présentent sous forme gazeuse, avec une teneur moyenne en CO_2 de 87,0 ± 20,7 % en volume sur 207 analyses de gaz (Aiuppa et al., 2021). En général, le volume restant (1-20 %) est constitué d'autres gaz ou éléments associés aux émissions volcaniques, tels que l'azote (N_2), l'oxygène (O_2), l'argon (Ar), le dihydrogène (H_2), l'hélium (He), le mercure (Hg), le méthane (CH_4), le sulfure d'hydrogène (H_2S) (González-Delgado and Hernández, 2018). La dissolution du CO_2 dans l'eau de mer entraîne l'acidification de l'eau. Un pH plus bas, et donc des différences dans d'autres paramètres chimiques, ont été particulièrement détectés dans le système de dégazage de l'île de Shikine, au Japon, où le pH ambiant a diminué de 1,3 unités (Agostini et al., 2015). Étant donné que ces éruptions volcaniques se trouvent à faible profondeur, elles entraînent le rejet de CO_2 et d'espèces réductrices (H_2S, CH_4 et H_2) dans les océans de surface, où elles influencent la chimie et la productivité de la surface de l'océan. L'augmentation de la pression partielle de CO_2 dans l'eau de mer réduit la concentration en ions carbonate et l'état de saturation des minéraux de carbonate de calcium, qui sont essentiels pour la calcification chez les invertébrés qui

accumulent du carbonate, tels que les coraux. Il a été démontré que certains organismes peuvent bénéficier de ces conditions changeantes, mais que de nombreux autres sont entravés (ex. réduction de la diversité des coraux), ce qui entraîne des changements complexes dans les communautés et le fonctionnement de l'écosystème (Fabricius et al., 2011; Morrow et al., 2015). En plus des apports chimiques, les gaz dissous dans l'eau de mer proviennent de bullages continues dans les zones d'activité volcanique. Cela peut à la fois empêcher l'établissement de certains organismes et générer une turbulence acoustique qui peut altérer la perception de l'environnement par certains animaux, affectant ainsi le développement et le comportement des larves et des juvéniles cherchant refuge ou nourriture (De Soto et al., 2013).

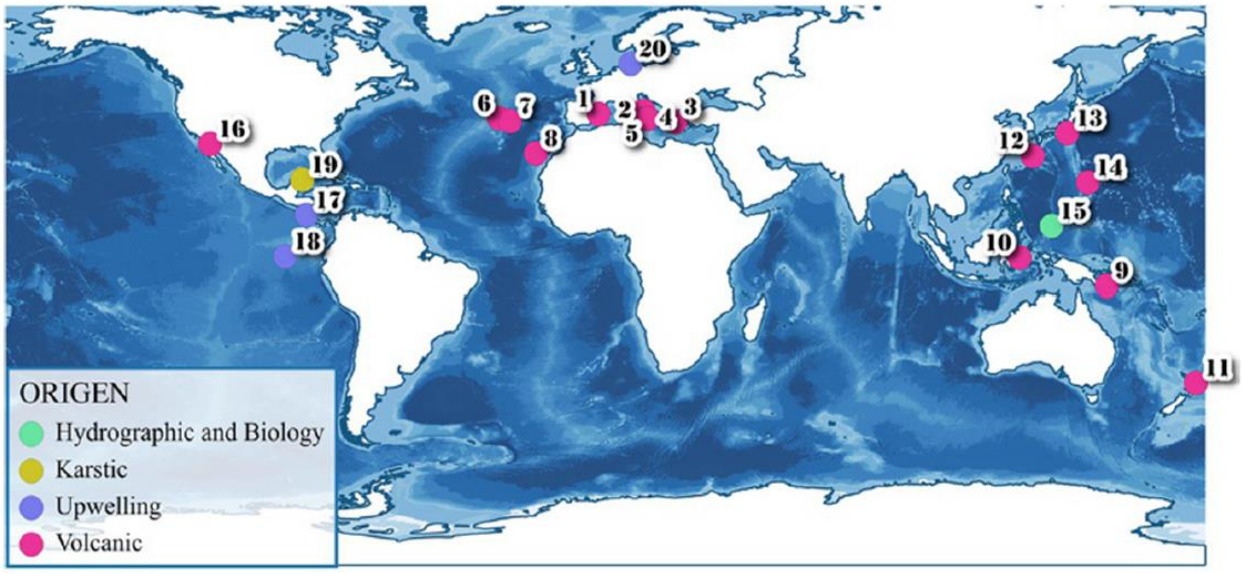

1	Columbretes Islands (Spain)	8	La Palma (Canary Islands)	15	Palau (Oceania)
2	Ischia (Italy)	9	Papua New Guinea	16	Wagner Basin (Northern Gulf of California)
3	Methana (Greece)	10	Indonesia	17	Bahia Culebra (Gulf of Papagayo)
4	Panarea (Italy)	11	White Island (New Zealand)	18	Eastern Tropical Pacific
5	Vulcano (Italy)	12	Iwatorishima (Japan)	19	Puerto Morelos (Mexico)
6	Faial (Azores)	13	Shikine Island (Japan)	20	Kiel Fjord (Baltic Sea)
7	San Miguel (Azores)	14	Maug (Mariana Islands)		

Figure 1. 5. Carte mondiale des emplacements des dégazages de CO_2 peu profonds, d'après González-Delgado and Hernández (2018).

D'autres systèmes d'émissions comparables de CO_2 ont été observés dans d'autres systèmes volcaniques (Tableau 1. 2), tels qu'au niveau du volcan sous-marin d'intraplaque El Hierro, aux îles Canaries, qui a particulièrement été étudié vis-à-vis de l'acidification des océans, montrant un dégazage significatif de CO_2 à environ 350 m de profondeur (Santana-Casiano et al., 2016). Des

courants de bulles ont également été observés au volcan sous-marin Kick'em Jenny, dans la mer des Caraïbes. Deux sites, nommés Champagne vent et Shrimp vent, présentent des bulles principalement composées de CO_2 d'origine magmatique qui ont été observés à environ 265 m en profondeur, avec des mesures de flux individuels variant de 10 à 100 kg de CO_2 par jour (Carey et al., 2016; Michel et al., 2018). De nombreux sites de dégazages de CO_2 ont été identifiés à environ 500 m dans le cratère du volcan sous-marin Kolumbo, dans la mer Égée (Grèce), induisant des valeurs de pH aussi basses que 5 unités de pH, et indiquant des conditions acides à l'intérieur du cratère (Carey et al., 2013). Rizzo et al. (2019) suggèrent que les gaz émis proviennent d'un manteau homogène chargé en CO_2, probablement en raison de la décarbonatation du calcaire en subduction. Également dans l'arc volcanique hellénique, des émissions de bulles avec du CO_2 comme composant majeur, et à haute température, ont été trouvés à faible profondeur autour de l'île de Milos (Dando et al., 1995). De plus, Lupton et al. (2008) a apporté des preuves de l'émission de bulles de gaz riches en CO_2 sur trois volcans sous-marins situés sur l'arc des Mariannes (NW Rota-1, Nikko et Daikoku) et deux volcans sur l'arc de Tonga-Kermadec (Giggenbach et Volcano-1).

Au niveau de ces sites de dégazage, le CO_2 est émis sous forme de bulles de gaz et les températures au niveau des sorties présentent des températures élevées. Cependant, dans certains cas rares, des décharges ont été observées en profondeur dans l'océan (> 1300 m) sous forme de gouttelettes froides de CO_2 liquide (Tableau 1. 2). Le premier cas a été observé dans le champ hydrothermal JADE, dans la fosse d'Okinawa, et pour lequel les auteurs suggèrent la présence d'hydrates de CO_2 dans le sédiment associé au CO_2 liquide (Sakai et al., 1990a; Sakai et al., 1990b). L'émission de CO_2 liquide a ensuite été observée dans le système hydrothermal de Yonaguni Knoll IV, également dans la fosse d'Okinawa, où il a été suggéré que ce CO_2 liquide pourrait résulter d'une série de processus sous-marins, notamment la séparation de phase du fluide hydrothermal due à l'ébullition, la formation de d'hydrate de CO_2 due au refroidissement de la phase vapeur, et la fusion d'hydrate de CO_2 en CO_2 liquide due à une augmentation de la température dans la couche sédimentaire (Sakai et al., 1990a; Sakai et al., 1990b; Konno et al., 2006). Le troisième site rapporté est le site Champagne sur le volcan NW Eifuku dans l'arc nord des Mariannes, qui décharge des gouttelettes froides de CO_2 liquide à un débit estimé de 23 mol CO_2/s, soit environ 0,1 % du flux mondial de carbone des dorsales médio-océaniques. Ici aussi, les auteurs supposent que le CO_2 provient directement du dégazage d'une chambre magmatique, puis est refroidi en migrant vers le fond marin, formant finalement du CO_2 liquide et de l'hydrate près de la surface (Lupton et al., 2006) (Figure 1. 6.B).

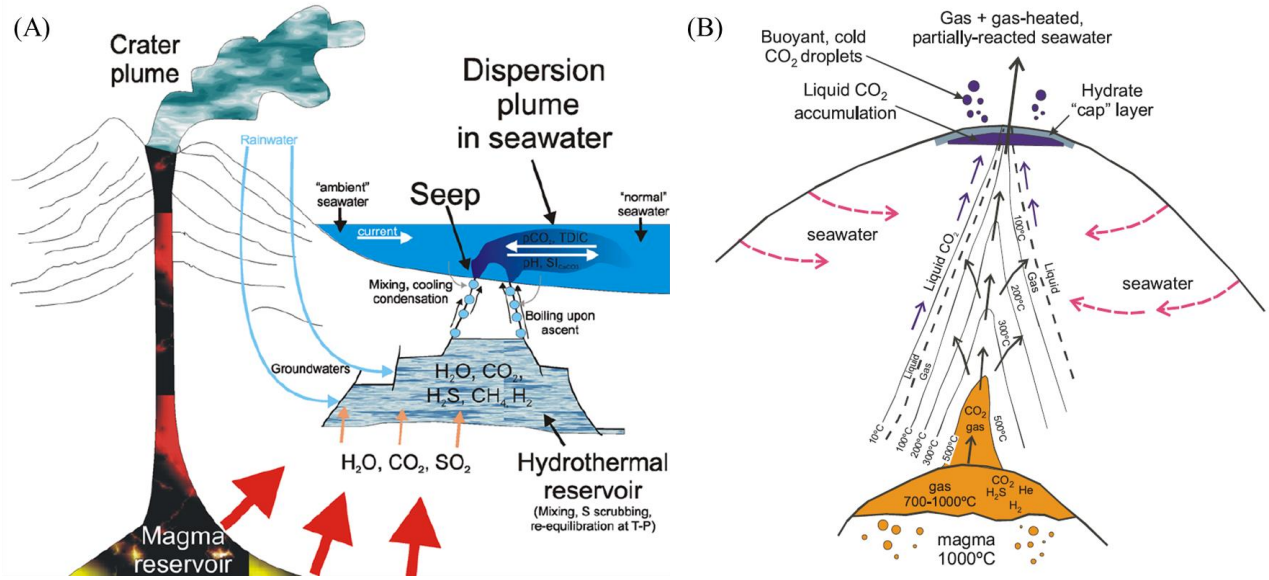

Figure 1. 6. Schémas du mécanisme sous-jacent suggéré pour (A) le dégazage du CO_2 au niveau des volcans côtiers et insulaires, d'après Aiuppa et al. (2021), et (B) le dégazage du CO_2 liquide dans les systèmes volcaniques profonds, d'après Lupton et al. (2006).

Tableau 1. 2. Synthèse des caractéristiques physico-chimiques de quelques sites de dégazage de CO_2.

Nom du site	Localisation	Profondeur	Contexte	CO_2	Phase	Température	Références
Champagne and Shrimp vents, Kick'em Jenny submarine volcano	Caribbean Sea, Lesser Antilles	265 m	Back-arc	93-96%	gaz	160-180°C	(Carey et al., 2016; Michel et al., 2018)
Kolumbo submarine volcano	Aegean Sea, Greece	500 m	Hellenic Volcanic Arc	>97%	gaz	>220°C	(Carey et al., 2013; Rizzo et al., 2019)
Island of Milos	Greece	3-110 m	Hellenic Volcanic Arc	54.9-91.9%	gaz	~80-110°C	(Dando et al., 1995)
Champagne vent field, NW Eifuku	Mariana Arc	1600 m	Arc	98%	liquide	<4°C	(Lupton et al., 2006)
JADE hydrothermal field	Mid-Okinawa Trough	1335-1550m	Back-arc	86%	liquide		(Sakai et al., 1990a; Sakai et al., 1990b)
Yonaguni Knoll IV hydrothermal system	Okinawa Trough	1360-1400 m	Back-arc	85%	liquide		(Konno et al., 2006)

Dans l'ensemble, l'émission de bulles de gaz riches en CO_2 et de gouttelettes de CO_2 liquide est probablement plus courante dans les zones volcaniques sous-marines que nous ne le pensions, mais les observations restent limitées en raison du manque de ressources et de la difficulté d'accès aux sites. De manière plus générale, l'impact des éruptions volcaniques sous-marines sur le bilan mondial du carbone, sur l'acidification des océans et sur les écosystèmes océaniques est encore très peu connu.

1.2.3. Géochimie des émissions de fluides

Les éruptions volcaniques sous-marines sont associées à l'émission de fluides et de gaz qui présentent diverses compositions chimiques contrôlées par de nombreuses caractéristiques telles que le contexte géotectonique, les processus tectoniques, la profondeur, l'échantillonnage spatial et temporel, ou la composition de la lave (Karl et al., 1988; Massoth et al., 1989; Malahoff et al., 2006; Kilias et al., 2013). Les émissions de fluides et de gaz volcaniques sont généralement caractérisées par une concentration élevée de volatils (y compris H_2O, CH_4, CO_2, SO2, H_2S, ^3He, H_2), un enrichissement en métaux (Fe, Mn), des précipités hydrothermaux (y compris du soufre particulaire) et de fortes baisses de l'alcalinité et des valeurs de pH par rapport à l'eau de mer ambiante (Massoth et al., 2003; Resing et al., 2009; Resing et al., 2011; Wen et al., 2016). Cette section présente un aperçu des composés chimiques présents dans le contexte volcanique sous-marin, qui fournissent des informations sur leur origine, les processus inhérents de génération, ainsi que leur impact sur la géochimie de l'eau de mer.

1.2.3.1. Gaz rares : hélium (He) et néon (Ne)

L'hélium est un traceur très efficace pour l'étude des sources de volatiles en raison de son état gazeux, de son inertie et de ses multiples origines (radiogéniques, magmatiques ; Figure 1. 7). L'hélium est un nucléide stable et conservatif qui ne participe à aucun processus chimique ou biologique. L'hélium possède deux isotopes stables : l'hélium-3 (^3He) et l'hélium-4 (^4He). Le ^3He est essentiellement primordial, stocké dans le manteau terrestre depuis l'accrétion, mais peut également être produit par la désintégration radioactive du tritium (^3H) (Jenkins and Clarke, 1976 ; Jenkins et al., 2019). Le ^3He peut également être produit par des réactions de spallation induites par les rayons cosmiques (cosmogéniques) à la surface des planètes, produisant du ^3H et du ^3He en proportions égales, avec la décomposition ultérieure du ^3H en ^3He, mais c'est une source relativement mineure de gaz nobles. Le ^4He est principalement radiogénique, produit par la désintégration radioactive de l'uranium (U) et du thorium (Th) (Craig and Weiss, 1971).

Par conséquent, l'hélium dans l'océan provient de trois sources différentes (Figure 1. 7) : (i) la dissolution gazeuse en équilibre avec l'hélium atmosphérique (He_{eq}), (ii) la désintégration radioactive du tritium formant de l'hélium tritiogénique (^3He), et (iii) l'injection d'hélium terrigène ^3He et ^4He par l'activité volcanique sous-marine et l'ajout d'hélium radiogénique ^4He provenant de la croûte et de la couverture sédimentaire (Lupton, 1983 ; Ayache et al., 2015).

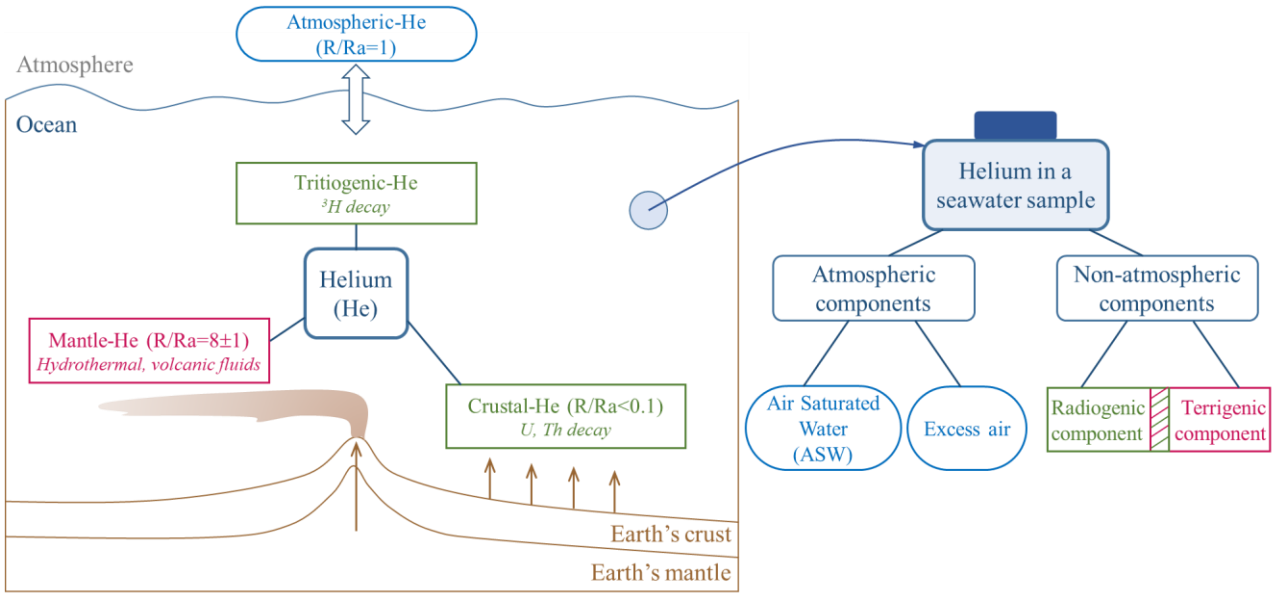

Figure 1. 7. Schéma des composants de l'hélium dans l'océan, et terminologie et classification des composants d'hélium pouvant être trouvés dans un échantillon d'eau de mer, adapté de Ayache et al. (2015) et Brennwald et al. (2013). Les gaz rares radiogéniques sont souvent, mais pas toujours, d'origine terrigène (ex. le ^3He tritiogénique n'est pas terrigène). À la surface de l'océan, l'hélium est essentiellement en équilibre de solubilité avec l'hélium atmosphérique.

En dehors de l'origine terrigène, la principale source de gaz nobles dans l'océan provient de l'atmosphère par le processus d'échange gazeux air-océan (Figure 1. 7). Les gaz rares sont généralement en quasi-équilibre avec l'atmosphère, conformément aux constantes de la loi de Henry, bien que le réchauffement ou le refroidissement rapide, la formation ou la fonte de glace et l'injection de bulles puissent entraîner des écarts par rapport à l'équilibre (Stanley and Jenkins, 2013). Les gaz rares se répartissent entre l'atmosphère et l'eau par échange à la surface air-eau. L'eau saturée en air (ASW) correspond à l'équilibre de solubilité du gaz noble entre l'atmosphère et l'eau de mer. L'excès d'air est formé par la dissolution (partielle) de bulles d'air dans l'eau (Brennwald et al., 2013). La concentration globale d'hélium (c'est-à-dire les mesures) dans l'eau de mer est ainsi donnée par la

somme de la concentration ASW (notée He_{eq} ci-après), du composant d'excès d'air (He_{air}), du composant d'hélium terrigène (He_{xs}) et du ^{3}He tritiogénique (Brennwald et al., 2013).

Le néon possède trois isotopes, ^{20}Ne, ^{21}Ne et ^{22}Ne. Ces trois isotopes peuvent être produits par des réactions cosmogéniques mais sont également nucléogéniques dans le manteau, bien que les taux de production de ^{20}Ne et de ^{22}Ne soient négligeables dans le manteau terrestre par rapport à leurs abondances naturelles. Le ^{21}Ne est un isotope rare et est donc plus affecté par la production cosmogénique et nucléogénique, contrairement aux abondants ^{20}Ne et ^{22}Ne. Dans la Terre solide, la production de ^{21}Ne nucléogénique est couplée à celle du ^{4}He radiogénique. En effet, la production de ^{21}Ne est directement proportionnelle au rapport de production de particules α des séries de l'uranium et du thorium (Hilton and Porcelli, 2003). Les isotopes du néon sont souvent utilisés pour corriger la contamination atmosphérique (c.-à-d. les composants d'hélium atmosphérique). En effet, les rapports isotopiques $^{20}Ne/^{22}Ne$ peuvent être considérés comme un rapport isotopique stable dans le manteau. Les ^{20}Ne et ^{22}Ne sont produits par des voies nucléogéniques, mais ces productions sont suffisamment lentes pour être considérées comme négligeables. La correction est généralement effectuée en supposant que tout le néon est atmosphérique et en exploitant le contraste entre les rapports He/Ne du manteau (> 1000, (Sano and Fischer, 2013)) et de l'air (0,226, (Weiss, 1971; Hilton, 1996)) (Marty et al., 1989; Ozima and Podosek, 2002; Moreira and Kurz, 2013).

À la surface de l'océan, l'hélium est essentiellement en équilibre de solubilité avec l'atmosphère. Cependant, plusieurs processus importants modifient le rapport isotopique de l'hélium ($^{3}He/^{4}He$) en fonction de la profondeur. Le manteau actuel contient à la fois des isotopes primordiaux (^{3}He) et radiogéniques (^{4}He), mais dans des proportions différentes selon le contexte géologique (Ayache et al., 2015). Les valeurs des isotopes d'hélium sont attribuées au mélange entre les composants radiogéniques d'origine mantellique et crustale. En conséquence, le rapport isotopique d'hélium dans les fluides et les gaz fournit des informations sur l'origine des volatiles (c.-à-d. manteau vs. croûte). Le relargage d'hélium provenant de l'activité volcanique sous-marine au niveau des dorsales médio-océaniques (MOR) et des centres volcaniques présente des rapports isotopiques d'hélium élevés caractéristiques de leur source mantellique, tandis que la libération de ^{4}He radiogénique à partir de la croûte et de la couverture sédimentaire conduit à l'ajout d'hélium à faible rapport isotopique d'hélium (Lupton et al., 1977b; a; Lupton, 1979; Craig and Lupton, 1981; Jean-Baptiste et al., 1991a; Jean-Baptiste et al., 1991b).

Le rapport isotopique de l'hélium atmosphérique (noté Ra) est de $1{,}384\times10^{-6}$ (Clarke et al., 1976) et peut être considéré comme constant en raison du temps de résidence élevé de l'hélium, qui est environ

10^6 fois plus long que le temps de mélange de l'atmosphère (basé sur la teneur totale en hélium de l'atmosphère et le flux global de dégazage d'hélium estimé par (Torgersen, 1989)). Par rapport à ce rapport atmosphérique, les rapports isotopiques typiques de l'hélium varient de < 0,1 Ra dans la croûte terrestre à une moyenne de 8,0 ± 1,5 Ra dans le manteau supérieur (c.-à-d. de type MORB), et jusqu'à environ 40 à 50 Ra dans les produits de volcans de points chauds, comme à Hawaï et en Islande (Ballentine and Burnard, 2002; Graham, 2002; Hilton et al., 2002; Sano and Fischer, 2013; Wang et al., 2020). Le rapport isotopique moyen de l'hélium dans le manteau lithosphérique subcontinental a été estimé à 6,1 ± 0,9 Ra (Gautheron and Moreira, 2002).

Parce que l'hélium est présent à une concentration élevée dans les fluides hydrothermaaux par rapport à l'eau de mer environnante, le ^{3}He peut être utilisé pour tracer les panaches hydrothermaux sur des milliers de kilomètres depuis les régions sources (Lupton, 1998). Les variations du rapport isotopique de l'hélium océanique sont généralement exprimées en tant que δ^3He, qui est l'écart en pourcentage au rapport atmosphérique, défini tel que $\delta^3 He = 100 \times \left(\frac{R_m}{R_a} - 1\right)$, où R_m correspond au rapport isotopique de l'hélium mesuré (Benson and Krause, 1980; Stanley and Jenkins, 2013). Dans plusieurs régions du Pacifique, comme la dorsale Est du Pacifique, la dorsale de Juan de Fuca ou le mont sous-marin Loihi, l'activité hydrothermale est suffisamment intense pour produire des panaches riches en ^{3}He, qui sont clairement associés à un enrichissement important en ^{3}He dans les masses d'eau profonde du Pacifique, soit environ 20% au-dessus des valeurs de l'eau de mer de fond (Lupton, 1998). Dans le canal du Mozambique, la valeur de δ^3He dans l'océan profond (à environ 2500 m) est d'environ 10-15 %, tandis que l'hélium tritiogénique apparaît négligeable (Jenkins et al., 2019).

1.2.3.2. Espèces volatiles

1.2.3.2.1. Dioxyde de carbone (CO_2)

Le CO_2 est le deuxième gaz le plus courant dans les émissions volcaniques après l'H_2O, généré par dégazage de la lave (Craig and Lupton, 1981; Symonds et al., 1994; Lowenstern, 2001), bien que dans les gaz exsolvés des magmas basaltiques, la concentration de CO_2 puisse dépasser celle de l'eau (Giggenbach, 1997), probablement en raison de son abondance plus élevée dans certaines régions sources du manteau. À mesure que le magma monte et refroidit, la faible solubilité du CO_2 par rapport à H_2O fait en sorte qu'il se partitionne préférentiellement dans toute phase de vapeur s'exsolvant et dans des bulles de gaz qui peuvent se séparer du liquide en fusion à différentes profondeurs

(Giggenbach, 1997). La composition de la phase gazeuse exsolvée change donc en fonction de la solubilité de chaque espèce volatile liée à la pression. Le CO_2 est largement perdu pendant la production de la phase gazeuse à haute pression et s'exsolve à toutes les profondeurs, avant l'H_2O (Métrich and Wallace, 2008). Étant donné que les fluides exsolvés sont moins denses que le liquide en fusion, ils montent plus rapidement à la surface, donnant lieu à des émissions fluides avec une concentration très élevée en volatiles. Le CO_2 peut également être généré par une phase gazeuse riche en CO_2 se dégazant directement de la chambre magmatique, comme cela a été observé à NW Rota-1, où des bulles de gaz riches en CO_2 s'exsolvent de la lave en éruption lente (Chadwick et al., 2008; Lupton et al., 2008). Lorsque la phase gazeuse riche en CO_2 rencontre l'eau de mer circulante lors de son ascension à travers l'édifice volcanique, un mélange biphasique de gaz riche en CO_2 et d'une phase aqueuse sous-saturée en CO_2 peut coexister à mesure que des bulles de gaz ascensionnelles échangent avec la phase aqueuse (Lupton et al., 2008). Le comportement du CO_2 libéré dans l'eau de mer est principalement régi par la pression (c.-à-d. la profondeur) et la température de l'eau dans laquelle il est libéré, et dans une moindre mesure par sa salinité.

Étant donné que le CO_2 émis par une éruption volcanique ou un fluide hydrothermal provient principalement du dégazage magmatique, la composition isotopique du dioxyde de carbone ($\delta^{13}C$-CO_2) d'origine magmatique varie entre -8 ‰ et -4 ‰ (Pineau and Javoy, 1983; Sano and Marty, 1995). Néanmoins, la composition isotopique du CO_2 peut résulter d'un mélange entre celle de la roche calcaire marine $\delta^{13}C$-CO_2 = 0 ‰ (Sano and Marty, 1995) et celle des sédiments riches en matière organique $\delta^{13}C$-CO_2 = -30 ‰ (Sano and Marty, 1995), en fonction du processus de fractionnement et du substrat à travers lequel les fluides et les gaz passent.

Une fois le plancher océanique atteint, le CO_2 peut exister sous différentes phases, selon les conditions de pression et de température (Figure 1. 8). Par exemple, il peut apparaître sous forme d'hydrates de CO_2 à l'intérieur des sédiments et sur le plancher océanique (Sakai et al., 1990a; Lupton et al., 2006), sous forme de gouttelettes de CO_2 liquide (Sakai et al., 1990a; Sakai et al., 1990b; Konno et al., 2006; Lupton et al., 2006), ou sous forme de CO_2 gazeux qui se produit généralement au-dessus de 500 m dans l'océan (Lupton et al., 2008).

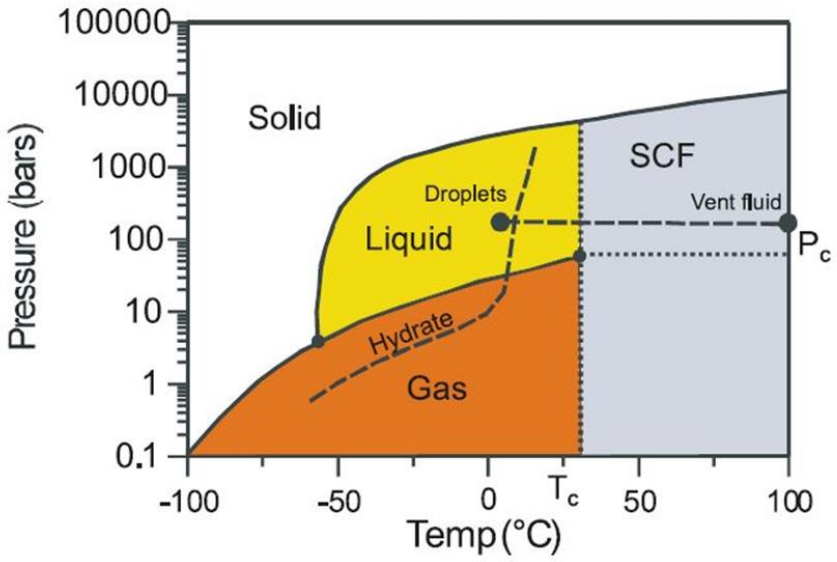

Figure 1. 8. Diagramme de phase du CO_2 (d'après Lupton et al. (2006)) montrant les régions où existent les phases solide, liquide, gazeuse et fluide supercritique (SCF). P_C et T_C désignent la pression critique et la température critique. La ligne en pointillés indique la limite de stabilité des hydrates. Ce diagramme présente également les conditions de pression et de température trouvées pour les gouttelettes liquides et le fluide à 103°C au site Champagne (Lupton et al., 2006).

1.2.3.2.2. Méthane (CH_4)

Le méthane peut être considéré comme un traceur des activités volcaniques et hydrothermales. Étant donné que les fluides émis sont riches en gaz et ont une composition globale très différente de celle de l'eau de mer environnante, ce traceur permet la détection de panaches dans la colonne d'eau sur des distances allant de quelques dizaines à des milliers de kilomètres.

Dans les systèmes volcaniques sous-marins, le CH_4 est généralement produit par la circulation hydrothermale qui est initiée après un événement éruptif, comme à Ahyi, NW Rota, West Mata, Nikko, Daikoku ou Kasuga-2 (Resing et al., 2009; Resing et al., 2011; Baumberger et al., 2014; Buck et al., 2018), bien qu'il soit également libéré pendant l'événement éruptif (Craig and Lupton, 1981; Baumberger et al., 2014; Baumberger et al., 2020).

Quatre processus sont généralement considérés pour la production de CH_4 dans les systèmes volcaniques et hydrothermaux (Schoell, 1988; Welhan, 1988; Fiebig et al., 2004) :

(i) la production biologique de CH_4 par des bactéries à des températures inférieures à 100 °C (Rice and Claypool, 1981; Schoell, 1988; McLaughlin-West et al., 1999);

(ii) la production thermogénique de CH_4 par la décomposition thermique de la matière organique à des températures supérieures à 100 °C (Schoell, 1980; 1988);

(iii) le dégazage du carbone juvénile à mesure que le CH_4 monte à travers le manteau, similaire à celui de l'hélium juvénile (Craig and Lupton, 1981);

(iv) la synthèse inorganique à des températures élevées (> 300-400 °C) impliquant le CO_2 et l'H_2 ou d'autres molécules C-H provenant de sources diverses. Un exemple de synthèse inorganique est la formation d'hydrocarbures et d'autres composés organiques dans les environnements géologiques lors de réactions chimiques telles que la réaction de Fischer-Tropsch : $CO_2 + 4H_2 \leftrightharpoons CH_4 + 2H_2O$ (Craig, 1953; Zolotov and Shock, 2000; McCollom, 2013).

Ces processus peuvent être classés en deux catégories : (i) et (ii) sont considérés comme des sources biogéniques qui comprennent à la fois les activités bactériennes et thermocatalytiques, tandis que (iii) et (iv) sont des sources abiotiques (bien qu'une histoire du carbone biogène antérieure ne soit pas exclue sous (iv)).

En examinant la composition isotopique en carbone du méthane ($\delta^{13}C$-CH_4), le gaz dominé par un CH_4 avec des valeurs de $\delta^{13}C$ inférieures à -55 ‰ est généralement considéré comme ayant une origine microbienne, tandis que le gaz avec du CH_4 ayant des valeurs de $\delta^{13}C$ de -30 ‰ à -50 ‰ est généralement interprété comme étant thermogénique. Le CH_4 abiotique est généralement supposé être enrichi en ^{13}C, avec des valeurs de $\delta^{13}C$ supérieures à -20 ‰ (Schoell, 1980; 1988; Welhan, 1988). Cependant, des processus post-génération tels que le mélange, la migration, la biodégradation, la réduction thermochimique du sulfate et l'oxydation peuvent se produire, auquel cas l'interprétation de la signature isotopique est plus complexe. Milkov and Etiope (2018) ont proposé de nouveaux diagrammes couvrant la grande majorité des gaz contenant des hydrocarbures actuellement connus.

Les gaz observés dans les fluides hydrothermaux des régions de dorsales médio-océaniques présentent généralement des valeurs de $\delta^{13}C$-CH_4 entre -8,6 et -20 ‰, tandis que des valeurs de $\delta^{13}C$-CH_4 de -23 ± 6 ‰ sont rapportées le long de la dorsale Est du Pacifique (EPR) et de -12 ± 4 ‰ le long de la dorsale médio-atlantique (MAR) ((Kawagucci et al., 2008; Sano and Fischer, 2013; Wen et al., 2016), et références citées). De plus, des fluides chauds et des bulles de gaz provenant des volcans sous-marins en arc arrière avec des valeurs de $\delta^{13}C$-CH_4 variant de -24,8 ‰ à -41,4 ‰ ont été détectés, suggèrant une origine principalement thermogène pour le CH_4 (Michel et al., 2018).

1.2.3.2.3. Dihydrogène (H_2)

Dans les systèmes volcaniques sous-marins, le dihydrogène (H2) est décrit comme un traceur immédiat de l'activité éruptive et fournit des preuves solides de réactions en cours ou très récentes

entre l'eau de mer ou l'eau magmatique et les roches fondues ou extrêmement chaudes (Baker et al., 2011; Resing et al., 2011; Baumberger et al., 2014; Baumberger et al., 2020).

L'H_2 provient soit d'une source de gaz magmatique (Symonds et al., 1994), soit peut être généré par le contact entre la lave en fusion et l'eau de mer (Sansone and Resing, 1995). Plus généralement, le H_2 est produit par toutes les formes d'oxydation du Fe(II) (Truche et al., 2020), résultant de la réduction de l'eau par des composés contenant du fer, selon la réaction $2(FeO)_{magma} + (H_2O)_{seawater} \rightarrow (Fe_2O_3)_{rock} + H_2$ (Perfit et al., 2003; Baker et al., 2011; Worman et al., 2020).

Les processus abiogéniques possibles d'être à l'origine de l'H_2 ont récemment été répertoriés par Worman et al. (2020) (Figure 1. 9), et comprennent :

(i) Interaction lave-eau de mer : c'est le processus le plus courant de génération de H_2 lors d'une éruption volcanique, se produisant pendant l'interaction entre la lave à haute température et l'eau de mer (Sansone et al., 1991);

(ii) Serpentinisation : l'H_2 est libéré par des réactions d'hydratation de matériaux ultramafiques tels que l'olivine et la pyroxène (McCollom, 2016; McCollom and Donaldson, 2016). Ce mécanisme est généralement considéré comme la principale voie de production de H_2 pendant la circulation hydrothermale dans les dorsales lentes et ultra-lentes, mais nécessite probablement un système hydrothermal mature (Charlou et al., 2010);

(iii) Cristallisation du magma basaltique : la production d'H_2 se produit pendant le stade tardif de la cristallisation, car l'eau dissoute dans le magma oxyde le fer ferreux (Christie et al., 1986);

(iv) Altération à haute température du basalte : pendant l'altération à haute température (~350 à 400 °C) de la croûte océanique par l'eau de mer, un nombre de silicates ferreux se transforment en minéraux contenant du fer ferrique et produisent de l'H_2 (Reed and Palandri, 2008).

(v) Altération de la croûte : la croûte océanique est altérée par l'eau de mer à mesure qu'elle refroidit et vieillit, formant des minéraux contenant du fer ferrique à plus basse température (< 250 °C) et du H_2 (Bach and Edwards, 2003);

(vi) Dégazage magmatique : à des températures magmatiques (~1200 °C), l'équilibre de la réaction $CH_4 + 2H_2O \leftrightharpoons CO_2 + 4H_2$ est fortement déplacé vers la droite, suggérant que l'H_2 peut être un composant des magmas (Apps and Kamp, 1993);

(vii) Radiolyse : la radiation émise par la désintégration des éléments radioactifs présents dans les roches océaniques tels que l'uranium (238U et 235U), le thorium (232Th) et le potassium (40K) peut exciter et ioniser l'eau, produisant des radicaux libres qui peuvent entraîner la radiolyse de l'eau, source d'H_2 (Jørgensen and D'Hondt, 2006; Dzaugis et al., 2016);

(viii) Fracturation des roches : ce processus rompt les liaisons chimiques, produisant des radicaux qui peuvent réagir avec l'eau pour générer de l'H_2 (Kita et al., 1982; Hirose et al., 2011);

(ix) Formation de pyrite : l'H_2 peut être produit suite à des réactions de précipitation des minéraux sulfurés métalliques (comme la pyrite) à partir de fluides hydrothermaux (Gallant and Von Damm, 2006).

Indépendamment du mécanisme, une fois que l'H_2 est produit, il peut être consommé par oxydation à travers des réactions abiotiques ou des processus microbiens, généralement dans un délai de quelques heures à quelques jours (McLaughlin-West et al., 1999; Worman et al., 2020).

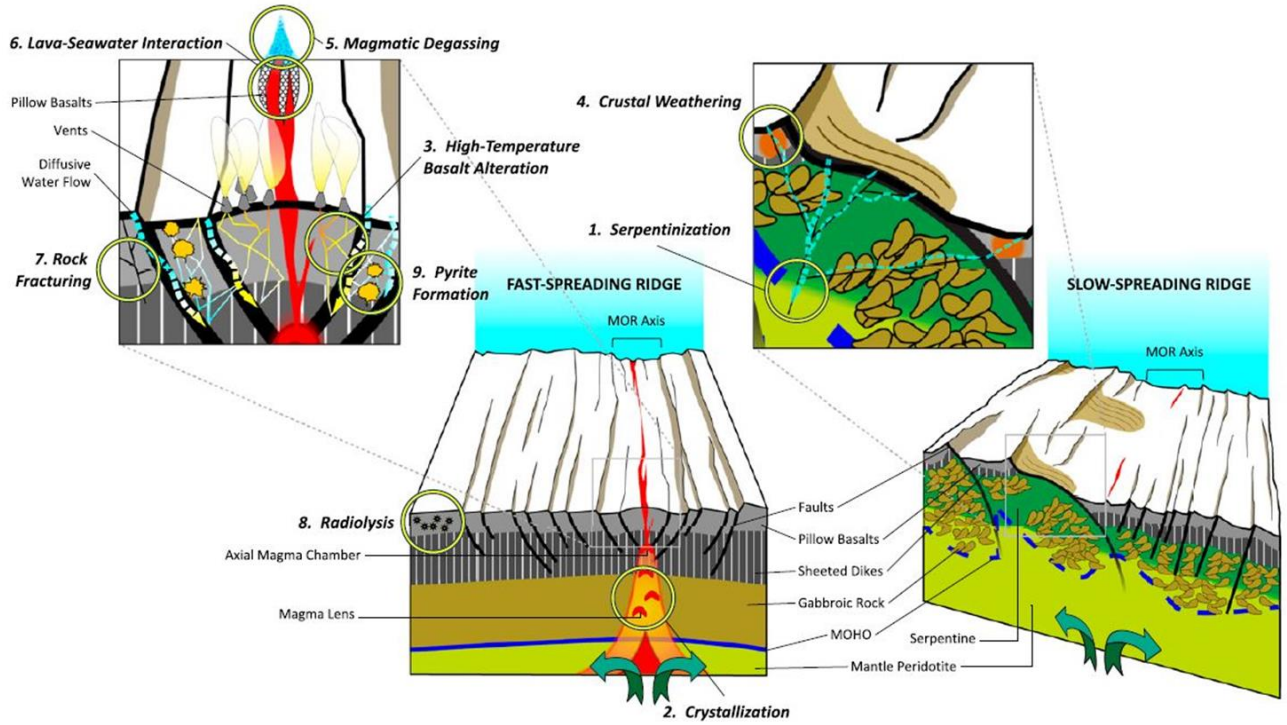

Figure 1. 9. Schéma des neuf différents processus abiogéniques qui peuvent produire de l'H_2 au sein de la croûte océanique, d'après Worman et al. (2020).

1.2.3.2.4. Sulfure d'hydrogène (H_2S) et dioxyde de soufre (SO_2)

Malgré son abondance réduite dans les magmas par rapport à l'eau ou au dioxyde de carbone, le dégazage des composés sulfurés liés aux éruptions volcaniques est un phénomène très important. En effet, il exerce une influence substantielle sur l'évolution des magmas (et leur potentiel éruptif) et a des impacts majeurs sur l'atmosphère (pour les volcans terrestres), le climat et les écosystèmes océaniques adjacents, à différentes échelles temporelles et spatiales. Le comportement complexe du soufre dans les magmas est en partie dû à ses multiples états d'oxydation (ex. -II, 0, IV, VI), à sa spéciation chimique (ex. S_2, H_2S, SO_2, OCS et SO_3 en phase gazeuse ; S^{2-}, SO_4^{2-} et SO_3^{2-}dans les laves et en phase liquide) et à ses variations dans la composition isotopique stable (^{32}S, ^{33}S, ^{34}S et ^{36}S ; par exemple Metrich and Mandeville (2010), Labidi et al. (2015)). Le rapport d'oxydoréduction (H_2S/SO_2) augmente notamment avec la pression (et donc la profondeur) et diminue avec la température du magma et la fugacité de l'oxygène, et dépend également du contexte tectonique (Hoshyaripour et al., 2012). Dans les systèmes hydrothermaux en fond de mer, le H_2S provient généralement de l'extraction de sulfure basaltique et de sulfate dérivé de l'eau de mer qui est réduit lors de l'interaction roche-eau à haute température (Shanks, 2001; Ono et al., 2007). Dans les environnements de dorsale d'arrière arc et d'arc, les volatils magmatiques enrichis en SO_2 peuvent produire des fluides hydrothermaux fortement acides et riches en H_2S par la réaction de dismutation (Herzig et al., 1998) : $4SO_2 + 4H_2O = 3H_2SO_4 + H_2S$.

L'impact de l'activité de dégazage des espèces soufrées sur la biosphère, lié au volcanisme, est également significatif, car une grande variété de microorganismes ont leur métabolisme basé sur la chimie d'oxydoréduction des sulfures : réduction des sulfures, du thiosulfate, du sulfite et du sulfate en H_2S, ou oxydation du soufre et du H_2S en sulfates (Amend and Shock, 2001; Shock et al., 2010). Comprendre le dégazage volcanique de sulfures revêt donc un intérêt primordial pour comprendre l'impact des processus magmatiques, volcaniques et hydrothermaux sur le système terrestre et les cycles biogéochimiques océaniques.

1.2.3.2.5. Fer (Fe) et manganèse (Mn)

Les éruptions sous-marines et la circulation hydrothermale produisent un dégagement important d'éléments traces tels que le fer (Fe) et le manganèse (Mn), qui sont essentiels sur le plan biologique. Dans les deux cas, la source des métaux est la lave, qu'elle soit solide ou en fusion, et les métaux sont libérés sous forme dissoute. Le fer et le manganèse sont les espèces ioniques (Fe^{2+} et Mn^{2+}) le plus couramment enrichies chimiquement dans les fluides de source hydrothermale, et le dégazage

hydrothermal est la principale source de ces métaux dans l'eau de mer. Ainsi, le fer et le manganèse sont des traceurs idéaux des émissions hydrothermales lorsqu'ils sont dilués au sein des panaches, où ils se transforment en composés particulaires qui jouent un rôle important dans la régulation des processus géochimiques dans l'eau de mer (Massoth et al., 2003).

Pendant longtemps, les émissions hydrothermales du plancher océanique n'ont pas été considérées comme une source majeure de fer dissous dans l'océan, contrairement au manganèse. Cependant, des études récentes ont montré le contraire. Dans la dorsale Est du Pacifique, l'activité hydrothermale pourrait être responsable de panaches de fer dissous s'étendant sur près de 4000 km (Resing et al., 2015). Dans la région de l'arc de Tonga, une source hydrothermale peu profonde est supposée être responsable de l'enrichissement en fer dissous des eaux photiques du Pacifique sud-ouest (Guieu et al., 2018).

À mesure que les panaches hydrothermaux vieillissent, le fer et le manganèse s'oxydent et sont captés par des particules. Il est supposé que le fer reste sous forme dissoute pendant des heures à des jours, tandis que le manganèse persiste pendant des mois (Klinkhammer et al., 1985; Cowen et al., 1990; Field and Sherrell, 2000; German and Von Damm, 2004).

Les concentrations de fer dissous dans l'océan ouvert sont très faibles, avec des valeurs typiques dans entre 0,02 et 2 nmol/L (ex. Wu et al. (2001)), tandis que les concentrations typiques de fer dissous dans les sources hydrothermales sont de l'ordre de 1 à 3 mmol/L, avec des valeurs extrêmes d'environ 18,7 mmol/L mesurées sur la dorsale Juan de Fuca (De Baar H. J, 2001). Dans les fluides hydrothermaux, le fer dissous se présente sous forme d'espèces stables de Fe(II) en raison des faibles valeurs de pH et des conditions de potentiel réduit. Après l'émission hydrothermale, le Fe(II) s'oxyde en présence d'oxygène dissous et précipite sous différentes formes minérales, principalement sous forme de sulfures de fer et d'oxyhydroxydes de fer. Les dépôts d'oxyhydroxydes de fer sont répandus dans les systèmes hydrothermaux en fond de mer le long des dorsales médio-océaniques et des centres d’expansion d'arrière arc, et constituent le principal type de dépôts hydrothermaux associés aux volcans sous-marins actifs. Les oxyhydroxydes de fer précipitent directement au fond de la mer à partir de fluides hydrothermaux diffus à basse température (de 10 à 100 °C) se mélangeant à l'eau froide de mer. Les oxyhydroxydes de fer ont été signalés le long de la dorsale Est du Pacifique (EPR), de la dorsale médio-atlantique (MAR), sur les monts sous-marins d'arc et d'arrière arc, ainsi que sur les volcans sous-marins intraplaques du Pacifique (Boyd and Scott, 2001; Kennedy et al., 2003; Edwards et al., 2011; Sun et al., 2011; Rouxel et al., 2018).

Environ 4% du fer émis total est stabilisé en solution grâce à la complexation par des ligands organiques dissous (Bennett et al., 2008; Resing et al., 2015; Fitzsimmons et al., 2017), ou par incorporation dans des colloïdes inorganiques ou organiques qui résident dans la fraction de taille dissoute (Resing et al., 2015). De plus, les espèces réduites de fer et de soufre forment un complexe colloïdal de FeS, qui reste en suspension dans l'eau et est modifié à mesure que le pH change (Luther et al., 2001). Ces nanoparticules peuvent rester en suspension dans les profondeurs marines pendant des années avec des taux de décantation plus lents (Yücel et al., 2011), solubilisant et libérant le Fe(II). La complexation augmente considérablement la teneur en métaux des systèmes hydrothermaux, augmentant le flux de métaux traces vers l'océan mondial. De grandes anomalies de fer en eau profonde, attribuées aux systèmes hydrothermaux en fond de mer, ont été trouvées dans les bassins du Pacifique, de l'Indien et de l'Atlantique (Tagliabue et al., 2010).

La relation entre Fe et Mn dans l'eau des panaches hydrothermaux est complexe et varie en fonction d'une multitude de conditions de réaction différentes. Le rapport Fe/Mn (en termes de fraction totale soluble) peut fournir des informations sur l'origine des fluides émis et l'état magmatique-hydrothermal. Les centres hydrothermaux actifs dans les îles Mariannes présentent des rapports variant de 5 à 30 (Buck et al., 2018), ce qui se situe dans la plage des rapports Fe/Mn mesurés dans les fluides à basse température au mont Loihi (Glazer and Rouxel, 2009). Les dorsales médio-océaniques et les systèmes hydrothermaux en profondeur ont des fluides avec des valeurs de pH plus élevées et des trajets de réaction eau-roche plus longs, et présentent donc des rapports de 0,2 à 4 (German and Seyfried, 2014). Les fluides magmatiques présents pendant l'éruption et l'évolution post-éruptive précoce, riches en SO_2 et CO_2, produisent des rapports Fe/Mn qui ont des valeurs similaires à celles de la roche hôte (Massoth et al., 2003; De Ronde et al., 2005). Les rapports Fe/Mn élevés dans les panaches hydrothermaux peuvent avoir plusieurs origines possibles : l'émission de volatils magmatiques riches en métaux (environ 54) (Rubin, 1997), la dissolution congruente de la roche hôte soit lors des interactions lave-eau de mer (environ 52) (Resing and Sansone, 2002) soit par la réaction entre les fluides riches en acide sulfurique chaud et la lave hôte (environ 50) (Butterfield et al., 2011). L'interaction entre la lave et l'eau de mer est régie par l'enrichissement des éléments majeurs de l'eau de mer en raison de la perte de vapeur d'eau, la libération de volatils magmatiques pour générer à la fois des enrichissements en éléments (Resing and Sansone, 2002) et en acidité (Resing and Sansone, 1999), l'échange d'ions entre l'eau de mer et la lave pour produire de l'acide (Resing and Sansone, 1999), la dissolution congruente de la lave (Resing and Sansone, 2002) et la réaction entre l'eau et le fer réduit de la lave pour produire de l'H_2 (Sansone and Resing, 1995).

1.2.3.3. Le système carbonaté

Dans l'étude des émissions de fluides et de gaz provenant des volcans sous-marins, le système carbonaté est crucial pour comprendre le dégazage de fluides riches en CO_2, en acide (H^+) et en alcalinité.

Le système carbonaté joue un rôle essentiel dans le contrôle de l'acidité de l'eau de mer et agit comme un régulateur fondamental du cycle du carbone (Emerson and Hedges, 2008). Au milieu de la multitude d'acides et de bases présents dans l'environnement en surface de la Terre, le système carbonaté agit comme le principal tampon pour l'acidité de l'eau, ce qui détermine la réactivité de la plupart des composés chimiques et des solides. Avec sa capacité à influencer la pression atmosphérique de CO_2, le système carbonaté de l'océan joue également un rôle critique dans la régulation de la température de la planète (Menon et al., 2007; Michard, 2008; Houghton, 2014). De plus, le taux de formation du minéral authigénique prévalent, le carbonate de calcium ($CaCO_3$), agit comme un puits majeur pour le carbone dissous, contribuant à l'équilibre mondial à long terme du carbone.

Essentiellement, le système carbonaté peut être décrit comme l'équilibre entre les formes dissoutes du CO_2 dans l'eau, le pH et les formes solides et dissoutes des carbonates. Les composés dissous qui constituent le système carbonaté dans l'eau (CO_2, HCO_3^- et CO_3^{2-}) sont en équilibre chimique sur des échelles de temps de quelques minutes (Emerson and Hedges, 2008).

Lorsque le CO_2 se dissout dans l'eau, de l'acide carbonique se forme et sa dissociation conduit à une diminution du pH :

$$CO_2 + H_2O \leftrightharpoons H_2CO_3 \leftrightharpoons HCO_3^- + H^+ \leftrightharpoons CO_3^{2-} + 2H^+ \qquad (1.14)$$

Dans l'eau de mer, cette acidification est atténuée en fonction de l'alcalinité totale (A_T) par rapport à la concentration de carbone inorganique dissous (DIC). L'A_T est la somme de toutes les bases faibles contenues dans l'eau qui peuvent être titrées par un acide fort jusqu'au point d'équivalence du CO_2. Dans l'eau de mer, la majorité de l'alcalinité est constituée d'ions carbonate et bicarbonate (Figure 1. 10). Les ions H^+ sont principalement neutralisés par la transformation des ions CO_3^{2-} en HCO_3^-. Ainsi, la concentration en ions CO_3^{2-} est un indicateur de la capacité tampon de l'eau de mer. Lorsque la concentration en ions carbonate devient limitante, le pH de l'eau de mer diminue. La dissociation de l'acide carbonique (HCO_3^-) augmente la capacité d'absorption du CO_2 atmosphérique par rapport à la dissolution du CO_2 telle que décrite par la loi de Henry. Cette capacité d'absorption est exprimée par

le facteur de Revelle, décrivant l'évolution des concentrations en DIC lorsque la pression partielle de CO_2 augmente dans l'eau de mer (Egleston et al., 2010).

Ainsi, l'eau de mer constitue un système tampon dans lequel différentes formes de DIC, d'A_T et de pH constituent le système carbonaté. Ce système est régi par un ensemble d'équilibres acido-basiques de l'acide carbonique, dépendant de la température et de la pression (Millero, 1979; Emerson and Hedges, 2008).

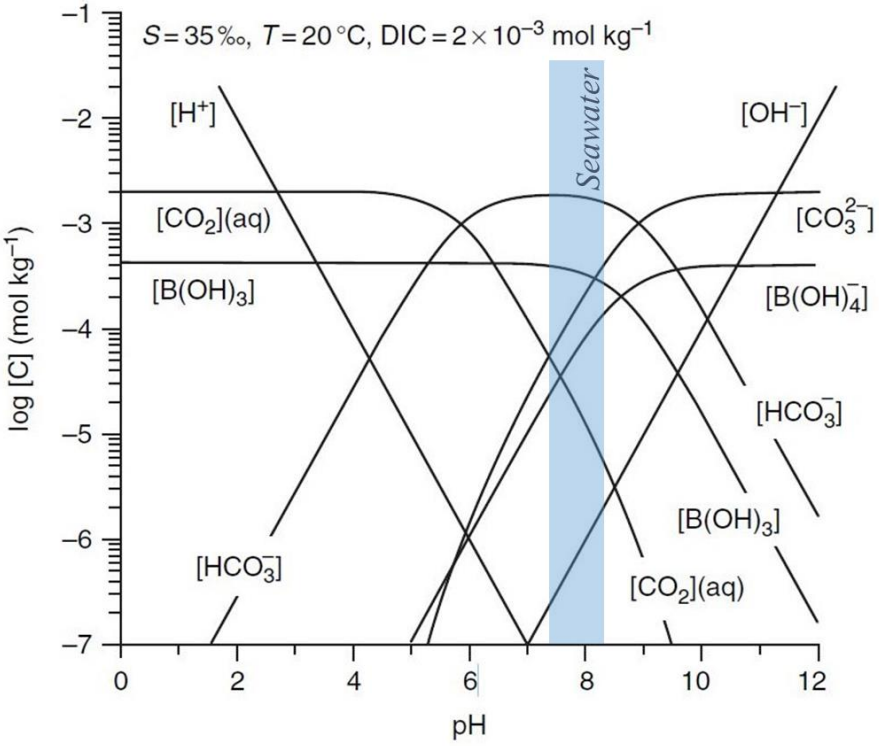

Figure 1. 10. centrations des couples acide-base de carbonate, borate et eau dans l'eau de mer en fonction du pH, pour une salinité (S) de 35 psu, une température (T) de 20 °C et un DIC de 2,0×10^{-3} mol/kg (modifié d'après Emerson and Hedges (2008)). Le pH de l'eau de mer se situe généralement entre 7,5 et 8,2, et le DIC pour cette plage est composé à plus de 90 % d'ions bicarbonate (HCO_3^-)

1.2.3.3.1. Le pH

Dans l'eau de mer, le pH est un paramètre crucial du système carbonaté car il détermine les équilibres chimiques des couples acide-base, tels que la spéciation du carbone inorganique dissous, et a donc une influence significative sur les écosystèmes marins.

La dissociation de l'acide carbonique (H_2CO_3) par abaissement du pH altère la spéciation normale du carbone dissous dans l'eau de mer et réduit l'état de saturation de la calcite et de l'aragonite dans l'eau de mer (Aiuppa et al., 2021). La diminution de cet état de saturation (Ω) affecte directement les organismes biocalcifiants (tels que les coraux, les foraminifères, les bivalves, etc.) en rendant difficile

la formation et le maintien de leurs coquilles. Cela peut conduire à la disparition locale d'espèces, entraînant une réorganisation complexe de la communauté avec des conséquences potentielles pour le fonctionnement de l'écosystème (Fabricius et al., 2011). Ainsi, l'équilibre des échanges de carbone entre l'océan, l'atmosphère et la lithosphère est directement lié aux conditions chimiques des écosystèmes marins (Mostofa et al., 2016).

1.2.3.3.2. Carbone inorganique dissous (DIC)

Dans l'eau de mer, le carbone inorganique existe sous quatre formes distinctes : le gaz en solution ou le dioxyde de carbone aqueux ($CO_{2\,(aq)}$), ainsi que les trois produits des réactions d'hydratation, à savoir l'acide carbonique (H_2CO_3), le bicarbonate (HCO_3^-) et le carbonate (CO_3^{2-}). Le carbone inorganique dissous (DIC), également appelé CO_2 total (ΣCO_2), est décrit comme la somme des formes dissoutes de CO_2 dans l'eau (Emerson and Hedges, 2008) :

$$DIC = \Sigma CO_2 = \left[CO_{2\,(aq)}\right] + [H_2CO_3] + [HCO_3^-] + [CO_3^{2-}] \qquad (1.15)$$

Les concentrations de ces formes dans l'eau de mer sont liées par des constantes d'équilibre qui dépendent du pH, de la salinité et de la température (Dickson et al., 2007; Emerson and Hedges, 2008) :

$$CO_{2\,(g)} \leftrightharpoons CO_{2\,(aq)} \qquad (1.16)$$

$$CO_{2\,(aq)} + H_2O \leftrightharpoons H_2CO_3 \qquad K'_{CO_2} = \frac{\left[CO_{2\,(aq)}\right]}{[H_2CO_3]} \qquad (1.17)$$

$$H_2CO_3 \leftrightharpoons HCO_3^- + H^+ \qquad K'_{H_2CO_3} = \frac{[HCO_3^-][H^+]}{[H_2CO_3]} \qquad (1.18)$$

$$HCO_3^- \leftrightharpoons CO_3^{2-} + H^+ \qquad K'_2 = \frac{[CO_3^{2-}][H^+]}{[HCO_3^-]} \qquad (1.19)$$

Il est difficile de distinguer analytiquement les espèces $CO_{2\,(aq)}$ et $H_2CO_{3\,(aq)}$. Il est donc courant de combiner les deux concentrations par leur somme et de la représenter soit avec le symbole $[CO_2]$ ou $H_2CO^*_3$, ce qui donne :

$$[CO_2] = \left[CO_{2\,(aq)}\right] + [H_2CO_3] \qquad (1.20)$$

Les équations (1.4) et (1.5) peuvent ensuite être combinées pour éliminer $[H_2CO_3]$ et obtenir une nouvelle constante de dissociation composite pour le CO_2 dans l'eau de mer. En supposant que $[CO_2$

$_{(aq)}$] = [CO_2], la première constante de dissociation de l'acide carbonique, K'1, est (Emerson and Hedges, 2008) :

$$CO_2 + H_2O \leftrightharpoons HCO_3^- + H^+ \qquad K_1' = \frac{[HCO_3^-][H^+]}{[CO_2]} \tag{1.21}$$

Trois processus importants (et les processus inverses correspondants) sont capables de modifier le DIC de l'eau de mer : la dissolution (dégazage) des gaz ; la respiration ou l'oxydation des organismes vivants (photosynthèse) ; la dissolution (précipitation) du $CaCO_3$ (Michard, 2008). Les ions carbonate réagissent avec les ions calcium pour former du carbonate de calcium solide sous deux formes possibles : la calcite et l'aragonite.

1.2.3.3.3. Alcalinité totale (A_T)

La concentration totale d'alcalinité dans l'eau de mer correspond à l'excès de bases (c'est-à-dire les accepteurs de protons) par rapport aux acides (c'est-à-dire les donneurs de protons) dans la solution (Emerson and Hedges, 2008). La définition précise de l'alcalinité totale selon (Dickson, 1981) est la suivante :

$$\begin{aligned} A_T = {} & [HCO_3^-] + 2[CO_3^{2-}] + [B(OH)_4^-] + [H_3SiO_4^-] + [HPO_4^{2-}] + 2[PO_4^{3-}] \\ & + [OH^-] - [H^+] - [HSO_4^-] - [HF] - [H_3PO_4] \end{aligned} \tag{1.22}$$

Cette expression inclut tous les accepteurs et donneurs de protons inorganiques connus dans l'eau de mer oxygénée (Dickson, 1981). Elle comprend deux espèces non chargées, la rendant pas exactement cohérente avec la définition précédente d'équilibre des charges ; cependant, en pratique, les concentrations des espèces acides dans l'eau de mer (H+, HSO4- , HF, et H_3PO_4) sont trop faibles dans la plage de pH de l'eau de mer de 7,0 à 8,0 pour être significatives et ne sont souvent pas incluses dans la définition de l'alcalinité.

$$A_T = [HCO_3^-] + 2[CO_3^{2-}] + [B(OH)_4^-] + [OH^-] - [H^+] \tag{1.23}$$

Dans l'eau de mer, les ions carbonate et borate représentent environ 99 % de l'alcalinité totale, tandis que les espèces de carbonate seules représentent environ 96 % de l'alcalinité totale et sont exprimées sous forme d'alcalinité carbonatée (AC) :

$$A_C = [HCO_3^-] + 2[CO_3^{2-}] \tag{1.24}$$

La principale source d'alcalinité pour de nombreuses eaux est le carbonate de calcium. La solubilité du carbonate de calcium est décrite par l'équation $CaCO_3 = Ca^{2+} + CO_3^{2-}$. Dans l'eau de mer, le

dioxyde de carbone réagit avec la calcite ($CaCO_3$) et la dolomite ($CaCO_3.MgCO_3$) pour former des ions bicarbonate (Boyd, 2015) :

$$CaCO_3 + CO_2 + H_2O \leftrightharpoons Ca^{2+} + 2HCO_3^- \quad (1.25)$$

$$CaCO_3 \cdot MgCO_3 + 2CO_2 + 2H_2O \leftrightharpoons Ca^{2+} + Mg^{2+} + 4HCO_3^- \quad (1.26)$$

1.2.4. Conséquences et dangers du volcanisme sous-marin

En comparaison aux éruptions subaériennes, les éruptions volcaniques sous-marines présentent un risque moindre pour la vie humaine, mais il existe toujours plusieurs dangers associés au volcanisme sous-marin. Les éruptions sous-marines peuvent entraîner des avalanches de débris sous-marins, des retombées de téphra, de forts séismes, des effondrements de flancs volcaniques, des instabilités de pente, des glissements de terrain sous-marins et même la génération de tsunamis (Lindsay et al., 2005; Paris et al., 2014). Les tsunamis d'origine éruptive se produisent lorsque l'énergie libérée lors d'une éruption est directement ou indirectement transmise à la mer, générant des vagues impulsionnelles par le déplacement de l'eau (Begét, 2000). Jusqu'à huit mécanismes sont impliqués dans la génération de tsunamis volcaniques : explosions sous-marines, coulées pyroclastiques entrant dans l'eau, séisme précédant ou se produisant pendant une éruption volcanique, effondrement de flanc, effondrement d'une plateforme côtière de lave, effondrement de caldeira et onde de choc produite par une forte explosion. De plus, une sismicité intense liée à l'éruption peut déclencher un effondrement de pente sous-marine (Nomikou et al., 2014; Paris et al., 2014; Mutaqin et al., 2019). De plus, la proximité des volcans des côtes peut présenter d'importants risques pour la population. Les dangers directs comprennent les éjections balistiques, les perturbations de l'eau et la diminution de la densité de l'eau due au dégazage, ce qui peut entraîner une diminution de la flottabilité des bateaux au-dessus du volcan (Lindsay et al., 2005).

Les activités volcaniques incluent l'émission de gaz, de particules et de fluides dans l'océan, qui sont acides et potentiellement toxiques pour de nombreuses espèces (ex. CO_2, CH_4, SO_2, H_2S, HS^-, HCl et HF) (Fischer, 2008; Oppenheimer et al., 2011; Buck et al., 2018; Romano et al., 2019; Aiuppa et al., 2021). Ces émissions peuvent perturber les caractéristiques physico-chimiques de l'océan environnant, avec des impacts potentiels sur le fonctionnement des écosystèmes présents sur le fond marin et/ou dans la colonne d'eau. Les panaches éruptifs sous-marins peuvent transporter de petites particules (par exemple, de la cendre) avec de faibles vitesses de sédimentation sur de grandes

échelles spatiales, le long des courants de gravité (White et al., 2001; Deardorff et al., 2011; Murch, 2018), s'éloignant à des centaines de kilomètres du lieu de l'éruption (Mittal and Delbridge, 2019). De plus, les éruptions sous-marines et les écoulements de lave ont été signalés comme un potentiel fertiliseur pour l'océan (Langmann et al., 2010b; Guieu et al., 2018; Wilson et al., 2019). Le volcanisme sous-marin soutient des communautés microbiennes diversifiées grâce aux émanations hydrothermales (Spietz et al., 2018), agissant comme une source exogène de nutriments et générant des blooms phytoplanctoniques en surface grâce à la remontée d'eaux profondes riches en nutriments et faibles en O2 (Wilson et al., 2019). Les zones de mélange entre le panache hydrothermal réduit et l'eau de mer fournissent des enrichissements locaux de donneurs d'électrons capables de nourrir des métabolismes chimiosynthétiques complexes (Jannasch and Wirsen, 1979; Dick et al., 2013). Des études ont suggéré la présence de processus autotrophes et de microorganismes impliqués dans l'oxydation des sulfures, de l'hydrogène, du méthane et de l'ammoniac, qui dominent ces zones de mélange (Baker et al., 2012; Li et al., 2014). À l'inverse, les éruptions sous-marines peuvent détruire des populations biologiques entières, avec des impacts significatifs sur la faune benthique sessile qui ne peut pas échapper à l'ensevelissement dans la lave, ou à l'exposition à la chaleur et aux gaz. La colonisation et le rétablissement des communautés benthiques sur le fond marin nouvellement créé dépendent de l'apport larvaire exogène d'autres populations et des modifications des conditions physico-chimiques dans l'eau de mer. Les changements observés dans les communautés benthiques entre l'état pré-éruptif et le rétablissement des communautés peuvent présenter des modifications drastiques (Kelley et al., 2002; Staudigel et al., 2006; Resing et al., 2011).

1.2.5. Synthèse des systèmes volcaniques sous-marins étudiés

Jusqu'à présent, seulement une douzaine d'éruptions sous-marines profondes ont été documentées dans le monde (Baker et al., 2011; Rubin et al., 2012). Elles ont été observées dans différents contextes tectoniques (centre de divergence, point chaud, contexte d'arc), mais très peu des volcans détectés se trouvent dans l’océan profond (>2000 m). Les principaux systèmes volcaniques sous-marins étudiés sont présentés dans le Tableau 1. 3.

Tableau 1. 3. Principaux systèmes volcaniques sous-marins étudiés. Données issues de Baker et al. (2012), Price and Giovannelli (2017), Rubin et al. (2012), Siebert et al. (2015b), Tepp and Dziak (2021), et des références citées dans le tableau. NA est utilisée pour les informations manquantes.

Volcan	Localisation	Contexte tectonique	Latitude	Longitude	Prof. de base (m)	Prof. du sommet (m)	Contexte géologique	Eruption observée
East Pacific Rise	Central Pacific	spreading center	9.83	-104.3	2500	NA	basalt	1991-1992, 2005-2006
Axial Seamount	Juan de Fuca Ridge	spreading center	45.95	-130	2200-2400	1540	basalt	1998, 2011, 2015
CoAxial Segment	Juan de Fuca Ridge	spreading center	46.52	-129.58	2400	NA	basalt	1993
Loihi Seamount	Hawaii	hotspot	18.92	-155.27	~1200	969	alkalic basalt	1996
Vailulu'u Seamount	American Samoa	hotspot/spreading center	-14.22	-169.06	1000	593	NA	2005, 1995, 1973
Macdonald	South Pacific, Austral Islands	hotspot	-28.98	-140.25	150	40	NA	1987-89
Tagoro	El Hierro, Canary Islands	hotspot	27.62	-17.99	350	88	basanite	2011-2012
Brothers Volcano	Kermadec Arc, New Zealand	arc	-34.86	179.06	1650	1500	NA	NA
Havre Seamount	Kermadec Arc, New Zealand	arc	-31.11	-179.04	1750-2000	650	rhyolite, dacite	2012
Kick 'em Jenny	Caribbean Sea, Lesser Antilles	back-arc	12.30	-61.64	265	NA	basaltic, andesite	12 times between 1939 and 2001
NW Rota-1	Mariana Arc	arc	14.6	144.78	2800	517	basaltic, andesite	2003-2010
Ahyi	Mariana Arc	arc	20.4375	145.0292	90	25	basaltic	2014
West Mata	NE Lau Basin, Tonga Islands	rear-arc	-15.1	-173.75	3000	1165	boninite	2008-2009
Northeast Lau Spreading Center	NE Lau Basin, Tonga Islands	back-arc	-15.4	-174.27	1800	NA	basaltic, andesite	2008
Fani Maoré Seamount	Comoros Archipelago, Indian Ocean	Intraplate, lithospheric deformation	-12.7	45.65	3500	2680	basaltic	2018-2019

Volcano	Activité observée	Géochimie de la colonne d'eau	Références
East Pacific Rise	Lava flow, hydrothermal activivity	High-temperature fluids (>410°C); High levels of CH_4; Presence of H_2S	(Tolstoy et al., 2006; Cowen et al., 2007; Dziak et al., 2009; Fornari et al., 2012; Wu et al., 2022)
Axial Seamount	Lava flow, hydrothermal plume	Low hydrothermal heat flux; Elevated ^3He/heat; Elevated CH_4, Mn and H_2	(Baker et al., 1990; McLaughlin-West et al., 1999; Baker et al., 2004; Wilcock et al., 2018)
CoAxial Segment	Megaplume, lava flow, microbial activity	Elevated dissolved Mn and CH_4; Fe-rich and H_2S-rich fluids	(Baker et al., 1995; Butterfield et al., 1997; Dziak et al., 2007)
Loihi Seamount	Lava flow, Hydrothermal fluid	High (~200°C) and low (<95°C) temperature hydrothermal fluids; Rich in CH_4, ^3He, CO_2, Fe, Mn	(Wheat et al., 2000; Garcia et al., 2006; Malahoff et al., 2006; Glazer and Rouxel, 2009; Schipper et al., 2010)
Vailulu'u Seamount	Hydrothermal activity, microbial communities	Low (~28°C) and high (~81°C) temperature hydrothermal fluids; Enrichment in particulates, ^3He and reduce Fe and Mn	(Staudigel et al., 2004; Staudigel et al., 2006; Connell et al., 2009)
Macdonald	Explosive eruption, hydrothermal activity, magmatic gases, volcanic ash	Large amount of CH_4, CO_2, SO_2; Enriched in H_2S, Fe, Mn and Si; Extremly low pH	(Cheminée et al., 1991)
Tagoro	Hydrothermal activity, active CO_2 degassing	Low temperature hydrothermal fluids (<40°C); Enriched in CO_2, CH_4, H_2S, Si, Fe^{2+}	(Santana-Casiano et al., 2013; Santana-Casiano et al., 2016; Santana-González et al., 2017; Santana-Casiano et al., 2018; González et al., 2020)
Brothers Volcano	Hydrothermal activity, episodic injection of magmatic fluid	Low (<200°C) and high (up to 320°C) temperature hydrothermal fluids; High levels of CO_2, H_2S, ^3He, particulate Cu, total dissolvable Fe	(De Ronde et al., 2003; Massoth et al., 2003; De Ronde et al., 2005; Stucker et al., 2022)
Havre Seamount	Eruption		(Murch, 2018; Mittal and Delbridge, 2019)
Kick 'em Jenny	Hydrothermal activity, cold seeps with chemosynthetic-based ecosystems, bacterial mats	Fluids up to 180°C; 93-96% CO_2; Diffuse venting of low temperature	(Lindsay et al., 2005; Carey et al., 2014; Carey et al., 2016; Michel et al., 2018)
NW Rota-1	Eruption, hydrothermal activivity, magma degassing	Gas-rich fluid; CO_2 bubble discharged, Fluid rich in Fe, Mn, CO_2, and ^3He; Acid flows rich in SO_2, Al, Si	(Embley et al., 2006; Resing et al., 2007; Chadwick et al., 2008; Resing et al., 2009; Chadwick et al., 2014)
Ahyi	Hydrothermal activity	Enriched concentrations of H_2, ^3He, CH_4, particulate S, Mn, and Fe	(Buck et al., 2018)
West Mata	Eruption, lava flow, strong effusive and explosive activity	Elevated volatile concentrations: H_2, CH_4, CO_2, He, Mn^{2+}, Fe^{2+}	(Clague et al., 2011; Resing et al., 2011; Baumberger et al., 2014; Embley et al., 2014; Dziak et al., 2015; Chadwick et al., 2019; Walker et al., 2019; Murch et al., 2022)
Northeast Lau Spreading Center	Possibly short-live explosive and effusive	Event plume rich in H_2, poor in ^3He; Diffuse plume rich in CH_4 and ^3He	(Baker et al., 2011; Embley and Rubin, 2018; Baumberger et al., 2020)
Fani Maoré Seamount	Eruption (possibly explosive and effusive), lava flow, liquid CO2 venting	Elevated concentrations of ^3He, CH_4, CO_2, H_2; Event plume with extremely high H_2; Fe and Mn enrichment near seafloor	(Feuillet et al., 2021); this thesis

1.3. Objectifs scientifiques

L'objectif global de cette thèse est de mieux comprendre comment un édifice volcanique se construit dans l'océan profond au cours du temps, comment les différents processus de construction influencent l'interaction entre les produits éruptifs et l'eau de mer, et quelle est l'ampleur de l'impact d'une telle éruption (Figure 1. 11).

À cette fin, nous avons profité du volcan sous-marin nouvellement formé – le mont Fani Maoré – situé à environ 50 km au large de l'île de Mayotte. L'éruption de Fani Maoré est la plus grande et la plus profonde éruption jamais rapportée à ce jour, et possiblement associée à un événement éruptif explosif. L'édifice du volcan est probablement le plus jeune jamais observé. De plus, le système volcanique est associé à des émissions de CO_2 liquides au sein d'une structure géologique appelée le Fer à Cheval, ce qui ne constitue que le quatrième cas observé.

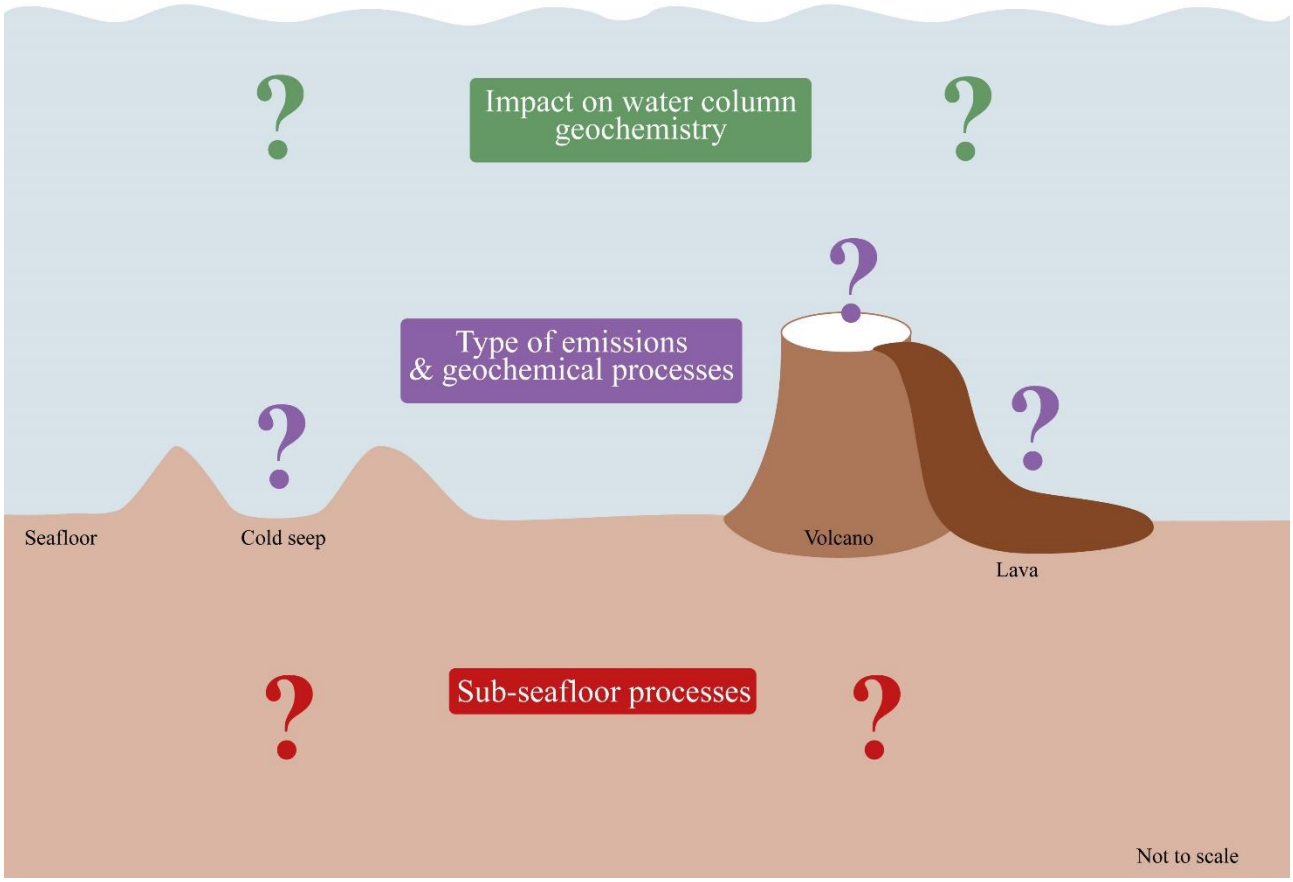

Figure 1. 11. Schéma des trois objectifs principaux qui ont motivé ce travail de doctorat. Ce diagramme est réutilisé pour la conclusion de ce manuscrit (Chapitre 7), et est complété d'après les résultats de cette thèse.

Par conséquent, l'étude du volcan Fani Maoré offre une opportunité unique pour répondre à l'objectif global de la thèse. Ci-dessous, nous détaillons les principales questions scientifiques associées au à l'objectif principal de la thèse, et qui consistent à s'interroger sur l'origine des émissions observées dans la colonne d'eau, sur les styles de manifestations des produits du volcanisme et leur composition géochimique, et sur l'impact global d'un volcan sous-marin profond sur la géochimie de la colonne d'eau (Figure 1. 11).

1.3.1. Origine des émissions observées dans la colonne d'eau

Le premier objectif de cette thèse est de déterminer, au sein de la colonne d'eau, l'origine des fluides et des gaz émis lors d'une éruption. Pour ce faire, nous utiliserons les isotopes d'hélium mesurés à partir d'échantillons prélevés dans la colonne d'eau sur la zone du système volcanique Fani Maoré. Grâce aux différentes campagnes réalisées dans cette zone, nous avons pu prélever des échantillons à différents stades de construction (éruption en cours et post-éruption à plusieurs moments) et de différentes manifestations d'activité (telles que panache éruptif, coulées de lave, circulation hydrothermale possible, émissions liquides de CO_2).

L'hélium est un gaz rare libéré via les fluides et les gaz magmatiques, et sa propriété non réactive en fait un traceur idéal de ces émissions dans la colonne d'eau. De plus, la composition isotopique de l'hélium (également appelée signature) fournit des informations précieuses sur l'origine des fluides et des gaz en apportant des preuves de matériaux dérivés du manteau ou de la croûte terrestre. Jusqu'à présent, l'utilisation des isotopes de l'hélium pour déterminer la signature était réalisée sur des échantillons de fluides et rarement sur des échantillons de colonne d'eau en raison de facteurs de dilution élevés impliquant de faibles concentrations en gaz rares. La quantification des isotopes d'hélium représente donc un défi et nécessite des choix d'échantillonnage minutieux.

La signature de l'hélium est très utile lorsqu'elle est associée aux émissions observées dans la colonne d'eau (émissions de fluide ou de gaz correspondant), et au mécanisme sous-marin, ce qui permet ainsi d'étudier le continuum depuis le réservoir sous-marin jusqu'à l'océan ouvert.

Dans cet objectif, nous cherchons à déterminer s'il existe (ou non) une homogénéité spatiale et temporelle de la signature du fluide observée dans la colonne d'eau. Pour cela, nous avons utilisé des données issues de d'échantillonnage réalisés pendant et après l'événement éruptif, ainsi que lors de diverses manifestations d'activité (ex. dégazage de CO_2 liquide). Un changement dans la signature

d'hélium de la colonne d'eau fournirait ainsi des informations sur le changement du chemin du magma ou des fluides associés. En fonction de la signature de la colonne d'eau, nous avons étudié si le mécanisme sous-marin responsable des émissions pouvait être défini.

Quelle est l'origine des émissions au sein de la colonne d'eau ?

Existe-t-il des variations spatiales et temporelles indiquant des changements dans les processus souterrains ?

Les processus sous le plancher océanique peuvent-ils être définis à partir de la signature en hélium de la colonne d'eau ?

1.3.2. Manifestations et processus géochimiques dans la colonne d'eau

Le deuxième objectif de cette thèse est de déterminer les différents types de manifestations de d'émissions volcaniques et les processus géochimiques associés. Les types de manifestations comprennent deux composantes : le style de manifestation et la composition des émissions. Le style de manifestation peut englober les panaches éruptifs, les fluides et les gaz libérés par les interactions entre la lave et l'eau de mer, les panaches hydrothermaux, les bulles de gaz, les gouttelettes, et bien plus encore. La composition des émissions comprend les caractéristiques physicochimiques, les concentrations en gaz, et en métaux. Les processus géochimiques contribuant aux émissions de fluides et de gaz peuvent impliquer le dégazage du magma, les interactions entre la lave et l'eau de mer, la circulation des fluides ou la libération de gaz à partir d'un réservoir sous-marin. Il a été observé que le type de manifestation influence significativement l'impact sur la colonne d'eau.

Pour atteindre cet objectif, nous avons utilisé un ensemble de données complet acquis lors de campagnes à la mer menées au niveau du système volcanique Fani Maoré. Cet ensemble de données englobe les concentrations de gaz (H_2, CH_4, CO_2), les concentrations en métaux traces (Fe, Mn) et les caractéristiques physicochimiques (pH, carbone inorganique dissous, alcalinité). Les gaz au sein d'un système volcanique résultent de processus divers, et leurs concentrations dans la colonne d'eau peuvent fournir des indications sur les processus impliqués. Cependant, la relation entre les concentrations de gaz et les processus reste encore mal déterminée. Par exemple, le fer et le manganèse sont des indicateurs efficaces qui peuvent refléter les interactions entre la lave et l'eau de mer, mais ils peuvent également indiquer le ré-entraînement de dépôts sous-marins. Les paramètres

physicochimiques fournissent des indices sur la nature du fluide. Par exemple, si les paramètres physicochimiques sont riches en acides, ils peuvent indiquer des interactions fluide-roche.

Dans cet aspect, nous avons spécifiquement étudié la corrélation entre les types de manifestations et les processus géochimiques intrinsèques observés dans la colonne d'eau. Cette analyse prend en compte diverses variables, notamment le niveau d'activité éruptive, la fraîcheur de la lave, la localisation (contexte géologique) et l'origine des émissions.

Comment les émissions volcaniques se manifestent-elles dans la colonne d'eau et quels sont les processus géochimiques impliqués ?

Quels sont les différents types de manifestations (style et composition) ?

Quels sont les processus géochimiques associés ?

Quel est le lien entre les caractéristiques géochimiques des émissions, les processus géochimiques, l'activité éruptive, le contexte géologique et l'origine des émissions ?

1.3.3. Impact sur la géochimie de la colonne d'eau

Le troisième objectif de cette thèse vise à évaluer l'impact d'une éruption sous-marine, et donc des fluides et des gaz volcaniques libérés, sur la géochimie de la colonne d'eau. Pour aborder cette question, nous nous sommes concentrés sur le système carbonaté (concentration de CO_2, carbone inorganique dissous, alcalinité) afin d'estimer le bilan du carbone libéré dans l'océan global, d'évaluer la capacité tampon de la colonne d'eau et d'estimer l'impact en termes d'acidification.

D'une part, nous avons évalué l'impact de l'éruption sous-marine de Fani Maoré sur la colonne d'eau, à la fois pendant et après l'événement. D'autre part, nous avons estimé l'impact de la libération exceptionnelle de CO_2 liquide présente au niveau de la structure du Fer à Cheval, à environ 40 km du volcan.

Dans les deux zones, nous avons étudié l'impact dans le temps et l'espace, et déterminé si le bilan carboné dans la colonne d'eau augmente, se dilue par exportation et renouvellement des masses d'eau, ou est tamponné par les composés chimiques présents dans l'eau de mer. Nous avons également évalué la relation entre le niveau d'impact et les caractéristiques géo-physicochimiques des émissions,

en tenant compte de la phase des émissions (gaz, liquide, dissous), de la composition chimique et du flux.

Quel est l'impact des émissions volcaniques sur la géochimie de la colonne d'eau?

Quel est l'impact dans le temps et dans l'espace?

Comment évolue le bilan carbone dans la zone locale?

Comment la colonne d'eau sera-t-elle affectée en fonction des caractéristiques géophysicochimiques des émissions?

1.4. Structure du manuscrit

Ce manuscrit est constitué de sept chapitres. Ils visent à mieux comprendre les émissions émises dans un contexte volcanique sous-marin et leur impact sur la géochimie de la colonne d'eau.

CHAPITRE 2. Site d'Etude & Contexte

Ce chapitre présente les paramètres géologiques régionaux de la zone de Mayotte. Il décrit les principales caractéristiques connues avant la crise sismo-volcanique, ainsi que le contexte géologique et sismique observé pendant crise. Ce chapitre aborde également les aspects sociétaux et la mobilisation scientifique qui en découle.

CHAPITRE 3. Méthodologie

Ce chapitre décrit les différents instruments utilisés pour l'observation, le prélèvement et l'analyse de la colonne d'eau, ainsi que les méthodes analytiques.

CHAPITRE 4. Fortes anomalies géochimiques suite à l'éruption sous-marine au large de Mayotte

Dans cette étude, nous présentons une compilation des données géochimiques acquises au volcan sous-marin Fani Maoré, lors de l'événement éruptif principal de mai 2019 et lors de deux campagnes à la mer réalisées en juillet 2019 et octobre 2020, conduisant à suivre l'installation de la coulée de lave en continu. Ces données apportent des informations précieuses sur les

mécanismes géochimiques lors de la mise en place d'un édifice volcanique et sur l'impact d'une activité éruptive sur la colonne d'eau à l'échelle locale.

CHAPITRE 5. Emissions sous-marines CO_2 liquide en contexte volcanique

Dans cette étude, nous présentons une compilation de données géochimiques acquises au-dessus des sites de dégazage du Fer à cheval et nous cherchons à déterminer l'origine des émissions de CO_2 liquide observées et la relation avec les émissions connues à proximité. Aussi, nous cherchons à comprendre les processus géochimiques qui se produisent dans l'eau de mer lors de l'ascension des gouttelettes de CO_2 liquide et, par conséquent, de leur dissolution. De plus, nous cherchons à évaluer l'impact de cette dissolution sur la colonne d'eau, en particulier en ce qui concerne l'acidification de la colonne d'eau à travers les échelles spatiales. En examinant de près les interactions entre les gouttelettes de CO_2 liquide et l'eau environnante, nous aspirons à mieux comprendre les implications environnementales de ces phénomènes.

CHAPITRE 6. Injection de CO_2 dans la colonne d'eau par les dégazages du Fer à Cheval : modélisation numérique

Dans ce chapitre, nous proposons une première approche pour donner une estimation de la quantité de dioxyde de carbone injectée tout au long de la colonne d'eau par le dégazage du Fer à cheval. Pour ce faire, nous utilisons le logiciel géochimique PHREEQC et la macro Excel CO2Sys, et nous comparons les données *in situ* avec les résultats du modèle. Nous réalisons d'abord cette approche à plusieurs profondeurs dans la colonne d'eau au-dessus de deux sites, l'un avec dégazage et l'autre sans présence de dégazage. Ensuite, nous testons le modèle pour différents sites à une profondeur donnée afin d'obtenir une analyse spatiale de la zone du Fer à Cheval. Enfin, nous extrapolons l'estimation du CO_2 injecté pour calculer les bilans de CO_2 dans la colonne d'eau.

CHAPITRE 7. Conclusions et Perspectives

Ce chapitre conclut le travail effectué au cours de cette thèse de doctorat, et présente quelques perspectives de recherche pour les travaux futurs.

1.5. Références Bibliographiques

Achterberg, E.P., Moore, C.M., Henson, S.A., Steigenberger, S., Stohl, A., Eckhardt, S., et al. (2013). Natural iron fertilization by the Eyjafjallajökull volcanic eruption. *Geophysical Research Letters* 40(5)**,** 921-926. doi: 10.1002/grl.50221.

Agostini, S., Wada, S., Kon, K., Omori, A., Kohtsuka, H., Fujimura, H., et al. (2015). Geochemistry of two shallow CO2 seeps in Shikine Island (Japan) and their potential for ocean acidification research. *Regional Studies in Marine Science* 2**,** 45-53. doi: 10.1016/j.rsma.2015.07.004.

Aiuppa, A., Hall-Spencer, J.M., Milazzo, M., Turco, G., Caliro, S., and Di Napoli, R. (2021). Volcanic CO2 seep geochemistry and use in understanding ocean acidification. *Biogeochemistry* 152(1)**,** 93-115. doi: 10.1007/s10533-020-00737-9.

Albright, R., Takeshita, Y., Koweek, D.A., Ninokawa, A., Wolfe, K., Rivlin, T., et al. (2018). Carbon dioxide addition to coral reef waters suppresses net community calcification. *Nature* 555(7697)**,** 516-519. doi: 10.1038/nature25968.

Amend, J.P., and Shock, E.L. (2001). Energetics of overall metabolic reactions of thermophilic and hyperthermophilic Archaea and Bacteria. *FEMS Microbiology Reviews* 25(2)**,** 175-243. doi: 10.1111/j.1574-6976.2001.tb00576.x.

Apps, J.A., and Kamp, P.C.v.d. (1993). Energy gases of abiogenic origin in the Earth's crust. *United States Geological Survey, Professional Paper; (United States)* 1570**,** Medium: X; Size: Pages: 81-132.

Ayache, M., Dutay, J.C., Jean-Baptiste, P., and Fourré, E. (2015). Simulation of the mantle and crustal helium isotope signature in the Mediterranean Sea using a high-resolution regional circulation model. *Ocean Science* 11(6)**,** 965-978. doi: 10.5194/os-11-965-2015.

Bach, W., and Edwards, K.J. (2003). Iron and sulfide oxidation within the basaltic ocean crust: implications for chemolithoautotrophic microbial biomass production. *Geochimica et Cosmochimica Acta* 67(20)**,** 3871-3887. doi: 10.1016/S0016-7037(03)00304-1.

Baker, E.T. (1998). Patterns of event and chronic hydrothermal venting following a magmatic intrusion: new perspectives from the 1996 Gorda Ridge eruption. *Deep Sea Research Part II: Topical Studies in Oceanography* 45(12)**,** 2599-2618. doi: 10.1016/S0967-0645(98)00085-X.

Baker, E.T., Chadwick, W.l.l.i.W.J., Cowen, J.P., Dziak, R.P., Rubin, K.H., and Fornari, D.J. (2012). Hydrothermal Discharge During Submarine Eruptions The Importance of Detection, Response, and New Technology. *Oceanography* 25(1)**,** 128-141. doi: 10.5670/oceanog.2012.11.

Baker, E.T., German, C.R., and Elderfield, H. (1995). "Hydrothermal Plumes Over Spreading-Center Axes: Global Distributions and Geological Inferences," in *Seafloor Hydrothermal Systems: Physical, Chemical, Biological, and Geological Interactions*.), 47-71.

Baker, E.T., Lowell, R.P., Resing, J.A., Feely, R.A., Embley, R.W., Massoth, G.J., et al. (2004). Decay of hydrothermal output following the 1998 seafloor eruption at Axial Volcano: Observations and models. *Journal of Geophysical Research: Solid Earth* 109(B1). doi: 10.1029/2003jb002618.

Baker, E.T., Lupton, J.E., Resing, J.A., Baumberger, T., Lilley, M.D., Walker, S.L., et al. (2011). Unique event plumes from a 2008 eruption on the Northeast Lau Spreading Center. *Geochemistry, Geophysics, Geosystems* 12(9). doi: 10.1029/2011gc003725.

Baker, E.T., Massoth, G.J., and Feely, R.A. (1987). Cataclysmic hydrothermal venting on the Juan de Fuca Ridge. *Nature* 329(6135)**,** 149-151. doi: 10.1038/329149a0.

Baker, E.T., McDuff, R.E., and Massoth, G.J. (1990). Hydrothermal venting from the summit of a ridge axis Seamount: Axial Volcano, Juan de Fuca Ridge. *Journal of Geophysical Research* 95(B8)**,** 12843. doi: 10.1029/jb095ib08p12843.

Ballentine, C.J., and Burnard, P.G. (2002). Production, Release and Transport of Noble

Gases in the Continental Crust. *Reviews in Mineralogy and Geochemistry* 47(1)**,** 481-538. doi: 10.2138/rmg.2002.47.12.

Batiza, R., and Vanko, D. (1983). Volcanic development of small oceanic central volcanoes on the flanks of the East Pacific Rise inferred from narrow-beam echo-sounder surveys. *Marine Geology* 54(1)**,** 53-90. doi: 10.1016/0025-3227(83)90008-7.

Baumberger, T., Lilley, M.D., Lupton, J.E., Baker, E.T., Resing, J.A., Buck, N.J., et al. (2020). Dissolved Gas and Metal Composition of Hydrothermal Plumes From a 2008 Submarine Eruption on the Northeast Lau Spreading Center. *Frontiers in Marine Science* 7. doi: 10.3389/fmars.2020.00171.

Baumberger, T., Lilley, M.D., Resing, J.A., Lupton, J.E., Baker, E.T., Butterfield, D.A., et al. (2014). Understanding a submarine eruption through time series hydrothermal plume sampling of dissolved and particulate constituents: West Mata, 2008-2012. *Geochemistry, Geophysics, Geosystems* 15(12)**,** 4631-4650. doi: 10.1002/2014gc005460.

Begét, J. (2000). "Volcanic tsunamis," in *Encyclopedia of volcanoes,* ed. H.B. Sigurdsson H, Mc Nutt SR, Rymer H, Stix J. (New York: Academic Press), 1005-1013.

Bennett, S.A., Achterberg, E.P., Connelly, D.P., Statham, P.J., Fones, G.R., and German, C.R. (2008). The distribution and stabilisation of dissolved Fe in deep-sea hydrothermal plumes. *Earth and Planetary Science Letters* 270(3-4)**,** 157-167. doi: 10.1016/j.epsl.2008.01.048.

Benson, B.B., and Krause, D. (1980). Isotopic fractionation of helium during solution: A probe for the liquid state. *Journal of Solution Chemistry* 9(12)**,** 895-909. doi: 10.1007/bf00646402.

Boatta, F., D'Alessandro, W., Gagliano, A.L., Liotta, M., Milazzo, M., Rodolfo-Metalpa, R., et al. (2013). Geochemical survey of Levante Bay, Vulcano Island (Italy), a natural laboratory for the study of ocean acidification. *Marine Pollution Bulletin* 73(2)**,** 485-494. doi: 10.1016/j.marpolbul.2013.01.029.

Bond, D.P.G., Wignall, P.B., Keller, G., and Kerr, A.C. (2014). "Large igneous provinces and mass extinctions: An update," in *Volcanism, Impacts, and Mass Extinctions: Causes and Effects*. Geological Society of America).

Boyd, C.E. (2015). "pH, Carbon Dioxide, and Alkalinity." Springer International Publishing), 153-178.

Boyd, T., and Scott, S. (2001). Microbial and hydrothermal aspects of ferric oxyhydroxides and ferrosic hydroxides: the example of Franklin Seamount, Western Woodlark Basin, Papua New Guinea. *Geochemical Transactions* 2(1). doi: 10.1186/1467-4866-2-45.

Brennwald, M.S., Vogel, N., Scheidegger, Y., Tomonaga, Y., Livingstone, D.M., and Kipfer, R. (2013). "Noble Gases as Environmental Tracers in Sediment Porewaters and Stalagmite Fluid Inclusions," in *The Noble Gases as Geochemical Tracers,* ed. P. Burnard. (Berlin, Heidelberg: Springer Berlin Heidelberg), 123-153.

Buck, N.J., Resing, J.A., Baker, E.T., and Lupton, J.E. (2018). Chemical Fluxes From a Recently Erupted Shallow Submarine Volcano on the Mariana Arc. *Geochemistry, Geophysics, Geosystems* 19(5)**,** 1660-1673. doi: 10.1029/2018gc007470.

Butterfield, D.A., Jonasson, I.R., Massoth, G.J., Feely, R.A., Roe, K.K., Embley, R.E., et al. (1997). Seafloor eruptions and evolution of hydrothermal fluid chemistry. *Philosophical Transactions of the Royal Society of London. Series A: Mathematical, Physical and Engineering Sciences* 355(1723)**,** 369-386. doi: doi:10.1098/rsta.1997.0013.

Butterfield, D.A., Nakamura, K.i., Takano, B., Lilley, M.D., Lupton, J.E., Resing, J.A., et al. (2011). High SO2 flux, sulfur accumulation, and gas fractionation at an erupting submarine volcano. *Geology* 39(9)**,** 803-806. doi: 10.1130/g31901.1.

Carey, S., Ballard, R., Bell, K.L.C., Bell, R.J., Connally, P., Dondin, F., et al. (2014). Cold seeps associated with a submarine debris avalanche deposit at Kick'em Jenny volcano, Grenada (Lesser Antilles). *Deep Sea Research Part I: Oceanographic Research Papers* 93**,** 156-160. doi: 10.1016/j.dsr.2014.08.002.

Carey, S., Nomikou, P., Bell, K.C., Lilley, M., Lupton, J., Roman, C., et al. (2013). CO2 degassing from hydrothermal vents at

Kolumbo submarine volcano, Greece, and the accumulation of acidic crater water. *Geology* 41(9), 1035-1038. doi: 10.1130/g34286.1.

Carey, S., Olsen, R., Bell, K.L.C., Ballard, R., Dondin, F., Roman, C., et al. (2016). Hydrothermal venting and mineralization in the crater of Kick'em Jenny submarine volcano, Grenada (Lesser Antilles). *Geochemistry, Geophysics, Geosystems* 17(3), 1000-1019. doi: 10.1002/2015gc006060.

Cas, R.A.F., and Giordano, G. (2014). Submarine Volcanism: a Review of the Constraints, Processes and Products, and Relevance to the Cabo de Gata Volcanic Succession. *Italian Journal of Geosciences* 133(3), 362-377. doi: 10.3301/Ijg.2014.46.

Cas, R.A.F., and Simmons, J.M. (2018). Why Deep-Water Eruptions Are So Different From Subaerial Eruptions. *Frontiers in Earth Science* 6. doi: 10.3389/feart.2018.00198.

Chadwick, W.W., Cashman, K.V., Embley, R.W., Matsumoto, H., Dziak, R.P., De Ronde, C.E.J., et al. (2008). Direct video and hydrophone observations of submarine explosive eruptions at NW Rota-1 volcano, Mariana arc. *Journal of Geophysical Research: Solid Earth* 113(B8). doi: 10.1029/2007jb005215.

Chadwick, W.W., Merle, S.G., Buck, N.J., Lavelle, J.W., Resing, J.A., and Ferrini, V. (2014). Imaging of CO2bubble plumes above an erupting submarine volcano, NW Rota-1, Mariana Arc. *Geochemistry, Geophysics, Geosystems* 15(11), 4325-4342. doi: 10.1002/2014gc005543.

Chadwick, W.W., Rubin, K.H., Merle, S.G., Bobbitt, A.M., Kwasnitschka, T., and Embley, R.W. (2019). Recent Eruptions Between 2012 and 2018 Discovered at West Mata Submarine Volcano (NE Lau Basin, SW Pacific) and Characterized by New Ship, AUV, and ROV Data. *Frontiers in Marine Science* 6. doi: 10.3389/fmars.2019.00495.

Charlou, J.L., Donval, J.P., Konn, C., OndréAs, H., Fouquet, Y., Jean-Baptiste, P., et al. (2010). "High production and fluxes of H2 and CH4 and evidence of abiotic hydrocarbon synthesis by serpentinization in ultramafic-hosted hydrothermal systems on the Mid-Atlantic Ridge," in *Diversity Of Hydrothermal Systems On Slow Spreading Ocean Ridges*.), 265-296.

Cheminée, J.L., Stoffers, P., McMurtry, G., Richnow, H., Puteanus, D., and Sedwick, P. (1991). Gas-rich submarine exhalations during the 1989 eruption of Macdonald Seamount. *Earth and Planetary Science Letters* 107(2), 318-327. doi: 10.1016/0012-821x(91)90079-w.

Christie, D.M., Carmichael, I.S.E., and Langmuir, C.H. (1986). Oxidation states of mid-ocean ridge basalt glasses. *Earth and Planetary Science Letters* 79(3), 397-411. doi: 10.1016/0012-821X(86)90195-0.

Clague, D.A., Paduan, J.B., Caress, D.W., Thomas, H., Chadwick, W.W., and Merle, S.G. (2011). Volcanic morphology of West Mata Volcano, NE Lau Basin, based on high-resolution bathymetry and depth changes. *Geochemistry, Geophysics, Geosystems* 12(11), n/a-n/a. doi: 10.1029/2011gc003791.

Clarke, W.B., Jenkins, W.J., and Top, Z. (1976). Determination of tritium by mass spectrometric measurement of 3He. *The International Journal of Applied Radiation and Isotopes* 27(9), 515-522. doi: 10.1016/0020-708x(76)90082-x.

Connell, L., Barrett, A., Templeton, A., and Staudigel, H. (2009). Fungal Diversity Associated with an Active Deep Sea Volcano: Vailulu'u Seamount, Samoa. *Geomicrobiology Journal* 26(8), 597-605. doi: 10.1080/01490450903316174.

Courtillot, V., Féraud, G., Maluski, H., Vandamme, D., Moreau, M.G., and Besse, J. (1988). Deccan flood basalts and the Cretaceous/Tertiary boundary. *Nature* 333(6176), 843-846. doi: 10.1038/333843a0.

Cowen, J.P., Fornari, D.J., Shank, T.M., Love, B., Glazer, B., Treusch, A., et al. (2007). Volcanic Eruptions at East Pacific Rise Near 9°50′N. *Eos, Transactions American Geophysical Union* 88(7), 81. doi: 10.1029/2007eo070001.

Cowen, J.P., Massoth, G.J., and Feely, R.A. (1990). Scavenging rates of dissolved manganese in a hydrothermal vent plume. *Deep Sea Research Part A. Oceanographic Research Papers* 37(10), 1619-1637. doi: 10.1016/0198-0149(90)90065-4.

Craig, H. (1953). The geochemistry of the stable carbon isotopes. *Geochimica et Cosmochimica Acta* 3(2)**,** 53-92. doi: 10.1016/0016-7037(53)90001-5.

Craig, H., and Lupton, J.E. (1981). Helium-3 and mantle volatiles in the ocean and the oceanic crust. *The oceanic lithosphere* 7**,** 391.

Craig, H., and Weiss, R.F. (1971). Dissolved gas saturation anomalies and excess helium in the ocean. *Earth and Planetary Science Letters* 10(3)**,** 289-296. doi: 10.1016/0012-821X(71)90033-1.

Dando, P.R., Hughes, J.A., Leahy, Y., Niven, S.J., Taylor, L.J., and Smith, C. (1995). Gas venting rates from submarine hydrothermal areas around the island of Milos, Hellenic Volcanic Arc. *Continental Shelf Research* 15(8)**,** 913-929. doi: 10.1016/0278-4343(95)80002-u.

Davis, A.S., and Clague, D.A. (1998). Changes in the hydrothermal system at Loihi Seamount after the formation of Pele's pit in 1996. *Geology* 26(5)**,** 399-402. doi: 10.1130/0091-7613(1998)026<0399:Cithsa>2.3.Co;2.

De Baar H. J, W. (2001). Distributions, sources and sinks of iron in seawater. *The Biogeochemistry of iron in seawater*.

De Ronde, C.E., Faure, K., Bray, C.J., Chappell, D.A., and Wright, I.C. (2003). Hydrothermal fluids associated with seafloor mineralization at two southern Kermadec arc volcanoes, offshore New Zealand. *Mineralium Deposita* 38(2)**,** 217-233. doi: 10.1007/s00126-002-0305-4.

De Ronde, C.E.J., Hannington, M.D., Stoffers, P., Wright, I.C., Ditchburn, R.G., Reyes, A.G., et al. (2005). Evolution of a Submarine Magmatic-Hydrothermal System: Brothers Volcano, Southern Kermadec Arc, New Zealand. *Economic Geology* 100(6)**,** 1097-1133. doi: 10.2113/gsecongeo.100.6.1097.

De Ronde, C.E.J., Humphris, S.E., Höfig, T.W., and Reyes, A.G. (2019). Critical role of caldera collapse in the formation of seafloor mineralization: The case of Brothers volcano. *Geology* 47(8)**,** 762-766. doi: 10.1130/g46047.1.

De Soto, N.A., Delorme, N., Atkins, J., Howard, S., Williams, J., and Johnson, M. (2013). Anthropogenic noise causes body malformations and delays development in marine larvae. *Scientific Reports* 3(1). doi: 10.1038/srep02831.

Deardorff, N.D., Cashman, K.V., and Chadwick, W.W. (2011). Observations of eruptive plume dynamics and pyroclastic deposits from submarine explosive eruptions at NW Rota-1, Mariana arc. *Journal of Volcanology and Geothermal Research* 202(1)**,** 47-59. doi: 10.1016/j.jvolgeores.2011.01.003.

Dick, G.J., Anantharaman, K., Baker, B.J., Li, M., Reed, D.C., and Sheik, C.S. (2013). The microbiology of deep-sea hydrothermal vent plumes: ecological and biogeographic linkages to seafloor and water column habitats. *Front Microbiol* 4**,** 124. doi: 10.3389/fmicb.2013.00124.

Dickson, A.G. (1981). An exact definition of total alkalinity and a procedure for the estimation of alkalinity and total inorganic carbon from titration data. *Deep Sea Research Part A. Oceanographic Research Papers* 28(6)**,** 609-623. doi: 10.1016/0198-0149(81)90121-7.

Dickson, A.G., Sabine, C.L., and Christian, J.R. (2007). "Guide to best practices for ocean CO2 measurements", in: *PICES Special Publication 3, IOCCP Report 8.* (North Pacific Marine Science Organization, Sidney, British Columbia).

Doney, S.C., Busch, D.S., Cooley, S.R., and Kroeker, K.J. (2020). The Impacts of Ocean Acidification on Marine Ecosystems and Reliant Human Communities. *Annual Review of Environment and Resources* 45(1)**,** 83-112. doi: 10.1146/annurev-environ-012320-083019.

Dzaugis, M.E., Spivack, A.J., Dunlea, A.G., Murray, R.W., and D'Hondt, S. (2016). Radiolytic Hydrogen Production in the Subseafloor Basaltic Aquifer. *Frontiers in Microbiology* 7. doi: 10.3389/fmicb.2016.00076.

Dziak, R.P., Bohnenstiehl, D.R., Baker, E.T., Matsumoto, H., Caplan-Auerbach, J., Embley, R.W., et al. (2015). Long-term explosive degassing and debris flow activity at West Mata submarine volcano. *Geophysical Research Letters* 42(5)**,** 1480-1487. doi: 10.1002/2014gl062603.

Dziak, R.P., Bohnenstiehl, D.R., Cowen, J.P., Baker, E.T., Rubin, K.H., Haxel, J.H., et al. (2007). Rapid dike emplacement leads to eruptions and hydrothermal plume release during

seafloor spreading events. *Geology* 35(7), 579-582. doi: 10.1130/g23476a.1.

Dziak, R.P., Bohnenstiehl, D.R., Matsumoto, H., Fowler, M.J., Haxel, J.H., Tolstoy, M., et al. (2009). January 2006 seafloor-spreading event at 9°50′N, East Pacific Rise: Ridge dike intrusion and transform fault interactions from regional hydroacoustic data. *Geochemistry, Geophysics, Geosystems* 10(6), n/a-n/a. doi: 10.1029/2009gc002388.

Edwards, K.J., Glazer, B.T., Rouxel, O.J., Bach, W., Emerson, D., Davis, R.E., et al. (2011). Ultra-diffuse hydrothermal venting supports Fe-oxidizing bacteria and massive umber deposition at 5000 m off Hawaii. *The ISME Journal* 5(11), 1748-1758. doi: 10.1038/ismej.2011.48.

Egleston, E.S., Sabine, C.L., and Morel, F.M.M. (2010). Revelle revisited: Buffer factors that quantify the response of ocean chemistry to changes in DIC and alkalinity. *Global Biogeochemical Cycles* 24(1), n/a-n/a. doi: 10.1029/2008gb003407.

Embley, R.W., Chadwick, W.W., Baker, E.T., Butterfield, D.A., Resing, J.A., de Ronde, C.E.J., et al. (2006). Long-term eruptive activity at a submarine arc volcano. *Nature* 441(7092), 494-497. doi: 10.1038/nature04762.

Embley, R.W., Merle, S.G., Baker, E.T., Rubin, K.H., Lupton, J.E., Resing, J.A., et al. (2014). Eruptive modes and hiatus of volcanism at West Mata seamount, NE Lau basin: 1996-2012. *Geochemistry, Geophysics, Geosystems* 15(10), 4093-4115. doi: 10.1002/2014gc005387.

Embley, R.W., and Rubin, K.H. (2018). Extensive young silicic volcanism produces large deep submarine lava flows in the NE Lau Basin. *Bulletin of Volcanology* 80(4). doi: 10.1007/s00445-018-1211-7.

Emerson, S., and Hedges, J. (2008). *Chemical Oceanography and the Marine Carbon Cycle.*

Fabricius, K.E., Langdon, C., Uthicke, S., Humphrey, C., Noonan, S., De'Ath, G., et al. (2011). Losers and winners in coral reefs acclimatized to elevated carbon dioxide concentrations. *Nature Climate Change* 1(3), 165-169. doi: 10.1038/nclimate1122.

Feuillet, N., Jorry, S., Crawford, W.C., Deplus, C., Thinon, I., Jacques, E., et al. (2021). Birth of a large volcanic edifice offshore Mayotte via lithosphere-scale dyke intrusion. *Nature Geoscience* 14, 787-795. doi: 10.1038/s41561-021-00809-x.

Fiebig, J., Chiodini, G., Caliro, S., Rizzo, A., Spangenberg, J., and Hunziker, J.C. (2004). Chemical and isotopic equilibrium between CO2 and CH4 in fumarolic gas discharges: Generation of CH4 in arc magmatic-hydrothermal systems 1 1Associate editor: M. Kusakabe. *Geochimica et Cosmochimica Acta* 68(10), 2321-2334. doi: 10.1016/j.gca.2003.10.035.

Field, M.P., and Sherrell, R.M. (2000). Dissolved and particulate Fe in a hydrothermal plume at 9°45′N, East Pacific Rise. *Geochimica et Cosmochimica Acta* 64(4), 619-628. doi: 10.1016/s0016-7037(99)00333-6.

Fischer, T.P. (2008). Fluxes of volatiles (H2O, CO2, N2, Cl, F) from arc volcanoes. *GEOCHEMICAL JOURNAL* 42(1), 21-38. doi: 10.2343/geochemj.42.21.

Fischer, T.P., and Aiuppa, A. (2020). AGU Centennial Grand Challenge: Volcanoes and Deep Carbon Global CO2 Emissions From Subaerial Volcanism—Recent Progress and Future Challenges. *Geochemistry, Geophysics, Geosystems* 21(3). doi: 10.1029/2019gc008690.

Fitzsimmons, J.N., John, S.G., Marsay, C.M., Hoffman, C.L., Sarah, Toner, B.M., et al. (2017). Iron persistence in a distal hydrothermal plume supported by dissolved–particulate exchange. *Nature Geoscience* 10(3), 195-201. doi: 10.1038/ngeo2900.

Fornari, D.J., Von Damm, K.L., Bryce, J.G., Cowen, J.P., Ferrini, V., Fundis, A., et al. (2012). The East Pacific Rise Between 9°N and 10°N: Twenty-five years of integrated, multidisciplinary oceanic spreading center studies. *Oceanography* 25(1), 18-43.

Gallant, R.M., and Von Damm, K.L. (2006). Geochemical controls on hydrothermal fluids from the Kairei and Edmond Vent Fields, 23°-25°S, Central Indian Ridge. *Geochemistry, Geophysics, Geosystems* 7(6), n/a-n/a. doi: 10.1029/2005gc001067.

Garcia, M.O., Caplan-Auerbach, J., De Carlo, E.H., Kurz, M.D., and Becker, N. (2006). Geology,

geochemistry and earthquake history of Lo̍ihi Seamount, Hawaìi's youngest volcano. *Geochemistry* 66(2)**,** 81-108. doi: 10.1016/j.chemer.2005.09.002.

Gautheron, C., and Moreira, M. (2002). Helium signature of the subcontinental lithospheric mantle. *Earth and Planetary Science Letters* 199(1)**,** 39-47. doi: 10.1016/S0012-821X(02)00563-0.

German, C.R., and Seyfried, W.E. (2014). "8.7 - Hydrothermal Processes," in *Treatise on Geochemistry (Second Edition)*, eds. H.D. Holland & K.K. Turekian. (Oxford: Elsevier), 191-233.

German, C.R., and Von Damm, K.L. (2004). "Hydrothermal processes," in *Treatise on geochemistry, Vol. 6. The oceans and marine geochemistry*, eds. H.D. Holland, K.K. Turekian & H. Elderfield. Elsevier-Pergamon), 181-222.

Giggenbach, W. (1997). The origin and evolution of fluids in magmatic-hydrothermal systems. *Geochemistry of hydrothermal ore deposits*.

Glazer, B.T., and Rouxel, O.J. (2009). Redox Speciation and Distribution within Diverse Iron-dominated Microbial Habitats at Loihi Seamount. *Geomicrobiology Journal* 26(8)**,** 606-622. doi: 10.1080/01490450903263392.

González-Delgado, S., and Hernández, J.C. (2018). "Chapter Two - The Importance of Natural Acidified Systems in the Study of Ocean Acidification: What Have We Learned?," in *Advances in Marine Biology*, ed. C. Sheppard. Academic Press), 57-99.

González, F.J., Rincón-Tomás, B., Somoza, L., Santofimia, E., Medialdea, T., Madureira, P., et al. (2020). Low-temperature, shallow-water hydrothermal vent mineralization following the recent submarine eruption of Tagoro volcano (El Hierro, Canary Islands). *Marine Geology* 430**,** 106333. doi: 10.1016/j.margeo.2020.106333.

Graham, D.W. (2002). Noble Gas Isotope Geochemistry of Mid-Ocean Ridge and Ocean Island Basalts: Characterization of Mantle Source Reservoirs. *Reviews in Mineralogy and Geochemistry* 47(1)**,** 247-317. doi: 10.2138/rmg.2002.47.8.

Guieu, C., Bonnet, S., Petrenko, A., Menkes, C., Chavagnac, V., Desboeufs, K., et al. (2018). Iron from a submarine source impacts the productive layer of the Western Tropical South Pacific (WTSP). *Scientific Reports* 8(1). doi: 10.1038/s41598-018-27407-z.

Hall-Spencer, J.M., and Harvey, B.P. (2019). Ocean acidification impacts on coastal ecosystem services due to habitat degradation. *Emerging Topics in Life Sciences* 3(2)**,** 197-206. doi: 10.1042/etls20180117.

Hawco, N.J., Yang, S.-C., Foreman, R.K., Funkey, C.P., Dugenne, M., White, A.E., et al. (2020). Metal isotope signatures from lava-seawater interaction during the 2018 eruption of Kīlauea. *Geochimica et Cosmochimica Acta* 282**,** 340-356. doi: 10.1016/j.gca.2020.05.005.

Herzig, P.M., Hannington, M.D., and Arribas Jr, A. (1998). Sulfur isotopic composition of hydrothermal precipitates from the Lau back-arc: implications for magmatic contributions to seafloor hydrothermal systems. *Mineralium Deposita* 33(3)**,** 226-237. doi: 10.1007/s001260050143.

Hilton, D.R. (1996). The helium and carbon isotope systematics of a continental geothermal system: results from monitoring studies at Long Valley caldera (California, U.S.A.). *Chemical Geology* 127(4)**,** 269-295. doi: 10.1016/0009-2541(95)00134-4.

Hilton, D.R., Fischer, T.P., and Marty, B. (2002). Noble Gases and Volatile Recycling at Subduction Zones. *Reviews in Mineralogy and Geochemistry* 47(1)**,** 319-370. doi: 10.2138/rmg.2002.47.9.

Hilton, D.R., and Porcelli, D. (2003). "2.06 - Noble Gases as Mantle Tracers," in *Treatise on Geochemistry*, eds. H.D. Holland & K.K. Turekian. (Oxford: Pergamon), 277-318.

Hirose, T., Kawagucci, S., and Suzuki, K. (2011). Mechanoradical H2 generation during simulated faulting: Implications for an earthquake-driven subsurface biosphere. *Geophysical Research Letters* 38(17)**,** n/a-n/a. doi: 10.1029/2011gl048850.

Honjo, S., Eglinton, T.I., Taylor, C.D., Ulmer, K.M., Sievert, S.M., Bracher, A., et al. (2014). Understanding the role of the biological pump in the global carbon cycle: An Imperative for Ocean Science. *Oceanography* 27(3)**,** 10-16.

Hoshyaripour, G., Hort, M., and Langmann, B. (2012). How does the hot core of a volcanic

plume control the sulfur speciation in volcanic emission? *Geochemistry, Geophysics, Geosystems* 13(7), n/a-n/a. doi: 10.1029/2011gc004020.

Houghton, R.A. (2014). "10.10 - The Contemporary Carbon Cycle," in *Treatise on Geochemistry (Second Edition)*, eds. H.D. Holland & K.K. Turekian. (Oxford: Elsevier), 399-435.

Hull, P.M., Bornemann, A., Penman, D.E., Henehan, M.J., Norris, R.D., Wilson, P.A., et al. (2020). On impact and volcanism across the Cretaceous-Paleogene boundary. *Science* 367(6475), 266-272. doi: doi:10.1126/science.aay5055.

Jannasch, H.W., and Wirsen, C.O. (1979). Chemosynthetic Primary Production at East Pacific Sea Floor Spreading Centers. *BioScience* 29(10), 592-598. doi: 10.2307/1307765.

Jean-Baptiste, P., Charlou, J.L., Stievenard, M., Donval, J.P., Bougault, H., and Mevel, C. (1991a). Helium and methane measurements in hydrothermal fluids from the mid-Atlantic ridge: The Snake Pit site at 23°N. *Earth and Planetary Science Letters* 106(1), 17-28. doi: 10.1016/0012-821X(91)90060-U.

Jean-Baptiste, P., Mantisi, F., Mémery, L., and Jamous, D. (1991b). 3He and chlorofluorocarbons (CFC) in the Southern Ocean: tracers of water masses. *Marine Chemistry* 35(1), 137-150. doi: 10.1016/S0304-4203(09)90013-5.

Jenkins, W.J., and Clarke, W.B. (1976). The distribution of 3He in the western Atlantic ocean. *Deep Sea Research and Oceanographic Abstracts* 23(6), 481-494. doi: 10.1016/0011-7471(76)90860-3.

Jenkins, W.J., Doney, S.C., Fendrock, M., Fine, R., Gamo, T., Jean-Baptiste, P., et al. (2019). A comprehensive global oceanic dataset of helium isotope and tritium measurements. *Earth System Science Data* 11(2), 441-454. doi: 10.5194/essd-11-441-2019.

Jørgensen, B.B., and D'Hondt, S. (2006). A Starving Majority Deep Beneath the Seafloor. *Science* 314(5801), 932-934. doi: 10.1126/science.1133796.

Karl, D.M., McMurtry, G.M., Malahoff, A., and Garcia, M.O. (1988). Loihi Seamount, Hawaii: a mid-plate volcano with a distinctive hydrothermal system. *Nature* 335(6190), 532-535. doi: 10.1038/335532a0.

Kawagucci, S., Okamura, K., Kiyota, K., Tsunogai, U., Sano, Y., Tamaki, K., et al. (2008). Methane, manganese, and helium-3 in newly discovered hydrothermal plumes over the Central Indian Ridge, 18°-20°S. *Geochemistry, Geophysics, Geosystems* 9(10). doi: 10.1029/2008gc002082.

Kelley, D.S., Baross, J.A., and Delaney, J.R. (2002). Volcanoes, Fluids, and Life at Mid-Ocean Ridge Spreading Centers. *Annual Review of Earth and Planetary Sciences* 30(1), 385-491. doi: 10.1146/annurev.earth.30.091201.141331.

Kelley, D.S., Delaney, J.R., and Juniper, S.K. (2014). Establishing a new era of submarine volcanic observatories: Cabling Axial Seamount and the Endeavour Segment of the Juan de Fuca Ridge. *Marine Geology* 352, 426-450. doi: 10.1016/j.margeo.2014.03.010.

Kennedy, C.B., Scott, S.D., and Ferris, F.G. (2003). Characterization of Bacteriogenic Iron Oxide Deposits from Axial Volcano, Juan de Fuca Ridge, Northeast Pacific Ocean. *Geomicrobiology Journal* 20(3), 199-214. doi: 10.1080/01490450303873.

Kilias, S.P., Nomikou, P., Papanikolaou, D., Polymenakou, P.N., Godelitsas, A., Argyraki, A., et al. (2013). New insights into hydrothermal vent processes in the unique shallow-submarine arc-volcano, Kolumbo (Santorini), Greece. *Scientific Reports* 3(1). doi: 10.1038/srep02421.

Kita, I., Matsuo, S., and Wakita, H. (1982). H2 generation by reaction between H2O and crushed rock: An experimental study on H2 degassing from the active fault zone. *Journal of Geophysical Research: Solid Earth* 87(B13), 10789-10795. doi: 10.1029/jb087ib13p10789.

Klinkhammer, G., Rona, P., Greaves, M., and Elderfield, H. (1985). Hydrothermal manganese plumes in the Mid-Atlantic Ridge rift valley. *Nature* 314(6013), 727-731. doi: 10.1038/314727a0.

Konno, U., Tsunogai, U., Nakagawa, F., Nakaseama, M., Ishibashi, J.-I., Nunoura, T., et al. (2006). Liquid CO2 venting on the seafloor: Yonaguni Knoll IV hydrothermal system,

Okinawa Trough. *Geophysical Research Letters* 33(16). doi: 10.1029/2006gl026115.

Labidi, J., Cartigny, P., and Jackson, M.G. (2015). Multiple sulfur isotope composition of oxidized Samoan melts and the implications of a sulfur isotope 'mantle array' in chemical geodynamics. *Earth and Planetary Science Letters* 417**,** 28-39. doi: 10.1016/j.epsl.2015.02.004.

Langmann, B., Zaksek, K., and Hort, M. (2010a). Atmospheric distribution and removal of volcanic ash after the eruption of Kasatochi volcano: A regional model study. *Journal of Geophysical Research-Atmospheres* 115. doi: 10.1029/2009jd013298.

Langmann, B., Zakšek, K., Hort, M., and Duggen, S. (2010b). Volcanic ash as fertiliser for the surface ocean. *Atmos. Chem. Phys.* 10(8)**,** 3891-3899. doi: 10.5194/acp-10-3891-2010.

Le Moigne, F.A.C. (2019). Pathways of Organic Carbon Downward Transport by the Oceanic Biological Carbon Pump. *Frontiers in Marine Science* 6. doi: 10.3389/fmars.2019.00634.

Lemasson, A.J., Hall-Spencer, J.M., Kuri, V., and Knights, A.M. (2019). Changes in the biochemical and nutrient composition of seafood due to ocean acidification and warming. *Marine Environmental Research* 143**,** 82-92. doi: 10.1016/j.marenvres.2018.11.006.

Li, J., Roche, B., Bull, J.M., White, P.R., Davis, J.W., Deponte, M., et al. (2020). Passive acoustic monitoring of a natural CO2 seep site – Implications for carbon capture and storage. *International Journal of Greenhouse Gas Control* 93**,** 102899. doi: 10.1016/j.ijggc.2019.102899.

Li, M., Toner, B.M., Baker, B.J., Breier, J.A., Sheik, C.S., and Dick, G.J. (2014). Microbial iron uptake as a mechanism for dispersing iron from deep-sea hydrothermal vents. *Nat Commun* 5. doi: 10.1038/ncomms4192.

Lindsay, J.M., Shepherd, J.B., and Wilson, D. (2005). Volcanic and Scientific Activity at Kick 'em Jenny Submarine Volcano 2001-2002: Implications for Volcanic Hazard in the Southern Grenadines, Lesser Antilles. *Natural Hazards* 34(1)**,** 1-24. doi: 10.1007/s11069-004-1566-2.

Longman, J., Palmer, M.R., Gernon, T.M., Manners, H.R., and Jones, M.T. (2022). Subaerial volcanism is a potentially major contributor to oceanic iron and manganese cycles. *Communications Earth & Environment* 3(1). doi: 10.1038/s43247-022-00389-7.

Lowenstern, J. (2001). Carbon dioxide in magmas and implications for hydrothermal systems. *Mineralium Deposita* 36(6)**,** 490-502. doi: 10.1007/s001260100185.

Lupton, J. (1998). Hydrothermal helium plumes in the Pacific Ocean. *Journal of Geophysical Research: Oceans* 103(C8)**,** 15853-15868. doi: 10.1029/98jc00146.

Lupton, J., Butterfield, D., Lilley, M., Evans, L., Nakamura, K.-I., Chadwick, W., et al. (2006). Submarine venting of liquid carbon dioxide on a Mariana Arc volcano. *Geochemistry, Geophysics, Geosystems* 7(8). doi: 10.1029/2005gc001152.

Lupton, J., Lilley, M., Butterfield, D., Evans, L., Embley, R., Massoth, G., et al. (2008). Venting of a separate CO2-rich gas phase from submarine arc volcanoes: Examples from the Mariana and Tonga-Kermadec arcs. *Journal of Geophysical Research: Solid Earth* 113(B8). doi: 10.1029/2007jb005467.

Lupton, J.E. (1979). Helium-3 in the Guaymas Basin: Evidence for injection of mantle volatiles in the Gulf of California. *Journal of Geophysical Research: Solid Earth* 84(B13)**,** 7446-7452. doi: 10.1029/jb084ib13p07446.

Lupton, J.E. (1983). TERRESTRIAL INERT GASES: Isotope Tracer Studies and Clues to Primordial Components in the Mantle. *Annual Review of Earth and Planetary Sciences* 11(1)**,** 371-414. doi: 10.1146/annurev.ea.11.050183.002103.

Lupton, J.E., Weiss, R.F., and Craig, H. (1977a). Mantle helium in hydrothermal plumes in the Galapagos Rift. *Nature* 267(5612)**,** 603-604. doi: 10.1038/267603a0.

Lupton, J.E., Weiss, R.F., and Craig, H. (1977b). Mantle helium in the Red Sea brines. *Nature* 266(5599)**,** 244-246. doi: 10.1038/266244a0.

Malahoff, A., Kolotyrkina, I.Y., Midson, B.P., and Massoth, G.J. (2006). A decade of exploring a submarine intraplate volcano: Hydrothermal manganese and iron at Lō'ihi volcano, Hawai'i. *Geochemistry, Geophysics,*

Geosystems 7(6), n/a-n/a. doi: 10.1029/2005gc001222.

Martinez, I., Shilobreeva, S., Alt, J., Polyakov, V., and Agrinier, P. (2021). The origin and fate of C during alteration of the oceanic crust. *Comptes Rendus. Géoscience* 353(1), 319-336. doi: 10.5802/crgeos.61.

Marty, B., Jambon, A., and Sano, Y. (1989). Helium isotopes and CO2 in volcanic gases of Japan. *Chemical Geology* 76(1-2), 25-40. doi: 10.1016/0009-2541(89)90125-3.

Masson-Delmotte, V.P., Zhai, P., Pirani, S.L., Connors, C., Péan, S., Berger, N., et al. (2021). IPCC, 2021, Climate Change 2021: The Physical Science Basis. Contribution of Working Group I to the Sixth Assessment Report of the Intergovernmental Panel on Climate Change.

Massoth, G.J., Butterfield, D.A., Lupton, J.E., McDuff, R.E., Lilley, M.D., and Jonasson, I.R. (1989). Submarine venting of phase-separated hydrothermal fluids at Axial Volcano, Juan de Fuca Ridge. *Nature* 340(6236), 702-705. doi: 10.1038/340702a0.

Massoth, G.J., Milburn, H.B., Hammond, S.R., Butterfield, D.A., McDuff, R.E., and Lupton, J.E. (1988). "The geochemistry of submarine venting fluids at Axial Volcano, Juan de Fuca Ridge: New sampling methods and a VENTS program rationale," in *Global venting, midwater, and benthic ecological processes*. NOAA Rockville, MD), 29-59.

Massoth, G.J., Ronde, C.E.J.D., Lupton, J.E., Feely, R.A., Baker, E.T., Lebon, G.T., et al. (2003). Chemically rich and diverse submarine hydrothermal plumes of the southern Kermadec volcanic arc (New Zealand). *Geological Society, London, Special Publications* 219(1), 119-139. doi: doi:10.1144/GSL.SP.2003.219.01.06.

McCollom, T.M. (2013). Laboratory Simulations of Abiotic Hydrocarbon Formation in Earth's Deep Subsurface. *Reviews in Mineralogy and Geochemistry* 75(1), 467-494. doi: 10.2138/rmg.2013.75.15.

McCollom, T.M. (2016). Abiotic methane formation during experimental serpentinization of olivine. *Proceedings of the National Academy of Sciences* 113(49), 13965-13970. doi: 10.1073/pnas.1611843113.

McCollom, T.M., and Donaldson, C. (2016). Generation of Hydrogen and Methane during Experimental Low-Temperature Reaction of Ultramafic Rocks with Water. *Astrobiology* 16(6), 389-406. doi: 10.1089/ast.2015.1382.

McGinnis, D.F., Schmidt, M., Delsontro, T., Themann, S., Rovelli, L., Reitz, A., et al. (2011). Discovery of a natural CO2seep in the German North Sea: Implications for shallow dissolved gas and seep detection. *Journal of Geophysical Research* 116(C3). doi: 10.1029/2010jc006557.

McLaughlin-West, E.A., Olson, E.J., Lilley, M.D., Resing, J.A., Lupton, J.E., Baker, E.T., et al. (1999). Variations in hydrothermal methane and hydrogen concentrations following the 1998 eruption at Axial Volcano. *Geophysical Research Letters* 26(23), 3453-3456. doi: 10.1029/1999gl002336.

Menon, S., Denman, K.L., Brasseur, G., Chidthaisong, A., Ciais, P., Cox, P.M., et al. (2007). *Couplings between changes in the climate system and biogeochemistry*. United States.

Metrich, N., and Mandeville, C.W. (2010). Sulfur in Magmas. *Elements* 6(2), 81-86. doi: 10.2113/gselements.6.2.81.

Métrich, N., and Wallace, P.J. (2008). Volatile Abundances in Basaltic Magmas and Their Degassing Paths Tracked by Melt Inclusions. *Reviews in Mineralogy and Geochemistry* 69(1), 363-402. doi: 10.2138/rmg.2008.69.10.

Michard, G. (2008). Can we explain atmospheric carbon dioxide oscillations during the past 400,000 years? *Comptes Rendus Geoscience* 340(8), 483-494. doi: 10.1016/j.crte.2008.06.004.

Michel, A.P.M., Wankel, S.D., Kapit, J., Sandwith, Z., and Girguis, P.R. (2018). In situ carbon isotopic exploration of an active submarine volcano. *Deep Sea Research Part II: Topical Studies in Oceanography* 150, 57-66. doi: 10.1016/j.dsr2.2017.10.004.

Milkov, A.V., and Etiope, G. (2018). Revised genetic diagrams for natural gases based on a global dataset of >20,000 samples. *Organic Geochemistry* 125, 109-120. doi: 10.1016/j.orggeochem.2018.09.002.

Millero, F.J. (1979). The thermodynamics of the carbonate system in seawater. *Geochimica et*

Cosmochimica Acta 43(10)**,** 1651-1661. doi: 10.1016/0016-7037(79)90184-4.

Mittal, T., and Delbridge, B. (2019). Detection of the 2012 Havre submarine eruption plume using Argo floats and its implications for ocean dynamics. *Earth and Planetary Science Letters* 511**,** 105-116. doi: 10.1016/j.epsl.2019.01.035.

Moreira, M.A., and Kurz, M.D. (2013). "Noble Gases as Tracers of Mantle Processes and Magmatic Degassing," in *The Noble Gases as Geochemical Tracers*, ed. P. Burnard. (Berlin, Heidelberg: Springer Berlin Heidelberg), 371-391.

Morrow, K.M., Bourne, D.G., Humphrey, C., Botté, E.S., Laffy, P., Zaneveld, J., et al. (2015). Natural volcanic CO2 seeps reveal future trajectories for host–microbial associations in corals and sponges. *The ISME Journal* 9(4)**,** 894-908. doi: 10.1038/ismej.2014.188.

Mostofa, K.M.G., Liu, C.-Q., Zhai, W., Minella, M., Vione, D., Gao, K., et al. (2016). Reviews and Syntheses: Ocean acidification and its potential impacts on marine ecosystems. *Biogeosciences* 13(6)**,** 1767-1786. doi: 10.5194/bg-13-1767-2016.

Murch, A. (2018). *Ash Generation in the 2012 Eruption of Havre Volcano, Kermadec Arc: The Largest Deep Subaqueous Eruption of the Last Century*. Doctor of Philosophy, University of Otago.

Murch, A.P., Portner, R.A., Rubin, K.H., and Clague, D.A. (2022). Deep-subaqueous implosive volcanism at West Mata seamount, Tonga. *Earth and Planetary Science Letters* 578**,** 117328. doi: 10.1016/j.epsl.2021.117328.

Mutaqin, B.W., Lavigne, F., Hadmoko, D.S., and Ngalawani, M.N. (2019). Volcanic Eruption-Induced Tsunami in Indonesia: A Review. *IOP Conference Series: Earth and Environmental Science* 256(1)**,** 012023. doi: 10.1088/1755-1315/256/1/012023.

Nomikou, P., Carey, S., Bell, K.L.C., Papanikolaou, D., Bejelou, K., Cantner, K., et al. (2014). Tsunami hazard risk of a future volcanic eruption of Kolumbo submarine volcano, NE of Santorini Caldera, Greece. *Natural Hazards* 72(3)**,** 1375-1390. doi: 10.1007/s11069-012-0405-0.

Ono, S., Shanks, W.C., Rouxel, O.J., and Rumble, D. (2007). S-33 constraints on the seawater sulfate contribution in modern seafloor hydrothermal vent sulfides. *Geochimica et Cosmochimica Acta* 71(5)**,** 1170-1182. doi: 10.1016/j.gca.2006.11.017.

Oppenheimer, C. (2003). Climatic, environmental and human consequences of the largest known historic eruption: Tambora volcano (Indonesia) 1815. *Progress in Physical Geography: Earth and Environment* 27(2)**,** 230-259. doi: 10.1191/0309133303pp379ra.

Oppenheimer, C., Scaillet, B., and Martin, R. (2011). *Sulfur Degassing From Volcanoes: Source Conditions, Surveillance, Plume Chemistry and Earth System Impacts*.

Ozima, M., and Podosek, F.A. (2002). *Noble gas geochemistry*. Cambridge University Press.

Paris, R., Switzer, A.D., Belousova, M., Belousov, A., Ontowirjo, B., Whelley, P.L., et al. (2014). Volcanic tsunami: a review of source mechanisms, past events and hazards in Southeast Asia (Indonesia, Philippines, Papua New Guinea). *Natural Hazards* 70(1)**,** 447-470. doi: 10.1007/s11069-013-0822-8.

Perfit, M.R., Cann, J.R., Fornari, D.J., Engels, J., Smith, D.K., Ian Ridley, W., et al. (2003). Interaction of sea water and lava during submarine eruptions at mid-ocean ridges. *Nature* 426(6962)**,** 62-65. doi: 10.1038/nature02032.

Pineau, F., and Javoy, M. (1983). Carbon isotopes and concentrations in mid-oceanic ridge basalts. *Earth and Planetary Science Letters* 62(2)**,** 239-257. doi: 10.1016/0012-821X(83)90087-0.

Pörtner, H.-O., Roberts, D.C., Tignor, M., Poloczanska, E.S., Mintenbeck, K., Alegría, A., et al. (2022). "IPCC, 2022, Climate Change 2022: Impacts, Adaptation and Vulnerability Working Group II Contribution to the Sixth Assessment Report of the Intergovernmental Panel on Climate Change", (ed.) C.U. Press. (Cambridge University Press, Cambridge, UK and New York, NY, USA).

Price, R.E., and Giovannelli, D. (2017). "A Review of the Geochemistry and Microbiology of Marine Shallow-Water Hydrothermal Vents," in *Reference Module in Earth Systems and Environmental Sciences*. Elsevier).

Raible, C.C., Brönnimann, S., Auchmann, R., Brohan, P., Frölicher, T.L., Graf, H.F., et al. (2016). Tambora 1815 as a test case for high impact volcanic eruptions: Earth system effects. *WIREs Climate Change* 7(4)**,** 569-589. doi: 10.1002/wcc.407.

Reed, M.H., and Palandri, J. (2008). Hydrogen Produced by Reduction of H2O in Rock Reaction: Peridotite vs Basalt. *AIP Conference Proceedings* 987(1)**,** 100-104. doi: 10.1063/1.2896951.

Resing, J.A., Baker, E.T., Lupton, J.E., Walker, S.L., Butterfield, D.A., Massoth, G.J., et al. (2009). Chemistry of hydrothermal plumes above submarine volcanoes of the Mariana Arc. *Geochemistry, Geophysics, Geosystems* 10(2). doi: 10.1029/2008gc002141.

Resing, J.A., Lebon, G., Baker, E.T., Lupton, J.E., Embley, R.W., Massoth, G.J., et al. (2007). Venting of Acid-Sulfate Fluids in a High-Sulfidation Setting at NW Rota-1 Submarine Volcano on the Mariana Arc. *Economic Geology* 102(6)**,** 1047-1061. doi: 10.2113/gsecongeo.102.6.1047.

Resing, J.A., Rubin, K.H., Embley, R.W., Lupton, J.E., Baker, E.T., Dziak, R.P., et al. (2011). Active submarine eruption of boninite in the northeastern Lau Basin. *Nature Geoscience* 4(11)**,** 799-806. doi: 10.1038/ngeo1275.

Resing, J.A., and Sansone, F.J. (1999). The chemistry of lava–seawater interactions: the generation of acidity. *Geochimica et Cosmochimica Acta* 63(15)**,** 2183-2198. doi: 10.1016/S0016-7037(99)00193-3.

Resing, J.A., and Sansone, F.J. (2002). The chemistry of lava-seawater interactions II: the elemental signature. *Geochimica et Cosmochimica Acta* 66(11)**,** 1925-1941. doi: 10.1016/S0016-7037(01)00897-3.

Resing, J.A., Sedwick, P.N., German, C.R., Jenkins, W.J., Moffett, J.W., Sohst, B.M., et al. (2015). Basin-scale transport of hydrothermal dissolved metals across the South Pacific Ocean. *Nature* 523(7559)**,** 200-203. doi: 10.1038/nature14577.

Rice, D.D., and Claypool, G.E. (1981). Generation, Accumulation, and Resource Potential of Biogenic Gas1. *AAPG Bulletin* 65(1)**,** 5-25. doi: 10.1306/2F919765-16CE-11D7-8645000102C1865D.

Rizzo, A.L., Caracausi, A., Chavagnac, V., Nomikou, P., Polymenakou, P.N., Mandalakis, M., et al. (2019). Geochemistry of CO2-Rich Gases Venting From Submarine Volcanism: The Case of Kolumbo (Hellenic Volcanic Arc, Greece). *Frontiers in Earth Science* 7. doi: 10.3389/feart.2019.00060.

Romano, D., Gattuso, A., Longo, M., Caruso, C., Lazzaro, G., Corbo, A., et al. (2019). Hazard Scenarios Related to Submarine Volcanic-Hydrothermal Activity and Advanced Monitoring Strategies: A Study Case from the Panarea Volcanic Group (Aeolian Islands, Italy). *Geofluids* 2019**,** 1-15. doi: 10.1155/2019/8728720.

Rouxel, O., Toner, B., Germain, Y., and Glazer, B. (2018). Geochemical and iron isotopic insights into hydrothermal iron oxyhydroxide deposit formation at Loihi Seamount. *Geochimica et Cosmochimica Acta* 220**,** 449-482. doi: 10.1016/j.gca.2017.09.050.

Rubin, K. (1997). Degassing of metals and metalloids from erupting seamount and mid-ocean ridge volcanoes: Observations and predictions. *Geochimica et Cosmochimica Acta* 61(17)**,** 3525-3542. doi: 10.1016/s0016-7037(97)00179-8.

Rubin, K.H., Soule, S.A., Chadwick, W.W., Fornari, D.J., Clague, D.A., Embley, R.W., et al. (2012). Volcanic Eruptions in the Deep Sea. *Oceanography* 25(1)**,** 142-157. doi: 10.5670/oceanog.2012.12.

Sakai, H., Gamo, T., Kim, E.-S., Tsutsumi, M., Tanaka, T., Ishibashi, J., et al. (1990a). Venting of Carbon Dioxide-Rich Fluid and Hydrate Formation in Mid-Okinawa Trough Backarc Basin. *Science* 248(4959)**,** 1093-1096. doi: doi:10.1126/science.248.4959.1093.

Sakai, H., Gamo, T., Kim, E.S., Shitashima, K., Yanagisawa, F., Tsutsumi, M., et al. (1990b). Unique chemistry of the hydrothermal solution in the mid-Okinawa Trough Backarc Basin. *Geophysical Research Letters* 17(12)**,** 2133-2136. doi: 10.1029/gl017i012p02133.

Sano, Y., and Fischer, T.P. (2013). "The Analysis and Interpretation of Noble Gases in Modern Hydrothermal Systems," in *The Noble Gases as Geochemical Tracers*, ed. P. Burnard. (Berlin, Heidelberg: Springer Berlin Heidelberg), 249-317.

Sano, Y., and Marty, B. (1995). Origin of carbon in fumarolic gas from island arcs. *Chemical Geology* 119(1)**,** 265-274. doi: 10.1016/0009-2541(94)00097-R.

Sansone, F.J., and Resing, J.A. (1995). Hydrography and geochemistry of sea surface hydrothermal plumes resulting from Hawaiian coastal volcanism. *Journal of Geophysical Research* 100(C7)**,** 13555. doi: 10.1029/95jc01120.

Sansone, F.J., Resing, J.A., Tribble, G.W., Sedwick, P.N., Kelly, K.M., and Hon, K. (1991). Lava-seawater interactions at shallow-water submarine lava flows. *Geophysical Research Letters* 18(9)**,** 1731-1734. doi: 10.1029/91gl01279.

Santana-Casiano, J.M., Fraile-Nuez, E., González-Dávila, M., Baker, E.T., Resing, J.A., and Walker, S.L. (2016). Significant discharge of CO2 from hydrothermalism associated with the submarine volcano of El Hierro Island. *Scientific Reports* 6(1)**,** 25686. doi: 10.1038/srep25686.

Santana-Casiano, J.M., González-Dávila, M., and Fraile-Nuez, E. (2018). "The Emissions of the Tagoro Submarine Volcano (Canary Islands, Atlantic Ocean): Effects on the Physical and Chemical Properties of the Seawater." InTech).

Santana-Casiano, J.M., González-Dávila, M., Fraile-Nuez, E., De Armas, D., González, A.G., Domínguez-Yanes, J.F., et al. (2013). The natural ocean acidification and fertilization event caused by the submarine eruption of El Hierro. *Scientific Reports* 3(1). doi: 10.1038/srep01140.

Santana-González, C., Santana-Casiano, J.M., González-Dávila, M., and Fraile-Nuez, E. (2017). Emissions of Fe(II) and its kinetic of oxidation at Tagoro submarine volcano, El Hierro. *Marine Chemistry* 195**,** 129-137. doi: 10.1016/j.marchem.2017.02.001.

Schipper, C.I., White, J.D.L., Houghton, B.F., Shimizu, N., and Stewart, R.B. (2010). Explosive submarine eruptions driven by volatile-coupled degassing at Lō`ihi Seamount, Hawai`i. *Earth and Planetary Science Letters* 295(3-4)**,** 497-510. doi: 10.1016/j.epsl.2010.04.031.

Schoell, M. (1980). The hydrogen and carbon isotopic composition of methane from natural gases of various origins. *Geochimica et Cosmochimica Acta* 44(5)**,** 649-661. doi: 10.1016/0016-7037(80)90155-6.

Schoell, M. (1988). Multiple origins of methane in the Earth. *Chemical Geology* 71(1)**,** 1-10. doi: 10.1016/0009-2541(88)90101-5.

Sedwick, P.N., McMurtry, G.M., and Macdougall, J.D. (1992). Chemistry of hydrothermal solutions from Pele's Vents, Loihi Seamount, Hawaii. *Geochimica et Cosmochimica Acta* 56(10)**,** 3643-3667. doi: 10.1016/0016-7037(92)90159-G.

Self, S., Zhao, J.-X., Holasek, R.E., Torres, R.C., and King, A.J. (1993). The atmospheric impact of the 1991 Mount Pinatubo eruption.

Shanks, W.C., III (2001). Stable Isotopes in Seafloor Hydrothermal Systems: Vent fluids, hydrothermal deposits, hydrothermal alteration, and microbial processes. *Reviews in Mineralogy and Geochemistry* 43(1)**,** 469-525. doi: 10.2138/gsrmg.43.1.469.

Shock, E.L., Holland, M., Meyer-Dombard, D.A., Amend, J.P., Osburn, G.R., and Fischer, T.P. (2010). Quantifying inorganic sources of geochemical energy in hydrothermal ecosystems, Yellowstone National Park, USA. *Geochimica et Cosmochimica Acta* 74(14)**,** 4005-4043. doi: 10.1016/j.gca.2009.08.036.

Siebert, L., Cottrell, E., Venzke, E., and Andrews, B. (2015a). "Chapter 12 - Earth's Volcanoes and Their Eruptions: An Overview," in *The Encyclopedia of Volcanoes (Second Edition)*, ed. H. Sigurdsson. (Amsterdam: Academic Press), 239-255.

Siebert, L., Cottrell, E., Venzke, E., and Edwards, B. (2015b). "Appendix 2 - Catalog of Earth's Documented Holocene Eruptions," in *The Encyclopedia of Volcanoes (Second Edition)*, ed. H. Sigurdsson. (Amsterdam: Academic Press), 1367-1400.

Siegel, D.A., Devries, T., Cetinić, I., and Bisson, K.M. (2023). Quantifying the Ocean's Biological Pump and Its Carbon Cycle Impacts on Global Scales. *Annual Review of Marine Science* 15(1)**,** 329-356. doi: 10.1146/annurev-marine-040722-115226.

Soule, S.A. (2015). "Chapter 21 - Mid-Ocean Ridge Volcanism," in *The Encyclopedia of Volcanoes (Second Edition)*, ed. H.

Sigurdsson. (Amsterdam: Academic Press), 395-403.

Spietz, R.L., Butterfield, D.A., Buck, N.J., Larson, B.I., Chadwick, W.W., Walker, S.L., et al. (2018). Deep-Sea Volcanic Eruptions Create Unique Chemical and Biological Linkages Between the Subsurface Lithosphere and the Oceanic Hydrosphere. *Oceanography* 31(1)**,** 128-135.

Stanley, R.H.R., and Jenkins, W.J. (2013). "Noble Gases in Seawater as Tracers for Physical and Biogeochemical Ocean Processes," in *The Noble Gases as Geochemical Tracers*, ed. P. Burnard. (Berlin, Heidelberg: Springer Berlin Heidelberg), 55-79.

Staudigel, H., Hart, S.R., Koppers, A.A.P., Constable, C., Workman, R., Kurz, M., et al. (2004). Hydrothermal venting at Vailulu'u Seamount: The smoking end of the Samoan chain. *Geochemistry, Geophysics, Geosystems* 5(2)**,** n/a-n/a. doi: 10.1029/2003gc000626.

Staudigel, H., Hart, S.R., Pile, A., Bailey, B.E., Baker, E.T., Brooke, S., et al. (2006). Vailulu'u Seamount, Samoa: Life and death on an active submarine volcano. *Proceedings of the National Academy of Sciences* 103(17)**,** 6448-6453. doi: 10.1073/pnas.0600830103.

Staudigel, H., and Koppers, A.A.P. (2015). "Chapter 22 - Seamounts and Island Building," in *The Encyclopedia of Volcanoes (Second Edition)*, ed. H. Sigurdsson. (Amsterdam: Academic Press), 405-421.

Stucker, V.K., de Ronde, C.E.J., Laurence, K.J., and Phillips, A.M. (2022). Rare Time Series of Hydrothermal Fluids for a Submarine Volcano: 14 Years of Vent Fluid Compositions for Brothers Volcano, Kermadec Arc New Zealand. *Economic Geology*. doi: 10.5382/econgeo.4922.

Sun, Z., Zhou, H., Yang, Q., Sun, Z., Bao, S., and Yao, H. (2011). Hydrothermal Fe–Si–Mn oxide deposits from the Central and South Valu Fa Ridge, Lau Basin. *Applied Geochemistry* 26(7)**,** 1192-1204. doi: 10.1016/j.apgeochem.2011.04.008.

Symonds, R.B., Rose, W.I., Bluth, G.J.S., and Gerlach, T.M. (1994). Volcanic-gas studies; methods, results, and applications. *Reviews in Mineralogy and Geochemistry* 30(1)**,** 1-66.

Tagliabue, A., Bopp, L., Dutay, J.-C., Bowie, A.R., Chever, F., Jean-Baptiste, P., et al. (2010). Hydrothermal contribution to the oceanic dissolved iron inventory. *Nature Geoscience* 3(4)**,** 252-256. doi: 10.1038/ngeo818.

Tepp, G., and Dziak, R.P. (2021). The Seismo-Acoustics of Submarine Volcanic Eruptions. *Journal of Geophysical Research: Solid Earth* 126(4). doi: 10.1029/2020jb020912.

Tolstoy, M., Cowen, J.P., Baker, E.T., Fornari, D.J., Rubin, K.H., Shank, T.M., et al. (2006). A Sea-Floor Spreading Event Captured by Seismometers. *Science* 314(5807)**,** 1920-1922. doi: doi:10.1126/science.1133950.

Torgersen, T. (1989). Terrestrial helium degassing fluxes and the atmospheric helium budget: Implications with respect to the degassing processes of continental crust. *Chemical Geology: Isotope Geoscience section* 79(1)**,** 1-14. doi: 10.1016/0168-9622(89)90002-X.

Truche, L., McCollom, T.M., and Martinez, I. (2020). Hydrogen and Abiotic Hydrocarbons: Molecules that Change the World. *Elements* 16(1)**,** 13-18. doi: 10.2138/gselements.16.1.13.

Walker, S.L., Baker, E.T., Lupton, J.E., and Resing, J.A. (2019). Patterns of Fine Ash Dispersal Related to Volcanic Activity at West Mata Volcano, NE Lau Basin. *Frontiers in Marine Science* 6. doi: 10.3389/fmars.2019.00593.

Wang, Y., Liu, Y., Zhao, C., Li, Q., Zhou, Y., and Ran, H. (2020). Helium and carbon isotopic signatures of thermal spring gases in southeast Yunnan, China. *Journal of Volcanology and Geothermal Research* 402**,** 106995. doi: 10.1016/j.jvolgeores.2020.106995.

Weiss, R.F. (1971). Solubility of helium and neon in water and seawater. *Journal of Chemical & Engineering Data* 16(2)**,** 235-241. doi: 10.1021/je60049a019.

Welhan, J.A. (1988). Origins of methane in hydrothermal systems. *Chemical Geology* 71(1-3)**,** 183-198. doi: 10.1016/0009-2541(88)90114-3.

Wen, H.-Y., Sano, Y., Takahata, N., Tomonaga, Y., Ishida, A., Tanaka, K., et al. (2016). Helium and methane sources and fluxes of shallow submarine hydrothermal plumes near the Tokara Islands, Southern Japan. *Scientific*

Reports 6(1), 34126. doi: 10.1038/srep34126.

Wheat, C.G., Jannasch, H.W., Plant, J.N., Moyer, C.L., Sansone, F.J., and McMurtry, G.M. (2000). Continuous sampling of hydrothermal fluids from Loihi Seamount after the 1996 event. *Journal of Geophysical Research: Solid Earth* 105(B8), 19353-19367. doi: 10.1029/2000jb900088.

White, J.D., Manville, V., Wilson, C.J., Houghton, B.F., Riggs, N.R., and Ort, M. (2001). "Settling and Deposition of AD 181 Taupo Pumice in Lacustrine and Associated Environments," in *Volcaniclastic Sedimentation in Lacustrine Settings*.), 141-150.

White, J.D.L., McPhie, J., and Soule, S.A. (2015a). "Chapter 19 - Submarine Lavas and Hyaloclastite," in *The Encyclopedia of Volcanoes (Second Edition)*, ed. H. Sigurdsson. (Amsterdam: Academic Press), 363-375.

White, J.D.L., Schipper, C.I., and Kano, K. (2015b). "Chapter 31 - Submarine Explosive Eruptions," in *The Encyclopedia of Volcanoes (Second Edition)*, ed. H. Sigurdsson. (Amsterdam: Academic Press), 553-569.

Wilcock, W.S.D., Dziak, R.P., Tolstoy, M., Chadwick Jr., W.W., Nooner, S.L., Bohnenstiehl, D.R., et al. (2018). The Recent Volcanic History of Axial Seamount: Geophysical Insights into Past Eruption Dynamics with an Eye Toward Enhanced Observations of Future Eruptions. *Oceanography* 31.

Wilson, S.T., Hawco, N.J., Armbrust, E.V., Barone, B., Björkman, K.M., Boysen, A.K., et al. (2019). Kīlauea lava fuels phytoplankton bloom in the North Pacific Ocean. *Science* 365(6457), 1040-1044. doi: 10.1126/science.aax4767.

Worman, S.L., Pratson, L.F., Karson, J.A., and Schlesinger, W.H. (2020). Abiotic hydrogen (H2) sources and sinks near the Mid-Ocean Ridge (MOR) with implications for the subseafloor biosphere. *Proceedings of the National Academy of Sciences of the United States of America* 117(24), 13283-13293. doi: 10.1073/pnas.2002619117.

Wu, J., Boyle, E., Sunda, W., and Wen, L.-S. (2001). Soluble and Colloidal Iron in the Oligotrophic North Atlantic and North Pacific. *Science* 293(5531), 847-849. doi: 10.1126/science.1059251.

Wu, J.N., Parnell-Turner, R., Fornari, D.J., Kurras, G., Berrios-Rivera, N., Barreyre, T., et al. (2022). Extent and Volume of Lava Flows Erupted at 9°50′N, East Pacific Rise in 2005–2006 From Autonomous Underwater Vehicle Surveys. *Geochemistry, Geophysics, Geosystems* 23(3). doi: 10.1029/2021gc010213.

Yücel, M., Gartman, A., Chan, C.S., and Luther, G.W. (2011). Hydrothermal vents as a kinetically stable source of iron-sulphide-bearing nanoparticles to the ocean. *Nature Geoscience* 4(6), 367-371. doi: 10.1038/ngeo1148.

Zimanowski, B., Büttner, R., Dellino, P., White, J.D.L., and Wohletz, K.H. (2015). "Chapter 26 - Magma–Water Interaction and Phreatomagmatic Fragmentation," in *The Encyclopedia of Volcanoes (Second Edition)*, ed. H. Sigurdsson. (Amsterdam: Academic Press), 473-484.

Zolotov, M.Y., and Shock, E.L. (2000). A thermodynamic assessment of the potential synthesis of condensed hydrocarbons during cooling and dilution of volcanic gases. *Journal of Geophysical Research: Solid Earth* 105(B1), 539-559. doi: 10.1029/1999jb900369.

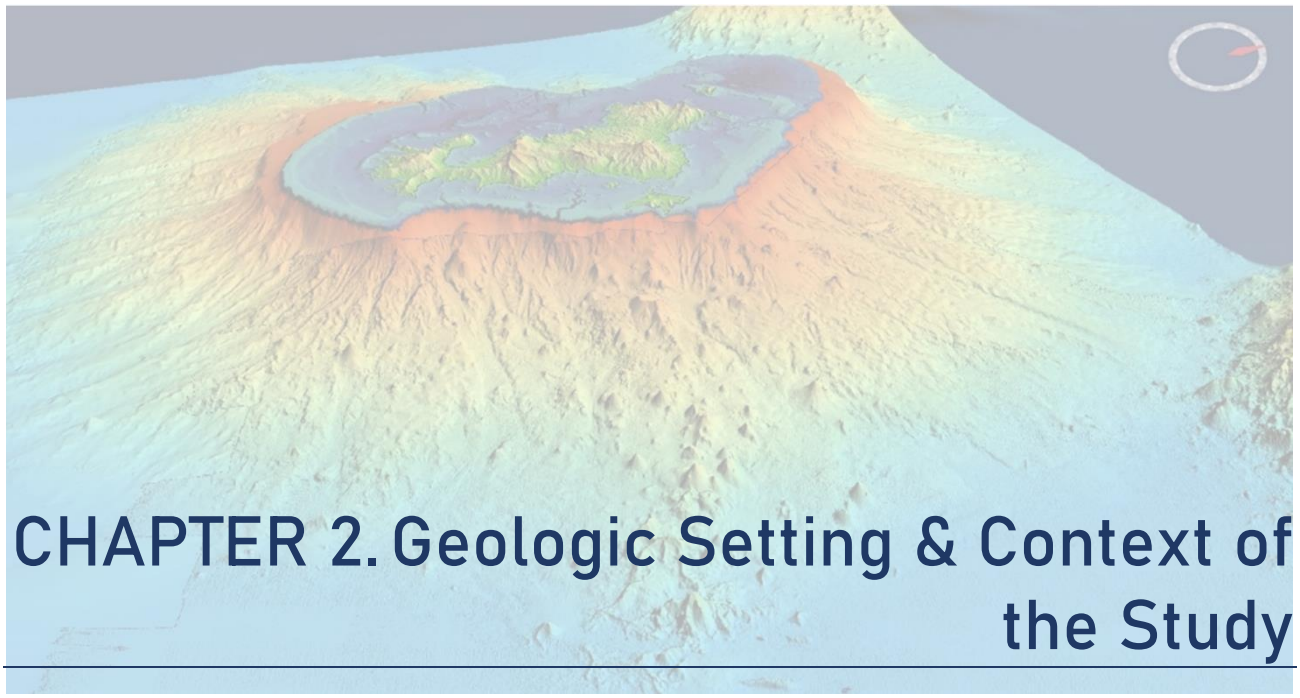

CHAPTER 2. Geologic Setting & Context of the Study

Abstract

The beginning of the seismo-volcanic crisis offshore Mayotte, in May 2018, has triggered a massive scientific mobilization. To date, numerous disciplines are studying the setup of the Fani Maoré Volcano, including seismology, geomorphology, geodesy, sedimentology, volcanology and petrology, underwater acoustics, water column geochemistry and ecology. As part of this PhD thesis, my interest focuses on the water column geochemistry and its variability, in a submarine volcanic context. Nonetheless, this aspect remains closely related to the other disciplines, and the understanding of the geochemistry requires knowledge on the global context.

In this objective, this chapter presents the regional geological settings of the Mayotte area. It describes the main features known before the seismo-volcanic crisis, as well as the geological and seismic context during the ongoing crisis. This chapter also includes the societal aspects and the scientific mobilization that ensues.

CHAPITRE 2. Site d'Etude & Contexte

Résumé

Le début de la crise sismo-volcanique au large de Mayotte, en mai 2018, a déclenché une mobilisation scientifique massive. À ce jour, de nombreuses disciplines étudient la mise en place du volcan Fani Maoré, dont la sismologie, la géomorphologie, la géodésie, la sédimentologie, la volcanologie et la pétrologie, l'acoustique sous-marine, la géochimie de la colonne d'eau et l'écologie. Dans le cadre de cette thèse de doctorat, mon intérêt se concentre sur la géochimie de la colonne d'eau et sa variabilité dans un contexte volcanique sous-marin. Néanmoins, cet aspect reste étroitement lié aux autres disciplines, et la compréhension de la géochimie nécessite une connaissance globale du contexte.

Dans cette optique, ce chapitre présente les paramètres géologiques régionaux de la zone de Mayotte. Il décrit les principales caractéristiques connues avant la crise sismo-volcanique, ainsi que le contexte géologique et sismique observé pendant crise. Ce chapitre aborde également les aspects sociétaux et la mobilisation scientifique qui en découle.

21. Geologic Setting

The Mayotte volcanic island is located in the Comoros archipelago, at the north of the Mozambique Channel (Indian Ocean), between the Mozambique and Madagascar (Figure 2. 1). The archipelago is composed of four volcanic islands, aligned in an overall East-West direction: Grande-Comore, Mohéli, Anjouan and Mayotte (Tzevahirtzian et al., 2021).

The Comoros Archipelago is characterized by active volcanism and tectonics associated with an area of active seismicity that connects the northern extremity of Madagascar in the east to the African coast in the west. This volcanic chain is interpreted as the NW–SE (northwest-southeast) boundary between the Lwandle microplate and the Somalia plate, on the periphery of the East African Rift System (Famin et al., 2020; Feuillet et al., 2021; Thinon et al., 2022) or as a zone of broad deformation extending up to the northern half of Madagascar (Stamps et al., 2021).

Mayotte comprises two main islands, Grande Terre and Petite Terre (Figure 2. 2). It is the easternmost island of the Comoros archipelago, and the eldest with a maximum age of 20 Ma for the onset of subaqueous volcanic activity and 11 Ma for the onset of subaerial volcanic activity (Nougier et al., 1986; Debeuf, 2004; Pelleter et al., 2014; Michon, 2016)

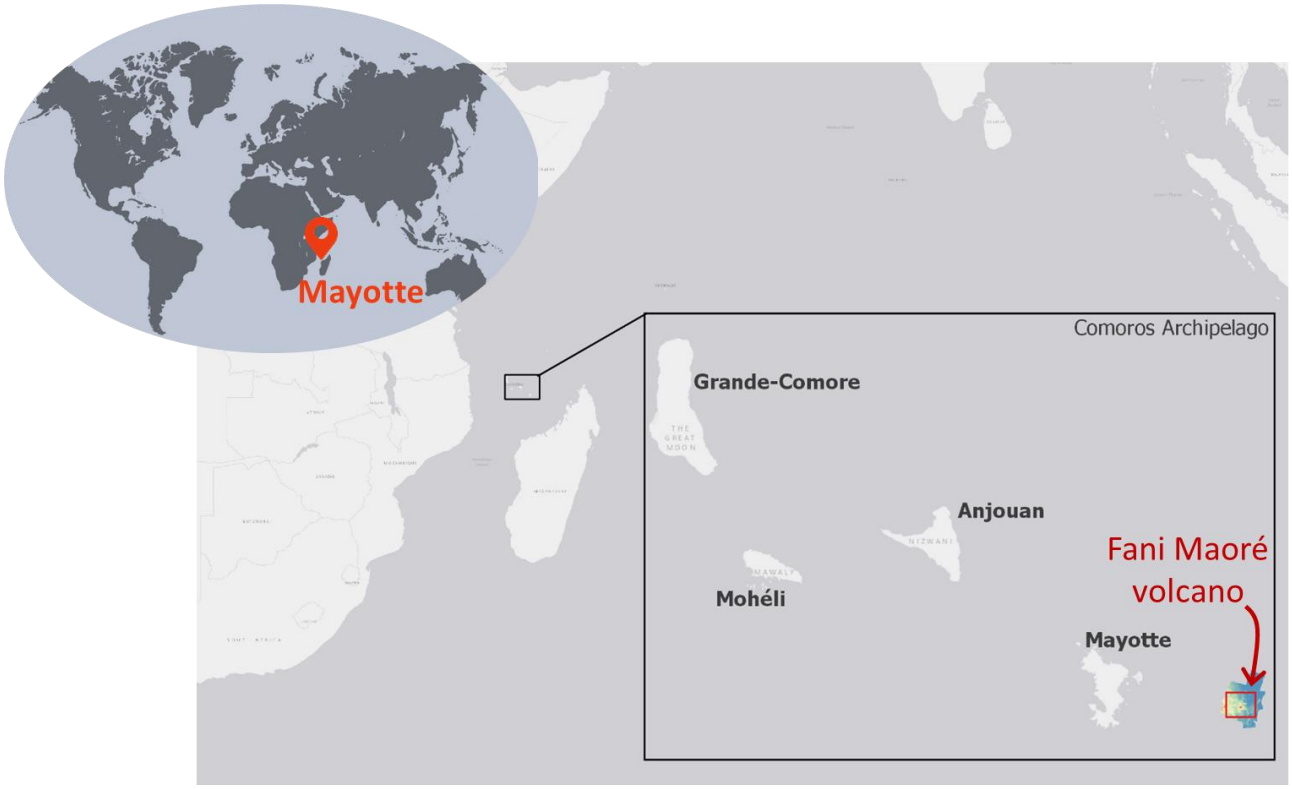

Figure 2. 1. World map and map of the Comoros Archipelago showing the location of Mayotte Island and of Fani Maoré submarine volcano.

The origin of the Comoros volcanism is not well established, and studies have discussed several competing mechanisms including i) the activity of a hot spot (Emerick and Duncan, 1982), ii) the presence of deep lithospheric fractures allowing magma migrations (Nougier et al., 1986), or iii) the coupling of both processes, with the interaction of extensional tectonics and deeper asthenospheric processes (Phethean et al., 2016). Recent works suggest that the volcanism is associated with lithospheric deformation rather than the result of a deep mantle plume (Michon, 2016; Famin et al., 2020; Lemoine et al., 2020; Tzevahirtzian et al., 2021). Indeed, values of heat flow measured by (Rolandone et al., 2022) do not support a regional thermal anomaly and so do not favor a hotspot model to explain Mayotte volcanism. Heat flow values are rather consistent with a Jurassic oceanic lithosphere around Mayotte, although the presence of very thin continental crust or continental fragments could also explain the observed heat flow (Rolandone et al., 2022).

The last documented volcanic and explosive activity on land is thought to have occurred less than 7000 years before present, in Petite-Terre, east of Mayotte (Zinke et al., 2003; Zinke et al., 2005), and probably between 4000 and 6000 years ago (Zinke et al., 2000). This volcanic activity extends offshore, east of Petite-Terre, where dozens of submarine volcanic edifices are observed in the insular slope of Mayotte (Audru et al, 2006) and particularly aligned along a 50 km long west-northwest–east-southeast (WNW-ESE) trending volcanic ridge (Feuillet et al., 2021).

2.2. Context of the Study

2.2.1. The seismo-volcanic crisis

Mayotte island has experienced a major seismic crisis that started on May 2018, the 10th (Lemoine et al., 2020). Subsequent offshore survey led to the discovery in May 2019 of a newly born volcanic edifice 50 km East of Mayotte (Figure 2. 2), at about 3600 m below sea level, the Fani Maoré Seamount (Feuillet et al., 2021) – see below part 2.2.3.1. At this time of the monitoring (May 2019), this submarine volcano appeared to be in eruption, with the detection of an exceptional acoustic plume ascending about 2 km height within the water column. The characteristics of this submarine eruption make it the largest active eruption ever documented since the Laki eruption in 1783 (Thordarson and Self, 1993; Feuillet et al., 2021).

Over the first year of the crisis, 32 earthquakes of magnitude $M_w \geq 5$ were recorded, including the largest seismic event ever recorded in the Comoros Archipelago on the 15th of May 2018 with M_w =

5.9 (Cesca et al., 2020; Lemoine et al., 2020; Feuillet et al., 2021). These earthquakes are distributed into two swarms, one proximal and one distal, whose epicenters are respectively located 5-15 km and about 25 km east of Petite-Terre, at 25-50 km depth (Feuillet et al., 2021; Lavayssière et al., 2022). Since July 2018, the number of earthquakes has decreased although continued seismicity persists, fluctuating and generating earthquakes of magnitudes up to $M_w \sim 4$ felt on land (REVOSIMA, 2023).

The seismo-volcanic crisis has been associated to a horizontal displacement of the island and to a subsidence. These effects have been observed using an on-land GNSS network (i.e. GPS stations) on Mayotte island. Since 1 July 2018, the displacement is estimated to be between 21 to 25 cm to the east, depending on the station location. The subsidence of the island is for its part estimated of about 10 to 19 cm. A slowdown of the displacement is observed since April-May 2019. Since the end of 2020, the deformation signals are too weak and remain within the noise. The origin of the seismic crisis is proposed to be magmatic, and studies have shown that the displacements of the first months of the crisis could result from the deflation of a deep magmatic reservoir east of Mayotte (Peltier et al., 2022).

About 30 km east of the new Fani Maore volcano, a particularly high heat flow measured by Rolandone et al. (2022) stands out. It could be the signature of a local magmatic process and/or a circulation of hot fluids in the crust (Emerick and Duncan, 1982). These observations testify to a renewed activity of the volcanic chain of Mayotte or to the intrusion of magmatic material within the crust (Rolandone et al., 2022).

Investigating the new volcano provides therefore a unique opportunity to better understand the formation of a volcanic edifice in deep-sea environment and the complex interactions between eruptive products, sea-water and local ecosystems.

2.2.2. In-depth monitoring through oceanographic cruises

The seismic crisis associated with the Fani Maore volcano birth had significant societal impacts. Several events of moderate magnitude were strongly felt by the population and damaged some buildings, also causing panic among the population (Miki, 2022; Taillefer et al., 2022). A strong concern lied in the potential of tsunami generation associated with earthquakes. Indeed, the intense seismic activity could weaken the submarine slopes of Mayotte and trigger submarine landslides potentially producing tsunamis. First results from Poulain et al., (2022) have shown that for the worst-case scenarios, the generated elevations of the water level are generally around 1 m, except in Petite Terre where they can reach very locally more than 15 m in an uninhabited area.

In response to this major seismo-volcanic crisis, the Mayotte volcanological and seismological monitoring network, named REVOSIMA (2021) was created. This network is a partnership between the Institut de Physique du Globe de Paris (IPGP), the Bureau de Recherches Géologiques et Minières (BRGM), the Observatoire Volcanologique du Piton de la Fournaise (OVPF-IPGP), the Centre National de la Recherche Scientifique (CNRS), and the Institut Français de Recherche pour l'Exploitation de la Mer (IFREMER). Both the scientific interest and crucial need for risk assessment drove the objectives and work of the REVOSIMA network.

Many topics are studied by scientists, including seismology, geomorphology, geodesy, sedimentology, volcanology and petrology, underwater acoustics, water column geochemistry and ecology (Van Der Woerd et al., 2023). This multidisciplinary work has the objective to understand the context of this major seismo-volcanic crisis and to define the interactions between magmatism, tectonics and fluids circulation processes at the scale of the lithosphere on several spatial and temporal scales. The purpose of the work is also to examine the environmental implications of this event by looking at the impact on physical-chemical properties of the water column and the ecosystem evolution.

Since the beginning of the scientific mobilization and creation of the REVOSIMA, a large series of survey cruises, called MAYOBS (Feuillet et al., 2019) was carried out. These cruises were dedicated to the maintenance of in-situ monitoring seismic apparatus (such sea-bottom seismometers (OBS), hydrophones) and to bathymetric survey, and a part of these cruises was devoted for multidisciplinary operations. This part concerns MAYOBS1, 4, 15 and 21 (for cruises that occurred before 2022). In addition, a scientific cruise named GeoFLAMME (Rinnert et al., 2021) took place for multidisciplinary operations using ROV. The main objectives and these cruises and operations are presented below:

MAYOBS1 (Feuillet, 2019) was conducted onboard the *R/V Marion Dufresne*, from May 2 to 22, 2019. The volcano edifice was discovered during this campaign.

MAYOBS4 (Fouquet and Feuillet, 2019) occurred on the *R/V Marion Dufresne*, from 19 July to 4 August 2019.

MAYOBS15 (Rinnert et al., 2020), was organized onboard the *R/V Marion Dufresne*, from the 1 to 27 October 2020.

MAYOBS21 (Rinnert et al., 2021b) was carried onboard the *R/V Marion Dufresne*, from 13 September to 4 October 2021.

These four campaigns were part of the REVOSIMA operations to monitor the evolution of the seismic and volcanic phenomenon that has been affected the island of Mayotte since May 2018. These campaigns aim to acquire marine geophysical data allowing the production of bathymetric and reflectivity maps of the sea floor, and the analysis of acoustic plumes caused by fluid or particle emissions in the water column. Their purpose is also to acquire samples (e.g. lava, rocks, fluid, seawater) to investigate magmatic processes through petrogeological analyses of lava, to monitor the water column geochemistry, to characterize the sediment composition and geotechnical properties, and to observe the seafloor using deep-towed camera in order to understand better the phenomenon. These sea expeditions also aim to maintain a network of underwater instruments including ocean bottom seismometers and acquire high-resolution bathymetric maps.

GeoFlamme (Rinnert et al., 2021a) was conducted onboard the *R/V Pourquoi Pas ?*, from 17 April to 26 May 2021. This is a scientific cruise taking part of the CNFH (Commission Nationale Flotte Hauturière) process. The main objective of the GeoFlamme project was to investigate the interactions between magmatism, tectonics and fluids circulation processes at the scale of the lithosphere and the implications on the physical-chemical properties of the sediment and water column (biogeochemical cycles, gas fluxes), and the marine ecosystem evolution. To complete this objective, this campaign aimed to provide the first ROV observations of the seafloor following the massive eruptive event that gave birth to the volcano. This project provides a combined study of solid, gas and liquid samples to document the entire chain of interactions between volcanic products, magmatic gases, seawater circulation and the water column, which is rarely done within the same project in the context of a deep-sea eruption, active or very recent.

The operations performed during all those cruises consist of dredges, water column sampling, bottom and water column imaging, bathymetric survey, sediment sounder, core drilling, seismicity. The principle of these operations is briefly explained below.

Ocean Bottom Seismometers (OBS): Six of these apparatus were deployed between 1000 and 3500 m on the seafloor, over the area of seismic activity. They record the waves generated by earthquakes and allow the location of their source with precision. This network completes the stations already installed on land to give more accuracy in the seismic location process. The first deployments were in February 2019. The recovery operations for maintenance and data backup, as well as their redeployment on the seafloor, are carried out approximately every 4 to 6 months.

A-0-A pressure sensor: This instrument is used to record very precise measurements of the vertical movements (i.e. inflation/deflation) of the seafloor above the location of the proximal seismic swarm with an accuracy of the order of cm.

Hydrophones: A network of hydrophones (about four) is deployed at sea around the volcanic activity. They are located at a depth of 1300 m, where the sound propagates most efficiently. They allow to record sounds made by earthquakes, underwater landslides, marine mammal calls (e.g. whales), and human-induced noises (e.g. ships). In our study case, they allow us to identify sounds related to lava flows or underwater explosions. These data must be recovered once or twice a year.

Acoustic survey from ship and from autonomous underwater vehicle (AUV): This operation maps the topography of the seafloor, allows the identification of lava flows and detects anomalies in the water column that may be related to fluid emissions. The mapping performed using an AUV allows to obtain a high definition of the bathymetry in comparison to the one performed from the surface using the ship's multibeam echosounder.

Bubseafloor stratigraphy: The multichannel seismic reflection profile gives an acoustic picture of the subsurface beneath the seafloor (i.e. superficial sediment layer). This technique uses sound waves that behave differently depending on the nature of the rocks in which they propagate. The reflected waves are collected by sensors (i.e. hydrophones), which allow the identification of different geological interfaces and the estimation of their thickness and depth. The images obtained show a vertical section of the subsurface, with the faults and the succession and geometry of the geological layers. Its second use is to provide the best possible image of the coring site and to identify if the conditions are favorable for the realization of a corer.

Bottom and water column imaging: A live observation of seafloor and water column images is carry out using an underwater camera mounted either on the submersible interactive camera system (SCAMPI, Ifremer) or on the ROV Remotely Operated underwater Vehicle (ROV Victor 6000, Ifremer).

Cores: Corers are used to collect sediments for analysis. This is performed on the superficial sediment layer (~0-10 m long) and allow the determination of the nature of the sediments and their conditions of deposition. There are two types of corers: (i) the multitube, which allows us to sample superficial sediments (the first few tens of centimeters below the seabed) using 8 tubes; and (ii) the gravity corer, equipped with a steel tube (in our case 13 to 15 m long), which allows the

acquisition of a continuous sedimentary sequence of about ten meters if the operation goes well and if the nature of the deposits allows it.

Dredges: This operation consists of taking rocks from the seabed. The dredge consists of a toothed steel collar at least 1 meter in diameter and 15 centimeters high, attached to a basket made of a mesh of steel rings. The dredge is connected to the ship by a steel cable and is launched by the articulated gantry at the back of the ship. Once the dredge is placed on the bottom, it is slowly dragged over the area to be sampled. After scraping the ground for several tens of minutes, the dredge is raised to the rear deck where it is emptied. This sampling is performed in order to carry out laboratory analyses on the composition of these rocks (e.g. gas content, metals). The dredges are conducted both on old structures and on new lava flows.

Hydrocasts: The hydrocasts performed with a CTD-rosette allow the sampling of seawater at different depths while measuring *in situ* physicochemical parameters. Deployments are performed on strategic sites, where volcanic activity or fluid/gas emission have been previously detected. The collected seawater is then analyzed in laboratory (onboard or onshore) and the results allow to evaluate the origin of the emissions, the processes within the water column and the possible change over time. This thesis focuses on this aspect of the monitoring.

2.2.3. Sites of activity with fluid emission

In the context of this seismo-volcanic crisis, and based on the monitoring operations, scientists have defined several areas of interest where gas and fluid emissions, acoustic signals, or distinctive geologic structures have first been observed. These areas are presented in Figure 2. 2 and include the main areas studied in this manuscript – the Fani Maoré Volcano and the Horseshoe structure –, the Crown structure and the Volcanic Ridge, and areas on Petite-Terre Island – the Dziani Dzaha lake and the Airport tidal flat.

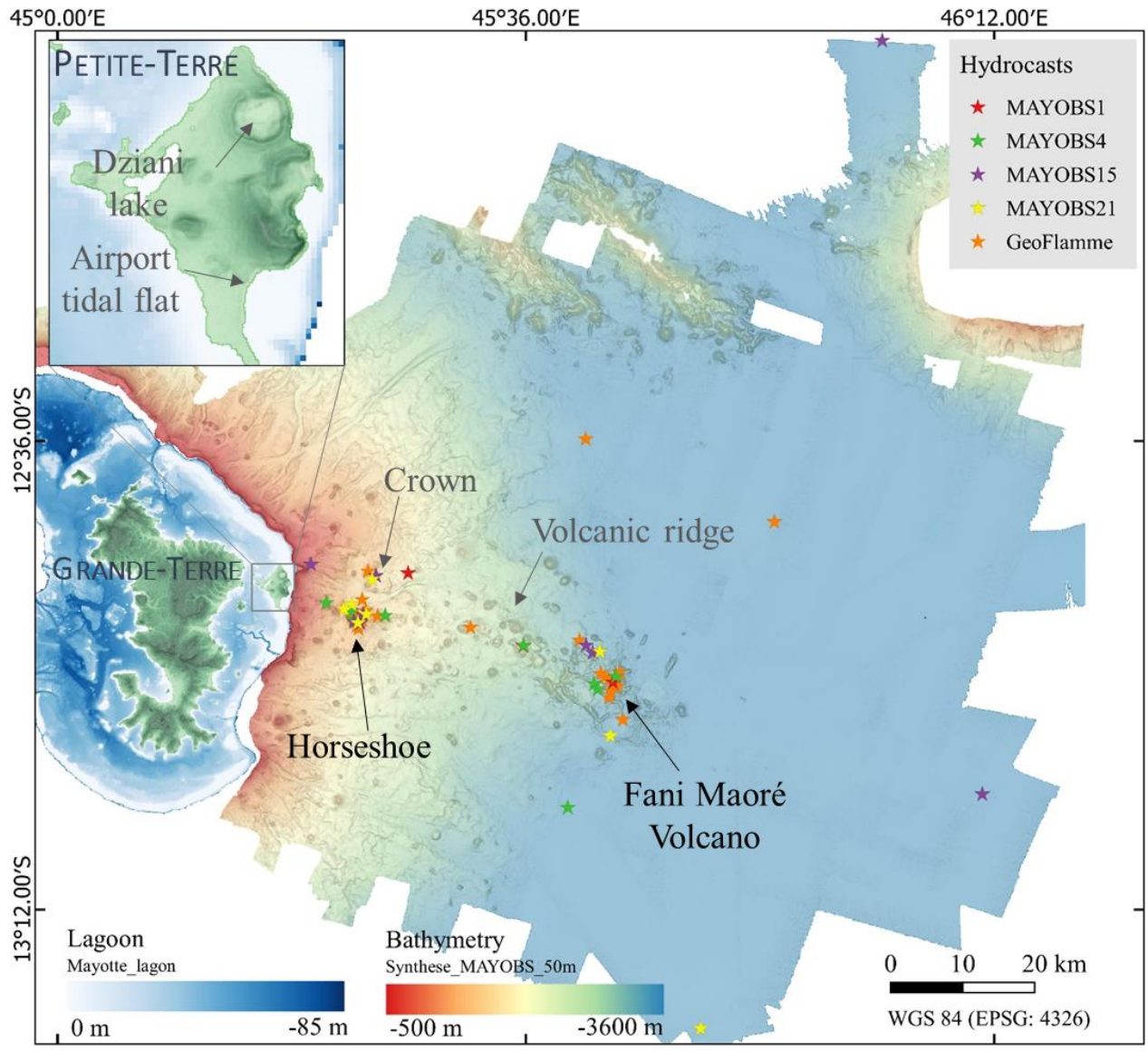

Figure 2. 2. Map of the studied area offshore Mayotte Island with the different areas of interest. The 50m-resolution bathymetry (Geo-Ocean (Ifremer), 2022) is represented using WGS 84 geodetic system. CTD casts performed throughout the MAYOBS and GeoFlamme cruises are represented by the colored stars.

2.2.3.1. Fani Maoré Seamount

Fani Maoré Seamount was discovered in May 2019 during the first oceanographic cruise, MAYOBS1 (Feuillet, 2019), as part of the REVOSIMA survey program. This volcanic edifice is located 50 km east offshore Mayotte, at the geographic coordinates 12°54'37 S and 45°42'42 E (Figure 2. 2). It is emplaced on the seafloor at about 3500 m below sea level, and rises to 820 m with a diameter of about 5 km. This new volcano is located on the WNW-ESE submarine volcanic ridge, cutting the

eastern flank of Mayotte Island (Cesca et al., 2020; Lemoine et al., 2020; Feuillet et al., 2021). The Fani Maore volcanic edifice wasn't present in 2014 during the survey operated by the French Naval Hydrographic and Oceanographic Service (SHOM) (SHOM, 2014; Feuillet et al., 2021). It was discovered using the multibeam ship echo sounder that caught an exceptional acoustic plume of about 2 km rising within the water column and attesting for the ongoing eruption of the volcano.

Initial studies on this submarine eruption have proposed that the eruptive activity has been going on from June-July 2018 to May 2019 (Cesca et al., 2020; Lemoine et al., 2020). From July 2018 (i.e. the first surface deformation recorded in Mayotte) to May 18, 2019, the average minimum eruptive flow of lava was about 172-181 m^3/s over a maximum duration of 320-336 days. At the onset of the crisis the eruptive volumes and fluxes were exceptional and were, despite uncertainties, among the highest observed on an effusive volcano since the eruption of Laki (Iceland) in 1783. This makes the Fani Maoré eruption, the biggest submarine eruption ever documented.

The acoustic plume at the summit of Fani Maoré Seamount ended in the beginning of June 2019 during MAYOBS2 cruise (Jorry, 2019), indicating the cessation of the eruption at the summit of the edifice. It was followed from May 2019 to October 2020, by a chronological lava flow installation around the edifice. Four distant exit points of magma have been observed in a chronological order, as follow (REVOSIMA, 2023) (Figure 2. 3 and Figure 2. 4):

(i) **South of the volcano** with ~0.2 km^3 of lava extruded from May 19th to June 17th 2019.

(ii) **West of the volcano** with ~0.3 km^3 of lava emitted from June 18th to July 30th 2019.

(iii) **North of the volcano** with ~0.08 km^3 of lava discharged from July 31st to August 20th 2019.

(iv) **Northwest of the volcano** with ~0.8 km^3 of lava released from August 21st 2019 to May 11th 2020.

(v) **Northwest of the volcano** with ~0.1-0.2 km^3 of lava discharged from May 11th to October 11th 2020.

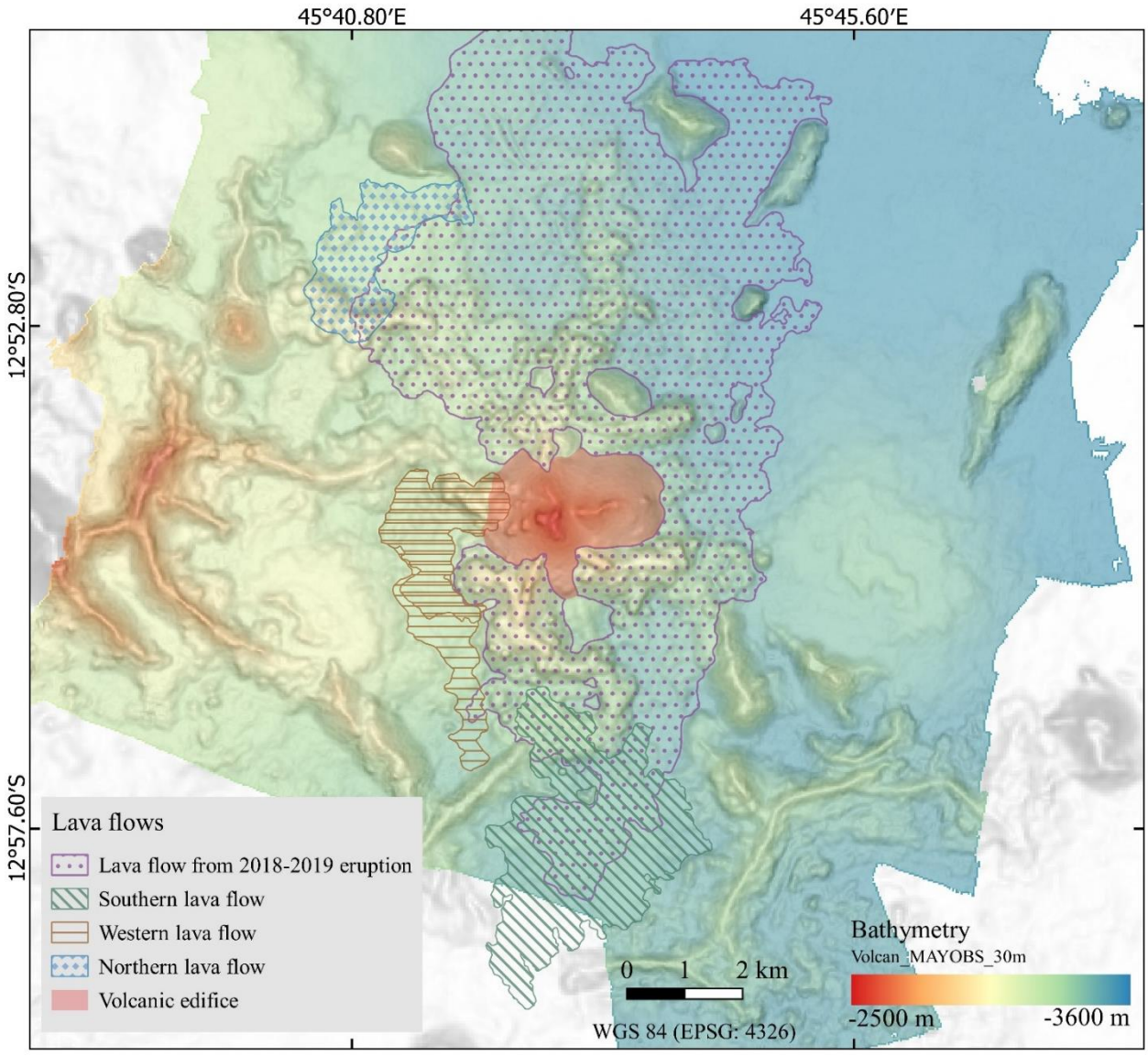

Figure 2. 3. Map of the area of Fani Maoré volcano with the distinct lava flows identified from bathymetry data collected during the MAYOBS (Feuillet et al., 2019; Fouquet and Feuillet, 2019; Jorry, 2019; Rinnert et al., 2020). The 30m-resolution bathymetry acquired during the MAYOBS15 cruise (Rinnert et al., 2020) is represented using WGS 84 geodetic system. Distinct lava flows.

Since the beginning of the eruptive activity, the volume of erupted magma is estimated to be about 6.55 km^3 (REVOSIMA, 2023). The last recorded lava flow occurred between October 2020 (MAYOBS15, (Rinnert et al., 2020)) and January 2021 (MAYOBS17, (Thinon et al., 2021)). Therefore, since the beginning of 2021, the eruption has probably stopped. However, given the persistent seismic activity and the fluid emissions on the Horseshoe structure, at this time no hypothesis is excluded regarding the evolution of the situation in the future (e.g. definitive stop of the activity, renewal of the eruptive activity on the same site or on another site) (REVOSIMA, 2023).

Although the effusive eruptive activity has stopped, an initiation of water-rock interactions in the sub-seafloor might occurs maintaining a release of chemical species into the water column.

Figure 2. 4. Chronology of the eruptive activity of Fani Maoré volcano from May 2018 to October 2020, and the corresponding monitoring campaigns.

Through the series of MAYOBS monitoring campaigns and the GeoFlamme scientific cruises, scientists are strongly mobilized to understand the origin of the Fani Maoré eruption and to investigate the interactions between magmatism, tectonics and fluid circulation processes.

To date, studies of petrological signatures of dredged lavas combined with geophysical data suggest the existence of a deep (≥37 km) and large (≥10 km^3) mantle reservoir located 15-20 km east of Petite-Terre that fed the large eruption of Fani Maoré Seamount which was tectonically triggered (Berthod et al., 2021; Lavayssière et al., 2022). Other petrological studies also suggest the presence of an intermediate shallower reservoir between the main magma chamber and the surface (Berthod et al., 2022). Dofal et al. (2022) have proposed that a shallow magma reservoir lies at the interface between the lithospheric mantle and the overlying crust, favoring the formation of thick magma underplating, and that two other magma reservoirs occur at~17km and 28 km at the upper and lower boundaries of this underplating (Figure 2. 5).

The very long period seismic events (VLP) that were frequently recorded suggest fluid migration at the lithospheric scale, resulting from active magmatic or hydrothermal processes (Lemoine et al., 2020). The displacements measured during the first months of the crisis could be induced by the deflation of the deep magma reservoir east of Mayotte (Peltier et al., 2022).

Seismic reflection images have shown that Fani Maore volcano is sitting on an older basaltic layer, itself sitting on a 3.5 km thick sedimentary cover (Masquelet et al., 2022). The construction of the edifice is believed to be the result of several successive eruptions from a single magma channel between May 2018 and May 2019. The 2018-2019 volcanic eruption would have occurred after about 4.6 million years of a seismic period in this area (Masquelet et al., 2022).

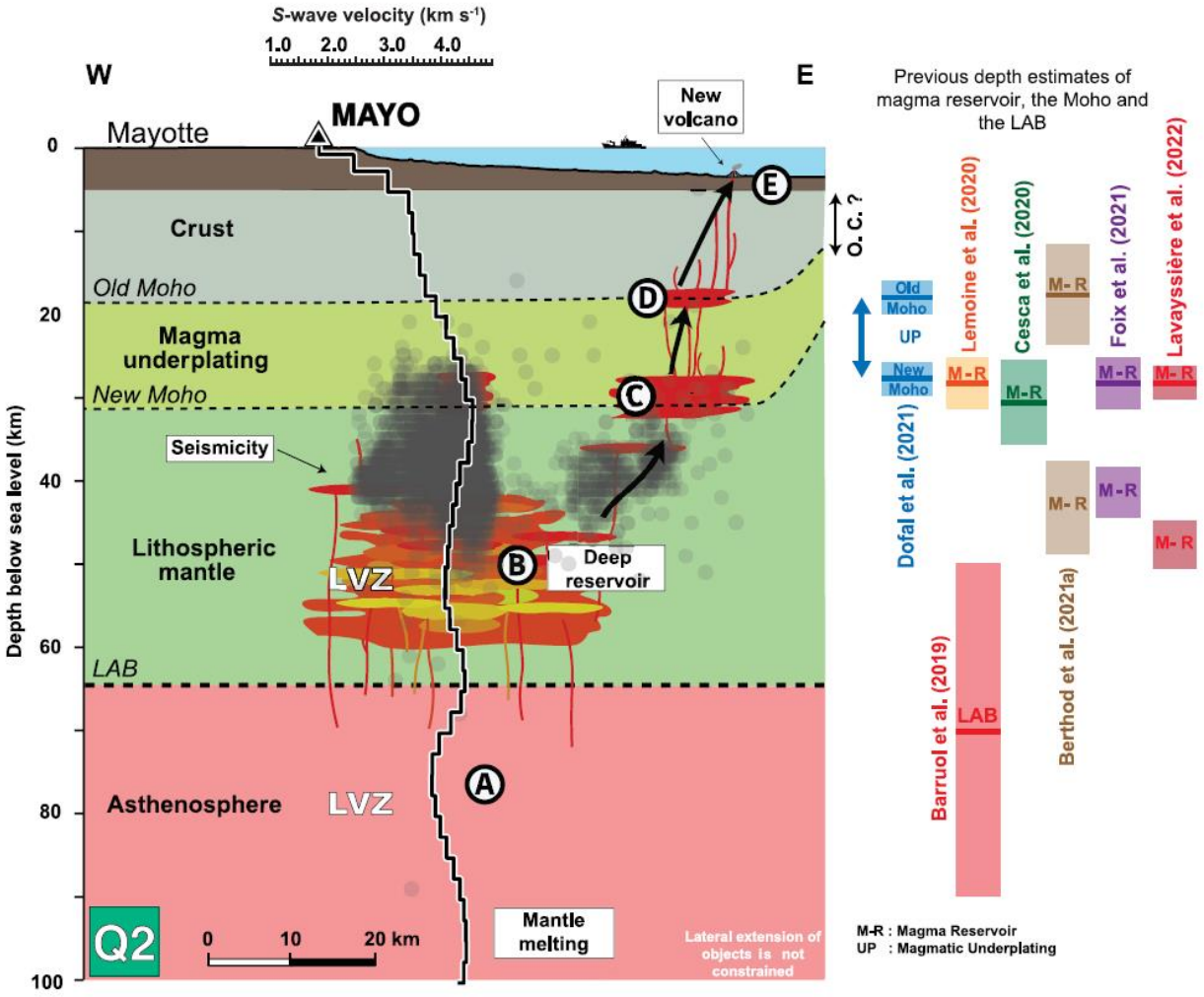

Figure 2. 5. Conceptual model of the magmatic plumbing system below the currently active eruptive zone of Mayotte from Dofal et al. (2022). Grey dots indicate the hypocenters of the seismicity recorded during the Mayotte seismo-volcanic crisis from February 2019 to May 2020. The red shapes represent areas of potential magma accumulation. Black arrows indicate possible magma migration paths from 80 km depth to the surface. On the right, the depth location of some interfaces provided by the literature.

Fani Maore provides a crucial addition of the relatively restricted list of seamount associated with known active hydrothermal activity, such as Tagoro volcano (El Hierro, Canary Islands) (González et al., 2020); Bounty seamount (Pitcairn Island hotspot) (Stoffers et al., 1990); Loihi seamount (Hawai'i, (Sedwick et al., 1992); Macdonald Seamount (Austral Islands) (Cheminée et al., 1991); Teahitia Seamount (Society Islands) (German et al., 2020); Vailulu'u Seamount (Samoan archipelago) (Staudigel et al., 2006). It is also the second major seafloor eruption witnessed after the discovery of the West Mata volcano (Chadwick et al., 2019).

2.2.3.2. Horseshoe structure

The Horseshoe ("Fer à Cheval" in French) is an ancient volcanic edifice located at about 10km east of Petite Terre (Figure 2. 2). It is a 4 km-wide cone, with steep slopes and a large collapse-induced scar (Feuillet et al., 2021) (Figure 2. 6). It is part of a submarine volcanic chain that extends from West to East over a distance of about 50 km, from ancient volcanoes of Petite-Terre (Dziani in particular) to the site of the new volcano (Fani Maore) discovered in 2019 (Feuillet et al., 2021). The Horseshoe is believed to have originated from several explosive submarine eruptions that reflect an intense volcanic activity in the past, characterized by a wide variety of eruptive styles and erupted magma composition (Feuillet et al., 2021; Puzenat et al., 2022). The Horseshoe shape, from which its name derives, is the result of several volcanic processes, including instability of the flanks, which took place in the past (Feuillet et al., 2021).

Since July 2019 (Fouquet and Feuillet, 2019), emissions of carbon dioxide (CO_2) have been observed on the ocean seafloor of the Horseshoe structure, suggesting the presence of magmatic activity. These emissions are in the form of droplets ascending the water column from the seafloor (Figure 2. 7). The detection of these emissions within the water column was first made by ship echo sounder survey (Kongsberg® and Reson Seabat® Multibeam acoustic echo-sounders), then by direct ocean bottom observations using towed camera SCAMPI during MAYOBS4 and MAYOBS15, and by the Victor 6000 ROV during GeoFlamme.

The Horseshoe being located over the proximal deep seismic swarm (recorded by the seismometers' network installed on/offshore Mayotte), it is suggested that it exists a strong link between the presence of the venting sites and the Fani Maoré eruption. The study of the location of these emissions at the seafloor, and their dispersion throughout the water column, as well as the emitted quantity and composition of the droplets is essential to understand the evolution of the fluid venting (in term of composition and flux), to determine the link with Fani Maoré eruption, and to evaluate the impact on the water column geochemistry.

Since its discovery at the beginning of the crisis, the number of venting sites is constantly increasing. Sites of venting were monitored from 02 May 2019 to 22 July 2022 over several cruises (MAYOBS cruises (Feuillet et al., 2019) and GeoFlamme cruise (Rinnert et al., 2021a)) (Figure 2. 6). It is important to note that the discovery of each venting site does not corresponds to the beginning of its activity but to the time of its first observation. In general, a venting site is composed of several seeps. Sites A_0 and B_0 were discovered in May 2019, the site C_0 in August 2019, sites D_0 and E_0 in May

2020, sites C_1 and F_0 in October 2020 simultaneously to an expansion toward the northwest of the A_0 and B_0 sites, with new sites called B_1, A_1 and A_2. The sites G_0, D_1, C_2+C_3 and C_4 were first observed between January and May 2021.

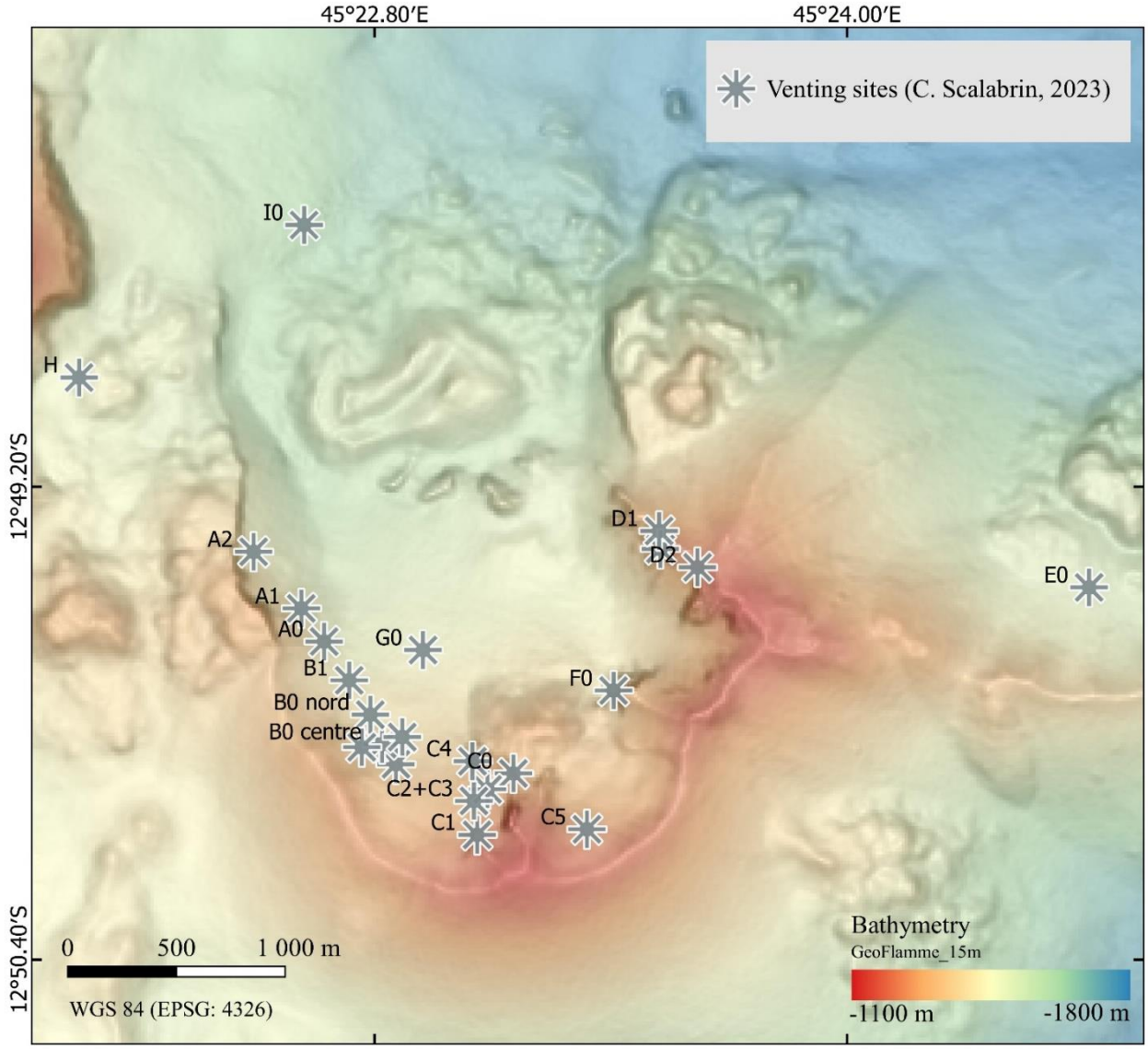

Figure 2. 6. Map of the Horseshoe structure area with identification of the various venting sites of liquid CO_2 (Scalabrin, 2023). The 15m-resolution bathymetry acquired during the GeoFlamme cruise (Rinnert et al., 2021a) is represented using WGS 84 geodetic system.

First geochemical analyses of emitted droplets at the seafloor have shown that these droplets are mainly composed of carbone dioxide CO_2 (99.0 ± 0.3 $\%_{vol}$), with a small contribution of methane CH_4 (0.8 ± 0.2 $\%_{vol}$) and dihydrogen H_2 (10 to 1000 ppm_{vol}) (Cathalot et al., in prep.). The stable carbon isotopic signature ($\delta^{13}C$) shows that CO_2 is of mantle origin ($\delta^{13}C$-CO_2 = -3.7 ± 0.2 ‰, ^{14}C-CO_2 aging > 40 kyrs) and suggests that CH_4 is of abiotic origin, although a mixed

biogenic/thermogenic contribution (i.e. from organic matter transformation) cannot be completely excluded ($\delta^{13}C\text{-}CH_4$ = -19.1 ± 0.4‰, $\delta D\text{-}CH_4$ = -140 ± 2‰). The helium isotopic signature ($^3He/^4He$) indicates a mantle source, confirming the deep magmatic origin of the fluids, obtained with the stable carbon isotopes (REVOSIMA, 2023).

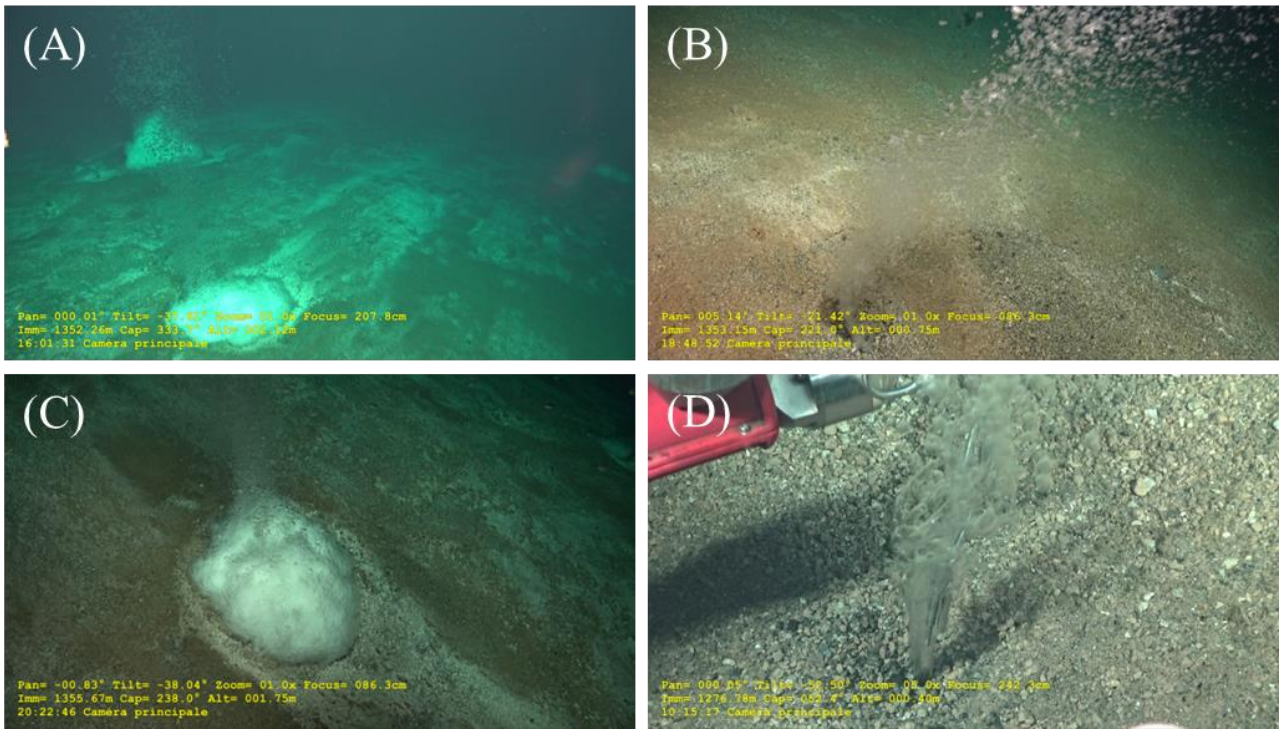

Figure 2. 7. Photography of some liquid CO_2 venting sites taken from the Victor 6000 ROV camera during the GeoFlamme cruise. In picture (A) and (C), venting is associated with the presence of CO_2 hydrates on the seafloor. In picture (D), the temperature of the vent is measured using the probe mounted on the Victor 6000 ROV.

In the literature, and based on our knowledge (see CHAPTER 1), only three sites of CO_2 deep seeps (i.e. < 500 m bsl) seems comparable to the droplet emissions occurring in the Horseshoe structure. The Champagne vent site, on NW Eifuku in the northern Mariana Arc, presents discharged of cold droplets (<4°C) of liquid CO_2, at 1600 m depth. These droplets are composed of about 98% of CO_2, 1% of H_2S and trace amounts of CH_4 and H_2 (Lupton et al., 2006; Lupton et al., 2008). The JADE hydrothermal field, in the Mid-Okinawa Trough Backarc Basin, presents carbon dioxide-rich fluid bubbles composed of about 86% of CO_2, 3% of H_2S and 11% of residual gas (CH_4, H_2). These emissions were observed on the seafloor between 1335 and 1550 m depth, with the presence of hydrates (Sakai et al., 1990a; Sakai et al., 1990b). In Yonaguni Knoll IV hydrothermal system, also located in the Okinawa Trough, liquid CO_2 droplets are emitted at ~1360-1400 m on the seafloor and are composed of ~85% of CO_2, ~14% of CH_4, and less than 0,02 % of H_2 (Konno et al., 2006).

2.2.3.3. Surrounding activity: Lake Dziani Dziaha and airport tidal flat at Petite Terre Island

On land, the most recent volcanic activity occurred in the Holocene on the eastern side of Mayotte, corresponding to the small Petite Terre Island, where two main and persistent areas of low-temperature CO_2-rich gas seeps are present: the airport tidal flat and the Dziani Dzaha intracrateric lake (Liuzzo et al., 2022).

2.2.3.3.1. Lake Dziani Dzaha

Lake Dziani Dzaha (Figure 2. 2) is a meromictic lake inside the volcanic crater of phonolitic maar, with maximum depth ranging between 4.5 m to around 18 m in a subcentral narrow depression. The bubbling emissions are heterogeneously distributed along the lake margins and in the central area. Several CO_2-rich and high-flux bubbling areas occur along the lake margins and a main CH_4-rich spot occurs close to the deepest part of the lake for which a strong increase in the bubbling activity has been observed since 2020 (Cadeau et al., 2020; Milesi et al., 2020; Liuzzo et al., 2021; Liuzzo et al., 2022).

2.2.3.3.2. Airport tidal flat

The bubbling area of Airport tidal flat (Figure 2. 2) was first described in 1998. First geochemical studies of this emissions occurred in 2005 (Traineau et al., 2006; Sanjuan et al., 2008). The composition of the emitted gas have been measured in 2006, 2008, and several times between 2018 and 2019 in the framework of the volcanic crisis monitoring (Liuzzo et al., 2021; Cadeau et al., 2022; Liuzzo et al., 2022).

This area is composed by tens of bubbling spots with variable flux on a muddy flat area exposed to significant tide (Liuzzo et al., 2022). Geochemical studies have shown the magmatic origin of these bubbles, mainly composed of carbon dioxide with low amounts of methane and helium (Traineau et al., 2006; Sanjuan et al., 2008; Liuzzo et al., 2022). In 2005, the lowest pH value of the seawater in association to this bubbling was 5.85 (Traineau et al., 2006).

2.3. Oceanographic Setting

Water masses of the Comoros Basin have been described by Collins et al. (2016) during a dedicated research cruise in the basin (Table 2. 1). The water masses of our study site (Figure 2. 8) can be

associated to the western part of the S7 transect and the northern part of the S5 presented in Figure 1 of their publication.

The upper ~200m of the Comoros Basin is dominated by warm, low-salinity, high-oxygen **Tropical Surface Water** (TSW), but also by warm and saline **Arabian Sea High Salinity Water** (ASHSW). Nonetheless, the influence of this water mass at the Horseshoe area remains weak. Below, the Comoros Basin is dominated by high-salinity, low-oxygen **Subtropical Surface Water** (STSW), which generally occurs in the 150-350 m depth range. The influence of **Equatorial Indian Ocean Water** (EIOW) is also observed at these depths. This water mass has elevated nutrient values compared to TSW, with temperatures similar to that of STSW, and has a less extreme salinity maximum and lower oxygen values compared to STSW. The dominant water mass in the 300-600 m depth range is **South Indian Central Water** (SICW) with its characteristic oxygen maximum.

The intermediate layers (600-1500 m) in the Comoros Basin are characterized by low-salinity **Antarctic Intermediate Water** (AAIW) and high-salinity **Red Sea Intermediate Water** (RSIW). Mixing between both water mases can occurs due to the presence of mesoscale eddies.

The deep and bottom waters of the Comoros Basin are found for background hydrocasts and at the Volcano area, and comprised high-salinity, oxygen-rich **North Atlantic Deep Water** (NADW) as well as **Upper Circumpolar Deep Water** (UCDW).

Table 2. 1. Characteristics of the major water masses found in the Comoros Basin, after Collins et al. (2016).

Water mass	**Depth range** m	**Temperature** °C	**Salinity** psu	**Oxygen** µmol/L
TSW	0–180	>22	<35.3	>160
ASHSW	0–180	>22	>35.4	>160
STSW	100–350	13–22	35.5–35.7	<180
EIOW	150–350	13–22	35.12–35.5	<150
SICW	300–700	8–14	34.8–35.4	140–220
AAIW	550–1000	7–8.5	34.7–34.9	120–180
RSIW	600–1400	4–8	34.9–35.1	<120
NADW	2300–2900	2–2.5	34.92–34.95	>200
UCDW	>2500	<2	34.9–34.92	<220

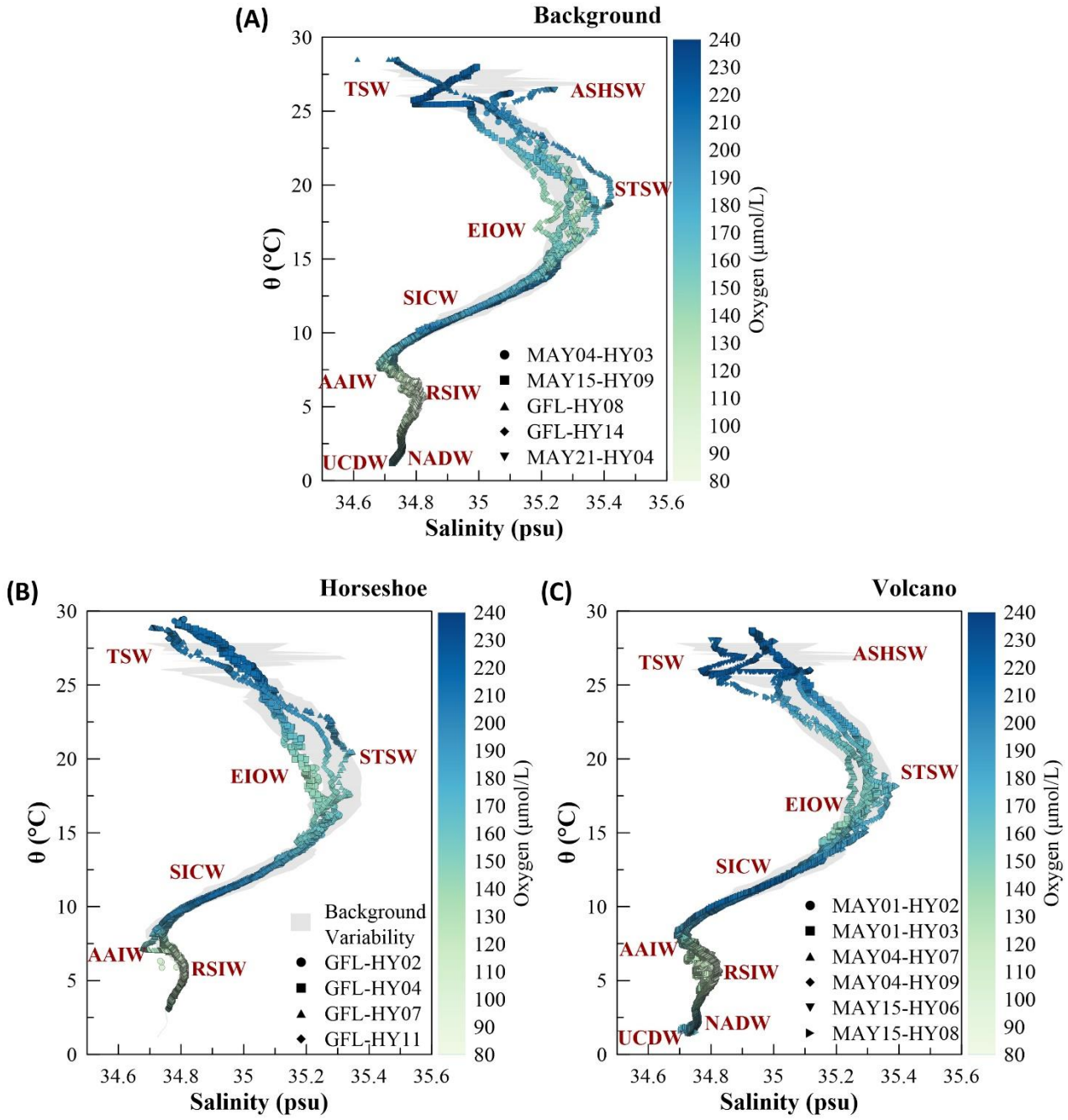

Figure 2. 8. Diagrams of potential temperature (θ) versus salinity for (A) background hydrocasts performed during MAYOBS4, MAYOBS15, MAYOBS21 and GeoFlamme cruises, (B) hydrocasts performed at the Horseshoe during GeoFlamme cruise, and (C) hydrocasts performed in the Volcano area during MAYOBS4, MAYOBS15, and MAYOBS21 cruises. Oxygen concentration is represented by the color scale. Water masses are identified on the diagrams. Methodology for data acquisition and treatment is describe in Chapter 3.

2.4. Highlights

The eruption of Fani Maoré Seamount is unique compared to any other deep submarine eruptions documented so far, as it presents exceptional characteristics.

(i) **The depth:** this new volcano lies on the seafloor at about 3500 m bsl.

(ii) **The duration:** the volcano was actively erupting during about one year, from June-July 2018 to May 2019.

(iii) **The erupted volume**: more than 6.55 km^3 of magma erupted, making this eruption the largest submarine eruption ever documented and the second reported worldwide after the 1783 Laki eruption in Iceland in terms of volumes.

(iv) **The eruptive flux**: 172-181 m^3/s estimated over 11 months, making these observed estimated fluxes the highest for an effusive eruption since the Laki eruption.

(v) **The plume height**: more than 2 km-high acoustic plumes were observed in the water column in May and June 2019.

(vi) **The depth of the involved sources and volcanic plumbing system**. This eruption is associated to a magma reservoir exceptionally deep (≥37 km).

In addition to these features, the eruption is associated with large fluid/gas emissions on the seafloor, and above the magma chamber. Studying the volcanic area of Mayotte is thus a unique opportunity to better understand the volcanic context of such extreme events, and evaluate the impact on the water column geochemistry.

2.5. Bibliographical References

Berthod, C., Komorowski, J.-C., Gurioli, L., Médard, E., Bachèlery, P., Besson, P., et al. (2022). Temporal magmatic evolution of the Fani Maoré submarine eruption 50 km east of Mayotte revealed by in situ sampling and petrological monitoring. *Comptes Rendus. Géoscience* 354(S2)**,** 195-223. doi: 10.5802/crgeos.155.

Berthod, C., Médard, E., Bachèlery, P., Gurioli, L., Di Muro, A., Peltier, A., et al. (2021). The 2018-ongoing Mayotte submarine eruption: Magma migration imaged by petrological monitoring. *Earth and Planetary Science Letters* 571**,** 117085. doi: 10.1016/j.epsl.2021.117085.

Cadeau, P., Jézéquel, D., Groleau, A., Muro, A.D., and Ader, M. (2022). Impact of the seismo-volcanic crisis offshore Mayotte on the Dziani Dzaha Lake. *Comptes Rendus. Géoscience* 354(S2)**,** 299-316. doi: 10.5802/crgeos.172.

Cadeau, P., Jézéquel, D., Leboulanger, C., Fouilland, E., Le Floc'H, E., Chaduteau, C., et al. (2020). Carbon isotope evidence for large methane emissions to the Proterozoic

atmosphere. *Scientific Reports* 10(1). doi: 10.1038/s41598-020-75100-x.

Cesca, S., Letort, J., Razafindrakoto, H.N.T., Heimann, S., Rivalta, E., Isken, M.P., et al. (2020). Drainage of a deep magma reservoir near Mayotte inferred from seismicity and deformation. *Nature Geoscience* 13(1)**,** 87-93. doi: 10.1038/s41561-019-0505-5.

Chadwick, W.W., Rubin, K.H., Merle, S.G., Bobbitt, A.M., Kwasnitschka, T., and Embley, R.W. (2019). Recent Eruptions Between 2012 and 2018 Discovered at West Mata Submarine Volcano (NE Lau Basin, SW Pacific) and Characterized by New Ship, AUV, and ROV Data. *Frontiers in Marine Science* 6. doi: 10.3389/fmars.2019.00495.

Cheminée, J.L., Stoffers, P., McMurtry, G., Richnow, H., Puteanus, D., and Sedwick, P. (1991). Gas-rich submarine exhalations during the 1989 eruption of Macdonald Seamount. *Earth and Planetary Science Letters* 107(2)**,** 318-327. doi: 10.1016/0012-821x(91)90079-w.

Collins, C., Hermes, J.C., Roman, R.E., and Reason, C.J.C. (2016). First dedicated hydrographic survey of the Comoros Basin. *Journal of Geophysical Research: Oceans* 121(2)**,** 1291-1305. doi: 10.1002/2015jc011418.

Debeuf, D. (2004). Étude de l'évolution volcano-structurale et magmatique de Mayotte (archipel des Comores, océan Indien). *Université de la Reunion* 277.

Dofal, A., Michon, L., Fontaine, F.R., Rindraharisaona, E., Barruol, G., and Tkalčić, H. (2022). Imaging the lithospheric structure and plumbing system below the Mayotte volcanic zone. *Comptes Rendus. Géoscience* 354(S2)**,** 47-64. doi: 10.5802/crgeos.190.

Emerick, C.M., and Duncan, R.A. (1982). Age progressive volcanism in the Comores Archipelago, western Indian Ocean and implications for Somali plate tectonics. *Earth and Planetary Science Letters* 60(3)**,** 415-428. doi: 10.1016/0012-821x(82)90077-2.

Famin, V., Michon, L., and Bourhane, A. (2020). The Comoros archipelago: a right-lateral transform boundary between the Somalia and Lwandle plates. *Tectonophysics* 789**,** 228539. doi: 10.1016/j.tecto.2020.228539.

Feuillet, N. (2019). MAYOBS1 cruise, RV Marion Dufresne. doi: 10.17600/18001217.

Feuillet, N., Jorry, S., Crawford, W.C., Deplus, C., Thinon, I., Jacques, E., et al. (2021). Birth of a large volcanic edifice offshore Mayotte via lithosphere-scale dyke intrusion. *Nature Geoscience* 14**,** 787-795. doi: 10.1038/s41561-021-00809-x.

Feuillet, N., Jorry, S., Rinnert, E., Thinon, I., and Fouquet, Y. (2019). MAYOBS cruises, RV Marion Dufresne. doi: 10.18142/291.

Fouquet, Y., and Feuillet, N. (2019). MAYOBS4 cruise, RV Marion Dufresne. doi: 10.17600/18001238.

Geo-Ocean (Ifremer) (2022). Bathymétrie - Mayotte (synthèse, 2021). doi: 10.12770/0085f83d-cc3e-4c3c-b19a-6c93bca97be9.

German, C.R., Resing, J.A., Xu, G., Yeo, I.A., Walker, S.L., Devey, C.W., et al. (2020). Hydrothermal Activity and Seismicity at Teahitia Seamount: Reactivation of the Society Islands Hotspot? *Frontiers in Marine Science* 7. doi: 10.3389/fmars.2020.00073.

González, F.J., Rincón-Tomás, B., Somoza, L., Santofimia, E., Medialdea, T., Madureira, P., et al. (2020). Low-temperature, shallow-water hydrothermal vent mineralization following the recent submarine eruption of Tagoro volcano (El Hierro, Canary Islands). *Marine Geology* 430**,** 106333. doi: 10.1016/j.margeo.2020.106333.

Jorry, S. (2019). MAYOBS2 cruise, RV Marion Dufresne. doi: 10.17600/18001222.

Konno, U., Tsunogai, U., Nakagawa, F., Nakaseama, M., Ishibashi, J.-I., Nunoura, T., et al. (2006). Liquid CO2 venting on the seafloor: Yonaguni Knoll IV hydrothermal system, Okinawa Trough. *Geophysical Research Letters* 33(16). doi: 10.1029/2006gl026115.

Lavayssière, A., Crawford, W.C., Saurel, J.-M., Satriano, C., Feuillet, N., Jacques, E., et al. (2022). A new 1D velocity model and absolute locations image the Mayotte seismo-volcanic region. *Journal of Volcanology and Geothermal Research* 421**,** 107440. doi: 10.1016/j.jvolgeores.2021.107440.

Lemoine, A., Briole, P., Bertil, D., Roullé, A., Foumelis, M., Thinon, I., et al. (2020). The 2018–2019 seismo-volcanic crisis east of

Mayotte, Comoros islands: seismicity and ground deformation markers of an exceptional submarine eruption. *Geophysical Journal International* 223(1)**,** 22-44. doi: 10.1093/gji/ggaa273.

Liuzzo, M., Di Muro, A., Rizzo, A.L., Caracausi, A., Grassa, F., Fournier, N., et al. (2021). Gas Geochemistry at Grande Comore and Mayotte Volcanic Islands (Comoros Archipelago), Indian Ocean. *Geochemistry, Geophysics, Geosystems* 22(8). doi: 10.1029/2021gc009870.

Liuzzo, M., Muro, A.D., Rizzo, A.L., Grassa, F., Coltorti, M., and Ader, M. (2022). The composition of gas emissions at Petite Terre (Mayotte, Comoros): inference on magmatic fingerprints. *Comptes Rendus. Géoscience* 354(S2). doi: 10.5802/crgeos.148.

Lupton, J., Butterfield, D., Lilley, M., Evans, L., Nakamura, K.-I., Chadwick, W., et al. (2006). Submarine venting of liquid carbon dioxide on a Mariana Arc volcano. *Geochemistry, Geophysics, Geosystems* 7(8). doi: 10.1029/2005gc001152.

Lupton, J., Lilley, M., Butterfield, D., Evans, L., Embley, R., Massoth, G., et al. (2008). Venting of a separate CO2-rich gas phase from submarine arc volcanoes: Examples from the Mariana and Tonga-Kermadec arcs. *Journal of Geophysical Research: Solid Earth* 113(B8). doi: 10.1029/2007jb005467.

Masquelet, C., Leroy, S., Delescluse, M., Chamot-Rooke, N., Thinon, I., Lemoine, A., et al. (2022). The East-Mayotte new volcano in the Comoros Archipelago: structure and timing of magmatic phases inferred from seismic reflection data. *Comptes Rendus. Géoscience* 354(S2)**,** 65-79. doi: 10.5802/crgeos.154.

Mayotte Volcanological And Seismological Monitoring Network (REVOSIMA), Institut de physique du globe de Paris (IPGP), Bureau de recherches géologiques et minières (BRGM), Institut français de recherche pour l'exploitation de la mer (IFREMER), and Centre national de la recherche scientifique (CNRS) (2021). Data collection of the Mayotte volcanological and seismological monitoring network (REVOSIMA). doi: 10.18715/MAYOTTE.REVOSIMA.

Michon, L. (2016). "The Volcanism of the Comoros Archipelago Integrated at a Regional Scale." Springer Berlin Heidelberg), 333-344.

Miki, M. (2022). Storytelling, language, and the earthquake swarm of May 2018: Insights into Shimaore and Kibushi from narrative analysis. *Comptes Rendus. Géoscience* 354(S2)**,** 417-437. doi: 10.5802/crgeos.131.

Milesi, V.P., Debure, M., Marty, N.C.M., Capano, M., Jézéquel, D., Steefel, C., et al. (2020). Early Diagenesis of Lacustrine Carbonates in Volcanic Settings: The Role of Magmatic CO2 (Lake Dziani Dzaha, Mayotte, Indian Ocean). *ACS Earth and Space Chemistry* 4(3)**,** 363-378. doi: 10.1021/acsearthspacechem.9b00279.

Nougier, J., Cantagrel, J.M., and Karche, J.P. (1986). The Comores archipelago in the western Indian Ocean: volcanology, geochronology and geodynamic setting. *Journal of African Earth Sciences (1983)* 5(2)**,** 135-145. doi: 10.1016/0899-5362(86)90003-5.

Pelleter, A.-A., Caroff, M., Cordier, C., Bachelery, P., Nehlig, P., Debeuf, D., et al. (2014). Melilite-bearing lavas in Mayotte (France): An insight into the mantle source below the Comores. *Lithos* 208-209**,** 281-297. doi: 10.1016/j.lithos.2014.09.012.

Peltier, A., Saur, S., Ballu, V., Beauducel, F., Briole, P., Chanard, K., et al. (2022). Ground deformation monitoring of the eruption offshore Mayotte. *Comptes Rendus. Géoscience* 354(S2)**,** 171-193. doi: 10.5802/crgeos.176.

Phethean, J.J.J., Kalnins, L.M., Van Hunen, J., Biffi, P.G., Davies, R.J., and McCaffrey, K.J.W. (2016). Madagascar's escape from Africa: A high-resolution plate reconstruction for the Western Somali Basin and implications for supercontinent dispersal. *Geochemistry, Geophysics, Geosystems* 17(12)**,** 5036-5055. doi: 10.1002/2016gc006624.

Poulain, P., Friant, A.L., Pedreros, R., Mangeney, A., Filippini, A.G., Grandjean, G., et al. (2022). Numerical simulation of submarine landslides and generated tsunamis: application to the on-going Mayotte seismo-volcanic crisis. *Comptes Rendus. Géoscience* 354(S2)**,** 361-390. doi: 10.5802/crgeos.138.

Puzenat, V., Feuillet, N., Komorowski, J.-C., Escartín, J., Deplus, C., Bachèlery, P., et al.

(2022). Volcano-tectonic structures of Mayotte's upper submarine slope: insights from high-resolution bathymetry and in-situ imagery from a deep-towed camera. *Comptes Rendus. Géoscience* 354(S2)**,** 81-104. doi: 10.5802/crgeos.175.

REVOSIMA (2023). *Bulletin mensuel de l'activité sismo-volcanique à Mayotte : Mars 2023* [Online]. Available: www.ipgp.fr/revosima [Accessed].

Rinnert, E., Cathalot, C., and Feuillet, N. (2021a). GEOFLAMME cruise, RV Pourquoi pas ? doi: 10.17600/18001297.

Rinnert, E., Thinon, I., and Feuillet, N. (2020). MD 228 / MAYOBS15 cruise, RV Marion Dufresne. doi: 10.17600/18001745.

Rinnert, E., Thinon, I., and Lebas, E. (2021b). MAYOBS21 cruise, RV Marion Dufresne. doi: 10.17600/18001986.

Rolandone, F., Poort, J., Masquelet, C., Leroy, S., Thinon, I., Lemoine, A., et al. (2022). Heat flow measurements in the Northern Mozambique Channel. *Comptes Rendus. Géoscience* 354(S2)**,** 35-46. doi: 10.5802/crgeos.130.

Sakai, H., Gamo, T., Kim, E.-S., Tsutsumi, M., Tanaka, T., Ishibashi, J., et al. (1990a). Venting of Carbon Dioxide-Rich Fluid and Hydrate Formation in Mid-Okinawa Trough Backarc Basin. *Science* 248(4959)**,** 1093-1096. doi: doi:10.1126/science.248.4959.1093.

Sakai, H., Gamo, T., Kim, E.S., Shitashima, K., Yanagisawa, F., Tsutsumi, M., et al. (1990b). Unique chemistry of the hydrothermal solution in the mid-Okinawa Trough Backarc Basin. *Geophysical Research Letters* 17(12)**,** 2133-2136. doi: 10.1029/gl017i012p02133.

Sanjuan, B., Baltassat, J.-M., Bezelgues, S., Brach, M., Girard, J.-F., and Mathieu, F. (2008). Estimation du potentiel géothermique de Mayotte: phase 2-étape2. Investigations géologiques, géochimiques et géophysiques complémentaires, synthèse des résultats. *Synthèse des Résultats (BRGM, 2008)*.

[Dataset] Scalabrin, C. (2023). *Site d'émissions de fluides, Mayotte, zone Fer à Cheval (C. Scalabrin, 2022).* doi: 10.12770/070818f6-6520-49e4-bafd-9d4d0609bf7d. Available: https://doi.org/10.12770/070818f6-6520-49e4-bafd-9d4d0609bf7d.

Sedwick, P.N., McMurtry, G.M., and Macdougall, J.D. (1992). Chemistry of hydrothermal solutions from Pele's Vents, Loihi Seamount, Hawaii. *Geochimica et Cosmochimica Acta* 56(10)**,** 3643-3667. doi: 10.1016/0016-7037(92)90159-G.

SHOM (2014). "Transit valorisé de Mayotte à Brest".).

Stamps, D.S., Kreemer, C., Fernandes, R., Rajaonarison, T.A., and Rambolamanana, G. (2021). Redefining East African Rift System kinematics. *Geology* 49(2)**,** 150-155. doi: 10.1130/g47985.1.

Staudigel, H., Hart, S.R., Pile, A., Bailey, B.E., Baker, E.T., Brooke, S., et al. (2006). Vailulu'u Seamount, Samoa: Life and death on an active submarine volcano. *Proceedings of the National Academy of Sciences* 103(17)**,** 6448-6453. doi: 10.1073/pnas.0600830103.

Stoffers, P., Hekinian, R., Ackermand, D., Binard, N., Botz, R., Devey, C., et al. (1990). Active Pitcairn hotspot found. *Mar. Geol* 95(1)**,** 51-55.

Taillefer, N., Bertil, D., Negulescu, C., Roullé, A., Iasio, C., Auclair, S., et al. (2022). Seismic damage scenarios for Mayotte: a tool for disaster management. *Comptes Rendus. Géoscience* 354(S2)**,** 343-359. doi: 10.5802/crgeos.120.

Thinon, I., Lemoine, A., Leroy, S., Paquet, F., Berthod, C., Zaragosi, S., et al. (2022). Volcanism and tectonics unveiled in the Comoros Archipelago between Africa and Madagascar. *Comptes Rendus. Géoscience* 354(S2)**,** 7-34. doi: 10.5802/crgeos.159.

Thinon, I., Rinnert, E., and Feuillet, N. (2021). MAYOBS17 cruise, RV Pourquoi Pas ? doi: 10.17600/18001983.

Thordarson, T., and Self, S. (1993). The Laki (Skaftár Fires) and Grímsvötn eruptions in 1783-1785. *Bulletin of Volcanology* 55(4)**,** 233-263. doi: 10.1007/bf00624353.

Traineau, H., Sanjuan, B., Brach, M., and Andru, J. (2006). "Etat des connaissances du potentiel géithermique de Mayotte". Rapport BRGM/RP-54700-Fr).

Tzevahirtzian, A., Zaragosi, S., Bachèlery, P., Biscara, L., and Marchès, E. (2021). Submarine morphology of the Comoros volcanic archipelago. *Marine Geology* 432**,**

106383. doi: 10.1016/j.margeo.2020.106383.

Van Der Woerd, J., Famin, V., and Humler, E. (2023). Special issue Comptes-Rendus Geoscience: The Mayotte seismo-volcanic crisis of 2018–2021 in the eastern Comoros archipelago (Mozambique channel). *Comptes Rendus. Géoscience* 354(S2)**,** 1-6. doi: 10.5802/crgeos.196.

Zinke, J., Reijmer, J., Dullo, W.-C., and Thomassin, B. (2000). Paleoenvironmental changes in the lagoon of Mayotte associated with the Holocene transgression. *Geolines* 11**,** 150-153.

Zinke, J., Reijmer, J.J.G., Taviani, M., Dullo, W.-C., and Thomassin, B. (2005). Facies and faunal assemblage changes in response to the Holocene transgression in the Lagoon of Mayotte (Comoro Archipelago, SW Indian Ocean). *Facies* 50(3-4)**,** 391-408. doi: 10.1007/s10347-004-0040-7.

Zinke, J., Reijmer, J.J.G., and Thomassin, B.A. (2003). Systems tracts sedimentology in the lagoon of Mayotte associated with the Holocene transgression. *Sedimentary Geology* 160(1-3)**,** 57-79. doi: 10.1016/s0037-0738(02)00336-6.

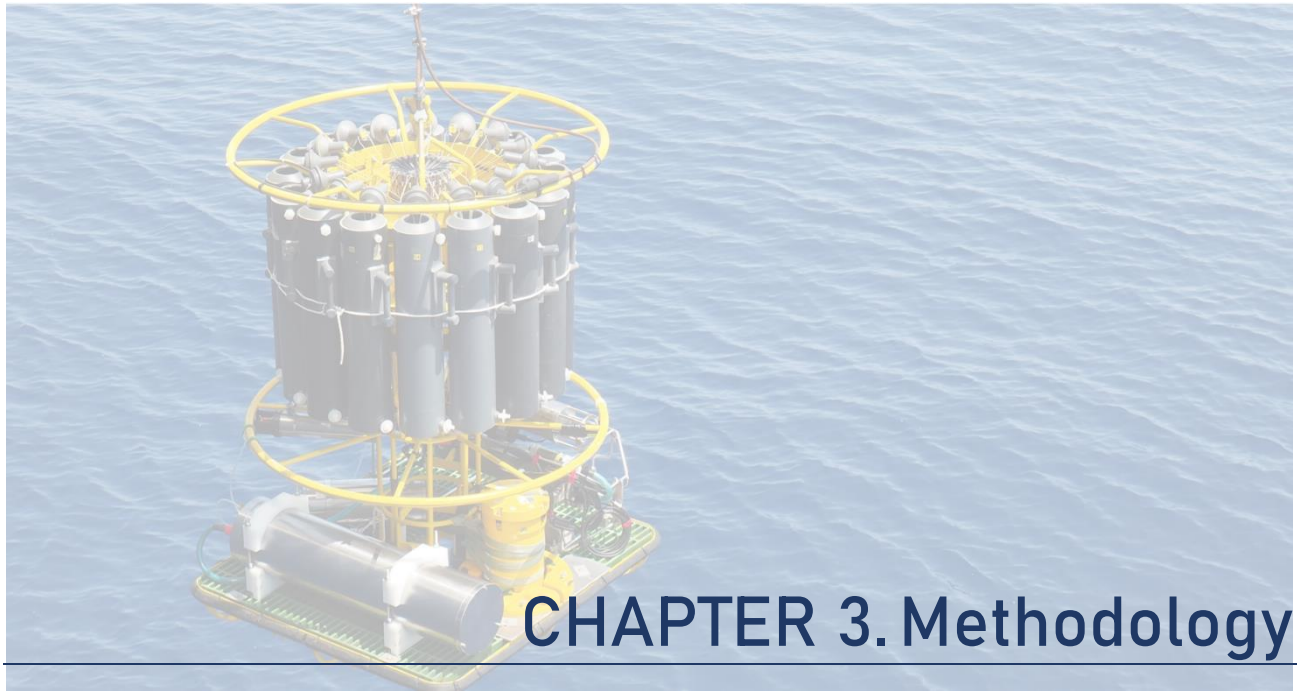

CHAPTER 3. Methodology

Abstract

As part of this PhD work, water column samples were taken both in the area of the Fani Maoré volcano for the study of the water column geochemistry in the context of a submarine eruption, and in the area of the Horseshoe for the study of liquid CO2 emissions. Sampling of the water column was performed using a CTD-rosette. Locations of the CTD-rosette casts were chosen from acoustic (using multibeam ship echo sounder) and visual (using the SCAMPI submersible camera and ROV observations) surveys for evidences of fluid and/or gas emissions. Samples were analyzed onboard and onshore for the determination of the concentrations of gases, metals, physicochemical parameters, while CTD (Conductivity, Temperature, Depth) data were computer-processed. Hereafter, this chapter describes the different instruments used for the observation, the sampling and the analysis of the water column, as well as the analytical methods.

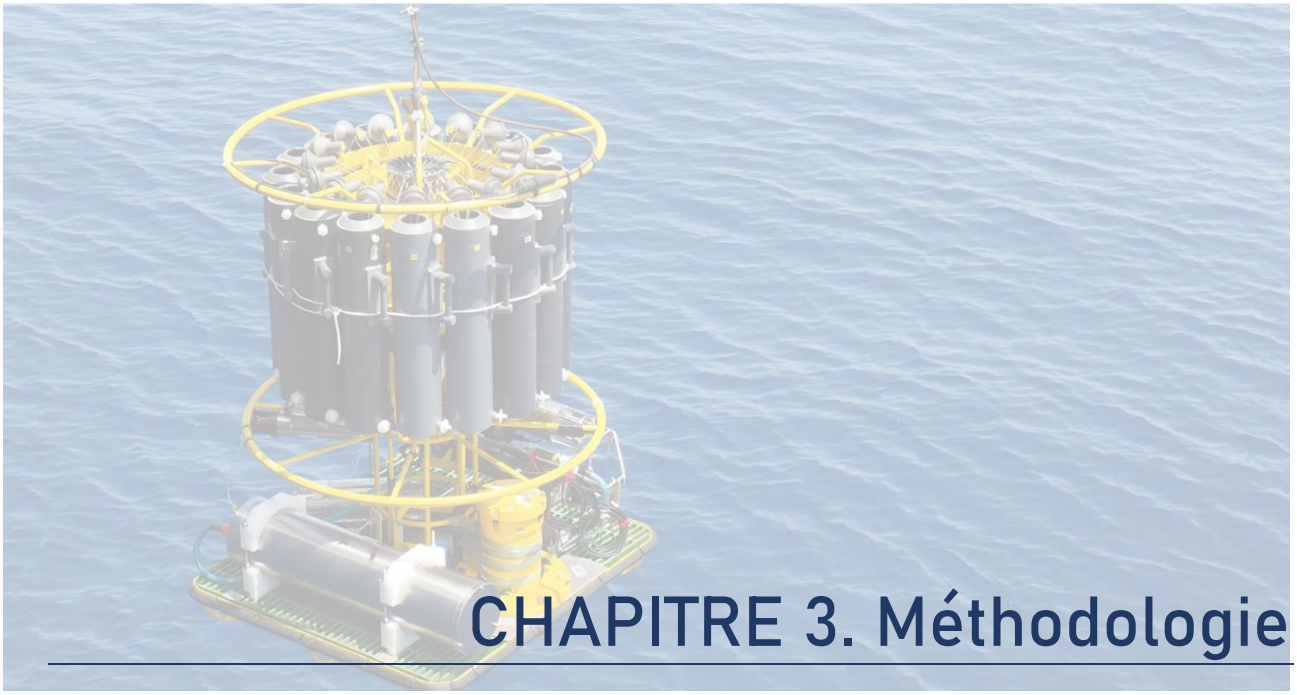

CHAPITRE 3. Méthodologie

Résumé

Dans le cadre de cette thèse de doctorat, la colonne d'eau a été échantillonnée à la fois dans la zone du volcan Fani Maoré pour l'étude de la géochimie de la colonne d'eau dans le contexte d'une éruption sous-marine, et dans la zone du Fec à Cheval pour l'étude des émissions de CO_2 liquide. Les prélèvement de la colonne d'eau ont été réalisés à l'aide d'une CTD-rosette. Les emplacements des opérations de déploiement de la CTD-rosette ont été choisis à partir d'études acoustiques (à l'aide d'un sondeur multifaisceaux) et visuelles (à l'aide de la caméra submersible SCAMPI et des observations du ROV) donnant des indices sur la présence d'émissions de fluides et/ou de gaz. Les échantillons ont été analysés à bord et à terre pour déterminer les concentrations de gaz, de métaux et des paramètres physico-chimiques, tandis que les données CTD (Conductivité, Température, Profondeur) ont été traitées informatiquement. Ce chapitre décrit les différents instruments utilisés pour l'observation, le prélèvement et l'analyse de la colonne d'eau, ainsi que les méthodes analytiques employées.

3.1. Water Column Sampling

3.1.1. The CTD-rosette

The CTD, stands for Conductivity Temperature Depth and refers to an *in situ* instrument that measures these parameters. The rosette is a seawater sampler. CTD-rosette hence indicates a combination of both instruments that acquires physical and chemical data throughout the water column and collects water samples in special bottles at different depths, from the ocean floor to the surface.

During MAYOBS01, MAYOBS04 and MAYOBS15 sea expeditions, the rosette was composed of 16 Niskin® bottles of 8 L each. During the GeoFlamme campaign, non-metallic bottles from Ocean Test Equipment® were used to improve the quality of the sampling dedicated to analyses of metals. The rosette was thus composed of 20 to 24 of these bottles of 10 L (Figure 3. 1).

In both configurations, we used a Seabird 911 + as CTD equipped with sensors for measurement of turbidity (Seapoint Turbidity Meter), fluorescence (WET Labs ECO-AFL), oxygen (Optode Aanderaa 4831F) and oxidation-reduction potential (ORP) (Figure 3. 1). The CTD was also coupled with an *In Situ* Mass Spectrometer (ISMS) for *in situ* measurements of gases along the water column. Measurements of currents were made using L-ADCP (Lowered-Acoustic Doppler Current Profiler) sensors attached to the rosette frame, one for the MAYOBS campaigns and two for the GeoFlamme campaign, one looking upward fixed at the top of the structure, and one fixed at the bottom and looking downward (Figure 3. 1).

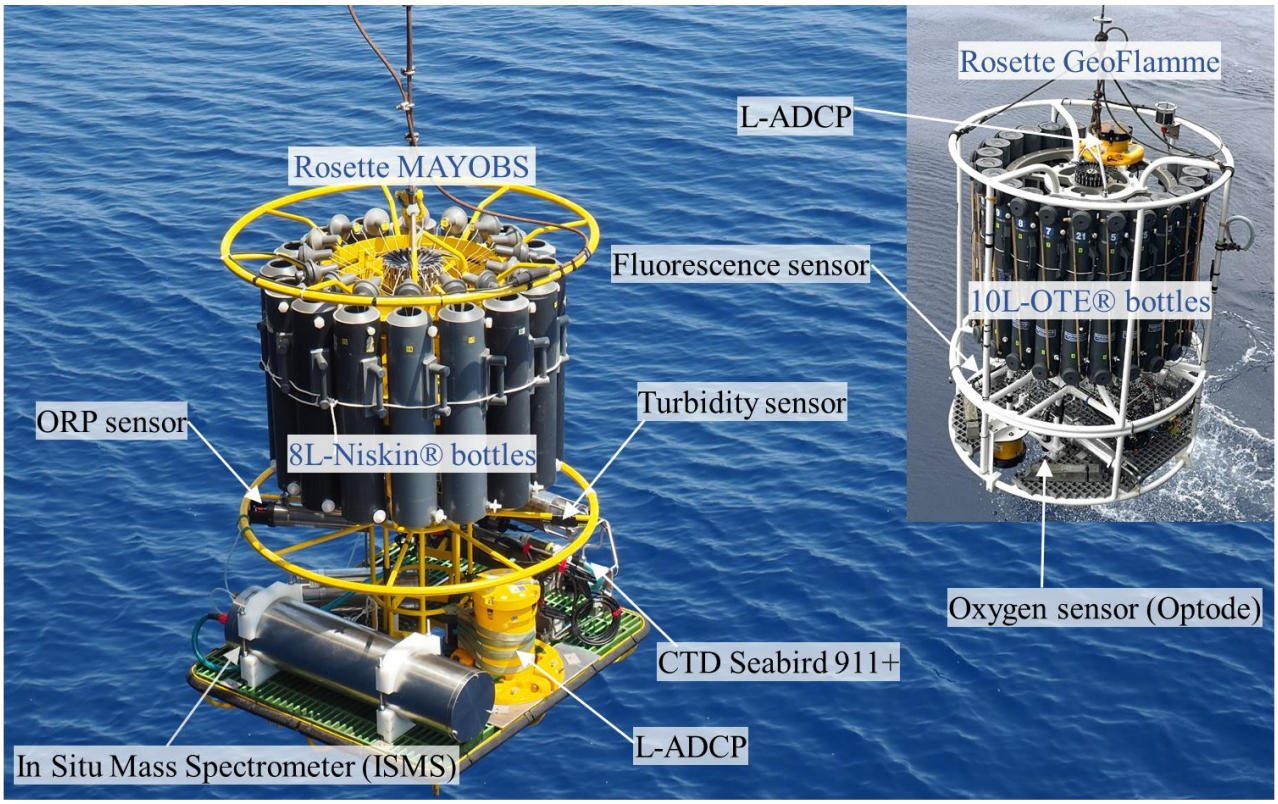

Figure 3. 1. Photography of the CTD-rosettes used on the MAYOBS and GeoFlamme cruises with annotations of sensors and instruments.

3.1.2. CTD-rosette deployment

During the different sea expedition, water column acoustic surveys served to identify fluid or droplets emissions from the seafloor and determine the locations for the CTD-rosette deployments. Multibeam ship echo sounders of the *R/V Marion Dufresne* and the *R/V Pourquoi Pas ?* were used to identify fluids discharging from the seafloor (Figure 3. 2). The ability to visualize an echo generated by a fluid discharged depends on the physicochemical characteristics of the target, the performance of the sounder, the distance of the target from the ship sounder and the morphology of the seabed. In this study, acoustic acquisitions for the observation of the water column onboard the *R/V Marion Dufresne* (cruises MAYOBS01, MAYOBS04 and MAYOBS15 in this study) were carried out with the shallow-sea and deep-sea multibeam sounders , the Kongsberg EM122 and EM710, and the Simrad EK80 single beam sounders operating from 18, 38, 70, 120 to 200 kHz, with adapted configurations at the depths of the studied sites. Onboard the *R/V Pourquoi Pas ?* (GeoFlamme cruise in this study) equivalent multibeam echo sounders were used, the Reson Seabat 7150 operating at 12 kHz for depths up to 12000 m and at 24 kHz for depths up to 5000 m, and the Seabat 7111 operating at 100kHz for depths up to 800 m.

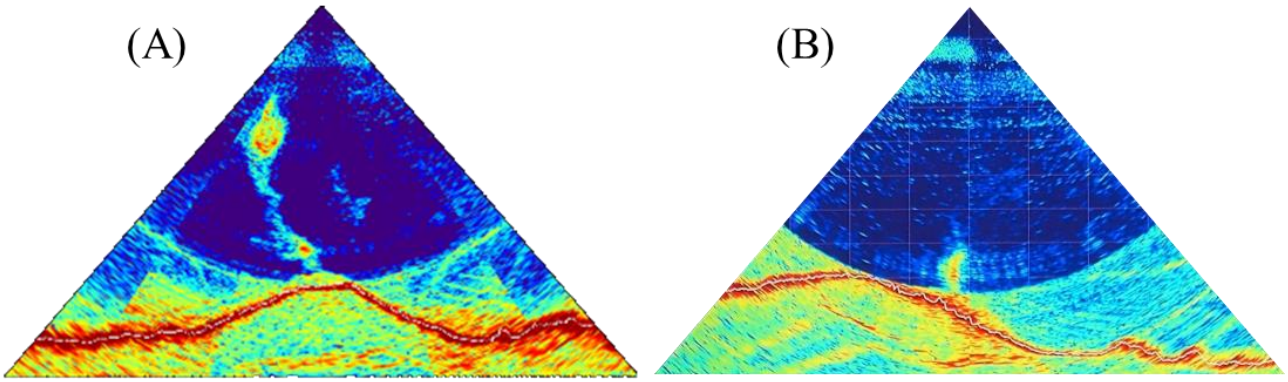

Figure 3. 2. Example of two echograms from ship echo sounder surveys. (A) Acoustic signal from the eruptive plume (~2 km high), (B) Acoustic signals detected above the Horseshoe degassing.

The acoustic survey was also very useful during the operations of CTD-rosette deployment for deploying the CTD-rosette inside the identified plumes. At the volcano area, we tried as well as possible to deploy the CTD-rosette within acoustic plumes in order to sample the fluid emissions. On the contrary, at the Horseshoe area, acoustic survey was used to identify the sites emplacement and the CTD-rosette has not been emplaced directly inside the droplet emissions, as the objective was to sample the dissolved part around the droplet emissions (Figure 3. 3.A and C).

Onboard the MAYOBS04 and MAYOBS15 cruises, a submersible interactive camera system, called SCAMPI, was used to investigate the presence of fluid vents, to explore the lava flows, and to help in the determination of the emplacement of the next CTD-rosette deployment. This submersible camera is designed to perform visual survey of the seafloor at a maximum operating depth of 5000 m. It is towed by the vessel and controlled from the ship.

Hydrocasts for water column study were carried out on the strategic emplacements and consist of deploying the CTD-rosette from the surface to the seabed at about 1m/s speed. A survey of hydrographic parameters (i.e. temperature, oxygen, turbidity, ORP) is done during the descent and resulting profiles allow to define the depths at which the bottles will be closed during the ascent. These depths are chosen according to the anomalies observed and the consistency with the other hydrocasts.

The CTD-rosette has been mainly deployed in vertical casts except during the GeoFlamme expedition where tow-yos were performed over the Horseshoe area (presented as West- and East- in CHAPTER 5) and the Volcano area. The principle of a tow-yo operation is to tow the CTD-rosette between the seafloor and a chosen depth (i.e. by rising and lowering the CTD rosette) as the ship proceeds on a

transect (Figure 3. 3.B). This operation allows to obtain a 2D-section composed by several profiles (named P1 to P6 for example).

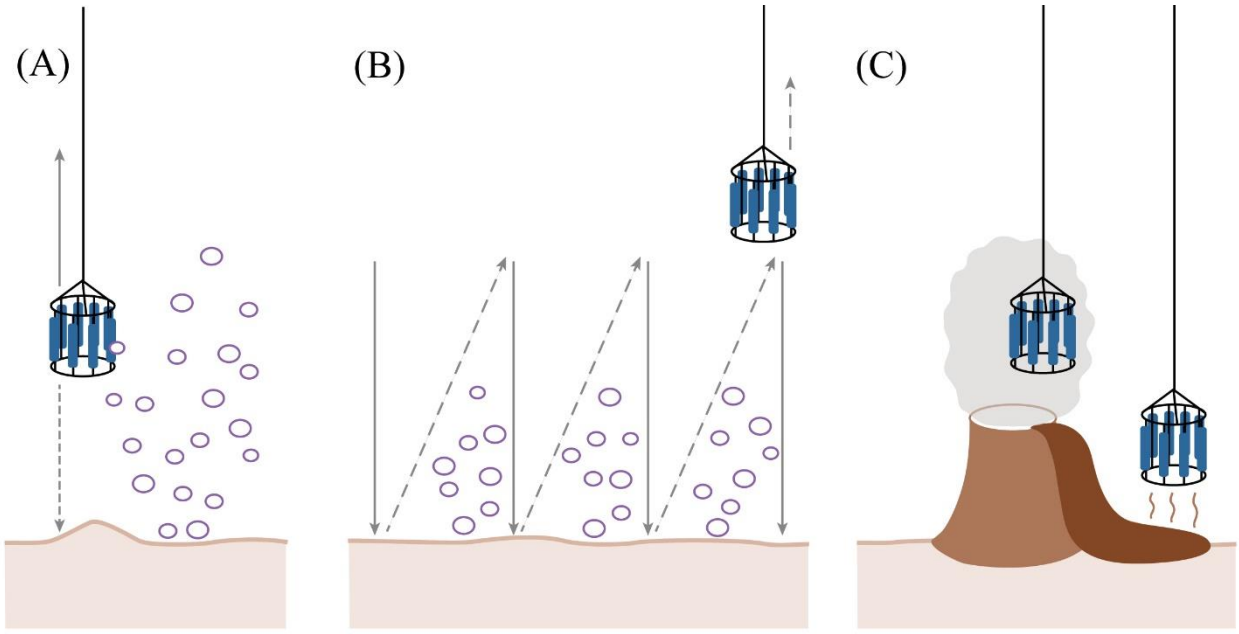

Figure 3. 3. Graphical representation of (A) vertical CTD-rosette cast above a liquid CO_2 venting site, (B) tow-yo operation above liquid CO_2 venting sites, (C) vertical CTD-rosette cast within the eruptive plume and above lava flow at the volcano.

To obtain a large spectra of geochemical parameters, we sampled the water column with the CTD-rosette over the Volcano area, the Horseshoe area, and on the Crown structure and the Volcanic Ridge (Figure 2. 2in CHAPTER 2). Background CTD-rosette casts were also performed outside the influence of fluid and/or gas emissions from the Fani Maoré volcano and the Horseshoe. It should be noted that those casts are used to give an approximation of a background reference but may not represent exactly the background of the studied areas as it was before any fluid or gas emission.

In this study, we focus on the Volcano and the Horseshoe areas. To investigate the submarine eruption and its impact on the water column, we used the CTD-rosette casts performed in the Volcano area during the first three cruises, MAYOBS01, MAYOBS04 and MAYOBS15. This gives an overview of the spatial and temporal variability in the water column. For the study of the gas emissions from the Horseshoe area, we choose to focused on the GeoFlamme cruise that offers a well defined screening of the area by sampling the majority of the venting site in a minimum of time.

3.1.3. CTD data processes

During CTD-rosette deployments, data from the CTD and associated sensors were recorded at a frequency of 24 Hz or 1 Hz. All data files were processed according to the following protocol:

In a first step, data profiles of temperature, conductivity, pressure, turbidity, oxygen and ORP are exported using the SBE Data Processing® software.

In a second step, data files are processed using a homemade R® script to downsize the data frequency from 24 Hz to 1 Hz, and separate if needed the downward and upward profiles.

In a third step, turbidity signals are processed with R to obtain smoothed turbidity profiles. Baseline of turbidity signals is set to zero for all casts. This correction is based on the near-zero signal values encountered below the euphotic zone and above turbidity anomalies linked to the venting activity (i.e. around 700 m depth for the Horseshoe area, and around 1500 m for the Volcano area and the background hydrocasts). We calculated the average of 100 turbidity values (acquired at a frequency of 1 Hz, for a CTD rosette ascent velocity of 1 m/s) at the aforementioned depths and subtracted it to the entire turbidity profile. To avoid the presence of erratic peaks in the turbidity profiles, turbidity profiles were also block averaged over 5 seconds along the 1 Hz-profiles.

In a fourth step, we calculated the potential temperature (θ) and potential density (σ_0) on each profile using the R® software according to the relation given by McDougall et al. (2003), and taking the ocean surface as the reference value.

3.2. Sample collection and analyses for water column study

Deployments of the CTD-rosette were carried out to study the physicochemical and geochemical parameters of the water column by taking samples and performing analysis of gas concentrations, metals and non-metals, pH, Dissolved Inorganic Carbon (DIC), total alkalinity (A_T), silicates, etc (Figure 3. 4). Sub-sampling from the CTD-rosette bottles was performed immediately after the CTD-rosette retrieval to preserve the integrity of the samples.

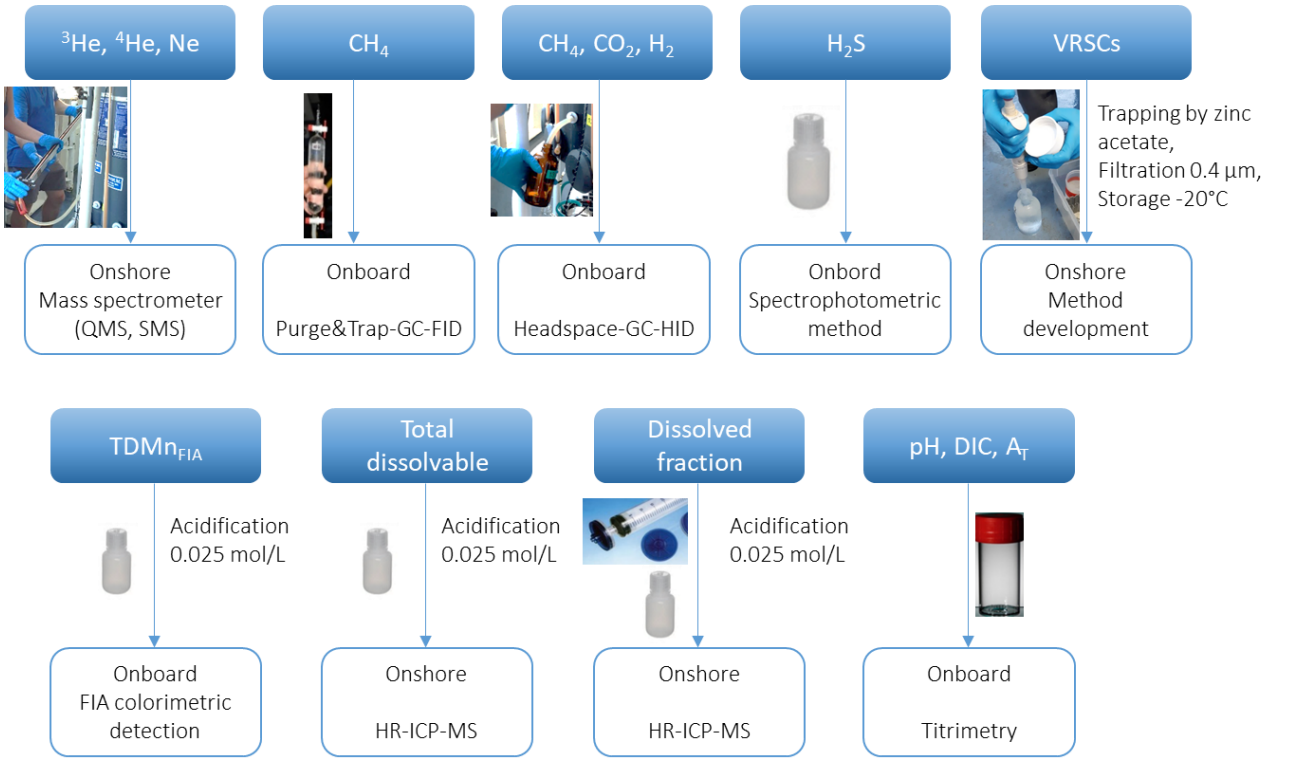

Figure 3. 4. Conceptual scheme of the methodology of sub-sampling from the CTD-rosette, and of the analyses performed.

3.2.1. Gas collection & analyses

3.2.1.1. Noble gas: sample collection and analyses

Sampling for helium analysis was carried out at specific depths, chosen mostly were CTD anomalies were the strongest, in order to capture the footprint of volcanic activity in the water column. Because helium is a highly volatile gas, samples for noble gases analyses were the first samples collected from the CTD-rosette bottles. Sampling was done by flushing the seawater from the CTD bottles directly into copper tubes, carefully checking for the absence of air bubbles (inclusion of air in the sampling procedure is particularly critical for ocean samples), and then sealed using special stainless clamps (Sültenfuß, 2016). These containers allow safe sample storage for extended periods, as exposure to elevated temperature and gas super-saturation has little effect. However, the clamping and sealing is a critical step and so is the rinsing of the copper tubes before storage in order to prevent their oxidation. Quantification of helium and neon isotopes (^{3}He, ^{4}He, ^{20}Ne, ^{22}Ne) was performed at the Helis Laboratory (Helium isotopes studies, Bremen, Germany) using a mass spectrometric system composed of a quadrupole mass spectrometer (QMS, Balzers QMG112a®) and a sector field mass spectrometer (SMS, MAP 215-50®). Briefly, the gases contained in the seawater samples are extracted and transferred from the copper tubes into glass ampoules. This transfer requires the

completion of a high vacuum (10^{-6} mbar) and leak control over the extraction system. During the transfer, the seawater samples are allowed to expand into 250 mL glass bulbs beneath the copper tubes that are flame-heated, whereas the ampoules are immersed in liquid nitrogen. The glass bulbs are gently shaken to help the gas transfer to the ampoules, which are flame-sealed at the end of the transfer. The recovery rate of this procedure exceeds 99.9 % (Sültenfuß et al., 2009).

Then, the ampoules are attached to a sample multi-port unit and transferred by water vapor flow into the separation unit of the system (Figure 3. 5). Gases and water vapor pass two cold traps and a chemical getter: the first trap (of 133 K) allows to stop almost all of the water vapor, while the second trap (of 25 K) stops all other interfering gases or bring them to tolerable concentrations. Then, a fraction of the sample is diverted via a gas pipette into the QMS to measure helium and neon, and the remainder is collected into a third trap (of 14 K) containing charcoal. Upon raising the trap temperature to 45 K, all the helium and a small fraction of the neon are released into SMS to measure the ^{3}He and ^{4}He concentrations, checking also the ^{20}Ne. The SMS is capable of a sufficient relative mass resolution to separate ^{3}He from the mass-3 hydrogen species (i.e. HD and H_3). The principle of the quadrupole mass spectrometer involves filtering ions based on their mass-to-charge ratio using a quadrupole analyzer consisting of four parallel rods or electrodes. The mass analyzer in a sector field mass spectrometer consists of a magnetic sector, where the ions travel along the circular path. The magnetic field strength and the radius of the circular path determine the mass resolution of the instrument

Instrument calibration is performed by air aliquots admitted from the calibration unit, cryo-fractionated and measured exactly as for the samples. This method yields a precision of ±0.4 % for $^{3}He/^{4}He$ ratios and ±0.8 % for helium and neon concentrations (Sültenfuß et al., 2009).

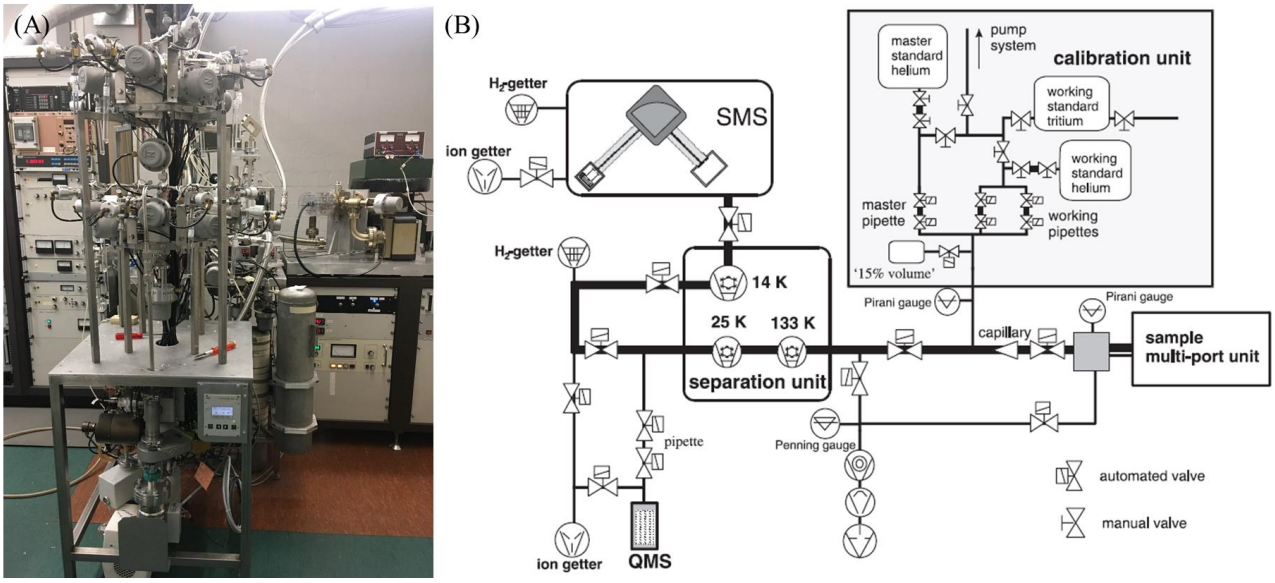

Figure 3. 5. (A) Photographic view of the Bremen mass spectrometric system for helium isotope, neon and tritium measurement. The sample multi-port unit is in the foreground with two levels of eight sample ports each. Behind it there is the inlet/cryo-fractionation unit which also carries the QMS. At the right is the SMS with the big magnet and to the left the electronic units. (B) Mass spectrometric system schematic from Sültenfuß et al. (2009). The thick line indicates the flow path of helium into the SMS.

Delta helium, noted δ^3He, corresponds to the measured ^{3}He/^{4}He isotope ratio (R_m) anomaly relative to the atmospheric standard (Ra = $(^3He/^4He)_{air}$ = 1.38×10^{-6}, Clarke et al. (1976)) and is calculated after the equation of Benson and Krause (1980):

$$\delta^3He = 100 \times \left(\frac{R_m}{R_a} - 1\right)$$

In this study, we choose to define each component of the measured concentrations of ^{3}He and ^{4}He (i.e. equilibrium, air contamination and non-atmospheric concentrations). Assuming that the entire Ne concentration comes from atmospheric air, the corrected He concentration from air contamination and atmospheric air in equilibrium is expressed as $^3He_{xs}$ and $^4He_{xs}$. Considering that the tritiogenic ^{3}He (i.e. resulting from the radioactive decay of tritium) is negligible in the Indian Ocean offshore Mayotte Island (Jenkins et al., 2019), the $^3He_{xs}$ and $^4He_{xs}$ should only corresponds to the supply of mantellic and crustal helium, and can be determined using the equation system as follows:

$$\begin{cases} Ne_m = Ne_{eq} + Ne_{air} \\ {}^4He_m = {}^4He_{eq} + {}^4He_{air} + {}^4He_{xs} \\ {}^3He_m = {}^3He_{eq} + {}^3He_{air} + {}^3He_{xs} \end{cases}$$

with *m* the measured concentration, *eq* the equilibrium concentration and *air* the concentration for air contamination. Equilibrium and air contamination neon concentrations were defined as Ne_{eq} =

$Ne_{atm} \times \beta_{Ne}$ and $Ne_{air} = Ne_m - Ne_{eq}$, and helium isotopes concentrations as ${}^{3,4}He_{eq} = {}^{3,4}He_{atm} \times \beta_{He}$ and ${}^{3,4}He_{air} = Ne_{air} \times \frac{{}^{3,4}He_{atm}}{Ne_{atm}}$.

We introduce solubility coefficients depending on the temperature and salinity conditions of sampling. Solubility coefficients of Ne and He in seawater (β_{Ne} and β_{He}, respectively) were determined for each sample according to the water temperature (T, in Kelvin) and salinity (S, in psu) of the sampling depth, using Weiss (1971) solubility equations:

$$ln\beta_{He} = -34.6261 + 43.0285\left(\frac{100}{T}\right) + 14.1391\ln\left(\frac{T}{100}\right) + S\left[-0.042340 + 0.022624\left(\frac{T}{100}\right) - 0.0033120\left(\frac{T}{100}\right)^2\right]$$

$$ln\beta_{Ne} = -39.1971 + 51.8013\left(\frac{100}{T}\right) + 15.7699\ln\left(\frac{T}{100}\right) + S\left[-0.124695 + 0.078374\left(\frac{T}{100}\right) - 0.0127972\left(\frac{T}{100}\right)^2\right]$$

For water column samples, the corrected ratio of helium (Rc/Ra) was determined by only applying the correction from atmospheric air contamination, as the equilibrium value (He_{eq}) is not negligible compare to He_{xs}. That is mean, $Rc = \frac{{}^3He_{xs} + {}^3He_{eq}}{{}^4He_{xs} + {}^4He_{eq}}$.

3.2.1.2. Methane: sample collection and analyses by Purge & Trap-GC-FID

For methane analysis, the seawater was transferred by gravity flow from the CTD-rosettes bottles into 125 mL two-valve glass ampoules. The ampoules were filled from below and allowed to overflow vertically about one third of their volume in order to avoid trapping air bubbles, and evacuate them promptly. For MAYOBS1 and MAYOBS4 cruises, analyses were performed onshore, back to the laboratory. In these cases, samples were poisoned with sodium azide (NaN_3) when collected in order to inhibit the microbial activity and stored at 4°C. During MAYOBS15 and GeoFlamme cruises, samples were analyzed onboard within two hours after samples retrieval, so poisoning was not necessary.

Both onshore and onboard analyses were carried out following the “purge and trap” method for methane extraction, and the quantification by Gas Chromatography - Flame Ionization Detection (GC-FID) (Figure 3. 6). This equipment is part of an on-board/onshore laboratory container. The technique has been modified after Swinnerton et al. (1962) as described in (Charlou et al., 1987). Samples are first degassed with purified helium and trapped onto activated charcoal at -80 °C. Then, gases are desorbed from the trap by increasing the temperature and then injected into a gas

chromatograph (Agilent 7890A, Agilent Technologies, USA) equipped with a porapack-Q packed column for component separation and a hydrocarbon-specific Flame Ionization Detector.

External calibration was performed using a gas standard of CH_4 injected using 50 µL and 2 mL loops at appropriate pressure and constant temperature. The analytical precision (i.e. RSD: Relative Standard Deviation) of the measurements established from replicate analyses (n=10) of standards is better than 0.5%. In the case of replicates of seawater analyses the RSD does not exceed 5%. The limit of detection of the method is 0.03 nmol/L and the limit of quantification is 0.1 nmol/L (Konn et al., 2016; Donval and Guyader, 2017). Therefore, this method allows the determination of CH_4 concentrations equivalent to those of open ocean seawater (0.3 nM).

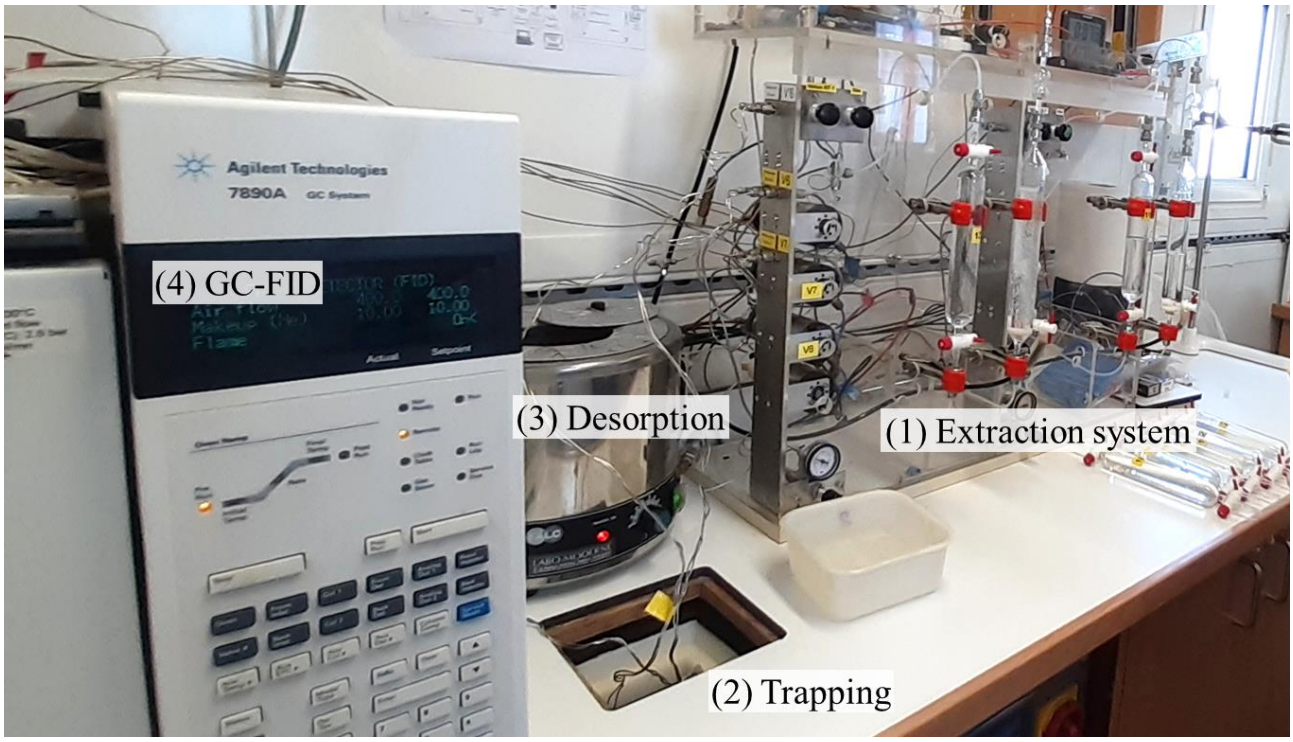

Figure 3. 6. Photography of the Purge & Trap-GC-FID instrument used for the methane analysis. Steps of the analytical procedure are identified: (1) gas extraction, (2) trapping onto activated charcoal, (3) desorption at high temperature, (4) injection into the Gas Chromatograph and detection by Flame Ionization Detector.

3.2.1.3. Carbon dioxide, methane and dihydrogen: sample collection and analyses by Headspace-GC-HID

During MAYOBS and GeoFlamme cruises, some of the seawater samples were dedicated to CO_2, CH_4 and H_2 analyses and were carefully collected from the CTD-rosette bottles into 240 mL brown

glass bottles, and closed by a screw cap fitted with a PTFE/silicone gas tight septum, avoiding injection of air bubble. Due to the rapid degradation of hydrogen in seawater samples, sampling and analysis must be carried out quickly after the CTD rosette has been retrieved. Prior to analyses, samples were prepared following the Headspace method developed by Donval and Guyader (2017), which consists of replacing ~20 mL of the seawater sample by a gaseous phase of pure helium. Samples are homogenized by shaking and then kept at room temperature (~20 °C) for at least one hour, to allow time for the dissolved gases to equilibrate with the helium phase according to the solubility coefficients at equilibrium temperature and water salinity.

Analyses for CO_2, CH_4 and H_2 were carried out by Gas Chromatography coupled to a Helium Ionization Detector (GC-HID) (Figure 3. 7. A and B). This technique is complementary to the purge and trap technique. It has been designed to be space-saving and easy to maintain. Less sensitive for methane quantification than the purge and trap method, nevertheless, it reveals anomalies of hydrogen, methane and carbon dioxide in the water column, and allows their quantification from Bunsen solubility coefficients. Step by step, an aliquot of the gas phase (i.e. headspace) is injected into the gas chromatographic system using an automatic headspace sampler. This injection is performed in two steps. First by using a 50 µL injection loop for the quantification of gases presenting elevated concentrations, and in a second step by using a 2 mL injection loop for the quantification of gases with lower concentrations, depending on the sample. Helium of 99.9995% grade is primarily purified and serves as the carrier gas for this method. After the gas injection through the system, the gas components are transferred into the gas chromatograph (Varian® 3900 GC) and separated by a Shincarbon packed column heated at 150°C, with a carrier gas flow of 20 mL/min. Compounds are eluted consecutively as follows: H_2, O_2, N_2, CH_4 and CO_2. Retention times are 1.22 min, 2.27 min and 3.23 min for H_2, CH_4 and CO_2, respectively. The detection is operated by the HID (Valco® Pulse Discharge Helium Ionization Detector, model PD-D2-I for packed columns). The resulting chromatogram is interpreted using the Chromeleon® software (Chromeleon™ CDS, Thermo Fisher Scientific) (Figure 3. 7.C). Both the areas (in mV*min) and pressure of injection are used to determine the gas concentrations.

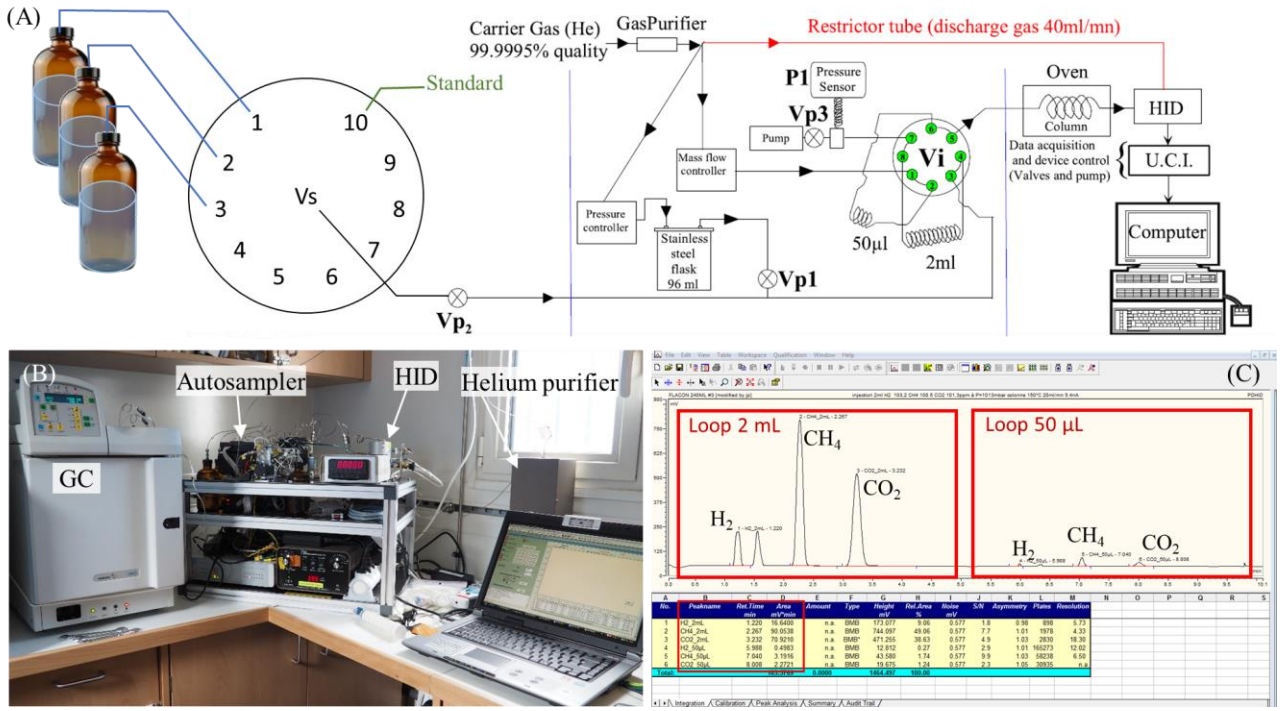

Figure 3. 7. (A) Schematic diagram of the Headspace-GC-HID analytical system (modified from Donval and Guyader (2017)). (B) Photography of the analytical system with identification of the instrument parts. (C) Resulting chromatogram from the gas standard analysis through the 2 mL and 50 µL injection loops.

External calibration was carried out using a standard gas mixture of H_2, CH_4 and CO_2, with respective concentrations of 103.2 ppmv, 100.5 ppmv and 101.3 ppmv. This standard was injected through both 50 µL and 2 mL injection loops at appropriate pressure and constant temperature. Analytical precision of chromatographic measurements, established from replicate analyses of standard is better than 0.5 %. The detection limit in gas concentrations in seawater are 0.3 nmol/L for H_2, and 0.1 nmol/L for CH_4. Quantification limits were thus evaluated at 1.0 nmol/L for H_2, and 0.3 nmol/L for CH_4 a. Based on replicate sample analyses, the global analytical precision (i.e. RSD) does not exceed 5 %.

3.2.1.4. Carbone dioxide and methane isotopic analyses

Analyses of the isotopic composition of CH_4 and CO_2 on water column samples were carried out for characteristic samples presenting elevated gas concentrations compare to the background level. To do so, the headspace phases of these samples were transferred in 12-mL pre-evacuated vials from Labco®, and completed with helium above the atmospheric pressure. To transfer the headspace phases to the Labco Exetainer® tubes, a special circuit (Figure 3. 8) was designed and added to the existing GC-HID analytical system. The headspace bottle and the Labco Exetainer® tube were

connected to the ten positions valve and coupled with two other valves (one for each container). This circuit allows for the completion of a high vacuum in the Labco Exetainer® tube, the transfer of the headspace phase according to pressure difference and equilibrium, and the addition of helium (or argon) in the Labco Exetainer® tube to reach a pressure higher than the atmospheric one.

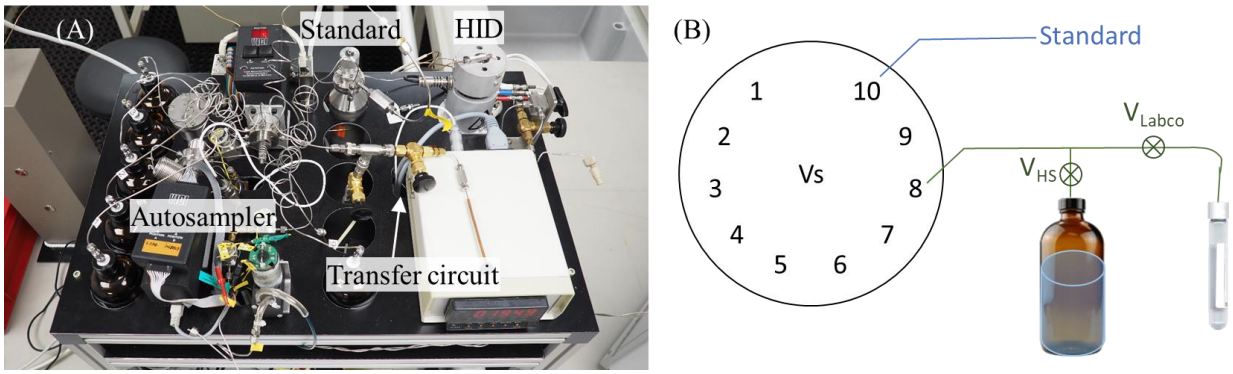

Figure 3. 8. (A) Photography of the analytical system with the transfer circuit of headspace phase into Labco Exetainer® tube. (B) Schematic of the headspace phase transfer into a Labco Exetainer® tube dedicated for isotopic analyses. The emplacement 10 in the sample valve (Vs) is for the gas standard bottle, the 8 is for headspace phase transfer, and the others are used for headspace phase analyses.

The Labco Exetainer® tubes were sent to the Isolab b.v. laboratory (Stable isotopes and geochemical laboratory services, The Netherlands) for the determination of the stable carbon ($\delta^{13}C$) and hydrogen (δD) isotope ratios of CH_4 and CO_2, mentioned hereafter as $\delta^{13}C\text{-}CH_4$, $\delta D\text{-}CH_4$ and $\delta^{13}CO_2$.

The analyses were carried out on a gas chromatograph - isotope ratio - mass spectrometers (GC-IR-MS). Carbon isotopes of methane ($\delta^{13}C\text{-}CH_4$) were analyzed with an Agilent 6890N gas chromatograph (Agilent Technologies, Santa Clara, US) interfaced with a Finigan Delta S IRMS (Thermo Scientific, Bremen, Germany) and a Finigan GC-C II interface (Thermo Scientific, Bremen, Germany). The separation from the GC was conducted with a 12 m long and 0.32 mm diameter Molsieve column (Agilent). Samples are calibrated regularly against a calibration standard and results are reported in promille vs. vPDB (Vienna PeeDee Belemnite Standard). The minimum concentration required was of 25-50 ppm.

Carbon isotopes of carbon dioxide ($\delta^{13}CO_2$) were analyzed on an Agilent 7890A GC (Agilent Technologies, Santa Clara, US) interfaced to a MAT 253 IRMS (Thermo Scientific, Bremen, Germany) using a GC-Isolink or a Finigan GC-C III interface. The GC is equipped with a 25 m, 0.32 mm Porabond-Q column (Agilent) and an injection valve. Cold trapping is used to pre-concentrate the sample when necessary. Samples are run at least three times after which the average of the results is calculated. The system is calibrated at least once a day using an in house natural gas standard and

results are reported in per mille vs. vPDB. The minimum concentrations needed to perform the analysis depends on sample composition.

Deuterium isotopes of methane (δD-CH_4) were measured on an Agilent 7890A GC (Agilent Technologies, Santa Clara, US) interfaced with a MAT 253 IRMS (Thermo Scientific, Bremen, Germany) and using a GC-Isolink interface (Thermo Scientific, Bremen, Germany). The GC was equipped with a 25 m long and 0.32 mm diameter Molsieve column (Agilent Technologies, Santa Clara, US) and an injection valve. Samples are calibrated regularly against a calibration standard and results are reported in per mille vs. vSMOW (Vienna Standard Mean Ocean Water). The minimum concentration required was about 300 ppm.

The uncertainties in the $\delta^{13}C$ and δD measurements are ± 0.3 ‰ and ± 1 ‰, respectively.

3.2.2. Metals: sample collection & analyses

Sampling was performed for the analysis of both total dissolvable and dissolved metals fractions. The Total Dissolvable fraction, noted with the prefix *TD*, represents the dissolved fraction and all particles that may dissolved under light acidification (2‰ v/v). The dissolved fraction, noted with the prefix *d*, represents the dissolved fraction filtered through 0.22 µm. We analyzed a large panel of major, metal and non-metal elements, such as magnesium (Mg), silicon (Si), phosphorous (P), sulfur (S), potassium (K), calcium (Ca), manganese (Mn), iron (Fe), lithium (Li), boron (B), rubidium (Rb), strontium (Sr), molybdenum (Mo), barium (Ba), or uranium (U). Aluminum (Al), lead (Pb), cobalt (Co), nickel (Ni), copper (Cu) and zinc (Zn) were also quantified but with lower resolution due to their low concentration levels and the risk of contamination. Although those results are available, in this study, concentrations from these last elements were mainly used as estimates and proxies to identify possible contamination during sampling preparation or analysis. In this study, we mainly focus on the total dissolvable fraction, of iron and manganese for the investigation of plume distribution and fluid-rock interactions.

3.2.2.1. Sample collection for dissolved and total dissolvable fractions

Sampling for analysis of the total dissolvable fraction, was carried out in 30 mL low or high density polyethylene bottles (LDPE/HDPE, Nalgene®) previously washed with 10%$_{v/v}$ hydrochloric acid (HCl 37%, Analytical Grade, Merck) then rinsed a minimum of three times with ultrapure water (Milli-Q Millipore element system). Sampling from the CTD-rosette bottles was performed in

duplicate, one sample being dedicated to onboard total dissolvable manganese analysis and one to onshore metals analyses.

The dissolved fraction was sampled using 60 mL low density polyethylene syringes (LDPE, Nalgene®) and 30 mL low density polyethylene bottles (LDPE, Nalgene®), both washed in the same way than the bottles used for the total dissolvable fraction. Syringe filters were mounted on the 60 mL syringes, and consist of a Supor® membrane (hydrophilic polyethersulfone) with a porosity of 0.22 µm (Ø 25mm, Acrodisc®, PALL Corporation®). These syringe filters were rinsed with 2% hydrochloric acid (HCl 37%, Analytical Grade, Merck®), then rinsed a minimum of three times with ultrapure water (Milli-Q element system).

For both total dissolvable and dissolved fractions, all raw samples for metal analysis were acidified to 0.025 mol/L hydrochloric acid (HCl 30% ultrapur® grade, Merck) within 6 hours of sampling.

3.2.2.2. Onboard analyses of the Total dissolvable manganese by Flow Injection Analyses

A first manganese quantification was carried out onboard using flow injection analysis (FIA) and the colorimetric detection method developed by Aguilar-Islas et al. (2006) and adapted from Resing and Mottl (1992). Recently, it has been adapted at Ifremer on a dedicated flow injection analyzer from MLE GmbH Dresden®, driven by the FIA Studio® software (MLE GmbH Dresden®) (Figure 3. 9). This method is based on the catalytic effect of manganese on the green leucomalachite oxidation by the periodate ions. Containers of 15 mL seawater samples are placed on an autosampler (PS 61F, MLE GmbH Dresden®). This sample quantity allows to perform three analyses runs (i.e. replicates). Reagents and samples are pumped using a peristaltic pump mounted on the analysis device. Primarily, preconcentration of manganese is performed by loading the sample mixed with an ammonium borate buffer onto an iminodiacetate resin (Toyopearl AF-chelate-650M) that retains metals (including manganese) and ions contained in seawater. The column is then rinsed with a less concentrated ammonium borate buffer to desorb the ions contained in the seawater. The sample is then desorbed using a carrier solution made of hydrochloric acid, and it is mixed with leucomalachite green reagent. The sample mixing then meets a combined solution of nitrilotriacetic acid and sodium periodate that activate the reaction. The flux passed through a thermostated reaction loop at 35°C. The absorbance of the fluid is then measured at a wavelength of 620 nm through a flux spectrophotometric cell (nominal volume of 0.018 mL), and peak height are pointed for concentration determination. External calibration was performed from a set of standards made of $MnCl_2.4H_2O_{(s)}$ dissolved in ultrapure water

(Milli-Q element system) and ranging from 0 to 40 nmol/L. This calibration gives a polynomic relationship between the absorbance peak height and the manganese concentration. The detection limit of this method has been evaluated to 3 nmol/L over the analysis of ten blanks (acidified ultrapure water), and validation was performed using a seawater certified reference material for trace metals, the NRCC (National Research Council Canada) NASS 7 standard (Nadeau et al., 2016) with a manganese concentration of 13.65 nmol/L. Using the FIA method we obtained a Mn concentration of 13.16 ± 0.53 nmol/L.

Samples analyses were run in duplicate and within the few hours following the sample acidification and the resulting concentration represents then mainly the dissolved manganese fraction (noted Mn_{FIA}). This method highlights geochemical anomalies in the water column that can be explained by volcanic and/or hydrothermal activity.

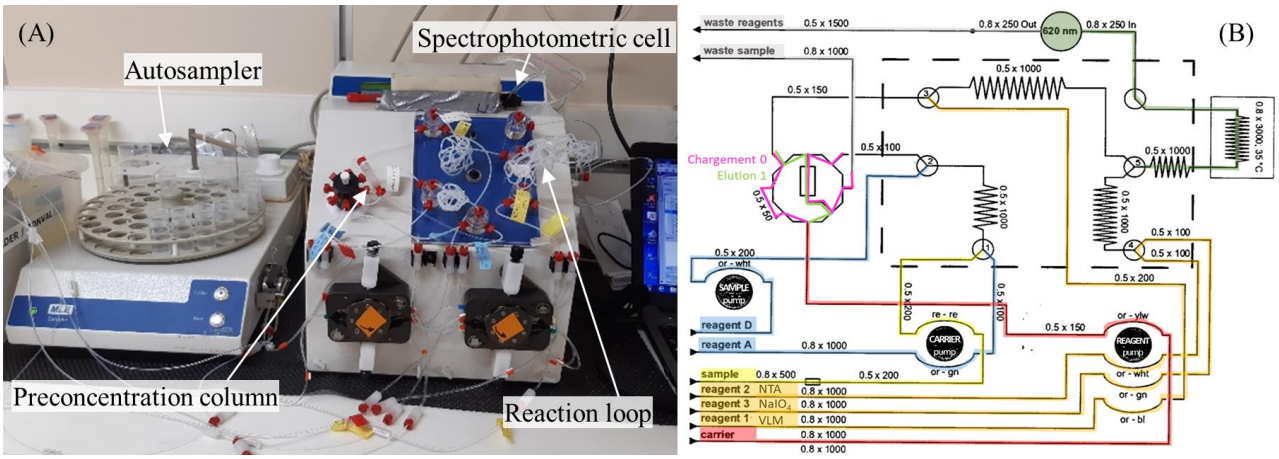

Figure 3. 9. (A) Photography of the flow injection analysis instrument with identification of the various components. (B) Schematic diagram of the analytical method.

3.2.2.3. Onshore analysis by ICP-MS

Samples collected for both total dissolvable and dissolved fractions were analyzed onshore at the Pôle Spectrométrie Océan (PSO, Ifremer, Brest, France), using HR-ICP-MS (High Resolution Inductively Coupled Plasma Mass Spectrometry; Element XR, ThermoFisher Scientific). Prior to the analyses, 20 µL of sample was diluted in 1.980 mL of 0.28 mol/L distilled nitric acid spiked with Indium (In) at 2 ppb, resulting in a dilution of factor 100. This method allows for the quantification of metal concentrations in seawater, with detection limits at sub-micromolar order (about 10 nmol/L for Mn and 100 nmol/L for Fe), and was used for MAYOBS and GeoFlamme cruises.

However, samples taken during the GeoFlamme cruise present lower Fe and Mn concentrations, making the dilution method not adequate for the quantification of both elements. Therefore, for this cruise, Fe and Mn were quantified using a pre-concentration method.

Samples were prepared in lab for analysis about a year after sampling, using the magnesium precipitation method for iron and manganese pre-concentration of seawater developed by Saito and Schneider (2006). This method consists of firstly adding a ^{57}Fe spike to 1.8 mL sample and then separate the trace metals from the matrix using concentrated ammonium hydroxide (50 µL of NH_4OH, Optima grade) that results in the precipitation of the Mg present in seawater as $Mg(OH)_2$. Finally, the pellet obtained after centrifugation was rinsed with 1 mL ultrapure water then dissolved with nitric acid (distilled ultrapure 0.28 mol/L HNO_3). The use of preconcentration allows to lower the detection limit during the quantification of Fe and Mn while removing the seawater matrix compared to dilution method for which open ocean Fe and Mn concentrations are difficult to reach.

Using this pre-concentration method, dissolved and total dissolvable iron and manganese (dFe, dMn, TDFe and TDMn, respectively) Quantification of TDFe and TDMn was carried out at the Pôle Spectrométrie Océan (PSO, Ifremer, Brest, France), using HR-ICP-MS (High Resolution Inductively Coupled Plasma Mass Spectrometry; Element XR, Thermo Fisher Scientific).

The principle of the HR-ICP-MS is based on the separation of elements in ionized form in a mass spectrometer according to their mass-to-charge ratio (m/z) (Figure 3. 10). The injected sample is transformed into an aerosol and then transport by a gas stream to an argon ion plasma at a temperature of 6000 to 8000 K. In this plasma, the sample undergoes a vaporization, dissociation, atomization and ionization. The ionized atoms pass through a dual focusing system combining a magnetic and an electrostatic sector, and are then quantified using a detector, which is either a Faraday cage or an ion counter, depending of the required sensitivity.

A set of certified seawater reference materials were used for determining analytical precision and accuracy, including NRCC (National Research Council Canada) standards NASS-05 and CASS-05, and GEOTRACES Intercalibration seawater GSI (Boyle et al., 2012). For Mn concentrations, we obtained 50.7 ± 2.0 nmol/L, 20.2 ± 0.8 nmol/L and 1.5 ± 0.6 nmol/L for CASS-05, NASS-05 and GSI respectively (2SD). For Fe concentrations, we obtained 32.3 ± 1.2 nmol/L, 5.3 ± 1.8 nmol/L and 0.8 ± 0.8 nmol/L for CASS-05, NASS-05 and GSI respectively (2SD). Both Fe and Mn concentrations are similar, within analytical uncertainty, to certified or accepted values.

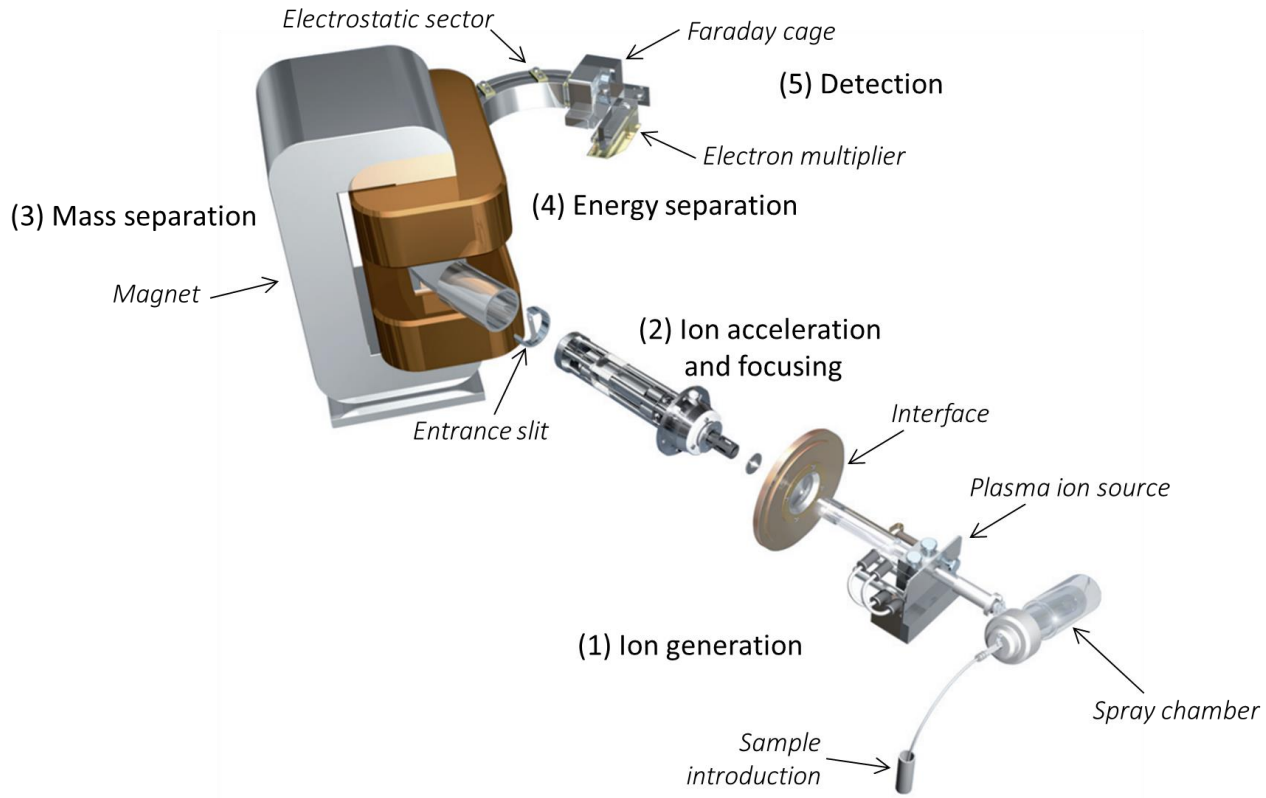

Figure 3. 10. Schematic diagram of the analytical principle of High Resolution Inductively Coupled Plasma Mass Spectrometry (HR-ICP-MS), modified from Thermo Fisher Scientific diagram.

3.2.3. Physicochemical parameters: sample collection & analyses

3.2.3.1. pH

Sampling for the study of pH was carried out in 30 mL polyethylene bottles (LDPE, Nalgene®) previously rinsed a minimum of three times with ultrapure water (Milli-Q Millipore element system) and dried.

Analyses for pH were performed onboard using pH electrode (Metrohm®). This electrode consists of a combined glass electrode filled with 3 mol/L KCl solution as reference electrolyte. The glass membrane of the electrode is ion-sensitive for H^+, thus responding to hydrogen ions. For pH calibration, buffer solutions of pH values at 4.00 ± 0.02, 7.00 ± 0.02, 9.00 ± 0.02 were used. Calibration and sample measurements were performer in a thermostatic laboratory, with solutions equilibrated to room temperature at 25 ± 2 °C. The *in situ* pH, denoted pH_{corr}, was deducted from the pH measured in the lab and following Lui and Chen (2017) equation:

$$pH_{in\ situ} = pH_{25} + a_1(T - 25°C)$$

Where a_1 is a considered as a constant of -0.0151 pH unit °C^{-1}.

Standard deviation of pH measurements was determined according to the calibration prior to measurements, and do not exceed 1 % for all cruises.

3.2.3.2. Dissolved Inorganic Carbon (DIC) and Total Alkalinity (A_T)

Sampling for the study of total alkalinity (A_T) and dissolved inorganic carbon (DIC) was carried out in 30 mL polyethylene bottles (LDPE, Nalgene®) previously rinsed a minimum of three times with ultrapure water (Milli-Q Millipore element system) and dried.

Samples were analyzed onboard for titration of dissolved alkaline species with hydrochloric acid solution (0.01 mol/L HCl Titrinorm®) using a titrimeter (Titrino 848, Metrohm®) combined with a pH electrode (Metrohm®) (Figure 3. 11). Total alkalinity and ΣCO_2 were determined from titration equivalence volumes, according to the following equations:

$$DIC = \frac{(EP_2 - EP_1) \times [HCl] \times 1000}{V_{sample}}$$

$$A_T = \frac{EP_2 \times [HCl] \times 1000}{V_{sample}}$$

With EP_1 and EP_2 the volumes of hydrochloric acid added to reach the two equivalence points, and V_{sample} the amount of sample titrated.

The certified reference material for oceanic DIC, Batch #178, was used to test the performance of both the total inorganic carbon and total alkalinity (Certified Reference Material, delivered by the Scripps Research Institute at the University of San Diego under the responsibility of A. Dickson, https://www.nodc.noaa.gov/ocads/oceans/Dickson_CRM/batches.html).

Standard deviations for DIC and A_T measurements were calculated on replicates analyses of the certified reference material. For MAYOBS4, standard deviations were respectively of 2.1 and 1.6 %, for DIC and A_T. During MAYOBS15, standard deviation was from 0.3 to 0.4 % for DIC and from 0.3 to 0.9 % for A_T. For GeoFlamme cruise, standard deviation were respectively of 0.08 and 0.19 %, for DIC and A_T.

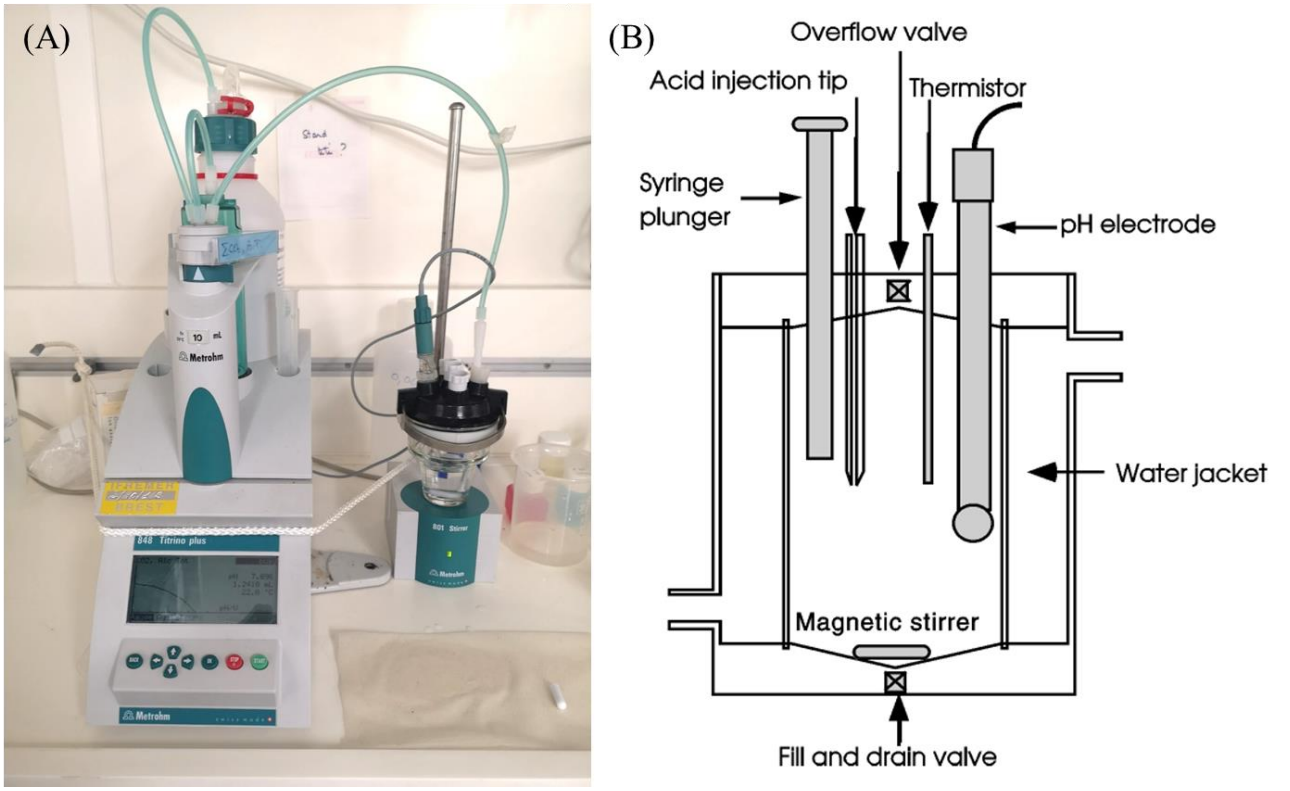

Figure 3. 11. (A) Photography of the titrimeter (Titrino 848, Metrohm®). (B) Schematic diagram of the titration cell for the determination of DIC and A_T, from Dickson et al. (2007).

3.2.3.3. Silicates

Silicates usually present a nutritive-type profile within the water column (Roy-Barman and Jeandel, 2016), in the present study this parameter has mostly been used to confirm the sampling depths of the CTD-rosette bottles. Samples for the quantification of silicates (SiO_2) were taken in 60 mL polyethylene bottles previously rinsed a minimum of three times with ultrapure water (Milli-Q Millipore element system) and dried. Analyses were done onboard during MAYOBS1, MAYOBS4 and GeoFlamme (hydrocasts HY01 to HY08) cruises, while during MAYOBS15 and GeoFlamme (HY09 to HY16) cruises the analyses were performed onshore.

Both onboard and onshore analyses were carried out by a segmented continuous flow analysis technique using an autoanalyzer (SEAL AutoAnalyzer 3 HR, SEAL Analytical®) based on the spectrophotometry detection by Aminot and Kérouel (2007) (Figure 3. 12). This method enables the determination of dissolved silicon which, at the usual pH of seawater, is 95% in the form of orthosilicic acid $Si(OH)_4$ and 5% in the ionized form $SiO(OH)_3^-$. The determination is based on the formation of a silico-molybdic complex which, after reduction by ascorbic acid, yields molybdenum

blue, creating a blue coloration. The addition of oxalic acid before ascorbic acid decomposes any phospho-molybdates formed, minimizing interference with phosphates. Absorbance is measured in a 10 mm cell at a wavelength of 820 nm. According to replicate measurements, the uncertainties of this method is of 0.2%. The detection limit is of 0,50 µmol/L and the quantification limit is of 1,60 µmol/L.

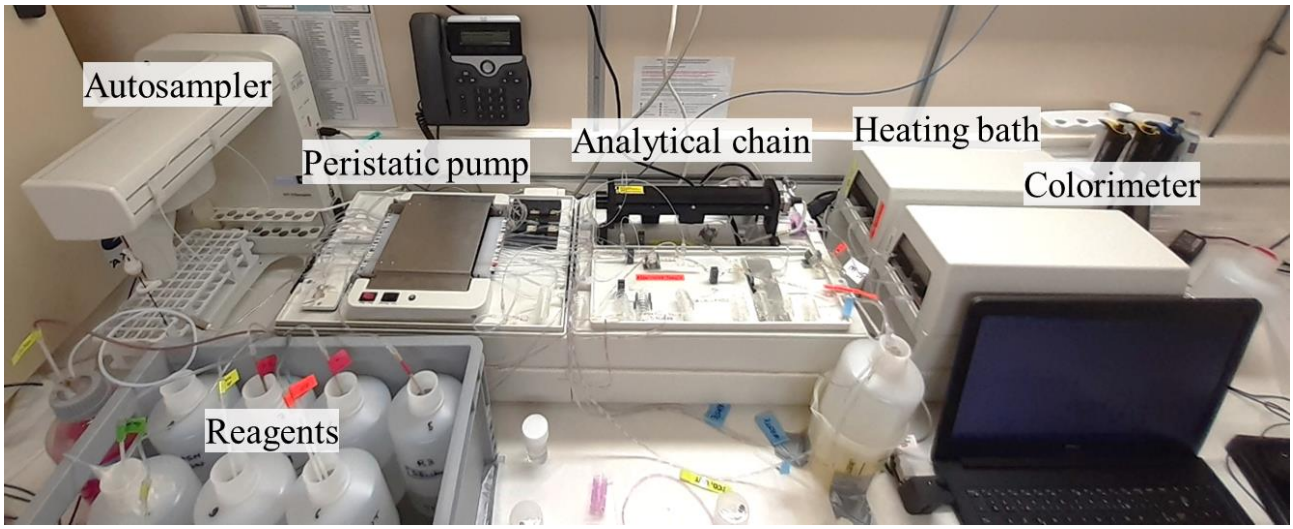

Figure 3. 12. Photography of the autoanalyzer used for the quantification of silicates by segmented continuous flow analysis. The various components of the analytical system are identified.

The silicate results from MAYOBS15 were compared to MAYOBS4. However, due to onshore analyses performed about a year after sampling, a shift of 0.856 ($y = 0.8561x$, $R^2 = 0.994$) was observed between the cruises, for the corresponding depths (Figure 3. 13). This decrease in silicates within the sample may be due to scavenging or adsorption on particles or on the botte walls as the samples have not been filtered. Concentrations of silicates from MAYOBS15 were thus corrected by multiplying by this coefficient. The GeoFlamme onshore measurements were not corrected as it was only used for bottle depth validation.

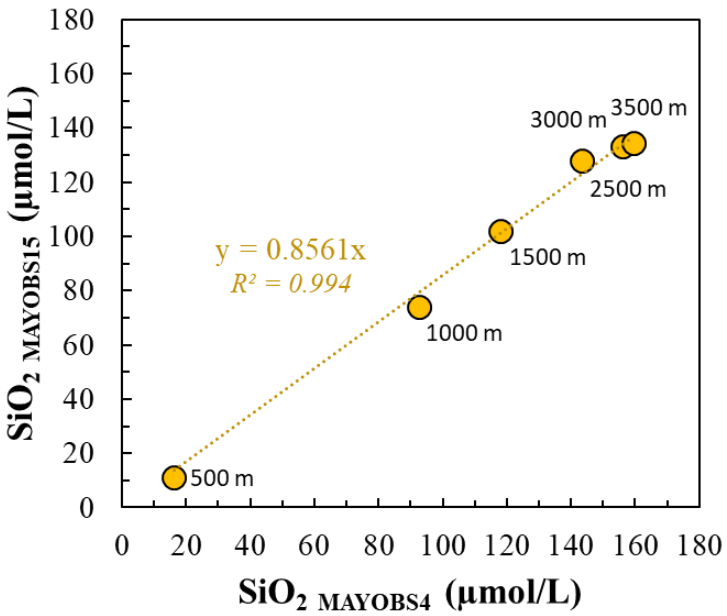

Figure 3. 13. Plot of silicate concentrations measured onboard MAYOBS4 cruise versus concentrations measured onshore on MAYOBS15 samples, for various depths within the water column.

3.2.4. Toward the development of volatile sulfur compounds analyses by GC-PFPD

During MAYOBS4 and MAYOBS15 cruises, concentrations of dissolved hydrogen sulfides ($\Sigma H_2S = H_2S + HS^- + S^{2-}$), also called total sulfides (ΣH_2S), were investigated. Sub-samples were taken from the CTD-rosette bottles with 60 mL low density polyethylene syringes (LDPE, Nalgene®) previously washed with 10%$_{v/v}$ hydrochloric acid (HCl 37%, Analytical Grade, Merck) then rinsed a minimum of three times with ultrapure water (Milli-Q Millipore element system). Measurements were performed using a classical spectrophotometric method developed by Cline (1969) and improved by Fonselius et al. (1999). This method is based on the formation reaction of methylene blue (i.e. 3,7-bis(dimethylamino)phenothiazine-5-onium chloride). Methylene blue is formed from dimethyl-p-phenylenediamine, with an indammonium salt (Bindschedler's green) as an intermediate. This condenses with hydrogen sulfide giving the thiazine coloration. Iron (III) chloride is the usual oxidant for the condensation and cyclization reactions, but iron (III) sulfate or oxalate may be used instead. The coloration intensity is pH dependent, and is optimal at 0.35 pH unit, according to Cline (1969). The absorbance of the blue complex is measured using a spectrophotometer at 670 nm, and is proportional to the sulfide concentration.

Cline's method is easy to use for routine work at sea and can be used for determining high concentrations of hydrogen sulfide, from 200 µmol/L to 1000 µmol/L. The Fonselius method is more suitable for measuring low concentrations of hydrogen sulfide. The blank values are negligible and determinations is possible up to 300 µmol/L.

Overall, quantification of dissolved hydrogen sulfides by those methods remains at the micromolar level and do not allows to access to the nanomolar level as it can exist within the water column in volcanic context. Thus, for the study of dissolved hydrogen sulfides in the submarine volcanic context of Mayotte, it was necessary to lower the detection limit by the development of a method.

The internal IsBlue MAYSOUFRE project was set up for the GeoFlamme cruise and consisted in applying an analytical method for quantifying sulfur compounds at sub-nanomolar resolution using GC-PFPD (Gas Chromatography - Pulsed Flame Photometric Detector). This project was supported by ISblue project, Interdisciplinary graduate school for the blue planet (ANR-17-EURE-0015) and co-funded by a grant from the French government under the program "Investissements d'Avenir".

The objective of this project, was to propose a fine characterization of volatile reduced sulfur compounds induced by volcanic activity, to establish their distribution in the fluid-panache continuum and to extract new knowledge on their behavior in this same continuum, to finally understand the processes involved in setting up the submarine volcanic system present offshore Mayotte.

3.2.4.1. Adaptation from a method used in fresh water

The analytical method for quantifying Volatile Reduced Sulfur Compounds (VRSCs) at sub-nanomolar resolution using a Gas Chromatography - Pulsed Flame Photometric Detector (GC-PFPD), was primarily developed at LBCM Laboratory (Ifremer Nantes) for the study of natural water and described by Cozic et al. (2008). This method enables, on a same sample, the simultaneous determination of the VRSCs, including hydrogen sulfide (H_2S), carbonyl sulfide (COS) and methane thiol (MeSH).

The principle of this analytical method consists firstly of extracting the dissolved gases from the water sample using the "purge and trap" technique, i.e. bubbling the sample with helium that is used as the carrier gas for the extracted volatile compounds (Figure 3. 14). Then, these compounds are trapped in a cryogenic trap consisting of a Teflon tube stuffed with Teflon wool and immersed in liquid nitrogen (-196°C). The second stage involves separating the VRSCs in a capillary column (CP-PoraBONDQ) after passing through a drying membrane (NafionTM, Perma pure) to remove all traces

of moisture. Finally, the separated compounds are sent to the pulsed flame photometric detector for quantification through an air-hydrogen flame at 250°C. According to previous studies, the analysis technique offers rapid analysis, up to six samples per hour, and requires only a small sample volume (15 mL). It is a sensitive method, with high precision (2.1%) and a detection limit below 100 pmol/L. The instrument is stable and can be taken onboard during cruises.

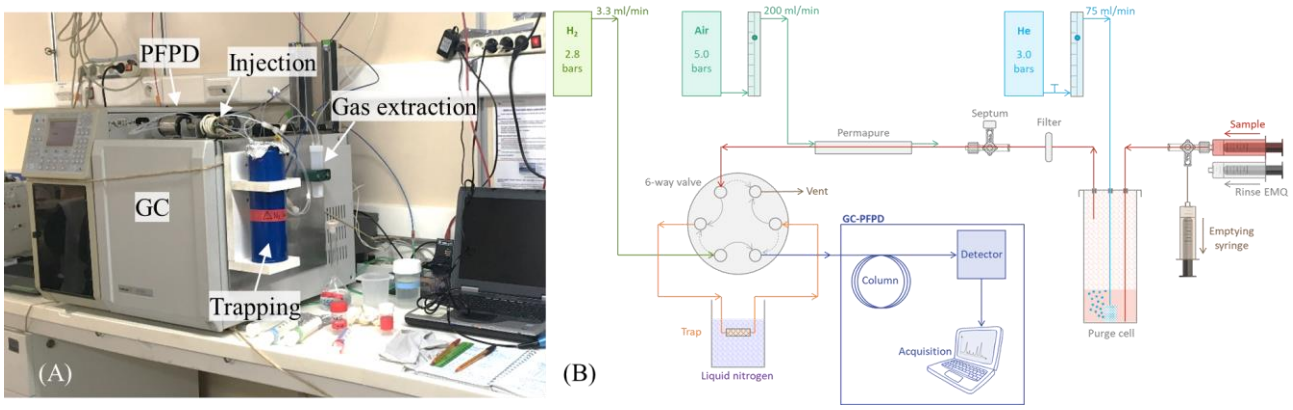

Figure 3. 14. (A) Photography of the Gas Chromatography - Pulsed Flame Photometric Detector (GC-PFPD) analytical system with identification of the various components. (B) Schematic diagram of the analytical principle.

3.2.4.2. Current development & Suggestions for future work

The aim of using this method on the GeoFlamme cruise was to apply it to the study of fluid and gas emissions present offshore Mayotte. This in order to provide the first quantifications of these compounds in the water column and to investigate the impact of the current eruption on the biogeochemical cycle of sulfur on a local and regional scale, in relation to the volcano-tectonic context at stake. The aim was therefore to carry out direct GC-PFPD analyses on samples collected with the CTD-rosette, and to make duplicates by trapping sulfides in zinc acetate, so that they could be analyzed by the same method on return to land to validate the method.

However, since the instrument had not been in operation for almost ten years, and most parts had to be replaced or restored to working order, the analyses carried out on the first samples showed unreliable or even random results. Solutions for calibration were made up using a standard solution of Na_2S, but results remained erratic. During the campaign, tests were carried out, but direct analyses were discontinued and replaced by the zinc acetate trapping method. To this end, samples

corresponding to the depths at which helium would be analyzed were taken in 250 or 300 mL glass flasks (of the BOD type), into which a solution of zinc acetate ($ZnC_4H_6O_4$) was added in excess. The samples were filtered within the hour on a polycarbonate membrane filter (Nuclepore®) with a diameter of 47 mm and a pore size of 0.4 µm, and the filters were frozen for future onshore analysis, after the instrument will be restarted.

Unfortunately, important issues with the apparatus functioning were encountered, and development could not be pursued at this time. Nevertheless, the project was reworked through exchanges with the project collaborators, as well as the realization of a bibliographical work for listing and comparing the analytical parameters used in different studies and contexts. The aim was to assess the consistency of the parameters with our project and their feasibility. This enabled us to determine the parameters to be used or tested in our case for this analytical development.

3.3. Gas Collection at the seafloor and Analyses

Liquid carbon dioxide droplets emitted at the seafloor in the Horseshoe area were observed and sampled using the deep-water Remotely Operated Vehicle (ROV) Victor 6000 – Ifremer (Figure 3. 15) The ROV was used during GeoFlamme cruise for seafloor exploration and sampling. It is equipped with a high-resolution optical imaging system for photo and video, as well as various sampling tools for geochemistry, including PEGAZ samplers.

Sampling of liquid carbon dioxide droplets directly at the seafloor was performed using gas-bubble sampler embedded on the ROV that has been developed at Ifremer and named PEGAZ, for *PrElèvement de GAZ* (Ruffine et al., 2018a) (Figure 3. 16). This sampler was designed to collect gas bubbles and preserve the sample at the *in situ* pressure until its recovery (Lanteri et al., 2007; Ruffine et al., 2018b). This device allows taking pressurized samples of gas, and/or liquids, and/or solids (i.e. hydrates), without suction, or mixing of the initial volume. It comprises a sampling enclosure consisting of a liner and piston that capture, when it is activated, the fluid/gas inside the 50 mL cylindrical sampling chamber. This sampler is proven to pressures of up to 550 bar. To be taken, the fluids/gas must be must be less dense than the surrounding seawater, so they can raised into the enclosure.

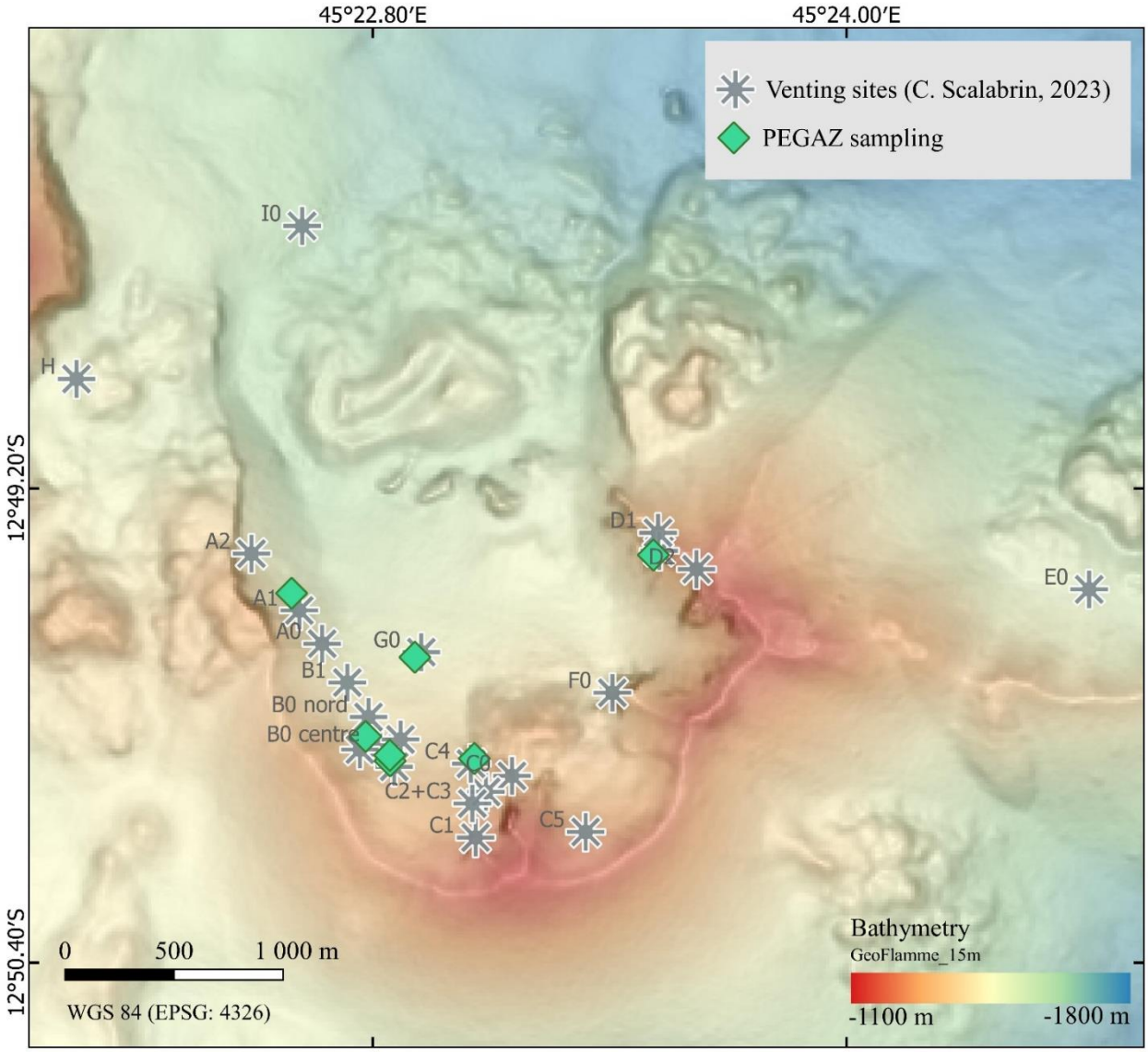

Figure 3. 15. Map of the PEGAZ sampling performed over the Horseshoe area with identification of the various venting sites of liquid CO_2 (Scalabrin, 2023). The 15m-resolution bathymetry acquired during the GeoFlamme cruise (Rinnert et al., 2021) is represented using WGS 84 geodetic system.

On board, the gases were extracted on an extraction line comprising an expansion bellows, enabling aliquots to be taken for helium, gas and isotope composition analyses. During GeoFlamme cruise, this sampling was exploratory. Indeed, the risk was relatively high, since the volume of a liquid CO_2 droplet sampled at a depth of 1600 m is multiplied by around 500 when at ambient pressure and temperature. Only a few droplets (between 4 and 6) were therefore collected for each site studied. The pressure obtained in the PEGAZ cell on return on board was equal to the saturation vapor pressure of CO_2, i.e. 68 bar, meaning that the CO_2 in the cell was still in liquid form on board.

Figure 3. 16. Photography of the PEGAZ sampler taken during an ROV exploration dive. (A) Sampling of liquid CO_2 droplets above hydrates, (B) sampling of liquid CO_2 droplets at a direct output from seafloor, (C) PEGAZ sampler in collection position, (D) PEGAZ sampler in activated position.

Gas composition analysis was carried out both on-board and onshore at Ifremer. A gas chromatograph µGC R3000 from SRA equipped with a µTCD and a PoraPlot U capillary column was used on-board to determine nitrogen, oxygen, methane to hexane and carbon dioxide concentrations. Hydrocarbons at low concentrations in the samples (<1%-mol) were analyzed onshore using a gas chromatograph (Agilent 7890A, Agilent Technologies, USA) equipped with a 32 m, 0.32 mm Porapack-Q packed column for component separation and a hydrocarbon-specific Flame Ionization. The uncertainty in the measurements was of ±2 % for methane and carbon dioxide concentrations, and ±4 % for the heavier hydrocarbons.

Aliquots of gas were then subsampled at low pressure (2- 4 bars) in 12-mL pre-evacuated vials from Labco Exetainer ® by connecting the PEGAZ sampler to a custom-made gas transfer system (Charlou et al., 2004). Isotopic composition was analyses by Isolab according to the same procedure as describe for water column samples (paragraph 3.2.1.4).

3.4. Data Mapping

During the MAYOBS cruises, coordinates from the ship were assumed to correspond to the CTD-rosette position, as hydrocasts were performed vertically. For the GeoFlamme cruise, tow-yow operations were performed: during those, the CTD-rosette position cannot be derived from the ship position, the wire out being way too long compared to the actual depth of the instrument. Therefore, an USBL (Ultra short baseline) transmitter from Exail® was mounted on the CTD-rosette, offering a precision of 3D positioning of 0.5 % of the depth. For all hydrocasts performed during the GeoFlamme cruise, the latitude and longitude of each sampling depth were extracted from the

CASINO+ database (onboard operation monitoring software) using the sampling time to correlate with the CTD-rosette data.

Mapping of the bathymetry and positioning of the hydrocasts was carried out using QGIS® software and the databases from MAYOBS and GeoFlamme cruises. The global bathymetry (Geo-Ocean (Ifremer), 2022) used on maps is the synthesis of several MAYOBS cruises acquired using multibeam echo sounder acoustics, from 2018 to 2020, with a resolution of 50 m. Ship-echo sounder characteristics are presented above in this chapter, in paragraph 3.1.2. Lower bathymetry resolution is used for Volcano and Horseshoe area mapping. The Volcano area is represented with a 30 m-resolution from the MAYOBS15 cruise ((Rinnert et al., 2020), Metadata available on *Sextant*) and the Horseshoe area with a 15 m-resolution from GeoFlamme cruise (Rinnert et al., 2021).

3.5. Bibliographical References

Aguilar-Islas, A.M., Resing, J.A., and Bruland, K.W. (2006). Catalytically enhanced spectrophotometric determination of manganese in seawater by flow-injection analysis with a commercially available resin for on-line preconcentration. *Limnology and Oceanography-Methods* 4**,** 105-113. doi: 10.4319/lom.2006.4.105.

Aminot, A., and Kérouel, R. (2007). *Dosage automatique des nutriments dans les eaux marines: méthodes en flux continu.* Editions Quae.

Benson, B.B., and Krause, D. (1980). Isotopic fractionation of helium during solution: A probe for the liquid state. *Journal of Solution Chemistry* 9(12)**,** 895-909. doi: 10.1007/bf00646402.

Boyle, E.A., John, S., Abouchami, W., Adkins, J.F., Echegoyen-Sanz, Y., Ellwood, M., et al. (2012). GEOTRACES IC1 (BATS) contamination-prone trace element isotopes Cd, Fe, Pb, Zn, Cu, and Mo intercalibration. *Limnology and Oceanography: Methods* 10(9)**,** 653-665. doi: 10.4319/lom.2012.10.653.

Charlou, J.L., Donval, J.P., Fouquet, Y., Ondreas, H., Knoery, J., Cochonat, P., et al. (2004). Physical and chemical characterization of gas hydrates and associated methane plumes in the Congo–Angola Basin. *Chemical Geology* 205(3)**,** 405-425. doi: 10.1016/j.chemgeo.2003.12.033.

Charlou, J.L., Rona, P., and Bougault, H. (1987). Methane anomalies over TAG hydrothermal field on Mid Atlantic Ridge. *Journal of Marine Research* 45(2)**,** 461-472. doi: 10.1357/002224087788401179.

Clarke, W.B., Jenkins, W.J., and Top, Z. (1976). Determination of tritium by mass spectrometric measurement of 3He. *The International Journal of Applied Radiation and Isotopes* 27(9)**,** 515-522. doi: 10.1016/0020-708x(76)90082-x.

Cline, J.D. (1969). Spectrophotometric determination of hydrogen sulfide in natural waters. *Limnology and Oceanography* 14(3)**,** 454-458. doi: 10.4319/lo.1969.14.3.0454.

Cozic, A., Viollier, E., Chiffoleau, J.-F., Knoery, J., and Rozuel, E. (2008). Interactions between Volatile Reduced Sulfur Compounds and Metals in the Seine Estuary (France). *Estuaries and Coasts* 31(6)**,** 1063-1071. doi: 10.1007/s12237-008-9099-7.

Dickson, A.G., Sabine, C.L., and Christian, J.R. (2007). "Guide to best practices for ocean CO2 measurements", in: *PICES Special Publication 3, IOCCP Report 8.* (North

Pacific Marine Science Organization, Sidney, British Columbia).

Donval, J.P., and Guyader, V. (2017). Analysis of hydrogen and methane in seawater by "Headspace" method: Determination at trace level with an automatic headspace sampler. *Talanta* 162**,** 408-414. doi: 10.1016/j.talanta.2016.10.034.

Fonselius, S., Dyrssen, D., and Yhlen, B. (1999). "Determination of hydrogen sulphide," in *Methods of Seawater Analysis*.), 91-100.

Geo-Ocean (Ifremer) (2022). Bathymétrie - Mayotte (synthèse, 2021). doi: 10.12770/0085f83d-cc3e-4c3c-b19a-6c93bca97be9.

Jenkins, W.J., Doney, S.C., Fendrock, M., Fine, R., Gamo, T., Jean-Baptiste, P., et al. (2019). A comprehensive global oceanic dataset of helium isotope and tritium measurements. *Earth System Science Data* 11(2)**,** 441-454. doi: 10.5194/essd-11-441-2019.

Konn, C., Fourré, E., Jean-Baptiste, P., Donval, J.P., Guyader, V., Birot, D., et al. (2016). Extensive hydrothermal activity revealed by multi-tracer survey in the Wallis and Futuna region (SW Pacific). *Deep Sea Research Part I: Oceanographic Research Papers* 116**,** 127-144. doi: 10.1016/j.dsr.2016.07.012.

Lanteri, N., Bignon, L., and Dupont, J. (2007). *Device for taking pressurized samples. European Patent WO/2007/128891*.

Lui, H.-K., and Chen, C.-T.A. (2017). Reconciliation of pH25 and pHinsitu acidification rates of the surface oceans: A simple conversion using only in situ temperature. *Limnology and Oceanography: Methods* 15(3)**,** 328-335. doi: 10.1002/lom3.10170.

McDougall, T.J., Jackett, D.R., Wright, D.G., and Feistel, R. (2003). Accurate and Computationally Efficient Algorithms for Potential Temperature and Density of Seawater. *Journal of Atmospheric and Oceanic Technology* 20(5)**,** 730-741. doi: 10.1175/1520-0426(2003)20<730:aaceaf>2.0.co;2.

Nadeau, K., Brophy, C., Yang, L., Grinberg, P., Pihillagawa Gedara, I., Meija, J., et al. (2016). NASS-7: Seawater Certified Reference Material for Trace Metals and other Constituents. doi: 10.4224/crm.2016.nass-7.

Resing, J.A., and Mottl, M.J. (1992). Determination of manganese in seawater using flow injection analysis with on-line preconcentration and spectrophotometric detection. *Analytical Chemistry* 64(22)**,** 2682-2687. doi: 10.1021/ac00046a006.

Rinnert, E., Cathalot, C., and Feuillet, N. (2021). GEOFLAMME cruise, RV Pourquoi pas ? doi: 10.17600/18001297.

Rinnert, E., Thinon, I., and Feuillet, N. (2020). MD 228 / MAYOBS15 cruise, RV Marion Dufresne. doi: 10.17600/18001745.

Roy-Barman, M., and Jeandel, C. (2016). *Marine geochemistry: ocean circulation, carbon cycle and climate change.* Oxford University Press.

Ruffine, L., Donval, J.-P., Croguennec, C., Burnard, P., Lu, H., Germain, Y., et al. (2018a). Multiple gas reservoirs are responsible for the gas emissions along the Marmara fault network. *Deep Sea Research Part II: Topical Studies in Oceanography* 153**,** 48-60. doi: 10.1016/j.dsr2.2017.11.011.

Ruffine, L., Ondreas, H., Blanc-Valleron, M.-M., Teichert, B.M.A., Scalabrin, C., Rinnert, E., et al. (2018b). Multidisciplinary investigation on cold seeps with vigorous gas emissions in the Sea of Marmara (MarsiteCruise): Strategy for site detection and sampling and first scientific outcome. *Deep Sea Research Part II: Topical Studies in Oceanography* 153**,** 36-47. doi: 10.1016/j.dsr2.2018.03.006.

Saito, M.A., and Schneider, D.L. (2006). Examination of precipitation chemistry and improvements in precision using the Mg(OH)2 preconcentration inductively coupled plasma mass spectrometry (ICP-MS) method for high-throughput analysis of open-ocean Fe and Mn in seawater. *Analytica Chimica Acta* 565(2)**,** 222-233. doi: 10.1016/j.aca.2006.02.028.

[Dataset] Scalabrin, C. (2023). *Site d'émissions de fluides, Mayotte, zone Fer à Cheval (C. Scalabrin, 2022).* doi: 10.12770/070818f6-6520-49e4-bafd-9d4d0609bf7d. Available: https://doi.org/10.12770/070818f6-6520-49e4-bafd-9d4d0609bf7d.

Sültenfuß, J. (2016). "Hints for sampling". Helis - helium isotopes studies Bremen).

Sültenfuß, J., Roether, W., and Rhein, M. (2009). The Bremen mass spectrometric facility for the

measurement of helium isotopes, neon, and tritium in water. *Isotopes in Environmental and Health Studies* 45(2)**,** 83-95. doi: 10.1080/10256010902871929.

Swinnerton, J., Linnenbom, V., and Cheek, C. (1962). Determination of Dissolved Gases in Aqueous Solutions by Gas Chromatography. *Analytical Chemistry* 34(4)**,** 483-485.

Weiss, R.F. (1971). Solubility of helium and neon in water and seawater. *Journal of Chemical & Engineering Data* 16(2)**,** 235-241. doi: 10.1021/je60049a019.

CHAPTER 4. Strong Geochemical Anomalies Following Active Submarine Eruption offshore Mayotte

This chapter has been published in *Chemical Geology*.

Received 20 February 2023; Received in revised form 28 August 2023; Accepted 17 September 2023; Available online 20 September 2023

Manon Mastin[1], Cécile Cathalot[1], Olivia Fandino[1], Thomas Giunta[1], Jean-Pierre Donval[1], Vivien Guyader[1], Yoan Germain[1], Carla Scalabrin[1], Sébastien Dehez[2], Stéphane Jouenne[2], Eric C. Gaucher[3], Olivier Rouxel[1], Emmanuel Rinnert[1]

[1]Geo-Ocean UMR 6538 CNRS - Ifremer - UBO - UBS, F-29280 Plouzané, France

[2]TotalEnergies, CSTJF EB 437, Avenue Larribau, F-64018 Pau Cedex, France

[3] Lavoisier H_2 Geoconsult, FR-74400 Chamonix, France

Mastin, M., Cathalot, C., Fandino, O., Giunta, T., Donval, J.-P., Guyader, V., Germain, Y., Scalabrin, C., Dehez, S., Jouenne, S., Gaucher, E. C., Rouxel, O., & Rinnert, E. (2023). Strong geochemical anomalies following active submarine eruption offshore Mayotte. *Chemical Geology*, 640, 121739. https://doi.org/10.1016/j.chemgeo.2023.121739

CHAPTER 4. Strong Geochemical Anomalies Following Active Submarine Eruption offshore Mayotte

Abstract

Submarine volcanic activity releases large amounts of gases and metals in the water column, affecting biogeochemical cycles and ecosystems at a regional and local scale. In 2018, Fani Maoré submarine volcano erupted 50 km offshore Mayotte Island (Comoros Archipelago, Indian Ocean). Active eruptive plumes were observed in May 2019 at and around the summit with acoustic plumes rising 2 km into the water column coupled to strong geochemical anomalies. Between May 2019 and October 2020, three research cruises monitored the eruptive activity.

Here, we report spatial and temporal variability of water column chemistry above the volcano, focusing on dissolved gases, trace metal concentrations, and physico-chemical parameters. In May 2019, concentrations above 800 nM in CH_4 and H_2 were measured throughout the water column, with Total Dissolvable Mn and Total Dissolvable Fe concentrations above 500 nM, and CO_2 values of 265 µM. Strong water column acidification was measured (0.6 pH unit) compared to the regional background. From May 2019 to October 2020, we observed a general decrease in gas concentrations, and an evolution of the TDMn/TDFe ratios similar to previously reported values in other submarine volcanic contexts, and consistent with a decrease of the eruptive activity at the volcano. In October 2020, a rebound of high H_2 concentrations resulted from new lava flows, which were identified by seafloor observation using deep-towed camera, 5 km further than the volcano summit. During 2 years timespan of our observations (2019-2020), He, CO_2 and CH_4 concentrations correlate highlighting a magmatic origin of dissolved gases. δ^{13}C-CH_4 values of -34‰ vs. vPDB might suggest magma/sediments interaction during the magma ascent, and potential thermal cracking of organic matter, although abiotic methane generation cannot be ruled out given the volcanic context.

Weak correlations between H_2 and excess of ^{3}He suggest complex processes of H_2 from magmatic degassing, lava/seawater interaction, and oxidation processes in the water column. Strong and correlated Fe, Mn and Si water column anomalies are also consistent with fluid-rock reactions induced by acidic fluids rich in magmatic volatiles. Water column acidification appears to be associated with the release of CO_2-rich fluids. A year after the main eruptive event, the system seems to be back to steady-state highlighting the buffer capacity and resilience of the seawater column environment.

CHAPITRE 4. Fortes Anomalies Géochimiques suite à l'Eruption Sous-Marine au Large de Mayotte

Résumé

L'activité volcanique sous-marine libère de grandes quantités de gaz et de métaux dans la colonne d'eau, impactant les cycles biogéochimiques et les écosystèmes à l'échelle régionale et locale. En 2018, le volcan sous-marin Fani Maoré est entré en éruption, à 50 km au large de l'île de Mayotte (archipel des Comores, océan Indien). Des panaches éruptifs actifs ont été observés en mai 2019 au sommet et autour de celui-ci, avec des panaches acoustiques s'élevant à 2 km dans la colonne d'eau, associés à de fortes anomalies géochimiques. Entre mai 2019 et octobre 2020, trois campagnes de recherche ont surveillé l'activité éruptive.

Dans cette étude, nous examinons la variabilité spatiale et temporelle de la chimie de la colonne d'eau au-dessus du volcan, en nous concentrant sur les gaz dissous, les concentrations en métaux traces et les paramètres physico-chimiques. En mai 2019, des concentrations en CH_4 et H_2 supérieures à 800 nM ont été mesurées dans toute la colonne d'eau, avec des concentrations totales en Mn et en Fe dissous supérieures à 500 nM, et des valeurs de CO_2 de 265 µM. Une forte acidification de la colonne d'eau a été mesurée (0,6 unité pH) par rapport au contexte régional. De mai 2019 à octobre 2020, nous avons observé une diminution générale des concentrations de gaz et une évolution des rapports TDMn/TDFe similaires aux valeurs précédemment rapportées dans d'autres contextes volcaniques sous-marins, en accord avec une diminution de l'activité éruptive du volcan. En octobre 2020, une hausse des concentrations élevées en H_2 a résulté de nouvelles coulées de lave, qui ont été identifiées par observation du fond marin, à 5 km du sommet du volcan.

La corrélation entre les concentrations en He, CO_2 et CH_4 démontre une origine magmatique des gaz dissous, tandis qu'une valeur en $\delta^{13}C$-CH_4 de -34‰ suggère une contribution sédimentaire probablement due à une interaction magma/sédiments pendant la remontée du magma. La faible corrélation entre H_2 et ^3He suggèrent des processus complexes de dégazage magmatique, d'interaction lave/eau de mer et de processus d'oxydation dans la colonne d'eau. La corrélation de fortes anomalies en Fe, Mn et Si dans la colonne d'eau, sont également cohérentes avec des réactions entre les fluides acides riches en volatiles magmatiques et les roches. L'acidification de la colonne d'eau semble être associée à la libération de fluides riches en CO_2. Un an après l'événement éruptif principal, le système semble être revenu à un état stable, mettant en évidence le pouvoir tampon et la résilience de la colonne d'eau.

4.1. Introduction

Submarine volcanism represents about 85% of the global Earth volcanism (White et al., 2015). It is responsible for the transfer of chemicals from the crust to the water column, including volatile elements or reduced transition metals, and is also the main mechanism responsible for deep stored carbon release to the surface (Baker et al., 2012; Rubin et al., 2012). Water column geochemical signatures of submarine eruptions are quite different from one site to another but generally exhibit increases in magmatic volatile gases (^3He, CO_2), enrichments in H_2 and CH_4, decreases in pH by the addition of CO_2, SO_2 and mineral acidity (H^+), and discharges of reduced species including H_2S (Baumberger et al., 2014; Buck et al., 2018; Resing et al., 2009; Resing et al., 2007). Each of these compounds are valuable tracers for submarine eruptions and hydrothermal circulation: combining them bring insights of their origin and generation mechanisms involved.

Studies on submarine eruptions started in the 1980's, but deep-sea eruptions are very difficult to detect and observe due to their shortness (Baker et al., 2012; Rubin et al., 2012). They have mostly been sampled after the end of the eruption, often capturing the hydrothermal activity state instead of the eruptive state (Rubin et al., 2012). Before the Mayotte submarine eruption, only three active submarine eruptions have been observed: NW Rota-1 (an explosive shallow eruption – at ~500 m deep – in the Mariana arc (Chadwick et al., 2008)),West-Mata (a deeper explosive eruption – at ~1200 m deep – in the Lau basin (Embley et al., 2014; Resing et al., 2011)), and event plumes at the NE Lau Spreading Center eruption (rising from summits between 1600 and 1300 m deep, Baker et al (2011)). The Mayotte submarine eruption and the significant scientist mobilization that followed offer well-defined temporal and spatial constrains on the birth of a volcanic edifice, and constitutes therefore a great opportunity to study the origin and processes responsible for gas release, their impact in the water column and the carbonate system response.

After a few thousand years of aseismicity, (Zinke et al., 2003a), in May 2018, Mayotte Island started to experience a major seismic crisis. This phenomenon was associated with the birth of a volcano edifice 50 km East offshore Mayotte, with characteristics that make it the largest active eruption ever documented since the Laki eruption in 1783 (Thordarson and Self, 1993). Indeed, this volcano stands 820 m above the seafloor, with a magma released estimated to be about 6.5 km^3, inducing strong geochemical anomalies through the water column (Cesca et al., 2020; Feuillet et al., 2021; Lemoine et al., 2020). We present here for the first time a comprehensive survey of gas chemistry (H_2, CO_2, CH_4 and He)

in the water column and its evolution from the birth of the volcano (i.e. eruptive state) to the initiation of hydrothermal activity, covering a time period of about 30 months, from May 2018 to October 2020. We aim to discuss the concomitant evolution of water column chemistry over the course of the eruption and discuss the geochemical mechanisms involved. For instance, the isotopic composition of He provides a valuable and reliable indicator of its own origin but can be decoupled from the more reactive gases (Giggenbach et al., 1993). Indeed, the presence of primordial ^{3}He within the water column indicates input of magmatic gases from the mantle (Craig and Lupton, 1981), whereas radiogenic ^{4}He indicates gas inputs originating from the crust (Barry et al., 2020). Aside from hydrothermal reactions (e.g. serpentinization), generation of H_2 occurs during lava and seawater interactions, generally associated with gas-rich eruptions (Sansone et al., 1991). In submarine volcanic systems, H_2 is therefore the typical tracer for ongoing eruption, with a short residence time as it is rapidly consumed by microorganisms and chemical oxidation over hourly or daily timescales (Baumberger et al., 2020; Baumberger et al., 2014). On another hand, methane can be a major component of hydrothermal gases but is usually present in trace amounts in volcanic gases. In natural systems, CH_4 may originate from thermocatalytic decomposition of organic matter, microbial production or from abiotic processes that may involve various chemical reactions (Fiebig et al. (2004) and references therein). In marine hydrothermal systems for instance, methane is thought to be generated abiotically during fluid-rock interactions involving serpentinization reactions and Fischer-Tropsch-type chemical reactions (Giggenbach, 1996; Truche et al., 2020). It is a potent greenhouse gas, 28 times more than CO_2 (Pörtner et al., 2022), with a potential significant effect on past climate change with volcanic basins providing a setting for rapid disruptions in the release of carbon from sedimentary reservoirs (Raynaud et al., 1993; Svensen et al., 2004).

The carbon dioxide is generally the predominant dissolved gases in submarine volcanic fluids, generated through lava outgassing (Craig and Lupton, 1981). Therefore, volcanic activity contributes to local ocean acidification, in particular by the discharge of CO_2-rich fluids into the seawater column (Resing et al., 2009; Santana-Casiano et al., 2016). Carbone dioxide is an acid gas that reacts with water to produce carbonic acid (H_2CO_3) which is dissociated into hydrogenocarbonate (HCO_3^-) and carbonate (CO_3^{2-}) ions depending on pH and buffer capacity of the solution. When CO_2 is added to a solution, it gives a mixture of these three species that results in an increase of the quantity of total dissolved inorganic carbon (expressed as ΣCO_2). Those dissolved

compounds make up the carbonate system in water. The carbonate system of the ocean is the primary buffer for the acidity of seawater and acts as a governor for the carbon cycle by controlling the partial pressure of CO_2 in the atmosphere, which helps to regulate the temperature of the planet. The formation rate of the most prevalent authigenic mineral in the environment, $CaCO_3$, is also the major sink for dissolved carbon in the long-term global carbon balance (Emerson and Hedges, 2008). The emission of CO_2 from submarine volcanoes generates local ocean acidification and a change in the carbonate system equilibrium that could affect biological communities, with especially important consequences for organisms that use calcium carbonate in their structures (Santana-Casiano et al., 2016). This process also favors the photosynthesis (Jansson and Northen, 2010; Suzuki, 1998).

In this study, we present a compilation of geochemical data taken at the Fani Maoré submarine volcano, during the main eruptive event in May 2019 and from two cruises performed in July 2019 and October 2020, leading to monitor the continuous lava flow installation. These data provide valuable information on geochemical mechanisms during the setup of a volcanic edifice and on the impact of an eruptive activity on the water column at a local scale.

4.2. Geological setting and overview on the eruptive activity offshore Mayotte

Mayotte Island is located in the Comoros Archipelago, within the Mozambique Channel (Indian Ocean) between the eastern coast of the Mozambique Channel and the northern tip of Madagascar (Figure 4. 1. A). The four islands that compose the Comoros Archipelago are aligned along a NW-SE axis (Tzevahirtzian et al., 2021). Mayotte is the easternmost island of the archipelago, and the eldest with a maximum age of 20 Ma for the onset of subaqueous volcanic activity and 11 Ma for the onset of subaerial volcanic activity (Debeuf, 2004; Michon, 2016; Nougier et al., 1986; Pelleter et al., 2014). The last reported volcanic event occurred 4-6 thousand years ago (ka) at Petite-Terre, east of Mayotte (Zinke et al., 2003b).

The origin of the Comoros volcanism is not yet well understood. Two main hypothesis have been developed to explain its origin: (1) a mantle plume that interacts with the oceanic lithosphere (Emerick and Duncan, 1982); (2) a lithospheric deformation that reactivated transform faults and controlled the magma path (Nougier et al., 1986). Recent works suggest that the volcanism is associated with lithospheric deformation rather than the result of a deep mantle plume (Famin et al., 2020;

Lemoine et al., 2020; Michon, 2016; Tzevahirtzian et al., 2021).

On May 10th, 2018, the major seismo-volcanic crisis that began on Mayotte Island has sparked the interest of scientists and led to the establishment of the Mayotte volcanological and seismological monitoring network, named REVOSIMA (2021). Over a year, 32 earthquakes of $M_w \geq 5$ were recorded, included the largest event ever recorded in the Comoros Archipelago on the 15th of May 2018 with M_w = 5.9 (Cesca et al., 2020; Feuillet et al., 2021; Lemoine et al., 2020). These earthquakes are distributed into two swarms, one proximal and one distal, whose epicenters are respectively located 5-15 km and about 25 km east of Petite-Terre, at 25-50 km depth (Feuillet et al., 2021; Lavayssière et al., 2022). Very long period seismic events (VLP) were frequently recorded suggesting a fluid migration from active magmatic or hydrothermal processes (Lemoine et al., 2020).

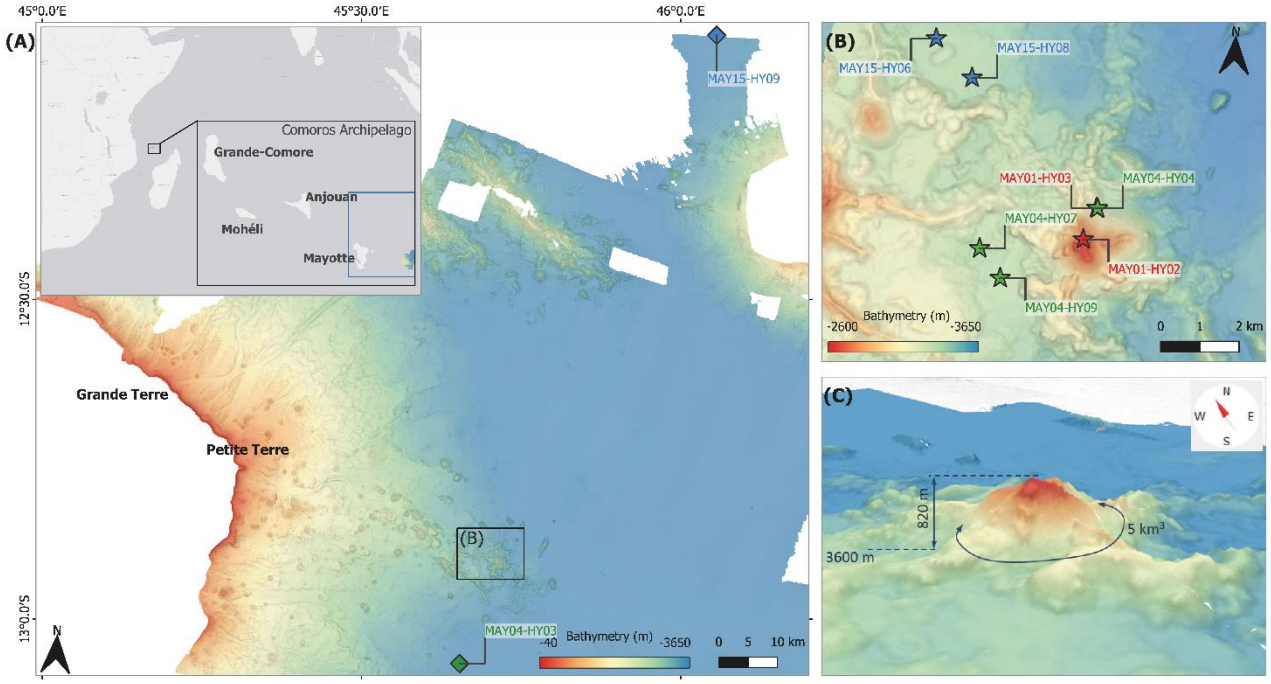

Figure 4. 1. (A) Map of the site with reference CTD casts and 50m-resolution bathymetry using WGS 84 geodetic system (Geo-Ocean (Ifremer), 2022), (B) Bathymetry (30m-resolution) of the volcano edifice with CTD casts performed above the volcano and above lava flows, (C) 3D representation of the volcano edifice (vertical exaggeration x2).

This seismo-volcanic crisis is associated with the birth of a volcanic edifice, the Fani Maoré Seamount, discovered in May 2019 during the MAYOBS1 oceanographic cruise (Feuillet, 2019), that was not present in 2014 during the survey operated by the French Naval Hydrographic and Oceanographic Service (SHOM) (Feuillet et al., 2021) (Figure 4. 1.B

and C). The edifice is located 50 km east of Mayotte (-12°54'37; 45°42'42) and rises to 820 m at about 3500 m depth. The ongoing eruption was captured in May 2019 by the ship echo sounder with an exceptional acoustic plume of about 2 km high within the water column associated with strong geochemical anomalies (Feuillet et al., 2021). Lemoine et al. (2020) and Cesca et al. (2020) proposed that the eruptive activity has been going on from June-July 2018 to May 2019, and was fed by a magma reservoir of 10 to 15 km diameter located at 25 to 35 km depth. Dofal et al. (2021) suggested that this magmatic reservoir developed beneath the interface between the mantle lithosphere and the subplateau.

The eruption was followed, from May 2019 to October 2020, by a chronological lava flow emission (REVOSIMA, Février 2021) associated with four new distant exit points: (1) south of the volcano (~ 0.2 km^3 of lava from May 19th to June 17th 2019); (2) west of the volcano (~ 0.3 km^3 of lava from June 18th to July 30th 2019); (3) north of the volcano (~ 0.08 km^3 of lava from July 31st to August 20th 2019); (4) northwest of the volcano (~ 0.8 km^3 of lava from August 21st 2019 to May 11th 2020); (5) northwest of the volcano (~ 0.1-0.2 km^3 of lava from May 11th to October 11th 2020). From the beginning of the eruptive activity, the volume of erupted magma is estimated to be about 6.5 km^3 (REVOSIMA, Février 2021). The Fani Maoré acoustic plumes ended in the beginning of June 2019 during MAYOBS2 cruise (Jorry, 2019) and the last recorded lava flow occurred between October 2020 (MAYOBS15, Rinnert et al. (2020)) and January 2021 (MAYOBS17, Thinon et al. (2021)).

4.3. Materials and Methods

The water column above the volcano was monitored during three oceanographic cruises on board the *R/V Marion Dufresne*. The first cruise, *MAYOBS1*, was conducted in 2019 from May 2nd to 22nd (Feuillet, 2019); the second, *MAYOBS4*, in 2019 from July 19th to August 4th (Fouquet and Feuillet, 2019); and the third, *MAYOBS15*, in 2020 from October 1st to 27th (Rinnert et al., 2020). These *MAYOBS* cruises are part of the REVOSIMA survey program with the aim of monitoring this seismic and volcanic crisis which affects Mayotte Island (Feuillet et al., 2019).

4.3.1. Sampling sites

Stations for hydrocasts were determined according to the presence of acoustic signals from ship echo sounder surveys (Kongsberg EM122 1° × 1°) and to seafloor observations from the submersible interactive camera system (SCAMPI, Ifremer). During the first cruise in May 2019, one hydrocast was performed within the 2000 m-height acoustic plume imaged at the volcano summit (MAY01-HY02), and one other above the

northern flank of the volcano (MAY01-HY03) (Figure 1B). In July 2019, three CTD (Conductivity, Temperature, and Depth) casts were carried out, one in the same location as MAY01-HY03 (cast MAY04-HY04) and two at the west of the volcano (MAY04-HY07, MAY04-HY09), above the recent lava flow from June 18th to July 30th 2019, detected by ship echo sounder. The third cruise focused on the northwest new lava flow from May 11th to October 11th 2020, with a CTD cast performed above incandescent lava (MAY15-HY08) and very recent lava flow (MAY15-HY06).

CTD casts for background water column evaluation (i.e. remote from volcanic activity) were performed in July 2019 and October 2020, tens of kilometers away from the study site. During MAYOBS4, the background cast was done about 20 km southward from the volcano (MAY04-HY03), whereas during MAYOBS15 the background cast was realized about 100 km northeastward (MAY-HY09).

4.3.2. Sampling methods and analysis

We studied physico-chemical parameters of the water column using a Seabird 911 Plus CTD combined with a Seapoint Turbidity Meter sensor. Turbidity measurements are reported as Nephelometric Turbidity Unit (NTU). Discrete water samples were collected using a 16-bottles carousel equipped with 8 L Niskin water sampling bottles.

Turbidity signals were homogenized by setting the zero value for all hydrocasts studied. This correction was based on the near-zero signal values encountered around 1500 m depth (i.e. below the euphotic zone and above turbidity anomalies linked to the volcanic activity). The average of 100 turbidity values (acquired at a frequency of 1 Hz, for a CTD rosette ascent velocity of 1 m/s) from 1500 m to deeper was determined and then subtracted to the entire turbidity depth profile.

Samples for noble gases, dissolved gases, metals, pH, alkalinity and silicates analyses were directly taken from the Niskin bottles, as described below. Hydrographic parameters are presented in Supplementary Figure 4. 1and 2.

4.3.2.1. Helium and Neon

Samples for noble gases analysis were collected immediately after the CTD-rosette was retrieved to conserve the integrity of the dissolved gases. Water was flushed into copper tubing carefully checking for the absence of air bubbles and sealed using special stainless clamps (Sültenfuß, 2016). Quantification of helium and neon isotopes (^{3}He, ^{4}He, ^{20}Ne, ^{22}Ne) was performed at the Helis Laboratory (Helium isotopes studies, Bremen, Germany) using a mass spectrometric system composed of a quadrupole mass spectrometer (QMS, Balzers QMG112a®) and a sector field mass spectrometer (SMS, MAP 215-50®). This method yields a precision of ±0.4 % for

$^3He/^4He$ ratios and ±0.8 % for helium and neon concentrations (Sültenfuß et al., 2009).

In this study, we choose to define each component of the measured concentrations of ^3He and ^4He (i.e. equilibrium, air contamination and non-atmospheric concentrations). Assuming that the entire Ne concentration comes from atmospheric air, the corrected He concentration from air contamination and atmospheric air in equilibrium is expressed as $^3He_{xs}$ and $^4He_{xs}$. Considering that the tritiogenic ^3He (i.e. resulting from the radioactive decay of tritium) is negligible in the Indian Ocean offshore Mayotte Island (Jenkins et al., 2019), the $^3He_{xs}$ and $^4He_{xs}$ should only corresponds to the supply of mantle and crustal helium. Therefore, the closure equations for neon and helium are:

$$\begin{cases} Ne_m = Ne_{eq} + Ne_{air} \\ {}^4He_m = {}^4He_{eq} + {}^4He_{air} + {}^4He_{xs} \\ {}^3He_m = {}^3He_{eq} + {}^3He_{air} + {}^3He_{xs} \end{cases}$$

with *m* the measured concentration, *eq* the equilibrium concentration and *air* the concentration for air contamination. Equilibrium and air contamination neon concentrations were defined as $Ne_{eq} = Ne_{atm} \times \beta_{Ne}$ and $Ne_{air} = Ne_m - Ne_{eq}$, and helium isotopes concentrations as ${}^{3,4}He_{eq} = {}^{3,4}He_{atm} \times \beta_{He}$ and ${}^{3,4}He_{air} = Ne_{air} \times \frac{{}^{3,4}He_{atm}}{Ne_{atm}}$.

We introduce solubility coefficients depending on the temperature and salinity conditions of sampling, which vary respectively from 1.44 to 10.82 °C and from 34.64 to 34.90 psu. Solubility coefficients of Ne and He in seawater (β_{Ne} and β_{He}, respectively) were determined for each sample according to the water temperature (T, in kelvin) and salinity (S, in psu) of the sampling depth, using Weiss (1971) solubility equations:

$$ln\beta_{He} = -34.6261 + 43.0285\left(\frac{100}{T}\right) + 14.1391\ln\left(\frac{T}{100}\right) + S\left[-0.042340 + 0.022624\left(\frac{T}{100}\right) - 0.0033120\left(\frac{T}{100}\right)^2\right]$$

$$ln\beta_{Ne} = -39.1971 + 51.8013\left(\frac{100}{T}\right) + 15.7699\ln\left(\frac{T}{100}\right) + S\left[-0.124695 + 0.078374\left(\frac{T}{100}\right) - 0.0127972\left(\frac{T}{100}\right)^2\right]$$

The corrected ratio of helium (Rc/Ra) was determined by only applying the correction from atmospheric air contamination, as the equilibrium value (He_{eq}) is not negligible compare to He_{xs}. That means, $Rc = \frac{{}^3He_{xs} + {}^3He_{eq}}{{}^4He_{xs} + {}^4He_{eq}}$.

4.3.2.2. Dissolved gases (CH_4, CO_2, H_2)

Water samples for CH_4 analyses were collected into 125 mL two-valve glass ampoules. During MAYOBS1 and MAYOBS4, samples were poisoned with NaN_3 before onshore analyses, whereas during

MAYOBS15, samples were analyzed onboard. Both onshore and onboard analyses were performed using the "purge and trap" method developed by Charlou et al. (1987). Dissolved gases were completely extracted by helium purging and trapped onto activated charcoal at -80°C. The CH_4 was desorbed from the trap by increasing the temperature and was injected into a gas chromatograph (GC) equipped with a flame ionization detector (FID) for quantitative analysis. External calibration was performed using a standard gas of CH_4 at appropriate pressure and constant temperature. This method allows the determination of CH_4 concentrations equivalent to those of open ocean seawater (0.3 nM), with residual standard deviation below 2%.

For onboard CO_2 and H_2 analyses, water samples were carefully collected from the Niskin bottles, without injecting air bubbles, in 240 mL brown glass bottles closed by a screw cap fitted with a PTFE/silicone gas tight septum. Analyses were run by gas chromatography coupled to an helium ionization detector (GC-HID) and using the Headspace method developed by Donval and Guyader (2017) which consists of replacing ~20 mL of the seawater sample by a gaseous phase of pure helium in which dissolved gases equilibrate according to solubility coefficients at equilibrium temperature and to water salinity. External calibration was carried out using a standard gas mixture of H_2, CO_2 injected through 0.50 mL and 2 ml injection loops at appropriate pressure and constant temperature. The detection limit was 1 nM for hydrogen and 0.1µM for CO_2 with a residual standard deviation of 3%.

For characteristic samples, the headspace phases were transferred in evacuated 12 mL Labco tubes, completed with helium above the atmospheric pressure, and sent to the Isolab b.v. laboratory (Stable isotopes and geochemical laboratory services, The Netherlands) for ^{13}C isotopic composition analysis of CH_4 and CO_2, mentioned hereafter as $\delta^{13}C\text{-}CH_4$ and $\delta^{13}CO_2$. Carbon isotopes of methane were analyzed with an Agilent 6890N GC (Agilent Technologies, Santa Clara, US) interfaced to a Finigan Delta S IRMS (Thermo Scientific, Bremen, Germany) using a Finigan GC-C II interface. The GC is equipped with a 12 m, 0.32 mm Molsieve column (Agilent) and an injection valve. Samples are calibrated regularly against a calibration standard and results are reported in promille vs. vPDB. The minimum concentration needed to perform the analysis is about 25-50 ppm. Carbon isotopes of CO_2 were analyzed on an Agilent 7890A GC (Agilent Technologies, Santa Clara, US) interfaced to a MAT 253 IRMS (Thermo Scientific, Bremen, Germany) using a GC-Isolink or a Finigan GC-C III interface. The GC is equipped with a 25 m, 0.32 mm Porabond-Q column (Agilent) and an injection valve. Cold trapping is used to pre-concentrate

the sample when necessary. Samples are run at least 3 times after which the average of the results is calculated. The system is calibrated at least once a day using an in house natural gas standard and results are reported in promille vs. vPDB. The minimum concentrations needed to perform the analysis depends on sample composition.

4.3.2.3. Total dissolvable iron and manganese (TDFe and TDMn)

Sampling for analysis of total dissolvable iron and manganese, respectively TDFe and TDMn, was carried out in 30 mL low density polyethylene bottles (LDPE, Nalgene®) previously washed with 10%$_{v/v}$ hydrochloric acid (HCl 37%, Analytical Grade, Merck) then rinsed with ultrapure water (Milli-Q Millipore element system). All raw samples for metal analysis were acidified to 0.025 mol/L hydrochloric acid (ultrapur® grade) within 6 hours of sampling. Quantification of TDFe and TDMn was carried out in laboratory at the Pôle Spectrométrie Océan (PSO, Ifremer, Brest, France), using HR-ICP-MS (High Resolution Inductively Coupled Plasma Mass Spectrometry; Element XR, ThermoFisher Scientific). Samples were spiked with Indium (In) at 2 ppb and diluted by a factor of 100 with 0.28 mol/L distilled nitric acid. This method allows the quantification of metal concentrations in seawater, with detection limits at sub-micromolar order (about 10 nmol/L for Mn and 100 nmol/L for Fe) and residual standard deviation of 3% for TDMn and 2% for TDFe.

4.3.2.4. pH, Total CO_2, Total Alkalinity, Silicates

Sampling for the study of pH, total alkalinity (A_T) and total CO_2 (ΣCO_2) was carried out in 30 mL polyethylene bottles (LDPE, Nalgene®) previously rinsed with ultrapure water (Milli-Q Millipore element system) and dried. Samples were analyzed onboard for titration of dissolved alkaline species with hydrochloric acid solution (0.01 mol/L HCl Titrinorm) using a titrimeter (Titrino 848, Metrohm®) combined with a pH electrode (Metrohm®). Total alkalinity and ΣCO_2 were determined from titration equivalence volumes. Residual standard deviations were of 1.04% for pH measurements, and below 2% for DIC and A_T measurements.

Samples for the quantification of silicates (SiO_2) were taken in 60 mL polyethylene bottles previously rinsed with ultrapure water (Milli-Q Millipore element system) and dried. Analyses were done onboard during MAYOBS1 and MAYOBS4 cruises, and onshore during MAYOBS15 cruise, by a segmented continuous flow analysis technique using an autoanalyzer (SEAL AutoAnalyzer 3 HR, SEAL Analytical®) based on the spectrophotometry detection (Aminot and

Kérouel, 2007). Residual standard deviation are below 0.2%.

4.3.3. Combined data for background evaluation

Background composition was evaluated by combining data from background hydrocasts performed both during MAYOBS4 (MAY04-HY03) and MAYOBS15 (MAY15-HY09) (Figure 4. 1). We defined the background as an envelope that integrates the variations of water masses and their movements through the seasons. The background reference for turbidity was determined by first combining the turbidity data from both hydrocasts recorded at 1Hz by the CTD. Then averaging over 40 values so that the standard deviation for depth did not exceed 10 m and that a signal frequency of 1/40Hz was obtained. For the chemical parameters studied, the background reference was determined by first combining the two background hydrocasts and then averaging the data over a close depth range. Same depth ranges were used for all parameters. The envelopes were defined by the standard deviations resulting from the combination of the two profiles (See Figure A 3).

4.4. Results

4.4.1. Seafloor observations

4.4.1.1. Identification of various lava flows

Hydrocast sampling was concomitant to lava flow emplacement occurring throughout the volcanic structure. To understand if geochemical anomalies in the water column could be attributed to active or recent lava flows at the bottom, it is important to evaluate the nature of the volcanic seafloor (Table 4. 1). The hydrocast on the northern flank in July 2019 (MAY04-HY04) was performed above an already emplaced lava flow, covered by a fine sediment deposit, with evidence for incipient fluid shimmering, identified during the SCAMPI exploration (Table 4. 1). At the western lava flow, where casts MAY04-HY07 and MAY04-HY09 were performed in July 2019, SCAMPI images show a more recent lava flow with yellowish staining and thin mats of probably microbial origin (Table 4. 1). In October 2020, the northeast lava flow captured at the hydrocast MAY15-HY06 was a very glossy black lava (Table 4. 1). Combining this visual aspect with bathymetric surveys gives evidence of the very recent nature of these lava flows. At the MAY15-HY08 cast, an active lava flow was identified by incandescent lava observation (Table 4. 1).

4.4.1.2. Strong turbidity layer

Monitoring of the turbidity (Figure 4. 2) shows a signal evolution from the regional background during the ongoing eruption and

Table 4. 1. Activity and lava flow characteristics associated to CTD-rosette sampling during MAYOBS1 cruise (May 2019), MAYOBS4 cruise (July 2019), and MAYOBS15 cruise (October 2020), Pictures of lava flows taken with the submersible interactive camera system (SCAMPI, Ifremer).

Lava picture	CTD station & sampling date	Site	Activity	Suggested lava age	Observations		
					Visual	Turbidity, heat, density	Chemicals
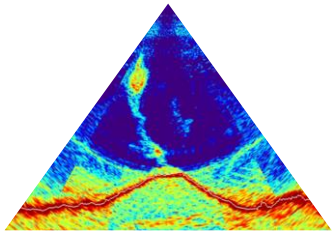 Ship echo souder	MAY01-HY02 (16/05/2019)	Summit	Eruption		Acoustic plume of ~2 km high	Turbidity up to 0.8 NTU Presence of temperature and density anomaly	Maximum concentrations: $^3He_{xs}$ = na CO_2 = 114.6 µmol/L CH_4 = 224.8 nmol/L H_2 = 5992.9 nmol/L
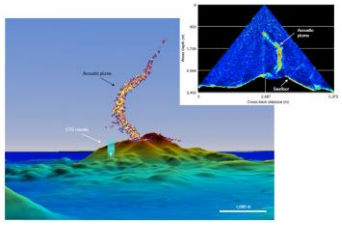 Figure from Feuillet et al., 2021	MAY01-HY03 (16/05/2019)	Northern flank	Eruption		1 km fronm the acoustic plume of ~2 km high	Turbidity up to 1.4 NTU from 2500 to 3000 m, and > 4.9 NTU for depths > 3000 m Presence of temperature and density anomaly	Maximum concentrations: $^3He_{xs}$ = na CO_2 = 264.7 µmol/L CH_4 = 830.5 nmol/L H_2 = 547.9 nmol/L
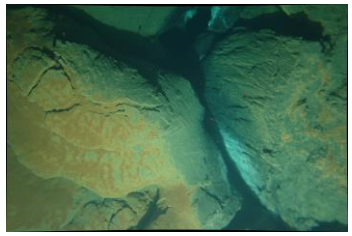	MAY04-HY04 (23/07/2019)	Northern flank	None	May 2019	Already emplaced lava flow, covered by a fine sediment deposit, with evidence for incipient fluid shimmering	Turbidity from 0.3 to 1.6 NTU Absence of temperature and density anomaly	Maximum concentrations: $^3He_{xs}$ = 11.33 fmol/L CO_2 = 32.7 µmol/L CH_4 = 173.8 nomol/L H_2 = 1.3

Lava picture	CTD station & sampling date	Site	Activity	Suggested lava age	Observations		
					Visual	Turbidity, heat, density	Chemicals
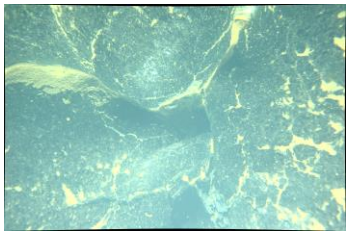	MAY04-HY07 (22/07/2019) MAY04-HY09 (29/07/2019)	West lava flow	Recent	June 18th to July 30th 2019	More recent lava flow with yellowish staining and thin mats of probably microbial origin	Turbidity from 0.3 to 1.6 NTU Presence of temperature and density anomaly	Maximum concentrations: $^{3}He_{xs}$ = 15.44 fmol/L CO_2 = 105.9 µmol/L CH_4 = 777.4 nmol/L H_2 = 39.3 noml/L
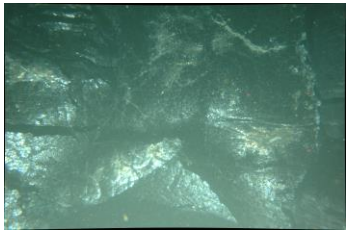	MAY15-HY06 (17/10/2020)	Northwest lava flow	Very recent	May 11th to October 11th 2020	Very glossy black lava	Turbidity up to 0.6 NTU Presence of temperature and density anomaly	Maximum concentrations: $^{3}He_{xs}$ = 5.49 fmol/L CO_2 = 69.6 µmol/L CH_4 = 204.4 nmol/L H_2 = 38.2 nmol/L
	MAY15-HY08 (21/10/2020)	Northwest lava flow	Active flow	May 11th to October 11th 2020	Incandescent lava	Turbidity up to 0.6 NTU Presence of temperature and density anomaly	Maximum concentrations: $^{3}He_{xs}$ = 7.78 fmol/L CO_2 = 53.2 µmol/L CH_4 = 283.6 nmol/L H_2 = 647.6 nmol/L

the lava flow installation. Outside the zone of influence of the volcano (i.e. background hydrocasts), turbidity does not exceed 0.06 NTU. Below 2000 m deep, maximum turbidity remains lower than 0.02 NTU. In May 2019, during the ongoing eruption, the turbidity at the volcano summit features maxima up to 0.8 NTU. However, these levels were not as significant compare to the turbidity values recorded at the northern flank of the volcano, with a maximum of 1.4 NTU between 2500 and 3000 m depth, reaching the saturation value of the sensor (> 4.9 NTU) over the last 200 m above seafloor. Two months later, in July 2019, at the same location in the northern flank, turbidity ranged from 0.3 to 1.6 NTU between 2000 m and the seafloor. Casts performed at the same time above the recent western lava flow shows the same turbidity pattern, with maximum turbidity zone starting at 2250 m deep. October 2020 monitoring highlight weaker turbidity signal measured above the new lava flow, with anomalies from 2500 m and only up to 0.6 NTU (Figure 4. 2).

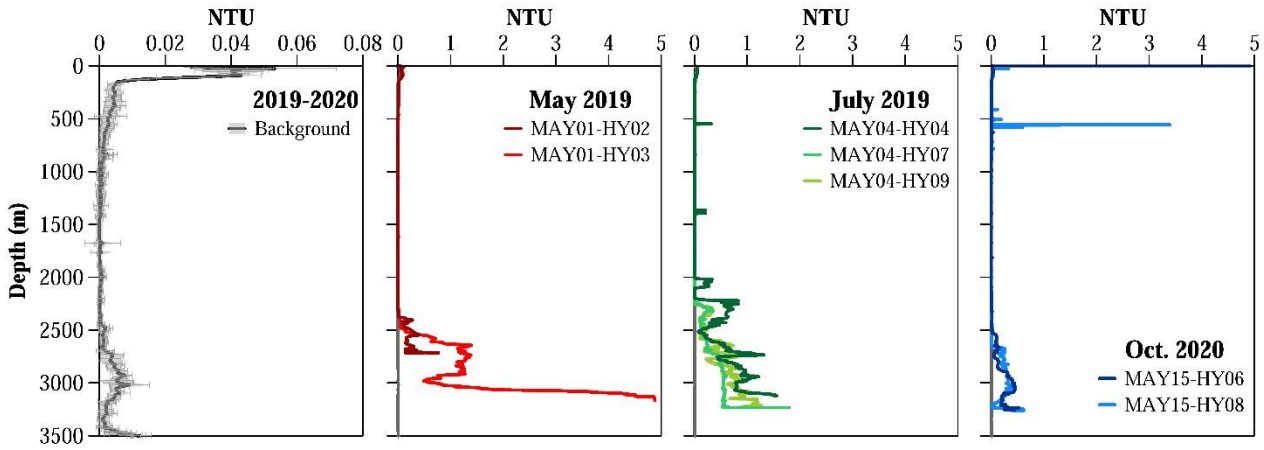

Figure 4. 2. Turbidity profiles determined by background evaluation, and measured for the studied hydrocasts from May 2019, July 2019 and October 2020 (MAYOBS1, MAYOBS4 and MAYOBS15 cruises, respectively). Please pay attention to the differences in NTU scales between the background profile and the others.

4.4.2. Concentration of gases within the water column

4.4.2.1. Helium measurements

From July 2019 to October 2020, $^{3}He_{xs}$ measurements for depths below 2000 m remain well distinct from the background value (~1.5 fmol/L) (Figure 4. 3; Table A 1). The highest $^{3}He_{xs}$ concentration of 15.4 fmol/L was measured in July above the western lava flow (cast MAY04-HY07), at 2924 m depth. Seawater samples taken during the same cruise above the northern flank of the edifice (cast MAY04-HY04) show lower $^{3}He_{xs}$ values of 11.3 fmol/L that were still higher than samples

from October 2020 taken above the northwest lava flow (casts MAY15-HY06 and MAY15-HY08). These two last CTD casts exhibit similar profiles with maximum $^3He_{xs}$ values around 8 fmol/L and 2900 m depth. TDMn concentrations are well correlated with $^3He_{xs}$ (TDMn = 8.97 $\times 10^{-6}$ $^3He_{xs}$, r^2=0.95), while CH_4 concentrations show weaker correlation with ^3He_x (CH_4 = 20.3 $\times 10^{-6}$ $^3He_{xs}$, r^2=0.78). CO_2 concentrations do not show any significant correlation with other gas concentrations (see Figure A 4).

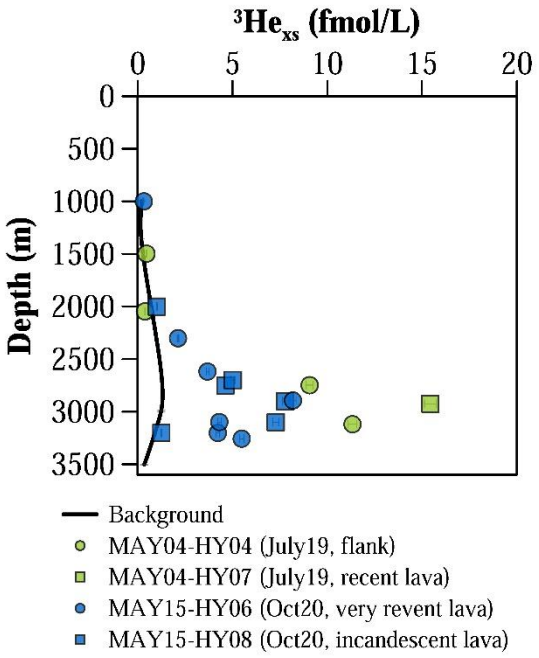

Figure 4. 3. Depth profiles of $^3He_{xs}$ concentration measured at the northern flank of the volcano and above the recent Western lava flow in July 2019 during MAYOBS4 cruise (in green), and above the North West very recent lava flow in October 2020 during MAYOBS15 cruise (in purple). The evaluated background for $^3He_{xs}$ concentrations is represented by the bold line.

4.4.2.2. Concentration of gases above the volcano edifice

During the May 2019 eruption, extremely high H_2 concentrations, up to 6000 nmol/L, were measured at the volcano summit (cast MAY01-HY02), inside the acoustic plume (Figure 4. 4; Table A 2) . Samples from the northern flank exhibit lower, but still strong H_2 concentrations up to 600 nmol/L. In both cases, maxima concentrations are located at remarkably shallow depths within the water column, whereas strong CO_2 and CH_4 anomalies are found deeper, near the seafloor, with maximum concentrations of 265 µmol/L and 830 nmol/L, respectively. The same cast above the northern flank was also investigated in July 2019 (cast MAY04-HY04) where no eruptive activity was identified. Concentrations of H_2 and CO_2 remain at background level whereas CH_4 anomalies were measured up to 180 nmol/L at depth 2250 m and below 2500 m.

4.4.2.3. Concentration of gases above new lava flow emplacements

Strong levels of H_2 were measured above the active lava flow in October 2020 (cast MAY15-HY08), with concentrations up to 650 nmol/L, between 2700 and 3260 m depth (Figure 4. 5; Table A 2). Lower H_2 concentrations, up to 40 nmol/L and near the seafloor, were found above the recent western lava flow in July 2019 (casts MAY04-HY07 and MAY04-HY09) and the very recent

western lava flow from October 2020 (cast MAY15-HY06).

The maxima concentrations in CO_2, from 95 to 106 µmol/L, were measured in July 2019 above the recent western lava flow (casts MAY04-HY07 and MAY04-HY09). Seawater samples from the very recent northwest lava flow site (cast MAY15-HY06) exhibit lower maximum concentrations, up to 70 µmol/L, while concentrations levels above the active northwest lava flow (cast MAY15-HY08) remains within the background envelope.

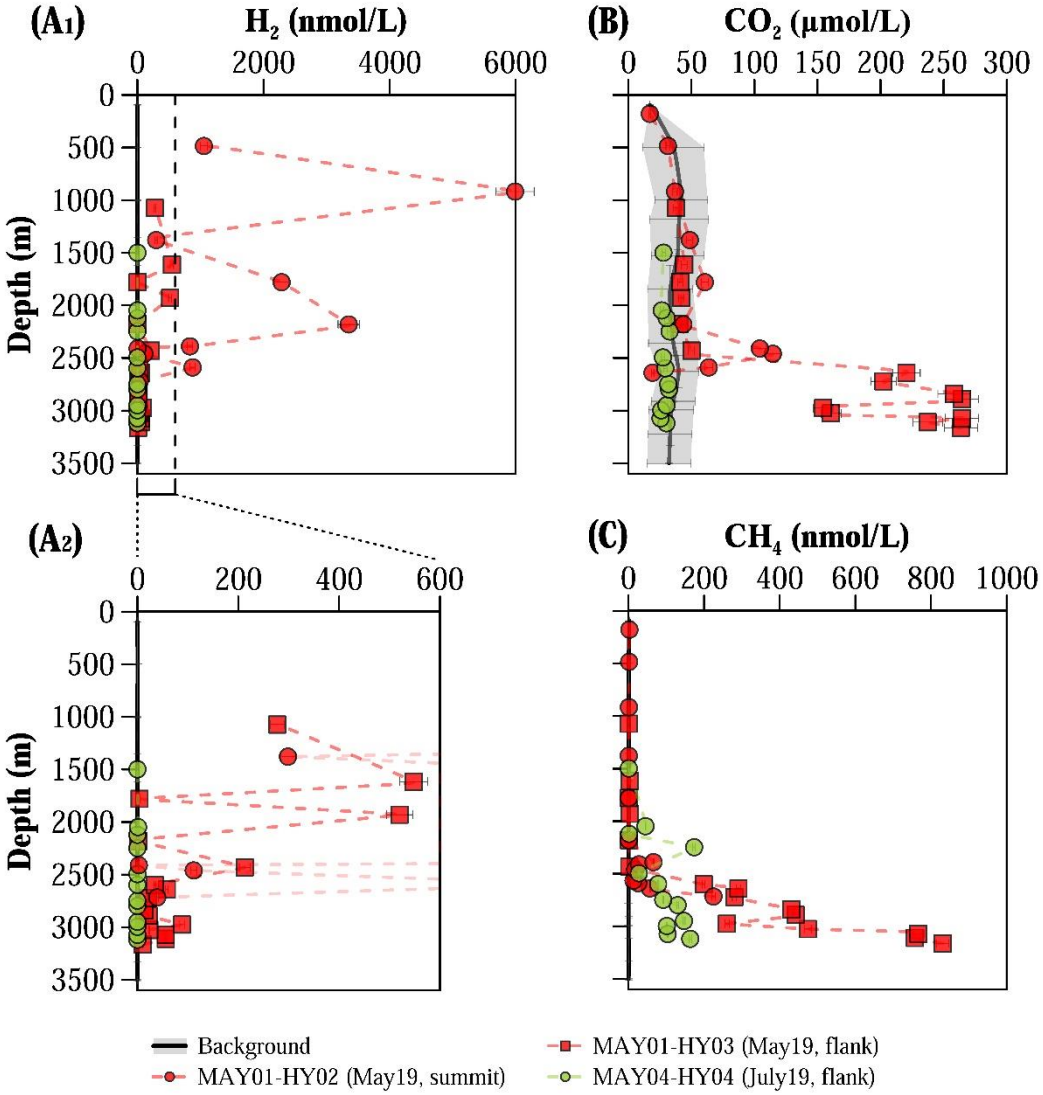

Figure 4. 4. Depth profiles of studied dissolved gases at the eruption site during the May 2019 eruption (in orange) and two months later (in green). MAY01-HY02 cast (from May 2019) was performed at the volcano summit while MAY01-HY03 (from May 2019) and MAY04-HY04 (from July 2019) were sampled at the northern flank of the volcano. (A_1) H_2 profiles; (A_2) Zoom in H_2 profiles for H_2 concentrations from 0 to 600 nmol/L; (B) CO_2 profiles; (C) CH_4 profiles. Evaluated background is represented by the bold line and the grey envelop.

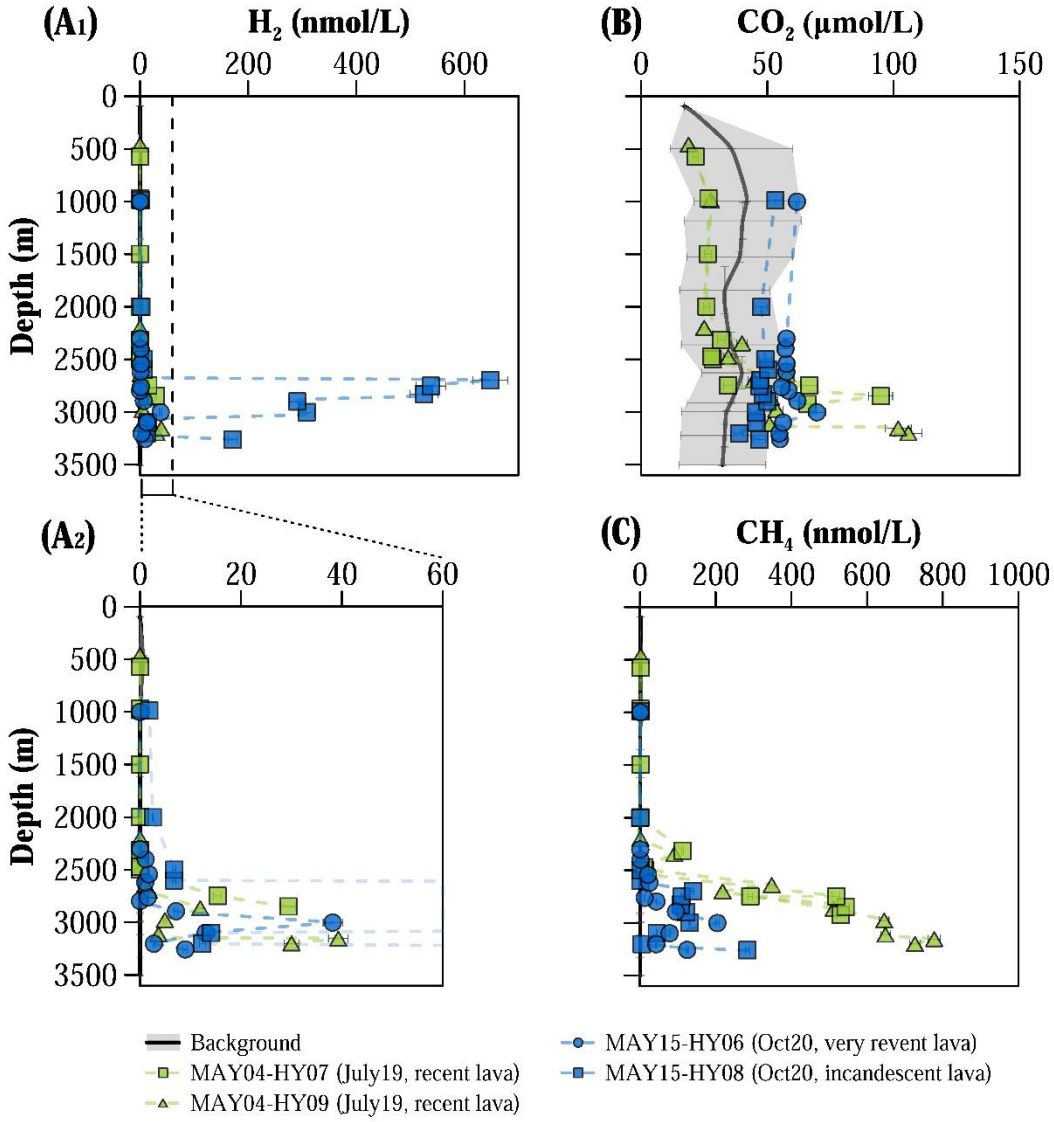

Figure 4. 5. Depth profiles of dissolved gases measured above recent (in green) and very recent lava flow (in purple). MAY04-HY07 (from July 2019) and MAY04-HY09 (from July 2019) casts were performed above the recent Western lava flow while MAY15-HY06 (from October 2020) was sampled above the very recent lava flow from and MAY15-HY08 (from October 2020) above the incandescent lava flow both from the North West site. (A_1) H_2 profiles; (A_2) Zoom in H_2 profiles for H_2 concentrations from 0 to 60 nmol/L; (B) CO_2 profiles; (C) CH_4 profiles. Evaluated background is represented by the bold line and the grey envelop.

Methane concentrations are at their highest level of 780 nmol/L above the recent western lava flow (casts MAY04-HY07 and MAY04-HY09), with an anomaly that seems to increase progressively as it goes deeper from 2500 to 3200 m below sea level. Lower anomalies, up to 280 nmol/L, were measured in October 2020 above the actively forming lava flow (casts MAY15-HY06 and MAY15-HY08).

4.4.3. Carbon isotope composition

Carbon isotope ratios of CH_4 and CO_2 throughout the water column (referred as $\delta^{13}C$-CH_4 and $\delta^{13}C$-CO_2 versus vPDB, respectively) display limited variability through time (

Table 4. 2). Mean $\delta^{13}C$-CH_4 is -34.4 ± 0.6 ‰ (2.s.d, n = 2), while $\delta^{13}C$-CO_2 is -1.0 ± 0.4 ‰ (2.s.d, n = 6). In this study, we will not use the signature of $\delta^{13}C$-CO_2 for data interpretation because, in our water column samples, the CO_2 emitted from the eruption is strongly diluted within the surrounding seawater where the CO_2 is about 30-40 µmol/L. As we do not have endmember values, the signature of the emitted CO_2 is hardly definable. We consider that $\delta^{13}C$-CO_2 values result from the mixing between a magmatic component (-8 ‰ < $\delta^{13}C$-CO_2 < -4 ‰; Sano and Marty (1995)), a marine limestone component (0 ‰; Sano and Marty (1995)), the remineralisation of the organic matter (mean $\delta^{13}C$- CO_2 of the marine organic matter is about-20 ‰; Degens et al. (1968)), and the Indian Ocean seawater composition (0.1 ‰ < $\delta^{13}C$- CO_2 < 1.5 ‰; Liu et al. (2021); Schmittner et al. (2013)).

Table 4. 2. Concentrations of CH_4 and CO_2 and their isotopic carbon composition, $\delta^{13}C$-CH_4 and $\delta^{13}C$-CO_2, in seawater samples taken above recent, very recent and active lava flows from July 2019 and October 2020 cruises.

Sample ID	Depth (m)	CH_4 (nmol/L)	CO_2 (µmol/L)	$\delta^{13}C$-CH_4 (‰, vs. vPDB)	$\delta^{13}C$-CO_2 (‰, vs. vPDB)
MAY4-HY07 (July 2019, Western recent lava flow)					
MAY4-HY07-B3	2924.0	530.4	66.0	-34.8	na
MAY4-HY07-B6	2746.8	518.0	66.7	na	-0.6
MAY15-HY06 (Oct. 2020, Northwest very recent lava flow)					
MAY15-HY06-B1	3257.1	124.8	55.0	na	-0.5
MAY15-HY06-B2	3202.8	42.8	54.7	na	-1.1
MAY15-HY08 (Oct. 2020, Northwest active lava flow)					
MAY15-HY08-B1	3259.2	283.6	46.9	-34	-1.4
MAY15-HY08-B4	3098.8	44.5	45.7	na	-1.3
MAY15-HY08-B7	2899.6	122.4	50.0	na	-1.3

na: not analyzed (due to low gas concentrations). $\delta^{13}C$-CO_2 values are corrected for carbon isotope fractionation between $CO_{2(g)}$ and $CO_{2(aq)}$, at 25°C and seawater salinity, following Eq. 4 from Assayag et al. (2006) and using fractionation factors from Zhang et al. (1995) and CO_2 solubilities from Weiss (1974).

4.4.4. Evolution of pH, Total alkalinity, ΣCO_2, silicates

During the ongoing eruption (May 2019), exceptional pH anomalies in water column up to -0.6 pH unit were measured both at the volcano summit and at the northern flank, for seawater samples taken below 2500 m (Figure 4. 6; Table A 2). Only one comparable anomaly was detected again, in July 2019 above the recent western lava flow, and was located between 3150 m deep and the seafloor (~ 3200 m). The strong pH anomalies observed during the eruption, are associated with a net increase in ΣCO_2, A_T and SiO_2, compare to background levels and to the other studied casts. Maximum ΣCO_2 of 2489 µmol/L has been observed at 2640 m deep, above the volcano summit in May 2019. Similar anomalies up to 2434 µmol/L were also observed during the eruption, above the northern flank but at deeper depths (~ 3160 m). This last anomaly level was found again in October 2020, at the same depth, above the active northwest lava flow. The strongest alkalinity addition happens during the eruption at the volcano summit, with concentrations up to 2700 µmol/L, associate to a strong silicate addition, up to 20 µmol/L.

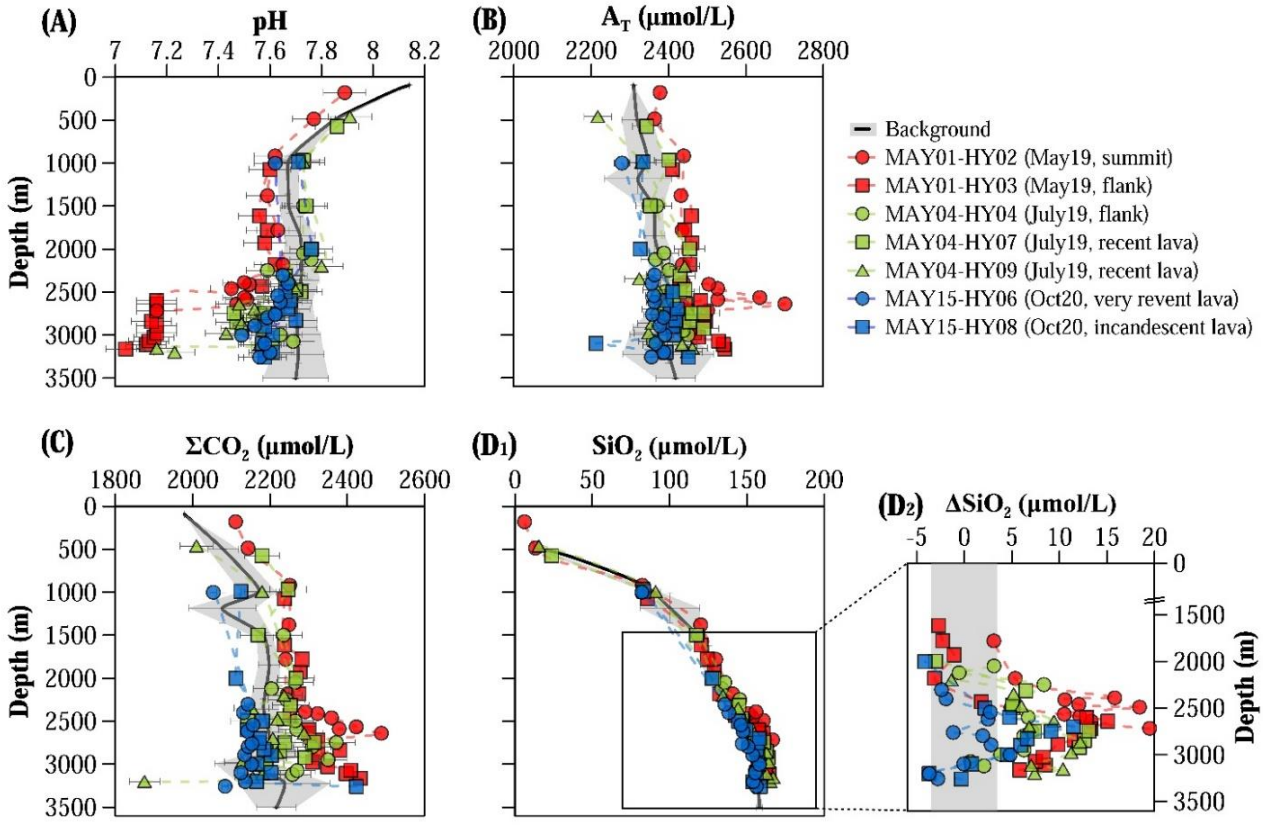

Figure 4. 6. Depth profiles of (A) pH; (B) Total alkalinity; (C) Total CO_2; (D_1) SiO_2 and (D_2) ΔSiO_2 that is the change in SiO_2 from the regional background. Seawater samples from all three cruises from May 2019

(MAYOBS1 in orange), July 2019 (MAYOBS4 in green) and October 2020 (MAYOBS15 in purple) are plotted. Background is represented by the bold line and the grey envelop, determined from two background hydrocasts.

In May 2019, while the strong anomalies are located below 2000 m depth, the entire water column seems to be impacted by the eruption with pH, ΣCO_2 and A_T levels outside the background envelope. July 2019 and October 2020 values, except for the few anomalies mentioned above, show moderate anomalies localized below 2000 m, with an acidification that does not exceed 0.3 pH unit, and ΣCO_2, A_T and ΔSiO_2 up to 2370 µmol/L, 2490 µmol/L and 14 µmol/L, respectively. Overall, anomaly levels were stronger in May 2019 than July 2019, which were themselves stronger than October 2020 levels.

4.4.5. Evolution of TDFe and TDMn

Whatever the sampling date or location, depth profiles of TDMn and TDFe (Figure 4. 7.A and B) show a similar trend with elevated concentrations below 2000 m deep compared to the local background, and with a strong enrichment near the seafloor (i.e. within the last 100 meters). The upper part of the water column presents low TDMn and TDFe concentrations (TDMn < 10 nmol/L ; TDFe < 200 nmol/L), close to background level. Depth profiles of TDMn and TDFe concentrations are indeed well correlated to those of $^3He_{xs}$ and CH_4 (see Figure A 4). Maximum TDMn and TDFe concentrations at the seafloor were of 560 nmol/L and 10575 nmol/L, respectively, found during the May 2019 eruption, above the northern flank of the edifice (at 3160 m deep). Shallower in the water column (i.e., between 2000 m and 3100 m), maximum TDMn and TDFe concentrations above lava flows were up to 160 nmol/L and 2380 nmol/L, respectively. Concentration levels decrease from hydrocasts taken in May 2019 to those taken in October 2020. Nonetheless, maximum TDMn and TDFe concentrations measured during the last cruise were still out of the background envelope with respective values up to 80 nmol/L and 880 nmol/L at 3000 m deep, and up to 120 nmol/L and 1880 nmol/L close to the seafloor (3260 m).

The significant correlation between iron and manganese concentrations allows to define a range of TDFe/TDMn ratios between ~11 and ~27 (Figure 4. 7. C_1 and C_2).). Elevated ratios were measured at deep water layers, close to the seafloor and near the surface of the volcano walls. The maximum TDFe/TDMn ratio of ~27 was found above the northern flank in May 2019 at depths between 3025 and 3110 m (MAY01-HY03), and was measured again in July 2019 at the same location for equivalent depths (cast MAY04-HY04). Within the layer from 2600 m to 2900 m deep, lower values of.

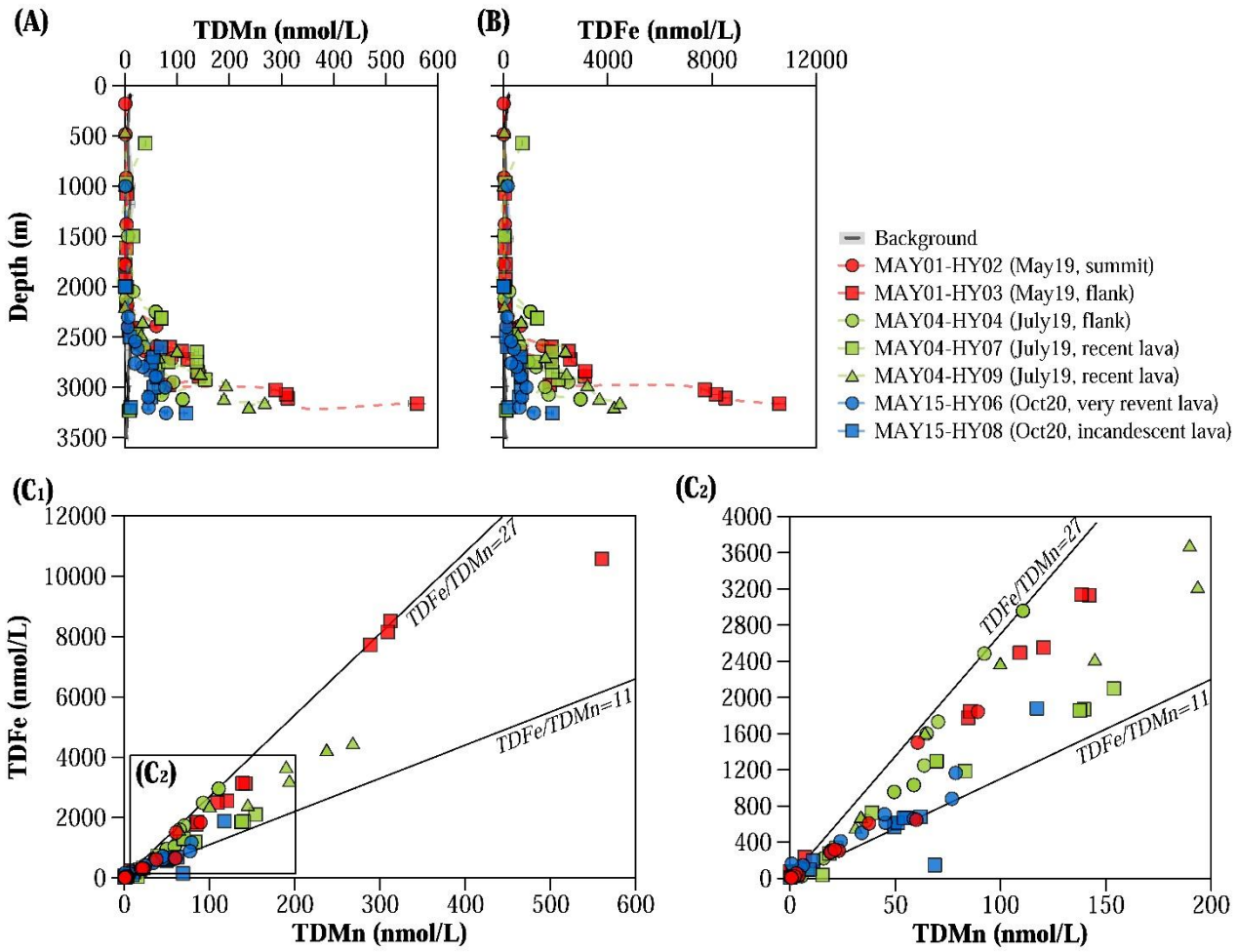

Figure 4. 7. Depth profiles of (A) Total Dissolvable Mn (TDMn) and (B) Total Dissolvable Fe (TDFe). (C) Plots of TDFe vs. TDMn. All hydrocasts performed during the three cruises are represented: May 2019 (MAYOBS1 in orange), July 2019 (MAYOBS4 in green), and October 2020 (MAYOBS15 in purple). (C1) shows the entire data set; (C2) focusses on smaller levels of TDFe and TDMn. Ratios of TDFe/TDMn evolve between 11 and 27 (in mol/mol). TDFe/TDMn ratios were determined for each cast: MAY01-HY02 (17.8, r^2= 0.94); MAY01-HY03 (22.5, r^2= 0.97); MAY04-HY04 (23.9, r^2= 0.98); MAY04-HY07 (13.9, r^2= 0.99); MAY04-HY09 (17.8, r^2= 0.99); MAY15-HY06 (13.4, r^2= 0.97); MAY15-HY08 (12.2, r^2= 0.89).

~22 are measured in May 2019 and ~ 20 in July 2019. Molar ratios from ~27 to ~20 were respectively measured from right above the volcano summit (at ~2720 m) to shallower depths (~ 2590 m) during the May 2019 eruption (cast MAY01-HY02). This ratio also decreases with decreasing sampling depth, with values from ~15 to ~11 for depths between 2500~2400 m. Intermediate ratios between ~14 and ~18 were found above the recent western lava flow in July 2019 (MAY04-HY07, MAY04-HY09) and the very recent northwest lava flow in October 2020 (MAY15-HY06). Although samples for the later hydrocast spread along a ratio of ~16, depletions in TDFe are observed giving a ratio

of ~11 at 2894 and 3002 m. Samples above the active northwest lava flow (cast MAY15-HY08) also exhibit a ratio of ~11, with the deepest sample (3260 m) that highlight a different pattern with a ratio of ~16.

4.5. Discussion

4.5.1. Rapid shift in magmatic fluid contribution

Fluid emissions at the seafloor are a source of helium to the water column, being either primordial (^{3}He) or radiogenic (^{4}He). Mantle and crustal contributions of these fluids are defined by the corrected isotopic helium ratio relative to the atmospheric ratio (Rc/Ra). Mantle MORB-like fluids are usually described by Rc = 8.0 ± 1.5 Ra and ^{4}He/Ne = 1000 (Sano and Fischer, 2013), while fluids originating from the crust present Rc values of 0.02 Ra and ^{4}He/Ne values of 1000 (Wang et al., 2020). Air saturated seawater (ASW) is defined by Rc = 1 Ra and ^{4}He/Ne = 0.226 (Hilton, 1996; Weiss, 1971). Therefore, a corrected ratio (Rc/Ra) close to 8 in seawater would imply that He source is dominated by a mantle-derived contribution with negligible assimilation of crust-derived materials which may occur during magma aging and/or interactions with ^{4}He-rich crustal rock, also referred as country rock (Hilton et al., 1993).

During the main eruptive event in May 2019, the magmatic contribution to the water column remains unknown as no helium isotope measurement were made at this time. However, a recent geochemical study of volcanic rocks from the volcano shows no evidence for crustal material assimilation, which could be explained by a direct and fast ascent of magma from the deep reservoir to the surface (Berthod et al., 2021). We however observe a change in magmatic fluid contribution (Figure 4. 8) between seawater samples taken above the recent western lava flow in July 2019 (casts MAY04-HY04 and MAY04-HY07) and those taken above the northwest active and very recent lava flow from October 2020 (casts MAY15-HY06 and MAY15-HY08). Extrapolating Rc values in our samples using the linear regressions in Figure 4. 8. A, down to a null Ne/He ratio, we approximate Rc_{fluid} values. Such extrapolated Rc_{fluid} values of 6.46 Ra in July 2019 suggest a higher crustal (i.e. radiogenic) contribution compared to October 2020 (extrapolated Rc_{fluid} = 8.52 Ra). Evidence for significant crustal material assimilation in the magmatic source in July 2019 is supported by petrogeochemical studies that have also shown a more crustal signature in those lavas. Authors explain this signature by the sampling of an evolved magma batch (i.e. that has assimilated crustal material during its aging), located on the magma path, during the magma ascent from the main reservoir to the seafloor (Berthod et

al., 2021). In October 2020, the return to less radiogenic (more primordial) helium signatures might be linked either to (i) a new magma path with direct ascent from the main reservoir to the seafloor, as seen in May 2019, or (ii) the passage of the magma through the same conduit as in July 2019 but with the secondary magma reservoir empty or newly recharged, and therefore no crustal assimilation (Berthod et al., 2022).

The measured helium water column composition yield the same range of Rc/Ra as Mayotte gaseous emissions in Petite-Terre (Rc/Ra = 6.4-7.5; (Liuzzo et al., 2021)) and Indian Ridge hydrothermal fluids (Rc/Ra = 7.8-8.0; (Gamo et al., 2001; Kawagucci et al., 2008)). Assuming that dissolved gas sources from the volcano exhibit a mantle MORB-like signature of Rc = 8.0±1.5 Ra (Sano and Fischer, 2013), we estimate from the isotopic helium ratios that the level of crustal contamination could be between 20~35 % in July 2019 (Figure 4. 8). However, this interpretation does not take into account the possible influence of the La Réunion hotspot where magma sources present Rc/Ra with a range from 12 to 14.5 (Boudoire et al., 2020; Marty et al., 1993). At this stage, as it was suggested by the recent studies (Famin et al., 2020; Lemoine et al., 2020; Michon, 2016; Tzevahirtzian et al., 2021), we hypothesize that there is no influence of this hotspot on Mayotte submarine eruption.

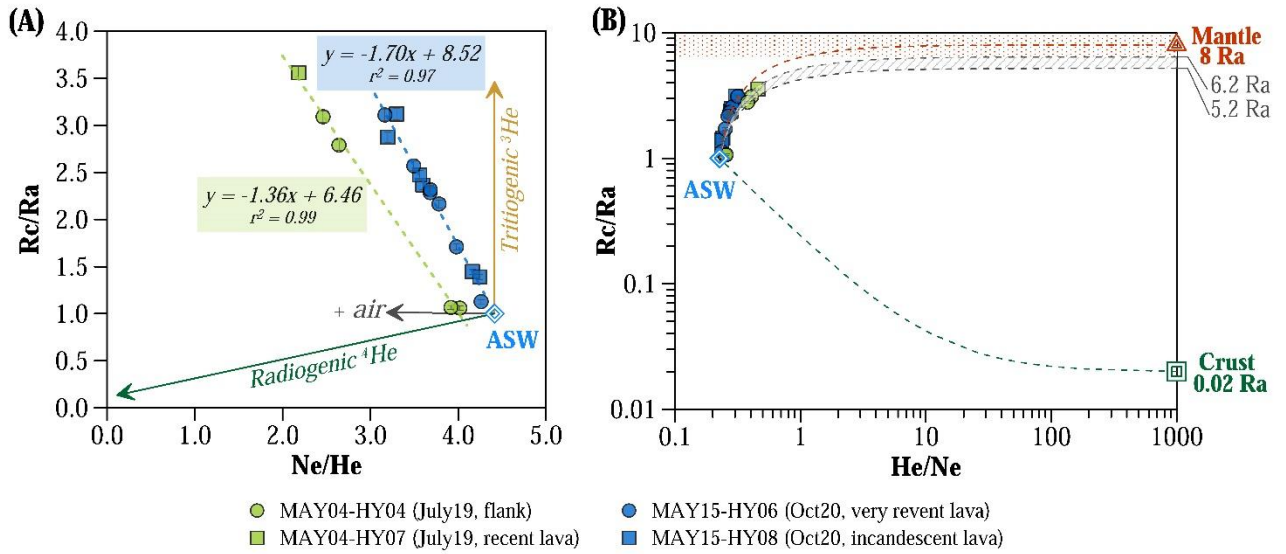

Figure 4. 8. Rc/Ra ratio versus Ne/He (A) and He/Ne (B) for seawater samples from July 2019 (MAYOBS4 in green) and October 2020 (MAYOBS15 in purple). ASW dot is the Air Saturated Water value. (A) The blue arrow shows helium enrichment due to air contamination, the green arrow would represent the addition of radiogenic ^{4}He, the gold arrow the addition of tritiogenic ^{3}He (from tritium radioactive decay). Our seawater samples are mainly driven by the addition of magmatic ^{3}He. (B) ASW, mantle and crust are isotopic ratios for corresponding end-members. ASW: Rc/Ra = 1, ^{4}He/Ne = 0.226 (Weiss, 1971; Hilton, 1996); upper mantle (MORB-like): Rc/Ra = 8 ± 1.5, ^{4}He/Ne = 1000 (Sano and Fischer, 2013); crust: Rc/Ra = 0.02, ^{4}He/Ne = 1000

(Wang et al., 2020). Dashed plots are the calculated binary mixing curves between the different endmembers. The uncertainty on Rc/Ra and He/Ne measurements is lower the size of the symbols.

4.5.2. Origin of contrasted behavior of gases

Using seafloor observations (SCAMPI pictures, Table 4. 1) and turbidity signals (Figure 4. 2), we interpret the geochemical anomalies in the water column according to two parameters: the freshness of lava, i.e., indicating the timing between lava flow emplacement and water column sampling; and the potential seawater-rock-lava interaction and their associated fluid emissions.

4.5.2.1. Ongoing eruption and active lava flow

4.5.2.1.1. Elevated H_2 levels

Exceptionally high H_2 concentrations were measured during the eruption (inside the acoustic plume, in May 2019) and above active lava flow (in October 2020), up to 5993 nmol/L and 648 nmol/L respectively.

Hydrogen is usually described as an immediate tracer of the eruptive activity and provides strong evidence for on-going or very recent reactions between seawater or magmatic water and molten or extremely hot rocks (Baker et al., 2011; Baumberger et al., 2020; Baumberger et al., 2014; Resing et al., 2011). Indeed, in marine environments, H_2 is produced from various sources, involving abiotic and biotic processes (Wang et al., 2023; Worman et al., 2020). In volcanic environments, with large magma inputs such as fast-spreading mid-ocean ridges or intraplate or hotspot volcanoes, hydrogen may originate from magmatic degassing as a result of magma crystallization, through the oxidation of ferrous iron contained within the magma by reduction of dissolved water (Hekinian et al., 1973; Klein et al., 2020; Symonds et al., 1994). H_2 may also be produced through the interaction between molten lava and seawater (Sansone and Resing, 1995), and more generally through the reduction of water during the oxidation of Fe(II)-bearing rocks (Truche et al., 2020). Indeed, some of the H_2 we observe might come from high temperature basalt alteration. During the high-temperature (~350 to 400 °C) alteration of oceanic crust by seawater, the majority of ferrous silicates alter to ferrous iron minerals (e.g., chlorite, amphibole), however, a small number, alter to ferric-bearing minerals and produce H_2. Other major sources of hydrogen in the ocean include the radiolysis of water due to radioactive decay of U, Th and K; crustal weathering or reaction of water with surface radicals during fracturing of silicate-bearing rocks (Klein et al. 202, Wang et al, 2023), all occurring in very distinct geological settings than ours. Decomposition of organic matter in sediment-hosted systems has also

been reported, but is very unlikely as sediment both in the lagoon and offshore Mayotte are mainly carbonateous with very low organic carbon contents (Dullo et al., 1998; Zinke et al., 2003b).

Production of hydrogen through serpentinization of ultramafic materials (i.e. hydration reactions of olivine and pyroxene, mostly) is very common in submarine settings. This mechanism is generally considered to be the main H_2 production route during hydrothermal circulation at slow and ultra-slow spreading ridges (e.g. Charlou et al. (2010)). The geological context here is of course very distinct and we did not find evidence, neither from dredge operations nor from direct seafloor observations, that would support exhumation of ultramafic materials. Although we cannot exclude a mechanism in which seawater is interacting at greater depth with ultramafic rocks, it should be noted that H_2 generation through serpentinization likely requires a mature hydrothermal system, which seems to be in contradiction with the young age (< 1 years) and the transient nature of the H_2 anomalies observed in the water column.

We therefore propose that H_2 is produced both from magmatic degassing and from water reduction by iron-bearing compounds in the extruding high temperature lava during its interaction with seawater, following the reaction (Baker et al., 2011; Perfit et al., 2003; Worman et al., 2020): $2(FeO)_{magma} + (H_2O)_{seawater} \rightarrow (Fe_2O_3)_{rock} + H_2$. Following its production, H_2 is likely to be consumed by oxidation through abiotic reactions or microbial processes, usually within the timespan of a few hours to a few days (McLaughlin-West et al., 1999; Worman et al., 2020).

Clague et al. (2009) documented submarine eruptions throughout the Pacific Ocean at depths from 1400 to 3800 m, and reported that an almost unfailing characteristic of submarine eruptions is the production of glassy pyroclastic fragments that are remnants of bubbles of magmatic gas. Also, Baker et al. (2011) showed that the production of pyroclastic fragments promotes extensive lava-seawater interaction during the eruption. At Mayotte submarine volcano, very fresh basanitic pillow lavas were dredged on the northeastern flank of the edifice and contain significant amounts of vesicle-trapped volatiles (Berthod et al., 2021; Feuillet et al., 2021). Such vesicular and gas-rich rocks, referred as 'popping rocks', may therefore provide larger effective surface area for seawater-lava interactions.

Additionally to the gas-rich characteristic of the rocks, the extremely high concentrations of H_2 probably testify for the explosive character of the Mayotte submarine eruption, as previously proposed by Baumberger et al. (2014) during the West Mata eruption and by Baumberger et al. (2020) during the Puipui

eruption. Submarine eruptions may generate massive megaplumes, of several kilometers height, as a the result of extremely high rates of energy discharge, including massive heat and magmatic and/or crustal fluids transfer (Baker et al., 2012; Pegler and Ferguson, 2021). Large fluxes of H_2 may have therefore been discharged into the water column as a result of a gas jet formation.

4.5.2.1.2. Elevated CO_2 and CH_4 levels

During the eruption, elevated concentrations of CO_2 and CH_4 were released, up to 265 µmol/L and 821 nmol/L, respectively. This positive correlation between CO_2 and CH_4 values might suggest a magmatic origin for both these gases. Carbone dioxide is most likely sourced from lava outgassing (Craig and Lupton, 1981), while methane may be present as a magma volatile or could reflect a production through Fischer-Tropsch-type reactions ($CO_2 + 4H_2 \rightleftharpoons CH_4 + 2H_2O$) associated with water-rock interactions (Craig, 1953; McCollom, 2013; Zolotov and Shock, 2000).

The carbon dioxide is one of the main volatiles dissolved in magma along with H_2O and SO_2. During the magma ascent, gas bubbles can segregate from the melt at different depths, so the volatile components fractionate according to their solubilities. The composition of the exsolved fluids will thus change as a function of the pressure-related solubility of each volatile species. Being the CO_2 less soluble in the melt than water, it will be exsolved at deeper levels (Métrich and Wallace, 2008). Because the exsolved fluids are less dense than the melt they ascent faster to the surface, leading to fluid emissions with a very high concentration in a specific volatile, that may be varying in time and space. Thus, CO_2 may be generated through a separate CO_2-rich gas phase directly degassing from the magma chamber, as it was observed at NW Rota-1, where CO_2-rich gas bubbles exsolve from slowly erupting lava (Chadwick et al., 2008). When the CO_2-rich gas phase encounters circulating seawater during its ascent through the volcano edifice, a two-phase mixture of CO_2–rich gas and an aqueous phase undersaturated with CO_2 can coexist as buoyant gas bubbles ascend through and exchange with the aqueous phase (Lupton et al., 2008). The behavior of CO_2 released into seawater will be governed primarily by the pressure (i.e., depth) and temperature of the water entity into which it is released, and to a lesser extent its salinity. Taking into account the salinity and temperature profiles of seawater obtained in the area with our CTD casts, CO_2 will become liquid at pressures of 45–50 bar, corresponding to water depths of ~450–500 m (Figure 4. 9). Above ~2700 m depth, density of liquid CO_2 is lower than the seawater density. When released into the water column at this depth or shallower, CO_2 will hence rise towards the surface. On the

contrary, the CO_2 emitted below ~2700 m depth will likely sink to the ocean floor. This threshold of 2700m corresponding to the summit depth of the Fani Maore volcano, we suggest that a significant amount of CO_2 emitted during the eruption sank and generated the high concentrations we observe at the bottom and the flanks of the volcano (Figure 4. 9). Eruptive megaplumes may involve the rapid evacuation of existing intracrustal fluid reservoirs (Baker et al., 2012; Lupton et al., 1999; Pegler and Ferguson, 2021). Such syn-eruptive release of mature hydrothermal fluids enriched in methane are usually observed in extensional tectonic settings, which promotes seafloor hydrothermal circulation and may be significantly enhanced by dyke intrusions (Curewitz and Karson, 1998; Delaney et al., 1998; Pegler and Ferguson, 2021). However, we did not find any signs of pre-eruptive hydrothermal active venting on the seafloor images we collected (no vent fauna, no sulfide deposits, no smokers, only surficial oxy-hydroxydes iron deposits on some of the freshly extruded lava flows). Although we cannot rule it out, it seems therefore unlikely that the concurrent release of significant crustal fluids as the generation process for methane was solely responsible for the elevated anomalies we observed during the eruption. Given the low organic matter content of the sediments in the area (Manoux et al., 2023), thermogenic cracking of organic matter during the magma ascent might not act as a significant source of methane released during the eruption.

A common pathway invoked for the formation of hydrocarbons and other organic compounds in geologic environments is the Fischer-Tropsch synthesis (McCollom, 2013). As originally described, Fischer-Tropsch type chemical reactions refer to the surface-catalyzed reduction of CO by H_2 in gas mixtures. In geological systems, dissolved CO_2 may be considered the primary carbon source for such abiotic organic synthesis (McCollom, 2013; Zolotov and Shock, 2000). Yet, despite a thermodynamic thrive for CO_2 reduction into CH_4 in conditions of hydrothermal circulation, it is now recognized that the process is likely slow and inhibited by strong kinetic barriers. For the process to overpass these kinetic barriers and produce significant amount of reduced carbon compounds such as methane (McCollom, 2016; McDermott et al., 2015), it may requires the presence of metal catalysts or of a co-existing H_2-rich gas phase (McCollom, 2016). Although speculative at this stage, we note that one or both of these conditions could be met in the case of the Fani Maoré eruption. First, the presence of large TDFe anomalies in the water-column supports sustained interactions of seawater with Fe-bearing phases that could act as catalyst for a Fischer-Tropsch type reaction. On the other hand, given the depth of Fani Maoré eruption, liquid and gaseous phases probably coexisted. Taken

together, we thus suggest that Fischer-Tropsch type reaction is a potential mechanism for the formation of methane observed in the water column.

4.5.2.1.3. Why such a dichotomy between H_2 versus CO_2, CH_4 profiles at the edifice?

During the eruption, concentration profiles of CH_4, CO_2 and H_2 were studied at two locations in the vicinity of the volcano: at the summit and above the northern flank (Figure 4. 4). From the water surface down to 2500 m depth, CH_4 and CO_2 concentrations are similar to those found in the local background. Below 2500 m, concentrations of both CH_4 and CO_2 increase, with maximum values at the seafloor. However, H_2 displays the opposite trend; very high anomalies (up to 6 µmol/L) are seen at depths above 2500 m while H_2 concentrations oscillate between 11 and 56 nmol/L below 2500 m.

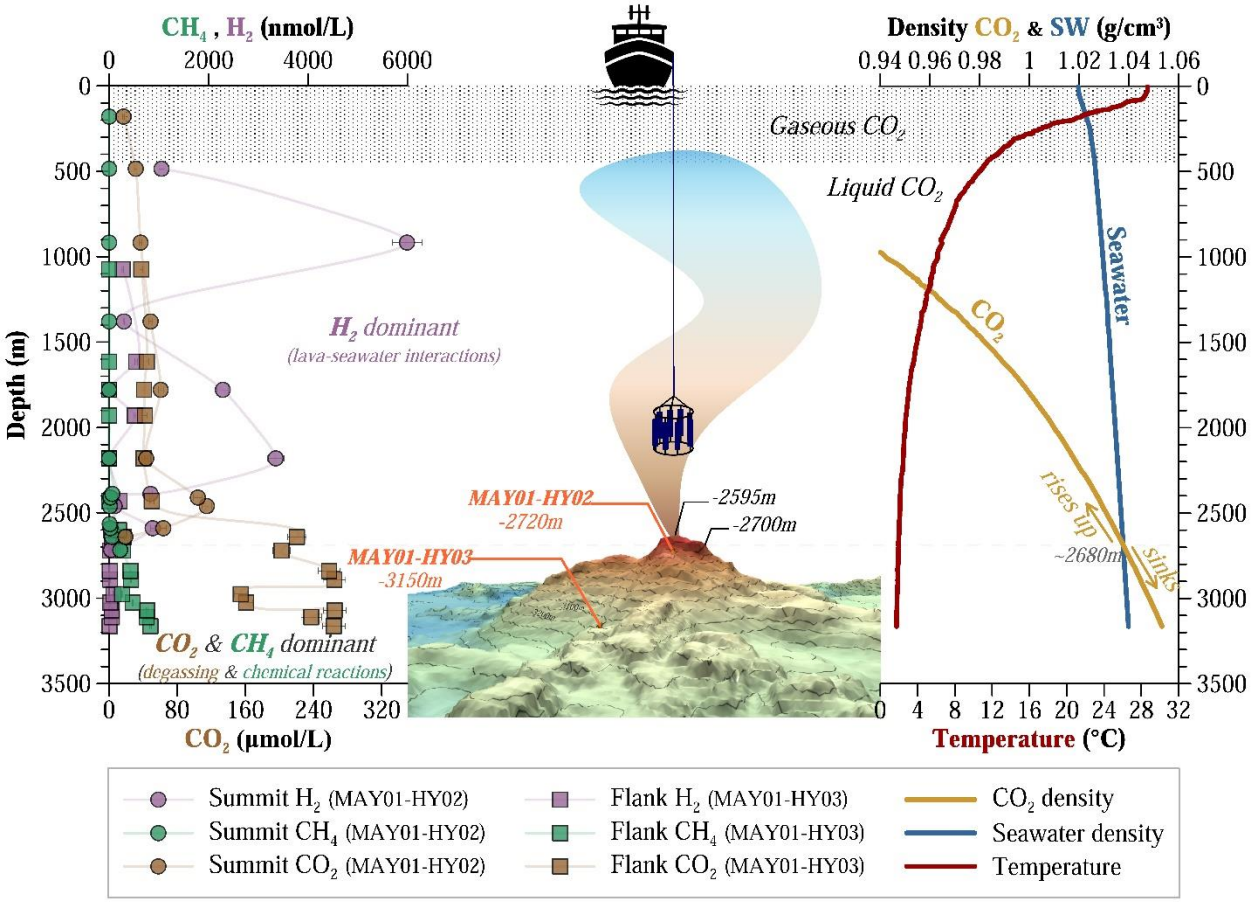

Figure 4. 9. Composite representation of gas concentration profiles, water column physical parameters and bathymetry of the Fani Maoré Seamount during the May 2019 eruption (MAYOBS1 cruise). Profiles of H_2, CO_2 and CH_4 were measured at the summit and above the northern flank of the volcano. Pure-CO_2 density changes with the water column depth at the volcano was calculated using Span and Wagner's equation of state (Span and Wagner, 1996). Standard-seawater density profile was calculated from CTD data recorded at both sites and Archer's thermodynamic model for NaCl (Archer, 1992). Temperature profile was extracted from

CTD data recorded at both sites. 3D representation of the volcano edifice was made using 30m-resolution bathymetry (vertical exaggeration x2), with counter lines at 50m intervals (Geo-Ocean (Ifremer), 2022).

To our knowledge, such dichotomy in gas behavior between H_2 on one hand and CO_2 and CH_4 on the other hand, has never been reported before in a context of deep submarine eruption. A plausible explanation is related both to different processes of gas generation and to the change in density equilibrium between liquid CO_2 and seawater around 2700 m depth (Figure 4. 9):

- On one hand, H_2 is generated as a free gas during lava quenching, i.e. at the exit point of the magma at the summit (2600~2700 m). H_2 dissolves in seawater and rises the water column, probably encouraged by the formation of a gas jet (Cahalan and Dufek, 2021). We observe no anomalies in potential temperature, potential densities (Figure A 2) nor turbidity anomalies (Figure 4. 2) between 2500 and 1300m although we do see some high dissolved H_2 concentrations randomly dispersed. Such features suggest that we did not capture the full tridimensional structure of the eruptive plume at these depths on this one cast (Pegler and Ferguson, 2021). The lower H_2 concentrations measured between 2500-1300 m compared to the very elevated one at 1000m may therefore simply result from the CTD-rosette emplacement outside the plume due to local currents and the turbulent 3D plume behavior.
- On the other hand, CO_2 is discharged through magma degassing, either from the exit point at the summit, from lavas flowing down the volcano flanks, or from fractures on the volcano flanks. Since the seafloor around the Fani Maoré new volcanic edifice is around 3400-3600 m depth and the top of the volcano is around 2600-2700 m, CO_2 emitted will likely sink to the ocean floor instead of rising up to the surface. At the same time, we expect that H_2 is generated by lava-seawater interactions from the lavas flowing down the volcano flanks. As its concentration does not exceed 56 nmol/L below 2500 m, we suggest that H_2 is consumed by the Fischer-Tropsch-type chemical reaction to generate CH_4 through the reduction of CO_2 (1 moles of dissolved CO_2 react with 4 moles of H_2). This reaction seems the most appropriate to explain why H_2 is lower at the bottom of the water column than at shallower depths. However, in this study, we are not able to estimate the amount of methane generated through this reaction. We discard microbial consumption of hydrogen as a significant process as the rates at stake and their

distribution in seawater cannot explain the discrepancy of hydrogen concentration over depth (Lappan et al., 2023).

Therefore, we suggest that the dichotomy in the generation processes of the various gases and the very specific settings of the Fani Maore volcano create a unique environment. At this stage of the eruption, past the initial eruptive outburst, lava are being emitted effusively from the summit down to the flanks (no explosive activity registered as turbidity anomalies are limited to 2500m ; Figure 4. 2) : CH_4 will likely be associated with the liquid CO_2 released by the volcano whereas H_2 will be released as a free gas in the water column. This would explain the high concentrations in methane found below 2500 m, while H_2 tends to stay in the gas phase and rises to the surface giving place to the H_2 anomalies aforementioned.

4.5.2.2. Continued lava flow

Above the northern flank, two months after the eruption, CO_2 and H_2 concentrations are back to background levels while CH_4 concentrations remains elevated (100-200 nmol/L, Figure 4. 5). Water column above the recent western lava flow (MAY04-HY07, MAY04-HY09) exhibit CH_4 anomalies up to 777 nmol/L (Figure 4. 5), which is more than twice the concentrations found above the very recent and active northwest lava flow for which maximum concentration was 284 nmol/L (Table 4. 1).

Above the northern flank, two months after the eruption, CO_2 and H_2 concentrations are back to background levels while CH_4 concentrations remains elevated (100-200 nmol/L, Figure 4. 5). Water column above the recent western lava flow (MAY04-HY07, MAY04-HY09) exhibit CH_4 anomalies up to 777 nmol/L (Figure 4. 5), which is more than twice the concentrations found above the very recent and active northwest lava flow for which maximum concentration was 284 nmol/L (Table 4. 1).

In submarine volcanic systems, CH_4 is generally produced through hydrothermal circulation that is initiated after an eruptive event. Buck et al. (2018) have compiled maximum CH_4 concentrations measured in hydrothermal plumes found above Ahyi, NW Rota, West Mata, Nikko, Daikoku and Kasuga-2 and concentrations do not exceed 22 nmol/L (Baumberger et al., 2014; Buck et al., 2018; Resing et al., 2009; Resing et al., 2011). The low H_2 levels (i.e. only up to 40 nmol/L) measured above the lava flows compared to those measured right during the ongoing eruption may be due to the weakening of the lava-seawater interaction processes and to the rapid oxidation and consumption of H_2 produced through these processes (McLaughlin-West et al., 1999; Worman et al., 2020). Moreover, the elevated concentrations

of CH_4 coupled with low concentrations of H_2 are consistent with a sudden release of subsurface fluids in which microbial processes could account for elevated CH_4 and low H_2. An alternative source for CH_4 is thermogenic decomposition of buried organic matter following the eruption and/or subsurface methanogenesis (McLaughlin-West et al., 1999).

CO_2 was the dominant dissolved gas measured above the western recent lava flow (MAY04-HY07 and MAY04-HY09, July 2019), and the northwest very recent (MAY15-HY06, October 2020) and active (MAY15-HY08, October 2020) lava flows (Figure 4. 5). Such emissions of CO_2 may originate from different sources such as mantle, oceanic crust, sedimentary carbonates and organic matter (de Hoog et al., 2001; Marty et al., 1989; Resing et al., 2007). The mean molar ratio of CO_2 to ^3He measured at the vicinity above recent (MAY04-HY07), very recent (MAY15-HY06) and active (MAY15-HY08) lava flows is at $6.82 \pm 2.32 \times 10^9$, which is elevated compared to the ratio found at the NW Rota-1 submarine volcano ($3.25 \pm 0.07 \times 10^9$, Resing et al. (2007)) or more generally at global magma outgassing at mid-ocean ridges (2×10^9, Marty and Jambon (1987)). As it is also outside the range of mid-ocean ridge hydrothermal fluids (0.7 to 4.6×10^9, Resing et al. (2004)), we argue that a hydrothermal fluid circulation is unlikely, or hasn't been emplaced yet, consistently with the very young age of the volcano. Our value is however within the range of submarine arc volcanoes (12×10^9 at Suiyo seamount, Tsunogai et al. (1994) ; 10×10^9 at NW Eifuku seamount, Lupton et al. (2006)) and subaerial arc volcanoes (about 6 to 34×10^9, Sano and Marty (1995)). Our value is also very similar to vent fluid value at Loihi seamount, where $CO_2/^3He$ ratio changed rapidly (i.e. increased) following a seismic crisis (Hilton et al., 1998). As it was demonstrated by Marty et al. (1989) the apparent excess of CO_2 relative to ^3He cannot be entirely due to the physical or chemical fractionation occurring during the transfer of gases from the magmatic source to the surface. Hilton et al. (1998) have shown that the degassing of an alkalic magma may explain $CO_2/^3He$ ratios (measured in fluids) higher than the initial magma ratio due to the solubility behavior of CO_2 and He in magmas of different chemistry. In low-SiO_2 alkali basalts, the solubility of CO_2 is significantly higher than in tholeiites, while helium solubility decreases with decreasing SiO_2. Thus, volatiles residual after a degassing event will have higher $CO_2/^3He$. A possible origin for excess carbon is the contribution (i.e. contamination) of carbonaceous sediments being a prominent source of CO_2 under the appropriate T-P-f_{O2} conditions (Marty et al., 1989). However, even if the contribution of crustal gases was more elevated for July 2019 samples than for the October 2020 samples, we

do not observe a significant change in $CO_2/^3He$ values between those both periods. Therefore we attribute the excess in CO_2 relative to ^3He to an enrichment of CO_2 originating likely from carbonates and organic matter of the thick sediment cover between the main volcanic layer, below the new volcano, and the top of the crust (2.2-2.5km, Masquelet et al. (2022a)).

The $\delta^{13}C\text{-}CH_4$ signatures of -34 ‰ in the water column are rather ambiguous and can point to both abiotic or thermogenic signature of methane (Etiope and Sherwood Lollar, 2013). Indeed, methane isotope signature observed in hydrothermal fluids from mid-ocean ridge regions, like the East Pacific Rise or Mid-Atlantic Ridge, generally display $\delta^{13}C\text{-}CH_4$ values between -8.6 -23 ‰ and ((Kawagucci et al., 2008; Sano and Fischer, 2013; Wen et al., 2016), and references therein). Our values are however more similar to warm vents and gas bubbles from back arc submarine volcano where $\delta^{13}C\text{-}CH_4$ ranging from -24.8‰ to -41.4‰ have been reported and suggest a primarily thermogenic origin for CH_4 (Michel et al., 2018).

With values of $\delta^{13}C\text{-}CH_4$ = -34.8 ‰ and -34.0 ‰ measured in July 2019, and October 2020 respectively, the stable carbon isotopic composition of methane measured in the water column above the Fani Maoré volcano falls in the range of -75‰ to -15‰ corresponding to early mature and very late mature thermogenic gases, but also within the -50‰ to +10‰ abiotic generation range (Milesi et al., 2020; Milkov and Etiope, 2018). Milkov and Etiope (2018) demonstrated that thermogenic gases are often mixed with microbial gases (in sediments at diagenetic to early catagenetic stages) and abiotic gases (e.g., in geothermal volcanic plumbing systems involving organic-rich rocks). The low organic carbon content of the sediment does not support extensive thermogenic generation of methane through magma/sediment interaction during the ascent. However, the volcano does lie above ~2.2-2.5 km thick sediment cover (Masquelet et al., 2022b), which depending on the magma ascent rate and conditions, may release enriched methane mature fluids of thermogenic signatures (Etiope and Sherwood Lollar, 2013; Pegler and Ferguson, 2021). With the current dataset, it is not possible to favor an abiotic over a thermogenic origin of CH_4.

4.5.3. Carbonate system response to high CO_2 discharges

Submarine volcanoes discharge acid-rich fluids (e.g. sulfuric acid originating form SO_2 disproportionation), CO_2 rich-fluids (e.g. magma CO_2 volatile), and fluids rich in CO_2 and alkalinity (e.g. mixture of magmatic volatiles and products of water/rock interactions). The addition of CO_2 within the water column results in acidification of the seawater, whereas the addition of alkalinity

increase the pH. When both CO_2 and carbonate alkalinity are added, pH decrease but less than when only CO_2 is added (Resing et al., 2009). Representation of the pH-CO_2 relationship as $\Delta\Sigma CO_2$ against ΔpH (delta values being the difference from the regional background) (Figure 4. 10) displays the three trends that might explain the significant water column acidification (Figure 4. 6): (1) CO_2 addition, (2) CO_2 and carbonate alkalinity addition, (3) mineral acid addition.

Samples taken above the northern flank during the eruption, between 2250 m and 2750 m depth (cast MAY01-HY03), exhibit a strong decrease in pH (-0.6 pH unit) that seems to be explained by an addition of CO_2 (showed by the red line, Figure 4. 10). According to the gas behavior study, at these pressure and temperature conditions (4.5.2.1.), we suppose that the CO_2 was mainly in the form of liquid CO_2 rising up through the water column. The absence of carbonate alkalinity addition suggests a limited fluid-rock interaction. Indeed, ΣCO_2 and A_T anomalies are just above the background level and the TDFe/TDMn ratio is about 2. Rather than originating from fluid-rock interaction, the significant anomalies in silicates we observe at the volcano northern flank (ΔSiO_2 up to 15 µmol/L) are likely due to basalt alteration at elevated temperature conditions. Indeed, as demonstrated by Resing et al. (2009), the presence of CO_2 without alkalinity suggests that the CO_2 does not react extensively with the host volcanic rocks to form alkalinity. Limited fluid-rock interaction is also consistent with the presence of pure CO_2 in liquid and clathrate forms that will limit CO_2 dissolution in seawater and facilitate CO_2 ascend in the water column due to density differences above 2700m (Figure 4. 9), thus preventing extensive surface reaction with the volcanic rocks.

Deeper than 2750 m above the northern flank, for the same cast (MAY01-HY03), pH is mainly controlled by CO_2 addition but shows a potential carbonate alkalinity addition that suggests rock weathering processes. This hypothesis is supported by the observation of moderate ΣCO_2 and A_T anomalies, the high TDFe/TDMn ratio of 27, and the significant correlation between ΣCO2 and TDMn for this cast (r^2=0.82, $p<0.0001$). This fluid-rock interaction might be explained by the liquid CO_2 that flows down the volcano flanks at these depths. Here, silicate anomalies are however lower, and can be explained by a lower temperature anomaly that does not enhance silicate alteration. The TDFe/TDMn ratio is similar to the one found at Ruby submarine volcano, at the Mariana arc (Fe/Mn = 26, Resing et al. (2009)), for which authors have attributed the elevated Fe levels to the carbonic acid dissolution of the host rocks as Ruby volcano shows evidence of being high alkalinity/high CO_2 systems. This ratio is also consistent with the one of ~30 found in

hydrothermal fluid from Pele's Vent (Loihi Seamount) where fluids were enriched in total dissolvable CO_2 and was attributed to chemical weathering of wall rock by magmatic volatiles entrained in the circulating hydrothermal fluids (Glazer and Rouxel, 2009).

At the volcano summit, between 2250 and 2750 m deep, the ongoing eruption led to a moderate acidification of about -0.3 pH unit. This pH anomaly is associated with a significant increase in ΣCO_2 (ΣCO_2 = 2644.2 µmol/L), which seems to have enhanced rocks weathering processes as indicated by a strong silicate anomaly (ΔSiO_2 = 20 µmol/L) and elevated alkalinity values (A_T = 2650.6 µmol/L). These maximum values of ΣCO_2, ΔSiO_2 and A_T are found at 2703 m, just above the summit and are associated with elevated TDFe/TDMn ratios of about 27, which is consistent with the hydrothermal fluid ratio value (i.e. ~30) from Pele's Vent (Loihi Seamount) where fluids were enriched in total dissolvable CO_2, as previously describe. At 2250 m, this ratio decreases down to 11, as well as ΣCO_2, ΔSiO_2 and A_T anomalies that decrease toward the background level. These observations seems to highlight the presence of strong water-rock interactions close to the summit of the volcano, which may have been enhanced by high temperature conditions during the ongoing eruption.

Higher than 2250 m in the water column, at the summit and above the northern flank during the ongoing eruption, pH anomalies are lower with maximum values of -0.26 pH unit, and seems to result both from CO_2 addition and carbonate alkalinity addition (brown arrow in Figure 4. 10). Actually, the majority of our samples (all cruises and casts) displays a pH that seems to be controlled by additions of both CO_2 and carbonate alkalinity. We suggest here, that acidification originates from the discharge through the water column of fluids rich in liquid CO_2 that slowly dissolves in seawater. This seawater, enriched in CO_2, then reacts with volcanic rocks to generate carbonate alkalinity and reach the carbonate equilibrium. This process might have occurred in contact with the seafloor, lava flows and volcano flanks, and got diluted when moving up into the water column. Such hypothesis is consistent with the low concentrations of TDFe and TDMn, and low anomalies of ΣCO_2, ΔSiO_2 and A_T observed above 2250m above the volcano. Samples taken above the western recent, and the northwest very recent and active lava flows display anomalies of pH, A_T, SiO_2 and ΣCO_2 located below 2250 m deep that are moderate to low, and that even reach the background envelope (as the ΔSiO_2 value for the northwest very recent lava, cast MAY15-HY06). The TDFe/TDMn ratios range between 17 and 11, and are lower than during the eruption. This ratio value corresponds to the NW Rota-1 ratio of 17 from Resing et al. (2009), where high acidity of fluids venting from the volcano likely

dissolved the host rock, producing fluids with elevated TDFe/TDMn. The depletion of TDFe from hydrocasts sampled above the recent lava flows compared to hydrocasts performed at the edifice during May 2019 eruption is either due to a decrease of the emitted TDFe or to the iron precipitation over time.

Some samples taken above the western recent (MAY04-HY09) and the northwest very recent (MAY15-HY06) lava flows align themselves along the blue arrow on Figure 4. 10.

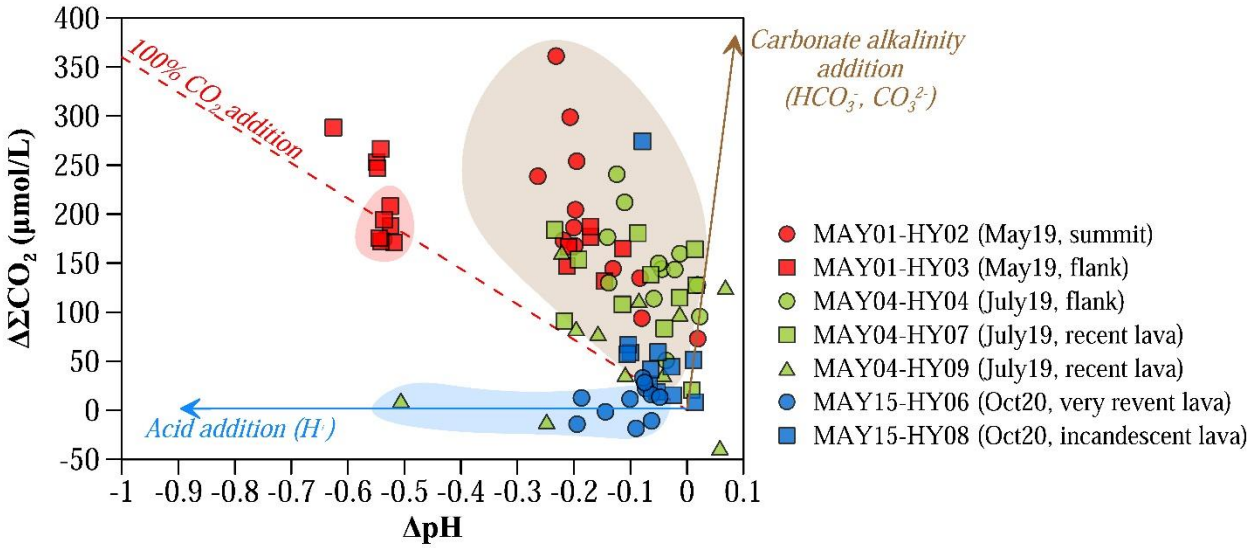

Figure 4. 10. Plot of ΔΣCO_2 vs. ΔpH for all seawater samples taken during the three cruises: May 2019 (MAYOBS1 in orange), July 2019 (MAYOBS4 in green) and October 2020 (MAYOBS15 in purple). Δ values are the change in ΣCO_2 and pH from the regional background. The blue arrow shows the decrease in pH caused by mineral acidity addition (H^+). The brown arrow represents the increase in pH due to carbonate alkalinity addition resulting from the rock weathering. The red dash line (-360 µmol/L per pH) shows the theoretical decrease in pH in the case of only CO_2 is added. When both carbonate alkalinity and CO_2 are added, pH decreases. (Theoretical trends from Resing et al. (2009)).

In particular, the sample taken at 3154 m above the western recent lava flow (MAY04-HY09) presents an acidification of -0.5 pH unit that is not linked with the total alkalinity and silicates. This behavior suggests that the acidification is controlled by the addition of mineral acid (H^+) likely generated by the emission of sulfur dioxide (SO_2) that produces sulfuric acid (H_2SO_4). In previous studies on submarine volcanoes at Mariana arc, authors determine that the mineral acidity (H^+) originates from the $SO_2 + H_2O = HSO_3^- + H^+$ reaction, when magmatic gases rich in SO_2 come in contact with water (Resing et al., 2007; Resing et al., 2009; Butterfield et al., 2011). In our study, we suggest that this reaction might have occurred

right above the emitted lava flows, implying the presence of magmatic gas rich in SO_2. H_2S which is also likely to be emitted during magma degassing may also generate acidity during its oxidation in the water column (e.g. Cline and Richards (1969)).

The major part of the samples taken above the lava flows, display pH and total dissolved inorganic carbon anomalies resulting from CO_2 and carbonate alkalinity addition. Even if effusive activity was detected at the northwest active lava flow (cast MAY15-HY08), acidification does not exceed -0.1 pH unit and the addition of CO_2 is also weak (< 70 µmol/L). Only one deeper sample (3259 m) appears to be strongly enriched in CO_2 (ΣCO_2 = 274.2 µmol/L) but displays a weak pH acidification (-0.08 pH unit). This is likely due to a possible rock weathering occurring during the contact between fluid and seafloor. This anomaly is coupled with a relatively high TDFe/TDMn ratio (~16) and a slight increase of ΔSiO_2 even if this value stays within the background envelope. In gas-rich hydrothermal systems, H^+ reacts first with the host rock followed by a CO_2-weathering reaction that produces alkalinity as HCO_3^-. The presence of alkalinity in deep samples collected above lava flows is consistent with long reaction paths where H^+ is completely consumed and CO_2 reacts with the host rocks (Resing et al., 2009).

Looking at the entire data set, the decrease of the overall eruptive activity intensity offshore Mayotte is clear during the investigated period. Indeed, even if lava flows from October 2020 are very recent and active, anomalies of pH, A_T, SiO_2 and ΣCO_2 are smaller than those measured in July 2019 above recent lava, which are themselves lower than those from May 2019. Concentrations of TDFe and TDMn are also decreasing over time. Therefore, after the eruption, the carbonate system seems to be back to steady-state highlighting either (i) that the initial eruptive impact has been exported/flushed away due to deep current, (ii) or that the impact has been indeed buffered within the seawater column environment. To answer this, models of the dissolution of $CaCO_3$ using water column geochemistry and/or correlation with local sediments analyses could be made. Although discharges of CO_2 at the deep Fani Maoré submarine volcano have generated a locally confined ocean acidification (< 27000 km²) that decrease over time (i.e. returning to a steady-state) over a few months, biological impacts on organisms incorporating calcium carbonate into their structures cannot be excluded.

4.6. Conclusion

The compilation of geochemical data from Fani Maoré submarine volcano has provided valuable information about the setup of a volcanic edifice and the impact of an eruptive

activity on the water column at a local scale. This study leads to the following conclusions:

(1) The turbidity signals translate the decrease of the eruptive activity intensity from May 2018 to October 2020 (about 30 months), starting from a strong eruptive event at the volcano summit to continued lava flow installation.

(2) A magma signature shift happens from crustal contamination to (pure) mantellic signature between the western recent lava flow seen in July 2019, and the very recent and active northwest lava flow seen in October 2020. This highlight a change to a direct magma ascent from the main reservoir to the seafloor, or a rapid recharge of the secondary magma reservoir.

(3) The May 2019 eruption has generated, by seawater-lava interaction and probably encouraged by the formation of a gas jet, a strong H_2 discharge nearly 1000 m high within the water column above the volcano summit. Due to temperature and pressure conditions above the volcano flanks, CO_2 was emitted in liquid phase and sank for depths less than about 2680 m. A strong acidification of the water column was linked to the high discharge of inorganic carbon to the water column. Fluids, including liquid CO_2, has interacted with the volcano walls producing high levels of metals, and elevated TDFe/TDMn ratios.

(4) The lava flows around the volcano edifice has generated significant gas inputs near the seafloor. H_2 levels highlighted the recent eruptive activity, produced through lava quenching, and was then rapidly found at low levels due to oxidation and microbial consumption. CO_2 was released by magma outgassing through a longer time scale. Origin of methane released in more ambiguous. Indeed, although magma outgassing as a methane source is obvious in this context, release of a more mature crustal fluid, originating from the thermogenic cracking of sedimentary organic matter during the magma ascent may also occur given the thick sediment cover that the volcano penetrated. Fluids emissions to the water column have led to a moderate acidification of the seawater mainly resulting from the addition of dissolved inorganic carbon and the addition of carbonate alkalinity released by rock weathering processes. Significant acidification for a part of the deep-water samples above lava flows appears to be controlled by the addition of mineral acid (H^+) from fluids rich in SO_2 and/or H_2S.

(5) About a year after the main eruptive event, with a decrease of the eruptive activity, the system appears to be approaching a steady-state where pH and total carbon

values are heading towards the evaluated local background.

(6) What is still unclear is whether this phenomenon is due to the decrease of the activity coupled with a renewing a water by the currents or to the buffering capacity and the resilience of the water column. To resolve this, future work could therefore focus on models of geochemical behavior of the water column under different scenarios and compare to sediment analyses for $CaCO_3$ investigation.

Besides the geological context that obviously drives the type of volcanism and emissions of associated magmatic volatiles, our findings clearly highlights how environmental settings (e.g. depth, morphobathymetry) might shape the manifestations of submarine eruptions and its impact on the water column. In addition to play a significant part in the eruption mode (Cas and Simmons, 2018), the hydrostatic pressure clearly constrains the behavior of magmatic or eruption-driven volatiles such as H_2, CO_2 or CH_4, and, therefore, how they affect the adjacent marine pelagic and benthic ecosystems.

4.7. Acknowledgments

We thank the crew members of the R/V Marion Dufresne (TAAF/IFREMER/LDA) and its Captain A. Eyssautier. We thank N. Feuillet, Y. Fouquet, E. Rinnert and I. Thinon the chief scientists of the MAYOBS01 cruise (May 2019, doi: 10.17600/18001217), the MAYOBS04 cruise (July 2019, doi: 10.17600/18001238), and the MAYOBS15 cruise (July 2019, doi: 10.17600/18001745). We also thank all the scientists involved. We thank Jürgen Sültenfuß from the Institute of Environmental Physics/Section of Oceanography at the University of Bremen who performed all helium and neon isotopic analyses. We thank Bart van der Haven from Isolab b.v. who carried out the carbon isotope analyses.

4.8. Funding sources

MAYOBS1 campaign was funded by the CNRS-INSU TELLUS Mayotte program (SISMAYOTTE project). *MAYOBS4* and *MAYOBS15* campaigns were conducted by several French research institutions and laboratories (IPGP/CNRS/BRGM/IFREMER) and were funded by the Mayotte volcanological and seismological monitoring network (REVOSIMA, doi: 10.18715/MAYOTTE.REVOSIMA), a partnership between the Institut de Physique du Globe de Paris (IPGP), the Bureau de Recherches Géologiques et Minières (BRGM),

the Observatoire Volcanologique du Piton de la Fournaise (OVPF-IPGP), the Centre National de la Recherche Scientifique (CNRS), and the Institut Français de Recherche pour l'Exploitation de la Mer (IFREMER). This study was funded by the REVOSIMA, IFREMER and TotalEnergies as part of the MAYFLUID PhD project (TOTAL ENERGIES FR000063751 // IFREMER 20/1001730).

4.9. Data availability

All data used in this study are presented in the tables, and/or will be deposited in SEANOE and SISMER online data repository.

4.10. Appendix A. Supplementary Material

Supplementary material presents vertical profiles of hydrographic parameters, and figure highlighting anomalies of potential temperature during the eruption and above the studied lava flows. Evaluation of background geochemistry is also presented through depth profiles. The relationship between TDMn, CO_2 and CH_4 with $^3He_{xs}$ are provided.

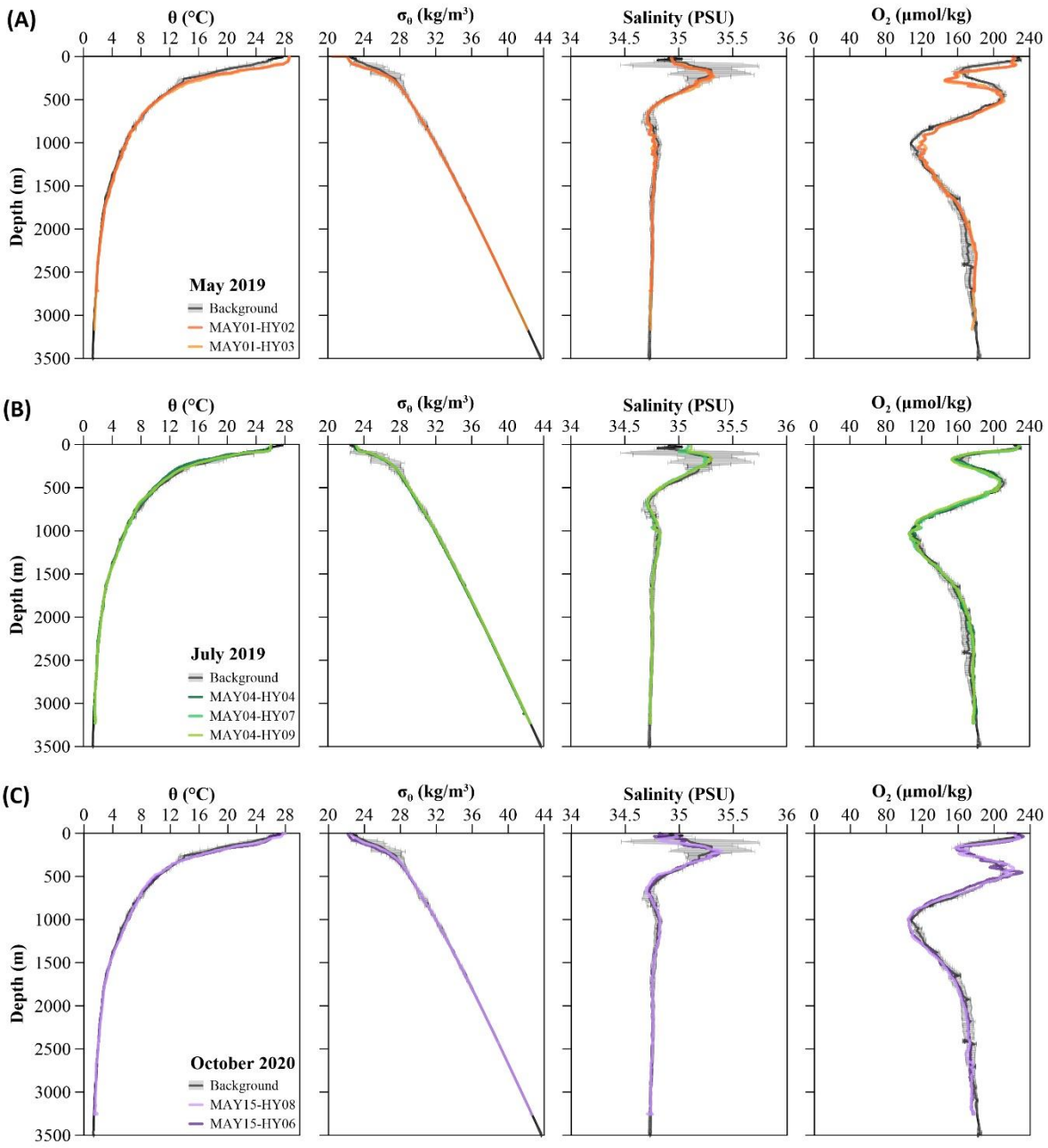

Figure A 1. Vertical profiles of potential temperature (θ), potential density (σ_θ), salinity and dissolved oxygen for the background evaluation and study casts from (A) May 2019 (MAYOBS1 cruise), (B) July 2019 (MAYOBS4 cruise) and (C) October 2020 (MAYOBS15 cruise).

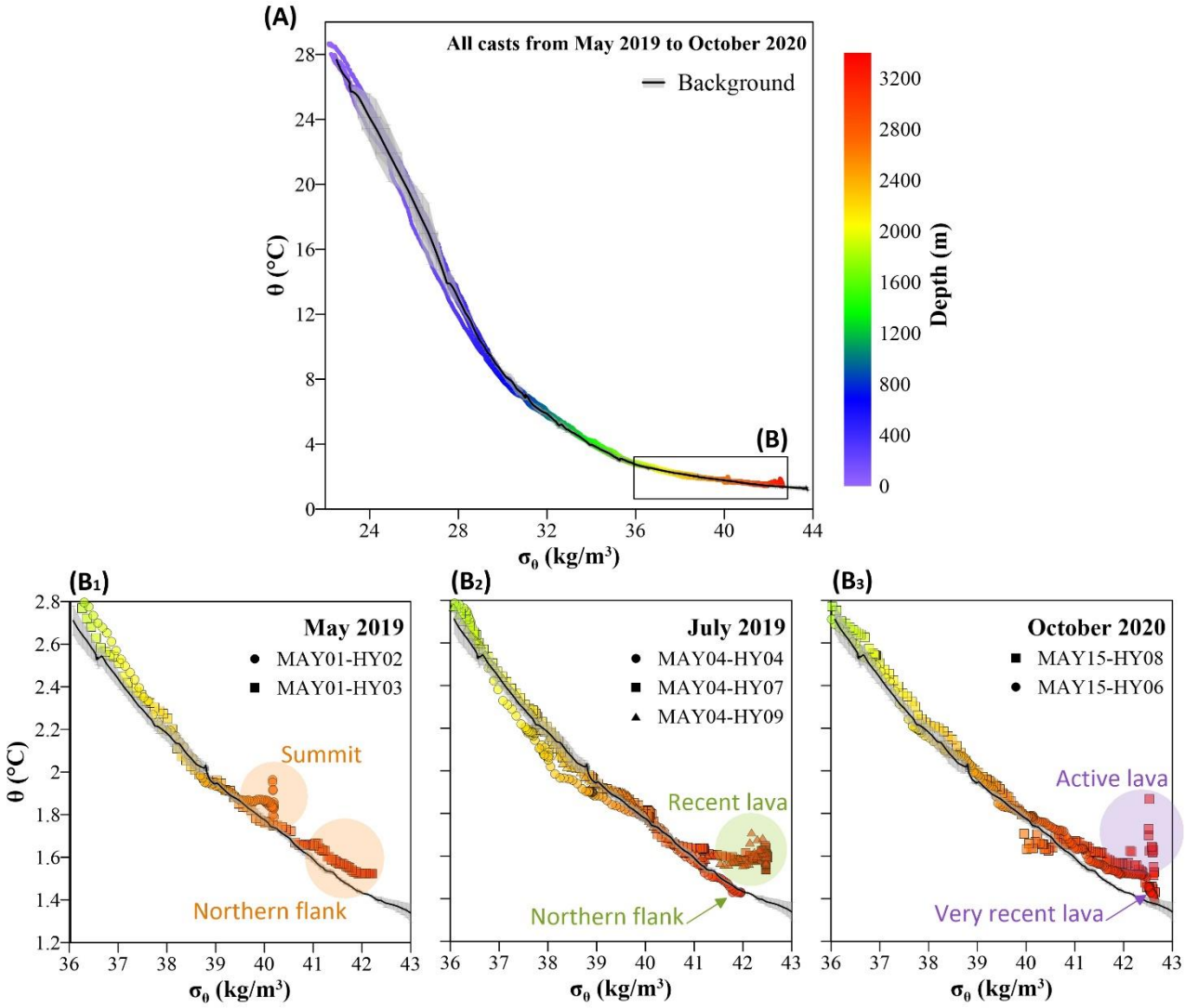

Figure A 2. Potential temperature (θ) vs. potential density (σ_θ) for background evaluation and study casts. (A) All casts from May 2019 to October 2020 are represented with color depth identification. Casts are also represented separately according to the sampling date and with a zoom on the (B) box, (B_1) May 2019 (MAYOBS1 cruise), (B_2) July 2019 (MAYOBS4 cruise) and (B_3) October 2020 (MAYOBS15 cruise). Anomalies of θ are observed at the volcano summit during the eruption, above the recent western lava flow from July 2019 cruise, and above the very recent and active northwest lava flow from October 2020 cruise with very high anomalies measured above the incandescent lava flow.

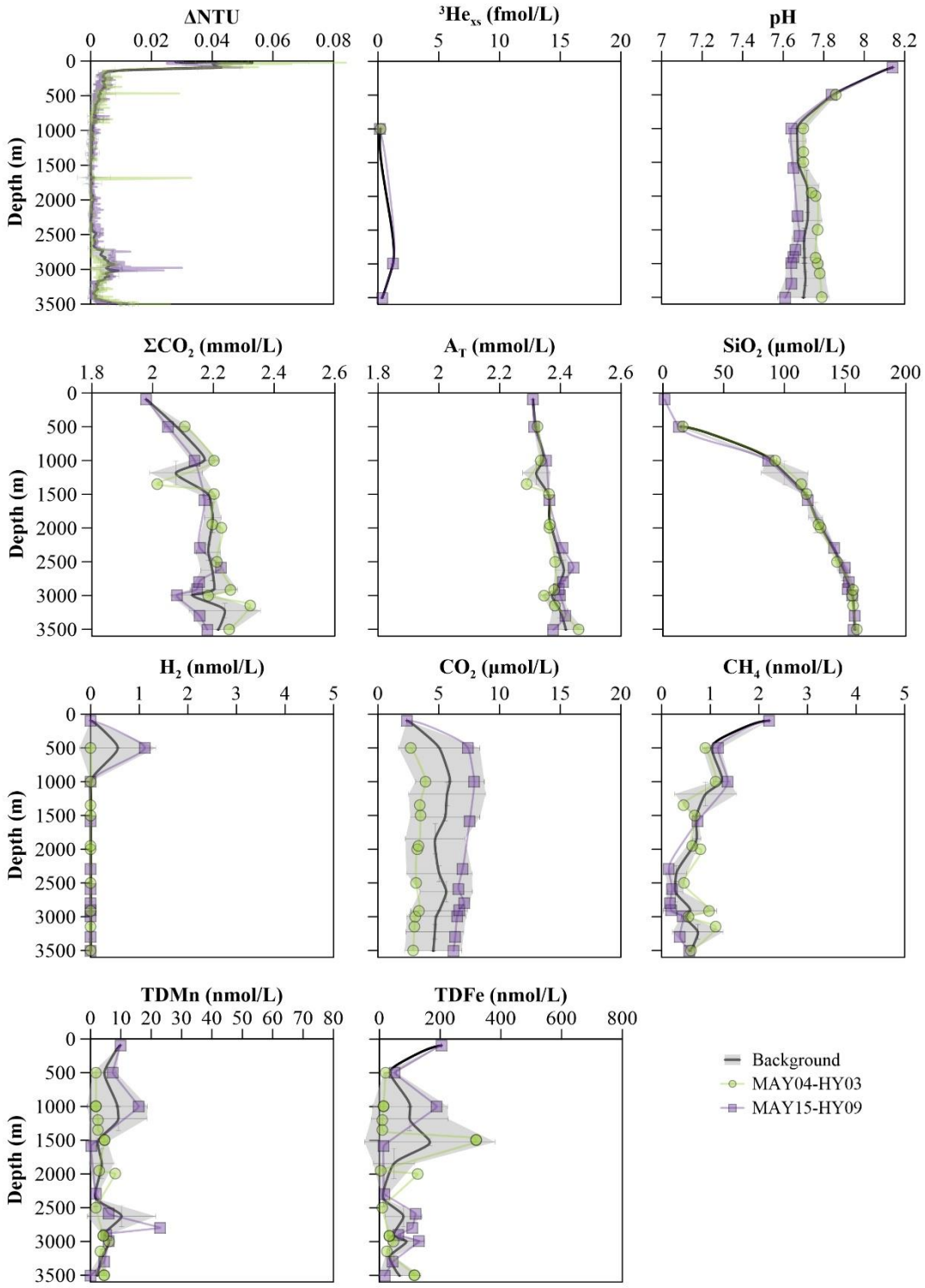

Figure A 3. Background geochemistry evaluation from two reference CTD casts performed outside the influence of the volcano: MAY04-HY03 from July 2019 and MAY15-HY09 from October 2020. The background geochemistry is then define by an envelope represented by the grey shape.

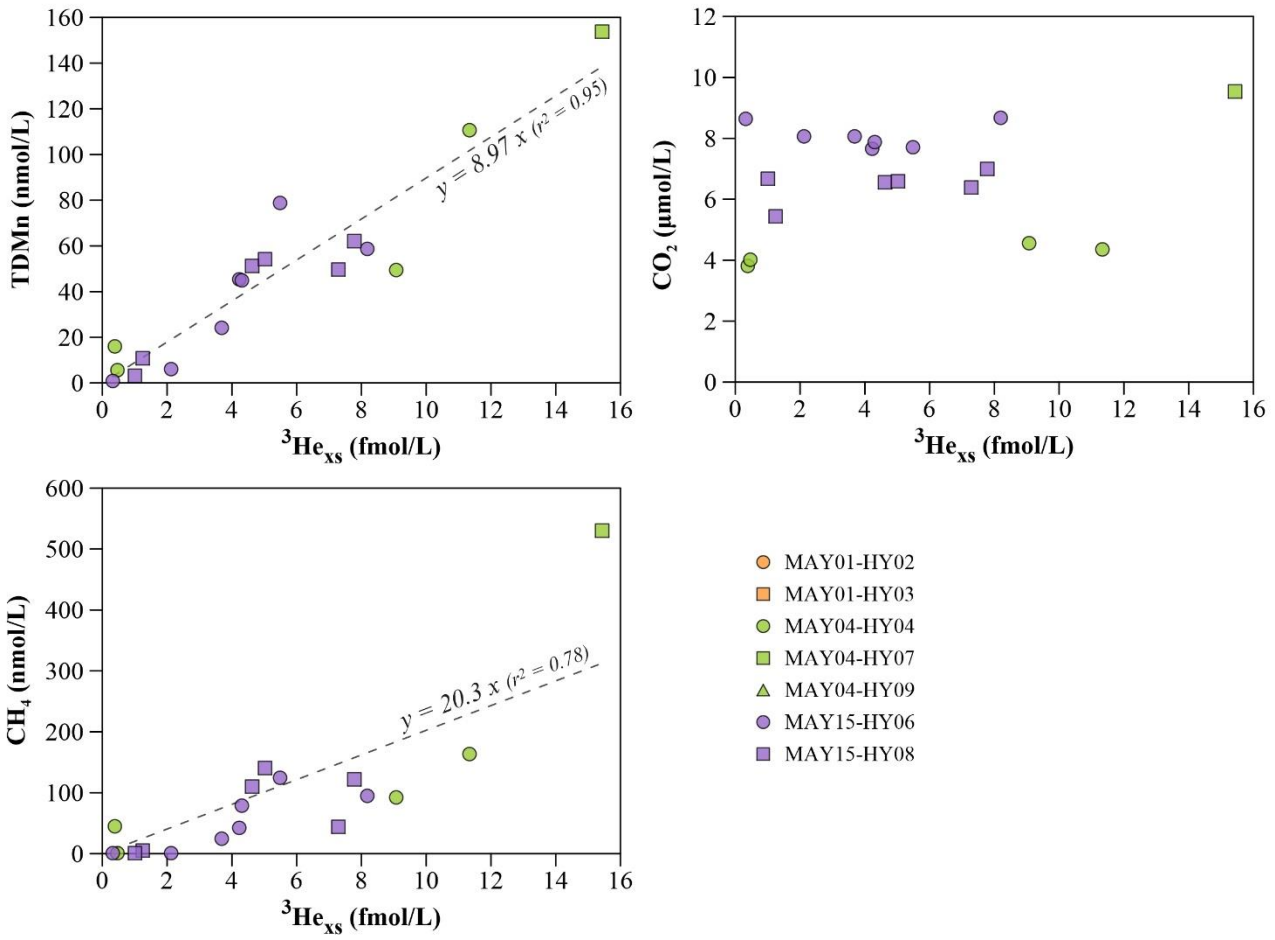

Figure A 4. Plots of TDMn, CO_2 and CH_4 vs. $^3He_{xs}$. Hydrocasts performed during MAYOBS1 (May 2019) and MAYOBS4 (July 2019) cruises are represented in orange and green, respectively. Linear regressions for TDMn vs. $^3He_{xs}$ ($y = 8.97\ x$, $r^2 = 0.95$) and CH_4 vs. $^3He_{xs}$ ($y = 20.3\ x$, $r^2 = 0.78$) were determined for the displayed dataset. No regression can be highlight for CO_2 vs. $^3He_{xs}$ global dataset.

Table A 1. Helium isotope concentrations, Neon concentrations and isotopic ratio calculations for seawater samples taken from July 2019 and October 2020 cruises at the northern volcano flank and above the various lava flows.

Sample ID	Depth (m)	^{3}He (mol/L)	^{4}He (mol/L)	Ne (mol/L)	^{3}He/^{4}He	He/Ne	*std He/Ne*	^{4}He/^{20}Ne	R/Ra	^{4}He$_{xs}$ (mol/L)	^{3}He$_{xs}$ (fmol/L)	*std ^{3}He$_{xs}$ (fmol/L)*	Rc/Ra	*std Rc/Ra*	CO$_2$/^{3}He
MAY4-HY04 (July 2019, northern volcano flank)															
MAY04-HY04-B01	3119.6	1.39×10^{-14}	3.34×10^{-9}	8.23×10^{-9}	4.17×10^{-6}	0.406	*0.008*	na	3.01	1.46×10^{-9}	11.33	*0.23*	3.09	*0.06*	2.16×10^{9}
MAY04-HY04-B07	2748.2	1.17×10^{-14}	3.10×10^{-9}	8.18×10^{-9}	3.77×10^{-6}	0.379	*0.008*	na	2.72	1.22×10^{-9}	9.07	*0.18*	2.79	*0.06*	2.70×10^{9}
MAY04-HY04-B14	2047.9	2.91×10^{-15}	1.99×10^{-9}	7.99×10^{-9}	1.46×10^{-6}	0.249	*0.005*	na	1.06	1.59×10^{-10}	0.38	*0.01*	1.06	*0.02*	9.09×10^{9}
MAY04-HY04-B15	1499.0	2.93×10^{-15}	1.99×10^{-9}	7.79×10^{-9}	1.47×10^{-6}	0.255	*0.005*	na	1.06	2.03×10^{-10}	0.46	*0.01*	1.07	*0.02*	9.49×10^{9}
MAY4-HY07 (July 2019, Western recent lava flow)															
MAY04-HY07-B03	2924.0	1.80×10^{-14}	3.74×10^{-9}	8.16×10^{-9}	4.82×10^{-6}	0.458	*0.009*	na	3.48	1.87×10^{-9}	15.44	*0.31*	3.56	*0.07*	3.66×10^{9}
MAY15-HY06 (Oct. 2020, Northwest very recent lava flow)															
MAY15-HY06-B01	3257.1	8.13×10^{-15}	2.38×10^{-9}	8.32×10^{-9}	3.42×10^{-6}	0.286	*0.006*	0.289	2.47	4.67×10^{-10}	5.49	*0.11*	2.57	*0.05*	6.76×10^{9}
MAY15-HY06-B02	3202.8	6.87×10^{-15}	2.26×10^{-9}	8.30×10^{-9}	3.04×10^{-6}	0.272	*0.005*	0.277	2.20	3.46×10^{-10}	4.22	*0.08*	2.29	*0.05*	7.96×10^{9}
MAY15-HY06-B04	3098.8	6.94×10^{-15}	2.25×10^{-9}	8.29×10^{-9}	3.08×10^{-6}	0.272	*0.005*	0.276	2.23	3.44×10^{-10}	4.30	*0.09*	2.31	*0.05*	8.10×10^{9}
MAY15-HY06-B08	2893.6	1.08×10^{-14}	2.60×10^{-9}	8.22×10^{-9}	4.16×10^{-6}	0.316	*0.006*	0.320	3.01	7.09×10^{-10}	8.19	*0.16*	3.11	*0.06*	5.73×10^{9}
MAY15-HY06-B11	2618.6	6.31×10^{-15}	2.19×10^{-9}	8.27×10^{-9}	2.89×10^{-6}	0.264	*0.005*	0.274	2.09	2.83×10^{-10}	3.68	*0.07*	2.16	*0.04*	9.11×10^{9}
MAY15-HY06-B14	2302.7	4.79×10^{-15}	2.09×10^{-9}	8.33×10^{-9}	2.29×10^{-6}	0.251	*0.005*	0.256	1.65	1.68×10^{-10}	2.12	*0.04*	1.71	*0.03*	1.20×10^{10}
MAY15-HY06-B16	1000.6	2.87×10^{-15}	1.85×10^{-9}	7.90×10^{-9}	1.55×10^{-6}	0.235	*0.005*	na	1.12	7.56×10^{-12}	0.32	*0.01*	1.13	*0.02*	2.15×10^{10}
MAY15-HY08 (Oct. 2020, Northwest active lava flow)															
MAY15-HY08-B02	3202.2	3.94×10^{-15}	2.03×10^{-9}	8.44×10^{-9}	1.94×10^{-6}	0.240	*0.005*	0.247	1.40	7.70×10^{-11}	1.24	*0.02*	1.45	*0.03*	9.85×10^{9}
MAY15-HY08-B04	3098.8	9.90×10^{-15}	2.57×10^{-9}	8.23×10^{-9}	3.85×10^{-6}	0.313	*0.006*	na	2.78	6.84×10^{-10}	7.29	*0.15*	2.88	*0.06*	4.61×10^{9}
MAY15-HY08-B07	2899.6	1.05×10^{-14}	2.54×10^{-9}	8.39×10^{-9}	4.11×10^{-6}	0.303	*0.006*	0.306	2.97	6.07×10^{-10}	7.78	*0.16*	3.12	*0.06*	4.78×10^{9}
MAY15-HY08-B09	2751.6	7.23×10^{-15}	2.28×10^{-9}	8.21×10^{-9}	3.17×10^{-6}	0.278	*0.006*	0.282	2.29	3.97×10^{-10}	4.62	*0.09*	2.36	*0.05*	6.48×10^{9}
MAY15-HY08-B11	2699.0	7.63×10^{-15}	2.30×10^{-9}	8.20×10^{-9}	3.31×10^{-6}	0.281	*0.006*	0.284	2.39	4.21×10^{-10}	5.02	*0.10*	2.47	*0.05*	6.18×10^{9}
MAY15-HY08-B14	2001.4	3.69×10^{-15}	1.97×10^{-9}	8.37×10^{-9}	1.87×10^{-6}	0.236	*0.005*	0.245	1.35	3.09×10^{-11}	1.01	*0.02*	1.39	*0.03*	1.29×10^{10}

nd: not determined ; na: not analyzed.

Table A 2. Summary of H_2, CH_4, CO_2, TDMn, TDFe concentrations and pH, A_T, ΣCO_2 and SiO_2 measured within the water column at the volcano summit, at the northern edifice flank and above the western and northwest lava flows, in May 2019, July 2019 and October 2020. These parameters are also presented for the both background hydrocasts used for background evaluation.

Station	Bottle	Site	Activity	Sampling Date (dd/mm/yyyy)	Latitude	Longitude	Depth (m)	CH_4 (nmol/L)	H_2 (nmol/L)	CO_2 (µmol/L)	pH	ΔpH	A_T (µmol/L)	ΣCO_2 (µmol/L)	$\Delta(\Sigma CO_2)$ (µmol/L)	SiO_2 (µmol/L)	ΔSiO_2 (µmol/L)	TdMn (nmol/L)	TdFe (nmol/L)
MAYOBS01 cruise (May 2019), ongoing eruption																			
MAY01-HY02	B01	Summit	Eruption	16/05/2019	-12.908872	45.71182	2717.0	224.8	39.2		7.16	-0.5	2501	2304	174.3	166.6	19.5	89.2	1841.8
MAY01-HY02	B02	Summit	Eruption	16/05/2019	-12.908831	45.71198	2640.3	56.6		19.1	7.47	-0.2	2701	2488	361.1	158.8	13.3	37.5	606.8
MAY01-HY02	B03	Summit	Eruption	16/05/2019	-12.908838	45.71196	2589.8	25.7	876.2	63.7	7.51	-0.2	2527	2379	253.9	156.5	12.1	60.6	1500.7
MAY01-HY02	B04	Summit	Eruption	16/05/2019	-12.90882	45.71198	2565.8	13.5			7.5	-0.2	2636	2423	298.8	154.3	10.5	23.2	306.1
MAY01-HY02	B05	Summit	Eruption	16/05/2019	-12.908835	45.71198	2490.4									160.6	18.4		
MAY01-HY02	B06	Summit	Eruption	16/05/2019	-12.90882	45.71198	2460.5	17.9	111.7	114.6	7.45	-0.3	2527	2359	238.6	153.6	12.0	19.3	287.0
MAY01-HY02	B07	Summit	Eruption	16/05/2019	-12.90883	45.71198	2410.7	27.8	2.8	104.2	7.52	-0.2	2504	2323	204.4	151.0	10.6	21.2	316.6
MAY01-HY02	B08	Summit	Eruption	16/05/2019	-12.90882	45.71198	2389.7	66.2	833.7		7.5	-0.2	2438	2291	173.1	155.8	15.8	60.0	647.3
MAY01-HY02	B09	Summit	Eruption	16/05/2019	-12.908822	45.71198	2181.0	0.9	3351.5	43.6	7.65	-0.1	2436	2245	134.7	140.8	5.4	4.2	37.0
MAY01-HY02	B10	Summit	Eruption	16/05/2019	-12.90882	45.71198	1779.9	0.9	2287.8	60.6	7.63	-0.1	2435	2240	144.1	129.8	3.1	0.0	18.1
MAY01-HY02	B13	Summit	Eruption	16/05/2019	-12.90882	45.71198	1378.9	0.9	298.5	48.7	7.59	-0.2	2432	2249	167.6	120.1	2.1	3.0	55.7
MAY01-HY02	B14	Summit	Eruption	16/05/2019	-12.90882	45.71198	917.4	1.3	5992.9	36.9	7.62	-0.2	2439	2251	186.3	82.4	-25.6	2.2	22.5
MAY01-HY02	B15	Summit	Eruption	16/05/2019	-12.908805	45.712	485.3	1.9	1054.5	31.3	7.77	-0.1	2364	2143	93.9	13.3	-85.2	0.8	7.1
MAY01-HY02	B16	Summit	Eruption	16/05/2019	-12.9088	45.712	179.4	2.6		17.0	7.89	0.0	2378	2111	72.9	6.2	-85.7	0.7	8.2
MAY01-HY03	B01	Northern flank	Eruption	16/05/2019	-12.90154	45.7149	3163.4	830.5	10.8	263.6	7.04	-0.6	2545	2434	288.2	162.7	5.8	560.2	10578.1
MAY01-HY03	B02	Northern flank	Eruption	16/05/2019	-12.90156	45.7149	3110.2	757.2	56.2	237.4	7.12	-0.5	2542	2397	253.1	164.2	8.5	312.2	8513.1
MAY01-HY03	B03	Northern flank	Eruption	16/05/2019	-12.90156	45.71494	3071.3	766.7	56.3	264.7	7.13	-0.5	2529	2409	266.5	162.3	7.5	309.1	8150.7
MAY01-HY03	B04	Northern flank	Eruption	16/05/2019	-12.90156	45.7149	3026.5	474.1	23.5	160.7	7.15	-0.5	2477	2349	208.2	162.1	8.3	288.7	7721.9
MAY01-HY03	B05	Northern flank	Eruption	16/05/2019	-12.90158	45.71494	2976.1	260.6	88.5	154.4	7.16	-0.5	2467	2310	171.0			84.6	1775.0
MAY01-HY03	B06	Northern flank	Eruption	16/05/2019	-12.90156	45.71494	2891.0	441.8	21.9	264.4	7.16	-0.5	2439	2324	188.1	160.7	9.8	142.1	3128.3
MAY01-HY03	B07	Northern flank	Eruption	16/05/2019	-12.90152	45.7149	2840.3	430.6	13.7	258.4	7.14	-0.5	2495	2381	246.9	161.4	11.6	138.4	3136.4
MAY01-HY03	B08	Northern flank	Eruption	16/05/2019	-12.90156	45.71492	2720.9	280.3	20.3	202.2	7.16	-0.5	2448	2324	194.2	160.5	13.3	120.5	2550.0
MAY01-HY03	B09	Northern flank	Eruption	16/05/2019	-12.90156	45.71492	2640.9	290.8	58.2	220.5	7.16	-0.5	2444	2299	172.1	160.5	15.1	109.2	2495.6
MAY01-HY03	B10	Northern flank	Eruption	16/05/2019	-12.90156	45.71492	2600.4	198.9	34.4		7.16	-0.5	2483	2301	175.5	157.4	12.8	85.5	1846.1
MAY01-HY03	B11	Northern flank	Eruption	16/05/2019	-12.90154	45.71492	2430.7	2.2	212.7	50.0	7.57	-0.1	2429	2251	131.7	142.7	1.8	7.0	232.5
MAY01-HY03	B12	Northern flank	Eruption	16/05/2019	-12.90156	45.71492	2180.1	1.6	1.8	40.4	7.62	-0.1	2455	2275	164.7	132.3	-3.1	2.8	74.2

Station	Bottle	Site	Activity	Sampling Date (dd/mm/yyyy)	Latitude	Longitude	Depth (m)	CH_4 (nmol/L)	H_2 (nmol/L)	CO_2 (µmol/L)	pH	ΔpH	A_T (µmol/L)	ΣCO_2 (µmol/L)	$\Delta(\Sigma CO_2)$ (µmol/L)	SiO_2 (µmol/L)	ΔSiO_2 (µmol/L)	TdMn (nmol/L)	TdFe (nmol/L)
MAY01-HY03	B13	Northern flank	Eruption	16/05/2019	-12.90156	45.7149	1929.6	2.6	519.8	42.1	7.58	-0.2	2461	2278	176.7	128.9	-1.1	0.9	73.2
MAY01-HY03	B14	Northern flank	Eruption	16/05/2019	-12.90156	45.7149	1779.6	1.0	4.3	41.0	7.59	-0.2	2442	2283	187.2	124.5	-2.3	0.0	79.5
MAY01-HY03	B15	Northern flank	Eruption	16/05/2019	-12.90156	45.71492	1614.7	3.7	547.9	44.3	7.56	-0.2	2459	2237	147.1	120.4	-2.7	3.0	49.1
MAY01-HY03	B16	Northern flank	Eruption	16/05/2019	-12.90162	45.71488	1074.0	1.0	277.3	37.7	7.6	-0.2	2410	2237	166.6	85.7	-25.7	3.3	56.9
MAYOBS04 cruise (July 2019)																			
MAY04-HY03	B01	Background	None	22/10/2019	-13.06938	45.65382	3498.7	0.6	0.0	20.0	7.79	0.15	2459.9	2251.8	93.9	159.5	-4.6	4.44	115.63
MAY04-HY03	B03	Background	None	22/10/2019	-13.06942	45.65388	3147.1	1.1	0.0	20.8	7.78	0.11	2381.2	2320.9	175.8	156.5	0.1	3.33	24.04
MAY04-HY03	B04	Background	None	22/10/2019	-13.06962	45.65376	2998.7	0.6		21.2	7.77	0.09	2346.8	2183.6	43.8	156.0	2.8	6.15	46.29
MAY04-HY03	B05	Background	None	22/10/2019	-13.06964	45.65374	2916.2	1.0	0.0	23.3	7.76	0.08	2380.3	2256.8	119.9	156.4	4.9	4.24	32.20
MAY04-HY03	B07	Background	None	22/10/2019	-13.06972	45.65356	2498.4	0.5	0.0	21.7	7.77	0.06	2383.2	2211.7	89.9	143.2	0.9	1.71	9.62
MAY04-HY03	B08	Background	None	22/10/2019	-13.06978	45.65352	1996.5	0.8	0.0	22.5	7.76	0.01	2363.5	2225.7	122.0	129.7	-1.7	8.10	126.34
MAY04-HY03	B09	Background	None	22/10/2019	-13.0698	45.65354	1948.5	0.6	0.0	23.2	7.74	-0.01	2364.5	2196.6	94.7	128.0	-2.4	2.81	3.90
MAY04-HY03	B10	Background	None	22/10/2019	-13.06982	45.65348	1496.8	0.7	0.0	24.2	7.7	-0.08	2362.6	2201.6	116.0	118.1	-2.5	4.66	318.16
MAY04-HY03	B12	Background	None	22/10/2019	-13.06978	45.6535	1347.2	0.5	0.0	23.9	7.7	-0.09	2288.8	2015.2	-65.1	113.8	-3.5	2.50	9.98
MAY04-HY03	B14	Background	None	22/10/2019	-13.06982	45.65354	998.4	1.1	0.0	27.1	7.7	-0.11	2335.0	2202.6	135.0	92.6	-17.1	1.83	13.91
MAY04-HY03	B16	Background	None	22/10/2019	-13.0698	45.6535	497.5	0.9	0.0	18.6	7.86	0.01	2324.2	2106.4	56.8	16.2	-82.6	1.83	20.61
MAY04-HY04	B01	Northern flank	None	23/10/2019	-12.90178	45.71518	3119.6	163.5	0.0	30.1	7.61	-0.06	2372.0	2257.9	113.7	157.9	2.1	110.61	2956.48
MAY04-HY04	B03	Northern flank	None	23/10/2019	-12.90174	45.7152	3074.0	103.7	0.0	25.4	7.69	0.02	2360.0	2270.2	127.6	155.5	0.6	70.32	1729.92
MAY04-HY04	B04	Northern flank	None	23/10/2019	-12.90174	45.7152	2997.4	101.6	0.0	26.0	7.64	-0.04	2451.0	2190.4	50.6	157.0	3.8	64.89	1599.10
MAY04-HY04	B05	Northern flank	None	23/10/2019	-12.90172	45.71522	2949.5	146.9	0.0	30.2	7.57	-0.11	2438.0	2350.0	211.9	158.5	6.3	92.29	2484.55
MAY04-HY04	B06	Northern flank	None	23/10/2019	-12.90176	45.71514	2798.8	130.2	0.0	32.2	7.55	-0.14	2394.0	2309.0	176.4	155.1	6.2	63.71	1248.33
MAY04-HY04	B07	Northern flank	None	23/10/2019	-12.90174	45.71514	2748.2	92.0	0.0	31.5	7.57	-0.12	2445.0	2371.5	240.7	154.9	7.1	49.48	956.23
MAY04-HY04	B09	Northern flank	None	23/10/2019	-12.90174	45.71516	2598.2	78.5	0.0	29.3	7.66	-0.04	2413.0	2269.1	143.8	151.2	6.7	35.96	635.77
MAY04-HY04	B10	Northern flank	None	23/10/2019	-12.90172	45.71518	2495.5	27.5	0.0	27.4	7.69	-0.02	2392.0	2265.1	143.4	147.2	4.9	19.76	311.75
MAY04-HY04	B11	Northern flank	None	23/10/2019	-12.90174	45.71516	2248.3	173.8	0.0	32.7	7.59	-0.14	2401.0	2242.5	129.8	145.3	8.4	58.83	1032.58
MAY04-HY04	B13	Northern flank	None	23/10/2019	-12.90174	45.71518	2121.7	1.9	0.0	30.4	7.76	0.02	2366.0	2203.7	95.5	133.6	-0.5	1.92	33.36
MAY04-HY04	B14	Northern flank	None	23/10/2019	-12.90174	45.71518	2047.9	45.1	1.3	26.4	7.73	-0.01	2388.0	2265.1	159.5	135.7	3.1	15.92	222.88
MAY04-HY04	B15	Northern flank	None	23/10/2019	-12.90174	45.71518	1499.0	0.8	0.0	27.8	7.73	-0.05	2370.0	2235.4	149.7	118.2	-2.4	5.53	25.26
MAY04-HY07	B03	West lava flow	Recent	27/07/2019	-12.91196	45.68738	2924.0	530.4		66.0	7.49	-0.19	2490.6	2290.7	153.5	163.7	12.1	153.81	2097.72
MAY04-HY07	B04	West lava flow	Recent	27/07/2019	-12.91196	45.68736	2848.4	543.1	29.4	94.9	7.47	-0.22	2453.5	2225.2	90.8	162.6	12.6	139.67	1870.03
MAY04-HY07	B05	West lava flow	Recent	27/07/2019	-12.91196	45.68738	2748.5	291.5	15.4	34.4	7.58	-0.11	2460.7	2238.7	107.9	155.2	7.4	83.09	1186.34

Station	Bottle	Site	Activity	Sampling Date (dd/mm/yyyy)	Latitude	Longitude	Depth (m)	CH_4 (nmol/L)	H_2 (nmol/L)	CO_2 (µmol/L)	pH	ΔpH	A_T (µmol/L)	ΣCO_2 (µmol/L)	$\Delta(\Sigma CO_2)$ (µmol/L)	SiO_2 (µmol/L)	ΔSiO_2 (µmol/L)	TdMn (nmol/L)	TdFe (nmol/L)
MAY04-HY07	B06	West lava flow	Recent	27/07/2019	-12.91196	45.68736	2746.8	518.0		66.7	7.46	-0.23	2491.6	2314.6	183.8	160.9	13.1	137.59	1856.08
MAY04-HY07	B08	West lava flow	Recent	27/07/2019	-12.91202	45.68736	2498.9	13.7	0.0	28.3	7.72	0.01	2428.9	2142.1	20.3	147.5	5.1	18.70	275.57
MAY04-HY07	B09	West lava flow	Recent	27/07/2019	-12.912	45.68736	2471.4	11.6	0.0	27.9	7.7	-0.01	2442.2	2235.6	114.8	146.8	5.0	21.91	334.12
MAY04-HY07	B10	West lava flow	Recent	27/07/2019	-12.912	45.68736	2313.6	112.4	0.0	31.7	7.66	-0.06	2429.9	2253.3	138.2	144.8	6.5	69.56	1295.62
MAY04-HY07	B12	West lava flow	Recent	27/07/2019	-12.912	45.68734	1997.6	1.1	0.0	25.9	7.76	0.01	2454.6	2267.8	164.1	128.4	-3.0	1.28	25.99
MAY04-HY07	B13	West lava flow	Recent	27/07/2019	-12.912	45.68732	1497.7	1.9	0.0	26.4	7.74	-0.04	2352.8	2169.1	83.4	117.5	-3.1	15.45	38.75
MAY04-HY07	B14	West lava flow	Recent	27/07/2019	-12.91202	45.68732	967.5	1.1	0.0	26.6	7.73	-0.09	2401.1	2247.0	180.5	82.7	-26.3	1.81	66.60
MAY04-HY07	B15	West lava flow	Recent	27/07/2019	-12.91196	45.6873	572.2	1.5	0.0	21.5	7.86	0.02	2343.5	2179.5	127.2	23.7	-76.8	38.92	723.30
MAY04-HY09	B01	West lava flow	Recent	29/07/2019	-12.9183	45.69218	3200.4	726.6	30.0	105.9	7.23	-0.43	2448.7	1875.2	-271.9	165.0	7.4	237.37	4244.69
MAY04-HY09	B03	West lava flow	Recent	29/07/2019	-12.9183	45.69218	3154.5	777.4	39.3	101.8	7.16	-0.51	2461.7	2155.5	10.0	167.0	10.4	268.03	4472.61
MAY04-HY09	B04	West lava flow	Recent	29/07/2019	-12.91828	45.69218	3112.7	648.6	3.7	50.9	7.56	-0.11	2434.8	2180.4	36.5	162.8	7.0	189.82	3682.72
MAY04-HY09	B05	West lava flow	Recent	29/07/2019	-12.9183	45.69218	2978.1	645.2	4.9	53.6	7.43	-0.25	2348.3	2127.6	-11.5	164.0	11.2	193.67	3222.76
MAY04-HY09	B06	West lava flow	Recent	29/07/2019	-12.91828	45.6922	2864.9	511.8	11.9	51.5	7.49	-0.20	2357.2	2218.3	83.3	162.5	12.2	144.78	2420.97
MAY04-HY09	B07	West lava flow	Recent	29/07/2019	-12.9183	45.69222	2700.4	218.3	1.8	44.6	7.54	-0.16	2369.2	2207.3	78.3	153.6	6.8	64.05	1608.02
MAY04-HY09	B09	West lava flow	Recent	29/07/2019	-12.9183	45.6922	2641.2	348.2	1.1	57.7	7.48	-0.22	2389.1	2288.1	161.2	154.9	9.4	99.87	2379.11
MAY04-HY09	B11	West lava flow	Recent	29/07/2019	-12.9183	45.6922	2478.0	9.5	0.0	34.5	7.7	-0.01	2372.2	2219.3	98.3	147.9	6.0	31.12	561.85
MAY04-HY09	B12	West lava flow	Recent	29/07/2019	-12.9183	45.6922	2348.1	90.7	0.0	40.0	7.68	-0.04	2324.4	2152.5	36.1	144.3	5.2	33.68	681.86
MAY04-HY09	B14	West lava flow	Recent	29/07/2019	-12.9183	45.69222	2199.9	1.1	0.0	25.0	7.8	0.07	2441.8	2236.3	125.3	134.5	-1.4	0.00	44.74
MAY04-HY09	B15	West lava flow	Recent	29/07/2019	-12.9183	45.69222	992.8	1.0	0.0	27.7	7.73	-0.09	2330.4	2179.4	112.0	90.9	-18.7	0.00	0.20
MAY04-HY09	B16	West lava flow	Recent	29/07/2019	-12.91832	45.69222	460.4	1.9	0.0	18.8	7.91	0.06	2217.0	2009.9	-38.4	15.5	-82.6	0.00	27.57
MAYOBS15 cruise (October 2020)																			
MAY15-HY06	B01	Northwest lava flow	Very recent	17/10/2020	-12.8616	45.6771	3257.1	124.8	9.0	55.0	7.56	-0.1	2356.1	2083.8	-65.3	156.1	-2.8	78.71	1165.50
MAY15-HY06	B02	Northwest lava flow	Very recent	17/10/2020	-12.8616	45.67712	3202.8	42.8	2.8	54.7	7.6	-0.1	2387.8	2136.2	-11.0	154.0	-3.7	45.30	614.48
MAY15-HY06	B04	Northwest lava flow	Very recent	17/10/2020	-12.86162	45.6771	3098.8	78.5	13.0	56.2	7.58	-0.1	2366.7	2124.8	-18.7	155.4	-0.1	44.89	707.64
MAY15-HY06	B06	Northwest lava flow	Very recent	17/10/2020	-12.8616	45.6771	3001.6	204.4	38.2	69.6	7.49	-0.2	2390.7	2152.4	12.4	158.1	4.8	76.89	880.66
MAY15-HY06	B08	Northwest lava flow	Very recent	17/10/2020	-12.8616	45.6771	2893.6	95.1	7.1	61.9	7.54	-0.1	2377.2	2134.3	-1.7	153.8	2.8	58.75	657.89
MAY15-HY06	B09	Northwest lava flow	Very recent	17/10/2020	-12.86162	45.6771	2796.8	43.5	0.0	58.5	7.59	-0.1	2386.8	2143.8	11.3	150.8	1.9	34.07	501.63
MAY15-HY06	B10	Northwest lava flow	Very recent	17/10/2020	-12.8616	45.6771	2762.0	12.3	1.5	55.7	7.62	-0.1	2358.0	2153.3	22.0	146.9	-1.2	19.06	294.75
MAY15-HY06	B11	Northwest lava flow	Very recent	17/10/2020	-12.86162	45.6771	2618.6	25.0	1.0	57.5	7.64	-0.1	2363.8	2141.9	15.8	147.5	2.5	24.05	409.64
MAY15-HY06	B12	Northwest lava flow	Very recent	17/10/2020	-12.86164	45.6771	2542.8	21.3	1.7	57.7	7.63	-0.1	2361.9	2156.2	32.8	146.1	2.7	19.68	294.61
MAY15-HY06	B13	Northwest lava flow	Very recent	17/10/2020	-12.8616	45.67712	2400.3	1.3	1.1	57.2	7.67	0.0	2357.1	2131.4	13.2	138.3	-1.9	5.11	115.23

Station	Bottle	Site	Activity	Sampling Date (dd/mm/yyyy)	Latitude	Longitude	Depth (m)	CH_4 (nmol/L)	H_2 (nmol/L)	CO_2 (µmol/L)	pH	ΔpH	A_T (µmol/L)	ΣCO_2 (µmol/L)	$\Delta(\Sigma CO_2)$ (µmol/L)	SiO_2 (µmol/L)	ΔSiO_2 (µmol/L)	TdMn (nmol/L)	TdFe (nmol/L)
MAY15-HY06	B14	Northwest lava flow	Very recent	17/10/2020	-12.86158	45.67712	2302.7	0.7	0.0	57.6	7.65	-0.1	2363.8	2142.9	28.1	135.7	-2.4	6.14	145.05
MAY15-HY06	B16	Northwest lava flow	Very recent	17/10/2020	-12.86162	45.6771	1000.6	1.2	0.0	61.7	7.62	-0.2	2279.3	2053.4	-14.4	82.1	-27.7	0.80	160.72
MAY15-HY08	B01	Northwest lava flow	Active flow	21/10/2020	-12.87088	45.6855	3259.2	283.6	171.3	46.9	7.58	-0.1	2451.6	2423.5	274.2	158.6	-0.3	117.26	1878.76
MAY15-HY08	B02	Northwest lava flow	Active flow	21/10/2020	-12.87088	45.6855	3202.2	5.0	12.4	38.8	7.61	-0.1	2393.4	2165.7	18.5	154.0	-3.7	10.91	194.94
MAY15-HY08	B04	Northwest lava flow	Active flow	21/10/2020	-12.87086	45.6855	3098.8	44.5	14.1	45.7	7.57	-0.1	2212.1	2202.1	58.7	156.2	0.8	49.67	600.08
MAY15-HY08	B06	Northwest lava flow	Active flow	21/10/2020	-12.87088	45.6855	2999.9	131.3	308.2	45.5	7.61	-0.1	2413.8	2166.7	26.8	157.8	4.5	55.13	673.76
MAY15-HY08	B07	Northwest lava flow	Active flow	21/10/2020	-12.87088	45.6855	2899.6	122.4	290.8	50.0	7.58	-0.1	2410.8	2203.1	66.8	157.0	5.9	61.99	682.35
MAY15-HY08	B08	Northwest lava flow	Active flow	21/10/2020	-12.87088	45.6855	2827.7	107.3	525.4	48.3	7.7	0.0	2418.6	2184.9	51.2	156.1	6.6	49.56	570.35
MAY15-HY08	B09	Northwest lava flow	Active flow	21/10/2020	-12.87088	45.6855	2751.6	110.6	537.9	46.9	7.63	-0.1	2404.1	2172.4	41.5	157.0	9.1	51.21	614.98
MAY15-HY08	B11	Northwest lava flow	Active flow	21/10/2020	-12.8709	45.68548	2699.0	140.6	647.6	47.1	7.67	0.0	2422.5	2173.4	44.3	158.2	11.5	54.13	666.90
MAY15-HY08	B12	Northwest lava flow	Active flow	21/10/2020	-12.8709	45.6855	2600.6	0.8	6.7	50.3	7.68	0.0	2393.4	2140.8	15.3	149.3	4.8	68.75	146.75
MAY15-HY08	B13	Northwest lava flow	Active flow	21/10/2020	-12.87088	45.6855	2499.2	2.3	6.8	49.2	7.66	-0.1	2410.8	2181.0	59.2	144.5	2.2	9.23	97.67
MAY15-HY08	B14	Northwest lava flow	Active flow	21/10/2020	-12.87086	45.6855	2001.4	0.6	2.5	47.7	7.76	0.0	2326.5	2112.0	8.2	127.4	-4.1	3.21	43.54
MAY15-HY08	B16	Northwest lava flow	Active flow	21/10/2020	-12.87088	45.6855	987.7	1.2	1.8	53.2	7.71	-0.1	2334.3	2124.5	57.2	83.5	-26.0		
MAY15-HY09	B01	Background	None	22/10/2020	-12.08746	46.0565	3507.0	0.6	0.0	44.4	7.61	0.0	2376.2	2179.9	21.7	156.8	-7.5	0.00	17.45
MAY15-HY09	B03	Background	None	22/10/2020	-12.08748	46.05648	3299.4	0.4	0.0	45.4	7.64	0.0	2417.1	2154.6	3.9	157.8	-2.0	4.51	43.77
MAY15-HY09	B04	Background	None	22/10/2020	-12.08746	46.0565	2992.2	0.4	0.0	46.6	7.64	0.0	2399.6	2079.8	-59.8	155.9	2.8	5.98	130.66
MAY15-HY09	B06	Background	None	22/10/2020	-12.08748	46.05648	2901.9	0.2	0.0	47.7	7.65	0.0	2394.7	2145.9	9.5	152.3	1.1	5.18	62.92
MAY15-HY09	B07	Background	None	22/10/2020	-12.08748	46.0565	2797.1	0.2	0.0	50.6	7.66	0.0	2408.3	2153.7	21.1	153.2	4.3	22.98	108.60
MAY15-HY09	B08	Background	None	22/10/2020	-12.08746	46.0565	2587.5	0.2	0.0	47.3	7.68	0.0	2443.4	2224.6	99.6	149.7	5.4	5.99	119.07
MAY15-HY09	B09	Background	None	22/10/2020	-12.0875	46.0565	2294.4	0.1	0.0	49.7	7.67	-0.1	2407.4	2155.6	41.2	141.1	3.2	1.74	15.64
MAY15-HY09	B11	Background	None	22/10/2020	-12.08748	46.05648	1585.5	0.7	0.0	53.9	7.65	-0.1	2363.5	2171.2	82.3	119.2	-3.3	0.22	14.08
MAY15-HY09	B12	Background	None	22/10/2020	-12.0875	46.05648	1000.1	1.4	0.0	56.6	7.64	-0.2	2352.8	2138.1	70.4	86.6	-23.1	15.86	188.82
MAY15-HY09	B14	Background	None	22/10/2020	-12.0875	46.0565	498.9	1.2	1.1	52.8	7.84	0.0	2313.9	2050.6	1.0	13.2	-85.7	7.34	50.05
MAY15-HY09	B15	Background	None	22/10/2020	-12.0875	46.0565	94.8	2.2	0.0	17.0	8.14	0.3	2310.0	1978.7	-56.3	1.5	-88.6	9.84	204.35

4.11. Bibliographical References

Aminot, A., Kérouel, R., 2007. Dosage automatique des nutriments dans les eaux marines: méthodes en flux continu. Editions Quae.

Archer, D.G., 1992. Thermodynamic Properties of the NaCl+H2O System. II. Thermodynamic Properties of NaCl(aq), NaCl·2H2(cr), and Phase Equilibria. Journal of Physical and Chemical Reference Data, 21(4): 793-829.

Assayag, N., Rivé, K., Ader, M., Jézéquel, D., Agrinier, P., 2006. Improved method for isotopic and quantitative analysis of dissolved inorganic carbon in natural water samples. Rapid Communications in Mass Spectrometry, 20(15): 2243-2251.

Baker, E.T. et al., 2012. Hydrothermal Discharge During Submarine Eruptions The Importance of Detection, Response, and New Technology. Oceanography, 25(1): 128-141.

Baker, E.T. et al., 2011. Unique event plumes from a 2008 eruption on the Northeast Lau Spreading Center. Geochemistry, Geophysics, Geosystems, 12(9).

Barry, P.H. et al., 2020. Volatile sources, sinks and pathways: A helium-carbon isotope study of Baja California fluids and gases. Chemical Geology, 550: 119722.

Baumberger, T. et al., 2020. Dissolved Gas and Metal Composition of Hydrothermal Plumes From a 2008 Submarine Eruption on the Northeast Lau Spreading Center. Frontiers in Marine Science, 7.

Baumberger, T. et al., 2014. Understanding a submarine eruption through time series hydrothermal plume sampling of dissolved and particulate constituents: West Mata, 2008-2012. Geochemistry, Geophysics, Geosystems, 15(12): 4631-4650.

Benson, B.B., Krause, D., 1980. Isotopic fractionation of helium during solution: A probe for the liquid state. Journal of Solution Chemistry, 9(12): 895-909.

Berthod, C. et al., 2022. Temporal magmatic evolution of the Fani Maoré submarine eruption 50 km east of Mayotte revealed by in situ sampling and petrological monitoring. Comptes Rendus. Géoscience, 354(S2): 195-223.

Berthod, C. et al., 2021. The 2018-ongoing Mayotte submarine eruption: Magma migration imaged by petrological monitoring. Earth and Planetary Science Letters, 571: 117085.

Boudoire, G., Rizzo, A.L., Arienzo, I., Di Muro, A., 2020. Paroxysmal eruptions tracked by variations of helium isotopes: inferences from Piton de la Fournaise (La Réunion island). Scientific Reports, 10(1).

Buck, N.J., Resing, J.A., Baker, E.T., Lupton, J.E., 2018. Chemical Fluxes From a Recently Erupted Shallow Submarine Volcano on the Mariana Arc. Geochemistry, Geophysics, Geosystems, 19(5): 1660-1673.

Butterfield, D.A. et al., 2011. High SO2 flux, sulfur accumulation, and gas fractionation at an erupting submarine volcano. Geology, 39(9): 803-806.

Cahalan, R.C., Dufek, J., 2021. Explosive Submarine Eruptions: The Role of Condensable Gas Jets in Underwater Eruptions. Journal of Geophysical Research: Solid Earth, 126(2).

Cas, R.A.F., Simmons, J.M., 2018. Why Deep-Water Eruptions Are So Different From Subaerial Eruptions. Frontiers in Earth Science, 6.

Cesca, S. et al., 2020. Drainage of a deep magma reservoir near Mayotte inferred from seismicity and deformation. Nature Geoscience, 13(1): 87-93.

Chadwick, W.W. et al., 2008. Direct video and hydrophone observations of submarine explosive eruptions at NW Rota-1 volcano, Mariana arc. Journal of Geophysical Research: Solid Earth, 113(B8).

Charlou, J.L. et al., 2010. High production and fluxes of H2 and CH4 and evidence of abiotic hydrocarbon synthesis by serpentinization in ultramafic-hosted hydrothermal systems on the Mid-Atlantic Ridge, Diversity Of Hydrothermal Systems On Slow Spreading Ocean Ridges, pp. 265-296.

Charlou, J.L., Rona, P., Bougault, H., 1987. Methane anomalies over TAG hydrothermal field on Mid Atlantic Ridge. Journal of Marine Research, 45(2): 461-472.

Clague, D.A., Paduan, J.B., Davis, A.S., 2009. Widespread strombolian eruptions of mid-ocean ridge basalt. Journal of Volcanology and Geothermal Research, 180(2): 171-188.

Clarke, W.B., Jenkins, W.J., Top, Z., 1976. Determination of tritium by mass spectrometric measurement of 3He. The International Journal of Applied Radiation and Isotopes, 27(9): 515-522.

Cline, J.D., Richards, F.A., 1969. Oxygenation of hydrogen sulfide in seawater at constant salinity, temperature and pH. Environmental Science & Technology, 3(9): 838-843.

Craig, H., 1953. The geochemistry of the stable carbon isotopes. Geochimica et Cosmochimica Acta, 3(2): 53-92.

Craig, H., Lupton, J.E., 1981. Helium-3 and mantle volatiles in the ocean and the oceanic crust. The oceanic lithosphere, 7: 391.

Curewitz, D., Karson, J.A., 1998. Geological Consequences of Dike Intrusion at Mid-Ocean Ridge Spreading Centers, Faulting and Magmatism at Mid-Ocean Ridges, pp. 117-136.

de Hoog, J.C.M., Taylor, B.E., van Bergen, M.J., 2001. Sulfur isotope systematics of basaltic lavas from Indonesia: implications for the sulfur cycle in subduction zones. Earth and Planetary Science Letters, 189(3): 237-252.

Debeuf, D., 2004. Étude de l'évolution volcano-structurale et magmatique de Mayotte (archipel des Comores, océan Indien). Université de la Reunion, 277.

Degens, E.T., Behrendt, M., Gotthardt, B., Reppmann, E., 1968. Metabolic fractionation of carbon isotopes in marine plankton—II. Data on samples collected off the coasts of Peru and Ecuador. Deep Sea Research and Oceanographic Abstracts, 15(1): 11-20.

Delaney, J.R. et al., 1998. The Quantum Event of Oceanic Crustal Accretion: Impacts of Diking at Mid-Ocean Ridges. Science, 281(5374): 222-230.

Dofal, A., Fontaine, F.R., Michon, L., Barruol, G., Tkalčić, H., 2021. Nature of the crust beneath the islands of the Mozambique Channel: Constraints from receiver functions. Journal of African Earth Sciences, 184: 104379.

Donval, J.P., Guyader, V., 2017. Analysis of hydrogen and methane in seawater by "Headspace" method: Determination at trace level with an automatic headspace sampler. Talanta, 162: 408-414.

Dullo, W.-C. et al., 1998. Morphology and Sediments of the Fore-Slopes of Mayotte, Comoro Islands: Direct Observations from a Submersible, Reefs and Carbonate Platforms in the Pacific and Indian Oceans, pp. 217-236.

Embley, R.W. et al., 2014. Eruptive modes and hiatus of volcanism at West Mata seamount, NE Lau basin: 1996-2012. Geochemistry, Geophysics, Geosystems, 15(10): 4093-4115.

Emerick, C.M., Duncan, R.A., 1982. Age progressive volcanism in the Comores Archipelago, western Indian Ocean and implications for Somali plate tectonics. Earth and Planetary Science Letters, 60(3): 415-428.

Emerson, S., Hedges, J., 2008. Chemical Oceanography and the Marine Carbon Cycle.

Etiope, G., Sherwood Lollar, B., 2013. Abiotic methane on Earth. Reviews of Geophysics, 51(2): 276-299.

Famin, V., Michon, L., Bourhane, A., 2020. The Comoros archipelago: a right-lateral transform boundary between the Somalia and Lwandle plates. Tectonophysics, 789: 228539.

Feuillet, N., 2019. MAYOBS1 cruise, RV Marion Dufresne.

Feuillet, N. et al., 2021. Birth of a large volcanic edifice offshore Mayotte via lithosphere-scale dyke intrusion. Nature Geoscience, 14: 787-795.

Feuillet, N., Jorry, S., Rinnert, E., Thinon, I., Fouquet, Y., 2019. MAYOBS cruises, RV Marion Dufresne.

Fiebig, J. et al., 2004. Chemical and isotopic equilibrium between CO2 and CH4 in fumarolic gas discharges: Generation of CH4 in arc magmatic-hydrothermal systems 1 1Associate editor: M. Kusakabe. Geochimica et Cosmochimica Acta, 68(10): 2321-2334.

Fouquet, Y., Feuillet, N., 2019. MAYOBS4 cruise, RV Marion Dufresne.

Gamo, T. et al., 2001. Chemical characteristics of newly discovered black smoker fluids and associated hydrothermal plumes at the

Rodriguez Triple Junction, Central Indian Ridge. Earth and Planetary Science Letters, 193(3): 371-379.

Geo-Ocean (Ifremer), 2022. Bathymétrie - Mayotte (synthèse, 2021).

Giggenbach, W.F., 1996. Chemical Composition of Volcanic Gases. In: Scarpa, R., Tilling, R.I. (Eds.), Monitoring and Mitigation of Volcano Hazards. Springer Berlin Heidelberg, Berlin, Heidelberg, pp. 221-256.

Giggenbach, W.F., Sano, Y., Wakita, H., 1993. Isotopic composition of helium, and CO2 and CH4 contents in gases produced along the New Zealand part of a convergent plate boundary. Geochimica et Cosmochimica Acta, 57(14): 3427-3455.

Glazer, B.T., Rouxel, O.J., 2009. Redox Speciation and Distribution within Diverse Iron-dominated Microbial Habitats at Loihi Seamount. Geomicrobiology Journal, 26(8): 606-622.

Hekinian, R., Chaigneau, M., Cheminee, J.L., 1973. Popping Rocks and Lava Tubes from the Mid-Atlantic Rift Valley at 36° N. Nature, 245(5425): 371-373.

Hilton, D.R., 1996. The helium and carbon isotope systematics of a continental geothermal system: results from monitoring studies at Long Valley caldera (California, U.S.A.). Chemical Geology, 127(4): 269-295.

Hilton, D.R., Hammerschmidt, K., Teufel, S., Friedrichsen, H., 1993. Helium isotope characteristics of Andean geothermal fluids and lavas. Earth and Planetary Science Letters, 120(3-4): 265-282.

Hilton, D.R., McMurtry, G.M., Goff, F., 1998. Large variations in vent fluid CO2/3He ratios signal rapid changes in magma chemistry at Loihi seamount, Hawaii. Nature, 396(6709): 359-362.

Jansson, C., Northen, T., 2010. Calcifying cyanobacteria—the potential of biomineralization for carbon capture and storage. Current Opinion in Biotechnology, 21(3): 365-371.

Jenkins, W.J. et al., 2019. A comprehensive global oceanic dataset of helium isotope and tritium measurements. Earth System Science Data, 11(2): 441-454.

Jorry, S., 2019. MAYOBS2 cruise, RV Marion Dufresne.

Kawagucci, S. et al., 2008. Methane, manganese, and helium-3 in newly discovered hydrothermal plumes over the Central Indian Ridge, 18°-20°S. Geochemistry, Geophysics, Geosystems, 9(10).

Klein, F., Tarnas, J.D., Bach, W., 2020. Abiotic Sources of Molecular Hydrogen on Earth. Elements, 16(1): 19-24.

Lappan, R. et al., 2023. Molecular hydrogen in seawater supports growth of diverse marine bacteria. Nature Microbiology, 8(4): 581-595.

Lavayssière, A. et al., 2022. A new 1D velocity model and absolute locations image the Mayotte seismo-volcanic region. Journal of Volcanology and Geothermal Research, 421: 107440.

Lemoine, A. et al., 2020. The 2018–2019 seismo-volcanic crisis east of Mayotte, Comoros islands: seismicity and ground deformation markers of an exceptional submarine eruption. Geophysical Journal International, 223(1): 22-44.

Liu, B., Six, K.D., Ilyina, T., 2021. Incorporating the stable carbon isotope 13C in the ocean biogeochemical component of the Max Planck Institute Earth System Model. Biogeosciences, 18(14): 4389-4429.

Liuzzo, M. et al., 2021. Gas Geochemistry at Grande Comore and Mayotte Volcanic Islands (Comoros Archipelago), Indian Ocean. Geochemistry, Geophysics, Geosystems, 22(8).

Lupton, J. et al., 2006. Submarine venting of liquid carbon dioxide on a Mariana Arc volcano. Geochemistry, Geophysics, Geosystems, 7(8).

Lupton, J. et al., 2008. Venting of a separate CO2-rich gas phase from submarine arc volcanoes: Examples from the Mariana and Tonga-Kermadec arcs. Journal of Geophysical Research: Solid Earth, 113(B8).

Lupton, J.E., Baker, E.T., Massoth, G.J., 1999. Helium, heat, and the generation of hydrothermal event plumes at mid-ocean ridges. Earth and Planetary Science Letters, 171(3): 343-350.

Manoux, M. et al., 2023. Impact of volcanism on sedimentary diagenesis, Session: 13dO1 - Hydrothermal vents from discharge to biogeochemical impacts, Goldschmidt Conference: Lyon France 9-14 July 2023.

Marty, B., Jambon, A., 1987. C/3He in volatile fluxes from the solid Earth: implications for carbon geodynamics. Earth and Planetary Science Letters, 83(1): 16-26.

Marty, B., Jambon, A., Sano, Y., 1989. Helium isotopes and CO2 in volcanic gases of Japan. Chemical Geology, 76(1-2): 25-40.

Marty, B., Meynier, V., Nicolini, E., Griesshaber, E., Toutain, J.P., 1993. Geochemistry of gas emanations: A case study of the Réunion Hot Spot, Indian Ocean. Applied Geochemistry, 8(2): 141-152.

Masquelet, C. et al., 2022a. The East-Mayotte new volcano in the Comoros Archipelago: structure and timing of magmatic phases inferred from seismic reflection data. Comptes Rendus. Géoscience, 354(S2): 65-79.

Masquelet, C. et al., 2022b. Structure of a new submarine volcano and magmatic phases to the East of Mayotte, in the Comoros Archipelago, Indian Ocean. EGU General Assembly 2022, Vienna, Austria, 23–27 May 2022, EGU22-10766.

Mayotte Volcanological And Seismological Monitoring Network (REVOSIMA), Institut de physique du globe de Paris (IPGP), Bureau de recherches géologiques et minières (BRGM), Institut français de recherche pour l'exploitation de la mer (IFREMER), Centre national de la recherche scientifique (CNRS), 2021. Data collection of the Mayotte volcanological and seismological monitoring network (REVOSIMA).

McCollom, T.M., 2013. Laboratory Simulations of Abiotic Hydrocarbon Formation in Earth's Deep Subsurface. Reviews in Mineralogy and Geochemistry, 75(1): 467-494.

McCollom, T.M., 2016. Abiotic methane formation during experimental serpentinization of olivine. Proceedings of the National Academy of Sciences, 113(49): 13965-13970.

McDermott, J.M., Seewald, J.S., German, C.R., Sylva, S.P., 2015. Pathways for abiotic organic synthesis at submarine hydrothermal fields. Proceedings of the National Academy of Sciences, 112(25): 7668-7672.

McLaughlin-West, E.A. et al., 1999. Variations in hydrothermal methane and hydrogen concentrations following the 1998 eruption at Axial Volcano. Geophysical Research Letters, 26(23): 3453-3456.

Métrich, N., Wallace, P.J., 2008. Volatile Abundances in Basaltic Magmas and Their Degassing Paths Tracked by Melt Inclusions. Reviews in Mineralogy and Geochemistry, 69(1): 363-402.

Michel, A.P.M., Wankel, S.D., Kapit, J., Sandwith, Z., Girguis, P.R., 2018. In situ carbon isotopic exploration of an active submarine volcano. Deep Sea Research Part II: Topical Studies in Oceanography, 150: 57-66.

Michon, L., 2016. The Volcanism of the Comoros Archipelago Integrated at a Regional Scale. Springer Berlin Heidelberg, pp. 333-344.

Milesi, V.P. et al., 2020. Early Diagenesis of Lacustrine Carbonates in Volcanic Settings: The Role of Magmatic CO2 (Lake Dziani Dzaha, Mayotte, Indian Ocean). ACS Earth and Space Chemistry, 4(3): 363-378.

Milkov, A.V., Etiope, G., 2018. Revised genetic diagrams for natural gases based on a global dataset of >20,000 samples. Organic Geochemistry, 125: 109-120.

Nougier, J., Cantagrel, J.M., Karche, J.P., 1986. The Comores archipelago in the western Indian Ocean: volcanology, geochronology and geodynamic setting. Journal of African Earth Sciences (1983), 5(2): 135-145.

Pegler, S.S., Ferguson, D.J., 2021. Rapid heat discharge during deep-sea eruptions generates megaplumes and disperses tephra. Nature Communications, 12(1).

Pelleter, A.-A. et al., 2014. Melilite-bearing lavas in Mayotte (France): An insight into the mantle source below the Comores. Lithos, 208-209: 281-297.

Perfit, M.R. et al., 2003. Interaction of sea water and lava during submarine eruptions at mid-ocean ridges. Nature, 426(6962): 62-65.

Pörtner, H.-O. et al., 2022. IPCC, 2022, Climate Change 2022: Impacts, Adaptation and Vulnerability Working Group II Contribution to the Sixth Assessment Report of the

Intergovernmental Panel on Climate Change, Cambridge University Press, Cambridge, UK and New York, NY, USA.

Raynaud, D. et al., 1993. The Ice Record of Greenhouse Gases. Science, 259(5097): 926-934.

Resing, J.A. et al., 2009. Chemistry of hydrothermal plumes above submarine volcanoes of the Mariana Arc. Geochemistry, Geophysics, Geosystems, 10(2).

Resing, J.A. et al., 2007. Venting of Acid-Sulfate Fluids in a High-Sulfidation Setting at NW Rota-1 Submarine Volcano on the Mariana Arc. Economic Geology, 102(6): 1047-1061.

Resing, J.A., Lupton, J.E., Feely, R.A., Lilley, M.D., 2004. CO2 and 3He in hydrothermal plumes: implications for mid-ocean ridge CO2 flux. Earth and Planetary Science Letters, 226(3): 449-464.

Resing, J.A. et al., 2011. Active submarine eruption of boninite in the northeastern Lau Basin. Nature Geoscience, 4(11): 799-806.

Resing, J.A. et al., 2015. Basin-scale transport of hydrothermal dissolved metals across the South Pacific Ocean. Nature, 523(7559): 200-U140.

REVOSIMA, Février 2021. Bulletin n°27 du 1er au 28 février 2021 : Bulletin de l'activité sismo-volcanique à Mayotte.

Rinnert, E., Thinon, I., Feuillet, N., 2020. MD 228 / MAYOBS15 cruise, RV Marion Dufresne.

Rubin, K.H. et al., 2012. Volcanic Eruptions in the Deep Sea. Oceanography, 25(1): 142-157.

Sano, Y., Fischer, T.P., 2013. The Analysis and Interpretation of Noble Gases in Modern Hydrothermal Systems. In: Burnard, P. (Ed.), The Noble Gases as Geochemical Tracers. Springer Berlin Heidelberg, Berlin, Heidelberg, pp. 249-317.

Sano, Y., Marty, B., 1995. Origin of carbon in fumarolic gas from island arcs. Chemical Geology, 119(1): 265-274.

Sansone, F.J., Resing, J.A., 1995. Hydrography and geochemistry of sea surface hydrothermal plumes resulting from Hawaiian coastal volcanism. Journal of Geophysical Research, 100(C7): 13555.

Sansone, F.J. et al., 1991. Lava-seawater interactions at shallow-water submarine lava flows. Geophysical Research Letters, 18(9): 1731-1734.

Santana-Casiano, J.M. et al., 2016. Significant discharge of CO2 from hydrothermalism associated with the submarine volcano of El Hierro Island. Scientific Reports, 6(1): 25686.

Schmittner, A. et al., 2013. Biology and air–sea gas exchange controls on the distribution of carbon isotope ratios (δ13C) in the ocean. Biogeosciences, 10(9): 5793-5816.

Span, R., Wagner, W., 1996. A New Equation of State for Carbon Dioxide Covering the Fluid Region from the Triple-Point Temperature to 1100 K at Pressures up to 800 MPa. Journal of Physical and Chemical Reference Data, 25(6): 1509-1596.

Sültenfuß, J., 2016. Hints for sampling, Helis - helium isotopes studies Bremen.

Sültenfuß, J., Roether, W., Rhein, M., 2009. The Bremen mass spectrometric facility for the measurement of helium isotopes, neon, and tritium in water. Isotopes in Environmental and Health Studies, 45(2): 83-95.

Suzuki, A., 1998. Combined effects of photosynthesis and calcification on the partial pressure of carbon dioxide in seawater. Journal of Oceanography, 54(1): 1-7.

Svensen, H. et al., 2004. Release of methane from a volcanic basin as a mechanism for initial Eocene global warming. Nature, 429(6991): 542-545.

Symonds, R.B., Rose, W.I., Bluth, G.J.S., Gerlach, T.M., 1994. Volcanic-gas studies; methods, results, and applications. Reviews in Mineralogy and Geochemistry, 30(1): 1-66.

Thinon, I., Rinnert, E., Feuillet, N., 2021. MAYOBS17 cruise, RV Pourquoi Pas ?

Thordarson, T., Self, S., 1993. The Laki (Skaftár Fires) and Grímsvötn eruptions in 1783-1785. Bulletin of Volcanology, 55(4): 233-263.

Truche, L., McCollom, T.M., Martinez, I., 2020. Hydrogen and Abiotic Hydrocarbons: Molecules that Change the World. Elements, 16(1): 13-18.

Tsunogai, U. et al., 1994. Peculiar features of Suiyo Seamount hydrothermal fluids, Izu-Bonin Arc: Differences from subaerial volcanism.

Earth and Planetary Science Letters, 126(4): 289-301.

Tzevahirtzian, A., Zaragosi, S., Bachèlery, P., Biscara, L., Marchès, E., 2021. Submarine morphology of the Comoros volcanic archipelago. Marine Geology, 432: 106383.

Wang, L., Jin, Z., Chen, X., Su, Y., Huang, X., 2023. The Origin and Occurrence of Natural Hydrogen. Energies, 16(5): 2400.

Wang, Y. et al., 2020. Helium and carbon isotopic signatures of thermal spring gases in southeast Yunnan, China. Journal of Volcanology and Geothermal Research, 402: 106995.

Weiss, R.F., 1971. Solubility of helium and neon in water and seawater. Journal of Chemical & Engineering Data, 16(2): 235-241.

Weiss, R.F., 1974. Carbon dioxide in water and seawater: the solubility of a non-ideal gas. Marine Chemistry, 2(3): 203-215.

Wen, H.-Y. et al., 2016. Helium and methane sources and fluxes of shallow submarine hydrothermal plumes near the Tokara Islands, Southern Japan. Scientific Reports, 6(1): 34126.

White, J.D.L., Schipper, C.I., Kano, K., 2015. Chapter 31 - Submarine Explosive Eruptions. In: Sigurdsson, H. (Ed.), The Encyclopedia of Volcanoes (Second Edition). Academic Press, Amsterdam, pp. 553-569.

Worman, S.L., Pratson, L.F., Karson, J.A., Schlesinger, W.H., 2020. Abiotic hydrogen (H2) sources and sinks near the Mid-Ocean Ridge (MOR) with implications for the subseafloor biosphere. Proceedings of the National Academy of Sciences of the United States of America, 117(24): 13283-13293.

Zhang, J., Quay, P.D., Wilbur, D.O., 1995. Carbon isotope fractionation during gas-water exchange and dissolution of CO2. Geochimica et Cosmochimica Acta, 59(1): 107-114.

Zinke, J., Reijmer, J.J.G., Thomassin, B.A., 2003a. Systems tracts sedimentology in the lagoon of Mayotte associated with the Holocene transgression. Sedimentary Geology, 160(1): 57-79.

Zinke, J., Reijmer, J.J.G., Thomassin, B.A., 2003b. Systems tracts sedimentology in the lagoon of Mayotte associated with the Holocene transgression. Sedimentary Geology, 160(1-3): 57-79.

Zolotov, M.Y., Shock, E.L., 2000. A thermodynamic assessment of the potential synthesis of condensed hydrocarbons during cooling and dilution of volcanic gases. Journal of Geophysical Research: Solid Earth, 105(B1): 539-559.

CHAPTER 5. Submarine Venting of Liquid Carbon Dioxide in a Volcanic Context

A version of this chapter will be submitted in *Geochimica et Chosmochimica Acta*.

Manon Mastin[1], Jean-Pierre Donval[1], Vivien Guyader[1], Yoan Germain[1], Thomas Giunta[1], Carla Scalabrin[1], Eric C. Gaucher[2], Stéphane Jouenne[3], Sébastien Dehez[3], Olivier Rouxel[1], Emmanuel Rinnert[1], Cécile Cathalot[1]

[1]Geo-Ocean UMR 6538 CNRS - Ifremer - UBO - UBS, F-29280 Plouzané, France

[2]Lavoisier H_2 Geoconsult, FR-74400 Chamonix, France

[3]TotalEnergies, CSTJF EB 437, Avenue Larribau, F-64018 Pau Cedex, France

CHAPTER 5. Submarine Venting of Liquid Carbon Dioxide in a Volcanic Context

Abstract

Although CO_2 is an abundant gas emitted during submarine volcanic eruptions or associated hydrothermal circulation, it has rarely been documented in the liquid form, which depends on pressure-temperature conditions of the site. Discharge of CO_2 in the ocean can lead to local perturbations in ocean acidity and alkalinity, with consequences on biogeochemical cycles, potential gas release at the ocean surface or sediment stability and geochemistry.

Here we document strong discharges of liquid CO_2 droplets recently discovered at about 1500 m below sea level, in the Horseshoe structure, on the eastern upper submarine slope of Mayotte Island (Comoros Archipelago, Indian Ocean). This area offers a natural laboratory to evaluate, through the study of dedicated geochemical processes, the impact of elevated level of CO_2 on the water column geochemistry. Water column geochemistry has been monitored above the vents in terms of dissolved gases, total dissolvable metals and physicochemical parameters. Excess of ^3He up to 19.4 fmol/kg in the water column were associated to strong pH anomalies (up to -0.8 pH unit) and elevated concentrations of dissolved gases with maximum measured of 191 µmol/kg for CO_2, 2956 nmol/kg for CH_4, and 175 nmol/kg for H_2.

This study investigates the liquid CO_2 emissions focusing on their origin, on the droplet dissolution processes during the ascent within the water column, and on their impact on the geochemistry. While isotopic helium composition have highlighted a homogeneous and dominant mantle-origin of the emissions, the droplet dissolution and inherently the impact on the water column geochemistry are strongly governed by the seafloor morphology and the local hydrodynamics.

CHAPITRE 5. Emissions Sous-Marines de CO_2 Liquide en Contexte Volcanique

Résumé

Bien que le CO_2 soit un gaz émis en abondance par les éruptions volcaniques sous-marines ou la circulation hydrothermale associée, il a rarement été documenté sous sa forme liquide, qui dépend des conditions de pression et de température du site. L'injection de CO_2 dans l'océan peut entraîner des perturbations locales sur l'acidité et l'alcalinité de l'océan, avec des conséquences sur les cycles biogéochimiques, le dégazage potentiel à la surface de l'océan, la stabilité des sédiments et la géochimie.

Nous documentons ici de fortes émissions de gouttelettes de CO_2 liquide récemment découvertes à environ 1500 mètres de profondeur, dans la structure du Fer à Cheval, sur le versant Est sous-marin de l'île de Mayotte (archipel des Comores, Océan Indien). Cette région offre un laboratoire naturel pour évaluer, grâce à l'étude de processus géochimiques dédiés, l'impact d'un niveau élevé de CO_2 sur la géochimie de la colonne d'eau. La géochimie de la colonne d'eau a été surveillée au-dessus des sites d'émissions en termes de gaz dissous, de métaux totaux dissolvables et de paramètres physico-chimiques. Un excès en ^3He allant jusqu'à 19,4 fmol/kg dans la colonne d'eau a été associé à des anomalies de pH importantes (jusqu'à -0,8 unité de pH) et à des concentrations élevées de gaz dissous, avec des mesures maximales de 191 µmol/kg pour le CO_2 et 2956 nmol/kg pour le CH_4.

Cette étude s'intéresse aux émissions de CO_2 liquide, plus particulièrement à leur origine, aux processus de dissolution des gouttelettes pendant leur ascension dans la colonne d'eau et à leur impact sur la géochimie. Alors que la composition isotopique de l'hélium a mis en évidence l'origine mantellique et homogène des émissions, la dissolution des gouttelettes et ainsi l'impact sur la géochimie de la colonne d'eau sont fortement régis par la morphologie du fond marin et l'hydrodynamique locale.

5.1. Introduction

Volcanic activity represents the primary mechanism for the transfer of carbon from the lithosphere to the atmosphere. While the global carbon dioxide (CO_2) flux from subaerial and submarine volcanoes remains poorly quantified, volcanic CO_2 emissions have been a key control on atmospheric-oceanic CO_2 levels over geological time scales, ultimately regulating the evolution of climate and life on Earth.

Currently, submarine volcanism has been estimated to represent about 85% of the global Earth volcanism (White et al., 2015), however the number of deep active submarine volcano remains uncertain, with a probable underestimation of intraplate volcanism (Rubin et al., 2012). In addition, more and more CO_2 degassing areas associated with recent underwater volcanic activity are being discovered, either at island arcs such as the CO_2 bubble venting of Kick'em Jenny submarine volcano in the Caribbean Sea (Carey et al., 2016; Michel et al., 2018), at intra-plate magmatism associated to the young submarine volcano of El Hierro in Canary Island (Santana-Casiano et al., 2016), along mid-oceanic ridges as CO_2-rich hydrothermal fluid (Massoth et al., 1989; Resing et al., 2004), or around active coastal or island volcano such as Island of Milos in Greece (Dando et al., 1995).

Such venting site are generally located at shallow depths (< 500 m) and lead to discharges of CO_2 and reducing species (H_2S, CH_4, and H_2) into the surface oceans where they influence surface ocean chemistry and productivity (González-Delgado and Hernández, 2018; Aiuppa et al., 2021). CO_2 discharges alter the ocean acidity (Carey et al., 2013; Agostini et al., 2015), with potential consequences on biogeochemical cycles and on processes of calcification of carbonate accreting invertebrates such as corals, and present a risk of gas release at the surface (Fabricius et al., 2011; Morrow et al., 2015; Santana-Casiano et al., 2016; Price and Giovannelli, 2017; González-Delgado and Hernández, 2018).

Although CO_2 is the most abundant dissolved gas found in the context of submarine volcanic eruption and the associated hydrothermal circulation or degassing, it is rarely found in its liquid phase due to inappropriate local pressure-temperature conditions (Brewer et al., 2002). To date, only three sites of liquid CO_2 venting have been discovered and studied: JADE hydrothermal field (Sakai et al., 1990a; Sakai et al., 1990b) and Yonaguni Knoll IV hydrothermal system (Konno et al., 2006) at the Okinawa Trough, and the Champagne vent site on NW Eifuku in the northern Mariana Arc (Lupton et al., 2006). Those liquid CO_2 discharges have been observed at depths of ~1300-1600 mbsl (below sea level) above the

ocean seafloor as cold droplets mainly constituted of CO_2 (>85%) with trace amounts of H_2S, CH_4 and H_2. Suggested sub-seafloor processes for such emissions includes the phase separation of hydrothermal fluid due to boiling or the directly degassing from a magma chamber, then a cooling during the migration to the seafloor, and ultimately the formation of CO_2 liquid and hydrate near the surface, with melting of the solid CO_2-hydrate to liquid CO_2 due to a temperature increase within the sedimentary layer.

Nonetheless, because of the low number of discovered sites, we still have a poor understanding of the extent to which these emissions could affect CO_2 cycling. Given the importance of CO_2 release in the atmosphere for climate (e.g. increasing temperature, or frequency of extreme events), better understanding the implication of submarine volcanic eruption on CO_2 release is of paramount importance.

Here we document strong discharges of liquid CO_2 droplets recently discovered at about 1500 m below sea level, in the Horseshoe structure, on the eastern upper submarine slope of Mayotte Island (Comoros Archipelago, Indian Ocean). Since the eruption of Fani Maoré seamount (~40 km to the east) in May 2018, the site has experienced an exceptionally deep seismic activity and a continuous increase of number of liquid CO_2 vent sites over time. This area is a natural laboratory to evaluate, through the study of dedicated geochemical processes, the impact of elevated level of CO_2 on the water column geochemistry at more global scales.

In this study, we present a compilation of geochemical data taken above the Horseshoe degassing sites and we aim to determine the origin of the liquid CO_2 emissions observed and the relationship with the known emissions in the area. In addition, we seek to understand the geochemical processes that occur in seawater during the ascent of the liquid CO_2 droplets and, consequently, their dissolution. Furthermore, we intend to assess the impact of this dissolution on the water column, particularly concerning water column acidification across spatial scales. By closely examining the interactions between liquid CO_2 droplets and the surrounding water, we aspire to gain a deeper understanding of the environmental implications of these phenomena.

5.2. Geologic setting

Sites of carbon dioxide venting have been recently discovered in May 2019 on the eastern upper submarine slope of Mayotte Island (Comoros Archipelago, Indian Ocean), at the beginning of the sismo-volcanic crisis linked to the submarine eruption of the Fani Maoré volcano (REVOSIMA, 2023; Scalabrin, 2023;

Cathalot et al., in prep.). The sites are located within a geologic structure - referred as Horseshoe due to its shape - about 10 km east from Petite Terre (Figure 5. 1) at 1100~1700m deep. The Horseshoe edifice is describe by Puzenat et al. (2022) as a 4 km wide volcanic cone that underwent a major collapse, resulting in the formation of a 2 km wide depression opened to the north. The Horseshoe area is a preexisting structure to the Fani Maoré volcano, that erupted from 2018 to 2021, experiencing both effusive and explosive eruptive activities (Feuillet et al., 2021; Puzenat et al., 2022).

Based on geomorphologic features and the location of the deep seismic swarm observed since 2018 below the Horseshoe area, Puzenat et al. (2022) suggest that the earlier deposits may result from the same deep magmatic system that fed the 2018 eruption of Fani Maoré.

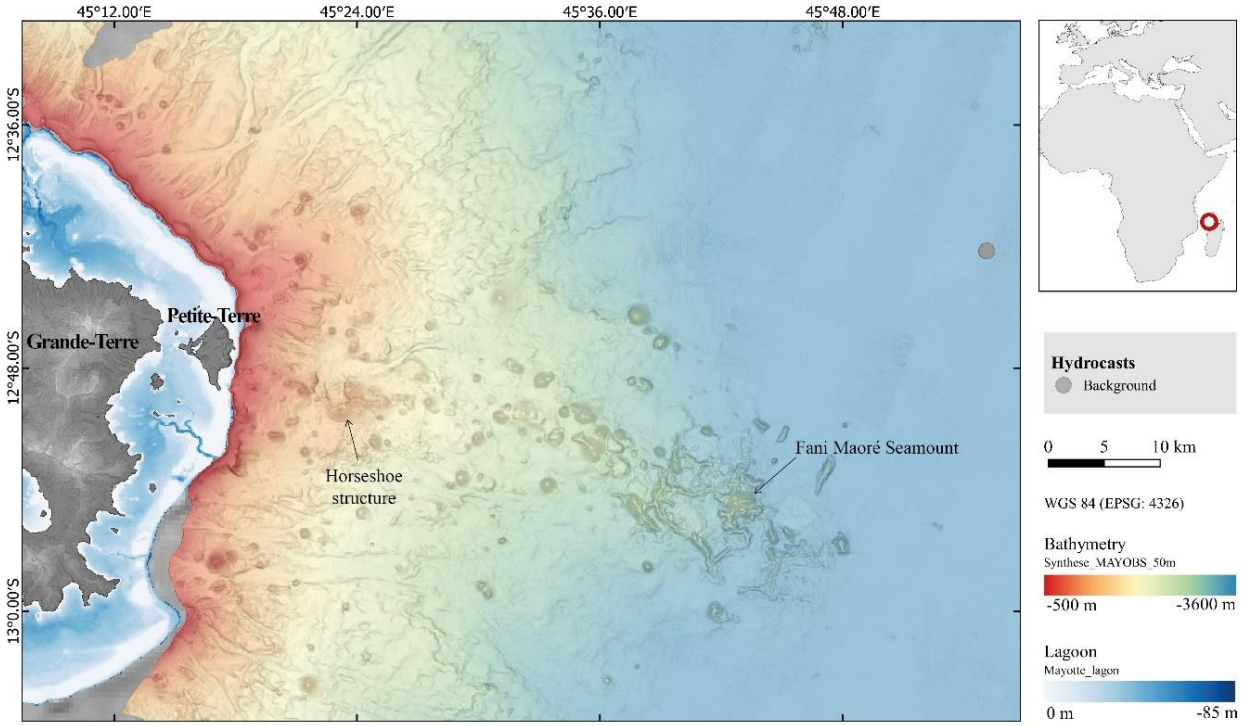

Figure 5. 1. Regional map of the study site with the background hydrocast and 50 m-resolution bathymetry (Geo-Ocean (Ifremer), 2022). Mayotte Island is composed of two islands, Grande-Terre and Petite-Terre. The Horseshoe structure is located ~10 km east of Petite-Terre, and Fani Maoré Seamount ~50 km.

Since the beginning of the crisis, the number of venting sites has been constantly increasing. Sites of venting were monitored from 2nd of May 2019 to 22nd of July 2022 along different survey (MAYOBS cruises, (Feuillet et al., 2019)) and scientific (GeoFLAMME cruise, (Rinnert et al., 2021)) cruises (Figure 5. 2). Sites A_0 and B_0 were discovered in May 2019,

the site C_0 in August 2019, the sites D_0 and E_0 in May 2020. Sites C_1 and F_0 were first observed in October 2020 simultaneously to an expansion toward the northwest of the A_0 and B_0 sites, with new sites called B_1, A_1 and A_2. The sites G_0, D_1, C_2+C_3 and C_4 were found between January and May 2021 (REVOSIMA, 2023; Scalabrin, 2023). The date of discovery of each venting site does not necessarily correspond to the date of the beginning of its activity but to the date of its first observation. It can therefore be older.

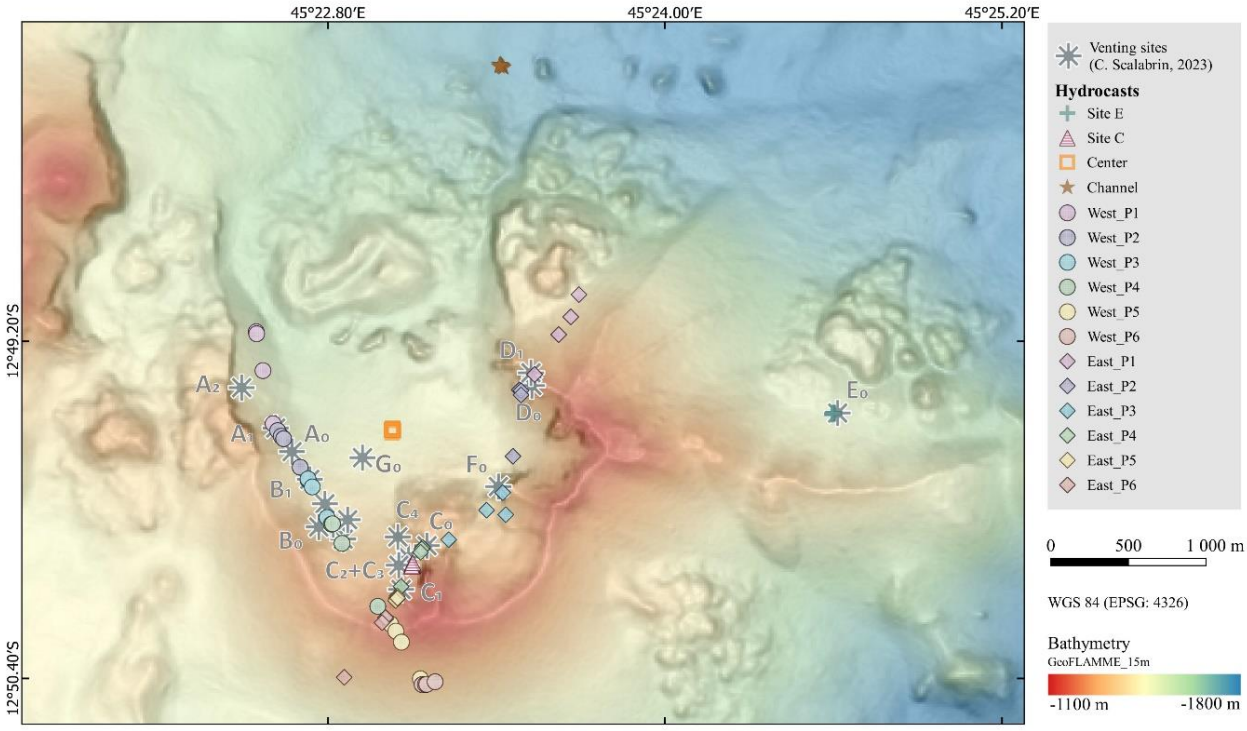

Figure 5. 2. Map of the Horseshoe area with 15 m-resolution bathymetry acquired during the GeoFLAMME cruise (Rinnert et al., 2021).Venting sites of liquid carbon dioxide identified before and during GeoFLAMME by Scalabrin (2023) are represented. The water column samples of this study taken in the Horseshoe area are shown, in association with the hydrocast label.

Carbon dioxide venting occurs in its liquid phase from the seafloor surface were carbon dioxide hydrates have also formed. First geochemical analyses on the venting droplets have shown that these droplets are mainly composed of carbon dioxide CO_2 (99.0 ± 0.3 $\%_{vol}$), with a small contribution of methane CH_4 (0.8 ± 0.2 $\%_{vol}$) and dihydrogen H_2 (10 to 1000 ppm_{vol}). The stable carbon isotopic signature ($\delta^{13}C$) showed that CO_2 is of magmatic origin with a mantle-like signature ($\delta^{13}CO_2$ ~4‰) while CH_4 appeared to be rather of abiotic origin, although a mixed biogenic/thermogenic contribution cannot be ruled out ($\delta^{13}CH_4$ ~19‰). However, the helium isotopic signature ($^3He/^4He$) clearly

points towards a deep magmatic origin of the venting droplets (i.e. from the mantle) (REVOSIMA, 2023; Cathalot et al., in prep.).

It is worth mentioning that this CO_2 venting activity is part of a larger volcano-tectonic context in which the Fani Maore submarine volcano located about 40 km to the east of the Horseshoe structure, at about 3500 m below sea level first erupted in 2018 ((Feuillet et al., 2021), (Figure 5. 1). The deep seismic activity associated with the eruption possibly corresponds to a single and large magmatic plumbing system with the presence of a main magma reservoir at mantle depths (38-54 km), 5–10 km east of Petite-Terre, thus right below the Horseshoe area (Dofal et al., 2022). The observation of persisting and increasing acoustic plumes in the Horseshoe area during the successive cruises seems linked to the position of the proximal cluster (Mercury et al., 2022; Puzenat et al., 2022).

West of the Horseshoe structure, onshore Mayotte,, the most recent volcanic activity occurred in the Holocene on the eastern side of the Island, on Petite Terre where two main and persistent areas of low-temperature CO_2-rich gas seeps are present: the Airport tidal flat and the Dziani Dzaha intracrateric lake (Liuzzo et al., 2022). First studies suggest that the bubbling zones found around the Mayotte volcanic system (Airport tidal flat, Dziani Dzaha lake and Horseshoe area) might be linked altogether by the same deep source, and their connection enhanced or increased by the seismo-volcanic crisis (Milesi et al., 2020; Liuzzo et al., 2021; Cadeau et al., 2022; Liuzzo et al., 2022).

5.3. Sampling, data treatment and analytical techniques

5.3.1. CTD-rosette sampling during GeoFlamme cruise

Data presented in this study were collected during the GeoFlamme scientific cruise that took place in 2021, from April 17th to May 26th, onboard the *R/V Pourquoi Pas ?* (Rinnert et al., 2021).

Study and sampling of the water column geochemistry was performed using a Seabird 911 Plus CTD (Conductivity Temperature Depth) mounted onto a rosette carousel equipped with 20 to 24 Ocean Test Equipment (OTE) bottles of 10 L. This CTD-rosette package was completed with a Seapoint Turbidity Meter sensor that measures turbidity reported as Nephelometric Turbidity Unit (NTU). It was also coupled with an Optode Aanderaa 4831F for the measurement of O_2 concentration.

Deployment sites for CTD/rosette casts were defined according to the presence of acoustic plumes observed from ship-born multibeam

echo sounder (RESON SB7150, 12 kHz). The objective was not to capture droplets within the CTD-rosette bottles but rather to capture the modified-seawater and to focus on the dissolved phase. In total, four vertical casts, two tow-yows (one on the western part and one on the eastern part of the Horseshoe structure) and one vertical hydrocast for background evaluation (away from the study site) were carried out (Figure 5. 1and Figure 5. 2). The purpose of tow-yo operations is to obtain a 2D-section by rising and lowering the CTD rosette as the ship proceeds on a transect. Here the CTD-rosette was towed between the seafloor and about 400 m below the sea level over 6 points (named P1 to P6 in this study).

Latitude and longitude of each sampling depth were extracted from a USBL (Ultra short baseline) (iXblue ®) transmitter mounted on the CTD-rosette.

5.3.2. Sub-sampling from CTD-rosette and analyses

5.3.2.1. Noble gas: He & Ne

Samples for noble gases analysis were collected immediately after the CTD-rosette recovery to conserve the integrity of the dissolved gases. Water was flushed into copper tubing carefully checking for the absence of air bubbles and sealed using special stainless clamps (Sültenfuß, 2016). Quantification of helium and neon isotopes (^{3}He, ^{4}He, ^{20}Ne, ^{22}Ne) was performed at the Helis Laboratory (Helium isotopes studies, Bremen, Germany) using a mass spectrometric system composed of a quadrupole mass spectrometer (QMS, Balzers QMG112a®) and a sector field mass spectrometer (SMS, MAP 215-50®). This method yields a precision of ± 0.4 % for ^{3}He/^{4}He ratios and ± 0.8 % for helium and neon concentrations (Sültenfuß et al., 2009).

The $^{3}He_{xs}$ is defined as the non-atmospheric ^{3}He over saturation that corresponds to the ^{3}He concentration corrected from air contamination and atmospheric air in equilibrium in the water column. Assuming that the entire Ne concentration comes from atmospheric air, and that the tritiogenic ^{3}He (i.e. resulting from the radioactive decay of tritium) is negligible in the Indian Ocean offshore Mayotte Island (Jenkins et al., 2019), the $^{3}He_{xs}$ should only corresponds to the supply of mantellic and crustal helium, and should be defined as follows:

$$\begin{cases} Ne_m = Ne_{eq} + Ne_{air} \\ {}^{3}He_m = {}^{3}He_{eq} + {}^{3}He_{air} + {}^{3}He_{xs} \end{cases}$$

with *m* the measured concentration, *eq* the equilibrium concentration and *air* the concentration for air contamination. Equilibrium and air contamination neon concentrations were defined as $Ne_{eq} = Ne_{atm} \times \beta_{Ne}$ and $Ne_{air} = Ne_m - Ne_{eq}$, and helium isotopes concentrations as ${}^{3}He_{eq} = {}^{3}He_{atm} \times \beta_{He}$ and ${}^{3}He_{air} = Ne_{air} \times \frac{{}^{3}He_{atm}}{Ne_{atm}}$.

Solubility coefficients of Ne and He in seawater (β_{Ne} and β_{He}, respectively) were determined for each sample according to the seawater temperature and salinity at the sampling depth, using Weiss (1971) solubility equations.

5.3.2.2. Dissolved gases: CO_2, CH_4

Water samples for CH_4 analyses were collected into 125 mL two-valve glass ampoules. Samples were analyzed onboard using the "purge and trap" method developed by Charlou et al. (1987). Briefly, dissolved gases were completely extracted by helium purging and trapped onto activated charcoal at -80°C. CH_4 was desorbed from the trap by increasing temperature and then injected into a gas chromatograph equipped with a flame ionization detector (FID) for quantitative analysis. This method allows for the determination of CH_4 concentrations equivalent to those of open ocean seawater (0.3 nM).

Onboard CO_2 analyses were performed by carefully collecting water samples from the Niskin bottles, without injecting air bubbles, in 240 mL brown glass bottles closed by a screw cap fitted with a PTFE/silicone gas tight septum. Analyses were run by gas chromatography coupled to an helium ionization detector (HID) and using the Headspace method developed by Donval and Guyader (2017) which consists of replacing 20 mL of the seawater sample by a gaseous phase of pure helium in which dissolved gases equilibrate according to solubility coefficients at equilibrium temperature and to water salinity.

5.3.2.3. pH, AT, DIC

Sampling for pH, total alkalinity (A_T) and Dissolved Inorganic Carbon (DIC) was carried out in 30 mL polyethylene bottles (LDPE, Nalgene®) previously rinsed with ultrapure water (Milli-Q Millipore element system) and dried. Samples were analyzed onboard for titration of dissolved alkaline species with hydrochloric acid solution (0.01 mol/L HCl Titrinorm) using a titrimeter (Titrino 848, Metrohm®) combined with a pH electrode (Metrohm®). Total alkalinity and DIC were determined from titration equivalence volumes. The certified reference material for oceanic DIC, Batch #178, was used to test the performance of both the total inorganic carbon and total alkalinity (Certified Reference Material, delivered by the Scripps Research Institute at the University of San Diego under the responsibility of A. Dickson, https://www.nodc.noaa.gov/ocads/oceans/Dickson_CRM/batches.html). pH was measured in lab, with solutions equilibrated to room temperature at 25 ± 2 °C. The *in situ* pH (denoted pH_{corr}) was deducted from the pH measured in the lab following Lui and Chen (2017). Standard deviation of pH, DIC and AT

measurements were respectively of 1.04, 0.08 and 0.19 %. Delta values of pH, DIC and A_T (ΔpH, ΔDIC and ΔA_T, respectively) represent the difference with the background profile. The use of this background cast has been previously validated for its comparison with the Horseshoe area profiles (see Supplementary Material, Figure S 2).

5.3.2.4. Total Dissolvable Manganese and Iron

Sampling for analysis of total dissolvable iron and manganese, respectively TDFe and TDMn, was carried out in 30 mL low density polyethylene bottles (LDPE, Nalgene®) previously washed with 10%$_{v/v}$ hydrochloric acid (HCl 37%, Analytical Grade, Merck) then rinsed a minimum of three times with ultrapure water (Milli-Q Millipore element system). All water samples for metal analysis were acidified to 0.025 mol/L hydrochloric acid (ultrapur® grade) within 6 hours of sampling.

Samples were prepared in lab for analysis about a year after sampling, using the magnesium precipitation method for iron and manganese pre-concentration of seawater developed by Saito and Schneider (2006). This method consists of firstly adding a ^{57}Fe spike to 1.8 mL sample and then separate the trace metals from the matrix using concentrated ammonium hydroxide (50 uL of NH_4OH, Optima grade) that results in the precipitation of the Mg present in seawater as $Mg(OH)_2$. Finally, the pellet obtained after centrifugation was rinsed with 1 mL ultrapure water then dissolved with nitric acid (distilled ultrapure 0.28 mol/L HNO_3). The use of preconcentration allows to lower the detection limit during the quantification of Fe and Mn while removing the seawater matrix compared to dilution method for which open ocean Fe and Mn concentrations are difficult to reach.

Quantification of TDFe and TDMn was carried out at the Pôle Spectrométrie Océan (PSO, Ifremer, Brest, France), using HR-ICP-MS (High Resolution Inductively Coupled Plasma Mass Spectrometry; Element XR, Thermo Fisher Scientific). A set of certified seawater reference materials were used for determining analytical precision and accuracy, including NRCC (National Research Council Canada) standards NASS-05 and CASS-05, and GEOTRACES Intercalibration seawater GSI (Boyle et al., 2012). For Mn concentrations we obtained 50.7 ± 2.0 nmol/L, 20.2 ± 0.8 nmol/L and 1.5 ± 0.6 nmol/L for CASS-05, NASS-05 and GSI respectively (2SD). For Fe concentrations we obtained 32.3 ± 1.2 nmol/L, 5.3 ± 1.8 nmol/L and 0.8 ± 0.8 nmol/L f for CASS-05, NASS-05 and GSI respectively (2SD). Both Fe and Mn concentrations are similar, within analytical uncertainty, to certified or accepted values.

5.4. Results

5.4.1. Helium isotopic ratio within the water column

Elevated concentrations of $^{3}He_{xs}$ compare to the background (i.e. < 2 fmol/kg) are found at depths higher than 1000m, all around the Horseshoe structure (Figure 5. 3.A). Most of the samples taken below 1000 m ranges from 2 to 10 fmol/kg. Maximum concentrations of up to 20 fmol/kg are encountered above the Site C and in the center of the Horseshoe structure, at about 1270 m and 1455 m deep respectively. Site E exhibits the lowest levels of $^{3}He_{xs}$ all along the water column, with maximal value of 5 fmol/kg at 1500 m. The channel shows concentrations of 8 fmol/kg at 1430 m deep, which is consistent with the profile trend of the cast performed at the center of the Horseshoe area.

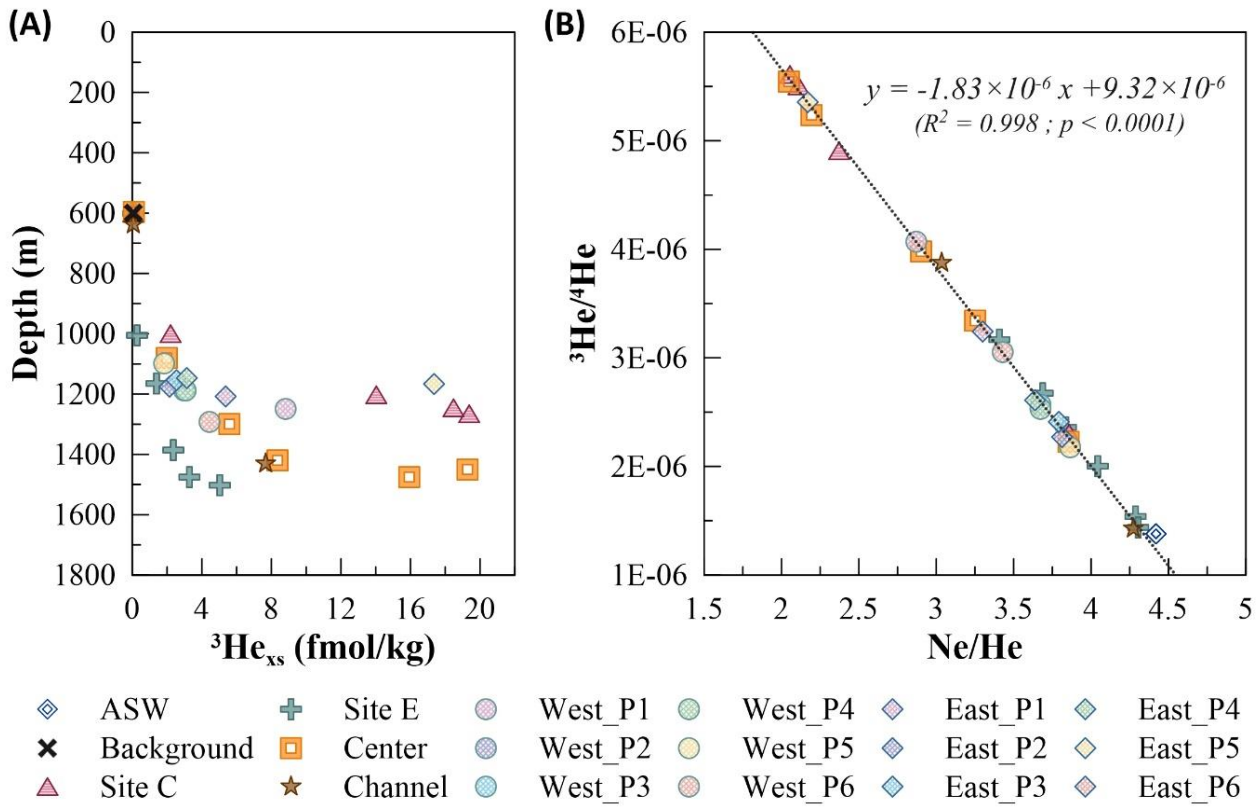

Figure 5. 3. (A) Depth profiles of $^{3}He_{xs}$, (B) Plot of helium isotopic ratio ($^{3}He/^{4}He$) versus Ne/He for seawater samples taken in the Horseshoe area and at the background hydrocast (hydrocasts presented in Figures 5.1 and 5.2) at depths > 600 m. The dashed line is the result of a linear regression adjusted on these data. ASW is the Air Saturated Water value, describe by Ne/He = 4.42 (Weiss, 1971; Hilton, 1996) and $^{3}He/^{4}He = 1.38\times10^{-6}$ (Clarke et al., 1976). The uncertainty on $^{3}He/^{4}He$ and Ne/He measurements is lower than the size of the symbols.

5.4.2. Water column geochemistry

Profiles of dissolved methane and carbon dioxide concentrations were studied over the Horseshoe area, as well as the total dissolvable iron and manganese (Figure 5. 4). Elevated concentrations compare to the background are mainly distributed below 1100 m deep over the different profiles. Gases present elevated levels from 1100 m to seafloor, while metals show enrichments mainly within the 100-150 m close to the seafloor, except for the cast at the center of the Horseshoe structure where relatively high levels of TDMn and TDFe are found around 1300 m and 1170 m.

Elevated concentrations of dissolved gases are mostly found within the Horseshoe structure with concentrations up to 105 µmol/kg for CO_2 and 1265 nmol/kg for CH_4. Nevertheless, a maximum value, out of the trendline, is observed above the Site C (West_P4, 1337 m) with 191 µmol/kg of CO_2 and 2951 nmol/kg of CH_4.

Looking at depths above 1500 m, the hydrocasts at Channel and Site E exhibit lower gases concentrations with levels up to 70 µmol/kg and 408 nmol/kg, respectively for CO_2 and CH_4. Below 1500m, gases concentrations increase for the Channel hydrocast, which is deeper than the others, with CO_2 up to 88 µmol/kg and CH_4 up to 617 nmol/kg.

Profiles of TDMn and TDFe remain below 5 nmol/kg and 40 nmol/kg respectively throughout the water column and show moderate enrichment close to the seafloor. The enrichments of TDMn and TDFe appears lower at site E than within the Horseshoe structure, with concentrations up to 7 nmol/kg in TDMn and 76 nmol/kg in TDFe for Site E, and up to 74 nmol/kg in TDMn and 1060 nmol/kg in TDFe for the Horseshoe structure.

Total Dissolvable Manganese was previously measured in October 2020 (Rinnert et al., 2020) using onboard flow injection analysis (FIA) with a colorimetric detection method developed by Aguilar-Islas et al. (2006), adapted from Resing and Mottl (1992). These $TDMn_{FIA}$ concentrations agree well with our TDMn data (this issue): indeed they show the same profile distributions with enrichments up to 80 nmol/kg within the first hundred meters above the seafloor (Supplementary Material, Figure S 3).

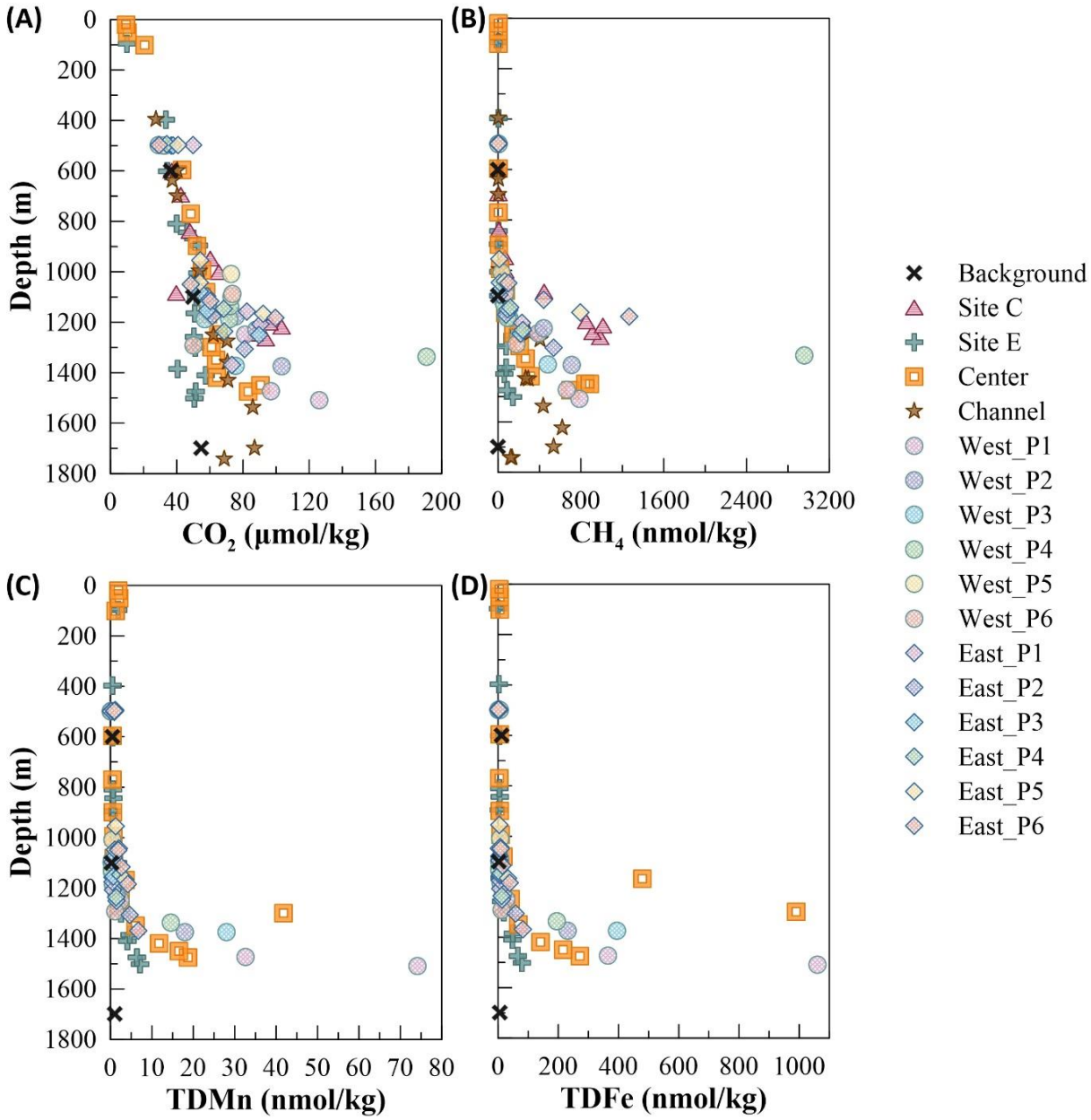

Figure 5. 4. Depth profiles of (A) CO_2, (B) CH_4, (C) Total Dissolvable Manganese (TDMn), and (D) Total Dissolvable Iron (TDFe) for all seawater samples taken in the Horseshoe area (hydrocasts presented in Figure 5.2) and for the background hydrocast (Figure 5.1).

5.4.3. Seawater carbonate system: pH, Total alkalinity (A_T) and Dissolved Inorganic Carbon (DIC)

Anomalies of pH, DIC and A_T from the regional background start to be significant below 1000 m deep (Figure 5. 5). Strong acidification is observed within the Horseshoe area, with a maximum ΔpH measured above Site C of -0.8 pH unit, and just above the seafloor at site B_0 (West_P4, 1337 m, Figure 5. 5) of -0.7 pH unit. These decreases in pH are

coupled with an increase in ΔDIC, up to 230 µmol/kg. The ΔA_T, however, do not exceed 25 µmol/kg.

At the center of the Horseshoe area, anomalies remain relatively low from 600 m to 1400 m deep, and then increase suddenly while going deeper with maximum values of -0.4 pH units, 150 µmol/kg and 26 µmol/kg, respectively for ΔpH, ΔDIC and ΔA_T.

Site E and Channel exhibit contrasted tendencies from the other sites. From 600 to 1500 m, while the ΔDIC remains under 75 µmol/kg for both sites, the ΔA_T shows elevated values (up to 40 µmol/kg) above Site E, whereas in the Channel, ΔA_T is close to zero or even negative relative to the background. The ΔpH does not show strong variations with a maximum value of -0.25 recorded between 600 m and 1500 m depths. At depths greater than 1500 m, at the Channel site, a maxima of -0.4 pH unit is observed, coupled to a maxima in ΔDIC of 100 µmol/kg along with a ΔA_T of 8 µmol/kg, which are small values compared to the other sites.

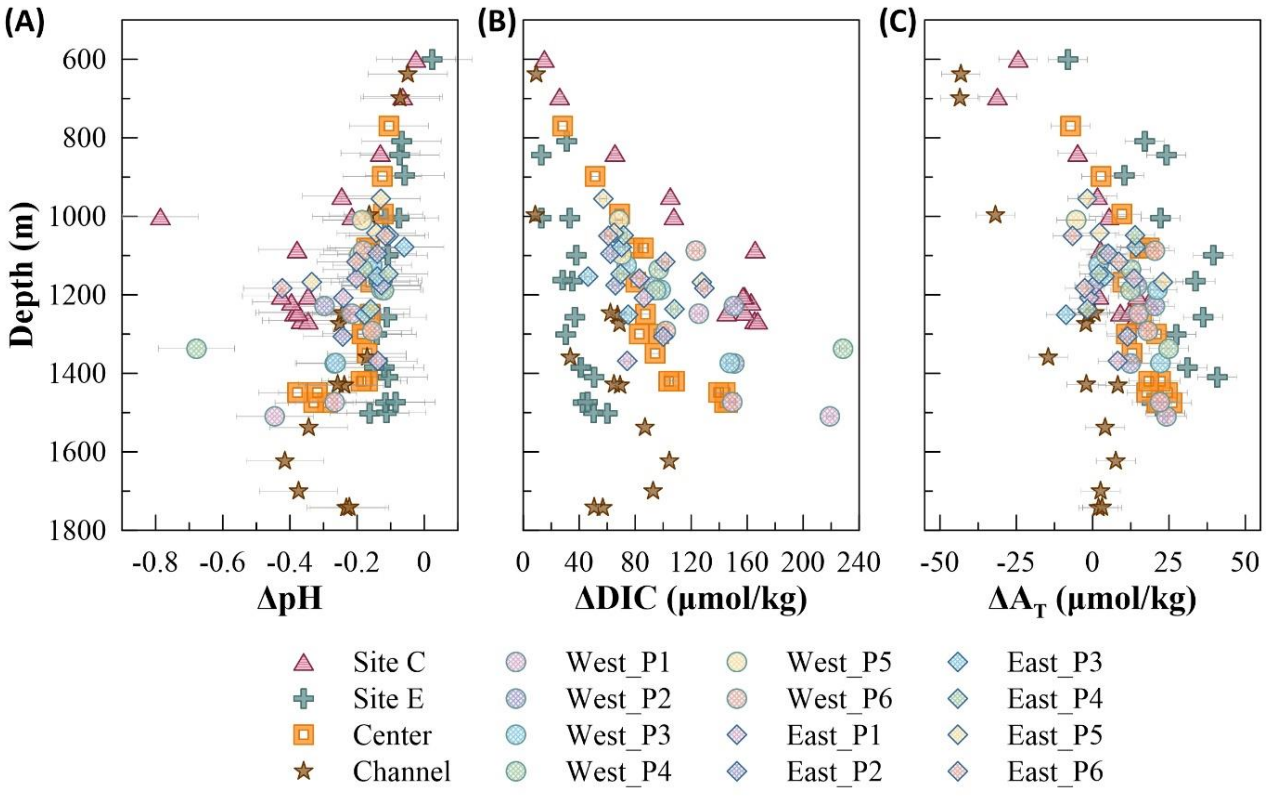

Figure 5. 5. Depth profiles of (A) ΔpH, (B) ΔDIC and (C) ΔA_T for all seawater samples taken in the Horseshoe area (hydrocasts presented in Figure 5.2). Δ values are the change in pH, DIC and A_T from the background hydrocast (Figure 5.1). Error bars are shown in grey, and were calculated based on the reproducibility of the batch analysis performed over all hydrocasts. Profiles of pH, DIC and A_T are shown if Supplementary Material (Figure S4), as well as the Normalization with salinity (34.8 PSU) that show no anomalies removed or added in DIC and A_T profiles, for depths under 600 m.

5.5. Discussion

5.5.1. Magmatic origin and signature of the emissions within the water column

Fluid emissions at the seafloor are a source of helium to the water column, being either primordial (^{3}He) or radiogenic (^{4}He). Here, data are aligned along a linear regression (Figure 5. 3.B) suggesting a single origin of the fluid emissions within the water column. We use this regression to determine the isotopic helium ratio relative to the atmospheric ratio (R/Ra) of the emissions. This ratio is an indicator of the level of mantellic or crustal contributions of these fluids. Mantle MORB-like fluids are usually described by R/Ra = 8.0 ± 1.5 (Sano and Fischer, 2013), while fluids originating from the crust present R/Ra values of 0.02 (Lin et al., 2020; Wang et al., 2020).

In this study, the determination of R/Ra from the linear regression gives a value of 6.75 (R/Ra = $9.32\times 10^{-6}/1.38\times10^{-6}$), suggesting that the helium source is dominated by a mantle-derived contribution with negligible crust-derived contribution. Therefore, fluid/gas emissions seem have a mantellic origin. This result is consistent with the helium isotopic signature of droplets sampled within the Horseshoe structure using a Remote Operated Vehicle (*ROV Victor 6000*, Ifremer) that gave a R/Ra of = 6.39 ± 0.50 (n=11) also suggesting a mantle source of the emitted droplets (Cathalot et al., in prep.). The droplet signature from the Horseshoe area is however distinct from the signature exhibited at the Fani Maoré volcanic edifice. Indeed, water column sampling above the Fani Maoré volcano have shown variations of R/Ra from 6.46 to 8.52 likely linked to a change of magma ascending path (Mastin et al., in review). Noble gas signatures of the Horseshoe area emissions are closer to the emissions on Petite-Terre Island, where R/Ra ratios were observed to vary between 5.45 and 7.5 in the Airport tidal flat area, and between 5.3 and 6.8 Ra in the Dziani Dzaha Lake (Liuzzo et al., 2022). Such similar values have been hypothesized to result from the presence of a shallow plumbing system with R/Ra fluid signature of about 6.6, feeding the two gas seep areas of Petite Terre (Airport tidal flat and Dziani Dzaha Lake). Our results do not give more insights regarding the plausibility of this hypothesis but they do suggest that this plumbing system and magmatic reservoir may also feed the Horseshoe area through their degassing.

The same range of R/Ra signatures has been previously observed in other liquid CO_2 venting systems with several hypotheses formulated regarding their origins. In the back-arc context of NW Eifuku in the northern Mariana Arc, droplets with a R/Ra signature of about 7.31 have been observed above the Champagne vent site (Lupton et al., 2006). The

authors suggest that these droplets come from CO_2 directly degassing from a magma chamber, that has then cooled while migrating to the seafloor, ultimately forming CO_2 liquid and hydrate near the surface (Lupton et al., 2006; Lupton et al., 2008). Also, in the back-arc basin of Mid-Okinawa Trough ratios of 6.6 and 5.8 were found respectively for two sites of bubbling of CO_2-rich fluid (Sakai et al., 1990a; Sakai et al., 1990b).

In the Horseshoe area, helium enrichments within the water column are coupled with an increase of the concentrations of dissolved CO_2 and CH_4 that modify the physicochemical characteristics of the surrounding water column. The low concentrations of TDMn and TDFe within the water column and the moderate enrichment close to the seafloor (Figure 5. 4) show that this distribution may be linked to a resuspension of metal-rich material due to the presence of internal currents, or to the stagnation of a modifies seawater, relatively acidified by the CO_2 emissions, that interact with the rocks of the seafloor and that releases metals. Samples taken over the Horseshoe area exhibit a mean TDFe/TDMn ratio of ~15 (R^2 = 0.88, Figure S 3). By mixing with seawater – either at the seafloor or within dikes –, CO_2 degassing produces acid-rich fluids that can percolate within Fe-rich volcanoclastic sediments or lead to chemical weathering of basaltic wall rock, and thus contribute to the high Fe/Mn values, as it was observed at Loihi Seamount (Malahoff et al., 2006). Another process responsible for such ratio value may be the exsolution of iron-rich brine, possibly coincident with magmatic degassing or generated by physical phase separation (Massoth et al., 2003).

5.5.2. Behavior of gases from the source to the water column

Within the Horseshoe area, concentrations of dissolved CH_4 measured in the water column are well correlated with concentrations of $^3He_{xs}$ ($y = 46.6\ x$; $R^2 = 0.982$), giving an average $CH_4/^3He_{xs}$ ratio of 4.66×10^7 (Figure 5. 6.A). Given the regression line, the presence of methane in the water column can be associated to the same emissions than the helium and thus to the same mantle-derived source. The composition of the droplets presents an average $CH_4/^3He_{xs}$ ratio of $6.01 \times 10^7 \pm 1.17 \times 10^7$ (Cathalot et al., in prep.). The $CH_4/^3He_{xs}$ ratios within the water column are slightly lower than the average droplet ratio, suggesting that the water column is preferentially enriched in $^3He_{xs}$ or depleted in CH_4 compared to the CO_2 droplets emitted at the seafloor. Two hypotheses may explain this difference, (i) the solubility of the two gases slightly differs from one to the other and CH_4 has preferentially dissolved in seawater during the droplet ascent in the water column, (ii) methane is a reactive gas whereas helium is an inert gas, and has started to oxidize (Craig and

Weiss, 1971; De Angelis et al., 1993). The sample from site C, with CH_4 = 850 nnmol/kg and $^3He_{xs}$=13.5 fmol/kg exhibit a ratio close to the average droplet ratio. It was taken at 1203 m deep, right above the venting site. Potentially, a droplet was sampled with the CTD and may explain the elevated ratio close to the one of the droplet.

Since the $^3He_{xs}$ is mantle-derived and, in contrast to the hydrocarbons, not affected by biogeochemical processes, $CH_4/^3He_{xs}$ ratio is indicative for potential sources of methane. The ratio reflects the relative importance of mantle-derived (i.e. abiogenic) CH_4, and CH_4 from other sources such as thermal breakdown of organic matter and microbial activity. The measured $CH_4/^3He_{xs}$ ratio point to additional methane sources as it is higher than the mean ratios of mid-ocean ridge hydrothermal systems (0.7-6.5 × 10^6) and much higher than in oceanic mantle plume environments as, such as Loihi seamount (1-4 × 10^5) (Gamo et al., 1987).

Concentrations of dissolved CO_2 measured in the water column within the Horseshoe area are not correlated with $^3He_{xs}$ concentrations (Figure 5. 6.B). However, two distinct behavior are observed in the $CO_2/^3He_{xs}$ ratios measured in the water column: (i) one group, sampled at depths with elevated concentrations both in CO_2 and $^3He_{xs}$, presents depleted CO_2 and/or enriched $^3He_{xs}$ compare to the mean ratio of the CO_2 droplets ; (ii) the other group, for which data are plotted above the droplet ratio (Figure 5. 6.B), presents ratios in the water column that are enriched in CO_2 and/or depleted $^3He_{xs}$ compare to the mean ratio of the CO_2 droplets. The first group can be explain by the preferential dissolution of helium at depths through the formation of hydrates, while at shallower depths, CO_2 is in excess in the water column due to droplets dissolution.

Droplets seeping from the seafloor are mainly composed of liquid CO_2 (99.0 ± 0.3 $\%_{vol}$) (Cathalot et al., in prep.). Dissolution of liquid CO_2 in seawater induces a reaction giving two separate compounds: HCO_3^- and CO_3^{2-}, that account for the Dissolved Inorganic Carbon (DIC) budget (Emerson and Hedges, 2008). There is no strict relationship between ΔDIC and $^3He_{xs}$ concentrations measured within the water column that exhibits higher ΔDIC levels (or lower in $^3He_{xs}$). The $\Delta DIC/^3He_{xs}$ ratio of the water column samples (i.e. in the seawater dissolved phase) is higher than in the droplet component, which can partly be explained by the much lower solubility of helium in seawater than CO_2. This observation was also found by Lupton et al. (2008) at Champagne site, NW Eifuku, where the dissolved gas ratios in the water column were much higher than the droplet ratio of 1.6×10^{10} mol/mol, and did not display any significant trend. Other CO_2 sources than droplets emissions may affect the $CO_2/^3He_{xs}$ and $\Delta DIC/^3He_{xs}$ ratios that we observe in the water column. Indeed,

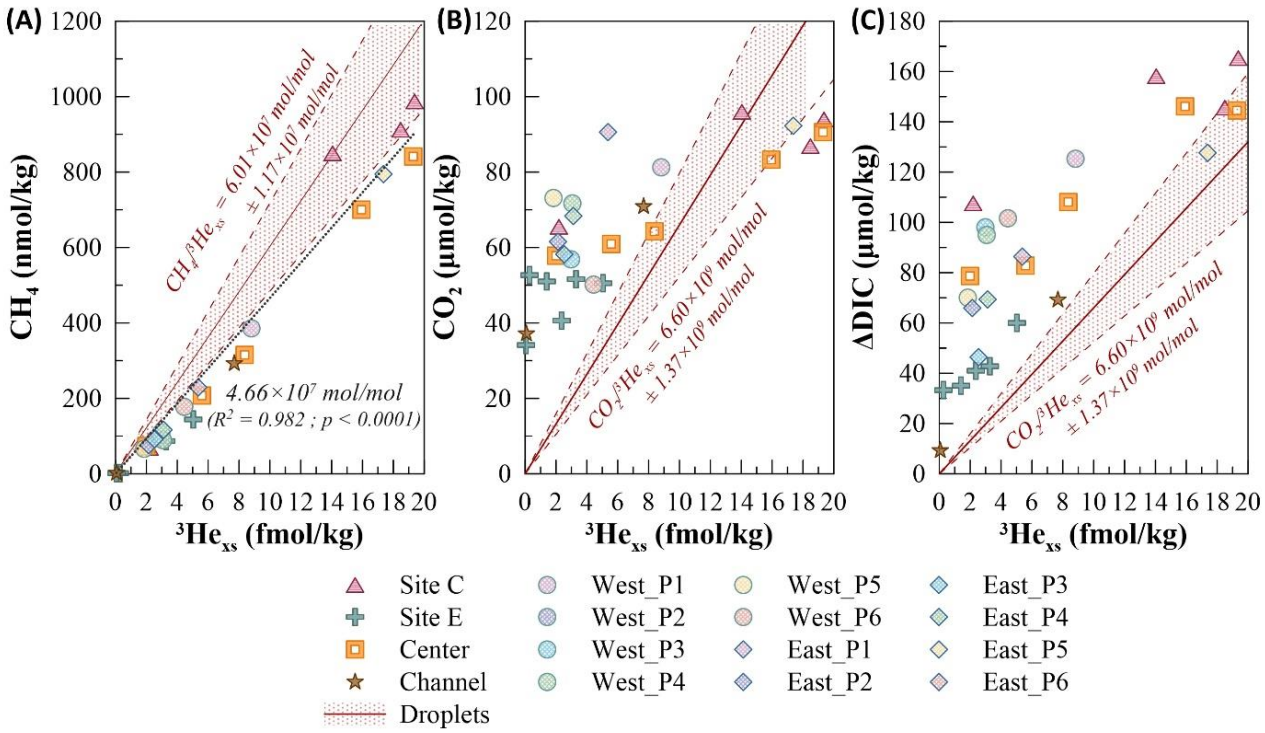

Figure 5. 6. Plots of (A) CH_4 vs. $^3He_{xs}$, (B) CO_2 vs. $^3He_{xs}$ and (C) ΔDIC vs. $^3He_{xs}$ for seawater samples taken in the Horseshoe area at depths > 600 m (hydrocasts presented in Figures 5.2). The dashed line is the linear regression of all Horseshoe data. The red line corresponds to the average gas ratio of the droplets issued from Cathalot et al. (in prep.) with the standard deviation represented by the red area between the dot lines.

additional CO_2 may originate from dissolved atmospheric CO_2 and water masses advection, or a stagnant background where CO_2 from older droplets has accumulated. (Figure 5. 6C).

The ratio $\Delta DIC/CH_4$ has been determined over the depth profile of the water column and compared to the droplet ratio ($1.11\times10^2 \pm 1.90\times10^1$, (Cathalot et al., in prep.)) (Figure 5. 7). Ascending the water column from the seafloor, the liquid CO_2 start dissolving slowly, and at about 1100-1000m it is strongly dissolved compared to CH_4, and thus $^3He_{xs}$. Pressure-temperature conditions are in part responsible for the destabilization of the liquid CO_2 to form gaseous CO_2 that instantly dissolve in seawater. Based on our local pressure and temperature conditions, liquid CO_2 is expected to change phase at about 450 m (Teng et al., 1996; Brewer et al., 2002). CO_2 or DIC contents are about a factor 10^3 below the CO_2 solubility range of 1.95-1.99 mol/kg, or 0.03 mol/mol when expressed in mol fraction, expected in the Horseshoe water column, arguing for a rapid dissolution with rates slightly below 1.309×10^3 $molCO_2$ m^{-2} s^{-1} (Teng et al., 1996; Brewer et al., 2002). However, differences are observed between the studied sites according to their location

inside/outside the Horseshoe structure, even if the water masses remains the same (Supplementary Material, Figure S 1). Studying four different behaviors of the ratio $\Delta DIC/CH_4$ over the water column ratio, it seems that bathymetric constraint and currents affect strongly the dissolution depth of liquid CO_2 by affecting the distribution of mass transfer rates in the water column.

(i) From 1600 to 1200 m (Figure 5. 7), the water column ratio is close to the droplet ratio while being slightly higher due to the preferential dissolution of CO_2 in seawater. Indeed, the methane hydrate solubility in the Horseshoe area is below 0.08 mol/kg much lower than the one for CO_2 (Sun and Duan, 2007). It is worth mentioning that at the local temperature, salinity and pressure conditions, we are within the methane hydrate stability range (Duan et al., 1992; Teng et al., 1996; Teng and Yamasaki, 1998). During those 400 m of ascending, the ratio increases very slowly or remains constant for the sites located inside the Horseshoe structure.

(ii) From 1200 to 1000 m, CO_2 dissolution seems to increase suddenly at 1000m deep at site E (as indicated by a strong increase in the $\Delta DIC/CH_4$ ratio), compared to other sites confined within the Horseshoe area where the ratio increases above 1000m. Tow-yo samples (East P2, P3, P4) from sites located east of the Horseshoe area at ~1100 m depth show the same behavior than site E, this depth corresponding to the rim crest depth in this area. Likely, the absence of bathymetric barriers and thus the presence of surrounding currents create horizontal shear flow and increase the travelled distance of a rising droplet, at a given depth (Alendal and Drange, 2001).

(iii) From 1000 to 600 m, a strong increase in the $\Delta DIC/CH_4$ is observed for all samples. At these depths we suggest that all gases are dissolved in seawater, linked to the bathymetry barrier removing and the presence of currents.

(iv) Deeper than 1600 m, in the Channel, a slightly increase in the $\Delta DIC/CH_4$ is observed toward the seafloor. Once again giving evidence of a plume-like water mass, which is possibly coming from the inside of the Horseshoe structure and exported through the Channel by currents. As a matter of fact, $\Delta^{14}C\text{-}_{DIC}$ in the channel area (determined by the LSCE – Laboratoire des Sciences du Climat et de l'Environnement, UMR 8212 – team) show values of 165-185 ‰ similar of those found at the reference site (background values) suggesting a strong dilution with adjacent water masses.

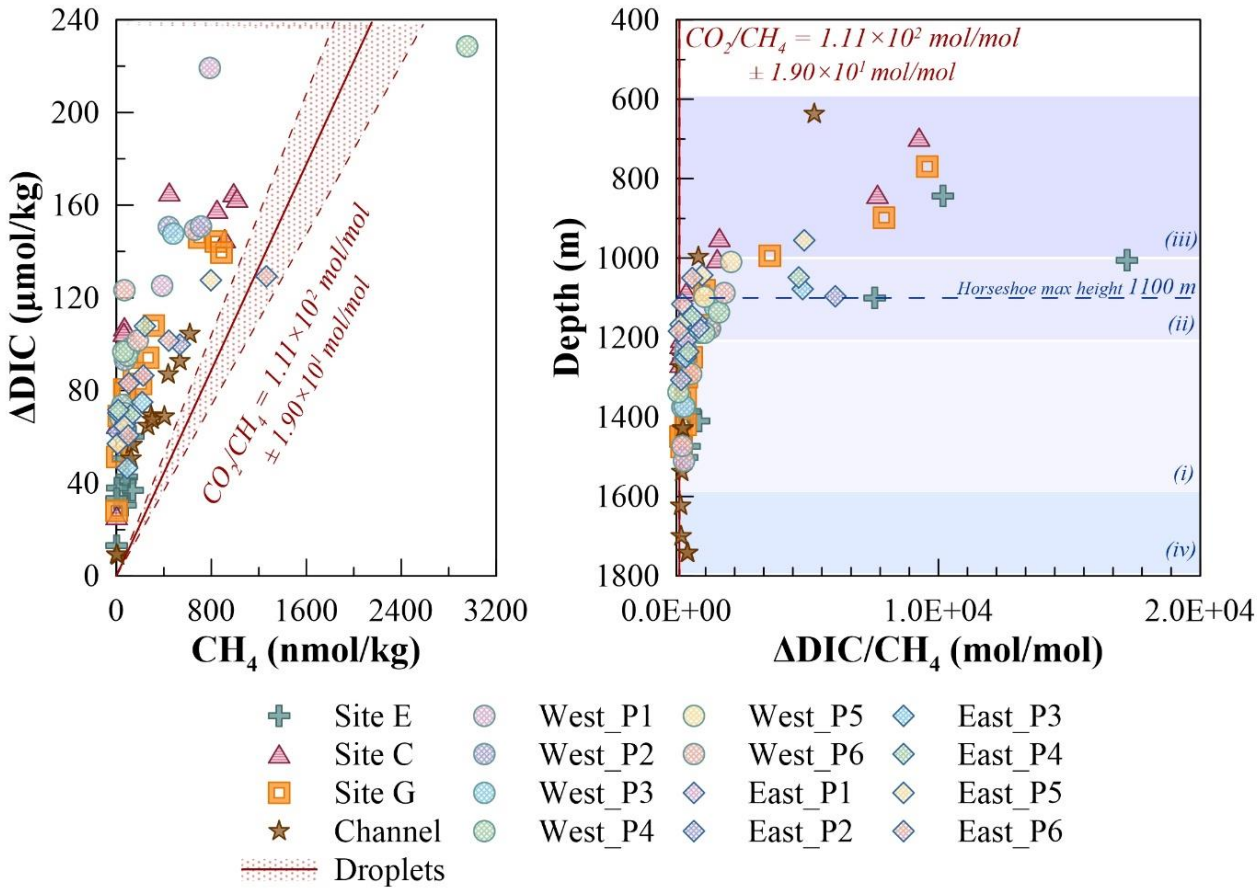

Figure 5. 7. (A) ΔDIC vs. CH_4 and (B) depth profiles of ΔDIC/CH_4 for seawater samples taken in the Horseshoe area at depths > 600 m (hydrocasts presented in Figures 5.2). The red line corresponds to the average gas ratio of the droplets issued from Cathalot et al. (in prep.) with the standard deviation represented by the red area between the dot lines. Different behaviors of the ratio are identified: (i) Ratio slowly increase during the droplet ascension, (ii) Dissolution start inside the structure while it is already strong outside the structure (site E), (iii) All gases are dissolved in the water column, (iv) Particular increase towards the seafloor in the Channel.

5.5.3. Spatial evaluation of the impact of CO_2 emission

We studied the spatial impact of the liquid CO_2 emissions within the Horseshoe structure by looking at the surface maps of pH, DIC and A_T anomalies measured over the water column and compared to the background level (Figure 5. 8).

Globally, the ΔpH and ΔDIC maps are well correlated, showing the direct link between the emissions of liquid CO_2 (that creates an increase in ΔDIC in the water column) and the water column acidification (observed as negative ΔpH values). Indeed, the addition of CO_2 to seawater leads to the formation of carbonic acid (H_2CO_3) that further decomposed into hydrogen (H^+) and hydrogenocarbonate (HCO_3^-) ions, and then

carbonate (CO_3^{2-}) ions. Therefore, as the concentration in dissolve CO_2 increases in the seawater, so does the concentration in H^+, leading to a decrease of the pH (Emerson and Hedges, 2008). The CO_2, HCO_3^- and CO_3^{2-} account for DIC budget, which can be only modify by the addition of CO_2 to the water column or by CO_2 production within the seawater.

The spatial dispersion of A_T anomalies are more difficult to relate to ΔpH and ΔDIC. In fact, the addition of CO_2 only leads to an increase of the A_T if one of the alkaline compound is produced. In seawater, ions of carbonate and borate define about 99% of the total alkalinity, while carbonate species alone account for 96% and is defined as carbonate alkalinity (A_C) (Emerson and Hedges, 2008).

Firstly, anomalies of pH, DIC and A_T have been integrated between 1000 m deep and the seafloor depth within the Horseshoe area (Figure 5. 8.A). Major anomalies for those three parameters are observed on sites C, B_0 and A_2 (north of the west Horseshoe branch, Figure 5. 2). Fluxes were estimated from the surface plot interpolations performed on the predefined water column heights. At site C, we estimate a flux of DIC about 40 mol/m^2 and of A_T about 3 mol/m^2, leading to an acidification up to –0.8 pH units. At site B_0, flux of DIC is about 56 mol/m^2 and A_T about 6 mol/m^2. At site A_2, flux of DIC is about 61 mol/m^2 and A_T about 6 mol/m^2. In the center of the Horseshoe, the ΔpH does not exceed -0.3 pH unit, while ΔDIC and ΔA_T are elevated compare to the background, with respective flux of 49 mol/m^2 and 8 mol/m^2.

Then, the integration of ΔpH, ΔDIC and ΔA_T was performed from 1000 m to 1300 m (Figure 5. 8.B), in order to study the anomalies measured above the geologic structure. The map of ΔpH shows that the water column for those depths is strongly impacted by acidification above site C (ΔpH about -0.6). This anomaly is coupled with elevated ΔDIC and ΔA_T, which are associated with flux of about 41 mol/m^2 and 3 mol/m^2 respectively. Sites A, B and Center show pH anomalies inferior to -0.3 pH unit, and moderate levels of ΔDIC and ΔA_T. At site B, flux of DIC is about 28 mol/m^2 and A_T about 3 mol/m^2. At site A2, flux of DIC is about 41 mol/m^2 and A_T about 5 mol/m^2. At the Center, flux of DIC is about 25 mol/m^2 and A_T about 4 mol/m^2. The fact that the acidification is low while the DIC and A_T are higher than the background seems to suggest that DIC and A_T levels may be the results of a water masses already buffered and that are stagnant within the structure. Finally, the integration between 1200 m and the seafloor mainly represent the part of the water column below the top level of the structure (Figure 5. 8.C). In that case, anomalies of pH, DIC and A_T above and around site B are strongly marked with flux of DIC is about 38 mol/m^2 and A_T about 4 mol/m^2. Anomalies are

also elevated above site A_2 with DIC of about 32 mol/m^2 and A_T about 3 mol/m^2.. At site C, flux of DIC is about 13 mol/m^2 and A_T about 1 mol/m^2. At the Center, flux of DIC is about 33 mol/m^2 and A_T about 5 mol/m^2.

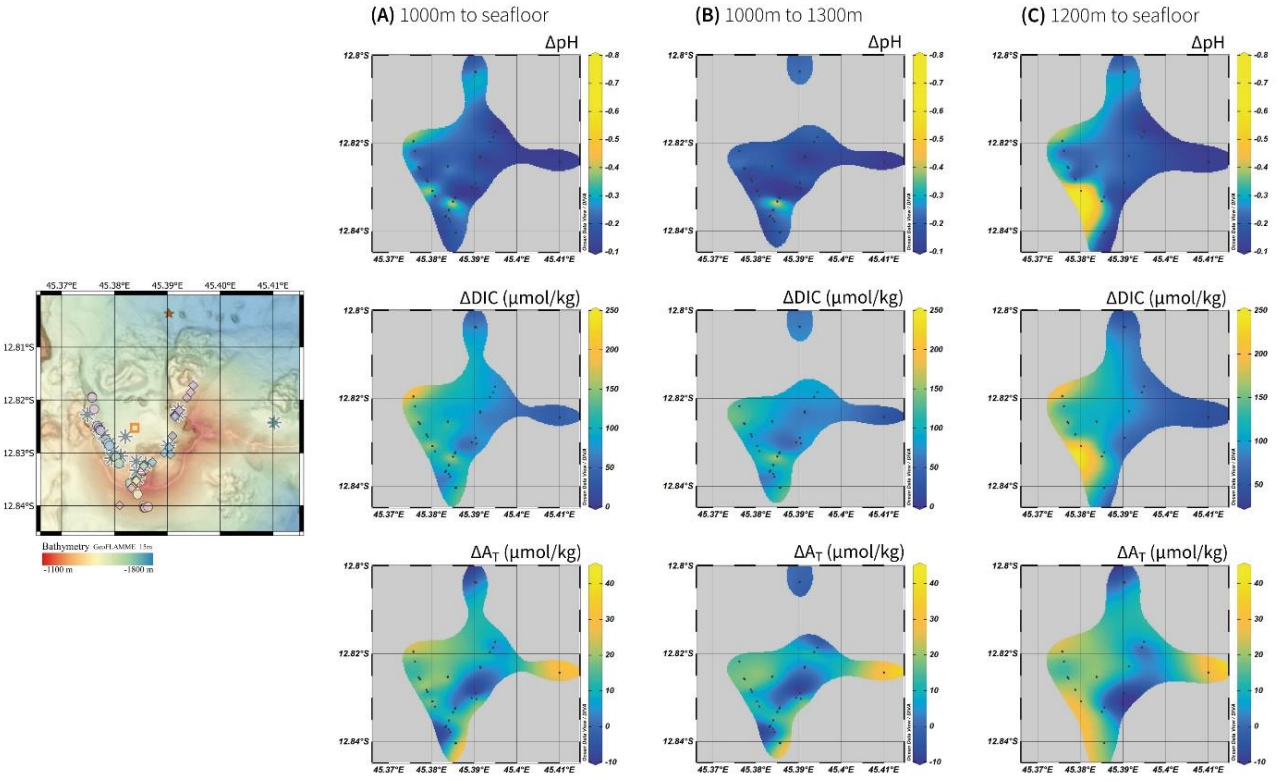

Figure 5. 8. Spatial distribution of ΔpH, ΔDIC, ΔA$_T$ (in rows) within the Horseshoe area, integrated from (A) 1000 m to the seafloor depth (first column), (B) 1000 m to 1300 m (second column), (C) 1200 m to the seafloor depth (third column). The maps were generated using Ocean Data View © (Schlitzer, 2023). Black dots on surface maps represent the sampling points. The map in the left shows the study area with the bathymetry, the venting sites and the location of the water column samples, according to the same legend as Figure 5.2.

Looking at the different integrations, we suggest that at site B, the emissions spread out on the seafloor and hardly pass over the geologic structure. This would lead to the stagnation of a modified seawater inside the Horseshoe structure, which is observed with an increase in DIC and A_T at the center of the structure. In addition, evidence of seafloor surface leaching possibly caused by the liquid CO_2 emissions have been observed during ROV surveys and appears as several white coverage zones at sites B and C. This rock alteration may be responsible for the TDMn, TDFe enrichments and the TDFe/TDMn ratio of ~15 all along the water column, with poor reaction processes highlighted by the low variations from this ratio value, which exclude the presence of hydrothermal fluid circulation (Figure S 3). Above 1300 m, the acidification effect seems to be diluted /or exported,

anomalies of DIC and A_T remains elevated compare to the background but are quite lower compare to the deeper part of the water column.

The Channel hydrocast presents minor anomalies of pH, DIC and A_T compare to the background, and even a negative anomaly in A_T. Moreover, geochemical profiles for this hydrocast (dissolved gases, ΔpH, ΔDIC, ΔA_T) present a maximum around 1600 m deep, giving suspicion of the presence of a plume or of the modification of the seawater over a water slice. We suggest that the Channel is strongly drove by currents that export water and potentially modified seawater from inside of the Horseshoe structure. The dilution process caused by currents is likely strong enough to flush away and buffer the CO_2 emissions coming from the inside of the Horseshoe structure.

Site E is distinct from the other sites as no or very low anomalies in pH and DIC are observed, while the ΔA_T stand at about 30 µmol/kg. In fact, the behavior of the A_T and DIC within the water column at site E appears to be associated to the background hydrocast (Figure S 5), while the sites inside the Horseshoe structure and the Channel show a different behavior. This suggest that due to its emplacement outside the Horseshoe structure, site E present a similar water column geochemistry compare to the background and highlights that site E is strongly influence by local hydrodynamics that may have flushed the emissions, avoiding the interactions between those emissions and the wall rocks. This hypothesis is confirmed by the low enrichment in TDFe and TDMn observed at site E (Figure 5. 4).

Clearly, the water column geochemistry in term of carbonate system differs from the inside of the Horseshoe structure to the outside. Inside the structure, DIC and AT are elevated due to the low renewing of the modified seawater. This stagnant water masses is likely to react with the surrounding wall rocks, which increase the DIC and AT budget, by the production of HCO_3^- and CO_3^{2-}, and lead to TDFe and TDMn enrichments. In contrary, outside the structure, the addition of DIC is weak because the water masses are easier flushed by currents and this limits the reaction of the modified-seawater by favoring dilution process.

5.6. Conclusion

The compilation of geochemical data taken above the Horseshoe degassing sites has provided valuable information on the origin of the emissions, on the dynamic of dissolution of a liquid CO_2 droplet released into the water column, and on the important role of local hydrodynamics in the way that those emissions of liquid CO_2 affect the water column

geochemistry. This study leads to the following conclusions:

(1) The liquid CO_2 droplets emitted within the Horseshoe area present an homogeneous magmatic signature of mantle-origin dominance that suggest the direct degassing of CO_2 from a sub-seafloor reservoir, potentially associated to the plumbing system feeding the gas emissions at Petite-Terre Island and/or feeding the Fani Maoré volcano system.

(2) The water column geochemistry at the Horseshoe is not characteristic of hydrothermal circulation and emissions mainly consist on gas discharges. Nonetheless, iron and manganese enrichments seems likely to have been released through interactions of acid-rich fluid resulting from droplet dissolution with surrounding wall rocks, either during the liquid CO_2 ascent within the sub-seafloor, or onto the seafloor surface after being discharged into seawater.

(3) The seafloor morphology and local hydrodynamics (e.g. tides, main currents) control the depth of the CO_2 droplet dissolution (Figure 5. 9). Dissolution rate, export and dilution processes are increased in the absence of a bathymetric structure that act as a protection against the current. As a result, the water column geochemistry is affected differently depending on the emission location and the seafloor morphology. To complete this study, a survey of the local currents would be very helpful to understand the CO_2 export and its impact at a more global scale.

(4) The morpho-bathymetric structures play an important role in the carbonate system by confining the emissions and further favoring accumulation, stagnation of modified seawater, and leaching processes through the interactions between liquid CO_2, seawater, and rocks (Figure 5. 9).

Overall, this study, which assesses the impact of one of the deepest site of carbon dioxide emission in liquid phase on the geochemistry of the water column, is unprecedented. Since those occurrences are likely associated to volcanic systems, the number of site of degassing might be as well underestimated, thus underestimating the global impact of such emissions on the ocean geochemistry. Therefore, the Horseshoe site offers a natural lab to expand our knowledge on liquid CO_2 emissions in the deep ocean, from the processes of generation to the impact on the ocean geochemistry at a global scale.

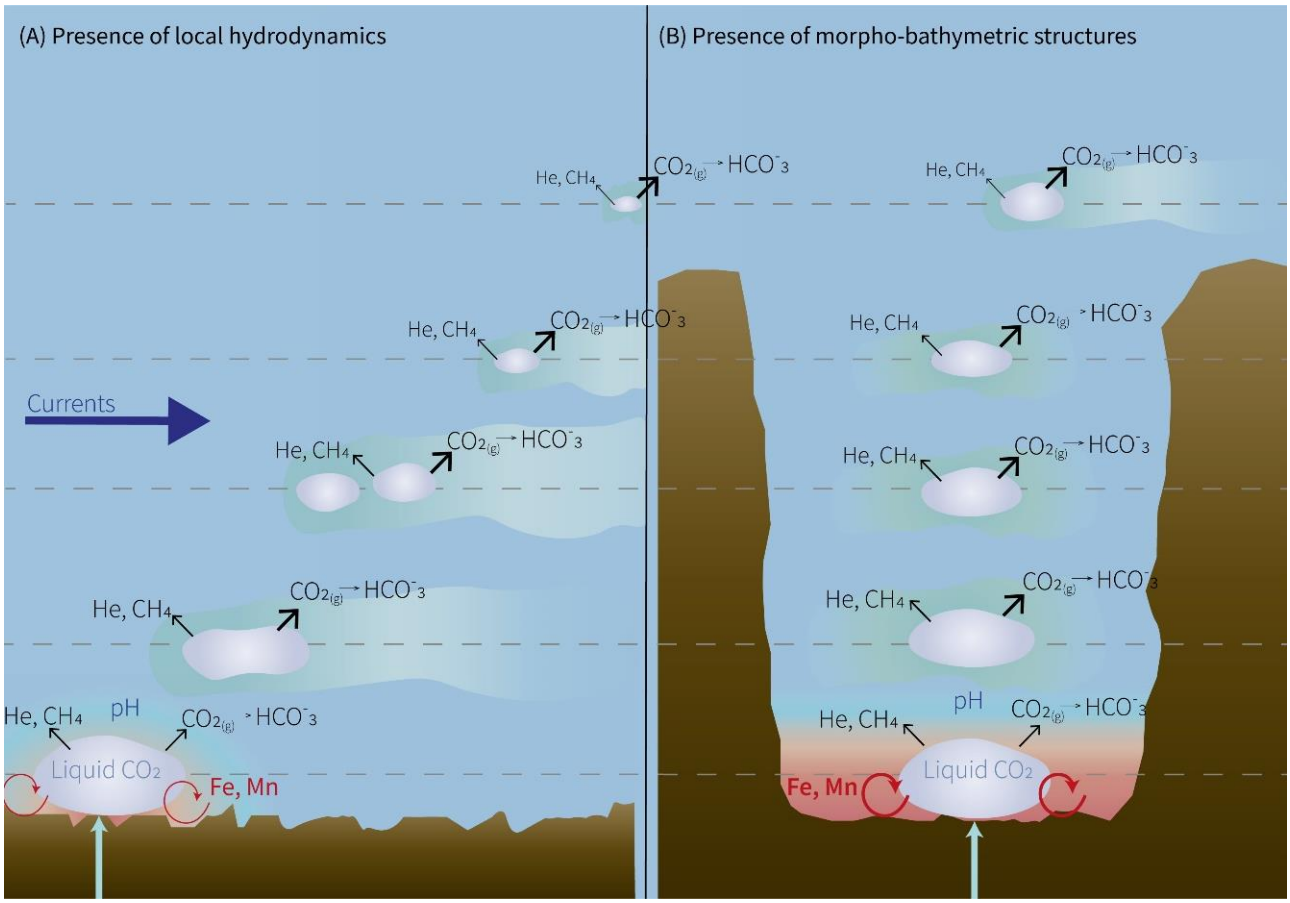

Figure 5. 9. Conceptual scheme representing the emission of a liquid CO_2 droplet in (A) presence of currents, and (B) presence of a morpho-bathymetric structures (protection from currents). Droplet goes up within the water column, whereas the dissolved part spreads horizontally and gets diluted. In case (A) currents favor dissolution, export and dilution processes, while in case (B) the bathymetric structures confines the emissions and favors accumulation, stagnation, leaching processes.

5.7. Acknowledgements

We thank the captain, crew members and all the scientists on the *R/V Pourquoi Pas ?* during the GeoFlamme cruise (April-May 2021, doi:10.17600/18001297). We also thank the French Oceanographic Fleet. We thank Jürgen Sültenfuß from Helis Laboratory, at the Institute of Environmental Physics/Section of Oceanography, University of Bremen (Germany) who performed all helium and neon isotopic analyses.

5.8. Supplementary material

5.8.1. Water column hydrography in the Horseshoe area

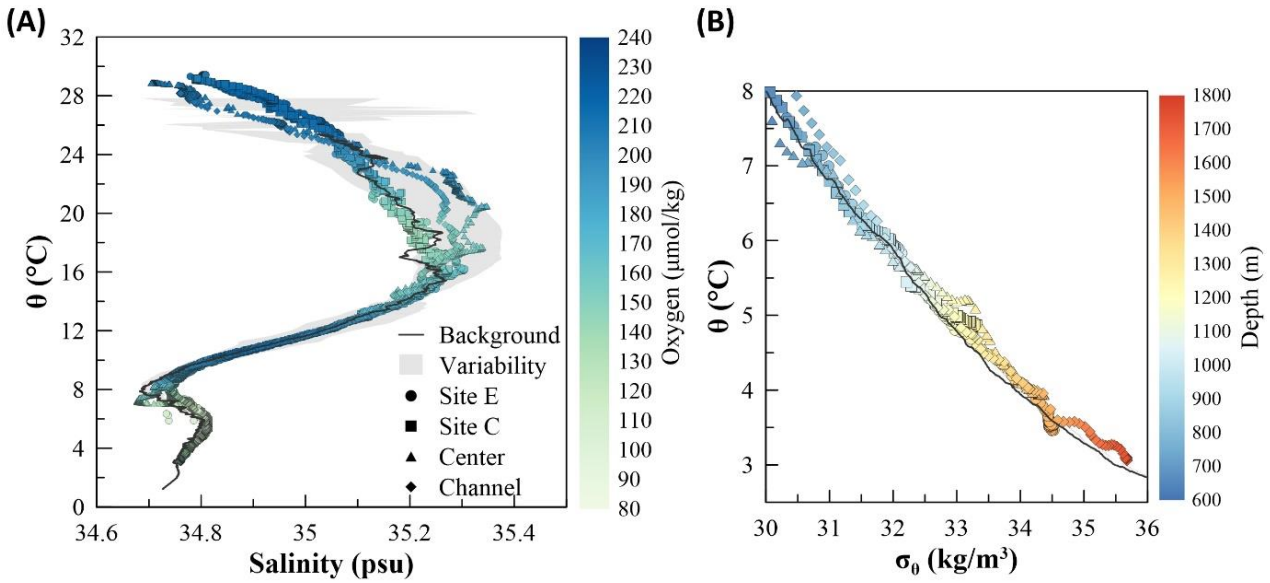

Figure S 1. (A) Plot of potential temperature (θ) versus salinity with color bar showing the oxygen concentration. (B) Plot of potential temperature (θ) versus potential density (σ_0) with color bar showing the depth of sampling. Data measured at sites C, E, Center and Channel are represented, as well as the background (black line) with its variation over time represented by the grey shadow (measured during several cruises from May 2019 to April-May 2021). θ and σ_0 have been computed after McDougall et al. (2003) and using ocean surface as the reference value.

5.8.2. Evaluation of the background geochemistry in the Horseshoe area

Dissolved CO_2 and DIC measured within the water column are supposed to be composed of the atmospheric equilibrium, the stagnant background and an excess from droplet emissions. The background hydrocast (Figure 5. 1) might not be a perfect reference as it is deeper and maybe not affect by same currents and geomorphology. Therefore, we want to validate the use of this background hydrocast for its comparison with the data measured in the Horseshoe area. The objective was to compare all data measured within the Horseshoe area, and that we consider as "very weakly influence by emissions", with the background hydrocast. Previous data over the Mozambique Channel have shown that the mean δ^3He value at approximately 2500 m in absence of fluid influence depth is about 10-15% (Jenkins et al., 2019). Thus, in our data, every sample with $^3He_{xs}$ < 0,5 fmol/kg was considered "very weakly influence by emissions". However, the helium measurement was not available for each depth sampled, so we use CH_4 concentration as the proxy since it is well correlated with $^3He_{xs}$. For $^3He_{xs}$ < 0,5 fmol/kg, concentrations of CH_4 remains under 20 nmol/kg.

Profiles of pH_{corr}, DIC, A_T and CO_2 for the data measured within the Horseshoe area and considered to be "very weakly influenced by emissions" (i.e. for CH_4 < 20 nmol/kg) were plotted (Figure S 2). In result, samples taken below 1100 m within the Horseshoe area are assumed to be impacted by the emissions as concentrations of methane are higher than 20 nmol/kg. Thus, profiles of "very weakly influence by emissions" samples within the Horseshoe area go from 0 to 1100 m depth. The comparison of the "very weakly influence by emissions" profiles of the Horseshoe with the background hydrocast show that profile are very closed one to each other even though a slight offset is observed for DIC and AT but can be explain by the presence of a stagnant background in the Horseshoe area. Also, both are constituted from the same water masses at same depths (Figure S 1). Thus, we assume that the background hydrocast can be used to calculate delta values (that is the difference from the background).

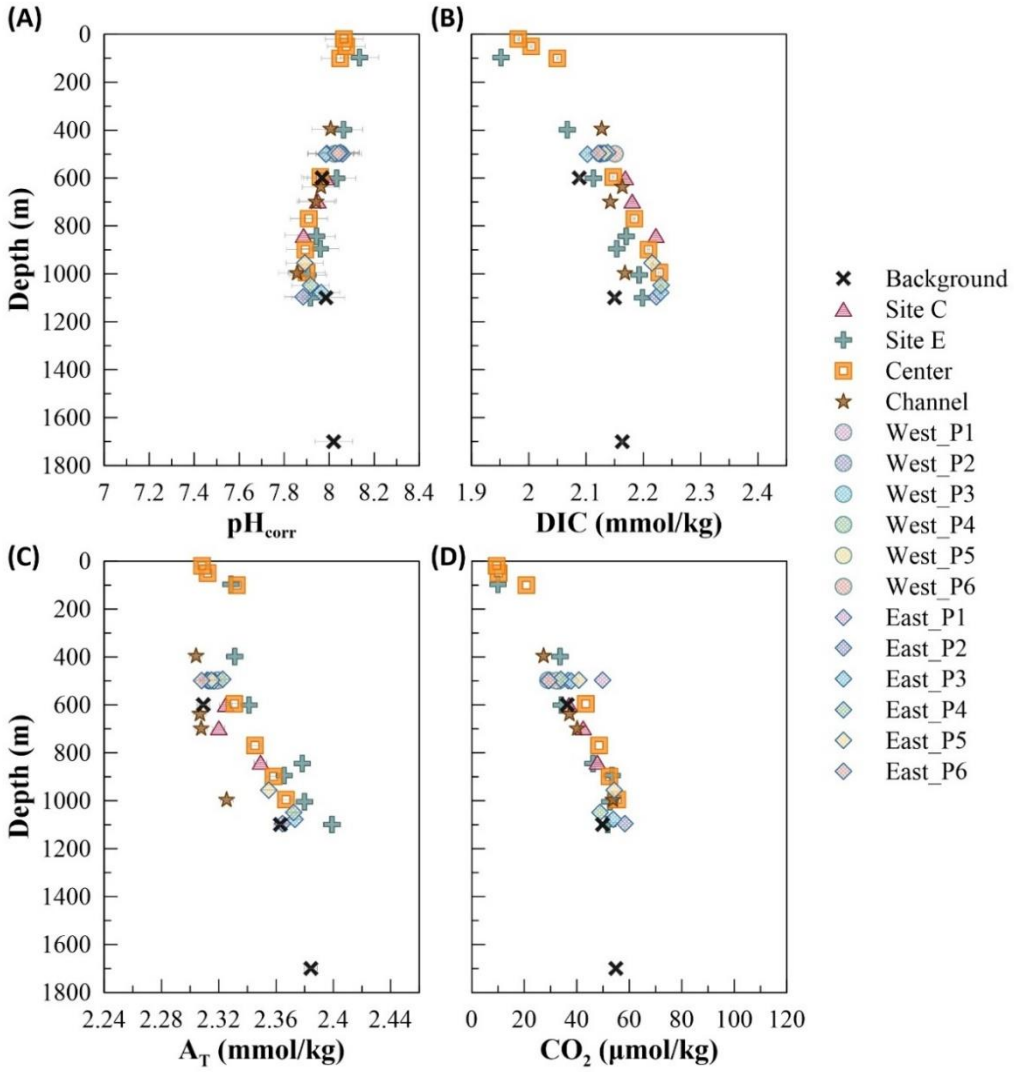

Figure S 2. Depth profiles of (A) pH_{corr}, (B) DIC, (C) A_T, and (D) CO_2 for all seawater samples taken in the Horseshoe area (hydrocasts presented in Figure 5.2) and for the background hydrocast (Figure 5.1), and for which CH_4 is < 20 nmol/kg. Those samples are thus considered to be "very weakly influenced by emissions".

5.8.3. Total dissolvable iron and manganese

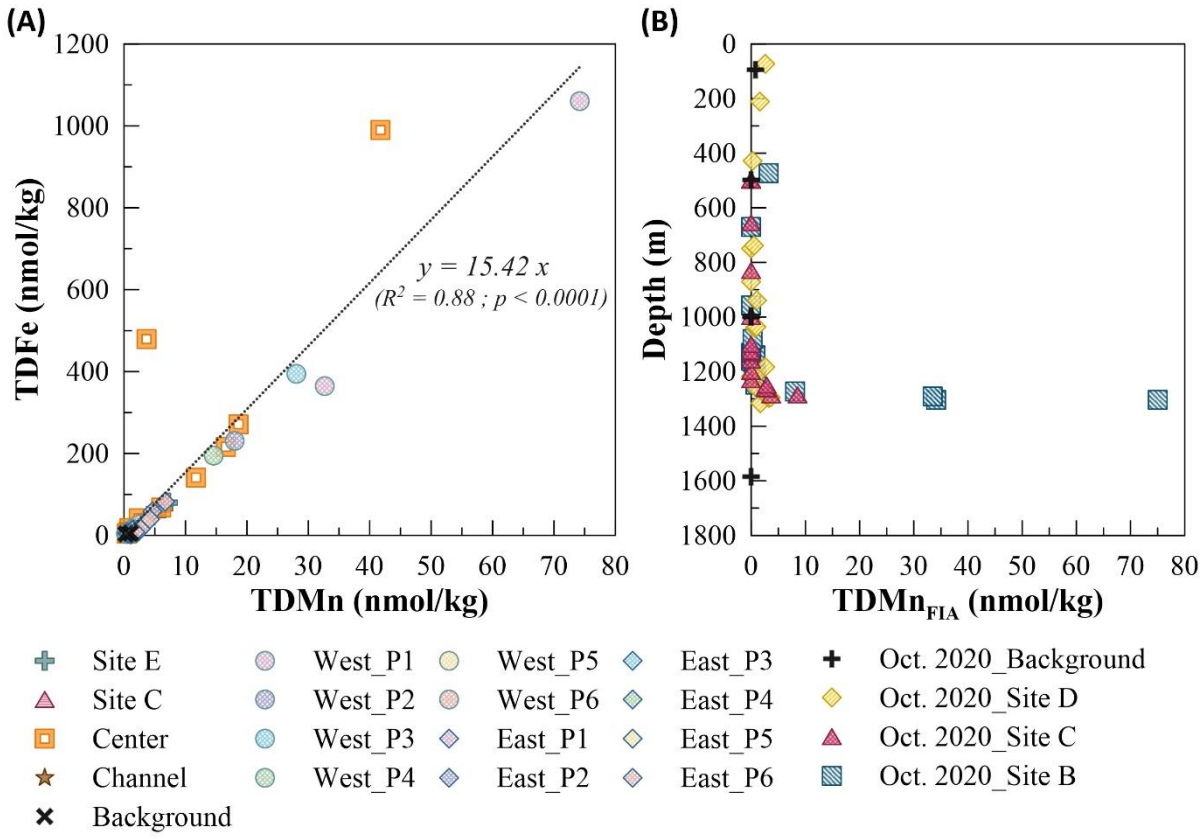

Figure S 3. (A) Plot of total dissolvable iron (TDFe) vs. total dissolvable manganese (TDMn) for seawater samples taken in the Horseshoe area and at the background hydrocast at depths between 600 m and 1800 m. The dashed line is the result of a linear regression adjusted on these data. (B) Depth profile of total dissolvable manganese obtained by onboard flow injection analysis ($TDMn_{FIA}$) in October 2020 during MAYOBS15 cruise (Rinnert et al., 2020).

5.8.4. Salinity normalization for DIC and A_T

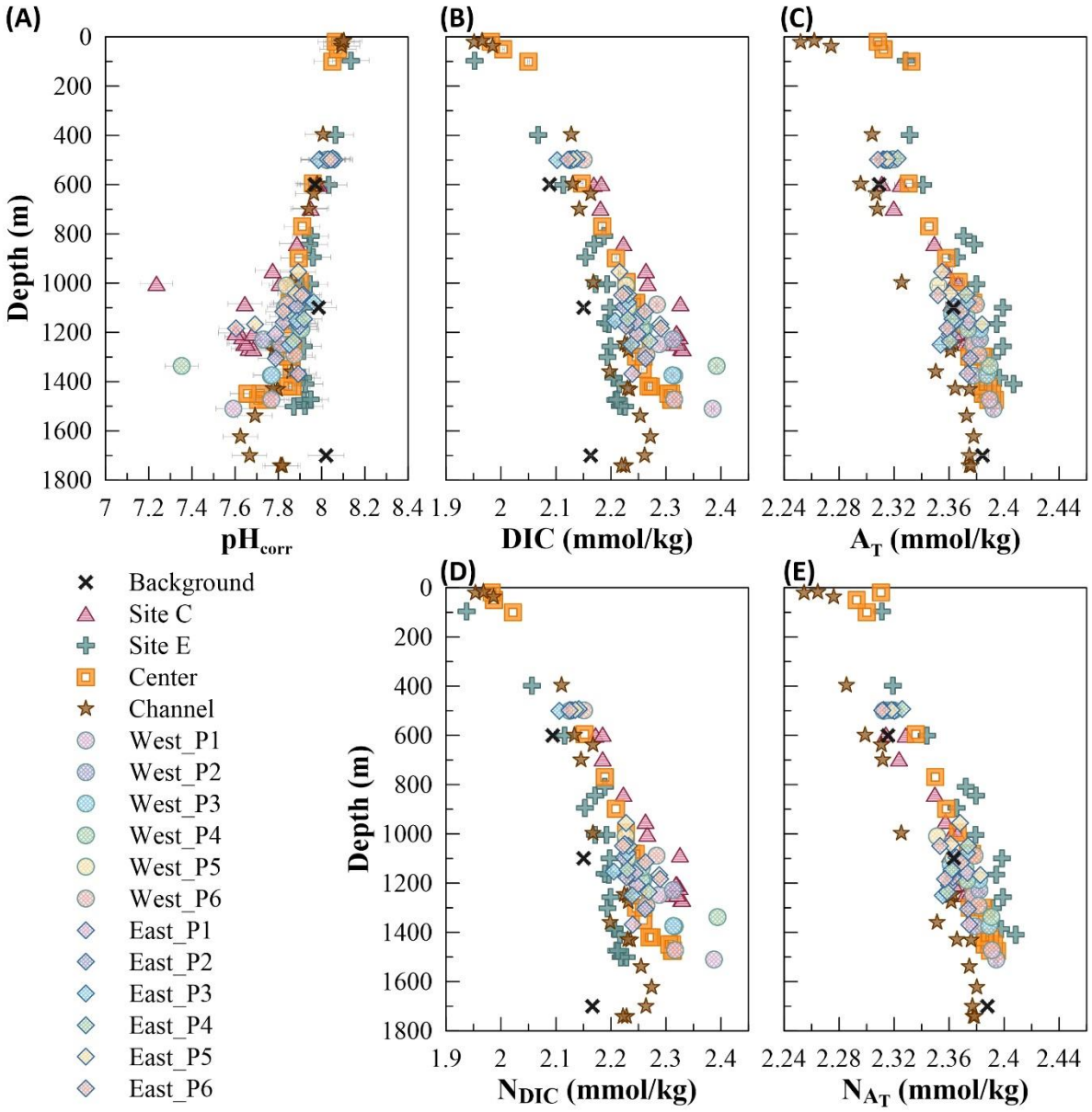

Figure S 4. Depth profiles of (A) pH_{corr}, (B) DIC, (C) A_T, (D) N_{DIC}, and (E) N_{AT} for all seawater samples taken in the Horseshoe area and for the background hydrocast. Normalization of DIC and A_T to a constant salinity of 34.8 (that is the global salinity measured under 1000 m depth) was performed using the relations N_{DIC} = (DIC/S)×34.8 and N_{AT} = (A_T/S)×34.8, with S the sample salinity. This correction is used in order to avoid the salinity effect due to the possible advection of different water masses. The normalized values showed the anomalies were not removed.

5.8.5. Relationship between DIC and A_T

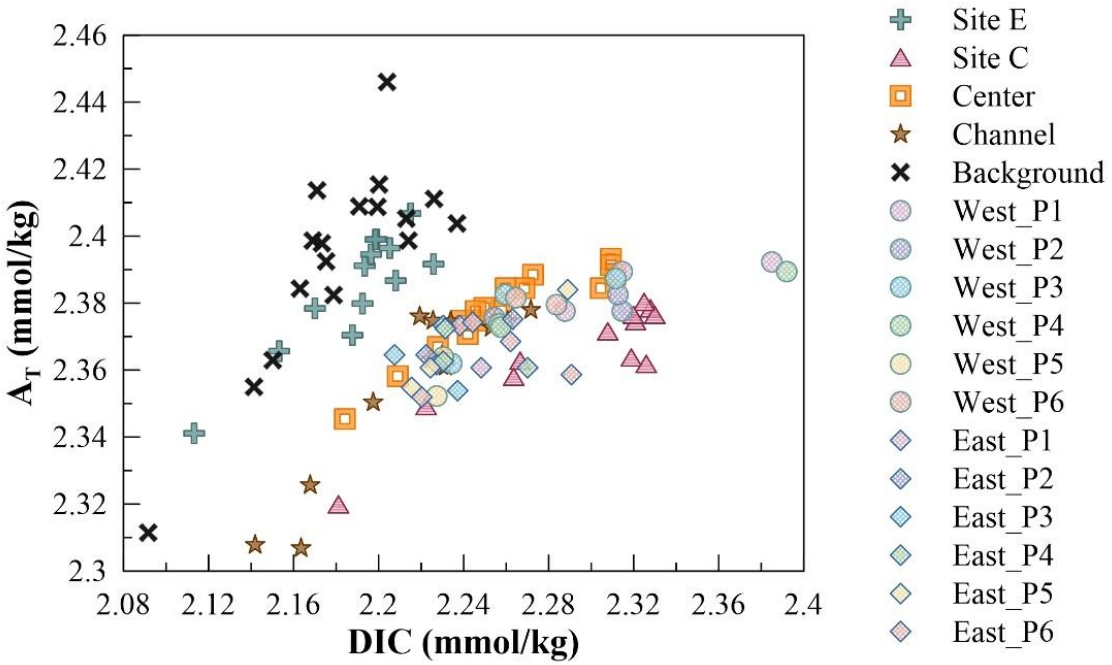

Figure S 5. Plot of A_T versus DIC for all seawater samples taken at depths > 600 m, in the Horseshoe area and for the background hydrocast.

5.8.6. Methodology for the integration of anomalies over space

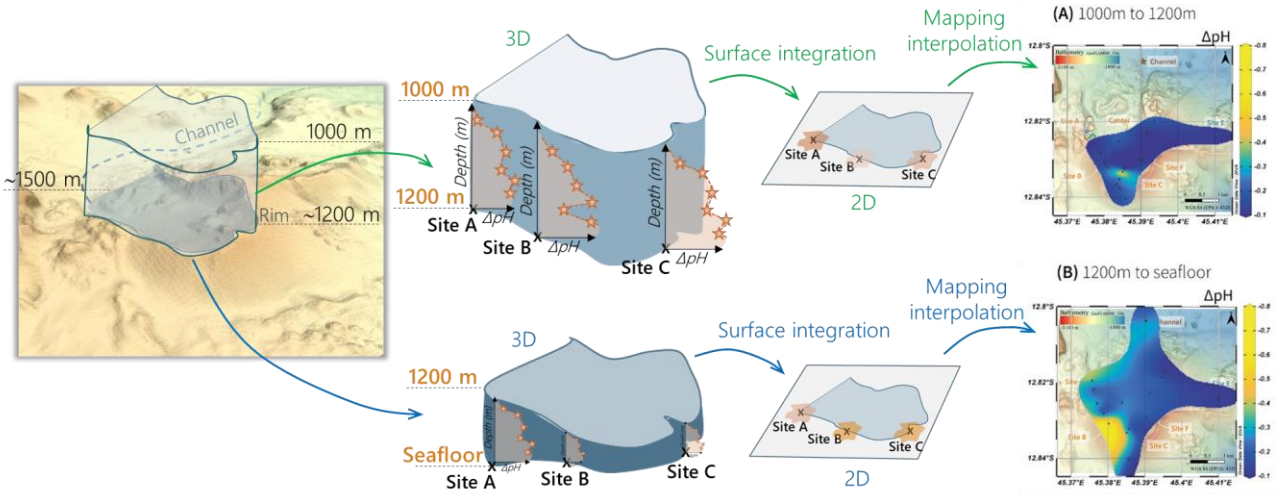

Figure S 6. 1.1.1. Methodology for the integration of pH, DIC and A_T anomalies and for the conception of surface map to study the spatiale distribution of the anomalies.

5.9. Bibliographical References

Agostini, S., Wada, S., Kon, K., Omori, A., Kohtsuka, H., Fujimura, H., et al. (2015). Geochemistry of two shallow CO2 seeps in Shikine Island (Japan) and their potential for ocean acidification research. *Regional Studies in Marine Science* 2**,** 45-53. doi: 10.1016/j.rsma.2015.07.004.

Aguilar-Islas, A.M., Resing, J.A., and Bruland, K.W. (2006). Catalytically enhanced spectrophotometric determination of manganese in seawater by flow-injection analysis with a commercially available resin for on-line preconcentration. *Limnology and Oceanography-Methods* 4**,** 105-113. doi: 10.4319/lom.2006.4.105.

Aiuppa, A., Hall-Spencer, J.M., Milazzo, M., Turco, G., Caliro, S., and Di Napoli, R. (2021). Volcanic CO2 seep geochemistry and use in understanding ocean acidification. *Biogeochemistry* 152(1)**,** 93-115. doi: 10.1007/s10533-020-00737-9.

Alendal, G., and Drange, H. (2001). Two-phase, near-field modeling of purposefully released CO2 in the ocean. *Journal of Geophysical Research: Oceans* 106(C1)**,** 1085-1096. doi: 10.1029/1999jc000290.

Boyle, E.A., John, S., Abouchami, W., Adkins, J.F., Echegoyen-Sanz, Y., Ellwood, M., et al. (2012). GEOTRACES IC1 (BATS) contamination-prone trace element isotopes Cd, Fe, Pb, Zn, Cu, and Mo intercalibration. *Limnology and Oceanography: Methods* 10(9)**,** 653-665. doi: 10.4319/lom.2012.10.653.

Brewer, P.G., Peltzer, E.T., Friederich, G., and Rehder, G. (2002). Experimental Determination of the Fate of Rising CO2 Droplets in Seawater. *Environmental Science & Technology* 36(24)**,** 5441-5446. doi: 10.1021/es025909r.

Cadeau, P., Jézéquel, D., Groleau, A., Muro, A.D., and Ader, M. (2022). Impact of the seismo-volcanic crisis offshore Mayotte on the Dziani Dzaha Lake. *Comptes Rendus. Géoscience* 354(S2)**,** 299-316. doi: 10.5802/crgeos.172.

Carey, S., Nomikou, P., Bell, K.C., Lilley, M., Lupton, J., Roman, C., et al. (2013). CO2 degassing from hydrothermal vents at

Kolumbo submarine volcano, Greece, and the accumulation of acidic crater water. *Geology* 41(9), 1035-1038. doi: 10.1130/g34286.1.

Carey, S., Olsen, R., Bell, K.L.C., Ballard, R., Dondin, F., Roman, C., et al. (2016). Hydrothermal venting and mineralization in the crater of Kick'em Jenny submarine volcano, Grenada (Lesser Antilles). *Geochemistry, Geophysics, Geosystems* 17(3), 1000-1019. doi: 10.1002/2015gc006060.

Cathalot, C., Rinnert, E., Fandiño, O., Scalabrin, C., Giunta, T., Ondreas, H., et al. (in prep.). Large CO2 hydrates field along the volcanic ridge offshore Mayotte Island.

Charlou, J.L., Rona, P., and Bougault, H. (1987). Methane anomalies over TAG hydrothermal field on Mid Atlantic Ridge. *Journal of Marine Research* 45(2), 461-472. doi: 10.1357/002224087788401179.

Clarke, W.B., Jenkins, W.J., and Top, Z. (1976). Determination of tritium by mass spectrometric measurement of 3He. *The International Journal of Applied Radiation and Isotopes* 27(9), 515-522. doi: 10.1016/0020-708x(76)90082-x.

Craig, H., and Weiss, R.F. (1971). Dissolved gas saturation anomalies and excess helium in the ocean. *Earth and Planetary Science Letters* 10(3), 289-296. doi: 10.1016/0012-821X(71)90033-1.

Dando, P.R., Hughes, J.A., Leahy, Y., Niven, S.J., Taylor, L.J., and Smith, C. (1995). Gas venting rates from submarine hydrothermal areas around the island of Milos, Hellenic Volcanic Arc. *Continental Shelf Research* 15(8), 913-929. doi: 10.1016/0278-4343(95)80002-u.

De Angelis, M.A., Lilley, M.D., and Baross, J.A. (1993). Methane oxidation in deep-sea hydrothermal plumes of the endeavour segment of the Juan de Fuca Ridge. *Deep Sea Research Part I: Oceanographic Research Papers* 40(6), 1169-1186. doi: 10.1016/0967-0637(93)90132-m.

Dofal, A., Michon, L., Fontaine, F.R., Rindraharisaona, E., Barruol, G., and Tkalčić, H. (2022). Imaging the lithospheric structure and plumbing system below the Mayotte volcanic zone. *Comptes Rendus. Géoscience* 354(S2), 47-64. doi: 10.5802/crgeos.190.

Donval, J.P., and Guyader, V. (2017). Analysis of hydrogen and methane in seawater by "Headspace" method: Determination at trace level with an automatic headspace sampler. *Talanta* 162, 408-414. doi: 10.1016/j.talanta.2016.10.034.

Duan, Z., Møller, N., Greenberg, J., and Weare, J.H. (1992). The prediction of methane solubility in natural waters to high ionic strength from 0 to 250°C and from 0 to 1600 bar. *Geochimica et Cosmochimica Acta* 56(4), 1451-1460. doi: 10.1016/0016-7037(92)90215-5.

Emerson, S., and Hedges, J. (2008). *Chemical Oceanography and the Marine Carbon Cycle*.

Fabricius, K.E., Langdon, C., Uthicke, S., Humphrey, C., Noonan, S., De'Ath, G., et al. (2011). Losers and winners in coral reefs acclimatized to elevated carbon dioxide concentrations. *Nature Climate Change* 1(3), 165-169. doi: 10.1038/nclimate1122.

Feuillet, N., Jorry, S., Crawford, W.C., Deplus, C., Thinon, I., Jacques, E., et al. (2021). Birth of a large volcanic edifice offshore Mayotte via lithosphere-scale dyke intrusion. *Nature Geoscience* 14, 787-795. doi: 10.1038/s41561-021-00809-x.

Feuillet, N., Jorry, S., Rinnert, E., Thinon, I., and Fouquet, Y. (2019). MAYOBS cruises, RV Marion Dufresne. doi: 10.18142/291.

Gamo, T., Ishibashi, J.-I., Sakai, H., and Tilbrook, B. (1987). Methane anomalies in seawater above the Loihi submarine summit area, Hawaii. *Geochimica et Cosmochimica Acta* 51(10), 2857-2864. doi: 10.1016/0016-7037(87)90163-3.

Geo-Ocean (Ifremer) (2022). Bathymétrie - Mayotte (synthèse, 2021). doi: 10.12770/0085f83d-cc3e-4c3c-b19a-6c93bca97be9.

González-Delgado, S., and Hernández, J.C. (2018). "Chapter Two - The Importance of Natural Acidified Systems in the Study of Ocean Acidification: What Have We Learned?," in *Advances in Marine Biology*, ed. C. Sheppard. Academic Press), 57-99.

Hilton, D.R. (1996). The helium and carbon isotope systematics of a continental geothermal

system: results from monitoring studies at Long Valley caldera (California, U.S.A.). *Chemical Geology* 127(4)**,** 269-295. doi: 10.1016/0009-2541(95)00134-4.

Jenkins, W.J., Doney, S.C., Fendrock, M., Fine, R., Gamo, T., Jean-Baptiste, P., et al. (2019). A comprehensive global oceanic dataset of helium isotope and tritium measurements. *Earth System Science Data* 11(2)**,** 441-454. doi: 10.5194/essd-11-441-2019.

Konno, U., Tsunogai, U., Nakagawa, F., Nakaseama, M., Ishibashi, J.-I., Nunoura, T., et al. (2006). Liquid CO2 venting on the seafloor: Yonaguni Knoll IV hydrothermal system, Okinawa Trough. *Geophysical Research Letters* 33(16). doi: 10.1029/2006gl026115.

Lin, H.-T., Lilley, M.D., Lupton, J.E., and Rappé, M.S. (2020). Mantle degassing of primordial helium through submarine ridge flank basaltic basement. *Earth and Planetary Science Letters* 546**,** 116386. doi: 10.1016/j.epsl.2020.116386.

Liuzzo, M., Di Muro, A., Rizzo, A.L., Caracausi, A., Grassa, F., Fournier, N., et al. (2021). Gas Geochemistry at Grande Comore and Mayotte Volcanic Islands (Comoros Archipelago), Indian Ocean. *Geochemistry, Geophysics, Geosystems* 22(8). doi: 10.1029/2021gc009870.

Liuzzo, M., Muro, A.D., Rizzo, A.L., Grassa, F., Coltorti, M., and Ader, M. (2022). The composition of gas emissions at Petite Terre (Mayotte, Comoros): inference on magmatic fingerprints. *Comptes Rendus. Géoscience* 354(S2). doi: 10.5802/crgeos.148.

Lui, H.-K., and Chen, C.-T.A. (2017). Reconciliation of pH25 and pHinsitu acidification rates of the surface oceans: A simple conversion using only in situ temperature. *Limnology and Oceanography: Methods* 15(3)**,** 328-335. doi: 10.1002/lom3.10170.

Lupton, J., Butterfield, D., Lilley, M., Evans, L., Nakamura, K.-I., Chadwick, W., et al. (2006). Submarine venting of liquid carbon dioxide on a Mariana Arc volcano. *Geochemistry, Geophysics, Geosystems* 7(8). doi: 10.1029/2005gc001152.

Lupton, J., Lilley, M., Butterfield, D., Evans, L., Embley, R., Massoth, G., et al. (2008). Venting of a separate CO2-rich gas phase from submarine arc volcanoes: Examples from the Mariana and Tonga-Kermadec arcs. *Journal of Geophysical Research: Solid Earth* 113(B8). doi: 10.1029/2007jb005467.

Malahoff, A., Kolotyrkina, I.Y., Midson, B.P., and Massoth, G.J. (2006). A decade of exploring a submarine intraplate volcano: Hydrothermal manganese and iron at Lō'ihi volcano, Hawai'i. *Geochemistry, Geophysics, Geosystems* 7(6)**,** n/a-n/a. doi: 10.1029/2005gc001222.

Massoth, G.J., Butterfield, D.A., Lupton, J.E., McDuff, R.E., Lilley, M.D., and Jonasson, I.R. (1989). Submarine venting of phase-separated hydrothermal fluids at Axial Volcano, Juan de Fuca Ridge. *Nature* 340(6236)**,** 702-705. doi: 10.1038/340702a0.

Massoth, G.J., Ronde, C.E.J.D., Lupton, J.E., Feely, R.A., Baker, E.T., Lebon, G.T., et al. (2003). Chemically rich and diverse submarine hydrothermal plumes of the southern Kermadec volcanic arc (New Zealand). *Geological Society, London, Special Publications* 219(1)**,** 119-139. doi: doi:10.1144/GSL.SP.2003.219.01.06.

Mastin, M., Cathalot, C., Fandino, O., Giunta, T., Donval, J.-P., Guyader, V., et al. (in review). Strong geochemical anomalies following active submarine eruption offshore Mayotte. *Chemical Geology*.

McDougall, T.J., Jackett, D.R., Wright, D.G., and Feistel, R. (2003). Accurate and Computationally Efficient Algorithms for Potential Temperature and Density of Seawater. *Journal of Atmospheric and Oceanic Technology* 20(5)**,** 730-741. doi: 10.1175/1520-0426(2003)20<730:aaceaf>2.0.co;2.

Mercury, N., Lemoine, A., Doubre, C., Bertil, D., Woerd, J.V.D., Hoste-Colomer, R., et al. (2022). Onset of a submarine eruption east of Mayotte, Comoros archipelago: the first ten months seismicity of the seismo-volcanic sequence (2018–2019). *Comptes Rendus. Géoscience* 354(S2)**,** 105-136. doi: 10.5802/crgeos.191.

Michel, A.P.M., Wankel, S.D., Kapit, J., Sandwith, Z., and Girguis, P.R. (2018). In situ carbon isotopic exploration of an active submarine volcano. *Deep Sea Research Part II: Topical Studies in Oceanography* 150**,** 57-66. doi: 10.1016/j.dsr2.2017.10.004.

Milesi, V.P., Debure, M., Marty, N.C.M., Capano, M., Jézéquel, D., Steefel, C., et al. (2020). Early Diagenesis of Lacustrine Carbonates in Volcanic Settings: The Role of Magmatic CO2 (Lake Dziani Dzaha, Mayotte, Indian Ocean). *ACS Earth and Space Chemistry* 4(3)**,** 363-378. doi: 10.1021/acsearthspacechem.9b00279.

Morrow, K.M., Bourne, D.G., Humphrey, C., Botté, E.S., Laffy, P., Zaneveld, J., et al. (2015). Natural volcanic CO2 seeps reveal future trajectories for host–microbial associations in corals and sponges. *The ISME Journal* 9(4)**,** 894-908. doi: 10.1038/ismej.2014.188.

Price, R.E., and Giovannelli, D. (2017). "A Review of the Geochemistry and Microbiology of Marine Shallow-Water Hydrothermal Vents," in *Reference Module in Earth Systems and Environmental Sciences*. Elsevier).

Puzenat, V., Feuillet, N., Komorowski, J.-C., Escartín, J., Deplus, C., Bachèlery, P., et al. (2022). Volcano-tectonic structures of Mayotte's upper submarine slope: insights from high-resolution bathymetry and in-situ imagery from a deep-towed camera. *Comptes Rendus. Géoscience* 354(S2)**,** 81-104. doi: 10.5802/crgeos.175.

Resing, J.A., Lupton, J.E., Feely, R.A., and Lilley, M.D. (2004). CO2 and 3He in hydrothermal plumes: implications for mid-ocean ridge CO2 flux. *Earth and Planetary Science Letters* 226(3)**,** 449-464. doi: 10.1016/j.epsl.2004.07.028.

Resing, J.A., and Mottl, M.J. (1992). Determination of manganese in seawater using flow injection analysis with on-line preconcentration and spectrophotometric detection. *Analytical Chemistry* 64(22)**,** 2682-2687. doi: 10.1021/ac00046a006.

REVOSIMA (2023). *Bulletin mensuel de l'activité sismo-volcanique à Mayotte : Mars 2023* [Online]. Available: www.ipgp.fr/revosima [Accessed].

Rinnert, E., Cathalot, C., and Feuillet, N. (2021). GEOFLAMME cruise, RV Pourquoi pas ? doi: 10.17600/18001297.

Rinnert, E., Thinon, I., and Feuillet, N. (2020). MD 228 / MAYOBS15 cruise, RV Marion Dufresne. doi: 10.17600/18001745.

Rubin, K.H., Soule, S.A., Chadwick, W.W., Fornari, D.J., Clague, D.A., Embley, R.W., et al. (2012). Volcanic Eruptions in the Deep Sea. *Oceanography* 25(1)**,** 142-157. doi: 10.5670/oceanog.2012.12.

Saito, M.A., and Schneider, D.L. (2006). Examination of precipitation chemistry and improvements in precision using the Mg(OH)2 preconcentration inductively coupled plasma mass spectrometry (ICP-MS) method for high-throughput analysis of open-ocean Fe and Mn in seawater. *Analytica Chimica Acta* 565(2)**,** 222-233. doi: 10.1016/j.aca.2006.02.028.

Sakai, H., Gamo, T., Kim, E.-S., Tsutsumi, M., Tanaka, T., Ishibashi, J., et al. (1990a). Venting of Carbon Dioxide-Rich Fluid and Hydrate Formation in Mid-Okinawa Trough Backarc Basin. *Science* 248(4959)**,** 1093-1096. doi: doi:10.1126/science.248.4959.1093.

Sakai, H., Gamo, T., Kim, E.S., Shitashima, K., Yanagisawa, F., Tsutsumi, M., et al. (1990b). Unique chemistry of the hydrothermal solution in the mid-Okinawa Trough Backarc Basin. *Geophysical Research Letters* 17(12)**,** 2133-2136. doi: 10.1029/gl017i012p02133.

Sano, Y., and Fischer, T.P. (2013). "The Analysis and Interpretation of Noble Gases in Modern Hydrothermal Systems," in *The Noble Gases as Geochemical Tracers*, ed. P. Burnard. (Berlin, Heidelberg: Springer Berlin Heidelberg), 249-317.

Santana-Casiano, J.M., Fraile-Nuez, E., González-Dávila, M., Baker, E.T., Resing, J.A., and Walker, S.L. (2016). Significant discharge of CO2 from hydrothermalism associated with the submarine volcano of El Hierro Island. *Scientific Reports* 6(1)**,** 25686. doi: 10.1038/srep25686.

[Dataset] Scalabrin, C. (2023). *Site d'émissions de fluides, Mayotte, zone Fer à Cheval (C. Scalabrin, 2022).* doi: 10.12770/070818f6-6520-49e4-bafd-9d4d0609bf7d. Available: https://doi.org/10.12770/070818f6-6520-49e4-bafd-9d4d0609bf7d.

Schlitzer, R. (2023). *Ocean Data View 5.6.5* [Online]. Available: https://odv.awi.de/ [Accessed].

Sültenfuß, J. (2016). "Hints for sampling". Helis - helium isotopes studies Bremen).

Sültenfuß, J., Roether, W., and Rhein, M. (2009). The Bremen mass spectrometric facility for the measurement of helium isotopes, neon, and tritium in water. *Isotopes in Environmental and Health Studies* 45(2)**,** 83-95. doi: 10.1080/10256010902871929.

Sun, R., and Duan, Z. (2007). An accurate model to predict the thermodynamic stability of methane hydrate and methane solubility in marine environments. *Chemical Geology* 244(1)**,** 248-262. doi: 10.1016/j.chemgeo.2007.06.021.

Teng, H., Masutani, S.M., Kinoshita, C.M., and Nihous, G.C. (1996). Solubility of CO2 in the ocean and its effect on CO2 dissolution. *Energy Conversion and Management* 37(6)**,** 1029-1038. doi: 10.1016/0196-8904(95)00294-4.

Teng, H., and Yamasaki, A. (1998). Solubility of Liquid CO2 in Synthetic Sea Water at Temperatures from 278 K to 293 K and Pressures from 6.44 MPa to 29.49 MPa, and Densities of the Corresponding Aqueous Solutions. *Journal of Chemical & Engineering Data* 43(1)**,** 2-5. doi: 10.1021/je9700737.

Wang, Y., Liu, Y., Zhao, C., Li, Q., Zhou, Y., and Ran, H. (2020). Helium and carbon isotopic signatures of thermal spring gases in southeast Yunnan, China. *Journal of Volcanology and Geothermal Research* 402**,** 106995. doi: 10.1016/j.jvolgeores.2020.106995.

Weiss, R.F. (1971). Solubility of helium and neon in water and seawater. *Journal of Chemical & Engineering Data* 16(2)**,** 235-241. doi: 10.1021/je60049a019.

White, J.D.L., Schipper, C.I., and Kano, K. (2015). "Chapter 31 - Submarine Explosive Eruptions," in *The Encyclopedia of Volcanoes (Second Edition)*, ed. H. Sigurdsson. (Amsterdam: Academic Press), 553-569.

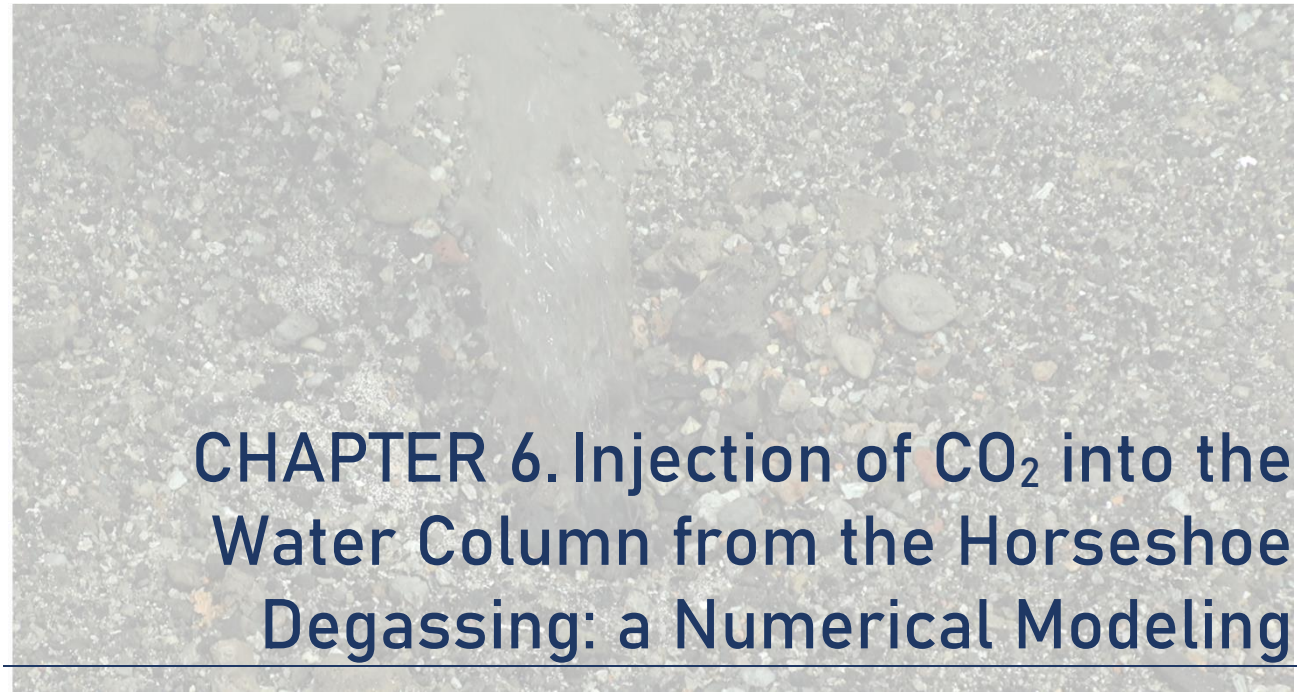

CHAPTER 6. Injection of CO_2 into the Water Column from the Horseshoe Degassing: a Numerical Modeling

Abstract

Emissions of liquid carbon dioxide (CO_2) in volcanic contexts are rare and have been observed only on four systems, including the Horseshoe venting site offshore Mayotte. However, it is possible that such occurrences are more common but overlooked due to their remote and inaccessible locations. Understanding these CO_2 injection, chemical reactions, export, and impact is crucial for assessing their contribution to the global ocean geochemistry.

This chapter is a first attempt at estimating the amount of carbon dioxide injected in the water column by the degassing seeps in the Horseshoe area. We use the PHREEQC geochemical software and the CO2Sys Excel Macro, to determine the pH and the concentrations of DIC and A_T depending on the amount of CO_2 injected in the water column. This approach was performed at several depths above two sites, and a focus was performed on depth at about 1200 m over multiple sites distributed in the Horseshoe area to give a spatial analysis.

The comparison of *in situ* data with the model results has highlight the strong influence of local hydrodynamics (transport, dilution processes) on the water column CO_2 budget, while the comparison of carbon budget and fluxes on one depth over the Horseshoe area has highlight a spatial differentiation of the water column impact depending on the site age and/or location.

CHAPITRE 6. Injection de CO_2 dans la Colonne d'Eau par les Dégazages du Fer à Cheval : Modélisation Numérique

Résumé

Les émissions en contexte volcanique de dioxyde de carbone (CO_2) liquide sont rares et n'ont été observées que dans quatre systèmes, incluant le Fer à Cheval au large de Mayotte. Cependant, il est possible que de telles occurrences soient plus courantes mais passent inaperçues en raison de leur localisation et de leur inaccessibilité. Comprendre ces injections de CO_2, les réactions chimiques, l'exportation et les impacts est crucial pour évaluer leur contribution à la géochimie globale de l'océan.

Ce chapitre présente une première approche pour l'estimation de la quantité de CO_2 injectée dans la colonne d'eau par les dégazage du Fer à Cheval. Le logiciels géochimique PHREEQC et CO2Sys ont été utilisés pour déterminer le pH ainsi que les concentrations en DIC et A_T en fonction de la quantité de CO_2 injectée dans la colonne d'eau. Cette approche a été appliquée à plusieurs profondeurs au-dessus de deux sites, puis à environ 1200 mètres sur plusieurs sites répartis sur la structure du Fer à Cheval afin d'obtenir une analyse spatiale.

La comparaison des données in situ avec les résultats du modèle a mis en évidence l'influence marquée de l'hydrodynamique locale (transport, processus de dilution) sur le budget en CO_2 de la colonne d'eau, tandis que la comparaison des budgets de CO_2 et des flux pour une profondeur a révélé une différenciation spatiale de l'impact sur la colonne d'eau en fonction de l'âge et/ou de l'emplacement du site.

6.1. Introduction

Emissions of liquid carbon dioxide in a volcanic context seem to be rare, or at least, a rare observation. The Mayotte liquid CO_2 venting site is only the fourth case where this type of emissions have been visually observed. But what if these occurrences were not that rare but rather a generality to all submarine volcanic context, and the scarcity of observations resulted only from their remote location and access difficulty (cost- and time-wise)?

Indeed, 70 shallow (< 200 m) volcano-related CO_2 seep locations have been reported (Price and Giovannelli, 2017). Those CO_2 seeps are described as subtidal areas affected by the emission of gases originated from the discharge at the seafloor of CO_2-rich volcanic-hydrothermal fluids (González-Delgado and Hernández, 2018). In the literature, these are also mentioned as shallow hydrothermal CO_2 seeps, steaming fumaroles or submerged seeps (Price and Giovannelli, 2017; González-Delgado and Hernández, 2018; Aiuppa et al., 2021). They are likely to exist around any active coastal or island volcano, or on top of shallow seamounts, such as mid-oceanic ridges or island arcs, or intra-plate magmatism (Price and Giovannelli, 2017). Price and Giovannelli (2017) have reported 70 shallow volcano-related seep locations. At those sites, emissions are in the gaseous form, with mean CO_2 content of 87.0 ± 20.7 vol% over 207 gas analyses (Aiuppa et al., 2021). For example: Baia di Levante in Vulcano Island (Aeolian Islands, Sicily) presents CO_2 seeps composed of CO_2 at ~90 mol% that are interpreted as vapors deriving from boiling of hydrothermal brines rising from a shallow geothermal aquifer (Boatta et al., 2013).

It is possible that the same manifestations occurs in a general way in the majority of volcanic context, and thus also in the deep ocean (>1000 m). It is probable that this has been observed only four times due to the difficulty to monitor and deploy observatory system at large depths in the ocean. Physicochemical properties of the venting are likely to be different in the deep ocean with CO_2 emitted in liquid form with positive or negative density compared to the surrounding seawater according to pressure and temperature conditions.

In CHAPTER 5 we discussed the liquid CO_2 droplets emitted from the seafloor as they rise vertically within the water column. During its ascend, liquid CO2 dissolves progressively, injecting carbon dioxide in the water column, resulting in aqueous CO_2 that reacts with water to give HCO_3^-, CO_3^{2-} and H^+ ions. This dissolved part likely spread horizontally depending on local stratification and is exported through local hydrodynamic processes such as tidal and regional currents, or oscillatory internal waves (Figure 6. 1). As

a result, this transport is likely to favor the incorporation of carbonate species into the surrounding water masses and further into the regional or global ocean circulation.

Although shallow gaseous CO_2 seeps are well studied for the evaluation of ocean acidification, knowledge on liquid CO_2 emissions, transport and impact are limited in the deep ocean. In order to evaluate the potential impact of these emissions on the global ocean circulation, it is first important to understand: (i) how much CO_2 has been injected into the ocean, at a 'site' scale and at local/regional scale ; (ii) how the CO_2 injected reacts in term of chemical species during its mixing with the ambient seawater ; (iii) to what extend are the CO_2 and the resulting chemical species exported, and where.

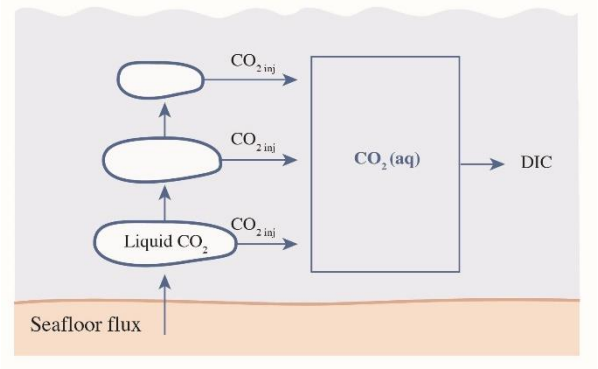

Figure 6. 1. Schematic of a droplet ascension, progressively injected aqueous CO_2 (named $CO_{2\ inj}$) into the surrounding seawater, and further reacting with seawater to give HCO_3^-, CO_3^{2-} and H^+ ions that account in the DIC budget.

In this chapter, we are exploring a first approach to give an estimate of the amount of carbon dioxide injected all along the water column by the Horseshoe degassing (Figure 6. 1). To this end, we use the PHREEQC geochemical software (Parkhurst and Appelo, 2013) and the CO2Sys Excel Macro (Lewis and Wallace, 1998), and we compare *in situ* data with model results.

We first perform this approach at several depths within the water column above two sites, one with venting and one without venting presence at seafloor. Then, we test the model for various sites at one depth to give a spatial analysis over the Horseshoe area. Finally, we extrapolate the estimation of the injected CO_2 for calculation of CO_2 budgets within the water column.

6.2. Material and Methods

6.2.1. Study site & data acquisition

Here we focus the study on the Horseshoe structure and the liquid CO_2 venting sites, which were previously presented in CHAPTER 2 *(Geologic Setting & Context of the Study)*, and in CHAPTER 5 *(Submarine venting of liquid carbon dioxide in a volcanic context)*.

The Horseshoe area is located at ~40 km offshore Petite-Terre Island, with a seafloor that evolves between 1100 and 1700 mbsl. The venting sites are mainly emplaced along the inside of the structure crest (CHAPTER 5,

Figure 5. 2). In this chapter, we focus on the sites presented in Table 6. 1 (venting sites characteristics). The Horseshoe Center and the Channel are both studied sites were there is no venting but where geochemical anomalies are observed within the water column. Discrete water column samples were taken during the GeoFlamme scientific cruise, from April 17th to May 26th 2021 (Rinnert et al., 2021), onboard the *R/V Pourquoi Pas ?*, using a CTD-rosette instrument.

Salinity, density, temperature, and oxygen were *in situ* recorded using a Seabird 911 Plus CTD (Conductivity Temperature Depth) coupled with an Optode Aanderaa 4831F for the measurement of oxygen concentration.

Sampling with the CTD-rosette and sub-sampling from the 10 L-Ocean Test Equipment (OTE) bottles for chemical analyses were performed according to the same procedure as describe in CHAPTER 5.

Quantification of total dissolvable boron (B), magnesium (Mg), silicon (Si), phosphorous (P), sulfur (S), potassium, (K), calcium (Ca) was carried out in laboratory at the Pôle Spectrométrie Océan (PSO, Ifremer, Brest, France), using HR-ICP-MS (High Resolution Inductively Coupled Plasma Mass Spectrometry; Element XR, ThermoFisher Scientific). According to the same procedure of sampling and quantification that the one used for TDMn and TDFe study (Method of dilution, CHAPTER 3).

Table 6. 1. Characteristics of the studied venting sites. The column first observation of venting sites gives information on the site age. Active site area and flux at seafloor have been determined in Cathalot et al. (in prep.).

	Liquid CO_2 venting	First observation	Emplacement	Characteristics	Seafloor depth (mbsl)	Active site area (m^2)	Flux at seafloor
Site C	Yes	August 2019 - May 2021	Horseshoe structure	C0, C1, C2, C3, C4	1288	20400	142208.3
Site A1	Yes	October 2020	Horseshoe structure		1441	2400	16730.4
Site A2	Yes	October 2020	Horseshoe structure		1428	2300	16033.3
Site B0	Yes	May 2019	Horseshoe structure	Multiple sites : center, south, north, east and west	1373	17500	121992.4
Site B1	Yes	October 2020	Horseshoe structure		1424	5600	39037.6
Site D0	Yes	May 2020	Horseshoe structure		1262	2600	18124.6
Site E0	Yes	May 2020	East of the structure	Subject to local hydrodynamics	1514	2800	19518.8
Site F0	Yes	October 2020	Horseshoe structure		1353	100	697.1
Channel	No	-	North of the structure	Local currents driving seawater from Horseshoe to the Channel	1747	-	-
Center	No	-	Center of the structure		1488	-	-

Total alkalinity (A_T) and Dissolved Inorganic Carbon (DIC) were determined onboard using a titrimeter (Titrino 848, Metrohm®) combined with a pH electrode (Metrohm®). The pH was measured in lab using a pH electrode (Metrohm®), with solutions at 25 ± 2 °C. Corrected pH (noted pH_{corr}) is the *in situ* pH calculated from the measured temperature at the depth of sampling according to Lui and Chen (2017).

Analyses for quantification of aqueous carbon dioxide (hereafter mentioned as $CO_{2\ (aq)}$) were performed onboard by gas chromatography coupled to an helium ionization detector and using the Headspace method developed by Donval and Guyader (2017).

Measured $CO_{2\ (aq)}$ is the dissolved part of the CO_2 that does not yet react with water to form HCO_3^-, CO_3^{2-}. It is associated with the form H_2CO_3. The DIC value represents the sum of the three forms in seawater ($CO_{2\ (aq)}$, HCO_3^- and CO_3^{2-}).

Complementary details on the sampling and the analytical methods are presented in the *Chapter 3 (Methodology)* and *Chapter 5* of this manuscript thesis.

6.2.2. Numerical modeling

6.2.2.1. PHREEQC

The geochemical computer model PHREEQC Version 3 (Parkhurst and Appelo, 2013) was used to simulate the injection of carbon dioxide by the venting sites into the water column. Such a model calculate the species distribution of the solution according to the complete analysis and the constants of the thermodynamic database used, in this study the PHREEQC database. All the PHREEQC modeling results represent equilibrium conditions. Models are run on a seawater batch of 1L.

We created a model program to estimate the amount of CO_2 injected by the venting sites into the seawater, at different depths within the horseshoe area. We focused on the depths between 1000 m and the seafloor, where geochemical anomalies are observed. The modelling sequence consists of the following three steps (Table 6. 2):

Step 1. Initial equilibrated solution called "SOLUTION 1": a background geochemical composition for seawater is defined. Here, we used data of the background hydrocast performed during the GeoFlamme sea expedition (see CHAPTER 5), which we assumed to be not impacted by the Horseshoe emissions. The needed parameters for the model are shown in Table 6. 2 and are expressed in mol/kg for concentration data.

Step 2. Equilibrate to *in situ* temperature called "REACTION TEMPERATURE": Temperature between background seawater and the chosen venting site may be slightly

different for a same depth. Thus, we modified the batch temperature of our initial solution to correspond to the in situ conditions measured at the venting site.

Step 3. Adding CO_2 and equilibrated with it called "REACTION add CO_2 to solution": A quantity of 150 µmol of $CO_{2\ (aq)}$ is injected progressively in 150 steps of 1 µmol each.

Table 6. 2. Example of PHREEQC model program for the modeling of the amount of injected CO_2 at Site C and at 1203 mbsl.

Modeling of CO_2 injection at Site C, 1203 mbsl

SOLUTION 1	Background hydrocast, 1203 mbsl
units	mol/kgw
temp	5.0
density	1.033
pH	7.99
Alkalinity	2.31e-03
Na	4.69e-01
Cl	5.46e-01
B	4.49e-04
Mg	5.64e-02
Si	1.12e-04
P	3.00e-06
S	2.82e-02
K	1.10e-02
Ca	1.06e-02
redox	O(0)/O(-2)
O(0)	1.13e-04
REACTION_TEMPERATURE	
5.09	
Save Solution 1	
REACTION Add carbon dioxide to solution	
CO2(g) 1.0	
150e-6 moles in 150 steps	
END	

As the model focuses only on the water column and since the Horseshoe degassing system at the seafloor is very young and maybe not at the equilibrium, reaction with carbonate solid phase such as calcite are considered as negligible and are not take into account in the model program. In addition, the seafloor in the Horseshoe area is characterized by pumice mixed bioclastic-volcanoclastic content, including phonolitic lava and bomb rims with negligible contribution of calcite.

As a result, the model gives, at each step, the seawater geochemical composition at equilibrium when 1 µmoles of $CO_{2\ (aq)}$ is injected from the previous step, starting from the initial conditions. In this study, we focus on the pH and DIC output parameters.

6.2.2.2. CO2Sys

For total alkalinity calculation we used the CO2 System Calculation Program (CO2Sys) (Lewis and Wallace, 1998).

CO2Sys is an Excel Macro spreadsheet that calculates the concentrations of the inorganic carbon system parameters if two of these parameters are provided along with temperature, pressure, total phosphate concentration, and total silicate concentration.

As we did not put a mineral phase in the PHREEQC modeling, the total alkalinity output does not vary. So we used CO2Sys to determine the A_T at each step of the model injection. To do this, pH and DIC resulting from the PHREEQC outputs were entered as

the two parameters of the inorganic carbon system.

As the input parameters in the PHREEQC model only include A_T and pH_{corr} but not DIC, and in order to stay coherent with the model processing and to ensure a consistent value of alkalinity, we also calculated the A_T of the background (in the PHREEQC input parameter) from our DIC and pH_{corr} values using CO2Sys (Table 6. 3).

The CO2Sys program uses CO_2 constants (K1, K2) from Mehrbach et al., 1973 refit by Dickson and Millero, 1987.

Table 6. 3. Example of CO2Sys spreadsheet for A_T determination using pH and DIC data. The first line correspond to background seawater at 1203 m, and the six following lines correspond to the six firsts step of $CO_{2\,(aq)}$ addition at site C and 1203 m depth. Each step refers to 1 µmol/kg of $CO_{2\,(aq)}$ being added into the 1L batch.

	INPUT CONDITIONS							RESULTS
Step	**Salinity**	**Temperature**	**Pressure**	**Total P**	**Total Si**	**DIC**	**pH**	**A_T**
		°C	dbars	µmol/kg	µmol/kg	µmol/kg		µmol/kg
Background	34.79	5	1203	3	112	2154.0	7.990	2307.8
1	34.79	5.09	1203	3	112	2249.7	7.990	2408.1
2	34.79	5.09	1203	3	112	2250.7	7.985	2406.9
3	34.79	5.09	1203	3	112	2251.7	7.981	2406.4
4	34.79	5.09	1203	3	112	2252.7	7.977	2405.9
5	34.79	5.09	1203	3	112	2253.7	7.974	2405.3
6	34.79	5.09	1203	3	112	2254.7	7.970	2404.8

6.3. Results & Discussion

6.3.1. CO_2 injection model applied on Site C and Center of the Horseshoe

We ran the PHREEQC model to study the evolution of A_T and DIC parameters at Site C and at the Horseshoe Center when CO_2 is progressively added to seawater. The model was tested every 100 m from 1000 mbsl to the seafloor depth of both sites. Water column geochemistry of the background hydrocast at the respective chosen depth fort each sites was used to defined the Solution 1 (Step 1) of the model. The input parameter for the reaction temperature was defined by *in situ* temperature measured at Site C and Horseshoe Center. Input parameters for this model program are presented in Table 6. 4 and Table 6. 5, respectively for Horseshoe Center and Site C.

Table 6. 4. Input parameters of the model for the estimation of the CO_2 that has been injected ($CO_{2\ inj}$) at the Horseshoe Center, at various depths. Data are from actual in situ *measurements. The estimation of $CO_{2\ inj}$ was carried out using the* in situ *pH_{corr} value that was projected on the model curve of pH versus $CO_{2\ inj}$.*

	HORSESHOE CENTER							
	Target depth	m	**1500**	**1400**	**1300**	**1200**	**1100**	**1000**
	Real depth	m	1475	1420	1299	1168	1080	995
BACKGROUND	Salinity	psu	34.77	34.77	34.78	34.8	34.8	34.8
	Density		1034	1034	1033	1033	1032	1032
	B	µmol/kg	448	448	448	449	450	450
	Mg	mmol/kg	56.6	56.6	56.4	56.3	56.3	56.5
	Si	µmol/kg	129	124	118	111	107	93
	P	µmol/kg	3.2	3.2	3	2.9	2.9	3
	S	mmol/kg	28.3	28.3	28.2	28.1	28.1	28.3
	K	mmol/kg	11.05	11.04	11.04	11.02	11.03	11.06
	Ca	mmol/kg	10.58	10.58	10.56	10.54	10.54	10.57
	Oxygen	µmol/kg	134	130	120	112	108	106
	Temperature	°C	3.8	4.2	4.6	5.1	5.4	6
	pH_{corr}		8.01	8.00	8.00	7.99	7.99	7.99
	$CO_{2(aq)}$	µmol/kg	52.6	52.3	51.2	50.3	49.1	46.7
	DIC	µmol/kg	2159	2157	2157	2153	2146	2139
	A_T	µmol/kg	2377	2375	2371	2366	2363	2352
	$A_{T\ CO2Sys}$	µmol/kg	2318	2314	2314	2307	2300	2295
VENTING SITE	Temperature	°C	4.06	4.14	4.82	5.38	5.71	5.85
	pH_{corr}		7.75	7.86	7.84	7.87	7.85	7.90
	$CO_{2(aq)}$	µmol/kg	83.3	64.3	61.0	59.0	57.8	55.4
	DIC	µmol/kg	2311	2273	2246	2242	2239	2228
	A_T	µmol/kg	2388	2388	2375	2371	2375	2367
MODEL	$CO_{2\ inj}$	µmol/kg	66	35	39	31	35	24

After processing the DIC and pH outputs from PRHEEQC with CO2Sys to obtain the A_T, we plotted the results onto 3D-plot graphs, with one graph per studied depth (Figure 6. 2).

Results of the model are plotted for total alkalinity (Figure 2, red lines) and Dissolved Inorganic Carbon (Figure 2, orange lines), both for site C (Figure 2, dotted lines) and the Horseshoe Center (Figure 2, plain lines). Due to its deeper depth, only the Center site is modelled at 1400 m and 1500 m: seafloor depth at site C is 1288 m. Variation of pH, DIC and A_T is dependent of the amount of $CO_{2\ (aq)}$ added in seawater. Addition of CO_2 decrease the pH value and increase the DIC, while A_T depend on the carbonate species that are favored according to pH

Model outputs are slightly different according to the studied depth. It is likely related with the input values (i.e. background values) of DIC and A_T increasing with depth. Nevertheless, at a single depth, there is no significant differences between Site C and the Horseshoe Center.

Table 6. 5. Input parameters of the model for the estimation of the CO_2 that has been injected ($CO_{2\ inj}$) at Site C, at various depths. Data are from actual in situ *measurements. The estimation of $CO_{2\ inj}$ was carried out using the* in situ *pH_{corr} value that was projected on the model curve of* pH *versus* $CO_{2\ inj}$.

			SITE C			
	Target depth	m	**1300**	**1200**	**1100**	**1000**
	Real depth	m	1265	1203	1084	1001
BACKGROUND	Salinity	psu	34.79	34.79	34.8	34.8
	Density		1033	1033	1032	1032
	B	µmol/kg	449	449	450	450
	Mg	mmol/kg	56.4	56.4	56.3	56.5
	Si	µmol/kg	116	112	107	93
	P	µmol/kg	3	3	2.9	3
	S	mmol/kg	28.2	28.2	28.1	28.3
	K	mmol/kg	11.04	11.04	11.03	11.06
	Ca	mmol/kg	10.55	10.55	10.54	10.57
	Oxygen	µmol/kg	118	113	108	106
	Temperature	°C	4.7	5	5.4	6
	pH_{corr}		8.00	7.99	7.98	7.98
	$CO_{2(aq)}$	µmol/kg	51	50.4	49.1	46.7
	DIC	µmol/kg	2156	2154	2146	2139
	A_T	µmol/kg	2369	2367	2363	2352
	$A_{T\ CO2Sys}$	µmol/kg	2313	2307	2296	2291
VENTING SITE	Temperature	°C	4.98	5.09	5.45	6.08
	pH_{corr}		7.66	7.68	7.65	7.81
	$CO_{2(aq)}$	µmol/kg	93.9	96.0	39.6	65.5
	DIC	µmol/kg	2328	2320	2326	2267
	A_T	µmol/kg	2378	2376	2362	2363
MODEL	$CO_{2\ inj}$	µmol/kg	86	79	84	44

6.3.1.1. Comparison of *in situ* measurements with the model curves

Figure 2 displays the *in situ* values of pH_{corr}, DIC and A_T along with the injected amount of CO_2 estimated using the pH_{corr} measured in the water column at our study sites and that was reported on the model curve of *$CO_{2\ inj}$ versus pH*. Results of this estimation is presented in Table 6. 4 and Table 6. 5 ($CO_{2\ inj}$) and in Figure 6. 3.

Comparison of *in situ* measurements with the model outputs shows that for Site C the model is in good compliance with the in situ measurements performed at the depths 1100 m and 1200 m (Figure 3. A and C). For the depths 1000 m and 1300 m (Figure 3. A and D), there is a slight divergence with the *in situ* DIC values that are slightly lower than the estimated value from the model.

For the Horseshoe Center, the A_T is well represented by the model at depths 1400 m and 1500 m, while *in situ* DIC values are slightly lower than the model outputs. However, differences between *in situ* DIC and A_T values, and model outputs increase at shallower depths.

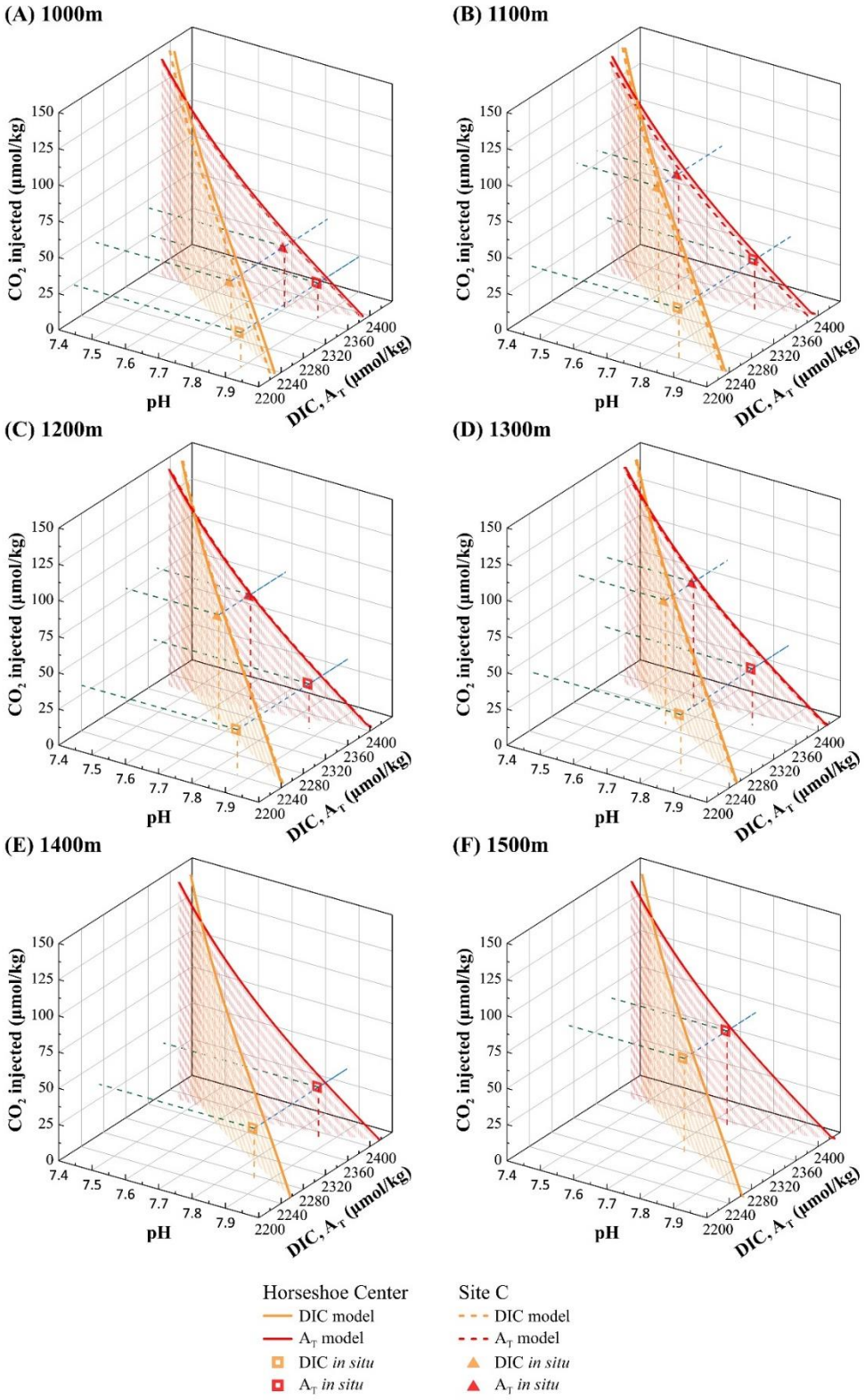

Figure 6. 2. 3D-plots of the model results with pH in x axis, *$CO_{2\ inj}$ in* y axis *and DIC and A_T in* z axis. *Model was run at various depths: (A) 1000 m, (B) 1100 m, (C) 1200 m, (D) 1300 m, (E) 1400 m, and (B) 1500m. Plotted lines are the results of the models, and* in situ *values of pH_{corr}, DIC and A_T are presented as symbols The red line and red symbols are for A_T, while the orange line and orange symbols are for DIC. Dotted lines and triangle symbols represent the Site C, while plain line and square symbols represent the Horseshoe Center. The value of injected CO_2 ($CO_{2\ inj}$) for* in situ *data has been estimated using the* in situ *pH_{corr} that was projected on the model curve of* pH versus $CO_{2\ inj}$.

Overall, *in situ* data are well modelled for depths close to the seafloor. We suggest that closer to the seafloor, dilution of the injected liquid CO_2 with the surrounding seawater remains low. The Horseshoe deep-water column is close to the actual model conditions: i.e. a closed batch system at equilibrium with CO_2 injection, with bathymetry at these depths offering a barrier against currents, therefore limiting transport and dispersion mechanisms.

Lower *in situ* DIC and A_T values than model outputs at higher depths are explained by transport, and more precisely by the export of the modified seawater and the input of 'fresh' unimpacted seawater inside the Horseshoe structure due to local hydrodynamic conditions. Indeed, in the model, the system reaches the equilibrium without any transport variable. On the contrary, *in situ* measurements represent a snapshot of the carbonate system within the Horseshoe area: they do not capture the total DIC linked to the CO_2 emissions, but rather the instantaneous budget between the continuous supply of CO_2 and the volume that may have already been flushed away by local transport (input of fresh seawater and output of already modified seawater). Since our modelled A_T values using CO2Sys are in accordance with our actual A_T *in situ* data, the Horseshoe carbonate system seems to be close to equilibrium, but we cannot exclude that part of the discrepancies observed between our model outputs and our data at shallower depths originates from the Horseshoe system being out of equilibrium.

6.3.1.2. Estimation of $CO_{2\ inj}$ at Site C and Horseshoe center

Figure 6. 3 shows the depth profiles of our model estimates of $CO_{2\ inj}$ at Site C and at the Horseshoe Center, from 1000 m to seafloor depths. Site C presents higher amount of $CO_{2\ inj}$ than Horseshoe Center. This is consistent with the high density of venting seeps with elevated flux observed at Site C, while the Horseshoe Center may rather represent the resultant or mixing of all venting sites over the entire Horseshoe area, as there is no direct venting observed at this site and as it is located in the middle of the Horseshoe structure.

For both Site C and Center, the amount of $CO_{2\ inj}$ remains constant between 1100 m and 1400 m. At 1000 m, a significant decrease is observed, and is consistent to the hypothesis of CHAPTER 5, where above the horseshoe structure, droplets and dissolved part are subject to local hydrodynamics that favor the export and the dilution processes.

In comparison to the $CO_{2\ (aq)}$ measured *in situ* (Table 6. 4 and Table 6. 5), the estimated $CO_{2\ inj}$ remains lower, whereas values of DIC calculated from the model are higher than the measured DIC.

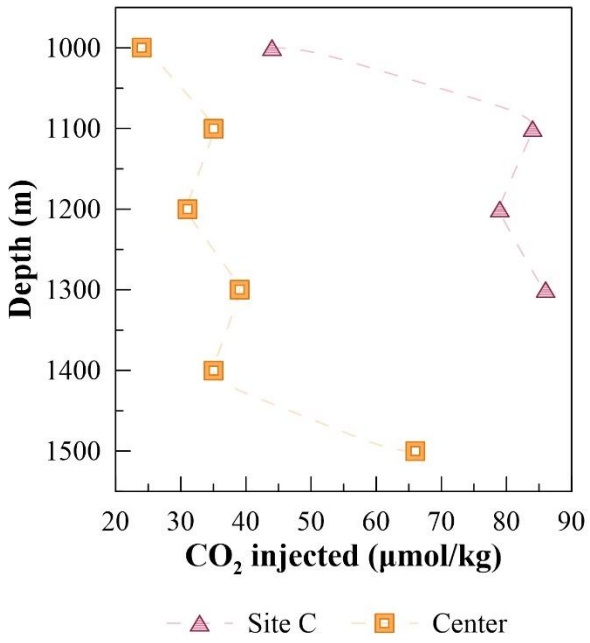

Figure 6. 3. Depth profile of the estimation of CO_2 injected within the water column for the Horseshoe Center and the Site C.

This observation is consistent with our previous finding where the model goes to the equilibrium without considering any transport variable or continuous supply of CO_2. This is why, in reality (i.e. *in situ* conditions), it seems that there is more CO_2 injected. The DIC is lower than the model DIC due to the presence of transport. If there was no flushing away we could expect an increase of DIC through time.

One should bear in mind that we do not consider kinetics of dissolution as we performed our batch simulations. Comparison with $CO_{2\,(aq)}$ can be impaired with part of our CO_2 injected being distributed into both the liquid and dissolved phase, and therefore already accounting for the entire DIC pool and not only the $CO_{2\,(aq)}$ or H_2CO_3.

However, we argue that such modelling approach is useful to i) highlight the equilibrium state of the system, and the transport intensity on the different sites, and ii) to study the response of the Horseshoe water column system and its spatial variability among sites.

6.3.2. Study of the overall Horseshoe area at 1200 m deep

Here we compare amounts of $CO_{2\,inj}$ between various sites over the entire Horseshoe area, at one depth, 1200 mbsl. We run the model at Site C at 1200 m and assume that the slight variation of depths in the collected data would lead to very little temperature changes that do not affect significantly the thermodynamic reactions of the model . Indeed, water samples collected at all sites from the Horseshoe area around 1200 m span over 1216 ± 35 m of sampling depth for a temperature of 5.1 ± 0.2 °C.

Figure 6. 4 shows the model outputs of pH, DIC, and A_T for a progressive addition of aqueous CO_2, at Site C and at a depth of 1200 m. *In situ* measurements performed at ~1200 m, at various sites within the Horseshoe area are compiled in this figure: based on our CO_2 injection curve, we estimated the $CO_{2\,inj}$ corresponding to these *in situ* conditions by reporting the *in situ* pH_{corr} on the model curves

of pH versus $CO_{2\ inj}$. These estimations of $CO_{2\ inj}$ are presented in Table 6. 6.

Sites C, A1 and A2 show the highest values of $CO_{2\ inj}$ (46 to 79 µmol/kg) among all the Horseshoe sites, and show a good agreement between DIC and A_T measurements and model outputs.

At the Channel, *in situ* DIC and A_T are significantly low compared to the model, which can be explained by the presence of strong local hydrodynamics at this site.

Although there has been no observation of venting at this site, it shows an elevated value of $CO_{2\ inj}$ (50 µmol/kg) compare to other sites where venting is present. This channelized area likely receive large amount of Horseshoe seawater exported off the rim. The modified seawater circulating in this path is enriched in CO_2 originating from the Horseshoe venting sites and exported offshore. ROV observation show occurrences of high bottom currents in the area (>1 m/s).

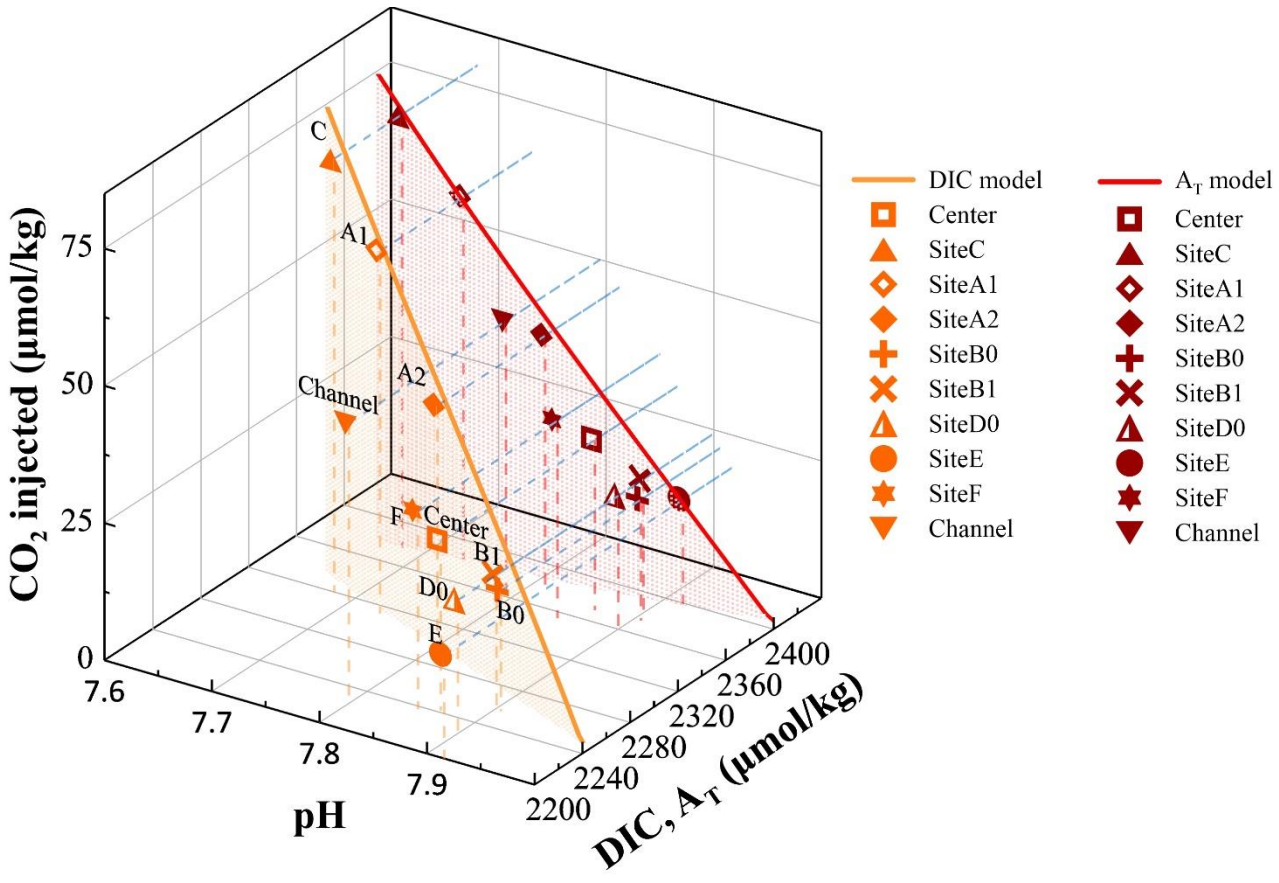

Figure 6. 4. 3D-plots of the model results with pH in x axis, *$CO_{2\ inj}$ in* y axis *and DIC and A_T in* z axis. *Plotted lines are the results of the model performed for Site C at 1203 mbsl. Symbols represent* in situ *values of pH_{corr}, DIC and A_T for various sites over the Horseshoe area, at ~1200 mbsl. The red line and red symbols are for A_T, while the orange line and orange symbols are for DIC. The value of injected CO_2 ($CO_{2\ inj}$) for* in situ *data has been estimated using the* in situ *pH_{corr} that was projected on the model curve of* pH versus $CO_{2\ inj}$.

The sites B0, B1, D0, F0 and Center present $CO_{2\ inj}$ values from 22 to 36 µmol/kg. The lower $CO_{2\ inj}$ compared to the other sites can not be explained by lower fluxes of venting at the seafloor since those fluxes are in the same order and even higher than the sites C, A1 and A2 (Flux at seafloor, Table 6. 7). However, the significant difference from the model (*in situ* DIC and A_T are lower than model outputs) suggest the presence of local hydrodynamics, and therefore, transport that potentially occurs horizontally and/or vertically.

Site E shows the lowest $CO_{2\ inj}$ and a significant difference between *in situ* values and the model, similar to what is observed within the Channel. According to CHAPTER 5, this would confirm that this site is subject to strong dilution processes associated to local hydrodynamics and the absence of bathymetric barrier.

6.3.3. Comparison with seafloor fluxes

Using our modelling results of CO_2 injection at 1200 m in the water column, we intend on estimating CO_2 budgets at this depth and for each site. To do so, the $CO_{2\ inj}$ determined at 1200 m has been extrapolated over each active site area, considering a height of 1 m and the surface of the active site determined by Cathalot et al. (in prep.). Those budgets, (and inherently, the concentrations of $CO_{2\ inj}$) can be compared to CO_2 fluxes measured at the seafloor of each sites by *Cathalot et al. (in prep.)*. Assuming that CO_2 fluxes remain constant along the water column, the necessary duration to supply an active site area at 1200 m have been estimated from seafloor fluxes and $CO_{2\ inj}$ budgets. Both surface of the active site and CO_2 fluxes at the seafloor were estimated by ROV images and gas measurements (Cathalot et al., in prep.).

Table 6. 6. In situ *data that have served as input parameters in the model program, and estimated $CO_{2\ inj}$ values for various sites at ~1200 mbsl. $CO_{2\ inj}$ values have been estimated using the* in situ *pH_{corr} that was projected on the model curve of* pH versus $CO_{2\ inj}$.

			Site C	Site A1	Site A2	Site B0	Site B1	Site D0	Site E0	Site F0	Channel	Center
	Real depth	m	1203	1229	1248	1188	1188	1176	1257	1250	1251	1168
	Height from seafloor	m	86	211	180	185	237	86	257	103	496	320
VENTING SITE	Temperature	°C	5.09	5.05	4.97	5.40	5.24	5.24	4.69	5.12	4.84	5.38
VENTING SITE	pH_{corr}		7.68	7.731	7.812	7.906	7.898	7.898	7.917	7.850	7.794	7.87
VENTING SITE	$CO_{2(aq)}$	µmol/kg	96.0	88.1	81.3	71.7	56.9	61.6	50.4	89.7	62.2	59.0
VENTING SITE	DIC	µmol/kg	2320	2313	2288	2257	2260	2227	2199	2237	2230	2242
VENTING SITE	A_T	µmol/kg	2376	2383	2378	2374	2383	2362	2399	2354	2361	2371
MODEL	$CO_{2\ inj}$	µmol/kg	79	66	46	22	24	24	19	36	50	31

The results of the budget determination is presented in Table 6. 7. The $CO_{2\,inj}$ budget over the sites evolve from 3.6 mol at site F0 to 1612 mol at site C. The sites A1, A2 and B1 leads to the same order of budget values (~100-160 mol) although B1 is about twice the area of A1 and A2. In addition, although the flux measured at the seafloor of B1 is higher than A1 and A2, the concentration of $CO_{2\,inj}$ at 1200 m is lower. This observation seems supporting the presence of transport, as suggested previously.

The most recent sites – D0, E0 and F0 – present the lowest $CO_{2\,inj}$ budgets. Those sites are located on the east branch of the Horseshoe, with E0 emplaced outside the structure. Although, sites D0 and E0 present seafloor fluxes higher than sites A1 and A2, the budget at 1200 m is weak. Thus, those results confirm that sites D0 and E0 are subject to local hydrodynamics. The low $CO_{2\,inj}$ budget at site F0 is trickier to explain, it seems that it result from both a low flux at the seafloor and the addition of transport variable.

Table 6. 7. Estimation of $CO_{2\,inj}$ budgets and fluxes at 1200 mbsl for the active venting sites and comparison to seafloor fluxes with the determination of an equivalent emission duration.

	Active site area*	**Flux at seafloor ***	**$CO_{2\,inj}$ at 1200 m**	**$CO_{2\,inj}$ budget at 1200 m**		**Equivalent emission duration****
	m^2	tCO_2/y	µmol/kg	mol	tCO_2	second
Site C	20400	142208.3	79	1611.6	7.09E-02	15.73
Site A1	2400	16730.4	66	158.4	6.97E-03	13.14
Site A2	2300	16033.3	46	105.8	4.66E-03	9.16
Site B0	17500	121992.4	22	385	1.69E-02	4.38
Site B1	5600	39037.6	24	134.4	5.91E-03	4.78
Site D0	2600	18124.6	24	62.4	2.75E-03	4.78
Site E0	2800	19518.8	19	53.2	2.34E-03	3.78
Site F0	100	697.1	36	3.6	1.58E-04	7.17

** Active site area and seafloor fluxes from Cathalot et al. (in prep.).*
*** Necessary duration to obtain $CO_{2\,inj}$ at 1200 m by assuming that the emission flux at the seafloor is equal to the one in the water column.*

Looking at the *equivalent emission duration* in Table 7, which represent the necessary time to supply the area at 1200 m up to the $CO_{2\,inj}$ budget with the CO_2 seafloor flux, it gives clues on the transport intensity. Indeed, sites C, A1 and A2, which seems to be less prone to transport according to the previous conclusion, present the higher durations of supply. This means that CO_2 has been injected with a minimum of flux disruption, and therefore suggesting a weak transport variable. On the contrary, for sites B0, B1, D0, and E0, the

budget is equivalent to only ~3-4 seconds of supply from the seafloor, highlighting the addition of local hydrodynamics that flushed away the $CO_{2\ inj}$ as CO_2 is discharged from the seafloor. Here again, site F0 shows an in-between position where the flux at the seafloor is weak and in addition, CO_2 budget at 1200 m may also be influence by transport.

6.4. Conclusion

In this study, we have used the PHREEQC geochemical software and the CO2Sys Excel Macro to give a first estimate of the amount of carbon dioxide injected within the water column by the Horseshoe degassing. In addition, this modelling approach was useful to study the dynamic of dissolution of the CO_2 injected within the water column, and to highlight the transport intensity and its spatial variability among sites.

In the deep-water column (i.e. close to the seafloor), the Horseshoe bathymetry offers a barrier against currents, limiting transport and dispersion mechanisms. On the contrary, upward in the water column, the emissions of CO_2 are subject to the local hydrodynamics, favoring transport and dispersion mechanisms.

Comparing the $CO_{2\ inj}$ budgets at 1200 m among sites, the stronger budgets are encountered for sites located on the western branch of the Horseshoe, which are also the oldest sites. Nonetheless, certain sites (B0 and B1) seems more subject to transport. On the east branch, sites are associated to lower $CO_{2\ inj}$ budgets, particularly explain by the presence of transport through local hydrodynamics.

Overall, although the initial CO_2 flux at the seafloor may be linked with site location and/or age, which is reflected on the $CO_{2\ inj}$ budgets within the water column, the budget at 1200 m appears to be governed by the presence and the intensity of local hydrodynamics.

This study should provide some clues to further determined the global carbon budget of this system, and its contribution to the global ocean. In this perspective, it would be necessary to complete this model of $CO_{2\ inj}$ calculation from in situ DIC and pH, with transport by local hydrodynamic and maybe two gas phases (liquid for droplet and dissolve part).

6.5. Bibliographical References

Aiuppa, A., Hall-Spencer, J.M., Milazzo, M., Turco, G., Caliro, S., and Di Napoli, R. (2021). Volcanic CO2 seep geochemistry and use in understanding ocean acidification. *Biogeochemistry* 152(1)**,** 93-115. doi: 10.1007/s10533-020-00737-9.

Boatta, F., D'Alessandro, W., Gagliano, A.L., Liotta, M., Milazzo, M., Rodolfo-Metalpa, R., et al. (2013). Geochemical survey of Levante Bay, Vulcano Island (Italy), a natural laboratory for the study of ocean acidification. *Marine Pollution Bulletin* 73(2)**,** 485-494. doi: 10.1016/j.marpolbul.2013.01.029.

Cathalot, C., Rinnert, E., Fandiño, O., Scalabrin, C., Giunta, T., Ondreas, H., et al. (in prep.). Large CO2 hydrates field along the volcanic ridge offshore Mayotte Island.

Donval, J.P., and Guyader, V. (2017). Analysis of hydrogen and methane in seawater by "Headspace" method: Determination at trace level with an automatic headspace sampler. *Talanta* 162**,** 408-414. doi: 10.1016/j.talanta.2016.10.034.

González-Delgado, S., and Hernández, J.C. (2018). "Chapter Two - The Importance of Natural Acidified Systems in the Study of Ocean Acidification: What Have We Learned?," in *Advances in Marine Biology*, ed. C. Sheppard. Academic Press), 57-99.

[Dataset] Lewis, E.R., and Wallace, D.W.R. (1998). *Program Developed for CO2 System Calculations.* doi: 10.15485/1464255. Available: https://www.osti.gov/biblio/1464255.

Lui, H.-K., and Chen, C.-T.A. (2017). Reconciliation of pH25 and pHinsitu acidification rates of the surface oceans: A simple conversion using only in situ temperature. *Limnology and Oceanography: Methods* 15(3)**,** 328-335. doi: 10.1002/lom3.10170.

Parkhurst, D.L., and Appelo, C.A.J. (2013). "Description of input and examples for PHREEQC version 3: a computer program for speciation, batch-reaction, one-dimensional transport, and inverse geochemical calculations", in: *Techniques and Methods.* (Reston, VA).

Price, R.E., and Giovannelli, D. (2017). "A Review of the Geochemistry and Microbiology of Marine Shallow-Water Hydrothermal Vents," in *Reference Module in Earth Systems and Environmental Sciences*. Elsevier).

Rinnert, E., Cathalot, C., and Feuillet, N. (2021). GEOFLAMME cruise, RV Pourquoi pas ? doi: 10.17600/18001297.

CHAPTER 7. Conclusions & Perspectives

Abstract

This PhD work on the submarine volcano system offshore Mayotte has provide valuable information on the chemicals discharged from a submarine eruption at different stage of eruptive activity, the various geochemical processes involved, and the impact on the water column geochemistry.

This chapter concludes with the work conducted during the course of this PhD thesis, and outlines a few perspectives of research for future work.

CHAPITRE 7. Conclusions & Perspectives

Résumé

Ce travail de thèse sur le système volcanique sous-marin au large de Mayotte a fourni des informations précieuses sur les éléments chimiques émis par les éruptions sous-marines à différents stades de l'activité éruptive, les divers processus géochimiques impliqués, et l'impact sur la géochimie de la colonne d'eau.

Ce chapitre conclut le travail effectué au cours de cette thèse de doctorat, et présente quelques perspectives de recherche pour les travaux futurs.

Submarine volcanism releases large amount of chemicals and heat through the water column. This is also the main mechanism responsible for deep carbon releases (Rubin et al., 2012; White et al., 2015). Deep submarine volcanoes are difficult to detect, to observe and to study, and thus very few have already been studied (Baker et al., 2012; Rubin et al., 2012). Although, very few deep submarine volcanoes have been geochemically studied, it is apparent that the chemical fluxes released into the ocean through submarine volcanism depend on the geotectonic context and the eruptive style (Gamo et al., 1987; Hilton et al., 1998; Wheat et al., 2000; De Ronde et al., 2005; Resing et al., 2009; Baumberger et al., 2014; Baumberger et al., 2020). However, the variety of fluid and gas discharged, as well as the associated geochemical mechanism, and the possible impact on the ocean are still poorly understood (Baker et al., 2012; Rubin et al., 2012). In addition, the number of deep active submarine volcano remains uncertain, with an underestimation of intraplate volcanoes (Rubin et al., 2012). As a result, the contribution of submarine volcanism in the release of gases into the ocean and the way it affects the geochemistry of the water column, are not well defined.

This thesis was conducted in the objective to gain knowledge on this issue. For this, we chose the Fani Maoré volcano and its associated volcanism system offshore Mayotte Island as study site. This volcano is the first submarine volcano ever observed only a few months/years after its appearance (< 6 years old, at the time of writing). It is also the deepest edifice (3500 m deep) and the largest submarine eruption (~6.5 km^3 of magma erupted) documented, which was captured right at the time of the volcano discovery (eruptive plume up to 2 km high) (Feuillet et al., 2021). This volcano is associated with strong releases of chemicals, in particular volatiles, emitted during the ongoing eruption (in 2018-2019), and during the continued lava flow installation (until the end of 2020). In addition, this volcano onset is associated with the setup of strong discharge of liquid carbon dioxide only a few tens of kilometers away, in a pre-existing volcanic structure, called the Horseshoe. Those features make it an exceptional site to study the geochemical manifestations occurring within the ocean water column during and after an eruptive event, as well as the impact of fluid and gas emissions on the water column geochemistry during the eruptive event and over time. It is also a great opportunity to study the link and feedbacks between this major volcanic eruption and adjacent carbon dioxide release in the marine environment.

In CHAPTER 4 of this thesis, we focused on the onset of the Fani Maoré volcano through the geochemistry of the water column. We gave evidence of the relationship between the degree of eruptive activity (i.e. ongoing eruption, date of lava flow installation, no activity) and the fluid emissions, gas basically, within the water column. During the eruption, we highlight an exceptional release of hydrogen up to shallow depths in the water column, which was dissociated from the

behavior of the other gaseous species (CH_4, CO_2) and which we explain by the generation processes involved and the physical properties of the water column (T, P, stratification). In addition, during the lava flow emplacement, we highlighted a temporal variation in the fluid origin through the helium isotopic composition of the fluid discharged into the water column. Through the study of the water column physicochemical composition, we show a strong perturbation (e.g. pH decrease, total inorganic dissolved carbon increase) caused by the eruptive activity, that was decreasing back to local background levels a year after (or less) the main eruptive event. However, it remains unclear whether this phenomenon was due to the decrease of the activity coupled with local hydrodynamics features and renewing of water masses by the currents or to the buffering capacity and the resilience of the water column, or a combination of both.

In CHAPTER 5, we studied the exceptional discharges of liquid CO_2 droplets occurring within the Horseshoe structure. We were interested into their origin, their behavior during their ascent in the water column, and their impact on the geochemistry of the surrounding seawater. We first found from the helium isotopic composition that those emissions had the same origin whatever the location on the Horseshoe structure. Then, we investigated the dissolution processes of the droplets during the ascent by describing the gas released and their proportion from each other, which highlighted the role of the seafloor morphology and the local hydrodynamics (e.g. tides, internal waves, geostrophic current) in controlling the depth of the CO_2 droplet dissolution. Finally, we shown that the spatial variations in the degree of impact of the carbonate system were also related to the seafloor bathymetry that act as a barrier against the current and confine the emissions, which is a very specific and unique feature of our study site.

In CHAPTER 6, we used a geochemical model that estimates from the carbonate system parameters the amount of aqueous CO_2 injected (before any reaction with seawater) within the water column by the seafloor discharges. We have shown differences in the amount of CO_2 injected depending on the site location and in agreement with the seafloor fluxes. In addition, from a comparison between the *in situ* data and the model results, we highlighted the presence of dilution processes caused by local hydrodynamics.

Overall, this thesis has enabled us to expand our understanding on the water column geochemistry above a complex system of submarine volcanism, although many questions remain unsolved.

7.1. Synthesis from the study of the submarine volcanic system offshore Mayotte

The study of the water column geochemistry in the volcanic system offshore Mayotte allows to answer the questions proposed in the CHAPTER 1, and to integrate these results in a general context for deep submarine volcanism assessment.

7.1.1. How do the volcanic emissions manifest within the water column?

First, we were interested on the different styles of manifestation affecting the water column that can exist in an active submarine volcanic context. Those manifestations were defined from the water column physical properties and the inherent anomalies (e.g. turbidity, temperature, density), and confirmed by acoustic and visual surveys. The various manifestations founded in Mayotte submarine volcanic system are summarized in the Figure 7. 1. A.

During the ongoing eruption (CHAPTER 4), the main manifestation was an eruptive plume at the summit of the volcano, rising up to 2 km high within the water column. In association to this eruption, the presence of sinking liquid CO_2 onto the volcano flanks have been further identified through the study of the geochemical water column composition (described in paragraph 7.1.3). Due to the hydrographic properties of the water column in the submarine volcanic context offshore Mayotte, the CO_2 emitted is in its liquid form below ~500 mbsl, (depending on the local pressure and temperature conditions). After the main eruptive event, lava flows have been continuously introduced onto the ocean seafloor around the volcano, leading to the formation of diffuse plumes right above them. In addition, emplaced at ~10 km from the coast and ~40 km from the volcano, the Horseshoe pre-existing structure presents numerous venting sites of liquid CO_2 droplets that rise within the water column (CHAPTER 5).

Despite the assessment of manifestation styles, it is not sufficient to determine the origin of such discharged and their chemical composition.

7.1.2. What is the origin of the emissions within the water column?

After having performed the assessment of all manifestation styles on the studied submarine volcanic system, we looked at their origin (i.e. mantellic or crustal-derived).

For this, we performed helium analyses on the seawater samples presenting the strongest anomalies in turbidity and volatiles (CO_2, CH_4 and H_2) contents, above different sites (e.g. summit, lava flows of various freshness, volcano flanks, Horseshoe degassing). Although the use of helium isotopes for

signature determination is usually favored on fluid samples and rarely in water column samples due to the elevated dilution factors (and thus the low concentrations of noble gases), in this study, the results were quite convincing with good estimation of the helium isotopic ratios at stake.

The study of the helium isotopic composition has shown variations in the origin of the emissions over time and space, which are represented in the Figure 7. 1. B, as well as the hypothesis for sub-seafloor processes. At the volcano (CHAPTER 4), the signature was mantellic with crustal-derived material (R/Ra = 6.46) for the western lava flow emplaced in June-July 2019. This isotopic signature is coherent with petrogeochemical studies on lava rocks that have shown evidences of a more crustal magma due to the presence of a secondary reservoir during the magma ascent from the deep reservoir to the surface (Berthod et al., 2022). In contrast, the signature of the fluid and gas emissions into the water column was mainly of mantellic origin for the northwest lava flow emplaced between May and October 2020 (R/Ra = 8.52), which was also confirmed by petrogeochemical studies. We suggested that for this lava flow, either the magma has rapidly ascent through a new dike that did not went through secondary reservoir (i.e. without crustal assimilation), either the secondary reservoir was empty of crustal-derived magma.

At the Horseshoe structure (CHAPTER 5), the emissions sampled within the water column display the same helium signature whatever the venting site (R/Ra = 6.75). This suggests that the degassing occurs from a unique reservoir of mantellic origin with a small contribution of crustal-derived material. Nonetheless, in this thesis, this area have only been studied over space because the GeoFlamme cruise offered the great opportunity to sample each venting sites. The study of temporal variations would be an interesting perspective using the complete series of cruises.

Therefore, the study of helium isotopic composition of the emissions discharged into the water column indicates signature variations over space and time along the Mayotte volcanic ridge, and suggesting changes in sub-seafloor processes. The helium isotopic composition in the water column is a valuable tool to be coupled with pretogeochemical data to estimate the sub-seafloor processes at the origin of the water column emissions.

7.1.3. What are the geochemical processes involved in water column manifestations?

Knowing the type of manifestations and the origin, the geochemical processes of fluid and gas generation occurring in water column were then investigated and associated to the emission composition. We have studied the volatile concentrations and their proportion (Figure 7. 1. C), and linked those parameters to their generation processes (Figure 7. 1. D).

During the eruptive event (CHAPTER 4), the intense magma-seawater interaction produce large amount of H_2, which can ascent exceptionally to very shallow depth within the water column, likely linked to the potentially explosive character of the eruption. Ongoing eruption also lead, through magma degassing, to large discharges of magmatic volatiles (e.g. CO_2, CH_4) for which the behavior in the water column depends on the hydrographic structure of the ocean. Depending on the depth of the discharge (and inherently to pressure, temperature and salinity), the carbon dioxide is emitted in liquid form and can have a larger density than the seawater, leading it to sink toward the seafloor and to govern the CH_4 behavior. In our case, the 'rise or sink' limit was determined to be at ~2700 mbsl. Although helium was not analyzed during the ongoing eruption, we assume that it is largely released through magma degassing since it is a common volatile included in magma.

Chemicals released by the lava flows strongly depend on the date of emission of the lava (CHAPTER 4). Submarine active lava flow emplacement involves lava-seawater interactions that generates H_2. Magma degassing releases mainly CO_2, which can persist for long periods after the lava flow emplacement. Older lava flow seems to present characteristics of the initiation of hydrothermal circulation with a dominance of CH_4 releases, likely to be generated from thermogenic and/or microbial origin, although the abiotic origin is not ruled out.

At the liquid CO_2 venting sites (CHAPTER 5), the water column composition is controlled by the droplet composition (99.0 ± 0.3 $\%_{vol}$ of CO_2, 0.8 ± 0.2 $\%_{vol}$ of CH_4, and trace amounts of H_2), which are degassed from a sub-seafloor reservoir. Surrounding seawater is governed by large CO_2 concentrations, although the amounts of ^3He and CH_4 are very significant.

According to our study, the geochemical characteristics of the emissions within the water column are linked to the eruptive activity, the geochemical processes involved, and to the geological context and the water column hydrography. At this point, it is likely that the impact on the water column geochemistry could be controlled by the geochemical characteristics of the emissions.

7.1.4. What is the impact of the volcanic emissions on the water column geochemistry?

We studied the impact of chemical discharges through volcanic activity on the surrounding seawater (Figure 7. 1. E). We focused mainly on the carbonate system and on iron and manganese concentrations.

At the liquid CO_2 venting sites, the droplets dissolved in seawater as they ascend the water column (CHAPTER 5 and CHAPTER 6). Aqueous carbon dioxide is injected into the water column

(CHAPTER 6) and reacts with the seawater, leading to a decrease of the surrounding pH (up to -0.8 pH unit) and an increase in dissolved inorganic carbon (DIC) and alkalinity (A_T) (CHAPTER 5 and CHAPTER 6). The degree of impact seems mainly driven by the local hydrodynamics that may export and dilute the chemicals released by water body renewing. Such effect is also driven by the local seafloor morphologies that act as a protective barrier from local currents and that contain chemicals within the bathymetric structures that may favor as a result leaching processes. Those interactions between rocks, seawater, and CO_2 and acidic species drive the release of Fe and Mn into seawater (CHAPTER 5).

At the volcano site (CHAPTER 4), , the surrounding seawater is also subject to acidification due to CO_2 being the main volatile released, although on various degrees this also depends on the intensity of the eruptive activity (up to -0.3 pH unit in the eruptive plume and in diffuse plume from lava flows, up to -0.6 pH unit where the CO_2 sinks on the volcano flank). We also highlight a significant increase in the budgets of DIC and A_T, with particularly elevated A_T values when associated with fluid-rock interactions such as at the summit of the volcano, on the flanks by the presence of sinking liquid CO_2, and on the surface of the lava flows. Nonetheless, the impact on the water column geochemistry seems to be buffered and to go towards a steady state approaching the background characteristics, quickly after the main eruptive event.

Overall, this work on the submarine volcano system offshore Mayotte has provide valuable information on the chemicals discharged from a submarine eruption at different stage of eruptive activity, the various geochemical processes involved, and the impact on the water column geochemistry. Those observations can be extrapolated to submarine volcanic systems in general. It seems clear that, in the case of a deep submarine eruption, the water column geochemistry will be affected depending on the origin of the fluid and gas discharged, the geochemical processed involved that controlled the manifestation types (styles and geochemical composition), the intensity of the eruption, and to the geological and hydrographic context.

7.2. Perspectives of the work

The study of the geochemistry of fluid and gas emissions in the submarine volcanic context of Mayotte, as well as the impact on the water column geochemistry, has raised further concerns. Indeed, this case study would be a useful tool for the estimation of the volatile and carbon budgets issued from a volcanic setting, and to extrapolate those budgets to global submarine volcanism. Those

estimations would provide new findings regarding the importance of the submarine volcanism carbon budget in the context of climate change. In addition, since the local hydrodynamics seems to play an important role in the impact of the volcanic emissions on the local water column, it would be useful to integrate this variable in the volatile and carbon budgets.

Throughout this study, we also found that it seems more common than we thought to found active volcano associated to near field CO_2 degassing, either in gaseous or in liquid form depending of the depth. It would be therefore interesting to investigate this relationship and to define if this setting only occurs in few volcanic systems, or if it is the commonplace. Finally, in a perspective of anthropogenic CO_2 removal through its sequestration into the ocean sub-seafloor, the liquid CO_2 discharged on the Horseshoe structure offers a natural laboratory to evaluate the impact of potential leakage.

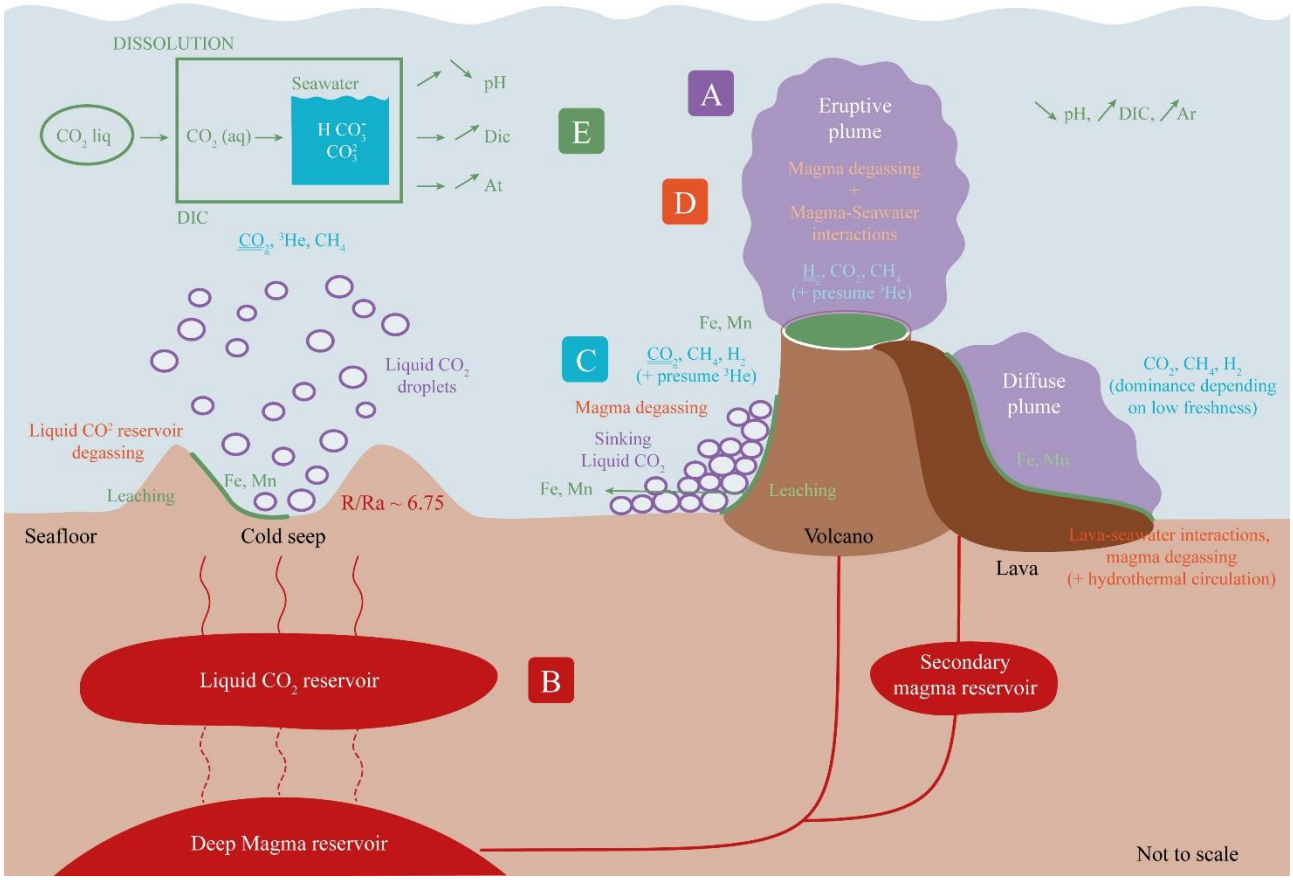

Figure 7. 1. Summary scheme representing the conclusions determined by the study of the submarine volcanic system offshore Mayotte and the associated fluid and gas emissions within the water column. (A) Styles of emission manifestation in the water column (in purple); (B) Hypothetic sub-seafloor processes and helium isotopic composition measured in the water column (in red); (C) Geochemical composition of the fluid and gas discharged (in blue); (D) Geochemical processes for fluid and gas generation (in orange); (E) Impacts and changes in the water column geochemistry (in green).

Although the study of Mayotte submarine volcanic system has provided new insights on the chemicals released by a deep submarine eruption and linked it to eruptive activity levels and types, this study only focused on one submarine volcanic system. One should keep in mind that tectonic (i.e. spreading center, hotspot, arc, intraplate) and geologic (i.e. nature of seafloor rocks) contexts may also control the geochemistry of fluid and gas released in the ocean.

7.2.1. Can we estimate budgets of volatiles released?

Budgets of volatiles in submarine volcanic contexts are not well established. Therefore, we proposed to estimate from the previous studies (Chapters 4, 5 and 6) and through a box model, the budget of volatiles (^{3}He, CO_2, CH_4, H_2) over the different areas of the submarine volcanic system offshore Mayotte. Those comprise the Horseshoe and the Volcano areas. Each area are considered as a unique box with a volume corresponding to the site surface and the chosen water column height. The methodology of this integration calculation is explain in the enclosure at the end of this *Synthesis* part.

7.2.1.1. The volcano area

The box model of data integration for the Volcano area is divided in three sub-boxes, covering the different periods of eruptive activity (Figure 7. 2). The first corresponds to the eruptive event (i.e. eruptive plume at the volcano summit) sampled during MAYOBS1 cruise. The second to the recent lava flow westward from the volcano, taken during MAYOBS4 cruise. And the third to the very recent and incandescent lava flows at the northwest of the volcano, during MAYOBS15 cruise. The global box model and the sub-boxes are dimensioned from the mean seafloor depth of each corresponding area to 900 mbsl, and over the surface of each corresponding area.

Volatile budgets and concentrations are determined for each box and sub-boxes, and are presented in Table 7. 1, and summarized in Figure 7. 2. During the eruptive event, CO_2 and H_2 were emitted in large amount, 470 and 23.7 mol/m^3 respectively, while CH_4 remains low with an estimated concentration of 0.83 mol/m^3. Above the northwest lava flow, which corresponds to very recent and active lava flows, the main released volatile remains the CO_2 with a concentration estimated at 93.4 mol/m^3. H_2 and CH_4 show estimated concentrations in the same order, 2.13 and 1.55 mol/m^3 respectively. Water column geochemistry above the lava considered less fresh (i.e. west lava flow), the estimated concentrations show a dominance of CH_4 against H_2, with values of 2.95 and 0.13 mol/m^3, respectively, while CO_2 is still released in abundance, at 470.3 mol/m^3.

CH_4 concentration is higher above the recent lava than the very recent or the eruptive plume, which is consistent with the initiation of hydrothermal circulation, as suggested in CHAPTER 4. H_2 and CO_2 budgets are also consistent with our study since they are higher in presence of fresh lava discharges (i.e. eruptive plume and very recent lavas). CO_2 being released mainly through magmatic degassing and H_2 through fresh lava-seawater interactions.

Overall, the Volcano box model shows that the CO_2 is the main volatile emitted over the area, with an elevated amount of aqueous CO_2 ($CO_{2\,(aq)}$ = 858 mol/m^3), and also of total carbon (ΔDIC = 1712 mol/m^3, which is the results of the aqueous carbon dioxide dissolution. Global concentration of H_2 is higher than the CH_4 concentration, with values of 21.6 and 5.37 mol/m^3 respectively, which is consistence with the dominance of the eruptive activity over the studied areas.

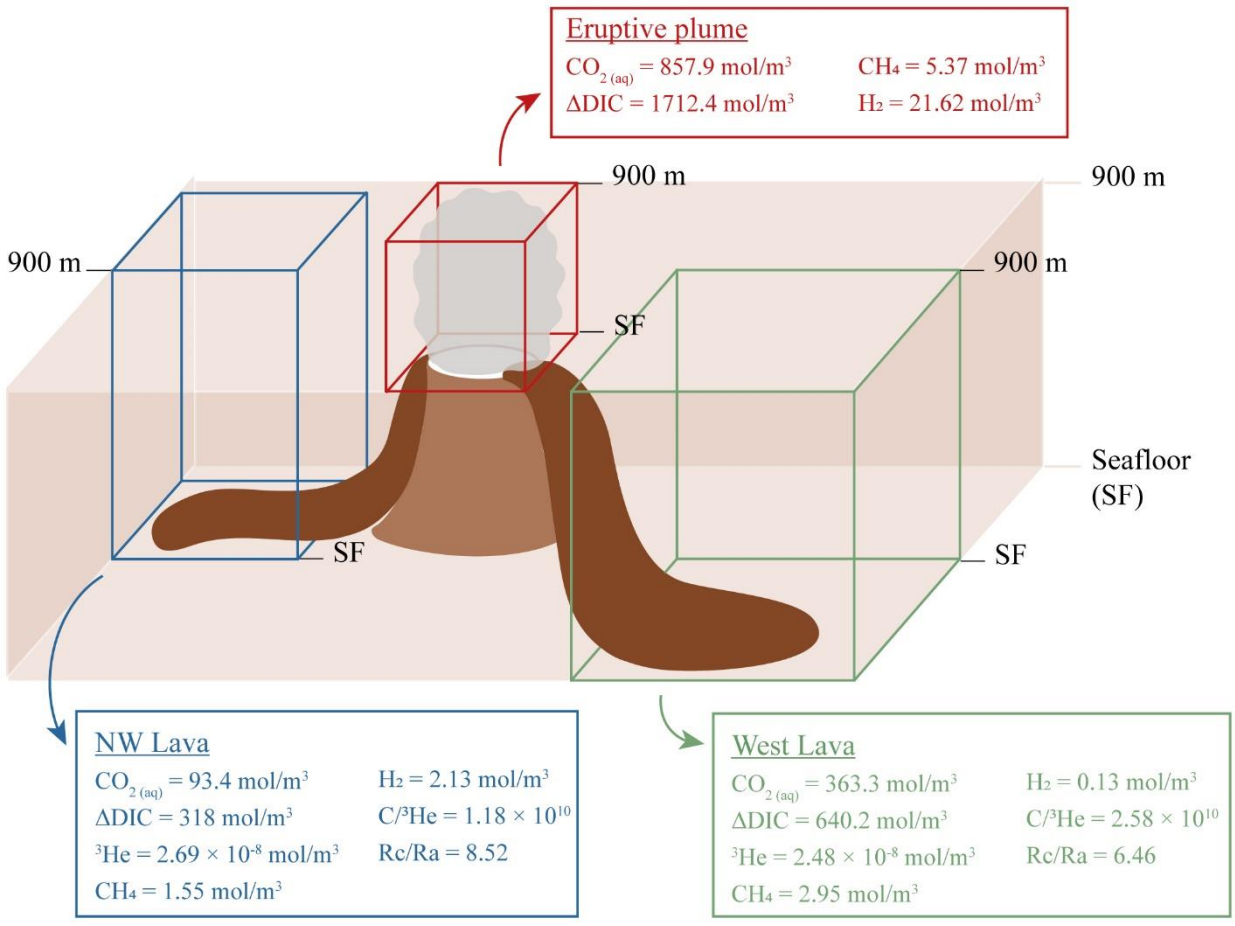

Figure 7. 2. Schematic of the box integration of the geochemical characteristics measured within the water column over the Volcano area.

7.2.1.2. The Horseshoe area

The geochemical study of the emissions at the Horseshoe area (CHAPTER 5) has highlighted a unique helium signature over the area, meaning that the emissions (i.e. the liquid CO_2 droplets) are likely of same origin and of the same composition. In addition, difference in fluxes between the venting sites is studied in the CHAPTER 6. For these two reasons, here, the volatile emissions within the Horseshoe structure are integrated using a single box (Figure 7. 3), covering the Horseshoe area and including the studied venting sites (C, A_1, A_2, B_0, B_1, D_0, F_0). Since there is no venting site at the Channel and Center location, those are not included in the box model. Site E is also not included, as it is located outside the structure and probably strongly influenced by the local currents. The global box model is dimensioned from the mean seafloor depth of the Horseshoe sites to 600 mbsl, and over the total surface. The input concentrations are the one taken during the GeoFlamme cruise and studied in CHAPTER 5 and CHAPTER 6. The box model thus represents the volatile budgets within a unique period.

Volatile budgets and concentrations determined for this global box are presented in Table 7. 1, and summarized in Figure 7. 3. The Horseshoe box model highlights the dominance of CO_2 within the area with estimated concentrations of 230 and 344 mol/m^3, respectively for $CO_{2\,(aq)}$ and ΔDIC. Methane concentration is higher than dihydrogen, with respective values of 2.93 and 0.14 mol/m^3. Those concentrations are consistent with the composition of the liquid CO_2 droplets discharged in the Horseshoe area (99.0 ± 0.3 $\%_{vol}$ of CO_2, 0.8 ± 0.2 $\%_{vol}$ of CH_4, and trace amounts of H_2).

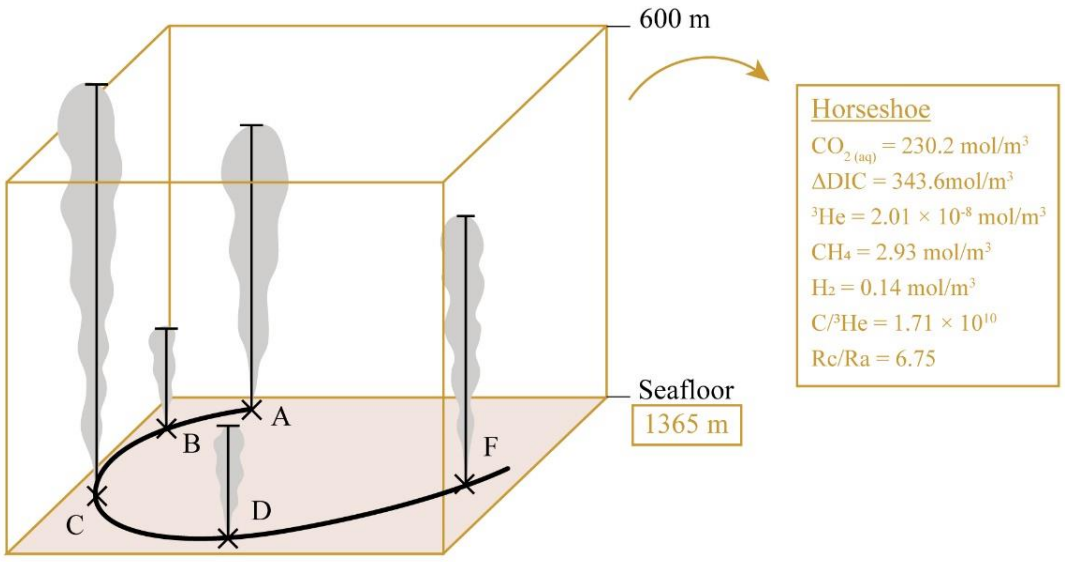

Figure 7. 3. Schematic of the box integration of the geochemical characteristics measured within the water column over the Horseshoe area.

Methodology of calculation

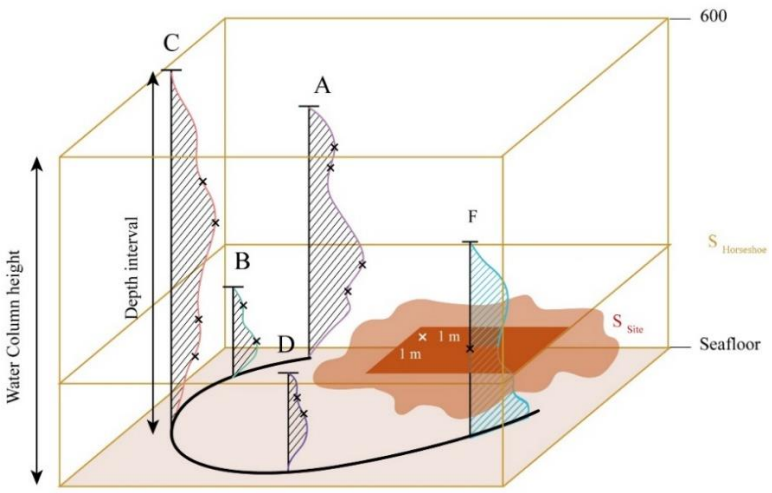

Figure 7. 4. Schematic of the methodology for the volatile concentration integration over the various box model. On this scheme, the methodology is applied on the Horseshoe box.

(i) Integration of concentrations over the water column at each studied site

Calculation of the area under the depth profile curve of the volatile concentration and conversion in mol/m^3 $\Rightarrow x$ mol/m^3

(ii) Determination of the integrated concentration for a surface of one meter square

x mol/m^3 × depth interval of the site profile (m) $\Rightarrow x$ mol/m^2

(iii) Budget determination over the site surface

x mol/m^2 × S_{site} (m^2) $\Rightarrow x$ mol/site

(iv) Budget determination over the area surface (i.e. over the Horseshoe or Volcano areas)

$\Sigma(x \text{ mol/m}^2)_{\text{all sites}} \times S_{area}$ (m^2) $\Rightarrow x$ mol/area

(v) Concentration estimation within the global box

x mol/area ÷ S_{area} (m^2) ÷ water column height (m) $\Rightarrow x$ mol/m^3

The water column height is defined from the mean seafloor depth of the area to the chosen depth within the water column (600 mbsl for Horseshoe, 900 mbsl for Volcano area). We consider that above these depths there is no anomaly.

Table 7. 1. Box model dimensions and results of volatile concentrations and budgets for the Horseshoe and the Volcano box models, as well as for the Volcano sub-boxes (Eruptive plume, West lava, NW lava).

	ZONE		VOLCANO				HORSESHOE
	Site			Eruptive plume	West lava	NW lava	
Box model dimensions	Surface	m2	1.24E+07	5.21E+06	3.28E+06	3.92E+06	5.09E+04
	Seafloor	m	3140	2720	3225	3265	1365
	Height	m	2240	1820	2325	2365	765
$CO_{2\,(aq)}$	Budget	mol	2.38E+13	4.46E+12	2.77E+12	8.65E+11	8.96E+09
	Conc	mol/m3	**857.9**	470.3	363.3	93.4	**230.2**
ΔDIC	Budget	mol	4.76E+13	8.31E+12	4.88E+12	2.94E+12	1.34E+10
	Conc	mol/m3	**1712.4**	876.5	640.2	318.0	**343.6**
^3He	Budget	mol	-	-	189.1	249.2	0.75
	Conc	mol/m3	-	-	2.48E-08	2.69E-08	**2.01E-08**
CH_4	Budget	mol	1.49E+11	7.88E+09	2.25E+10	1.44E+10	1.14E+08
	Conc	mol/m3	**5.37**	0.83	2.95	1.55	**2.93**
H_2	Budget	mol	6.01E+11	2.25E+11	971827451	1.97E+10	5.39E+06
	Conc	mol/m3	**21.62**	23.68	0.13	2.13	**0.14**
$C/^3He$			-	-	2.58E+10	1.18E+10	**1.71E+10**
$CO_2/^3He$			-	-	1.46E+10	3.47E+09	**1.15E+10**
$CH_4/^3He$			-	-	1.19E+08	5.77E+07	**1.46E+08**
R/Ra			-	-	6.46	8.52	**6.75**

Those box models seem to be useful tools to estimate global volatile budgets over an area and compare it to other areas. However, those are an instantaneous picture of the water column composition and do not take into account the fluxes of volatiles injection and other variables that may affect the budgets, such as local hydrodynamic conditions.

7.2.2. Does local hydrodynamics limit the impact on the water column geochemistry?

In CHAPTER 5 we have shown that the impact of liquid CO_2 emissions on the water column geochemistry is strongly controlled by local hydrodynamics that leads to water masses renewing and thus dilution of the chemicals released by the fluid and gas emissions.

Indeed, comparing the budget of total carbon accumulated in the Horseshoe area over 3 years (i.e. from the vents' discovery to the sampling time) that is of 1.34×10^{10} moles, with the total carbon input from the seafloor liquid CO_2 vents that would be of 2.42×10^{10} molC in three years (Cathalot et al., in prep.), there is a loss within the water column of 1.08×10^{10} molC (Figure 7. 5). This amount of carbon is likely to have been exported by the local hydrodynamics. Indeed, surveys of current

speed performed during MAYOBS15 from ADCP (Acoustic Doppler Current Profiler) mounted on the CTD-rosette gave evidence of a mean current speed of ~10 cm/s, in the both directions (South-North and East-West). This current is thus likely to have spawned water masses export and inherently water renewing, finally diluting the carbon budget of the Horseshoe area. Assuming that the water entry of the horseshoe consists of a surface of ~1700 m wide and 765 m of height, the renewing flux would be of 4.68×10^8 m^3/yr, and would correspond to an export of 3.22×10^{11} molC within three years. Although in the same order of magnitude, such outflow flux estimate is higher than our established C budget. Such overestimation may result from the improper estimate of the hydrodynamic flux (i.e. current speed or water surface entry overestimated), from the underestimation of the number and/or the flux of the seafloor emissions, or from the presence of physical protections from the currents and export out of the Horseshoe structure.

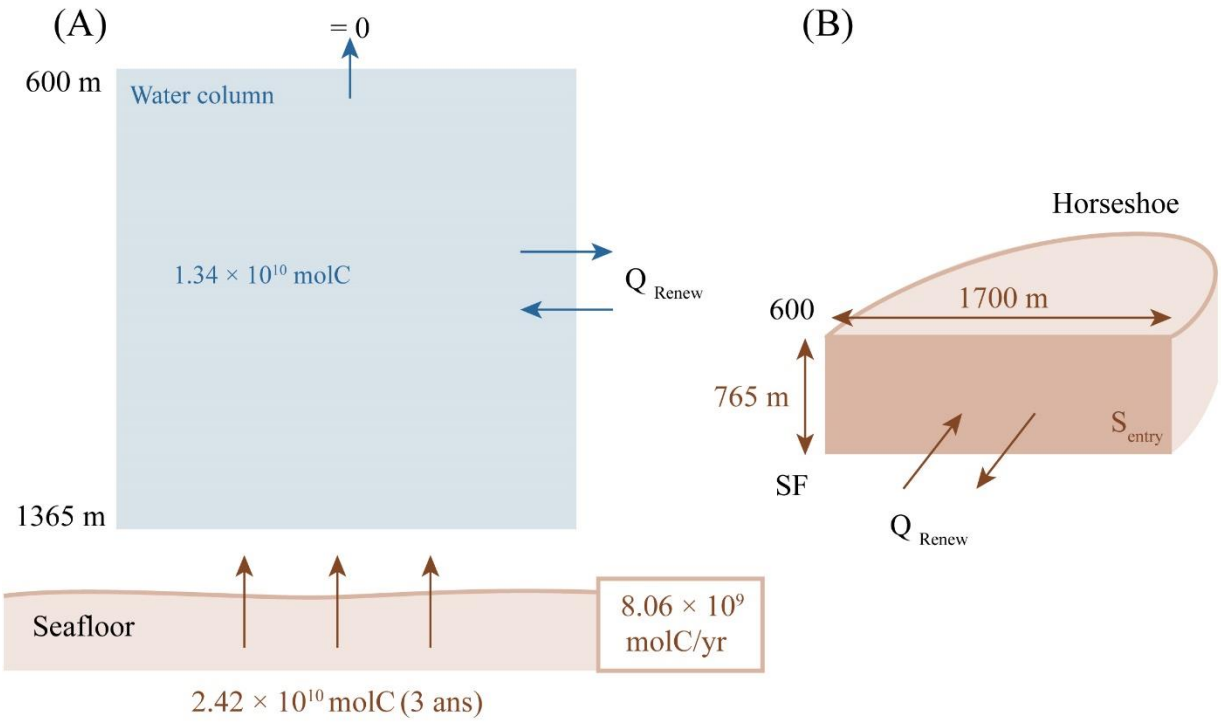

Figure 7. 5. Box model schematic. (A) Without water masses renewing, (B) with renewing.

Through the export by local hydrodynamics, the emissions of carbon are suggested to be incorporate into the water masses and to enter the global ocean circulation. Therefore, in the objective to quantify this impact, it would be interesting to run more complex models including the geochemical data obtained through this study, coupled with local and regional hydrodynamics and with the residence time and the reactivity of the chemicals. As a result, more accurate predictions on where the carbon

is going and which water body will be affected by volcanic emissions can be made. In addition to carbon export study, the impact evaluation could also be conducted on water density or heat fluxes. On another point of view, it would also be interesting to model the fluxes of chemicals injected using *in situ* budgets, local hydrodynamics, and thermodynamic reactions.

Methodology of calculation

This is a simplified model for the estimation of the carbon amount that would be exported from the Horseshoe area by the local hydrodynamics.

We consider the water column between 600 mbsl and the averaged seafloor depth (1365 m) as a unique box. Flux toward the upper level of the water column is assumed to be negligible due to the strong stratification and the absence of anomaly above 600 mbsl. The liquid CO_2 emissions are compare with the total carbon budget of the water column, so the budget takes into account all carbon species resulting from the reaction of CO_2 with seawater.

The renewing flux (Q_{renew}) was calculated as follow:

$Q_{renew} = v\ (m/yr) \times S_{entry}\ (m^2)$

With v the current speed and S_{entry} the considered water surface entry.

7.2.3. Volcano and Horseshoe: is there a link?

The submarine volcanic context offshore Mayotte includes the Fani Maoré volcano that erupted first in 2018-2019 followed by a continued lava flow installation until the end of 2020, and of the Horseshoe area where liquid CO_2 venting sites appeared at the beginning of the volcanic crisis and are continuously increasing in their number. Although, both the Volcano and the Horseshoe area released volatiles within the water column and are linked to the volcanic crisis timing, the link between the two structures remains unclear. Here, we attempt to compare the water column data of both areas and associate them to a common or to different sub-seafloor processes.

7.2.3.1. Through the study of the magmatic signature

Firstly, from the global box models performed on the Volcano and on the Horseshoe areas, we can compare the volatile concentrations released into the water column between both areas (Table 7. 1).

Overall, the Volcano areas presents concentrations higher by more than the twice of the Horseshoe concentrations. For example, concentrations of total carbon are of 1712 mol/m^3 at the Volcano and of 343.6 at the Horseshoe, and the ^{3}Heconcentration accounts respectively for 5.42 x 10^{-8} and 2.01 x 10^{-8} mol/m^3. This suggest that the volcanic eruption and the subsequent lava flows have led to strongest volatiles discharges within the water column than the liquid CO_2 emissions of the Horseshoe area.

Then, using the global box models, we can estimate the C/^{3}He ratios for the Volcano sub-sites (i.e. the lava flows), as well as for the Horseshoe area, C corresponding to the total carbon concentration (ΔDIC). Unfortunately, samples for helium analyses could not be taken during the eruptive event, so helium data for the eruptive plume-box are not available. The C/^{3}He ratios are presented in the Figure 7. 6. The box model for the northwest lava flow (NW lava on the figure), which is the fresher lava with presence of incandescent lava, highlight a ratio of 11.8 x 10^9, while the box model for the recent lava flow westward of the volcano (West lava on the figure) gives a higher ratio of 25.8 x 10^9. For the Horseshoe, the ratio estimation from the box model is of 17.1 x 10^9. Degassing of fresh lava flow is suggested to explain the lower C/^{3}He ratio observed at the NW lava. The fluid and gas discharged are thus mainly originating directly from the magma and are richer in ^{3}He. The West lava presents a relatively higher ratio, suggesting that there is higher CO_2 released compared to the ^{3}He, which may be explained by the addition of other reactions that produce CO_2 in addition to magma degassing.

The Figure 7. 6 also compare the results from the box model to various systems from the literature. The ratio obtained for the Horseshoe box model is consistent with the ratio of 16 x 10^9 found in the liquid CO_2 emissions of the submarine arc volcano, NW Eifuku seamount (Lupton et al., 2006). The ratios for the West lava, NW lava and Horseshoe are in the range of the vent fluid ratios from Loihi seamount, where CO_2/^{3}He ratio evolved from 2 x 10^9 to 27.3 x 10^9 (Hilton et al., 1998). However, our values remains higher than the ratios reported at Petite-Terre degassing areas of 5 x 10^9 (Liuzzo et al., 2021), or than the ratio range of mid-ocean ridge hydrothermal fluids (0.7 to 4.6 x 10^9, Resing et al. (2004), Marty and Jambon (1987)).

Finally, we can compare the helium isotopic ratio, R/Ra, measured at the different sites, and previously reported in CHAPTER 4 and CHAPTER 5. The water column above the NW lava flow presents an R/Ra of 8.52, typical of a mantellic-derived material. The Horseshoe emissions present an R/Ra of 6.75, which is close to the R/Ra of 6.46 measured above the West lava flow. It has been suggested that this lava has a more crustal signature than the NW lava flow due to the presence of a secondary reservoir where magma has assimilate crustal material. In addition, the Horseshoe

emissions could be associated with the shallow plumbing system feeding the gas emissions at Petite Terre that present an isotopic composition of the same order, R/Ra ~6.6 (Liuzzo et al., 2022).

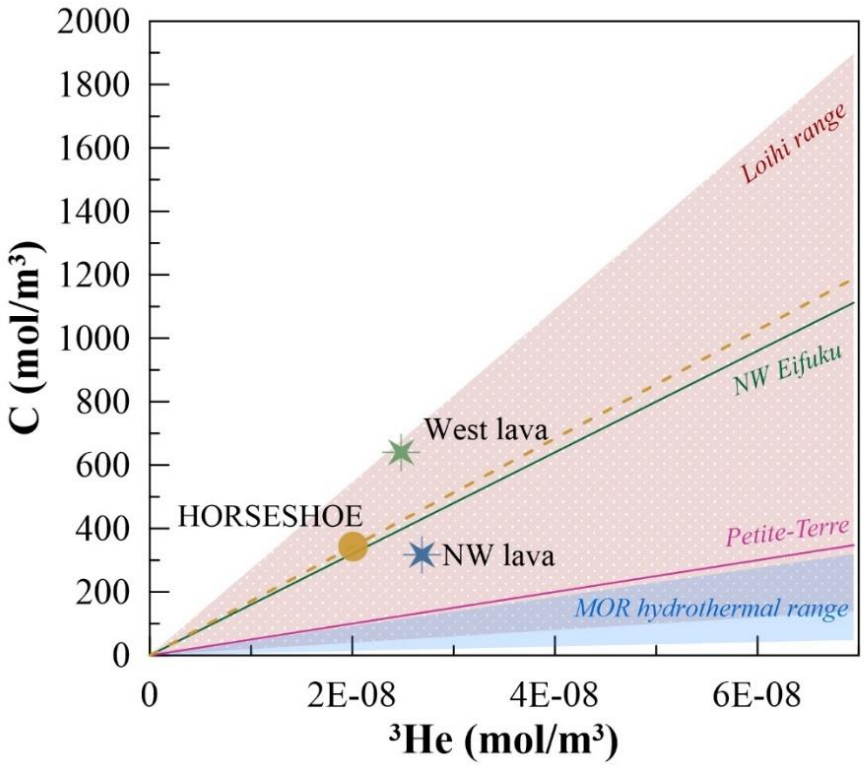

Figure 7. 6. Total carbon released (C) versus the ^{3}He concentrations. Results from the box models of the Horseshoe area and the West and NW lava flows. Ratios of various systems from the literature are represented: mid-ocean ridge (MOR) hydrothermal fluids (0.7 to 4.6 x 10^{9}) (Marty and Jambon, 1987; Resing et al., 2004), Petite-Terre degassing areas (5 x 10^{9}) (Liuzzo et al., 2021), NW Eifuku seamount (16 x 10^{9}) (Lupton et al., 2006), Loihi seamount(2 x 10^{9} to 27.3 x 10^{9}) (Hilton et al., 1998).

From those results, it seems that the emissions observed at the Horseshoe area are associated to the local plumbing system, with helium and carbon dioxide originating from a magmatic source mainly of mantellic origin (R/Ra = 6.75). We therefore suggest that the deep magma reservoir, located beneath the Horseshoe structure (Feuillet et al., 2021), may have degassed up to a sub-seafloor reservoir where the CO_2 is stored. We suggest that the degassing gas was of mantellic origin, and then by ascending within the crust and being stored, it assimilates crustal-derived material that lower the R/Ra signature from ~8 to ~6.75. It is also suggested that this CO_2 reservoir may be heated by the magma reservoir or destabilize by seismic events, leading to degassing at the seafloor of the Horseshoe structure, in the form of liquid CO_2, according to the pressure and temperature conditions. The age of this CO_2 sub-seafloor reservoir is however unknown

7.2.3.2. Emission of liquid CO_2 in volcanic context: rare or the norm?

Shallow submarine volcanoes have regularly been associated with CO_2 seeps with CO_2 emitted in its gaseous phase (Price and Giovannelli, 2017; González-Delgado and Hernández, 2018; Aiuppa et al., 2021). In contrast, only four cases of deep CO_2 venting, therefore in the liquid phase, have been observed (Sakai et al., 1990a; Sakai et al., 1990b; Konno et al., 2006; Lupton et al., 2006). These rare observations of liquid CO_2 venting can be explained either because it is hard to detect those emissions but they are in fact numerous hidden venting sites all over the globe at deep submarine volcanoes, or either because such emissions only happen in specific conditions that are rarely reached. Given the numerous volcanic systems that released gaseous CO_2 through cold seeps, we could hypothesize that it is likely that CO_2 emissions also occur in the deep ocean as liquid form. In that case, this would mean that deep active submarine volcanoes would release about 4.46×10^9 molC/yr in addition to their actual carbon releases (calculated from the carbon budget of the Horseshoe water column of 1.34×10^{10} molC after 3 years of degassing). Overall, it would largely increase the global carbon budget resulting from submarine volcanic discharges.

7.2.4. What is the contribution of submarine emissions to the global carbon cycle?

To date, the current global volcanic, hydrothermal, and tectonic CO_2 emissions from subaerial and submarine sources represents only a small fraction (< 2%) of the global anthropogenic CO_2 produced by burning of fossil fuel energy sources (10.9 ± 0.9 PgC/yr) (Burton et al., 2013; Masson-Delmotte et al., 2021). Nonetheless, the rate of CO_2 degassing from the Earth is considered to be a major factor controlling the partial pressure of atmospheric CO_2 over geological time, and therefore the long-term variation of climate (Berner et al., 1983; Huybers and Langmuir, 2009). Volcanic CO_2 degassing thus acts as a key regulator of climate and eventually leading to periods of long-term global warming.

In the ocean, the global volcanic flux of CO_2 is estimated to be about 176-440 Tg/yr considering mid-ocean ridges, arcs and plumes (Marty and Tolstikhin, 1998). It is estimated that mid-ocean ridge, arcs and plumes contribute for ~70-100 Tg/yr, 110 Tg/yr, and 132 Tg/yr, respectively (Marty and Tolstikhin, 1998). However, since the discovery of submarine volcanoes and CO_2 outputs increase in number each year, global estimates of submarine CO_2 emissions are extremely difficult to make. The vast extent of the surface of the ocean seafloor and our relatively poor knowledge on it suggest that there are many possibilities for unknown or little-known active volcanism (Burton et al., 2013). Therefore, it is a challenge to make quantitative estimates of the global submarine CO_2 emissions.

The study of the Fani Maoré eruption (this present thesis) would be a great opportunity for improving the global submarine CO_2 emissions. Taking the carbon budgets estimated previously, it gives us an idea of the CO_2 flux emitted from this submarine volcanic system to the ocean. The eruptive stage of Fani Maoré is estimated with a CO_2 flux of ~365 Tg/yr, while at the decrease of the activity the flux decrease to ~43.2 Tg/yr, which is therefore more or less the entire current volcanic CO_2 flux estimated at the global range. Our flux estimation may be strongly overestimated, since it is based solely on approximate box models that involve important data extrapolation and therefore strong error propagation, but the gap between actual global estimates and our fluxes may also result from the determination methods currently used in the literature. Indeed, the estimation made for the Horseshoe, of ~0.2 Tg/yr, appears to be in the range of CO_2 flux determined for other systems, such as El Hierro submarine volcano that presents flux of ~0.2 Tg/yr (Santana-Casiano et al., 2016), or NW Rota-1 for which the flux of CO_2 degassing was determined of 0.4 ± 0.1 Tg/yr (Dziak et al., 2012), giving us confidence in the methodology we used. The Horseshoe highlight a flux nearly ten times higher than the flux of 0.035 Tg/yr from NW Eifuku where liquid CO_2 discharges were also observed (Lupton et al., 2006). In this case, although an overestimation cannot be discarded, the elevated CO_2 flux from the Horseshoe may be related to the great extent of the degassing area.

Overall, the carbon emissions caused by submarine volcanism may not account for the majority of the increase in CO_2 in the atmosphere, but their contribution to the overall budget may be greater than the actual budget, especially if we take into account the total number of the detected active submarine volcanoes (119 seismo-acoustically recorded submarine eruptions since 1939 (Tepp and Dziak, 2021)), and those that have probably not been detected. In fact, it has been estimated that there may be more than a million active volcanoes on the ocean seafloor (Kim and Wessel, 2011).

7.2.5. Towards the storage of liquid CO_2 in the ocean seafloor: what would be the impacts?

In recent years, the storage of anthropogenic carbon dioxide within sub-seafloor reservoir has been identified as an important strategy to mitigate the increase in atmospheric CO_2, and to reduce global warming (Metz et al., 2005; Masson-Delmotte et al., 2021). The CO_2 capture and storage consist on the injection of CO_2 at great depth into the ocean, where most of it would remain isolated from the atmosphere for centuries. CO_2 can be transported via pipeline or ship for release in the ocean, on the seafloor or within sub-seafloor reservoirs. There have been small-scale field experiments, as well as

theoretical, laboratory, and modelling studies of intentional ocean storage of CO_2 (Teng et al., 1996; Teng and Yamasaki, 1998; Tohidi et al., 2010; Li et al., 2020), but ocean storage has not yet been deployed or thoroughly tested (Metz et al., 2005).

Since carbon dioxide in ocean can induce serious consequences such as ocean acidification and decrease of biodiversity, it is necessary to clearly understand the possible impact of a CO_2 leak from its storage. Leakage of CO_2 from the sub-seafloor reservoir to the water column may occur in different conditions, such as (i) the presence of a seepage through a porous sediment, (ii) the initiation of a fault connecting the reservoir to the ocean depths and leading to a leak along a line, or (iii) the presence of a well not properly sealed for which the leak will be located in on point.

The degassing observed at the Horseshoe structure represents a natural lab to study the impact of a potential CO_2 leak on the water column. The impact on the geochemistry are presented in this thesis and mainly consist on the increase of the carbon budget, the acidification and the perturbation of the carbonate system by increasing also the alkalinity budget, which is a consequence of rock alteration (i.e. carbonate dissolution). Complementarily, rock alteration takes part within the various CO_2-trapping and CO_2-consuming mechanisms in which minerals are either dissolved or precipitated to conserve a thermodynamic equilibrium.

Additionally, although the geochemical anomalies appears to be low above 1000 mbsl and the droplets should change to gaseous form above ~500 mbsl, signals associated to droplets or bubbles have been observed with ship echo sounder up to ~200 mbsl. Therefore, with CO_2 discharges at ~1300 mbsl, the impact on the ocean surface, and potentially on the atmosphere, must not be ignored.

Nonetheless, we suggest that the impact of a CO_2 leak would be mainly driven by the seafloor depth that control the behavior and the CO_2 phase, along with local hydrodynamics. As it was observed in the context of the Fani Maoré eruption, liquid CO_2 discharged at ~1300 mbsl at the Horseshoe structure ascent within the water column, while liquid CO_2 discharged at > 2700 mbsl at the volcano likely sink toward the seafloor. Finally, it should also be pointed out that, in the case of a storage within an old gas reservoir, the sequestered CO_2 might mixed with other gases (such as helium, methane, hydrocarbons, etc.), which could be released into the ocean through the leakage, and which might change its behavior in the water column.

Overall, many aspects on the impact of a CO_2 leakage on the water column geochemistry, and more generally on the global ocean, are still to be investigated. One of these aspects is the potential impact on the ocean acidification and further on the coral reef, which are subject to $CaCO_3$ dissolution.

Another aspect is the impact on the diversity of microorganisms and organisms in the ocean, which is mainly controlled by the geochemical composition of the seawater. Those questions could be explored further using the geochemical data from the present study. Moreover, the present degassing system is located close to a coral reef for which the impact has not yet be studied, at our knowledge, and would required more investigations.

7.3. Bibliographical References

Aiuppa, A., Hall-Spencer, J.M., Milazzo, M., Turco, G., Caliro, S., and Di Napoli, R. (2021). Volcanic CO2 seep geochemistry and use in understanding ocean acidification. *Biogeochemistry* 152(1)**,** 93-115. doi: 10.1007/s10533-020-00737-9.

Baker, E.T., Chadwick, W.l.l.i.W.J., Cowen, J.P., Dziak, R.P., Rubin, K.H., and Fornari, D.J. (2012). Hydrothermal Discharge During Submarine Eruptions The Importance of Detection, Response, and New Technology. *Oceanography* 25(1)**,** 128-141. doi: 10.5670/oceanog.2012.11.

Baumberger, T., Lilley, M.D., Lupton, J.E., Baker, E.T., Resing, J.A., Buck, N.J., et al. (2020). Dissolved Gas and Metal Composition of Hydrothermal Plumes From a 2008 Submarine Eruption on the Northeast Lau Spreading Center. *Frontiers in Marine Science* 7. doi: 10.3389/fmars.2020.00171.

Baumberger, T., Lilley, M.D., Resing, J.A., Lupton, J.E., Baker, E.T., Butterfield, D.A., et al. (2014). Understanding a submarine eruption through time series hydrothermal plume sampling of dissolved and particulate constituents: West Mata, 2008-2012. *Geochemistry, Geophysics, Geosystems* 15(12)**,** 4631-4650. doi: 10.1002/2014gc005460.

Berner, R.A., Lasaga, A.C., and Garrels, R.M. (1983). The carbonate-silicate geochemical cycle and its effect on atmospheric carbon dioxide over the past 100 million years. *American Journal of Science* 283(7)**,** 641-683. doi: 10.2475/ajs.283.7.641.

Berthod, C., Komorowski, J.-C., Gurioli, L., Médard, E., Bachèlery, P., Besson, P., et al. (2022). Temporal magmatic evolution of the Fani Maoré submarine eruption 50 km east of Mayotte revealed by in situ sampling and petrological monitoring. *Comptes Rendus. Géoscience* 354(S2)**,** 195-223. doi: 10.5802/crgeos.155.

Burton, M.R., Sawyer, G.M., and Granieri, D. (2013). Deep Carbon Emissions from Volcanoes. *Reviews in Mineralogy and Geochemistry* 75(1)**,** 323-354. doi: 10.2138/rmg.2013.75.11.

Cathalot, C., Rinnert, E., Fandiño, O., Scalabrin, C., Giunta, T., Ondreas, H., et al. (in prep.). Large CO2 hydrates field along the volcanic ridge offshore Mayotte Island.

De Ronde, C.E.J., Hannington, M.D., Stoffers, P., Wright, I.C., Ditchburn, R.G., Reyes, A.G., et al. (2005). Evolution of a Submarine Magmatic-Hydrothermal System: Brothers Volcano, Southern Kermadec Arc, New Zealand. *Economic Geology* 100(6)**,** 1097-1133. doi: 10.2113/gsecongeo.100.6.1097.

Dziak, R.P., Baker, E.T., Shaw, A.M., Bohnenstiehl, D.R., Chadwick, W.W., Haxel, J.H., et al. (2012). Flux measurements of explosive degassing using a yearlong hydroacoustic record at an erupting submarine volcano. *Geochemistry, Geophysics, Geosystems* 13(11). doi: 10.1029/2012gc004211.

Feuillet, N., Jorry, S., Crawford, W.C., Deplus, C., Thinon, I., Jacques, E., et al. (2021). Birth of a large volcanic edifice offshore Mayotte via lithosphere-scale dyke intrusion. *Nature Geoscience* 14**,** 787-795. doi: 10.1038/s41561-021-00809-x.

Gamo, T., Ishibashi, J.-I., Sakai, H., and Tilbrook, B. (1987). Methane anomalies in seawater above the Loihi submarine summit area, Hawaii. *Geochimica et Cosmochimica Acta* 51(10)**,** 2857-2864. doi: 10.1016/0016-7037(87)90163-3.

González-Delgado, S., and Hernández, J.C. (2018). "Chapter Two - The Importance of Natural Acidified Systems in the Study of Ocean Acidification: What Have We Learned?," in *Advances in Marine Biology*, ed. C. Sheppard. Academic Press), 57-99.

Hilton, D.R., McMurtry, G.M., and Goff, F. (1998). Large variations in vent fluid CO2/3He ratios signal rapid changes in magma chemistry at Loihi seamount, Hawaii. *Nature* 396(6709)**,** 359-362. doi: 10.1038/24603.

Huybers, P., and Langmuir, C. (2009). Feedback between deglaciation, volcanism, and atmospheric CO2. *Earth and Planetary Science Letters* 286(3-4)**,** 479-491. doi: 10.1016/j.epsl.2009.07.014.

Kim, S.-S., and Wessel, P. (2011). New global seamount census from altimetry-derived gravity data. *Geophysical Journal International* 186(2)**,** 615-631. doi: 10.1111/j.1365-246X.2011.05076.x.

Konno, U., Tsunogai, U., Nakagawa, F., Nakaseama, M., Ishibashi, J.-I., Nunoura, T., et al. (2006). Liquid CO2 venting on the seafloor: Yonaguni Knoll IV hydrothermal system, Okinawa Trough. *Geophysical Research Letters* 33(16). doi: 10.1029/2006gl026115.

Li, J., Roche, B., Bull, J.M., White, P.R., Davis, J.W., Deponte, M., et al. (2020). Passive acoustic monitoring of a natural CO2 seep site – Implications for carbon capture and storage. *International Journal of Greenhouse Gas Control* 93**,** 102899. doi: 10.1016/j.ijggc.2019.102899.

Liuzzo, M., Di Muro, A., Rizzo, A.L., Caracausi, A., Grassa, F., Fournier, N., et al. (2021). Gas Geochemistry at Grande Comore and Mayotte Volcanic Islands (Comoros Archipelago), Indian Ocean. *Geochemistry, Geophysics, Geosystems* 22(8). doi: 10.1029/2021gc009870.

Lupton, J., Butterfield, D., Lilley, M., Evans, L., Nakamura, K.-I., Chadwick, W., et al. (2006). Submarine venting of liquid carbon dioxide on a Mariana Arc volcano. *Geochemistry, Geophysics, Geosystems* 7(8). doi: 10.1029/2005gc001152.

Marty, B., and Jambon, A. (1987). C/3He in volatile fluxes from the solid Earth: implications for carbon geodynamics. *Earth and Planetary Science Letters* 83(1)**,** 16-26. doi: 10.1016/0012-821X(87)90047-1.

Marty, B., and Tolstikhin, I.N. (1998). CO2 fluxes from mid-ocean ridges, arcs and plumes. *Chemical Geology* 145(3)**,** 233-248. doi: 10.1016/S0009-2541(97)00145-9.

Masson-Delmotte, V.P., Zhai, P., Pirani, S.L., Connors, C., Péan, S., Berger, N., et al. (2021). IPCC, 2021, Climate Change 2021: The Physical Science Basis. Contribution of Working Group I to the Sixth Assessment Report of the Intergovernmental Panel on Climate Change.

Metz, B., Davidson, O., De Coninck, H., Loos, M., and Meyer, L. (2005). *IPCC special report on carbon dioxide capture and storage.* Cambridge: Cambridge University Press.

Price, R.E., and Giovannelli, D. (2017). "A Review of the Geochemistry and Microbiology of Marine Shallow-Water Hydrothermal Vents," in *Reference Module in Earth Systems and Environmental Sciences*. Elsevier).

Resing, J.A., Baker, E.T., Lupton, J.E., Walker, S.L., Butterfield, D.A., Massoth, G.J., et al. (2009). Chemistry of hydrothermal plumes above submarine volcanoes of the Mariana Arc. *Geochemistry, Geophysics, Geosystems* 10(2). doi: 10.1029/2008gc002141.

Resing, J.A., Lupton, J.E., Feely, R.A., and Lilley, M.D. (2004). CO2 and 3He in hydrothermal plumes: implications for mid-ocean ridge CO2 flux. *Earth and Planetary Science Letters* 226(3)**,** 449-464. doi: 10.1016/j.epsl.2004.07.028.

Rubin, K.H., Soule, S.A., Chadwick, W.W., Fornari, D.J., Clague, D.A., Embley, R.W., et al. (2012). Volcanic Eruptions in the Deep Sea. *Oceanography* 25(1)**,** 142-157. doi: 10.5670/oceanog.2012.12.

Sakai, H., Gamo, T., Kim, E.-S., Tsutsumi, M., Tanaka, T., Ishibashi, J., et al. (1990a). Venting of Carbon Dioxide-Rich Fluid and Hydrate Formation in Mid-Okinawa Trough Backarc Basin. *Science* 248(4959)**,** 1093-1096. doi: doi:10.1126/science.248.4959.1093.

Sakai, H., Gamo, T., Kim, E.S., Shitashima, K., Yanagisawa, F., Tsutsumi, M., et al. (1990b). Unique chemistry of the hydrothermal solution in the mid-Okinawa Trough Backarc Basin. *Geophysical Research Letters* 17(12)**,** 2133-2136. doi: 10.1029/gl017i012p02133.

Santana-Casiano, J.M., Fraile-Nuez, E., González-Dávila, M., Baker, E.T., Resing, J.A., and Walker, S.L. (2016). Significant discharge of CO2 from hydrothermalism associated with the submarine volcano of El Hierro Island. *Scientific Reports* 6(1)**,** 25686. doi: 10.1038/srep25686.

Teng, H., Masutani, S.M., Kinoshita, C.M., and Nihous, G.C. (1996). Solubility of CO2 in the ocean and its effect on CO2 dissolution. *Energy Conversion and Management* 37(6)**,** 1029-1038. doi: 10.1016/0196-8904(95)00294-4.

Teng, H., and Yamasaki, A. (1998). Solubility of Liquid CO2 in Synthetic Sea Water at Temperatures from 278 K to 293 K and Pressures from 6.44 MPa to 29.49 MPa, and Densities of the Corresponding Aqueous Solutions. *Journal of Chemical & Engineering Data* 43(1)**,** 2-5. doi: 10.1021/je9700737.

Tepp, G., and Dziak, R.P. (2021). The Seismo-Acoustics of Submarine Volcanic Eruptions. *Journal of Geophysical Research: Solid Earth* 126(4). doi: 10.1029/2020jb020912.

Tohidi, B., Yang, J., Salehabadi, M., Anderson, R., and Chapoy, A. (2010). CO2 Hydrates Could Provide Secondary Safety Factor in Subsurface Sequestration of CO2. *Environmental Science & Technology* 44(4)**,** 1509-1514. doi: 10.1021/es902450j.

Wheat, C.G., Jannasch, H.W., Plant, J.N., Moyer, C.L., Sansone, F.J., and McMurtry, G.M. (2000). Continuous sampling of hydrothermal fluids from Loihi Seamount after the 1996 event. *Journal of Geophysical Research: Solid Earth* 105(B8)**,** 19353-19367. doi: 10.1029/2000jb900088.

White, J.D.L., Schipper, C.I., and Kano, K. (2015). "Chapter 31 - Submarine Explosive Eruptions," in *The Encyclopedia of Volcanoes (Second Edition)*, ed. H. Sigurdsson. (Amsterdam: Academic Press), 553-569.

Appendices | Annexes

Scientific Publications | Publications Scientifiques

Mastin, M., Cathalot, C., Fandino, O., Giunta, T., Donval, J.-P., Guyader, V., Germain, Y., Scalabrin, C., Dehez, S., Jouenne, S., Gaucher, E., Rouxel, O., & Rinnert, E. (2023). Strong geochemical anomalies following active submarine eruption offshore Mayotte. *Chemical Geology*, 640, 121739. https://doi.org/10.1016/j.chemgeo.2023.121739

Mastin, M., Donval, J.-P., Guyader, V., Germain, Y., Giunta, T., Scalabrin, C., Gaucher, E., Dehez, S., Jouenne, S., Rouxel, O., Rinnert, E. & Cathalot, C., (in prep.). Strong geochemical anomalies following active submarine eruption offshore Mayotte. *Chemical Geology*.

Oral Presentations | Présentations Orales

Ocean Sciences Meeting 2022

Mastin, M., Cathalot, C., Rouxel, O., Gaucher, E., Donval, J., Guyader, V., Germain, Y., Scalabrin, C., Jouenne, S., Dehez, S. & Rinnert, E (2022). Strong geochemical anomalies following active submarine eruption offshore Mayotte. Ocean Sciences Meeting 2022, DS08 The Impact of Submarine Hydrothermal and Volcanic Activity on Ocean Chemistry and Biology 03. 24 February–4 March 2022.

Abstract

Submarine volcanic activity releases large amounts of gas and metals in the water column, affecting biogeochemical cycles and ecosystems at a regional and local scale. In 2018, a submarine volcano erupted ~50 km offshore Mayotte Island and an active eruptive plume was observed in May 2019 at the summit with acoustic plumes rising 2 km into the water column coupled to strong geochemical anomalies. Between May 2019 and October 2020, 3 cruises monitored the eruptive activity above the volcano, focusing on water column geochemistry using noble gas, volatile species and dissolved metals concentrations. Beginning of the eruption, concentrations of > 800 nM in CH_4 and H_2 were

coupled with TdMn and TdFe concentrations above 500 nM, and CO_2 values of 35 µM. In addition, strong water column acidification was measured (1 upH) compared to the regional background. From May 2019 to October 2020, we observed a general decrease in gas and metals concentrations, and an evolution of the TdMn:TdFe ratios consistent with a decrease in the eruptive activity at the volcano, similar to literature values observed in other volcanic contexts. In October 2020, a rebound of high H_2 concentrations was consistent with ship-echo sounder surveys showing new lava flow installations and pictures of active lava flows at the seafloor. Correlation between He, CO_2 and CH_4 concentrations demonstrates magmatic degassing origin, but a $\delta^{13}C$-CH_4 value of -34‰ suggests a biogenic contribution likely due to magma/sediments interaction during its ascent. Weak correlations between H_2 and He suggest complex processes of H_2 from magmatic degassing, lava/seawater interaction, and oxidation processes in water column. Water column acidification linked to the eruption seems to be associated with a release of silicates in the water column suggesting rock water interaction. After a year, the carbonate system seems to be back to steady-state highlighting the buffer capacity and resilience of the seawater column environment.

AGU Fall Meeting 2022

Mastin, M., Cathalot, C., Fandino, O., Gaucher, E., Donval, J.-P., Guyader, V., Germain, Y., Giunta, T., Scalabrin, C., Jouenne, S., Dehez, D., Rouxel, O. & Rinnert, E. (2022). Behavior of volatiles (H2, CO2, CH4) during the 2018-2019 Eruption of the Submarine Volcano Offshore Mayotte and response of the Carbonate System of the water column. AGU Fall Meeting 2022.

Abstract

Submarine volcanic activity releases large amounts of gases and metals through the water column, affecting biogeochemical cycles and ecosystems at local and regional scales. Here we study the Fani Maore volcano, a newly erupted submarine volcano located 50 km offshore Mayotte at 3500 m deep, 820 m high for a total volume of 6.55 km^3. The 2018-2019 eruption produced massive fluid emissions generated from the summit and deeper, associated with an acoustic plume rising 2 km into the water column. The MAYOBS1 cruise in May 2019 monitored the eruptive activity above the summit and northern flank of the edifice. The study focused on water column geochemistry using volatile species, total dissolvable metal concentrations, and physicochemical parameters. The deep location of the edifice is responsible for a dichotomy in gases' behavior near 2700 m deep, with one part rising while the other sinks. As a result of lava-seawater interactions, exceptionally high concentrations of H_2 (up

to 6 000 nmol/L) were measured in the upper part of the water column. High CO_2 and CH_4 concentrations, up to 35 µmol/L and 830 nmol/L, respectively, were found below 2500 m. Likely, these large amounts of CO_2 were in liquid form, driven by density differences with seawater, they rose or sank in water column depending on the depth of emission. Liquid CO_2 emitted below 2700 m may have flown downward, carrying along an important fraction of CH_4 due to its high solubility in liquid CO_2. H_2 is less likely to have been associated with liquid CO_2 and rose solely in the water column. Further, strong water column acidification (up to 0.6 upH) were attributed to CO_2 addition, whereas rock-water interactions may have contributed to increase the pH toward an equilibrium through carbonate alkalinity addition. These interactions are likely to be responsible for the high TDFe:TDMn ratios (27:1 to 11:1) observed from the base of the edifice to the surface. Silicate anomalies (up to 20 µmol/L) were found only at the volcano summit suggesting high temperature rock-water interaction. Numerical modelling with PHREEQC software gives us the water column chemical state during the eruption, and minerals that are likely to precipitate or dissolve. We thus calculate the water column chemistry in its state disturbed by volcanic gas emissions and evaluate the importance of these perturbations.

Poster Presentations | Présentation de Posters

Goldschmidt Conference 2023

Mastin, M., Donval, J.-P., Guyader, V., Germain, Y., Giunta, T., Scalabrin, C., Gaucher, E., Dehez, S., Jouenne, S., Rouxel, O., Rinnert, E. & Cathalot, C., (2023). Submarine Venting of Liquid Carbon Dioxide in a Volcanic Context. Goldschmidt Conference 2023.

Submarine Venting of Liquid Carbon Dioxide in a Volcanic Context

Manon Mastin[1], Jean-Pierre Donval[1], Vivien Guyader[1], Yoan Germain[1], Thomas Giunta[1], Carla Scalabrin[1], Eric C. Gaucher[2], Stéphane Jouenne[3], Sébastien Dehez[3], Olivier Rouxel[1], Emmanuel Rinnert[1], Cécile Cathalot[1]

[1] CYcles Biogéochimiques Et Ressources (CYBER), Geo-Ocean UMR 6538 CNRS - Ifremer - UBO - UBS, F-29280 Plouzané, France
[2] Lavoisier H_2 Geoconsult, FR-74400 Chamonix, France
[3] TotalEnergies, Centre Scientifique et Technique Jean Féger, EB 437, FR-64018 Pau Cedex, France

How do liquid CO_2 droplets behave in the ocean water column & what is their impact on the surrounding seawater geochemistry?

Context

New submarine volcano and 2018-2019 ongoing eruption associated with gas emissions (liquid CO_2) ~10 km offshore Mayotte.

Mayotte Island, Comoros Archipelago

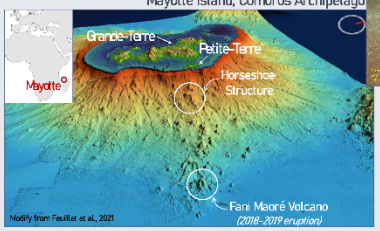

Emissions of liquid CO_2 droplets at the Horseshoe area

Droplet composition
CO_2 (99.0 ± 0.3 $\%_{vol}$)
CH_4 (0.8 ± 0.2 $\%_{vol}$)
H_2 (10 to 1000 ppm_{vol})
Magmatic origin (R/Ra = 6.39 ± 0.50)

Evolution of liquid CO_2 venting sites

May 2019	August 2019	May 2020	October 2020	January and May 2021	July 2022
2 sites	3 sites	5 sites	10 sites	15 sites	22 sites

Methodology

GeoFLAMME cruise (April-May 2021)
Ocean water column sampling

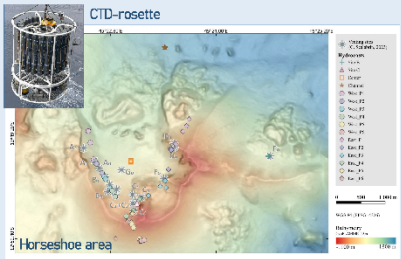

- Seafloor depths in the area from 1100 m to 1700 m bsl
- Crest of the Horseshoe structure from 1100 m to 1300 m bsl

4 vertical hydrocasts
2 Tow-yos
1 vertical hydrocast for background

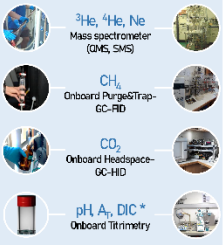

*A_T: Total Alkalinity ; DIC: Dissolved Inorganic Carbon

1 Nature of the emissions

- Homogeneous magmatic signature observed within the water column (R/Ra = 6.75, Fig. 1)
- No evidence of hydrothermal fluid circulation in the venting area of the Horseshoe
- Hypothesis : presence of a sub-seafloor reservoir of liquid CO_2

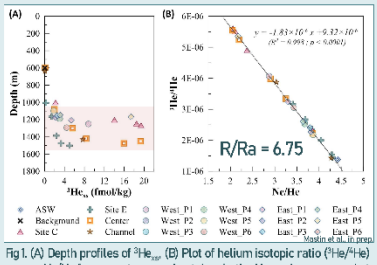

Fig 1. (A) Depth profiles of $^3He_{xs}$, (B) Plot of helium isotopic ratio ($^3He/^4He$) versus Ne/He for seawater samples taken in the Horseshoe area and at the background hydrocast.

✓ Horseshoe droplets
R/Ra = 6.39 ± 0.50

✓ Shallow plumbing system of Petite-Terre gas emissions
R/Ra ~6.6 *(Liuzzo et al., 2022)*

✓ Fani Maore fluid emissions
R/Ra ~8.52 (temporary shift to ~6.5 due to a change of magma path through a secondary reservoir) *(Mastin et al., 2022)*

➢ Horseshoe emissions could be associated with the plumbing system feeding the gas emissions at Petite Terre

Magmatic-derived gas emissions in the form of liquid CO_2

2 Droplet dissolution processes

- Elevated $CO_{2(aq)}$ and CH_4 dissolved concentrations in the water column between 1100 m bsl and the seafloor
- Profile dichotomy:

Sites inside Horseshoe (strong anomalies) ≠ Site outside Horseshoe (less affected) ≠ Channel (plume shape)

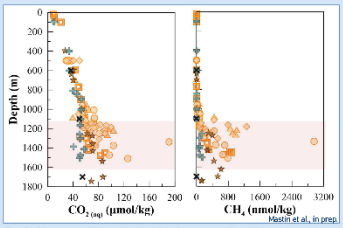

Fig 2. Depth profiles of dissolved carbon dioxide and methane concentrations within the water column.

- Preferential dissolution of CO_2 over CH_4

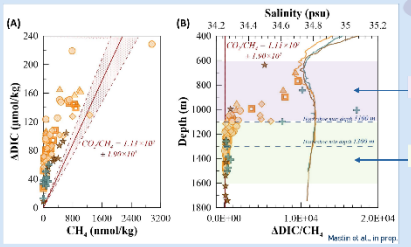

Fig 3. (A) ΔDIC versus CH_4, (B) Salinity profiles of the area and depth profiles of ΔDIC/CH_4 for seawater samples taken in the Horseshoe area at depths >600m. The red line corresponds to the average gas ratio of the droplets with the standard deviation represented by the red area between the dot lines.
Δ: delta is the difference from the background

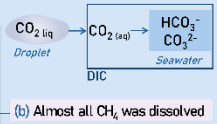

(b) Almost all CH_4 was dissolved

(a) CO_2 and CH_4 dissolved

- At a similar depth: more advance state of CO_2 dissolution in the absence of bathymetric barrier and presence of currents (Site E, outside Horseshoe)

Seafloor morphology and local hydrodynamics (e.g. tides, main currents) control the depth of the CO_2 droplet dissolution

3 Impact on the carbonate system

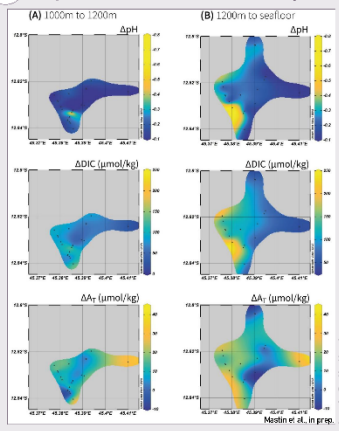

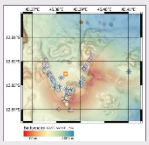

(A) Mainly above the Horseshoe rim
- Localized pH anomaly
- Moderate DIC and A_T anomalies

(B) Constrained/trapped by the structure
- Strong and large pH anomalies
- Strong DIC and A_T anomalies within the structure

➢ Accumulation of the emissions, stagnation of the modified seawater, leaching (interactions CO_2 liq/seawater/rocks)

Fig 4. Spatial distribution of ΔpH, ΔDIC, $ΔA_T$ integrated from (A) 1000 m to 1200 m, and (B) 1200 m to the seafloor depth using Ocean Data View©. Black dots on surface maps represent the sampling points. The map on the right shows the bathymetry of the study area, the venting sites and the water column samples.
Δ: delta is the difference from the background.

Stagnation and/or leaching within morpho-bathymetric structures

Conclusion

➢ Seafloor emissions from direct degassing of liquid CO_2, of magmatic origin
➢ Seafloor morphology and local hydrodynamics play an important role
- Currents: favor dissolution, export and dilution processes
- Bathymetry: confines the emissions and favors accumulation, stagnation, leaching processes

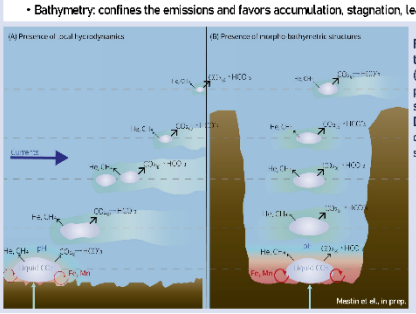

Fig 5. Conceptual scheme representing the emission of a liquid CO_2 droplet in (A) presence of currents, and (B) presence of a morpho-bathymetric structures (protection from currents). Droplet goes up within the water column, whereas the dissolved part spreads horizontally and gets diluted.

Acknowledgements & References

We thank the captain, crew members and all the scientists on the *RV Pourquoi Pas ? during* the GeoFlamme cruise (April-May 2021, doi: 10.17600/18001297). We thank the French Oceanographic Fleet. We thank Jürgen Süttenfuß from Helis Laboratory, at the Institute of Environmental Physics/Section of Oceanography, University of Bremen (Germany) who performed all helium and neon isotopic analyses.

Feuillet, N., Jorry, S., Crawford, W.C., Deplus, C., Thinon, I., Jacques, E., et al. (2021). Birth of a large volcanic edifice offshore Mayotte via lithosphere-scale dyke intrusion. Nature Geoscience 14, 787–795. doi: 10.1038/s41561-021-00809-x.
Liuzzo, M., Muro, A.D., Rizzo, A.L., Grassa, F., Coltorti, M., and Ader, M. (2022). The composition of gas emissions at Petite Terre (Mayotte, Comoros): inference on magmatic fingerprints. Comptes Rendus. Géoscience 354(S2). doi: 10.5802/crgeos.148.
Mastin, M., Cathalot, C., Rouxel, O., Gaucher, E., Donval, J., Guyader, V., et al. (2022). "Strong geochemical anomalies following active submarine eruption offshore Mayotte", in: Ocean Sciences Meeting 2022. OS08 The Impact of Submarine Hydrothermal and Volcanic Activity on Ocean Chemistry and Biology 03. 24 February–4 March 2022).
Rinnert, E., Cathalot, C., and Feuillet, N. (2021). GEOFLAMME cruise, RV Pourquoi pas ? doi: 10.17600/18001297.
Scalabrin, C. (2023). Site d'émissions de fluides, Mayotte, zone Fer à Cheval (C. Scalabrin, 2022). doi: 10.12770/070818f6-6520-49e4-befd-9d4d0609bf7d.

Goldschmidt Conference
9-14 July 2023, Lyon

COLLEGE SCIENCES DOCTORAL DE LA MER BRETAGNE ET DU LITTORAL

Université de Bretagne Occidentale

Titre : Etude des émissions de fluide et de gaz dans un contexte d'éruption sous-marine au large de l'Ile de Mayotte : impact géochimique sur la colonne d'eau

Mots clés :
Géochimie, Volcanisme sous-marin, Fani Maoré, Gaz dissous, CO_2 liquide, Colonne d'eau

Résumé : Le volcanisme sous-marin émet des flux significatifs d'éléments chimiques (ex. He, CO_2, CH_4, H_2, Fe^{2+}, Mn^{2+}) dans l'océan. Cependant, les processus géochimiques à l'origine de ces émissions et l'impact de ces rejets sur la géochimie de la colonne d'eau sont peu connus. Dans cette thèse, nous avons étudié le nouveau volcan sous-marin Fani Maoré, dont l'activité a débuté en 2018-2019 (île de Mayotte, Archipel des Comores, Océan Indien). Ce système est exceptionnel et unique car il permet d'étudier la géochimie de la colonne d'eau pendant l'éruption et la formation de l'édifice volcanique, ainsi qu'après l'événement éruptif (c.-à-d. pendant la mise en place des coulées de lave et l'initiation de la circulation hydrothermale). Nous avons étudié l'impact des émissions de CO_2 sur la géochimie de la colonne d'eau. Nous avons montré un lien entre le niveau d'activité éruptive (c.-à-d. éruption en cours, installation des coulées de lave) et l'impact des émissions de fluides et de gaz dans la colonne d'eau. L'activité volcanique influence également le système carbonaté, bien qu'un retour vers l'état de référence ait été observé un an après l'événement éruptif principal. Les dégazages de CO_2 liquide induisent une acidification significative, une augmentation de l'alcalinité et du carbone inorganique dissous. Cet impact sur la colonne d'eau dépend de la morphologie du fond marin et de l'hydrodynamique locale. Globalement, ce travail constitue une avancée vers une meilleure compréhension de l'impact du volcanisme sous-marin sur les processus géochimiques se déroulant dans la colonne d'eau et plus généralement sur la chimie des océans.

Title: Fluid and gas emissions in a submarine eruption context offshore Mayotte Island: Geochemical impact on the water column

Keywords :
Geochemistry, Submarine volcanism, Fani Maoré, Dissolved gases, Liquid CO_2, Water Column

Abstract: Submarine volcanism contributes significant fluxes of chemicals (e.g. He, CO_2, CH_4, H_2, Fe^{2+}, Mn^{2+}) in the ocean. However, the geochemical processes behind these emissions and the impact of these discharges on the water column geochemistry are poorly documented. In this PhD thesis, we took advantage of the Fani Maoré newly born submarine volcano whose activity started in 2018-2019 (Mayotte Island, Comoros Archipelago, Indian Ocean). This exceptional and unique setting offers the opportunity to study the water column geochemistry during the eruption and formation of a new volcanic edifice, and after the eruptive event (i.e. during lava flows installation and hydrothermal circulation initiation). In particular, we investigate the impact of elevated levels of CO_2 – major greenhouse gas involved in climate change and associated ocean acidification – on the water column geochemistry. We find evidence of the relationship between the degree of eruptive activity (i.e. ongoing eruption, lava flow installation) and the footprint of fluid and gas emissions within the water column. The volcanic activity also influences the carbonate system although a return toward local background levels was observed a year after the main eruptive event. Continuous discharge of liquid CO_2 at venting sites are responsible of significant acidification, increase in alkalinity and in dissolved inorganic carbon. This impact on the water column depends on seafloor morphology and local hydrodynamics. Overall, this work is a step toward a better understanding of the impact of submarine volcanism on geochemical processes taking place within the water column and more generally on the ocean chemistry.